A MODIFIED STIC MODEL FOR ESTIMATING CROP EVAPOTRANSPIRATION

A THESIS SUBMITTED BY

Simon Kelderman ***BEng(Ag), BBus***

FOR THE AWARD OF

Doctor of Philosophy

2021

ABSTRACT

A novel application of the STIC model (Mallick et al. 2014, 2015a) was developed by the author to estimate crop evapotranspiration, E, at a field or sub-field scale without recourse to any remote sensing (RS), i.e. all sensors were mounted near to the ground. This new 'Ground-Proximal STIC' (GPSTIC) system was evaluated against a Bowen Ratio Energy Balance (BREB) micro-meteorological system.

GPSTIC could make continuous estimates of E, day and night, and avoided problems associated with RS, such as limited spatiotemporal resolution, impacts of cloud cover, and intermittency of satellite overpasses.

The GPSTIC system was deployed into Australian irrigated cotton fields (118 - 185 ha) on three occasions (featuring partial canopy, bare soil, and full canopy conditions) for a total of 592 hours over the 2018/19 and 2019/20 summer seasons.

A five-height Profile BREB system, also developed by the author specifically for this research, was co-located with GPSTIC in the field. The Bowen ratio was determined from the slope of the linear regression

of the T vs. e plot. The Profile BREB system included a novel algorithm that accounted for the measurement uncertainties of T and e when assessing whether to include each (e, T) point in the linear regression.

Simultaneous 60 s measurements of environmental variables were made by the independent GPSTIC and Profile BREB systems, and 4 min averages were recorded. Thus 8880 modelled values of E were made by each of the GPSTIC and Profile BREB systems.

The results showed very good alignment between GPSTIC and Profile BREB. For the three field deployments the total accumulated values (daytime *and* nightime data) of E_{GPSTIC} and E_{BREB} were, respectively, 31.2 mm and 31.1 mm, 37.6 mm and 37.6 mm, and 51.2 mm and 50.6 mm. The accumulated discrepancy between GPSTIC and Profile BREB was never larger than 2 mm.

Advantages of this new GPSTIC system over existing technologies include its ease of use and deployment; a small number of simple and inexpensive sensors (relative to other systems such as eddy covariance); low power requirements; no need for a reference crop; and no need for complex post-processing of data. GPSTIC has potential to provide good quality, continuous, real-time, low-cost E data to irrigators and researchers.

CERTIFICATION OF THESIS

This thesis is entirely the work of Simon Kelderman except where otherwise acknowledged. The work is original and has not previously been submitted for any other award, except where acknowledged.

Principal Supervisor:
Assoc. Prof. Joseph Foley BEng *USQ*, MEng *UniSA*, PhD *USQ*

Associate Supervisor:
Assoc. Prof. Nigel Hancock BSc *VicUni Manchester*, PhD *Strathclyde*

Student's and supervisors' signatures of endorsement are held at the University.

This page intentionally left blank.

ACKNOWLEDGEMENTS

I wish to acknowledge the advice, insights and time given by Assoc. Prof. Joseph Foley and Assoc. Prof. Nigel Hancock during the course of this PhD program. I am grateful for your involvement and thank you.

The willingness of the farm managers and staff at 'Waverley' to have equipment for this research placed in their fields is gratefully acknowledged.

Also gratefully acknowledged is the financial support for this PhD research program that was received from the Commonwealth Government of Australia through the Researcher Training Program. This made it possible to undertake the PhD while having a young family at home.

This page intentionally left blank.

TABLE OF CONTENTS

LIST OF FIGURES

LIST OF TABLES

This page intentionally left blank.

ACRONYMS AND ABBREVIATIONS

Acronym	Meaning
ASTM	American Society for Testing and Materials
BREB	Bowen Ratio Energy Balance
BR-DTS	Bowen Ratio - Distributed Temperature Sensing
CI	Confidence Interval
CS	Campbell Scientific
CSV	Comma Separated Variable
DCHT	Double Concentric Horizontal-Tube
DIN EN	Deutsches Institut für Normung (English) standards
DS1	Data Set One
DS2	Data Set Two
DS3	Data Set Three
DS2	Model of Decagon (Meter) sonic anemometer
DTS	Distributed Temperature Sensing
EC	Eddy Covariance
EnSEB	Ensemble SEB
FAO	Food and Agriculture Organisation, United Nations
FAO-56	UN FAO Irrigation and Drainage Paper No. 56
FC	Field capacity
FoV	Field of View
FluxNet	A global network of EC stations

Acronym	Meaning
GPSTIC	Ground-Proximal STIC
HFP01SC	Self-calibrating heat flux plate by Hukseflux
HS3	Model of Michell capacitive hygrometer
IBL	Internal Boundary Layer.
IC	Integrated Circuit
IEC	International Electrotechnical Commission
IR01	The pyrgeometer model in the NR01
IRR	Infrared radiometer, also called an infrared thermometer (IRT).
ISO	International Organisation for Standardisation
LAI	Leaf Area Index
LoBF	Line of Best Fit
METRIC	Mapping EvapoTranspiration at high Resolution with Internalised Calibration
MOD16	MODIS evapotranspiration data set
MODIS	Moderate resolution Imaging Spectroradiometer
MPPT	Maximum Power Point Tracking
NE	North-East direction
NLDAS-2	North American Land Data Assimilation System, v2
NR01	Model of net radiometer by Hukseflux
NSW	New South Wales
NW	North-West direction
OzFlux	Australian EC flux tower network
PM	Penman-Monteith
PMBL	Penman-Monteith Bouchet Lhomme
PRT	Platinum Resistance Thermometer
PT	Priestley-Taylor
Pt100	Temperature sensing device with platinum sensing element and 100 Ω resistance at 0 °C
PVC	Polyvinyl chloride
RMSD	Root Mean Square Deviation

Acronym	Meaning
RS	Remote Sensing
RS-E	Remote Sensing for Evapotranspiration
RS485	Electrical standard in serial communications
RTD	Resistance Temperature Detector
SDI-12	Serial Digital Interface at 1200 baud,
SEBAL	Surface Energy Balance Algorithm for Land
SEB	Surface Energy Balance
SHF	Soil Heat Flux
S-SEBI	Simplified Surface Energy Balance Index
SEBS	Surface Energy Balance System
SI-411	Model of IRR with digital output by Apogee
SR01	The pyranometer model in the NR01
STIC	Surface Temperature Initiated Closure
SVP	Saturated Vapour Pressure curve
TBSHTPO4	Model of Tekbox barometer
TDR	Time Domain Reflectometry
TSEB	Two-Source Energy Balance
$\mathrm{T_S}$-VI	Surface Temperature - Vegetation Index
UKAS	United Kingdom Accreditation Service
UN	United Nations
VWC	Volumetric Water Content of soil [$\mathrm{m^3\,m^{-3}}$]
WMO	World Meteorological Organisation

This page intentionally left blank.

NOTATION AND CONVENTIONS

0.1 Notation (Roman Alphabet)

Notation	Meaning and Units
a_0	y-intercept of T vs. e plot [°C]
a_1	Slope of T vs. e plot [$°\mathrm{C\,hPa^{-1}}$]
c_{ds}	Volumetric specific heat capacity of dry soil [$\mathrm{J\,m^{-3}\,K^{-1}}$]
c_{in}	Concentration of incoming air [$\mathrm{qty\,vol^{-1}}$]
c_{out}	Concentration of outgoing air [$\mathrm{qty\,vol^{-1}}$]
c_0	Initial concentration of air inside chamber [$\mathrm{qty\,vol^{-1}}$]
c_P	Specific heat capacity of air [$\mathrm{J\,kg^{-1}\,K^{-1}}$]
c_v	Volumetric soil heat capacity [$\mathrm{J\,m^{-3}\,K^{-1}}$]

Notation	Meaning and Units
c_{water}	Volumetric specific heat capacity of water [$\mathrm{J\,m^{-3}\,K^{-1}}$]
d	Zero plane displacement [m]
d_{shf}	Depth of installation of soil heat flux sensors [m]
D	Discrepancy
$\overline{D}_{inst}$	Mean 'instantaneous' discrepancy (i.e. mean for a 4 min interval) [mm/4 min]
$\overline{D}_{daily}$	Mean daily discrepancy [$\mathrm{mm\,day^{-1}}$]
D_A	Water vapour pressure deficit [hPa]
D_x	Discriminant of quadratic function
e	Actual vapour pressure [hPa]
e_1	Actual vapour pressure at time t_1 [hPa]
$\bar{e}$	Mean vapour pressure [hPa]
e^*	Saturation vapour pressure [hPa]
e_S	Vapour pressure at surface [hPa]
e_S^*	Saturation vapour pressure at surface [hPa]
E	Evapotranspiration [$\mathrm{mm\,s^{-1}}$] This is the actual evapotranspiration, equivalent to ET_C in FAO-56 parlance.
ET_0	Reference evapotranspiration [$\mathrm{mm\,s^{-1}}$]
E_{BREB}	Evapotranspiration per the BREB method, usually [mm/4 min], sometimes [$\mathrm{mm\,s^{-1}}$]
E_{GPSTIC}	Evapotranspiration per the GPSTIC method usually [mm/4 min], sometimes [$\mathrm{mm\,s^{-1}}$]
E_{wbal}	Evaporation per water balance methods [mm]
f	Fetch distance [m]
fb	Grid bearing of long edge of field, measured clockwise from grid North [degrees]
g	Acceleration due to gravity [$\mathrm{m\,s^{-2}}$]
g_{av}	Aerodynamic conductance of water vapour [$\mathrm{m\,s^{-1}}$]
g_B	Bulk aerodynamic conductance [$\mathrm{m\,s^{-1}}$]
g_S	Bulk stomatal conductance [$\mathrm{m\,s^{-1}}$]

Notation	Meaning and Units
G	Soil heat flux [Wm^{-2}]
$G_{0.16\,\mathrm{m}}$	Soil heat flux at depth 0.16 m [Wm^{-2}]
H	Sensible heat flux [Wm^{-2}]
h	Height above the ground [m]
K_B	Clearness index for direct beam radiation
K_D	Transmissivity index for diffuse radiation
K_t	Turbidity coefficient
$LW_{downwelling}$	Downwelling (i.e. from sky) flux of longwave radiation [Wm^{-2}]
$LW_{upwelling}$	Upwelling (i.e. from ground) flux of longwave radiation [Wm^{-2}]
m	Optical path length [unitless ratio]
M	Moisture availability [unitless ratio]
M_{ratio}	Ratio of molecular mass of water vapour to that of dry air (0.622)
n	Number of samples
N	Julian date
P	Barometric pressure [hPa]
P_0	Barometric pressure at sea level [hPa]
q	Specific humidity [$\mathrm{kg\,kg}^{-1}$]
Q	Soil heat flux variable [Wm^{-2}]
R	Statistical correlation coefficient
R^2	Statistical coefficient of determination
RH	Relative humidity [%]
Ri	Richardson number
R_N	Net radiation flux [Wm^{-2}]
r_B	Bulk aerodynamic resistance [$\mathrm{s\,m}^{-1}$]
r_S	Bulk stomatal resistance [$\mathrm{s\,m}^{-1}$]
rw	Grid bearing of wind direction relative to field, clockwise from grid North [degrees]
s	Slope of saturation vapour pressure vs.

Notation	Meaning and Units
	temperature curve [hPa °C^{-1}]
s_1	Slope of line between points (T_D, e) and (T_{SD}, e_S) on saturation vapour pressure curve [hPa °C^{-1}]
s_2	Slope of line between points (T_D, e) and (T_S, e_S^*) on saturation vapour pressure curve [hPa °C^{-1}]
s_3	Slope of line between points (T_{SD}, e_S) and (T_S, e_S^*) on saturation vapour pressure curve [hPa °C^{-1}]
S_0	Solar constant (assumed 1367 Wm^{-2})
S_d	Diffuse shortwave radiation [Wm^{-2}]
S_p	Solar radiation perpendicular to horizontal plane at Earth's surface [Wm^{-2}]
S_p^*	Extra-terrestrial radiation perpendicular to a horizontal plane on Earth's surface [Wm^{-2}]
S_t	Total shortwave irradiance [Wm^{-2}]
$SW_{downwelling}$	Downwelling (i.e. from sky) flux of shortwave radiation [Wm^{-2}]
$SW_{upwelling}$	Upwelling (i.e. from ground) flux of shortwave radiation [Wm^{-2}]
t	Time [s]
t_1, t_2	Time 1, time 2 [s]
T	Ambient air temperature [°C]
T_0	Aerodynamic temperature [°C]
T_1	Ambient air temperature at time t_1 [°C]
$(T_{soil})_{t_1}$	Soil temperature at time t_1 [°C]
$\overline{T}$	Mean ambient air temperature [°C]
T_D	Dewpoint temperature of air [°C]
$T_{background}$	Background radiometric temperature, usually of the sky if outdoors [°C]
$T_{internal}$	Internal temperature of NR01 [°C]
T_{sky}	Radiometric temperature of the sky [°C]
T_S	Surface temperature of crop and/or soil [°C]

Notation	Meaning and Units
T_{SD}	Dewpoint temperature at the surface of crop and/or soil [°C]
$\partial T/\partial z$	Temperature gradient with respect to height [$\mathrm{K\,m^{-1}}$]
$\partial u/\partial z$	Wind speed gradient with respect to height [$\mathrm{s^{-1}}$]
W	Precipitable water in the atmosphere [mm]
wb	Grid bearing of wind direction, measured clockwise from grid North [degrees]
W_{dir}	Wind direction [degrees]
W_{speed}	Wind speed [$\mathrm{m\,s^{-1}}$]
x	X–ordinate of known point on ellipse [m]
X_f	Minimum fetch distance [m]
y	Y–ordinate of known point on ellipse [m]
z	Height [m]
z_{om}	Momentum roughness height [m]
Z	Maximum sensor height above ground [m]

0.2 Notation (Greek Alphabet)

Notation	Meaning and Units
α	Temperature coefficient of resistance [$\mathrm{°C^{-1}}$]
α	Half-angle of radiometer's field-of-view [°]
α_{PT}	Priestley-Taylor advection parameter
α_{*PT*}	Iteratively-solved Priestley-Taylor advection parameter
β	Bowen Ratio
γ	Psychrometric constant [$\mathrm{kPa\,°C^{-1}}$]

Notation	Meaning and Units
δ	Height of IBL [m]
δ_s	Solar declination angle [radians]
$\delta\{\cdot\}$	Absolute uncertainty in $\{\cdot\}$
$\Delta\{\cdot\}$	Change in $\{\cdot\}$
Δ_{PT}	A term in the PT equation
ϵ	Emissivity
θ	Volumetric water content of soil [$\mathrm{m^3\,m^{-3}}$]
θ	Angle of elevation [degree]
θ_s	Solar zenith angle [radians]
κ_H	Diffusivity of heat [$\mathrm{m^2\,s^{-1}}$]
κ_W	Diffusivity of water vapour [$\mathrm{m^2\,s^{-1}}$]
λ	Latent heat of vapourisation of water [$\mathrm{J\,kg^{-1}}$]
λE	Latent heat flux [$\mathrm{Wm^{-2}}$]
Λ	Evaporative fraction
μ	Statistical mean
ρ	Density [$\mathrm{kg\,m^{-3}}$]
ρ_{ds}	Density of dry soil [$\mathrm{kg\,m^{-3}}$]
ρ_{water}	Density of water [$\mathrm{kg\,m^{-3}}$]
σ	Stefan-Boltzmann constant [$\mathrm{Wm^{-2}\,K^{-4}}$]
σ	Statistical standard deviation
τ	System time constant [s]
τ_a	Aerosol extinction coefficient
τ_m	Molecular extinction coefficient
τ_r	Atmospheric transmissivity
ϕ	Available energy flux [$\mathrm{Wm^{-2}}$]
ψ	Soil water tension [kPa]
ψ	Angle to the normal of a surface [°]
ω	Solar time angle [radians]

0.3 Sign Convention

The convention for determining the sign of any flux is based upon Fig. 0.1. The control volume is a conceptual volume that encompasses the air above the soil (to a height that includes all of the crop), the crop, the soil surface, and the soil to a depth of several centimeters. Any flux that is entering the control volume is regarded as positive, and any leaving the control volume is regarded as negative.

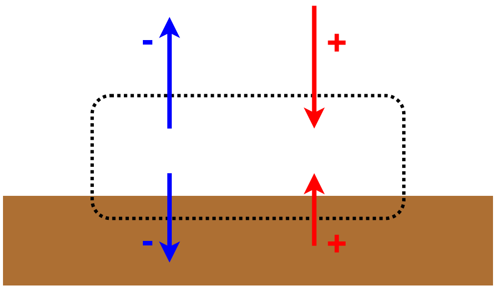

Figure 0.1: Control volume basis for sign convention. All fluxes entering the control volume have a positive sign; all fluxes leaving have a negative sign.

While some fluxes will always have the same sign (e.g. $SW_{downwelling}$ will always be positive) most fluxes will have a variable sign that depends on the direction of the net flow. For example, R_N will likely be positive during the day and negative at night, and G will likely be negative during the day (as heat moves out of the control volume down into the soil) and positive at night.

Storage quantities (e.g. Q) are always positive as negative storage is nonsensical. However, change in storage quantities (e.g. ΔQ) may be positively or negatively signed depending on whether the storage quantity is increasing or decreasing in magnitude.

0.4 Temperature and Vapour Pressure

In the interest of brevity, throughout this thesis the terms *temperature* and *vapour pressure* should be understood to mean *air temperature* and *water vapour pressure*, respectively, unless explicitly stated otherwise.

0.5 Third Person Convention

This thesis reports *my* experimental fieldwork, modelling, analyses and conclusions (except where otherwise acknowledged). In keeping with the common practice within scientific and academic literature to write in the passive and third-person grammatical forms, the use of the first person has been avoided in this thesis.

Accordingly, throughout this thesis 'the author' should be understood as referring to myself.

0.6 Guidelines to Interpreting the Plots

This thesis includes a large number of plots. Fig. 0.2 (p. xxxv) is provided to help explain the meaning of some features common to many of the plots, particularly those that have *time* on the horizontal axis.

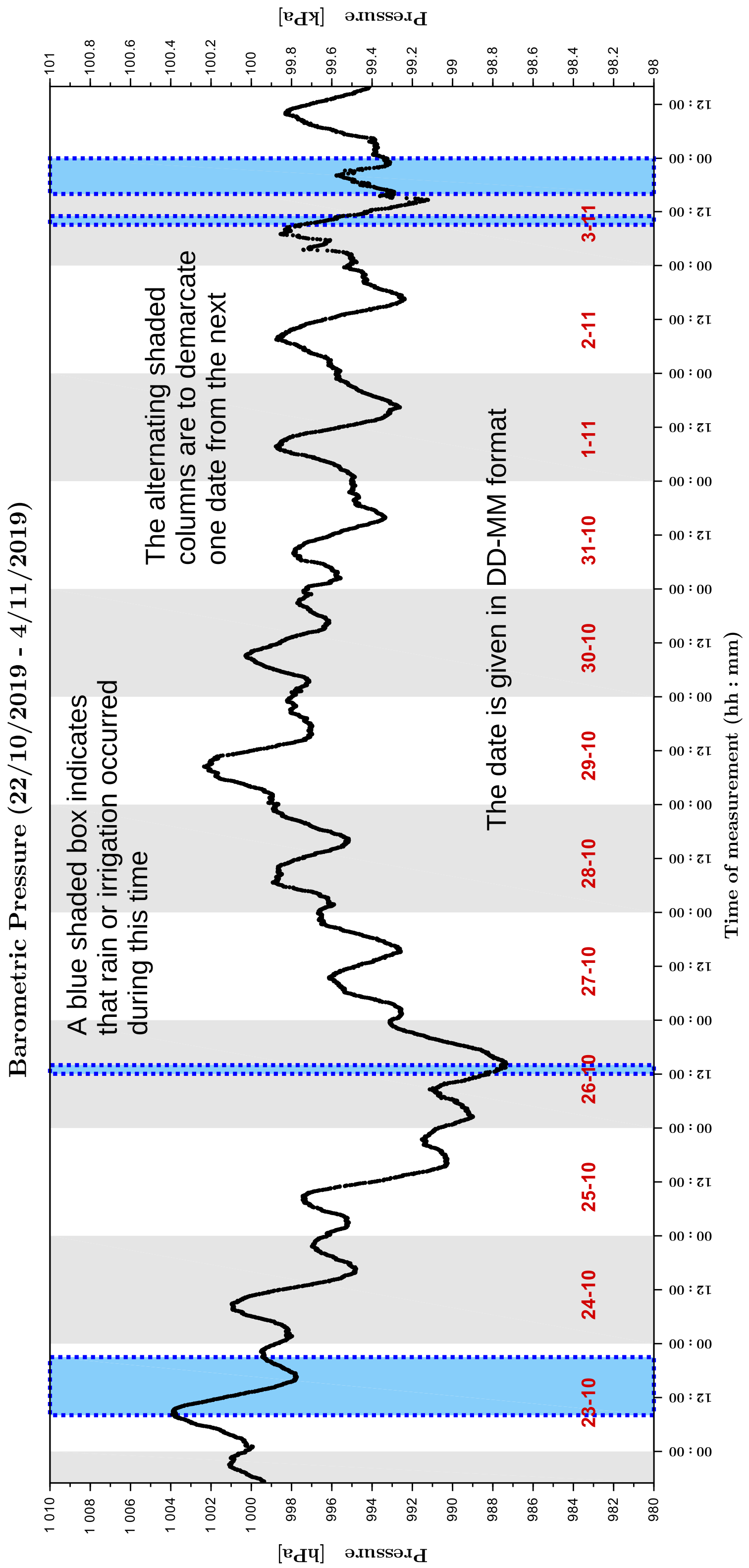

Figure 0.2: An example plot with explanatory comments of some features commonly used throughout this thesis.

This page intentionally left blank.

Chapter 1

INTRODUCTION

This thesis reports on the research efforts between 2018 - 2021 to evaluate a novel technique for applying the STIC model (Mallick et al. 2014) to estimate crop evapotranspiration from broadacre irrigated cotton in Australia. The novel technique is termed 'GPSTIC', an acronym for Ground-Proximal STIC.

1.1 Context and Motivation

The sustainable and equitable management of fresh water is a problematic and contentious issue, especially in water limited regions of the world such as Australia. Competing agronomic, ecological, social and economic interests make the issue of water management highly political and polarising in our society. This is likely to only become all the more so as the effects of climate change and population growth increasingly become manifest.

The efficient and effective management of what fresh water resources we have, within this context of scarcity and competition, is a pressing concern. Agriculture — especially irrigated agriculture — has a critical role in that it provides much of the necessary food and fibre for society but also consumes more fresh water than any other part of society.

One of the prerequisites to efficient and effective water management by growers and policy makers is the capability to measure and monitor water use. Ideally, this capability should be accurate and low cost so that it is accessible to more people. This thesis reports a research effort to contribute to that body of knowledge and further that capability by developing a new model (GPSTIC) to enable low-cost, accurate estimates of crop water use.

1.2 Proposed Model – GPSTIC

STIC ('Surface Temperature Initiated Closure') was a model developed by Mallick et al. (2014, 2015a) for the purpose of estimating evapotranspiration, E, using remotely sensed data (usually from satellites). It was derived after revisiting the Penman-Monteith model (Penman 1948, Monteith 1965) with a view to incorporating a surface temperature variable, T_S, in lieu of the aerodynamic and stomatal conductance terms, g_B and g_S, respectively. Mallick et al. were primarily interested in modelling at large-scales (i.e. kilometre grids) and to this end the STIC model appears to have performed well (§ 2.1.1, p. 20 and Appendix B, p. 339).

The GPSTIC model is being proposed here as an alternative, modified application of STIC whereby ground-based sensing is used in place of any remotely sensed data.

There are several reasons for proposing the new GPSTIC model:

1. In GPSTIC the exclusive use of ground-based sensing obviates any requirement for remotely-sensed data. There are several significant

advantages of taking this approach:

(a) The operation of GPSTIC will not be contingent upon having ideal weather conditions (such as clear skies). Cloud cover and atmospheric dust and aerosols will not be an issue to a ground-based system.

(b) Ground-based sensing avoids the technical difficulties typically associated with remotely-sensed data, namely having to deal with intermittent satellite coverage (and the need to interpolate data between satellite overpasses); the inability to directly measure key climatological variables (relying instead on models to infer those variables from radiometric data); and the time lag between when satellites measure data and when the data becomes available to the end user (in contrast, GPSTIC may be able to provide continuous, real-time, accurate estimations of E).

(c) The flux footprint for ground-based data collection is typically at the size of an individual cropping field (especially in Australian broadacre cropping where the size of irrigated fields is often in the order of 100 ha or larger). This makes it ideal when decisions for irrigation management of a particular field are required.

(d) The farmer/irrigator does not have to access their data from a third-party (such as from space-satellite systems) and they retain ownership and control of the data and its collection methods.

2. A GPSTIC system will be a practical and easily deployed tool that is suitable for use within annually cropped fields. The technical requirements of GPSTIC instrumentation will be low making it accessible to farmers and irrigators.

3. GPSTIC will use commonly available, inexpensive equipment.

Furthermore, it is also anticipated that this research will indirectly give greater insight into the STIC model itself. This is significant because STIC has been emerging as an important development in the remotely-sensed evapotranspiration modelling discipline.

1.3 Scope of the Research

The primary motivation for developing and evaluating GPSTIC was to help improve agricultural water management, particularly with respect to evaluating crop water use in order to guide irrigation management. Naturally, then, the scope of the research was defined to evaluate GPSTIC under irrigated agriculture scenarios.

The scope of research was further narrowed by several additional considerations:

1. There was an ongoing severe drought in Eastern Australia during 2018 - 2020. Only farmers with access to groundwater were growing crops and irrigated cotton predominated (due to the high prices paid for cotton at the time). Thus this research was limited to irrigated cotton.

2. A Bowen Ratio Energy Balance (BREB) system (Bowen 1926) was used to provide benchmark evapotranspiration data against which GPSTIC was evaluated. Accordingly, the present research was limited to field conditions that were ideal for BREB, i.e. large, flat, homogenously cropped, irrigated fields with extensive fetch in all directions.

3. Only high-quality, research-grade sensors were used for GPSTIC in this research. Evaluating how lower-quality, lower-cost sensors might affect the performance of GPSTIC was outside of the scope of this research.

Thus the scope of the research was limited to evaluating the performance of the proposed GPSTIC model for an irrigated, broadacre cotton crop under hot and semi-arid Australian summer conditions.

1.4 Scientific and Practical Relevance

Much research has already been undertaken with regard to providing models, methods and tools to assist researchers, growers and policy makers with estimating E. Probably the most widely adopted is the FAO-56 Penman-Monteith model (Allen et al. 1998) and its subsequent derivatives.

This research (i.e. the content of this thesis) differs from previous work and has scientific and practical value in several respects:

- Many of the existing models, methods and tools are effective for research purposes but are not suitable for practical implementation by growers.

- The ubiquitous FAO-56 PM model has a requirement that weather measurements be made over a crop that resembles the theoretical reference crop described in Allen et al. (1998). Such a crop may not be present near a field site and, under such circumstances, an easily implemented alternative to FAO-56 PM that does not require a reference crop would be valuable.

- The STIC model has not yet been independently evaluated, i.e. without the involvement of any of its original authors. A positive evaluation of GPSTIC will, by implication, help to affirm the theory and equations that form the basis of STIC.[1]

- It is envisaged that GPSTIC could develop into a practical tool to measure and monitor crop water use in real-time and so assist with improving water use efficiency on the farm.

[1] A negative evaluation of GPSTIC, however, does not necessarily imply a rejection of STIC because it was not originally developed with a ground-proximal configuration in mind.

1.5 Research Aims and Objectives

1.5.1 Research Methodology

This research comprised

1. development of hardware and software for a new GPSTIC system (and a new BREB system);

2. *quantitative* field measurement of environmental variables;

3. numerical computer modelling to compute values of evapotranspiration E; and

4. a comparative evaluation of the results for E from GPSTIC against those of BREB (serving as a benchmark).[2]

The comparative evaluation comprised regression analyses and discrepancy analyses. Regarding the latter, if the discrepancy between the results of two models was zero then the models were deemed as having equivalent performance. If not, then it became necessary to determine whether the discrepancy was significant in light of the uncertainties associated with each model's outputs.

1.5.2 Research Aims

The primary research aim was to answer the question 'Can GPSTIC effectively measure E from a broadacre, irrigated cotton crop?' The *effective* measurement of E implied some level of accuracy that was adequate for its purpose. Since the envisaged purpose of GPSTIC is to be a practical tool for irrigation and water management, where there are already significant uncertainties associated with measuring the depths of applied irrigation, runoff, deep drainage and rainfall, the measurement accuracy of GPSTIC realistically only needed to be in the order of $\pm 1\,\mathrm{mm\,day^{-1}}$.

[2] The term 'benchmark' is used in preference to 'reference' because in the context of evapotranspiration modelling *reference evapotranspiration* has come to have a special meaning, i.e. $\mathrm{ET_0}$ in FAO-56 Allen et al. (1998), and similar.

Thus the primary research aim was restated as follows to incorporate this criterion:

Primary Research Aim

> ‘Can the proposed model GPSTIC measure the cumulative evapotranspiration from a broadacre, irrigated cotton crop to within $\pm 1\,\mathrm{mm\,day^{-1}}$ of a quality benchmark measurement?’

Whilst not explicitly stated as a research aim it was also of interest to evaluate just how accurately GPSTIC could align with the benchmark measurements of E.

Secondary Research Aim

> Make an independent contribution — i.e. without the involvement of any of STIC’s developing authors (Mallick et al. 2014, 2015a) — to the body of knowledge regarding the STIC model.

The literature review (§ 2.1, p. 16) and Appendix B (p. 339) show that there has been little independent evaluation or application of the STIC model.

1.5.3 Research Objectives

Achievement of the research aims required completion of the following objectives:

1. Replicate the STIC model from Mallick et al. (2014, 2015a) and modify it to use high-frequency ground-proximal sensors.

2. Design and assemble the hardware and software for a GPSTIC system and a BREB micro-meteorological system (to provide benchmark evapotranspiration data). The BREB system must be able to make measurements at the same temporal resolution as the GPSTIC system, i.e. every 60 s.

3. Make measurements of physical environmental variables at the field sites, and use these data as inputs in the BREB and GPSTIC modelling.

4. Determine the uncertainties in the BREB and GPSTIC modelling that originate from known sensor uncertainties (which are propagated through the modelling to create an uncertainty in the models' outputs).

5. Make a comparative evaluation of the two models by regression and discrepancy analyses.

6. Draw conclusions about the performance of GPSTIC as a system to accurately estimate evapotranspiration for agricultural water management, especially irrigation.

Fig. 1.1 (p. 9) shows an overview of the process adopted to achieve the research aims.

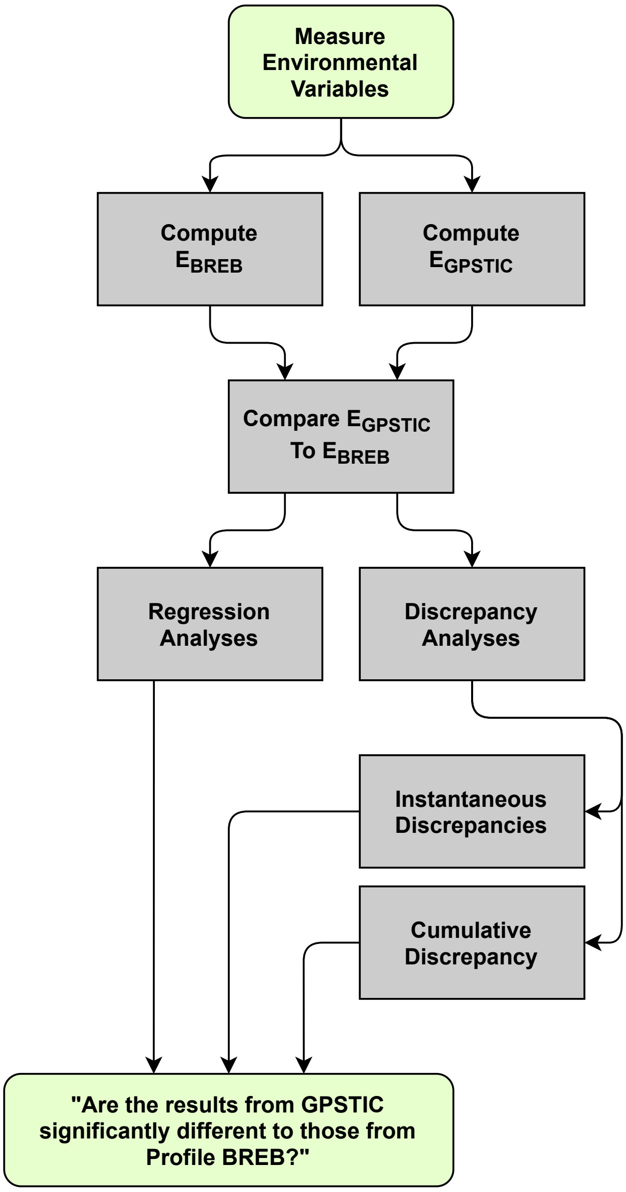

Figure 1.1: A broad overview of the process to achieve the research aims. E_{BREB} and E_{GPSTIC} are the modelled evapotranspiration per Profile BREB (§ 3.3, p. 85) and GPSTIC, respectively.

1.6 Overview of Thesis Structure

The body of the thesis is structured around seven chapters:

- ***Ch. 1 – Introduction***

- ***Ch. 2 – Literature Review*** shows that while the STIC model has repeatedly demonstrated its ability to perform well under a variety of conditions, the application of STIC at field or sub-field scales using ground-based sensors has not been reported. The literature review also leads to the deduction that BREB is a preferable method to provide the benchmark measurement of evapotranspiration for this research and identifies the historical precedence of the 'profile' approach to BREB.

- ***Ch. 3 – Materials and Methods*** comprises four sections:

  § 3.1 describes the two field sites at which field work was undertaken over three distinct periods. These sites were chosen primarily for the reason that they provided ideal conditions for BREB. They also had secure access to water which was significant given the ongoing severe drought. The two sites afforded an opportunity to evaluate the GPSTIC model under a variety of field conditions, i.e. bare soil; single-skip planting configuration[3] with partially-irrigated cotton; and a fully-planted, fully-irrigated, fully-grown cotton crop.

  § 3.2 details each of the sensors that were used by the BREB and GPSTIC systems. Significant instrumentation development by the author was a key part of this research and suitable sensor selection was central to this. Recent technological advances have meant that precise, field-deployable sensors had become available at a reasonable price. The sensors were carefully selected for their precision thereby reducing the uncertainty in the modelling results.

[3] In a single-skip planting configuration every third plant row is not planted, i.e. only 2/3 of the field is planted.

§ 3.3 describes the BREB system — specifically, a 'Profile' BREB system — that was custom developed by the author for the present research. Based upon well established theory, but leveraging newly available sensing technologies, a Profile BREB system[4] was designed and constructed. This included a novel algorithm and computer program that automated the process of assessing whether measured data needed to be excluded from the BREB modelling by accounting for the inherent measurement uncertainties in the sensors. (This automated process was necessary because 592 hours' worth of field data were collected and the assessment had to repeated 8880 times.)

§ 3.4 gives an explanation and description of the GPSTIC system. Some of GPSTIC's sensors were shared in common with Profile BREB — part of the attractiveness of using Profile BREB for this research. However, the GPSTIC and Profile BREB algorithms were entirely independent of each other and had very different computational processes. The algorithm for GPSTIC is described in detail.

- ***Ch. 4* – *Results*** is presented in three sections, each corresponding to a separate period of field work. The three distinct periods of field work were named 'Data Set One' (DS1), 'Data Set Two' (DS2) and 'Data Set Three' (DS3), comprising 165 hours, 311 hours and 116 hours of data collection, respectively. Each section in this chapter simply presents measurement data on the environmental conditions (with commentary as required) and the modelling results for GPSTIC and Profile BREB for the Data Set. To be clear, in Ch. 4 no analyses or comparisons of the GPSTIC and Profile BREB models are undertaken.

[4]As opposed to a 'two-height' BREB system that exchanged sensors between two heights.

- ***Ch. 5* – *Analysis*** is where the results from the GPSTIC model are evaluated against the results of the benchmark Profile BREB model. Specifically, it is each model's estimation of evapotranspiration (i.e. E_{GPSTIC} and E_{BREB}) that is being compared; this occurs on both a 4 min basis[5] and on a cumulative basis.

  § 5.1 analyses the 4 min results for the GPSTIC and Profile BREB systems by calculating linear regressions of E_{GPSTIC} against E_{BREB}. Exemplary regression plots and a table of all regression results are provided. These analyses were undertaken one Data Set at a time.

  § 5.2 presents the discrepancy analyses, one Data Set at a time. The analyses include plots and tables of the modelling results that allow a comparison of the 4 min and accumulated values of E_{GPSTIC} and E_{BREB}, and the discrepancy between them. The analyses include the associated 95 % confidence intervals (that were derived from the sensors' inherent measurement uncertainties) to help determine the significance of non-zero discrepancies between the models' results. The cumulative analyses were particularly effective at revealing how closely the two models aligned over time.

  § 5.3 serves to summarise and emphasise some of the key results from § 5.1 and § 5.2. It also highlights the differences in the crop status and the modelling results across the three Data Sets.

- ***Ch. 6* – *Discussion*** comprises seven sections that explain and expand upon key material from Chapters 4 and 5, particularly as they relate to GPSTIC:

  § 6.1 specifically addresses the two Research Aims from § 1.5.2 (p. 6).

  § 6.2 briefly summarises the performance of GPSTIC and Profile BREB. The latter discusses why there can be confidence that Pro-

[5] The environmental data were measured every 60 s and averaged in 4 min intervals (giving 15 averaged values per hour).

file BREB was, in fact, providing appropriate and adequately accurate evapotranspiration data.

§ 6.3 justifies the inclusion of modelling uncertainties with the results.

§ 6.4 discusses the α_{PT} advection parameter in the GPSTIC model (which was the only user-selectable parameter in the model). It was not within the scope of this research to establish a process for determining α_{PT} but it was, nevertheless, an important influence on the final results and thus deserving of some discussion.

§ 6.5 discusses the impacts of applying various exclusion criteria to the data. An explanation of how fieldwork dates were chosen is also given here.

§ 6.6 discusses the contributions to come from this research, particularly with respect to GPSTIC but also the implications for Profile BREB and STIC.

§ 6.7 discusses the limitations of this research.

- ***Ch. 7 – Conclusion*** recaps the achievement of the research aims and makes suggestions for future work.

This page intentionally left blank.

Chapter 2

LITERATURE REVIEW

This chapter reviews the literature that provide a background and context to the STIC model (Mallick et al. 2014, 2015a). The GPSTIC model – the subject of this thesis – is a modification and novel application of the STIC model.

Brief reviews of the literature pertaining to the Priestley-Taylor (PT) model, which played a minor but essential role in the derivation of STIC, and of Remote Sensing for Evapotranspiration (RS-E) models, are also presented. STIC is a RS-E model but GPSTIC is designedly not.[1] Thus the review of the RS-E literature is only for the limited purpose of showing where STIC sits within the (considerable) field of RS-E modelling.

Finally there is an extensive review of the Bowen Ratio Energy Balance (BREB) method for estimating evapotranspiration because BREB

[1]A key motivation for GPSTIC was to remove altogether the RS aspect from the STIC model so that it could be applied in real-time at field or sub-field scales.

was used in the present research to provide the benchmark evapotranspiration data against which GPSTIC was evaluated. A sizeable part of the review is given to providing a justification of the *Profile* approach to BREB – a relatively uncommon approach but well suited to present purposes. The rationale for the extensive BREB review is primarily to demonstrate from the literature that BREB (and particularly Profile BREB) is capable of providing quality benchmark evapotranspiration data; a secondary purpose is to justify the use of BREB in this research instead of other commonly used methods, notably eddy covariance (EC).[2] This review of BREB is supplemented by additional material in Appendix A (p. 331).

2.1 The STIC Model

When Monteith (1965) developed a physically-based model for evaporation over terrestrial surfaces, he sought to eliminate the need to measure surface temperature, T_S, because this was, at the time, the most difficult of all meteorological variables to measure at large scales. In so doing, however, it became necessary to specify the aerodynamic and bulk stomatal conductance terms (g_B and g_S respectively). These terms are difficult to accurately quantify and generally are not measurable at scales at which the PM equation is applied (Mallick et al. 2014). Mallick et al. (2014) describe the present models for g_B and g_S as speculative and requiring parameterisations to adapt them from leaf-scale to canopy-scale applications – parameterisations that are non-stationary due to biological controls and boundary layer dynamics. Schymanski and Or (2017) have shown that, even at the leaf-scale, the PM equation is subject to errors because of its omission of two-sided sensible heat flux from a planar leaf and because of its failure to represent hypostomatous leaves. The consequent errors in aerodynamic and bulk stomatal conductances at the leaf-scale often propagate into inaccurate canopy-scale sensitivities

[2] EC systems are expensive and not financially viable in a budget-restricted evapotranspiration monitoring system.

of latent and sensible heat fluxes to changing atmospheric conditions. Frequently it has been assumed that leaf-scale conductance terms can be replaced by their canopy scale counterparts with little change to the underlying physics model (Dhungel et al. 2014, Schymanski & Or 2017).

Because of these difficulties with the PM equation, and because technology for measurement of T_S had advanced since Monteith's seminal paper (Monteith 1965), Mallick et al. (2014) revisited the PM equation. Their aim was to replace the problematic exogenous inputs g_B and g_S with T_S (as the exogenous input). The justification, according to Mallick et al. (2015a), was that:

> ...the internal states (e.g. soil moisture and conductances) regulating λE are strongly temperature dependent (Monteith 1981, Huband & Monteith 1986, Blonquist et al. 2009) making T_S a primary state variable of surface energy balance closures.

Their efforts drew heavily upon the theories of Penman (1948), Monteith (1965), Priestley and Taylor (1972) and Brutsaert and Stricker (1979). The *Penman-Monteith-Bouchet-Lhomme (PMBL)* model (Mallick et al. 2013) emerged with promising results for estimating E even though it did not yet include T_S or remote sensing (data was retrieved from EC and meteorological towers). Their conclusions, however, indicated that the authors were already moving strongly toward the use of radiometric surface temperatures and remote sensing of data. This became manifest in the following year in the new *Surface Temperature Initiated Closure* ('STIC') model (Mallick et al. 2014).

The STIC model only required measurements of net radiation flux (R_N), soil heat flux (G), ambient air temperature (T), surface temperature (T_S), barometric pressure (P), and relative humidity (RH). A value for the Priestley-Taylor (Priestley & Taylor 1972) parameter (α_{PT}) was also required. In the original STIC model (Mallick et al. 2014) α_{PT} was assumed to be 1.26, but Mallick et al. (2015a) subsequently added a dynamic, interative procedure into STIC that avoided the use of a fixed, assumed, α_{PT}. Thus the model only required commonly measured meteorological variables, plus T_S.

A key part of the formulation of STIC was the use of three slopes of chords on the saturated vapour pressure (SVP) vs. temperature curve, as illustrated in Fig. 2.1 (p. 19). The relevant temperature variables here are

T	Ambient air temperature	[°C]
T_D	Ambient dewpoint temperature	[°C]
T_{SD}	Dewpoint temperature at the leaf surface	[°C]
T_S	Surface temperature	[°C]

The relevant water vapour pressure variables are

e	Ambient vapour pressure	[hPa]
e^*	Saturation ambient vapour pressure	[hPa]
e_S	Vapour pressure at leaf surface	[hPa]
e_S^*	Saturation vapour pressure at leaf surface	[hPa]

The superscripted * is used to denote saturation conditions because the subscripted S is used to denote surface variables. The three chord slopes in STIC are thus defined as

s_1	Slope of chord between T_D and T_{SD}	[hPa °C^{-1}]
s_2	Slope of chord between T_D and T_S	[hPa °C^{-1}]
s_3	Slope of chord between T_{SD} and T_S	[hPa °C^{-1}]

The point (T_{SD}, e_S) is unknown and so the slopes s_1 and s_3 are approximated by using the tangential (gradient) SVP slopes at (T_D, e) and (T_S, e_S^*). This approximation appears to work well but it could be a possible source of error in the model. As it stands, however, there is no alternative method to determine s_1 and s_3.

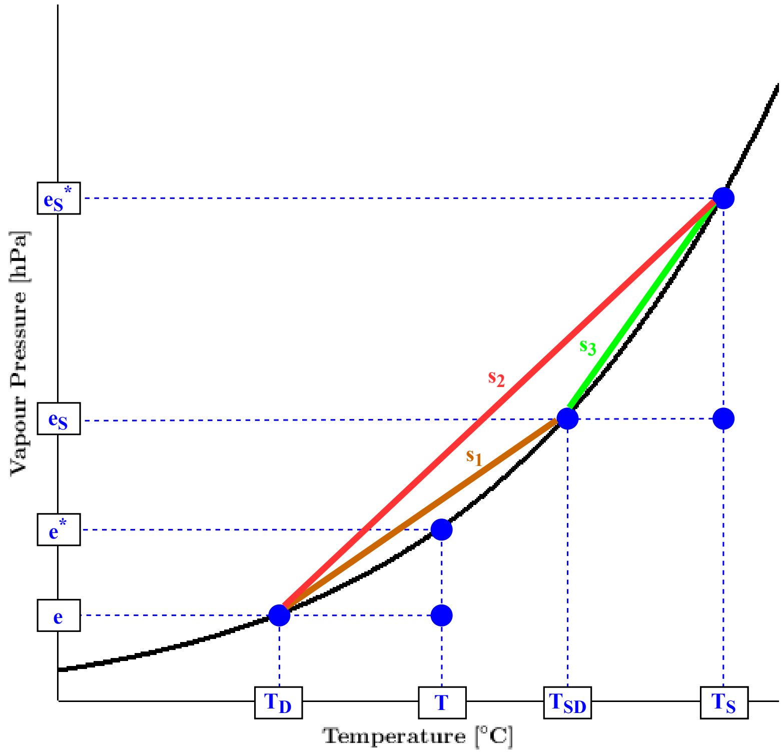

Figure 2.1: A saturation vapour pressure curve as an exponential function of temperature calculated by the Buck equation (Buck 1981, 1996). The relationships between dewpoint temperature (T_D), ambient temperature (T), dewpoint temperature at the leaf surface (T_{SD}) and leaf surface temperature (T_S) with the ambient vapour pressure (e), ambient saturation vapour pressure (e^*), vapour pressure at the leaf surface (e_S) and saturation vapour pressure at the leaf surface (e_S^*) have been reproduced from Mallick et al. (2014, 2015a). s_1, s_2 and s_3 are the slopes of the chords between various points on the curve.

Remotely sensed MODIS data from the satellites Terra and Aqua[3] were originally used in STIC (Mallick et al. 2014). The RMSD, compared to EC measurements at over 30 sites over natural and agricultural biomes, was 11 - 15 % for daily λE and 8 - 9 % for daily H. In a similar paper, Mallick et al. (2015a) reported RMSDs of 5 - 13 % in daily λE and 10 - 44 % in daily H – again using MODIS Terra and Aqua, with benchmark flux data coming from EC, BREB and scintillometry (e.g. McAneney

[3] https://terra.nasa.gov/about/terra-instruments/modis

et al. 1995, Meijninger et al. 2002) systems.

These good results were notable for several reasons. Firstly, in Mallick et al. (2014) and Mallick et al. (2015a) STIC had been applied and evaluated over a wide variety of landscapes, biomes and climates. Secondly, there was a considerable difference in the spatial and temporal resolutions of the data used for STIC (sourced from space-satellite sensors) and the EC data. And thirdly, STIC had no requirement for any knowledge of plant or field properties, such as crop height, stomatal and aerodynamic resistances, or antecedent soil moisture.

2.1.1 Summary of STIC Model Application and Performance

Mallick et al. (2016) applied the STIC model in the Amazon rainforest and regressed against EC data yielding R^2 values with respect to mean λE and H of 0.94 and 0.61 respectively. The larger errors in H were attributed to the greater sensitivity of H to errors in T_S due to poor emissivity correction (Mallick et al. 2015a, 2016).

Obringer et al. (2016), co-authored by Mallick, applied the STIC model to create regional estimates of E in a combined rural/urban district around Indianapolis, USA, with a view to producing better estimates of surface resistance, r_S, for PM modelling to assist with drought monitoring. An R^2 of 0.84 compared to EC towers was reported, all the more impressive given the 32 km resolution of the satellite data.

Udelhoven et al. (2017), co-authored by Mallick, used the 2016 version of STIC[4] to retrieve λE from lawn and soil plots. An airborne hyperspectral thermal imaging camera, at 1430 m altitude, was used instead of satellite thermal data. They reported strong correlation between STIC-retrieved E data and in-situ measurement, and concluded that accuracy requirements for absolute land surface temperatures when using STIC need to be better than ± 1 K.

[4]The Mallick et al. (2016) version of STIC differed slightly in that it included a new feedback loop coupling T_S, T, λE and e.

Bhattarai et al. (2018), co-authored by Mallick, acknowledged that STIC was yet to receive significant interest in the RS community, especially among those who are interested in modelling at the regional-level scale. Consequently, in this paper the 2016 version of STIC (referred to as 'STIC 1.2') was adapted to not require any data inputs from local flux towers or weather stations and rely only on data from NLDAS-2 and MODIS to estimate E at regional scales at $1\,\mathrm{km} \times 1\,\mathrm{km}$ resolution. STIC performed better than either SEBS or MOD16 when compared to EC flux towers, especially in forests and grasslands, but had 20 % and 40 % errors in croplands and woody savanna, respectively.

Mallick et al. (2018) reported the application of STIC in Australia at fifteen different OzFlux EC sites which afforded the opportunity to evaluate STIC across a range of dry to wet ecohydrological systems. At half-hourly intervals the mean RMSD of λE was 36 - 55 $\mathrm{Wm^{-2}}$ at the mesic and semi-arid sites ($R^2 = 0.60$ - 0.85) and 26 - 46 $\mathrm{Wm^{-2}}$ ($R^2 = 0.4$) at the arid sites. However, STIC had a larger relative error in arid ecosystems. At daily intervals the mean RMSD of λE was 17 $\mathrm{Wm^{-2}}$ (R^2 = 0.55 - 0.81) across mesic and semi-arid ecosystems and 11 $\mathrm{Wm^{-2}}$ (R^2 = 0.55) across arid ecosystems. The study showed that STIC was most sensitive to T_S in arid and semi-arid ecosystems. It also compared the 2016 version of STIC to earlier versions of STIC: the 2016 version showed improved performance for arid and semi-arid ecosystems.

Bhattarai et al. (2019), co-authored by Mallick, noted the difficulties created for remote sensing of E (including STIC) when there is cloud cover, lack of ground-based meteorological data, and lack of open source codes and automation. They also noted the lack of consensus on which Surface Energy Balance (SEB) model performs best under given conditions. The study compared seven individual SEB models (METRIC, SEBAL, SEBS, TSEB, Triangular, S-SEBI and STIC) with a new 'Ensemble SEB' (EnSEB) model, which was a mean of the seven individual SEB models. All were benchmarked against four BREB systems. EnSEB yielded hourly λE with RMSD of 59 $\mathrm{Wm^{-2}}$ which was lower than the individual SEB models (STIC was second best with a RMSD of 64 $\mathrm{Wm^{-2}}$).

The authors suggested the better performance by EnSEB was due to errors or biases associated with the individual SEB models cancelling each other out when averaged by EnSEB. STIC performed best out of all models in terms of being able to account for the variability in observed λE ($R^2_{STIC} = 0.6$, $R^2_{EnSEB} = 0.57$). The main part of the study only considered clear-sky conditions[5] and mainly comprised irrigated, high λE sites.

Renner et al. (2019), co-authored by Mallick, assessed the diurnal cycle of E under wet and dry conditions. STIC was used to calculate actual E and FAO-56 (Allen et al. 1998) was used to calculate potential E. Meteorological data were measured at 30 min intervals but no mention was made of how T_S was measured. Compared to EC (which was acknowledged to have problems with energy misclosure), STIC slightly overestimated λE in dry conditions (110 % of mean observed λE) and underestimated λE in wet conditions (83 % of observed mean λE). STIC showed relatively larger phase-lags under wet and dry conditions, and the diagnosed g_{av} (aerodynamic conductance of water vapour) did not vary between wet and dry conditions, which was suggested as being a possible problem for STIC.

At the time of writing no other papers in the available literature have reported the use of the STIC model *per se*. It appears that no authors besides Mallick have replicated STIC and that it has never been applied outside of the RS context, despite the positive results of the ground-based *Penman-Monteith-Bouchet-Lhomme (PMBL)* model in Mallick et al. (2013). These circumstances are surprising to me, as they were to Bhattarai et al. (2018), because STIC has shown strong performance and potential for application across a wide variety of scenarios. It may be that the RS research community has been flooded with new RS-E models (and STIC is just one of many such models), that there is a lack of communication with those outside of the RS research community,

[5]Other parts of the study used gap-filling when there were persistent cloudy conditions during the monsoon season. The authors acknowledged that this could result in additional biases in estimates of E by EnSEB.

and that there is not sufficient detail provided in published papers for readers to easily replicate the STIC model (especially if RS data is to be used).

An exhaustive, annotated list of all other papers citing STIC and/or Mallick et al. (2014, 2015a) is given in Appendix B (p. 339).

2.2 The Priestley-Taylor Model

The Priestley-Taylor (PT) model (Priestley & Taylor 1972) for estimating E in humid climates is reviewed here because the Priestley-Taylor α_{PT} is a significant parameter in the STIC model. The PT model has also been a significant model in its own right influencing the evolution of theory regarding E. It requires only radiation and air temperature data and, among the simplified reduced parameter models, it is considered to be one of the better performing models (Xu & Singh 1998, Sumner & Jacobs 2005, Aschonitis et al. 2015).

Priestley and Taylor were concerned with large-scale relationships in the atmosphere, particularly in numerical weather forecasting models whose grid sizes spanned hundreds of kilometres on each side. They argued (Priestley & Taylor 1972) that, at those scales, advective effects would be dominated by incoming radiant energy because

> The radiation received will increase as the square of grid-point separation, whereas advective effects will increase more or less linearly because the differences in horizontal fluxes of heat and vapour at the upwind and downwind edges of an area will not continue to increase indefinitely as the edges are moved further apart.

Priestley (1959) had already argued that over a surface with unlimited water supply the atmosphere would be saturated if

$$\lambda E = \frac{\Delta_{PT}}{1 + \Delta_{PT}} \left(R_N + G \right) \tag{2.1}$$

where

$$\Delta_{PT} = \frac{\lambda}{c_p}\frac{dq^*}{dT} \tag{2.2}$$

Here $\frac{dq^*}{dT}$ is the slope of the saturated specific humidity vs. air temperature curve. However, Priestley and Taylor (1972) recognised the importance of advection even at large scales and the need for a corrective advection coefficient. The Priestley-Taylor equation thus became

$$\lambda E = \alpha_{PT}\frac{\Delta_{PT}}{1+\Delta_{PT}}\left(R_N + G\right) \tag{2.3}$$

Incidentally, when $\alpha_{PT} = 1$ the Δ_{PT} term can be shown to be equivalent to the inverse of Bowen's ratio by assuming $(R_N + G) = (H + \lambda E)$ and combining with Eqn. 2.1:

$$\begin{aligned}
\lambda E + \Delta_{PT}\lambda E &= \alpha_{PT}\,\Delta_{PT}\left(H + \lambda E\right) \\
&= \Delta_{PT}\left(H + \lambda E\right) \\
\Delta_{PT} &= \frac{\lambda E}{H} \\
\therefore\ \Delta_{PT} &= \frac{1}{\beta} \qquad (\text{when } \alpha_{PT} = 1)
\end{aligned} \tag{2.4}$$

By empirical means they found a value of $\alpha_{PT} \approx 1.26$ best fitted the data from several sources and this has since been regarded as the default value, including by Mallick et al. (2014) in their original work on STIC. Eichinger et al. (1996) affirmed 1.26 for bare irrigated soil and Lhomme (1997) and McMahon et al. (2013) reported 1.26 from theoretical simulations where the contributions of advection were limited. Stewart and Rouse (1977) reported 1.26 for wet meadow, Davies and Allen (1973) reported 1.27 for irrigated ryegrass, Weiβ and Menzel (2008) reported 1.26 for wet conditions and Morari and Giardini (2001), Heinemann et al. (2002) and Utset et al. (2004) reported using 1.26 for estimating irrigation requirements in a variety of climates. However, Jury and Tanner (1975) reported 1.57 under strongly advective conditions, Weiβ and

Menzel (2008) reported using 1.75 for dry climates and Tabari and Talaee (2011) reported α_{PT} between 1.82 and 2.14 in dry, cold conditions in Iran. Singh and Irmak (2011) reported a lower value of 1.14 in Nebraska, and values between 1.08 and 1.34 have been reported for agricultural lands and grasslands (Mukammal & Neumann 1977, De Bruin & Holtslag 1982, Tateishi & Ahn 1996, Xu et al. 2013). Barton (1979) reported 1.04 for bare soil, and values between 0.72 and 1.18 have been reported for forests (McNaughton & Black 1973, Black 1979, Shuttleworth & Calder 1979, Giles et al. 1985, Flint & Childs 1991).

Thus there appears to be considerable spatial and temporal variation in α_{PT} (Castellvi et al. 2001, Moges et al. 2003, Pereira 2004). McAneney and Itier (1996) showed that the PT model tended to produce better results in more humid regions where daytime mean humidity deficit was less than $10\,\mathrm{g\,m^{-3}}$.

Mallick et al. (2015a) introduced an internal iterative process to their STIC model to optimise α_{PT} instead of adopting a fixed 1.26 as per their earlier work (Fig. 2.2, p. 26). However, the iterations tended to converge on values of $\alpha_{PT} < 1$. This is in contrast to other authors who consistently reported $\alpha_{PT} > 1$ except in the cases of forestry.

(It has also been the author's experience, when using the GPSTIC model, that this internal iterative process tended to produce $\alpha_{PT} < 1$ (§ 6.4.2, p. 280). Moreover, the use of values of $\alpha_{PT} < 1$ in GPSTIC invariably produced poor results for E; the best results generally occurred when $1.1 < \alpha_{PT} < 1.4$ which is consistent with Priestley and Taylor's recommended value and with the literature relating to agricultural lands.)

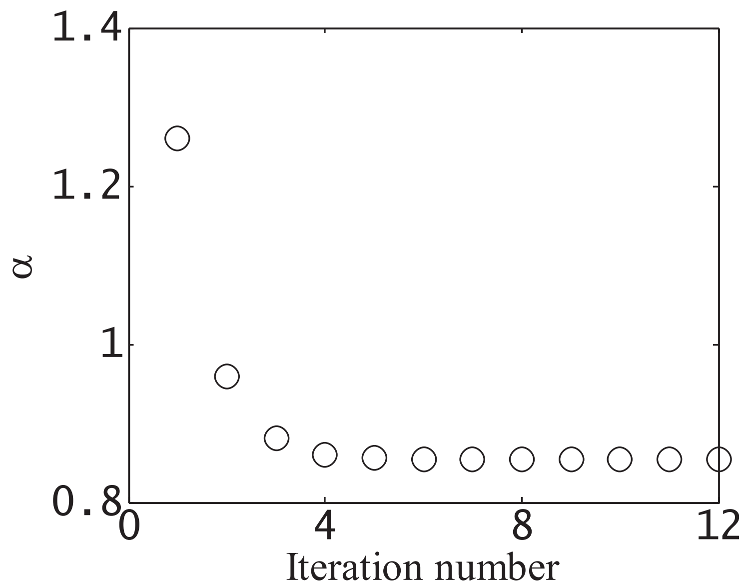

Figure 2.2: An example plot of the results of the iterative process for α_{PT} (denoted as α in this plot) as presented in Mallick et al. (2015a) showing the convergence of α_{PT} on a stable value of approx. 0.85.

2.3 Remote Sensing for Evapotranspiration

STIC was developed and has been implemented as a RS model since its inception.[6] It is a significant model within the rapidly expanding field of Remote Sensing of Evapotranspiration ('RS-E'). Reviews of this field of study include Kustas and Norman (1996), Courault et al. (2005), Li et al. (2009), Zhang et al. (2016) and McShane et al. (2017).

There are now numerous RS-E models and a variety of approaches to categorising them. Fig. 2.3 (p. 29) presents a timeline of key RS-E models prior to STIC and categorises the RS-E models into one of the following eight groups after Zhang et al. (2016):

- One-source RS-E models
- Two-source RS-E models
- $\mathrm{T_S}$-VI RS-E models
- Priestley-Taylor-based RS-E models
- Penman-Monteith-based RS-E models
- Empirical RS-Emodels
- Water balance RS-E models
- Water-carbon linkage RS-E models

These groups are not necessarily mutually exclusive and the STIC model can be categorised as a one-source PM-based RS-E model.

Just as for other models within the PM group, STIC had to find a way to determine the conductance parameters, g_B and g_S, in the PM equation:

$$E = \frac{s\,\phi + \rho\,c_P\,g_B\,(e^* - e)}{\lambda\left[s + \gamma\left(1 + \frac{g_B}{g_S}\right)\right]} \tag{2.5}$$

[6]Unlike STIC's precursor (Mallick et al. 2013) which made use of ground-proximal measurements of environmental variables.

Recognising, then, that E is controlled by both biological and physical processes (as described in the PM equation), and following the work of Jarvis (1976), Stewart (1988), Ball et al. (1987), Kelliher et al. (1995) and Leuning (1995) to relate the stomatal response to environmental variables and vegetation indices, a number of PM-based RS-E models were developed, e.g. Cleugh et al. (2007), Mu et al. (2007), Leuning et al. (2008), Sheffield et al. (2010), Mu et al. (2011), Zhang et al. (2015).[7]

In contrast, Mallick et al. (2013) decided to take a different approach and avoid mechanistic or empirical models for g_S and g_B in the PM equation by instead combining the PM equation with the PT equation, the diffusion equations of scalar transfer, and Bouchet's complementary hypothesis. This then formed the basis of STIC (Mallick et al. 2014) which finally incorporated the radiometric surface temperature, T_S, into the model. Despite the apparently good results it has achieved, however, STIC has subsequently received surprisingly little attention within the RS community, and less still outside of it – as noted by Udelhoven et al. (2017).

The major limitations of all of the RS-E models include the negative impacts of non-clear-sky conditions; the need for temporal integration and scaling of data between satellite overpasses; the lack of measurement of near-surface meteorological data; and the difficulty of validating model estimates due to lack of ground-based systems (especially over complex terrains).

[7]Zhang et al. (2015) and its precursors Zhang et al. (2009, 2010) were not PM-based RS-E models *per se*. Rather they incorporated an inverse solution of the PM equation (using data from EC towers) to determine key model parameters.

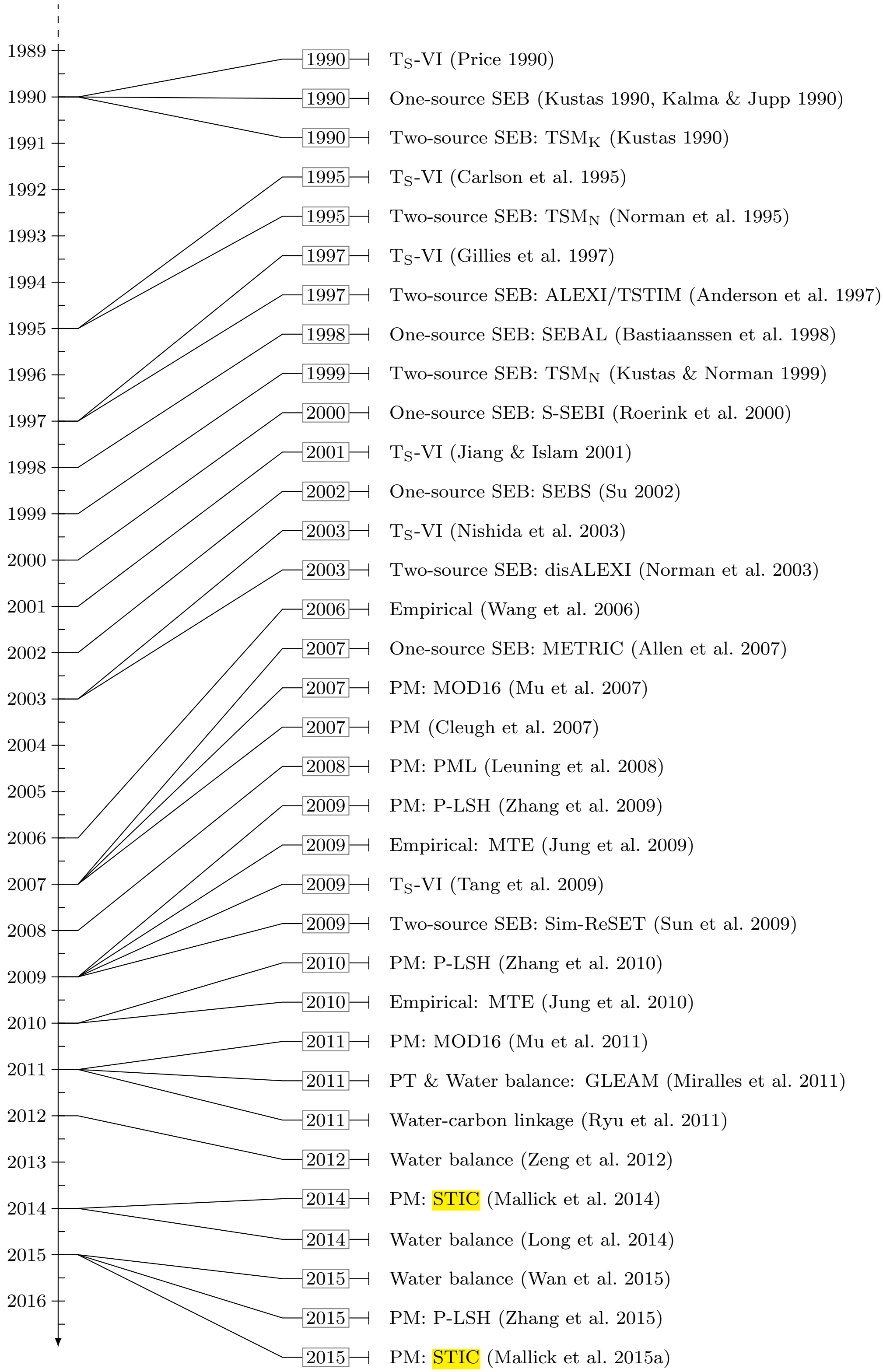

Figure 2.3: A timeline of key publications in the development of RS-E prior to STIC (Mallick et al. 2014, 2015a), adapted from Zhang et al. (2016). SEB = Surface Energy Balance; T$_S$-VI = Surface Temperature - Vegetation Index; PM = Penman-Monteith; PT = Priestley-Taylor.

2.4 The BREB Model

The Bowen Ratio Energy Balance (BREB) model (Bowen 1926) is a micrometeorological model used to estimate sensible and latent heat fluxes above a surface. BREB — specifically, the 'profile' approach to BREB (§ 2.4.6, p. 43) — was used in this research to provide benchmark evapotranspiration data against which GPSTIC was evaluated.

The 'two-height' approach to BREB has been regarded as the default approach to BREB. This review, however, presents an argument that Profile BREB has strong historical precedence in the published literature and is well suited to the current research.

Coverage of the theory and historical development of BREB, examples of its application, and a review of the default 'two-height' approach to BREB are presented in Appendix A (p. 331). Thus, with an assumption that the reader is already familiar with these aforementioned topics, this review will go immediately to cover key BREB issues arising in the literature, namely the assumption of equality of diffusivity, the adequacy of fetch, concerns pertaining to sensors, and the accuracy of BREB. Then § 2.4.6 (p. 43) will proceed to review the 'profile' approach to BREB which is particularly relevant to the current research.

2.4.1 Assumed Equality of Diffusivity

The most significant assumption in BREB is that the diffusivities of sensible heat (κ_H) and water vapour (κ_W) are equal all the time (McIlroy 1971). The basis of this assumption was that 'all energy scalars are carried by the same eddies and, therefore, these scalars are associated at the same boundary layer of the evaporating surface' (Irmak et al. 2014a). This assumption has often been justified by the similarity hypothesis of Monin and Obukhov (1954) but Bowen (1926) and Taylor (1938) had already argued in favour of assuming equality of κ_H and κ_W.

Many authors have subsequently agreed. Tanner (1960), Pruitt (1963), Fritschen (1965), Denmead and McIlroy (1970), McIlroy (1971) and Blad and Rosenberg (1974) argued that the good agreement between lysimetry and BREB lends support to the equality assumption. Swinbank and Dyer (1967), Garratt and Hicks (1973) and Sinclair et al. (1975) all reported that $\kappa_H \approx \kappa_W$. Rider and Robinson (1951) and Rider (1954) compared BREB and an aerodynamic technique and found $\kappa_H \approx \kappa_W$ for stable and unstable conditions. Pruitt and Aston (1963), Dyer (1967) and Swinbank and Dyer (1967) also concluded that $\kappa_H \approx \kappa_W$ for stable and unstable conditions. Denmead and McIlroy (1970) reported $\kappa_H \approx \kappa_W$ when the Richardson number, Ri,[8] was in the range $-0.001 < Ri < 0.026$ under conditions of non-potential evaporation. Campbell (1973) reported $\kappa_H \approx \kappa_W$ and errors in β were less than 10 % when $-2.5 < Ri < 0.025$, and Cellier and Brunet (1992) showed that $\kappa_H \approx \kappa_W$ even in the surface roughness layer just above the canopy. Dicken et al. (2013) used EC to determine that $\frac{\kappa_H}{\kappa_W}$ averaged 0.99 (standard error ± 0.02) inside a screen house.

It has, however, also been argued that κ_H does not equal κ_W all the time. For example, Blad and Rosenberg (1974) and Verma et al. (1978) concluded that $\kappa_H > \kappa_W$ during regional sensible heat advection. Lang et al. (1983b) found that $\kappa_H < \kappa_W$ under stable conditions but Pruitt and Aston (1963) and Campbell (1973) found that $\kappa_H > \kappa_W$ in very stable conditions. Perez et al. (1999) reasoned that atmospheric conditions at night are usually stable and consequently turbulence is less developed and the assumption that $\kappa_H \approx \kappa_W$ may not be valid. Irmak et al. (2014b) stated that the equality assumption may be invalid over some heterogeneous vegetation surfaces, and Katul et al. (1995) found that non-uniform sources of water vapour could cause dissimilar diffusivities.

[8] Atmospheric stability can be defined by the Richardson number (Ri) where

$$Ri = \frac{g\,\frac{\partial T}{\partial z}}{T\left(\frac{\partial u}{\partial z}\right)^2} \tag{2.6}$$

where g is gravity [$\mathrm{m\,s^{-2}}$], T is the ambient temperature [K], $\partial T/\partial z$ is the temperature gradient with respect to height [$\mathrm{K\,m^{-1}}$], and $\partial u/\partial z$ is the wind gradient with respect to height [$\mathrm{m\,s^{-1}\,m^{-1}}$]. The atmosphere is considered stable if $Ri > 0$, neutral if $-0.035 < Ri < 0$ and unstable if $Ri < -0.035$ (Blad & Rosenberg 1974).

The generally adopted practice for BREB is to assume that $\kappa_H = \kappa_W$. In many cases this is a valid and safe assumption because '...the equality (or similarity) assumption has been proven to be valid for a range of field and vegetation surfaces in various climates.' (Irmak et al. 2014a). There is also a significant practical consideration in this assumption: to reject the equality assumption will complicate the modelling and require the determination of κ_H and κ_W which typically are not known and can be extremely difficult to measure in the field (Irmak et al. 2014a).

2.4.2 Advection and Fetch in BREB

Another common assumption in BREB is that there is no significant horizontal advection[9] (Spittlehouse & Black 1980, Lang et al. 1983a). This is despite advective conditions reportedly being present 75 % of the time (Blad & Rosenberg 1974). Neutral stability atmospheric conditions[10] are generally preferred (and assumed) for BREB but 'the effects of non-neutral conditions on source areas of measurements made at typical BR heights are relatively small' (Stannard 1997, citing Leclerc and Thurtell (1990) and Schmid (1994)).

It is also assumed that the measurement sensors are located within the Internal Boundary Layer (IBL) where fluxes are constant with height (Dyer & Hicks 1970, Heilman et al. 1989, Irmak et al. 2014a). Fritschen (1965) acknowledged that his sensors were at times probably not inside the IBL and thus included horizontal fluxes. The issue of the IBL has spawned a lot of debate about adequate fetch, generally described in terms of fetch-to-height ratios. The generally agreed fetch-to-height ratio is 100:1 (Rosenberg et al. 1983) but some have advocated for ratios as large as 200:1 to 350:1 in stable conditions (Dyer 1965, Leclerc & Thurtell 1990). Fig. 2.4 (p. 33) from Poznikova et al. (2012) suggests that a 90 %

[9] Advection is 'the process of transport of an atmospheric property solely by the mass motion of the atmosphere' (Huschke et al. 1959) ...but has had a more limited meaning of transfer of energy in the horizontal plane in the downwind direction (Blad & Rosenberg 1974).

[10] which, strictly speaking, only occur when $H = 0$, i.e. $\beta = 0$ (Stannard 1997)

'pure' flux sample would be achieved by a 40:1 fetch-to-height ratio in unstable conditions and by a 100:1 ratio in stable conditions (based on a 2 m measurement height and 0.06 m crop height, i.e. grass turf), suggesting that the generally agreed 100:1 ratio is a conservative rule of thumb.

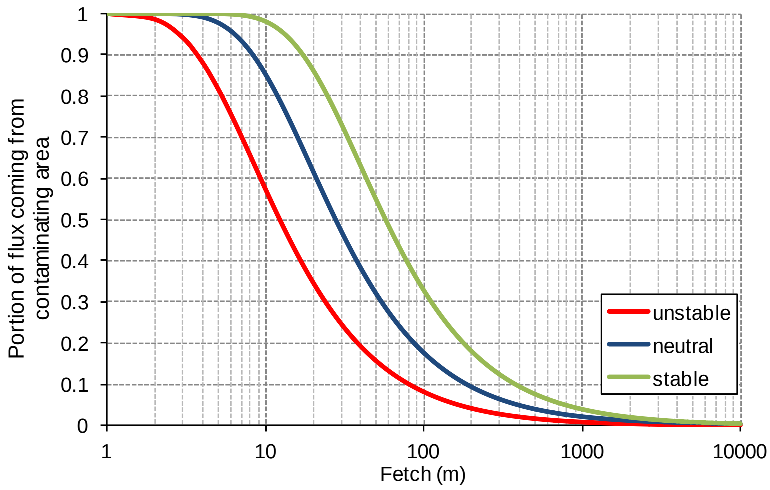

Figure 2.4: Footprint model based on Hsieh et al. (2000) showing the impact of fetch distance and atmospheric stability conditions on the proportion of flux that comes from an upwind 'contaminating' area. Image reproduced from Poznikova et al. (2012).

On the other hand Tanner (1960) did not believe fetch requirements to be critical to BREB; Yeh and Brutsaert (1971) argued that BREB is less sensitive to imperfect fetch conditions than other micrometeorological techniques when β is small; and the findings of Heilman et al. (1989) confirmed the results of Yeh and Brutsaert. Payero et al. (2003) reported that even when the fetch was only 41 % of requirements[11] there was a non-significant impact on BREB's estimates of λE as compared to a lysimeter. Poznikova et al. (2012) studied the applicability of BREB in

[11] An estimate of minimum fetch was calculated by Payero et al. (2003) according to Brutsaert (1982):

$$X_f = \left[\frac{30(Z-d)}{z_{om}^{0.125}}\right]^{1.14} \tag{2.7}$$

fetch limited conditions and disagreed with Hsieh et al. (2000) in Fig. 2.4 (p. 33):

> ...it seems that indeed the fetch to height ratio for BREB method is not so critical and probably lays closer to the values 10:1 - 20:1 given by Panofsky and Townsend (1964) or Heilman et al. (1989) and Stannard (1997) rather than the values 100:1 - 200:1 which are generally more deep-rooted and accepted within the scientific community.

Stannard (1997) noted that two-height BREB appears to have much shorter fetch requirements than EC (in contrast to Schmid (1994) who had argued quite the opposite):

> The primary finding of this work is in contradiction to Schmid's (1994) implication that the effective source area of a BR measurement is about an order of magnitude larger than an EC source area. ...equilibriation of a BR measurement to the surface of interest downwind of the discontinuity is roughly equal to equilibriation of an EC measurement made at the geometric mean of the two BR measurement heights ...[however] the relative advantage (in terms of required fetch) of the BR method over EC decreases as surface roughness increases.

Thus there are contradictory arguments in the literature regarding fetch requirements for BREB. However, there is a sense that the balance of the arguments favours the position that fetch-to-height ratios less than 100:1 are acceptable for BREB (especially under neutral and unstable atmospheres). In the fieldwork reported by this thesis the fetch-to-height

---

where X_f was the minimum fetch distance [m] required to complete boundary layer development, Z was maximum sensor height above the ground [m], d was zero plane displacement [m], and z_{om} was the momentum roughness height of the surface [m]. d and z_{om} can be estimated as 0.63 and 0.13 times the plant height, respectively (Monteith 1973).

ratios varied between approx. 50:1 and 240:1 (depending on wind direction) based on the highest sensors being at 5.2 m.[12]

2.4.3 Accuracy and Error in BREB

The accuracy of BREB has generally been reported against lysimetry or EC but the uncertainty, or margin of error, in BREB's estimates of λE and H has usually not been reported in the literature.

Fritschen (1965) reported BREB-determined λE to be within 5 % of a lysimeter, Tanner et al. (1987) reported λE within 15 % of EC, and Malek et al. (1990) reported that $E_{wbal} = 0.98\, E_{BREB}$ ($R^2 = 0.97$) where E_{wbal} was the evaporation calculated by water balance methods.

Sinclair et al. (1975) reported that the error in β was ± 12.6 % and the error in λE was ± 6.6 %. However, they had assumed that the error in available energy flux, ϕ, was only ± 5 % and that the errors in differential T and humidity were ± 0.01 K and ± 0.03 g m^{-3} respectively (which would be very good even for sensors made 45 years hence). It is not clear where their estimates of sensor errors came from.

Cellier and Olioso (1993) used an early-model capacitive hygrometer (Vaisala HMP35A) in a two-height aspirated BREB system. They excluded any times when available energy flux, ϕ, was less than 50 Wm^{-2} to avoid low T and e gradients. H was reportedly determined to be within 12 Wm^{-2} ($\sigma = 25$ Wm^{-2}) of that determined by EC. It is impressive that they obtained such close agreement with EC because the HMP35A has a relatively poor accuracy[13] of ± 2 % and ± $(0.1 + 0.002|T|)$ ℃ for RH and T, respectively.

Thus BREB has been shown to be capable of providing reasonably accurate estimates of λE. A 'representative opinion is that latent heat

[12]Stannard (1997) argued that the mean sensor height (which would be 3.2 m for the present research) should be used instead of the highest sensor. In that case the fetch-to-height ratios varied between approx. 80:1 and 400:1.

[13]`https://www.manualslib.com/manual/564277/Vaisala-Hmp-35a.html` The temperature sensor has 1/3 DIN Pt100 RTD specifications and the accuracy for T can be determined from Fig. 3.11 (p. 69).

flux can be estimated [by BREB] to within 10 %' (Sinclair et al. 1975, cited in Heilman et al. (1989)).

However, the accuracy of BREB has been shown to worsen under various conditions. Fritschen (1965), McIlroy (1971) and Spittlehouse and Black (1980) showed nighttime to be problematic. This may have been due, in part, to the technological limitations of sensors during the 1960's through 1980's that made it difficult to accurately measure the small T and e gradients that often occur at night. It may also be due to the increased fetch requirements at night when the atmosphere is more stable (Hsieh et al. 2000, Dicken et al. 2013). Cloudy conditions were occasionally reported as a source of error in BREB, but this was mainly due to the large time constants for sensors in the past. For example, Fritschen (1965) reported time constants of 5 min for T and e, and 12 s for R_N, and McIlroy (1971) noted high percentage errors following sharp changes in cloud cover. BREB can also be adversely affected under advective conditions, especially when there is a neutral and stable atmosphere and/or inadequate fetch (Tanner 1960, Slatyer et al. 1961, Blad & Rosenberg 1974, Payero et al. 2003, Escarabajal-Henarejos et al. 2015). Generally an underestimation of λE results when there is strong advection (Hanks et al. 1971, Blad & Rosenberg 1974) and λE can even exceed R_N under advective conditions (Slatyer et al. 1961).

A number of data rejection schemes have thus emerged. Ohmura (1982), Perez et al. (1999), Savage et al. (2009) and Comunian et al. (2018) made recommendations to deal with issues that arise from sensor inaccuracies, especially at times with low T and e gradients. Tanner (1988) and Cellier and Olioso (1993) suggested that a blanket rejection of data where $-1.25 < \beta < -0.75$ should be applied.[14] This can sometimes lead to a large loss of data, e.g. Dicken et al. (2013) discarded 36 % of their data based on this criterion.

[14] This rejection criterion was not applied to the data in the current research. Nevertheless, plots of β in Ch. 4, such as Fig. 4.12 (p. 133), highlight where $-1.25 < \beta < -0.75$.

2.4.4 Sensor Considerations in BREB

Three key considerations highlighted by the literature regarding sensors in BREB systems are:

1. BREB requires accurate measurement of available energy flux, ϕ. Ohmura (1982) noted that 'errors in evaluation of net radiation and subsurface fluxes are accumulated in the evaluation of turbulent fluxes', even if the determination of β was perfectly correct. Spittlehouse and Black (1980) noted that when $-0.6 < \beta < 2$ it is the error in ϕ that is the major contributor to total error in E. Euser et al. (2014) noted that the contribution of relative error in β into the relative error for λE and H is small, especially for $-0.3 < \beta < 0.7$. Sinclair et al. (1975) similarly noted that for $0 < \beta < 0.8$ the contributions of errors in ϕ are more significant than the contribution of error in β. That is, errors in measuring R_N and G may be more significant under low-β conditions than errors in β itself.[15]

2. The sensors used to determine β should ideally be identical and without bias — a technically challenging task (Schellenberg 2002). Remedies for this issue have thus included:

   - Repeatedly exchanging the position of the sensors to cancel out inherent sensor biases (Tanner 1960, Spittlehouse & Black 1980, Irmak 2010); or
   - Aspirating air from inlets at different heights, in an alternating fashion, to a common set of sensors (Sinclair et al. 1975, Tanner et al. 1987, Malek & Bingham 1993, Cellier & Olioso 1993, Wight et al. 1993, Tomlinson 1996, Payero et al. 2003); or
   - Fitting a line-of-best-fit through a multitude of sensors that are arranged in a vertical array or 'profile' (Blad & Rosenberg

[15] The measurement of G can be problematic and consequently the measurement error can be large (and difficult to quantify), as discussed in § 3.2.6, p. 79.

1974, McNeil & Shuttleworth 1975, Sinclair et al. 1975, Olejnik et al. 2001*b*).

Examples of the first two methods are given in Fig. 2.5, (p. 39) and examples of the ‘profile’ method are given in Fig. 2.6 (p. 40).

Another, rather unusual, approach to BREB explored by Euser et al. (2014), van Iersel et al. (2016) and Schilperoort et al. (2017, 2018) was to use a fibre-optic technology called distributed temperature sensing (DTS)[16] to measure very accurate dry- and wet-bulb temperatures in a vertical profile above a crop or forest. This was a very novel approach; however, given the high cost of DTS equipment and the need to maintain a long, moistened, cotton cloth (for wet-bulb measurements) it is hard to see application for this approach to BREB at remote sites or outside of a research context.

3. BREB instrumentation has often been regarded as more robust and reliable than EC instrumentation (Tanner et al. 1987, Cellier & Olioso 1993, Tomlinson 1996) and the trend is toward increasingly accurate and robust capacitive hygrometry and resistance thermometry (Savage 2010, Escarabajal-Henarejos et al. 2015).

2.4.5 Advantages and Disadvantages of BREB

A number of key advantages that the BREB method has relative to other evapotranspiration-modelling methods are identified in the literature:

- BREB is relatively simple (especially with respect to EC) in terms of the underlying theory, required instrumentation, data processing and data corrections, and technical know-how (Blad & Rosenberg 1974, Spittlehouse & Black 1980, Savage 2010, O’Dell et al. 2014, Irmak et al. 2014a, Escarabajal-Henarejos et al. 2015).

- Unlike lysimetry or sap-flow monitoring, BREB does not require alteration of the field or canopy (Fritschen 1965).

[16]e.g. `https://silixa.com/products/ultima-dts/`

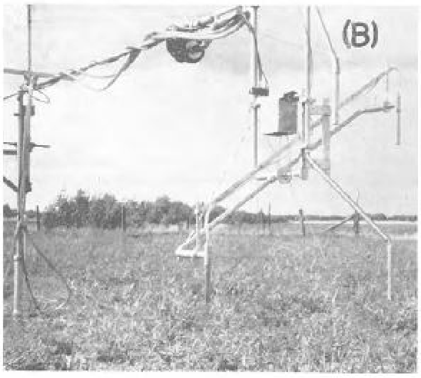

(a) Double psychrometer lift apparatus by Suomi (1957). Image from Tanner (1960).

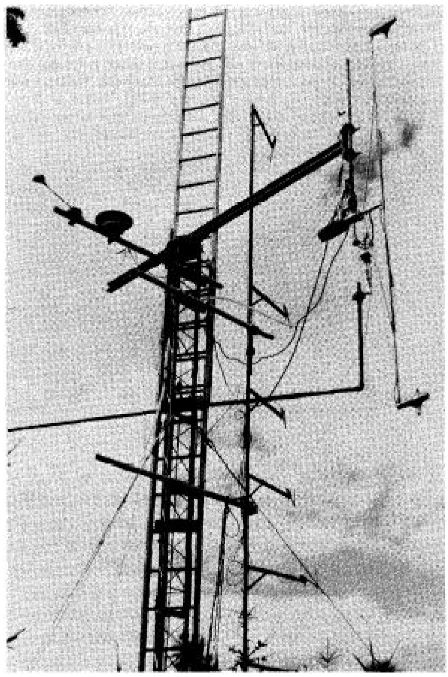

(b) Rotary arm apparatus from Spittlehouse and Black (1980).

(c) Reciprocating linear actuator from O'Dell et al. (2014).

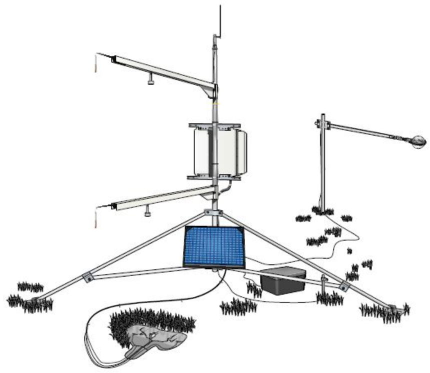

(d) Vacuum aspirated apparatus from Campbell Scientific (2005) which was based on Tanner et al. (1987).

Figure 2.5: Examples of two-height BREB systems.

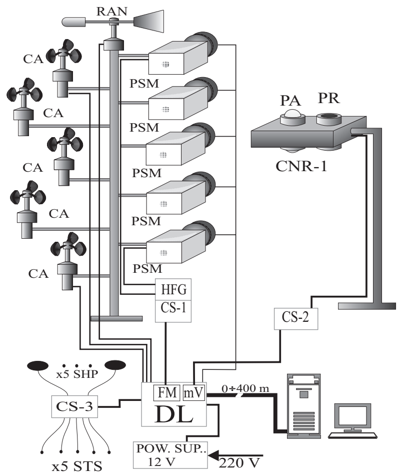

(a) Schematic diagram from Olejnik et al. (2001*a*) showing their Profile BREB setup. DL = data logger, PSM = psychrometer, CNR-1 = net radiometer, CA = cup anemometer, SHP = soil heat flux plates, STS = soil temperature sensors.

(b) Photograph of a 5.5 m tall, five-height Profile BREB system (structure on the right) that was designed and built for the fieldwork in this research.

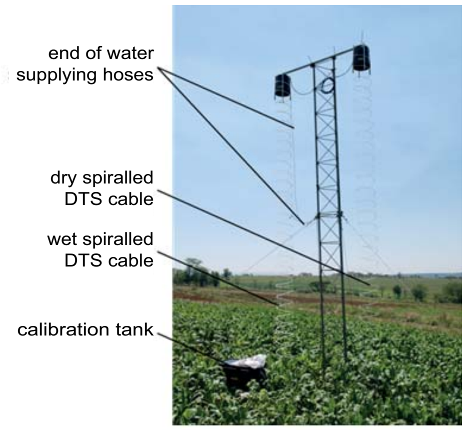

(c) BR-DTS (Bowen Ratio - Distributed Temperature Sensing) system by Euser et al. (2014), effectively a variant of Profile BREB.

Figure 2.6: Examples of Profile BREB systems.

- Fetch-to-height ratios are claimed to be equal to or less than for EC (Stannard 1997).

- BREB instruments can be closer to the top of the canopy than EC instruments (McIlroy 1971, Cellier & Brunet 1992, Stannard 1997).

- Unlike satellite-based RS modelling and water balance methods (e.g. catchment hydrology, isotopic measurements of soil moisture, gravimetric measurements of soil moisture) BREB can provide real-time and continuous records of E (McIlroy 1971). Indeed, as stated by Malek et al. (1990):

  > ...the Bowen ratio energy balance (BREB) method is the most appropriate for continuous measurement of micrometeorological elements and evapotranspiration over extensive homogenous surfaces throughout the season.

- BREB does not require exacting wind profile data unlike classical aerodynamic methods[17] (Fritschen 1965, Cellier & Olioso 1993) or the determination of parameters such as surface roughness, stomatal and aerodynamic resistances, or absolute values of eddy diffusivities[18] (Bowen 1926, Ohmura 1982, Heilman et al. 1989).

- In the BREB method reasonable limits on the values of λE and H are imposed by ϕ (Fritschen 1965), i.e. λE and H are constrained by the requirement that $\lambda E + H \approx \phi$ (in non-advective conditions).

A number of key disadvantages of the BREB method are also identified:

- BREB becomes indeterminate when $R_N + G \to 0$.

- BREB requires accurate determination of ϕ (as noted at Item 1 on p. 37).

[17] e.g. Thornthwaite and Holzman (1942), Brockamp and Wenner (1963), Biscoe et al. (1975)

[18] Provided that diffusivities are assumed to be equal.

- BREB can become difficult to apply when R_N is small, such as at nighttime (Monteith & Unsworth 2013).

- BREB can lose accuracy when temperature and humidity gradients are low. Angus and Watts (1984) argued that

  > ...it is evident that this method cannot accurately determine evapotranspiration rates under very dry conditions ... this degree of accuracy is extremely difficult to achieve under dry conditions if β is determined by dry- and wet-bulb psychrometry.

  Similarly, Spittlehouse and Black (1980) noted that for $\beta > 2$ (i.e. very dry conditions) or under conditions of high turbulent mixing (e.g. over forest canopy and other rough canopies) the temperature and humidity gradients can be very low and would require sensors of high accuracy and resolution or greater distances between sensor heights (constrained by the need for an adequate fetch-to-height ratio). Tomlinson (1996) conceded that EC was useful or even preferred in semi-arid areas with small humidity gradients. (It is significant that these criticisms of BREB under low-gradient conditions were made at a time when psychrometry was the primary method for making field measurements of humidity. Also significant was that these authors used two-height BREB systems with relatively small separation distances between the sensors.)

In summary, BREB is well established and recognised in the literature as a quality micrometeorological method capable of accurate determinations of λE. It has, nonetheless, been largely sidelined in recent decades by EC. As Shuttleworth (2007) put it,

> ...there has been, over the last 15 years, a huge explosion in the use of the eddy correlation method ... [and there is an] "irrational exuberance" to apply the eddy correlation technique.

But BREB continues to be used by a relatively small group of researchers. Its faults and limitations are generally well recognised (and some of those may no longer be relevant as they were due to sensing and logging technologies that have since been superseded). BREB has been shown in the literature as being quite capable of providing quality benchmark evapotranspiration data; in the context of large, irrigated, homogenously cropped agricultural fields within a broader flat topography (i.e. ideal conditions for BREB) and with modern, accurate sensors, all the more so.

2.4.6 The 'Profile' Approach to BREB

The 'two-height' approach to BREB is to repeatedly alternate the position of the sensors measuring e and T between two heights above a surface, thereby cancelling out inherent biases in the sensors. In contrast, the 'profile' approach is to have multiple pairs of temperature and humidity sensors positioned in a vertical array, or 'profile'. Paired (e, T) measurements are then simultaneously made at all heights in the profile. A straight line is fitted through the points $(e_1, T_1), (e_2, T_2), \ldots, (e_n, T_n)$ — e.g. Fig. 2.7 (p. 45) and Fig. 2.9 (p. 49) — the gradient of which can be used to calculate β by Eqn. 3.14 (p. 87).

Using the slope of a line fitted through multiple pairs of measurements helps to mitigate against the impact of erroneous or biased instruments. McNeil and Shuttleworth (1975) stated:

> The profile method uses temperature and humidity measurements at three or more heights . . . The rationale of this method assumes that although each measurement may be subject to systematic errors, over the whole profile these errors can be treated as pseudo–random deviations, and if sufficient sensors are used, a line fitted through the data should have an error less than any pair.

2.4.6.1 Historical Precedence for Profile BREB

Despite being a relatively uncommon approach, Profile BREB systems do have historical precedence. For example, Blad and Roseberg (1974) made Profile measurements at four heights (0 m, 0.25 m, 0.50 m, 1.00 m) above a soybean crop. Sinclair et al. (1975) used a hybrid air-aspirating Profile BREB system[19] at ten heights between 0.1 m and 4.0 m above a corn crop. Lafleur et al. (1992), Olejnik (1996), and Olejnik et al. (2001*b*) made measurements at five heights above forests, lucerne, wheat and sugarbeet crops. Oswald and Rouse (2004) in a pseudo-Profile approach made measurements at three heights above a water surface (0.5 m, 1.2 m, 1.8 m), and Euser et al. (2014) made measurements at thirteen heights above a forest canopy.

2.4.6.2 Advantages of the Profile Approach

There are two key advantages of the 'profile' approach to BREB vis-à-vis the 'two-height' approach.

Firstly, the 'profile' approach allows the researcher to assess whether the sensors were suitably positioned within the IBL. Olejnik et al. (2001*b*) stated:

> A disadvantage of only using two measurement points is that it is not possible to assess how reliable the Bowen ratio values are. In contrast, this is possible by using multiple measurement points in a vertical. [sic] . . . multiple measurements give more insight into the measured profiles and lead to more verifiable results.

It is difficult to determine the upper and lower extents of the IBL with certainty and two-height BREB systems are incapable of verifying that

[19] Their system had a profile of ten air inlets, each with its own temperature sensor. Air was aspirated from each inlet, in turn, to a common infrared gas analyser. A line-of-best-fit was then used on the T vs. e plot (Fig. 2.7, p. 45) as per regular Profile BREB procedure.

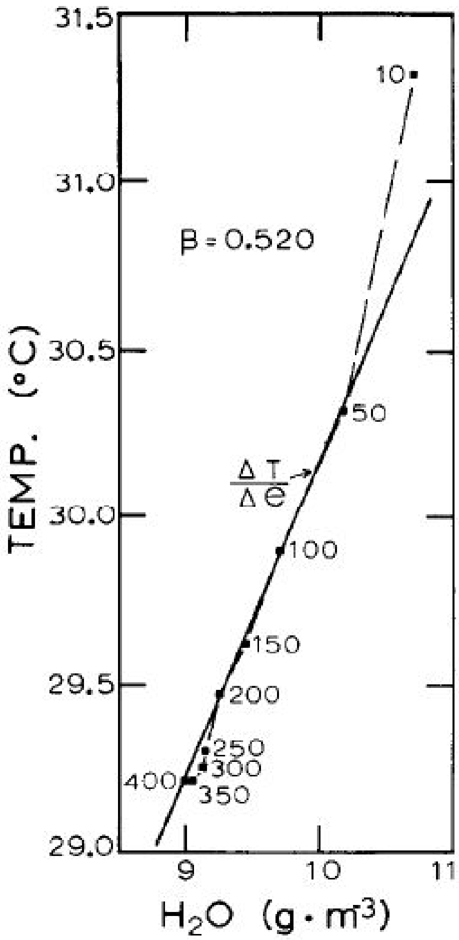

Figure 2.7: Example from Sinclair et al. (1975) of a T vs. e plot for determination of β using the profile method. The labels at each point (10, 50, ..., 400) give the height in centimetres of the sensors. It can be seen that only the sensors between 50 cm and 200 cm lie on the linear portion of the curve and so only those sensors are deemed to be situated inside the IBL.

the sensors are, in fact, within the IBL. Consequently the only recourse that two-height systems have is to

- set the height of the upper sensors so as to not exceed the fetch-to-height requirements[20] (Olejnik et al. 2001*b*); and

[20]Hence the debate over what constitutes an appropriate fetch-to-height ratio (§ 2.4.2, p. 32)

- set the height of the lower sensors so as to not be within the surface roughness layer (Stannard 1997).

Given the uncertainty surrounding the extents of the IBL, there is a tendency when using two-height BREB systems to position the sensors conservatively, i.e. not too low and not too high, guided by rules-of-thumb such as Munro and Ike (1975), Brutsaert (1982) and Payero et al. (2003). However, Cellier and Brunet (1992) noted that the eddy diffusivities κ_H and κ_W were effectively equal in the surface roughness layer between the canopy and the IBL, suggesting that locating the lower sensors very close to the crop may not be as significant a problem after all.

In Profile BREB, however, the lower and upper extents of the IBL can often be identified on a T vs. e plot (if enough measurement heights have been used). This allows the vertical span of the sensors to be maximised. Fig. 2.8 (p.48) is taken from Olejnik et al. (2001*b*) which shows the 40 measured pairs made at five above-ground heights: 0.7 m, 1.3 m, 2.0 m, 3.0 m and 4.0 m. These data have been reproduced into a more familiar T vs. e format in Fig. 2.9 (p.49) where the plotted points going from top-right to bottom-left correspond to increasing measurement height. The fitted line shows the nearly perfect linearity of the T vs. e data except for the point at the lowest measurement height. This suggests that the lowest sensors were probably in the surface roughness layer and should be excluded from calculations of β.

For argument's sake, if Olejnik et al. (2001*b*) had made measurements at only two heights, such as is done by two-height BREB systems, they would have had no way of determining whether the sensors at 0.7 m height were too low (or, for that matter, whether the sensors at 3.0 m and 4.0 m were too high). They would have had to resort to rules-of-thumb to guess the extents of the IBL. Because of the necessarily conservative nature of such rules-of-thumb, they would likely have foregone the opportunity to measure e and T at the 0.7 m position — which is where the temperature and humidity gradients are greatest. Plot (b) in Fig. 2.8 (p. 48) is a good example of how the magnitudes of ${}^{\delta e}/{}_{\delta z}$ and ${}^{\delta T}/{}_{\delta z}$ become larger as you approach the evaporating surface. Thus it is beneficial to measure as close to the evaporating surface as possible.

Fig. 2.7 (p. 45) also provided a striking example of this phenomenon. Sinclair et al. (1975) had made measurements at multiple heights which, when plotted, revealed which measurements were made within the surface roughness layer (below 50 cm) and which measurements were made above the IBL (above 200 cm).

Heilman et al. (1989) noted the need to stay clear of the surface roughness layer (what they termed 'equilibrium sublayer') but, because they were using a two-height BREB system, they had to rely on the following rule-of-thumb to select appropriate heights for their sensors:

$$0.05\, f^{0.8}\, z_0^{0.2} < \delta < f^{0.8}\, z_0^{0.2} \tag{2.8}$$

where δ is the above-crop height of the IBL [m], f is the fetch distance [m] and z_0 is the momentum roughness length [m] of the surface, estimated at 0.13 times the mean canopy height (Tanner & Pelton 1960). This rule-of-thumb for the IBL was based on Brutsaert (1982) and Munro and Ike (1975) and is illustrated in Fig. 2.10 (p. 50).[21]

There is a problem in this process that is demonstrated by an example: according to Eqn. 2.8 (p. 47) a wheat crop with a mean height of 0.7 m and a fetch of 80 m would have an IBL whose lower and upper extents are 1.0 m and 20.6 m above the crop, respectively. Whilst Olejnik et al. (2001*b*) didn't specify the fetch or field size, 0.7 m was the mean height for the wheat crop presented in Fig. 2.8 (p. 48). Yet Fig. 2.8 shows that the measurements at 1.3 m and 2.0 m above ground (i.e. 0.6 m and 1.3 m above the crop) were probably within the IBL, contradicting Eqn. 2.8 (p. 47). Interestingly, the results given in Sinclair et al. (1975) also suggest that it is possible, under some circumstances, for the lower extent of the IBL to go all the way down to the crop surface.[22]

The second key advantage of the 'profile' approach is more practical:

[21] The fetch distances in Fig. 2.10 (p. 50) were only 15 - 80 m.
[22] The results reported in this thesis also suggest likewise.

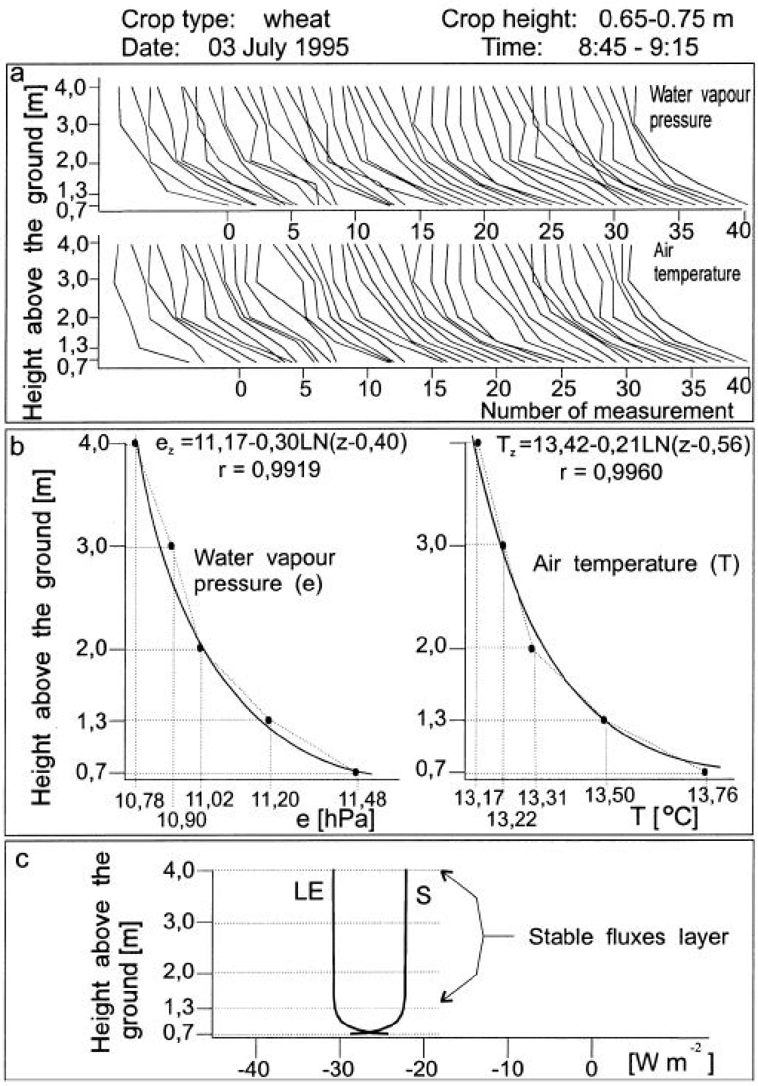

Figure 2.8: Original plots of Profile BREB data from Olejnik et al. (2001*b*). The larger gradients of T and e close to the ground are apparent.

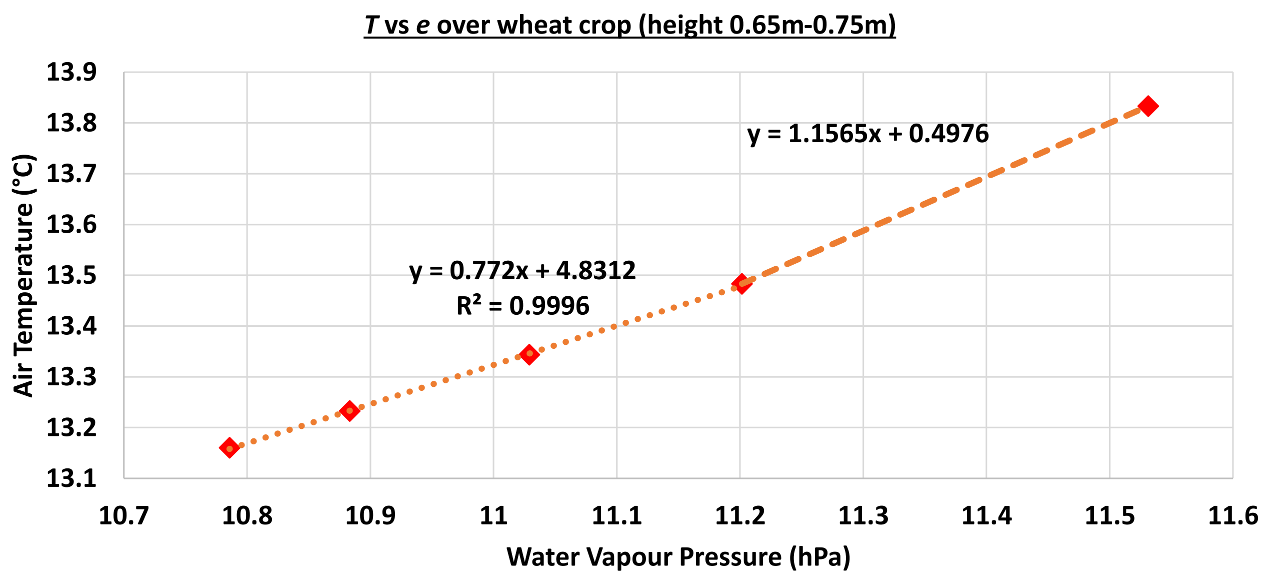

Figure 2.9: Data from Fig. 2.8 (p. 48) that has been re-plotted for this review to show the linear relationship between T and e for the upper four measurement heights. The height of the wheat crop was approx. 0.65 - 0.75 m.

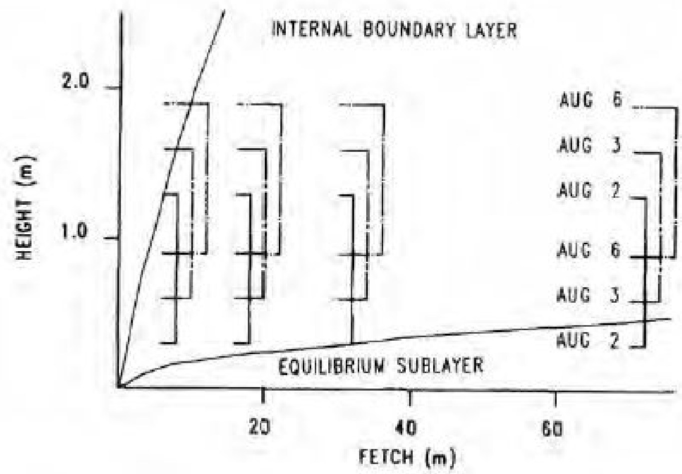

Figure 2.10: Illustration from Heilman et al. (1989) of the relationship between sensor heights for various two-height BREB systems, the internal boundary layer (IBL), and the surface roughness layer ('equilibrium sublayer'). The heights of the IBL and surface roughness layers were estimated using Eqn. 2.8 (p. 47).

sensors at multiple fixed heights require no exchange system, no vacuum pump, and no moving parts. Consequently Profile BREB is mechanically simpler, has lower power consumption, and does not have non-measurement periods after sensors have exchanged position (required for sensors to adjust to their new environment).

Why then, given these advantages, did Profile BREB not grow in popularity as did the two-height approaches to BREB? Several factors were probably responsible:

- Authors such as Spittlehouse and Black (1980) and Angus and Watts (1984) were openly critical of the 'profile' approach. In the former case, the authors modelled the error in β for $\beta > 0.8$ and found it to be 2 - 4 times greater when using Profile BREB than that using two-height BREB under low-gradient conditions over a forest canopy. However, they gave no details as to how their hypothetical Profile BREB system was arranged or how it was modelled. It is also worth pointing out that no actual testing of a Profile BREB system was reported and no explanation as to how they came by their results was given.

- Accurate measurement of vapour pressure in a field environment once required aspirated psychrometry or chilled-mirror instruments. These sensors were expensive, mechanically complex, had significant power requirements and required regular maintenance (Savage 2010, Escarabajal-Henarejos et al. 2015); a vertical array of such instruments was thus a difficult practical undertaking, especially for prolonged remote deployments.

- Two-height BREB systems were popularised by Tanner et al. (1987) and were effectively marketed by Campbell Scientific Pty Ltd.

- EC systems became more affordable and more popular, especially given their ability to operate in a wide variety of natural ecosystems.

2.4.7 Final Remarks for the BREB Review

Profile BREB had a significant and essential role to play in this research. A precise and accurate system was required to serve as a benchmark against which GPSTIC could be evaluated and § 2.4 (pp. 30 - 51) serves to establish that Profile BREB was capable and suitable for this purpose.

However, as reflected in the literature, Profile BREB systems are uncommon. No Profile BREB system was already on hand for this research and there were no suitable commercial offerings to be found. Consequently, the author took the opportunity — building on the ideas and principles reported in this literature review — to develop and construct a new Profile BREB system (§ 3.3, p. 85). There were features in the design of the new Profile BREB system that had significant novelty. Thus while its role in this research was only as a source of benchmark (or 'control') data, the reporting of its development and performance in this thesis might be of interest to some readers and add to the body of knowledge regarding BREB.

2.5 Chapter Conclusion

The STIC model has emerged within the context of two important and related trends: the increasing prominence of RS in the modelling of E, and an increasing focus on larger scale modelling (especially as part of hydrological, hydro-meteorological, water management and climate modelling).

The author has found no independent evaluation of STIC (i.e. without involvement by any of the original authors) in the public literature; furthermore, no application of STIC has been reported outside the RS discipline. These constitute two significant gaps in the literature — the perpetuation of which has possibly been aided by the shift toward large scale modelling of E (to which RS-based tools and processes are naturally suited) and by an apparent lack of awareness of STIC from outside the RS discipline.

It can be reasonably concluded that an evaluation of STIC as a tool for continuous monitoring of crop water use, utilising ground-based sensors (i.e. not remotely sensed), at the field or sub-field scale has not been undertaken. This thesis reports such an undertaking and will help to fill this knowledge gap. It will also provide an entirely independent evaluation of STIC which may be of interest to STIC's current and future users.

Chapter 3

MATERIALS AND METHODS

Two systems – GPSTIC and Profile BREB – were developed for this research (the latter for the purpose of providing benchmark, or 'control', data against which to evaluate GPSTIC). This chapter details the sensors and their configuration, and the algorithms to compute E, that made up each system. Information about the two field sites used is also given here.

Several measures were taken to improve the quality of the comparative evaluation of GPSTIC against Profile BREB:

1. GPSTIC and Profile BREB were always co-located in the field.

2. GPSTIC and Profile BREB determined E for the same instances of time.

3. Measurements of T, RH, R_N, and P — required by both GPSTIC and Profile BREB — were provided by a set of sensors that was common to both systems.

4. The sensors were specifically selected for their high accuracy and precision and their suitability to prolonged field deployment.

5. The field sites were specifically selected to provide ideal conditions for Profile BREB.

Chapter 3 is structured as follows:

The models' algorithms were computed using Scilab[1] v6.1.0 after each period of field data collection was completed.

[1]https://www.scilab.org/

3.1 Descriptions of Field Sites

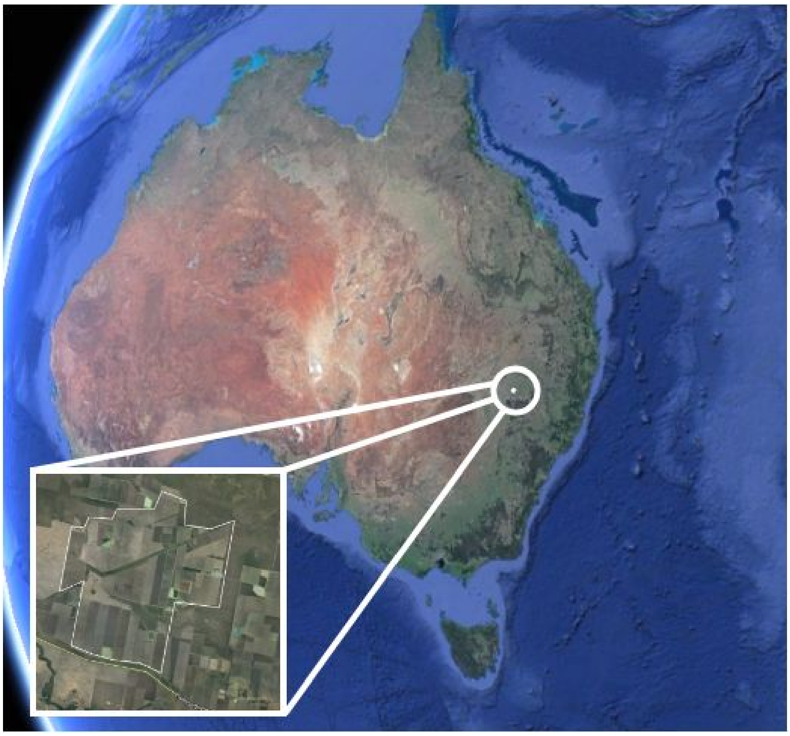

Figure 3.1: Google Earth images showing location of field site in northern New South Wales, Australia.

Two field sites were chosen at a 2200 ha cotton-growing farm that is located near the town of Wee Waa, Australia, which is approx. 600 km Northwest of Sydney and 380 km inland from the ocean (Fig. 3.1, p. 55).[2] Typical field sizes at the farm are 100 ha to 300 ha. The fields are irrigated by furrow irrigation and the historical mean annual rainfall was 575 mm. One of the key factors for selecting this site was its water security: in addition to sourcing water from the local river and from harvesting of on-farm rainfall runoff, it also has a bore capable of supplying 1500 ML $year^{-1}$ which was sufficient to irrigate one or two smaller fields during a drought.

The regional topography was very flat for over a hundred kilometres in

[2]Farm location is 30° 04' 14.41" S, 149° 09' 27.05" E

any direction. The landscape had been extensively cleared of vegetation for cropping; small pockets of native vegetation remained mainly along the river.

The climate at the field site is almost semi-arid. Historically, typical summer daytime temperatures ranged between 25 - 45 °C and summer rain frequently came in the form of short intense cumulonimbus storms; it was not uncommon for one part of a field to receive heavy rainfall and another part to receive nothing at all.

Figure 3.2: Photograph from a drone of the farm, taken in October 2017, showing the flat terrain typical of the region. A farm water storage reservoir reflecting the sun is in the background and partially-filled irrigation channels at left. The walls of the irrigation channels have a maximum height of 1.5 m above the adjacent field.

Two particular fields (Fields 14 and 16) were the sites for data collection. Both fields were large, flat and surrounded by extensive cropped or fallow fields, providing ideal conditions for Profile BREB.

Figure 3.3: Google Earth image of Field 14, with northeast at the top of the image. The field was 600 m wide by 3100 m long. The location of Profile BREB and GPSTIC is indicated by the yellow marker.

3.1.1 Site Description for Field 14

Field 14 (Fig. 3.3, p. 57 and Fig. 3.4, p. 58) was the site of Data Set One (DS1) which was collected during 18^{th} - 25^{th} February, 2019.

Field 14 was 600 m wide (east-west) by 3100 m long (north-south) for a total cropped area of 185 ha. The Profile BREB and GPSTIC equipment were located 280 m in from the nearest edge of the field. Ground elevation was 170 m above sea level. The field had a $^1/_{1000}$ (0.1 %) slope downwards from east to west. Plant rows were 1.0 m apart, oriented east-west, and irrigation water was supplied to every second furrow from a channel at the eastern end of the field. The field received approx. 120 mm of infiltrated irrigation six days prior to DS1.

The farm had a reduced supply of water during the 2018/19 summer season because of the ongoing drought in eastern Australia. Consequently, every third plant row in Field 14 was not planted (Fig. 3.4b, p. 58 and Fig. 3.5, p. 59), sometimes referred to as a 'single-skip configuration'.[3] The cotton crop was 125 days old and had a canopy height of

[3]The agronomic rationale for omitting every third row during planting was that crop water use would be one-third less and so irrigation could be done less frequently, supplemented by rainfall between irrigation events.

(a) Looking north. The white Profile BREB structures are just visible, located one-quarter up from the bottom of the photo, near the centre.

(b) Looking east. The white Profile BREB structures are barely visible, located in line with the vehicle. The 'single-skip' planting configuration is evident from this viewpoint.

Figure 3.4: Photographs from a drone of Field 14 during February 2019.

(a) Looking west down the furrows. The 5.5 m tall white Profile BREB/GP-STIC structure is closest in the photo. The second structure is 6 m beyond and supports two NR01 net radiometers at the end of its horizontal arm.

(b) Looking southwest. The 5.5 m tall white Profile BREB/GPSTIC structure is on the right.

Figure 3.5: Photographs from a drone of the Profile BREB/GPSTIC structures in Field 14 during February 2019.

approx. 1.0 m. The plants appeared healthy with a few flowers emerging, were free of pest pressures, and not demonstrating any signs of water stress.

The soil at Field 14 was classified according to the Australian Soil Classification as a Vertosol (Isbell 2016), presenting as a highly uniform, grey-coloured shrink-swell clay comprising 50 - 60 % clay particles and 25 - 30 % sand particles. The soil had a field capacity of 49 - 51 % volumetric water content (VWC), and was prone to large, deep cracking as it dried. The cracking facilitated rapid infiltration of irrigation water deep into the soil profile.

3.1.2 Site Description for Field 16

Field 16 (Fig. 3.6, p. 61, Fig. 3.7, p. 62 and Fig. 3.8, p. 63) was the site of Data Set Two (DS2) and Data Set Three (DS3) which were collected between the 22nd October and 4th November, 2019, and 31st January and 5th February, 2020, respectively. Field 16 was approx. 1.2 km west of Field 14.

(a) Rotated image of Field 16 with northeast at the top.

(b) Field 16 with overlaid yield map after harvesting in May 2020.

Figure 3.6: Google Earth images of Field 16, the site for Data Set Two (DS2) and Data Set Three (DS3). In each image, the position of Profile BREB/GPSTIC is indicated by the white marker.

(a) Looking northeast. The white Profile BREB structures are just visible near the right edge of the photo.

(b) Looking eastwards down the furrows. The Profile BREB structures are just visible at the centre of the photo.

Figure 3.7: Photographs from a drone of Field 16 during November 2019, two weeks after planting.

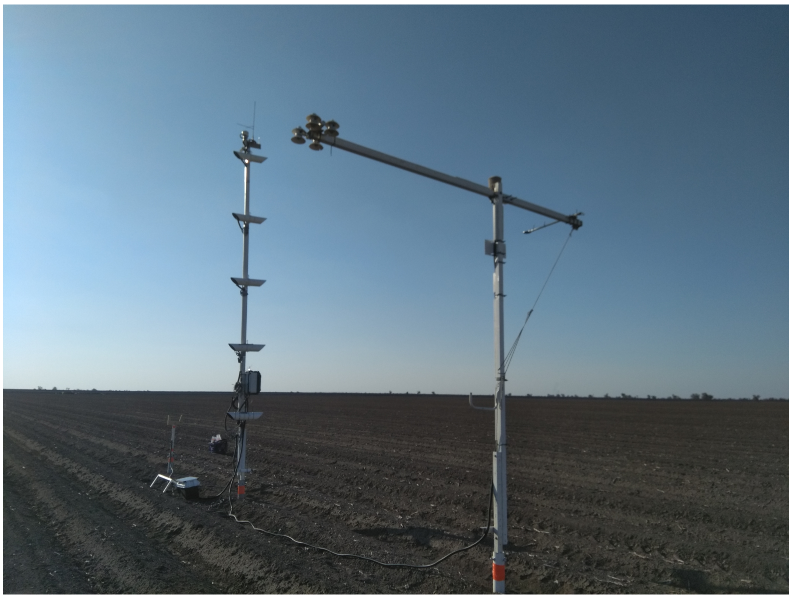

(a) Facing northwest, taken on 22$^{\text{nd}}$ October 2019 after planting was completed but prior to the first irrigation.

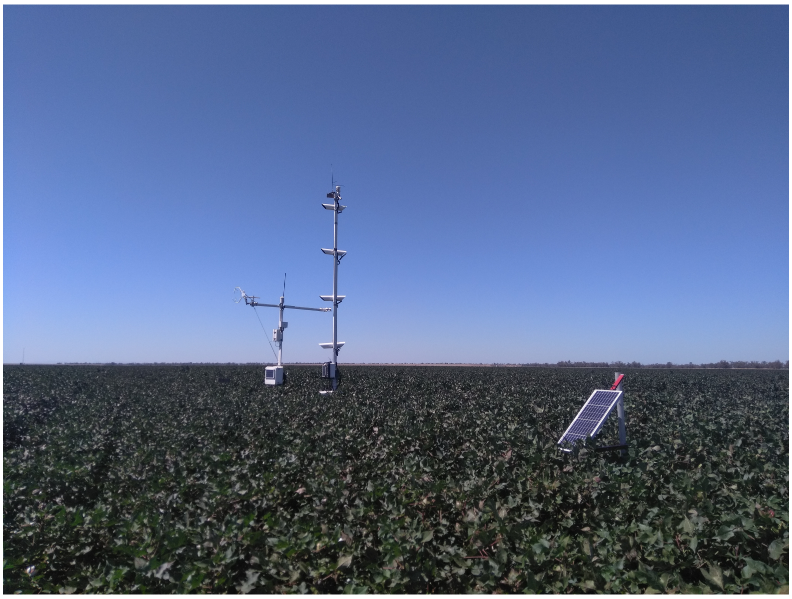

(b) Facing southeast, taken on 5$^{\text{th}}$ February, 2020. A continuous crop canopy was approx. 1.0 - 1.2 m tall and no soil was visible from above. The elevated solar panel was located 20 m away from the Profile BREB/GPSTIC equipment to not interfere with radiation measurements or disrupt air flows.

Figure 3.8: Photographs of Field 16 at different stages during the 2019/20 summer season.

Field 16 was 640 m wide (east-west) by 2000 m long (north-south), for a total cropped area of 118 ha. The Profile BREB/GPSTIC structures were located 260 m in from the nearest edge of the field. The field had a $^1/_{1000}$ (0.1 %) slope downwards from east to west. Plant rows were 1.0 m apart, oriented east-west, and irrigation water was supplied to every second furrow from a channel at the eastern end of the field. The crop was irrigated regularly by furrow irrigation throughout the season, and the final irrigation occurred on 2nd February, 2020, which was during DS3.

A cotton crop had been planted in every row on the 21st October. Field 16 was bare, cultivated soil at the start of DS2 and by the end of DS2 the newly emerged seedlings were several centimetres tall. The field was pre-irrigated during September and the field was again irrigated on the 23rd October (two days after planting).

At the start of DS3 the crop was 100 days old and had formed a continuous canopy of approx. 1.0 - 1.2 m height (which was an unusually tall cotton crop for this farm).

There were no pest pressures during DS2 and DS3. Regular rain through the latter half of the season (after DS3) delayed picking and the yield at Field 16 was mostly in the range of 13.7 - 15.3 bales ha^{-1} (Fig. 3.6b, p. 61). This yield was slightly higher than the regional average.

The soil type and the surrounding landscape at Field 16 were the same as that of Field 14.

Figure 3.9: Looking east at Field 16, from the tail end of the field, on 23$^{\text{rd}}$ October, 2019, one day after planting. Irrigation water advancing down the furrows was being met by water backing up from the tail drain. Also visible on the horizon is the smoke from distant bushfires.

3.2 Sensors

All data required by the Profile BREB and GPSTIC models to calculate E were measured by sensors at the field sites, i.e. there were no remotely-sensed data.

Profile BREB required the following twelve sensors:

1. Pt100 resistance thermometer detectors (RTD) $\times 5$
2. capacitive hygrometers $\times 5$
3. barometer $\times 1$
4. net radiometer $\times 1$

GPSTIC required the following five sensors:

1. Pt100 resistance thermometer detector (RTD) $\times 1$
2. capacitive hygrometer $\times 1$
3. barometer $\times 1$
4. net radiometer $\times 1$
5. infrared radiometer (IRR) $\times 1$

The first four sensors listed for GPSTIC were, by design, the very same sensors used for Profile BREB. The commonality of sensors allowed a fair comparison of the two models to be made.

Wind and rainfall data were also collected although these were not actually required by either model. These data were used only to provide some context for the modelling conditions.

The Profile BREB and GPSTIC systems of sensors were controlled and logged by the same data logger.

Table 3.1 (p. 67) provides a summary of all of the sensors; further details on each sensor are provided in the subsequent sections.

Table 3.1: Sensors used for Profile BREB and GPSTIC. Website links for each of the sensors are provided in § 3.2.1 - § 3.2.8 (pp. 68 - 83).

Sensor	Brand & Model	Measurand	Accuracy	Qty
Pt100 RTD[a]	TC Measurement & Control 4-wire Pt100 1/10 DIN Class B	T [°C]	$\pm(0.03 + 0.0005\,\lvert T\rvert)$°C ($\alpha = 0.003\,85\,°\mathrm{C}^{-1}$)	5
Capacitive hygrometer	Michell Hygrosmart HS3 w/ Modbus RS485 output	RH [%]	$\pm\,0.8\,\%\,RH$ (between 5 - 95 % RH)	5
Barometer	Tekbox TBSHTP04 w/ SDI-12 output	P [hPa]	± 1 hPa (between 300 - 1100 hPa)	1
Infrared radiometer[b]	Apogee SI-411 w/ SDI-12 output	T_S [°C]	± 0.12°C (between -30 °C to 65 °C)	1
Net radiometer	Hukseflux NR01	$SW_{downwelling}$ [Wm^{-2}] $LW_{downwelling}$ [Wm^{-2}] $SW_{upwelling}$ [Wm^{-2}] $LW_{upwelling}$ [Wm^{-2}]	SW (0.285 - 3.0 µm): ± 3% LW (4.5 - 40.0 µm): ± 8% $T_{internal}$: $\pm(0.15 + 0.002\,\lvert T\rvert)$ °C	1[c]
2D sonic anemometer	Decagon (Meter) DS2 w/ SDI-12 output	W_{speed} [m s^{-1}] W_{dir} [degrees]	W_{speed}: ± 0.3 m s^{-1} W_{dir}: ± 3°	1

[a] Resistance Thermometer Detector, also known as a Resistance Temperature Detector, Resistive Temperature Device, or a Platinum Resistance Thermometer (PRT).
[b] Only GPSTIC required an infrared radiometer (IRR).
[c] One NR01 net radiometer was shared by Profile BREB and GPSTIC. A second NR01 net radiometer was also used as a backup.

3.2.1 Ambient Temperature

Accurate measurements of ambient temperature, T, were required for Profile BREB and GPSTIC. The sensor selected was a 4-wire Pt100 $^1/_{10}$ DIN Class B EN RTD[4] with $\alpha = 0.003\,85\,°\mathrm{C}^{-1}$ (Fig. 3.10, p. 68), manufactured by TC Measurement & Control[5] in Victoria, Australia.

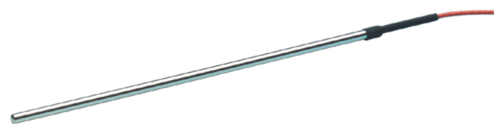

Figure 3.10: Photograph (from `www.tcdirect.net.au`) of the precision 4-wire Pt100 $^1/_{10}$ DIN Class B EN RTD.

According to IEC 60751 the guaranteed manufacturing tolerance (for temperature) of these RTDs is no greater than $(0.03 + 0.0005\,|T|)\,°\mathrm{C}$ (Fig. 3.11, p. 69). A factory 3-point calibration (Fig. C.8, p. 354) at 0 °C, 30 °C and 60 °C found the RTDs had an error up to 0.02 °C across the full temperature range, traceable to ITS-90 (UKAS) standards, i.e. well within the acceptable tolerance. Summer daytime temperatures at the field sites were typically around 30 - 40 °C. Under these conditions the RTDs were expected to have a 2σ measurement uncertainty of ± 0.045 °C to ± 0.050 °C.

Five RTDs were used for Profile BREB; one of those five (the one closest to the crop) was also used for GPSTIC. All of the RTDs were housed inside radiation shields (§ 3.3.2.2, p. 91), each one adjacent to a capacitive hygrometer. The RTDs were 200 mm long and 6 mm diameter (only the final 20 mm contained the sensing components). This diameter was chosen over the thinner 3 mm option for mechanical robustness; the resultant slower response time due to increased thermal inertia was not

[4]Depending on the source, RTD is an acronym for Resistance Thermometer Detector or a Resistive Temperature Device. It may also be referred to as a Platinum Resistance Thermometer (PRT).

[5]`https://www.tcdirect.net.au/`

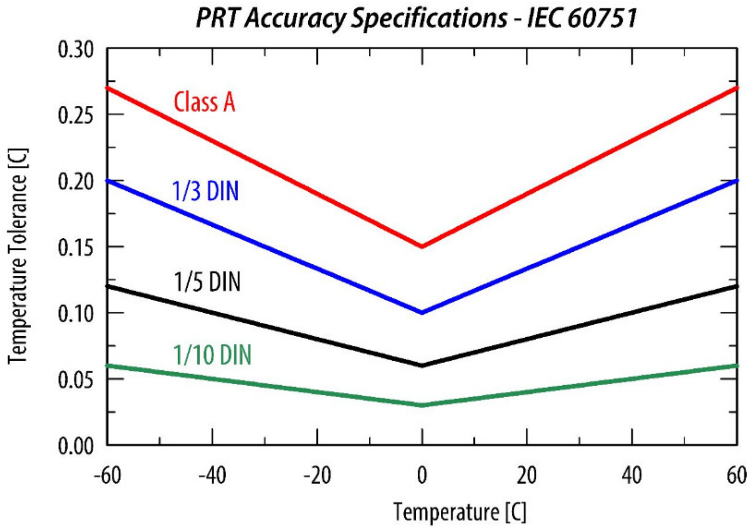

Figure 3.11: IEC 60751 accuracy specifications for RTDs (PRTs), (`https://www.iec.ch/`). The RTDs used for this research were $^1/_{10}$ DIN instruments.

significant for Profile BREB and GPSTIC because measurements of T were only required every 60 s.

RTDs were preferred over thermocouples, thermistors and IC sensors because RTDs are more accurate and more stable. According to Omega (2019):

> …the 4-wire bridge design fully compensates for all resistance found in the lead wires and the connectors between them. A 4-wire RTD configuration is primarily used in laboratories and other settings where great accuracy is necessary.

Whilst self-heating can sometimes be an issue for RTDs it was not the case in this research as each RTD had current going through it for only several milliseconds per minute.

3.2.2 Relative Humidity and Vapour Pressure

Accurate measurements of water vapour pressure, e, were required for Profile BREB. GPSTIC required measurements of RH. Vapour pressure, however, was not measured directly. Rather, it was derived from RH and T according to

$$e = e^* \left(\frac{RH}{100}\right) \tag{3.1}$$

where e^* is the saturation vapour pressure [hPa] per Buck (1981, 1996):

$$e^* = 6.1121 \ \exp\left[\left(18.678 - \frac{T}{234.5}\right)\left(\frac{T}{257.14 + T}\right)\right] \tag{3.2}$$

where T was accurately measured by the RTD sensors.

The Michell Hygrosmart HS3[6] capacitive hygrometer (Fig. 3.12, p. 71) was the sensor selected to measure RH because of its excellent accuracy. This was stated by the manufacturer to be $\pm\,0.8\,\%\,RH$ although the factory-provided calibration certificates (Figs. C.3 - C.7, pp. 349 - 353) showed all HS3 sensors to be better than $\pm\,0.6\,\%\ RH$.[7]

Five HS3 sensors were used to determine e for Profile BREB, and one of those HS3's (the one closest to the crop) was also used to measure RH for GPSTIC. All of the HS3s were housed inside the radiation shields, each one adjacent to a RTD.

The HS3 had a measurement response time of approx. 1 s and communicated using the Modbus RTU protocol with RS485 connection, allowing all five sensors to be powered and communicate on a common multi-core

[6] `http://www.michell.com/uk/products/hygrosmart_hs3_probe.htm`

[7] By contrast, the well regarded Vaisala HMP155 (`https://www.vaisala.com/sites/default/files/documents/HMP155-Datasheet-B210752EN.pdf`) has a stated accuracy (δRH) of

$$\delta RH = \begin{cases} \pm\,(1.0 + 0.008 \times \text{reading})\,\%\,RH & -40 \leq T \leq 40\,^\circ\text{C} \\ \pm\,(1.2 + 0.012 \times \text{reading})\,\%\,RH & 40 \leq T \leq 60\,^\circ\text{C} \end{cases} \tag{3.3}$$

Thus if conditions were 35 °C and 40 % RH, such as often was the case at the field sites in this study, an HMP155 would have an expected accuracy of $\pm\,1.3\,\%\ RH$.

cable. (The HS3 could be used with either analog or digital communications. Despite being slower, the latter was preferred because it avoided problems with varying electrical resistance in the cables as they heated and cooled in the field environment.) The HS3 was also a cost effective solution for accurate humidity measurement.

(a) Michell HS3 capacitive hygrometer. Image from `www.michell.com`

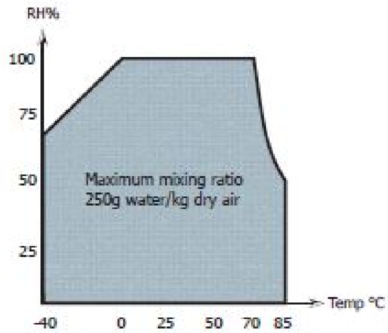

(b) Acceptable operating conditions for Michell HS3 capacitive hygrometer. Image from Michell Instruments (2017).

Figure 3.12: The Michell Hygrosmart HS3 capacitive hygrometer was used to measure RH with high accuracy, i.e. better than $\pm\,0.8\,\%\,RH$.

3.2.3 Barometric Pressure

Barometric pressure, P, was measured using a TekBox TBSHTP04 barometer with SDI-12 output (Fig. 3.13, p. 72). Measurements of P were required for calculation of the psychrometric constant, γ [hPa °C^{-1}], by the following equation:

$$\gamma = \frac{c_P\, P}{M_{ratio}\, \lambda} \tag{3.4}$$

where c_P is the specific heat of air (taken to be a constant 1010 J kg^{-1}K^{-1}), P is the barometric pressure in hPa, M_{ratio} is the molecular mass ratio of water vapour to dry air (taken to be 0.622) and λ, in J kg^{-1}, is the latent heat of vapourisation when $-5 < T < 45$ °C given by:

$$\lambda \approx 1000\left(2500.9 - 2.4007\,T + 0.0007\,T^2\right) \tag{3.5}$$

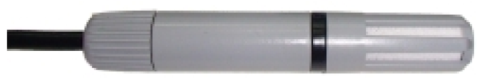

Figure 3.13: Photograph of a Tekbox TBSHTP04 digital sensor (from `www.tekbox.com`) which was used to measure barometric pressure with an accuracy of ± 1 hPa.

The TBSHTP04 has a stated accuracy of ± 1 hPa over the range 300 - 1100 hPa. (Other measurands provided by this instrument, T and RH, were not used in the modelling as they did not have the accuracy of the RTD and HS3 sensors.) The sensor was housed inside the logger's enclosure, which was vented to the surrounding environment, at 1.6 m above the ground.

3.2.4 Radiometric Surface Temperature

Measurements of the surface temperature, T_S, of the soil and plant canopy were required for GPSTIC (not Profile BREB). The sensor selected was the Apogee SI-411 Infrared Radiometer (IRR) with SDI-12 digital output (Fig. 3.14, p. 73). This sensor was mounted at the top of the Profile BREB mast, i.e. 5.5 m above the ground, and was oriented so that it pointed down 45° below the horizontal and at a bearing of 45° (i.e. northeast). The area of ground visible to the IRR was 57 m^2 (calculated in Appendix D, p. 357).

(a) Photograph from `https://www.apogeeinstruments.com/`.

(b) Photograph from a drone, taken February 2019, of the IRR visible just above the top radiation shield of the Profile BREB mast.

Figure 3.14: The Apogee SI-411 digital infrared radiometer (IRR) was used to measure the surface temperatures of soil and plant canopy for GPSTIC.

The Apogee SI-411 IRR had been designed specifically for measuring terrestrial temperatures. A germanium filter was fitted (by the manufacturer) to limit the sensor's spectral window to 8 - 14 µm so as to minimise interference by atmospheric water vapour and CO_2 that occur outside of this spectral window (Fig. 3.15, p. 74). Whilst terrestrial surfaces emit radiation wavelengths between 4 - 50 µm, the proportion of terrestrial radiation that is within the 8 - 14 µm wavelengths is sufficiently large that errors from the omission are small (Apogee 2018).

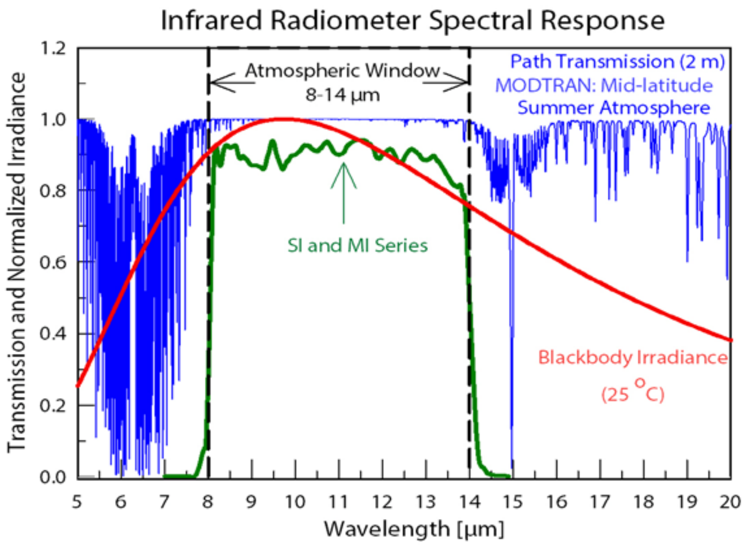

Figure 3.15: Spectral window of Apogee SI-411 infrared radiometer. Image from `https://www.apogeeinstruments.com/content/SI-400-manual.pdf`.

The SI-411 sensor's 2σ measurement uncertainty inside the temperature range of −30 °C to 65 °C was certified to be ± 0.12 °C with a maximum absolute error of 0.179 °C (Fig. C.1, p. 347) which is very good for radiometric temperature sensing.

3.2.4.1 Emissivity Considerations

The value of emissivity, ϵ, set by the factory for the SI-411 is 0.96 as this is suitable for many plants. For soil, however, ϵ can sometimes be lower and inaccurate measurements of T_S may result if soil constitutes a large proportion of the sensor's field of view.

A more accurate T_S can be calculated if a surface-specific value for ϵ is known and if the background temperature, $T_{background}$, is known (when outdoors, the sky is usually the background).[8] A correction (Apogee 2018) to the measured T_S can then be calculated by

$$(T_S)_{corrected} = \left[\frac{{T_S}^4 - (1-\epsilon)\,{T_{background}}^4}{\epsilon}\right]^{\frac{1}{4}} \tag{3.6}$$

where all temperature variables are in Kelvin. This correction, however, quickly becomes impractical when surface-specific values for ϵ are not known or if the SI-411's field of view is a composite of plant canopy and soil (each with different values for ϵ). A soil's ϵ may even change temporally based on its moisture content (Sánchez et al. 2011, Tian et al. 2019). Furthermore, the background temperature must be measured with the same waveband as is used to measure the target surface. For all these reasons, no corrections were made in this research to the SI-411's standard measurement of T_S.

T_S can also be calculated using the downward-facing pyrgeometer of the Hukseflux NR01 net radiometer by

$$T_S = \left(\frac{LW_{upwelling}}{\epsilon\,\sigma}\right)^{\frac{1}{4}} - 273.15 \qquad [^\circ\mathrm{C}] \tag{3.7}$$

where the Stefan-Boltzmann constant, σ, is $5.6704 \times 10^{-8}\,\mathrm{Wm^{-2}K^{-4}}$. It is probable, however, that using the NR01's pyrgeometer (i.e. the IR01 sensor) to measure T_S will produce slightly different results to the SI-411. The IR01 has a considerably larger infrared spectral window (4.5 - 40 µm) than the SI-411 and is not designed to exclude emitted radiation by water vapour and CO_2. The IR01 is designed to be oriented straight down and has a very wide field of view (with greatest sensitivity to the ground directly beneath it), whereas the SI-411 tends to be at an oblique

[8] $T_{background}$ is required because the measured radiation is the sum of the surface's emitted longwave radiation and the reflected longwave radiation from the background. If $\epsilon_{target} = 0.96$ then this implies that 4 % of T_S is not due to the target's temperature itself but what has originated from the environment and been reflected off the target.

orientation and equally sensitive across its full field of view. Because the SI-411 was expressly designed to measure terrestrial temperatures, it was used as the primary source for T_S; the IR01 was a backup in case the SI-411 malfunctioned (which it did not).

The bearing of the SI-411 was not overly significant because the SI-411 measures emitted and reflected longwave radiation, not reflected shortwave radiation. The small zenith angle of the midday sun meant that a north-facing IRR had only slightly more shade in its field-of-view than a south-facing IRR (in the Southern Hemisphere). Furthermore, the shaded ground/canopy only occupied a small proportion of the IRR's field of view.

GPSTIC did not require a 'two-source' partitioning of the surface temperature into its soil and crop components. A composite T_S was sufficient.

3.2.5 Net Radiation

Accurate measurements of net radiation, R_N, were required for Profile BREB and GPSTIC. The sensor used was the Hukseflux NR01 four-component net radiometer (Fig. 3.16, p. 77).

Four-component net radiometers such as the NR01 are widely used because they offer a good compromise between the less costly, less accurate two-component or single-component net radiometers and the more accurate, more costly Secondary Standard or First Class sensors (Blonquist et al. 2009, Vignola et al. 2016). Hukseflux cites World Meteorological Organisation (1983) estimates of achievable measurement uncertainty for the NR01 at ± 5 % for daily totals of R_N, although the origin of this figure is unknown and probably only applies under favourable conditions when the shortwave components are dominant (Hukseflux 2017).[9]

Measurements of global horizontal irradiance by the NR01's pair of

[9]Michel et al. (2008) could not achieve daily R_N uncertainties below 10 % with an unheated and unventilated Kipp & Zonen CNR1 four-component net radiometer, which is comparable to the NR01.

(a) Photograph from `www.hukseflux.com`. The pyrgeometers are at left and the pyranometers at right.

(b) Photograph from a drone, taken February 2019, of two NR01 net radiometers suspended 2.0 m above the canopy.

Figure 3.16: Hukseflux NR01 four-component net radiometer, used for measuring net radiation for Profile BREB and GPSTIC.

Second Class SR01 pyranometers[10] are reported to have a measurement uncertainty of ± 6.2 % for daily totals and ± 8.4 % for minutely totals at mid-latitudes during the summer; uncertainty worsens in winter and closer to the poles (Hukseflux 2017). Hukseflux states that these values are for best-case scenarios when the NR01 is maintained in accordance with ASTM G183-15 (ASTM International 2015) and that individual device performance can vary. The NR01 net radiometer calibrated for this research (serial #1830) was reported to have a 2σ pyranometer measurement uncertainty of ± 3 % (Fig. C.2, p. 348).

The NR01 also has a pair of identical pyrgeometers, model IR01, for measuring $LW_{downwelling}$ and $LW_{upwelling}$. There is no ISO or WMO classification for pyrgeometers equivalent to that for pyranometers and there is no formal process for evaluating the uncertainty of measurements. Hukseflux cites a calibration uncertainty of approximately ± 7 % for its

[10]ISO-9060:1990 classifies pyranometers (in descending order of performance) as 'Secondary Standard', 'First Class', then 'Second Class'.

upfacing pyrgeometers, and a 'far larger' uncertainty for its downfacing pyrgeometers (Hukseflux 2017). The internal temperature of each pyrgeometer is measured by a Pt100 IEC 60751 Class A RTD (Fig. 3.11, p. 69). The NR01 net radiometer calibrated for this research (serial #1830) was reported to have a 2σ pyrgeometer measurement uncertainty of ± 8 %.

The pyranometers in the NR01 have a 180° field of view and cover the spectral range of 0.285 - 3.00 µm (the full range of the shortwave spectrum is 0.100 - 3.00 µm). The pyrgeometers in the IR01 have a 150° field of view and cover the spectral range of 4.5 - 40 µm (the full range of the longwave spectrum is 4.0 - 50 µm). The pyrgeometers' reduced field of view is because the required interference filter is better deposited on a flat surface than on a convex surface (Vignola et al. 2016). Because of the wide fields of view it is necessary that the NR01 is located as far as practically possible from the supporting ground structures.

In fact, two NR01 net radiometers (serial #1830 and serial #1236) were deployed to the field sites in this research. However, #1236 was only intended to be used as a backup. The two net radiometers were positioned side-by-side at the end of a 2.5 m horizontal arm, suspended 3.0 m above the ground, on a secondary mast that was 6.0 m away from the Profile BREB mast (Fig. 3.16b, p. 77). The net radiometers were levelled using their built-in bubble level (which was viewed by standing on a ladder). The analogue signal outputs from both net radiometers were measured and recorded by the same data logger.

3.2.6 Soil Heat Flux

Available energy flux, ϕ, is a variable required by both the GPSTIC and Profile BREB algorithms. ϕ is calculated by

$$\phi = R_N + G \qquad [\mathrm{Wm}^{-2}] \tag{3.8}$$

where G is an estimate of soil heat flux. (It is also common to see ϕ defined as $\phi = R_N - G$. However, Eqn. 3.8 is consistent with the sign convention described in § 0.3, p. xxxiii.)

A recommended process for estimating G is to bury soil heat flux plates (such as the Hukseflux HFP01SC), soil moisture sensors and soil temperature sensors into the soil as illustrated in Fig. 3.17 (p. 79).

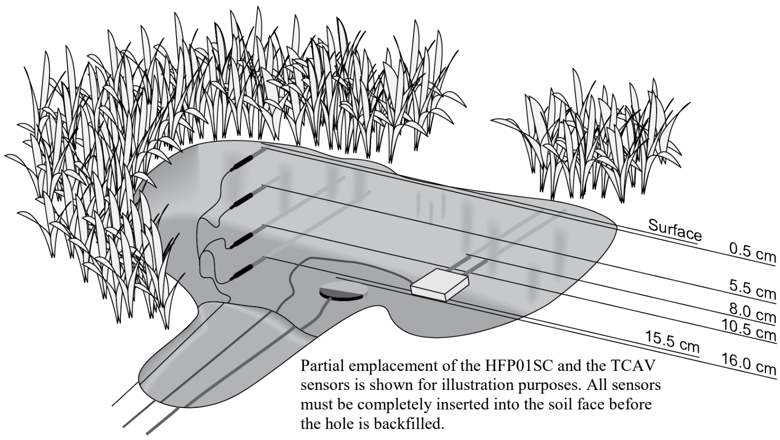

Figure 3.17: Recommended placement of soil heat flux plates (HFPS01SC), soil moisture sensor, and averaging soil thermocouples (TCAV). Image from `https://s.campbellsci.com/documents/us/manuals/hfp01sc.pdf`.

After measuring these sensors G can then be estimated per Hukseflux (2016):

$$c_v = \rho_{ds}\, c_{ds} + \rho_{water}\, c_{water}\, \theta \tag{3.9}$$

$$\Delta Q = c_v\, d_{shf}\, \frac{(T_{soil})_{t_2} - (T_{soil})_{t_1}}{t_2 - t_1} \tag{3.10}$$

$$G = G_{0.16\,\mathrm{m}} + \Delta Q \tag{3.11}$$

where c_v is the volumetric heat capacity of the soil [$\mathrm{J\,m^{-3}\,K^{-1}}$], ρ_{ds} is the soil's dry density [$\mathrm{kg\,m^{-3}}$], c_{ds} is the soil's dry volumetric heat capacity [$\mathrm{J\,m^{-3}\,K^{-1}}$], ρ_{water} is the density of water [$\mathrm{kg\,m^{-3}}$], c_{water} is the volumetric heat capacity of water [$\mathrm{J\,m^{-3}\,K^{-1}}$], θ is volumetric water content [$\mathrm{m^3\,m^{-3}}$], ΔQ is the change in soil heat flux [$\mathrm{Wm^{-2}}$], d_{shf} is the depth to the soil heat flux plate [m], $(T_{soil})_{t_1}$ and $(T_{soil})_{t_2}$ are the soil temperatures [°C] at times t_1 and t_2, and $G_{0.16\,\mathrm{m}}$ is the heat flux [$\mathrm{Wm^{-2}}$] through the soil heat flux plate buried at 0.16 m depth.

The description of G as an 'estimate' is appropriate. Besides the difficulty of accurately measuring $G_{0.16\,\mathrm{m}}$ (Ochsner et al. 2006), especially in cracking clay soils, the variable c_{ds} must typically be estimated from tables (it is otherwise a difficult quantity to measure in the field) (Savage 2009). Determining c_{ds} from a table is also problematic because it is known to not only vary from one soil to another but also as a function of moisture content and density. For example, Yadaz and Saxena (1973) and Abu-Hamdeh (2003) found c_{ds} to vary between $1.5 \times 10^6\,\mathrm{J\,m^{-3}\,K^{-1}}$ and $3.5 \times 10^6\,\mathrm{J\,m^{-3}\,K^{-1}}$ for clay soils. Even ρ_{ds}, d_{shf} and θ are difficult to accurately measure near the surface of shrink-swell clay soils.

ΔQ should not be ignored when calculating G. Tanner and Pelton (1960) claimed its magnitude can be up to 15 % of R_N and Hukseflux (2016) claimed that up to 50 % of G can be attributed to ΔQ. Mean soil temperatures generally do not change by large amounts from day to day but ΔQ may account for a large portion of R_N at any one time during the day, particularly under short and sparse vegetation (Hillel 1971).

Furthermore, there can be a time lag in the order of 20 min between changes in environmental conditions at the surface and subsequent changes in Q. The response time for Q increases, approximately, in proportion to the square of the depth between the surface and the soil heat flux sensors (Hukseflux 2016). The time lag introduces further error especially when above-surface environmental conditions are changing rapidly.

All of these factors are problematic in themselves. During the current research there was the additional difficulty that there were also ongoing soil cultivation activities in Field 14 and Field 16 (for weed control).

The Profile BREB and GPSTIC equipment, including the masts, had to be removed from the field for each soil cultivation. This made it impractical to have heat flux plates, soil thermometers, moisture sensors, and associated cabling buried in the field ...especially at the sorts of depths detailed by Fig. 3.17 (p. 79).

Consequently, the use of the simplified procedure by Allen et al. (1998) to estimate G, i.e.

$$G \approx \begin{cases} -0.1|R_n| & \text{at daytime} \\ 0.5|R_n| & \text{at nighttime} \end{cases} \tag{3.12}$$

was adopted in this research. This was not only justifiable but even preferable given the high likelihood of cultivation implements damaging buried sensors and cables. It was deemed to be nighttime when $SW_{downwelling} \leq 0\,\mathrm{Wm}^{-2}$.[11]

An important mitigating factor regarding the impact of using Eqn. 3.12 (instead of Eqns. 3.9 - 3.11) on the comparative performance of GPSTIC and Profile BREB in this research is that the very same values of ϕ were used as inputs to each of the GPSTIC *and* Profile BREB models. Thus while an erroneous estimate of G will affect the absolute outputs of GPSTIC and Profile BREB, there will be a much smaller impact on the output of GPSTIC *relative to* the output of Profile BREB.

[11] A more sophisticated approach, such as tapering G between day and night, was not warranted because the simplified procedure in Eqn. 3.12 was already an approximation.

3.2.7 Wind and Rain

Measurements of wind and rain were not required by either Profile BREB or GPSTIC, per se. However, they helped to provide context for the modelling results.

Horizontal wind speed and direction were measured at the top of the Profile BREB mast, i.e. at a height of 5.5 m, by a Decagon (Meter) DS2 two-dimensional sonic anemometer[12] with SDI-12 output (Fig. 3.18, p. 82).

Rainfall was measured by a Davis tipping-bucket raingauge (0.2 mm/tip resolution) adjacent to Field 14, mounted on a star picket 1.2 m above the ground. The rainfall data were logged as part of a wireless raingauge network on the farm.

(a) Photograph from www.metergroup.com

(b) Photograph from a drone, taken February 2019, at Field 14. The DS2 is at the top of the mast.

Figure 3.18: Decagon DS2 two-dimensional sonic anemometer.

[12] http://library.metergroup.com/Manuals/14586_DS2_Web.pdf

3.2.8 Data Logging

A DataTaker DT85M Series 4 programmable data logger (Fig. 3.19, p. 84) was used to control, measure and log all sensors used by Profile BREB and GPSTIC. No real-time computing of the Profile BREB or GPSTIC algorithms was done by the logger; all computing was done at a later date using Scilab.

The logger could measure and log at 40 Hz, had 18 bit analogue-to-digital resolution, low power demand, and an integrated 3G cellular modem (with an external high gain antenna). The logger included 48 analogue input channels (expandable to 960 analogue inputs), and 12 bi-directional digital channels supporting Modbus and SDI-12 sensors. The large number of analogue input channels was necessary because the two NR01 net radiometers each required 12 analogue channels (since they did not require heating) and the five 4-wire RTDs each required 4 analogue channels. That is, 44 of the 48 analogue channels were used in addition to SDI-12 and Modbus channels.

The logger was externally powered from a 12 V deep-cycle battery sitting at the base of the Profile BREB structure. The battery's charge was maintained by a 20 W solar panel (which was located approx. 20 m away from the Profile BREB structure) and a Victron MPPT solar regulator.[13] The logger was housed inside a weather-proof enclosure that was actively vented (during the daytime) to the environment using an extractor fan.

The logger was new and had been recently calibrated by the manufacturer (Fig. C.9, p. 355).

[13] `https://www.victronenergy.com.au/solar-charge-controllers/mppt7510`

Figure 3.19: Photograph of a DataTaker DT85M Series 4 data logger, shared by the GPSTIC and Profile BREB systems. (Image is from https://media.lontek.com.au/uploads/pages/datataker/DT85M-Series4.pdf.)

3.3 Profile BREB System

In this research the benchmark evapotranspiration data against which GPSTIC was evaluated was provided by a 'Profile BREB' system. § 2.4 (p. 30) and Appendix A (p. 331) provide a background to the BREB method.

Several factors were significant in the decision to use a Profile BREB system in this research (rather than an EC system). Foremost among these was that an EC system was not available for use for this research. However, even if an EC system had been available, there were several practical reasons why a Profile BREB system would still have been preferred for this particular research:

1. The farm's manager stated a requirement that any in-field equipment could be removed from the field by farm workers if so required (since the author lived 550 km from the field site). This was because there were ongoing inter-row soil cultivation and crop spraying activities at the field sites, whose scheduling was subject to change. Removal of the Profile BREB system was quite straightforward since it could be carried into and out of the field by a single person without very little disassembly required. Removal of an EC system would, by contrast, require considerable disassembly – a relatively complex and time consuming task which would be inappropriate to expect of the farm's workers.

2. The electrical power requirement of the Profile BREB system was approx. 590 times smaller than that of the EC system (4.4 kJ each day vs. 2592 kJ each day, respectively). The Profile BREB system had a maximum power draw of approx. 1.5 W while the sensors were being actively measured, which occurred for approx. 1 s each minute. Between measurements, the quiescent power draw of the Profile BREB system was a constant 50 mW. In contrast the EC system had a continuous power draw of approx. 30 W. The lower power requirement of the Profile BREB system was a significant

practical advantage given that the power had to come from a solar–battery system at the centre of a large, furrow-irrigated cropping field.

3. The purchase price of an EC system was high (approx. $60000AUD). The full cost of a Profile BREB system was approx. $9000AUD (including the $5000 logger and the power supply).

Furthermore, in this research the fields were large, flat, and homogenously cropped with extensive fetch in all directions, i.e. ideal conditions for Profile BREB.

There were also several reasons for custom developing a Profile BREB system instead of using the more common two-height design of Tanner et al. (1987), produced by Campbell Scientific (CS) and shown in Fig. 2.5d (p. 39).

1. A CS two-height air-aspirated BREB system was not available during this research and the purchase price was prohibitive.

2. The air intakes for the CS two-height air-aspirated system had a relatively small vertical separation (compared to the full span of a Profile BREB system). This meant that modelling uncertainty due to sensor error can be a greater issue, particularly at times when temperature and/or humidity gradients are very low, e.g. around dawn and dusk.

3. The CS BREB system had to continually aspirate air using a vacuum pump, which meant that the electrical power requirement of the system was greater than Profile BREB.

4. There was a risk that condensation could form and accumulate inside either of the two unheated air aspiration tubes, two mixing chambers, or single measurement chamber. This is more likely to occur when temperatures fall below dewpoint and would invalidate vapour pressure measurements. On clear-sky nights there is an additional risk that condensation can form on the CS BREB system's

exposed thermocouples due to radiative heat transfer to the cold night sky.

5. The CS BREB system required relatively long ‘quiet’ periods after switching the air inlets during which no measurements could be taken. Given the 5 min time constant of the system (Tanner et al. 1987), 15 min of quiet period is required before making measurements to ensure that the measurement chamber has achieved at least 95 % equalisation with the outside ambient conditions (see Fig. A.1, p. 337).

3.3.1 Method for Profile BREB

The ‘two-height’ approach to BREB is to repeatedly alternate the sensors measuring e and T between two heights above a surface, thereby cancelling out inherent biases in the sensors. In contrast, the ‘profile’ approach is to have a vertical array, or ‘profile’, of sensors to simultaneously measure e and T. A straight line-of-best-fit (LoBF) is fitted through $(e_1, T_1), (e_2, T_2), \ldots, (e_n, T_n)$, e.g. Fig. 2.7 (p. 45) and Fig. 4.55 (p. 186). The gradient, a_1, of the LoBF can be calculated following Taylor (1997):

$$a_1 = \frac{n \sum e_i T_i - \sum e_i \sum T_i}{n \sum {e_i}^2 - \left(\sum e_i\right)^2} \tag{3.13}$$

where n is the number of heights that (e, T) were measured at. Then the Bowen ratio, β, can be calculated by

$$\beta = \frac{c_P \, P}{M_{ratio} \, \lambda \left(\overline{T}\right)} \, a_1 \tag{3.14}$$

where c_P is the specific heat capacity of air [J kg^{-1} K^{-1}], P is the barometric pressure [hPa],[14] M_{ratio} is ratio of molecular masses of water vapour to dry air (taken to be 0.622), $\overline{T}$ is the mean air temperature across the

[14]Barometric pressure normally has units of Pa or kPa. hPa are used here because e was measured in hPa and thus a_1 had units of °C hPa^{-1}.

profile [°C], and $\lambda\left(\overline{T}\right)$ is the latent heat of vapourisation of water at the mean air temperature [J kg^{-1}].

A minimum of three measurement heights is needed for Profile BREB but the quality of the estimate of β improves as the number of measurement heights increases. Fig. 2.7 (p. 45), for example, shows a line fitted by Sinclair et al. (1975) through nine pairs of (e, T). In this research five measurement heights were used.

Profile BREB obviates the need to alternate the positions of sensors. This reduces the mechanical complexity of the system and also allows measurements to be made more frequently than 'two-height' BREB systems because there is no need for the sensors to equilibriate to their new environment after exchange.

3.3.2 Physical Design of the Profile BREB System

Profile BREB consisted of a primary mast that supported a vertical array of precision temperature and humidity sensors, as well as a secondary mast that suspended a net radiometer out over the crop (Fig. 3.20, p. 89 and Fig. 3.21, p. 90).

Profile BREB had a relatively simple physical design with low power requirements, no moving parts and was quite robust (surviving wind speeds up to 127 km h^{-1} during the development phases, i.e. before DS1). The farm at which the field sites were located was not a research facility; consequently it was necessary that Profile BREB would be of minimal interference to the ongoing agronomic and machinery activities at the site and could be easily removed from the field as required.

3.3.2.1 Masts

The masts were constructed of 50 mm×50 mm aluminium square hollow section. They were painted gloss white and had white cable duct affixed to their southern faces to protect the sensors' cables from solar radiation and from wildlife.

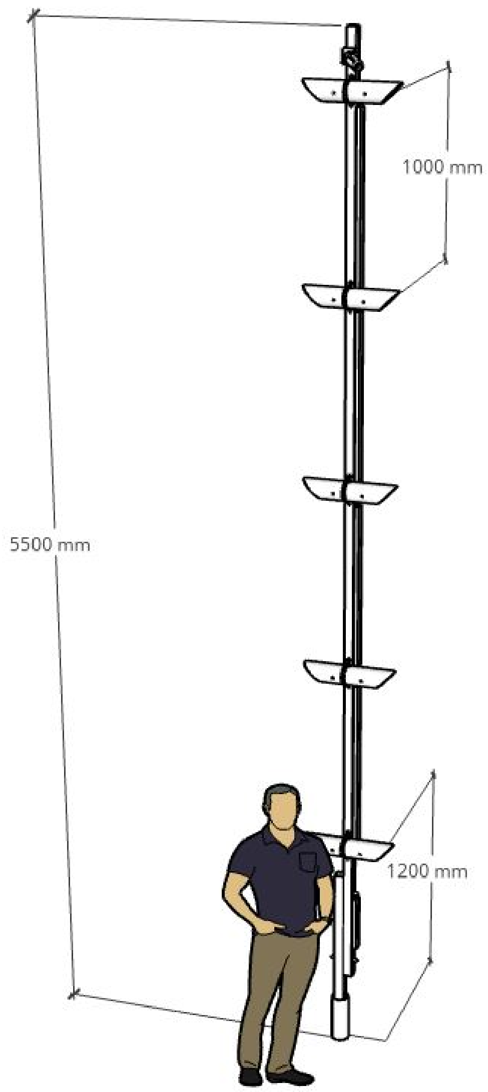

Figure 3.20: Design sketch, drawn to scale, of the Profile BREB mast showing the five radiation shields. The GPSTIC's IRR is also mounted near the top of the mast. Not shown in this sketch are the two-dimensional sonic anemometer (mounted at the top of the mast) or the data logger (mounted between the lowest two radiation shields). The net radiometer was mounted on a separate mast (not shown).

Figure 3.21: Photograph from a drone of the 5.5 m tall Profile BREB operating in the field. Radiation shields and sensors were at five heights, spaced 1.0 m apart. The logger was between the two lowest radiation shields and the two-dimensional sonic anemometer was at the top of the tall mast. On the shorter mast the net radiometers were mounted at the end of the horizontal arm at 3.0 m above the ground. The deep-cycle battery was at the base of the tall mast and the solar panel was 20 m away (out of photo).

The bottom of each mast was supported by a groundscrew[15] which was installed in the plant line. The primary mast was 5.5 m tall and had an omni-directional 7.5 dBi 3G antenna protruding from the top to permit data telemetry in this remote location. The secondary mast, located 6.0 m away, was 3.0 m tall with a 2.5 m long horizontal arm that supported the two NR01 net radiometers at approx. 2.0 m above the crop.

3.3.2.2 Radiation Shields

The primary mast supported a vertical array of five radiation shields (Fig. 3.22, p. 92 and Fig. 3.23, p. 93) for Profile BREB. GPSTIC also used the sensors in the lowest of these radiation shields. The shields were positioned at 1.2 m, 2.2 m, 3.2 m, 4.2 m and 5.2 m above the ground (labelled 'A' to 'E', respectively, in the algorithm in § 3.3.3, p. 95). The height of the lowest shield (1.2 m) was set so that it would be just above a fully grown cotton canopy.

The five radiation shields were custom designed and built for this research. Essential in their design was that they provided protection from direct, reflected and emitted radiation whilst ensuring that air freely exchanged with the surrounding environment even in relatively calm conditions. It was also important that heating of the radiation shield itself was minimised so that it would not become a net source of longwave radiation to the sensors.[16]

The shields were made of two concentric PVC tubes in horizontal alignment (referred to as 'Double Concentric Horizontal Alignment', or DCHA, shields).[17] The inner and outer tubes were each painted gloss white on the outer surface and matt black on the inner surface. The ends

[15] https://www.krinner.io/en/products/detail/g-89x1000-4xm12/

[16] Some non-aspirated multi-plate or stacked-plate type shields can experience elevated internal temperatures under relatively calm conditions, especially when constructed out of materials that have high thermal conductivity or low specific heat capacity such as steel or aluminium (Nakamura & Mahrt 2005, Erell et al. 2005, Tarara & Hoheisel 2007, Huwald et al. 2009).

[17] Tarara and Hoheisel (2007) also reported on the use of horizontal tubes for radiation shields, finding their performance to be comparable to commercial 'Gill' stacked-plate shields.

Figure 3.22: Photographs (not at the field site) of the radiation shields, end view. The sensor cables were on the south side of the mast and inside white cable duct to protect them from direct sun.

of the outer tube were cut at 45° to ensure that no direct solar radiation reached the inner surfaces or the sensors.[18] The 80 mm diameter inner tube was fixed in position with pieces of wooden dowel and there was a 10 mm air gap between the two tubes.

Solar heating of the radiation shield was managed in three ways.

- PVC material was selected because its thermal conductivity is approx. 0.092 $\mathrm{Wm^{-1}K^{-1}}$ which is over 2500 times less thermally conductive than aluminium, and its specific heat capacity of 840 - 1170 $\mathrm{J\,kg^{-1}K^{-1}}$ is either equal to or greater than aluminium and is at least twice that of steel (Jones 2013). Wooden dowel was used to fix the inner tube in position instead of steel stand-offs because the thermal conductivity of wooden dowel is over 50 times less than steel.[19]

[18] The site lattitude was 30° 04' 14.41" S. From October through to February the sun's altitude was approx. 75 - 80° at solar noon.

[19] The thermal conductivity of wooden dowel is approx. 0.3 $\mathrm{Wm^{-1}K^{-1}}$ and steel is approx. 16 - 50 $\mathrm{Wm^{-1}K^{-1}}$

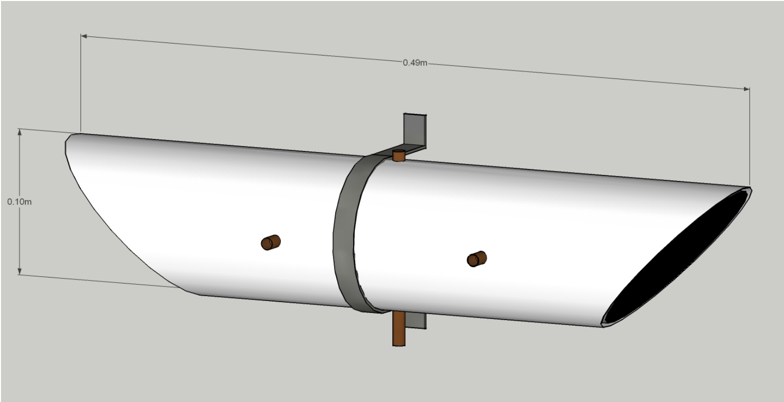

(a) Opaque view.

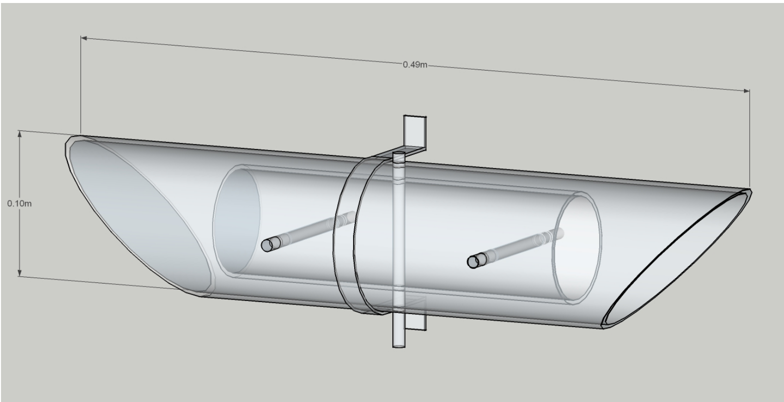

(b) 'X-ray' view.

Figure 3.23: Design sketches of the radiation shields. The outer tube had a diameter of 100 mm and a length of 450 mm along its top surface. The inner tube had a diameter of 80 mm and a length of 200 mm. The inner tube was fixed in position by vertical and horizontal pieces of wooden dowel.

- The external gloss-white paint was considered to have a high (but unknown) reflectivity and emissivity while the internal matt black paint was considered to have a low reflectivity. These helped to maximise reflection and emission of radiation from outer surfaces and minimise reflection of radiation from interior surfaces back onto the sensors.

- The radiation shields were oriented with their openings in a north-south direction. This prevented direct solar radiation from entering the tubes early and late in the day when the sun's altitude was low.

Air could move freely through the radiation shields, including around the sensors and through the space between the two concentric tubes. The sensors were tied (using plastic cable ties) onto the horizontal pieces of dowel inside the inner tube. They were not in contact with any other surface and the sensing tips were well in from the mouth of the tubes.

3.3.2.3 Sensor Installation and Configuration

Inside each radiation shield was a 4-wire Pt100 RTD and a capacitive hygrometer. The sensors' cables ran down the south face of the mast, inside white cable duct, to minimise the direct radiation load on them from the sun.

Profile BREB had twelve essential sensors: five RTDs, five capacitive hygrometers, a net radiometer[20] and a barometer (Table 3.1, p. 67). The barometer was housed inside the logger box (which was open to the atmosphere), the net radiometer was mounted on a secondary mast, and a RTD + hygrometer combination was inside each of the radiation shields. Every sensor was logged once every 60 s.

Measurements from a two-dimensional sonic anemometer, mounted at the top of the 5.5 m mast, were also logged every 60 s. These were not required measurements for either Profile BREB or GPSTIC but helped to give context for the modelling.

Power for the sensors and data logger was provided by a 20 W solar panel, MPPT regulator, and deep cycle battery. (The power system was well over-specified in case of prolonged overcast weather.) The solar panel was positioned approx. 20 m away from the masts so that it wouldn't interfere with air flows around the Profile BREB vertical array or with measurements of net radiation.

[20] In fact, two NR01 net radiometers were used side-by-side, for redundancy.

3.3.3 An Algorithm for Profile BREB

The procedure to determine β and λE using Profile BREB was essentially very simple: simultaneously measure T and e at each of five heights above the soil or crop, and find the slope of the linear regression line through a plot of T vs. e in order to calculate β and λE (§ 3.3.1, p. 87).

The Profile BREB algorithm is detailed step-by-step in § 3.3.3.2 and the flow diagram in Fig. 3.24 (pp. 97 - 98). First, however, the LoBF (sub)algorithm, which is an important part of Profile BREB, is described.

3.3.3.1 The LoBF Sub-Algorithm within Profile BREB

Profile BREB included within its computational algorithm a sub-procedure (the 'LoBF sub-algorithm') to assess whether (e, T) data points should be excluded from the linear regression line (whose slope was used to calculate the Bowen ratio β). The reason why some (e, T) data points needed to be excluded from the regression was usually because (a) the respective sensors were below the lower extents of the IBL, or (b) the respective sensors were above the upper extents of the IBL.[21] This situation could change depending on the atmospheric stability regime.

The question that needed to be answered was whether, on a two-dimensional T vs. e plot, a particular (e, T) data point was too far out of line with the others. As an example, Fig. 3.26 (p. 104) shows an instance where the (e, T) data points at heights 'A' and 'E' (i.e. the lowest and highest sensors, respectively) were both clearly out of line with heights 'B', 'C' and 'D'.

The idea behind the LoBF sub-algorithm was to recognise that there was an uncertainty in the plotted position of each of the five (e, T) data points, best represented by a two-dimensional ellipse (Cook & Weisberg 1994, Taylor 1997). Because of the sensors' inherent measurement uncer-

[21] This accounted for the vast majority of instances when (e, T) data points were out of line. Very occasionally, however, the profile was all jumbled up, as though a violent gust of wind had smashed through and temporarily mixed up the atmospheric profile. Such (rare) instances were removed from the Data Set because β could not be reliably calculated.

tainties there was a 95 % chance that the true position of a given (e, T) data point was somewhere within the ellipse. The LoBF sub-algorithm then started by first fitting a regression line through the middle three points ('B', 'C' and 'D'). When this line was extended in each direction, it was checked if it also intersected with either of the ellipses at 'A' and 'E'. If so, the regression line would be recalculated to also include the additional point(s), e.g. Fig. 3.25 (p. 103).

As far as the author is aware, this research was the first time that an automated process for inspecting profiles of (e, T) data points (using 2σ ellipses based upon sensors' inherent measurement uncertainties) had been included in a BREB system. The fact that the process could be automated as a sub-algorithm within the Profile BREB algorithm allowed a numerical 'examination' of thousands of profiles of data points to be undertaken efficiently using a computer program.

The LoBF sub-algorithm was computed at Steps 5 - 8 (pp. 99 - 100) in the Profile BREB algorithm for every 4 min interval of (averaged) data.

3.3.3.2 Computing E_{BREB}

This Profile BREB algorithm to compute E_{BREB} was repeated every 60 s:

1. Measure and log ambient temperature, T [°C], and relative humidity, RH [%], at each of the five heights ('A' ... 'E'). Also measure net radiation, R_N [Wm^{-2}], and barometric pressure, P [hPa].

2. Every 4 min calculate the 4 min averages for T, RH, R_N and P. These averaged values are used in subsequent calculations.

3. Calculate actual vapour pressure, e [hPa], by the Buck Equation (Buck 1981, 1996)[22]:

$$e^* = 6.1121 \exp\left[\left(18.678 - \frac{T}{234.5}\right)\left(\frac{T}{257.14 + T}\right)\right] \tag{3.15}$$

[22] Over the limited temperature range of $0 < T < 50$ °C the Buck equation is more accurate than that of Tetens (1930) – used, e.g., in FAO56 (Allen et al. 1998) – which was itself a refinement of the August-Roche-Magnus formula (Lawrence 2005).

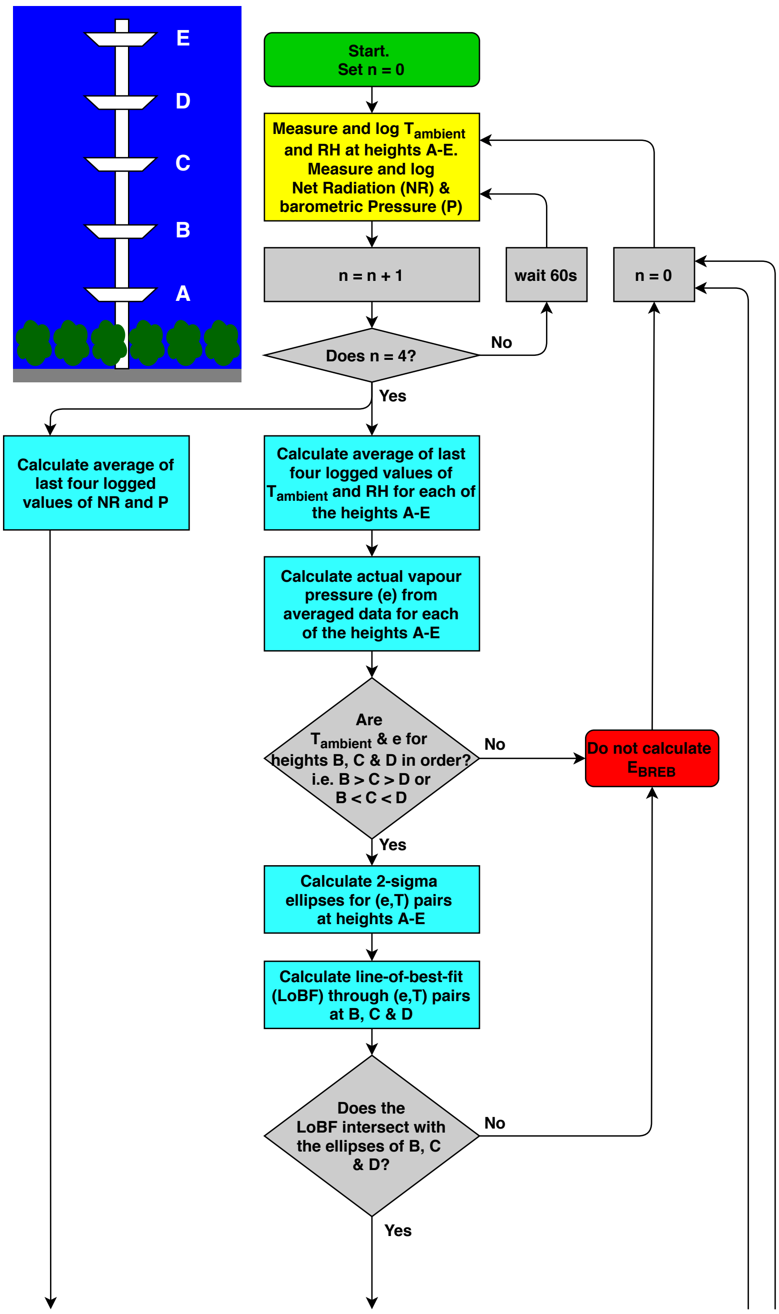

Figure 3.24: Flow diagram of the algorithm to compute Profile BREB (continued on following page).

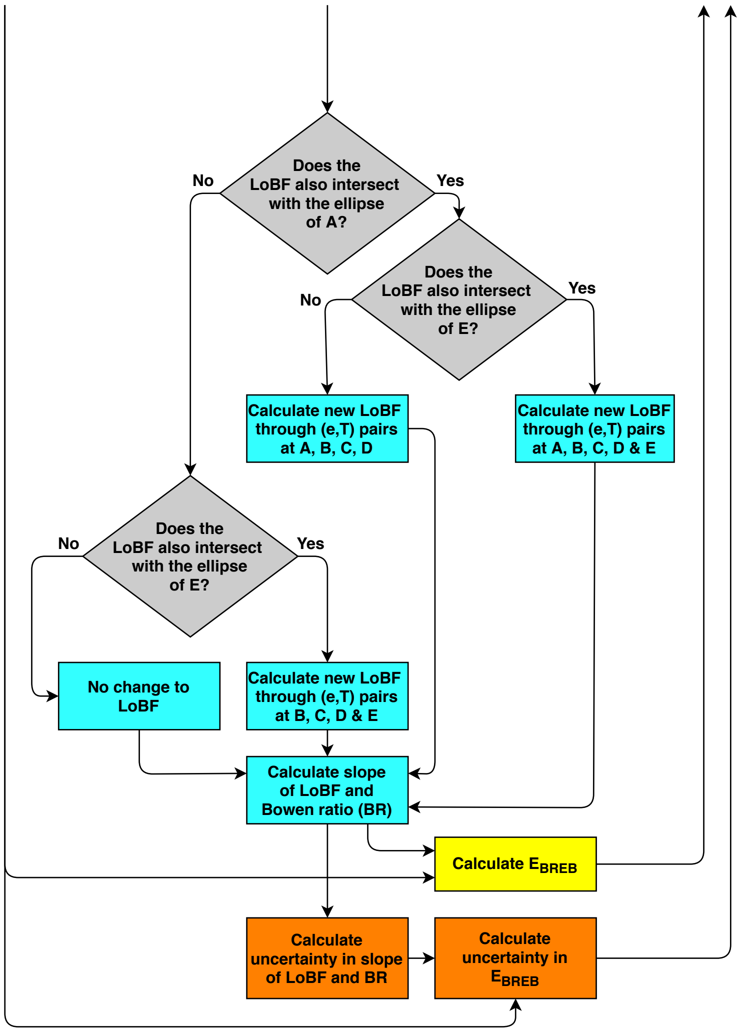

Figure 3.24: Flow diagram of the algorithm to compute Profile BREB (continuing from previous page).

$$e = e^* \left(\frac{RH}{100} \right) \tag{3.16}$$

where e^* is the saturation vapour pressure [hPa]. exp[·] denotes the natural exponential function to avoid confusion with e which denotes vapour pressure.

4. Check if T and e are in sequential order for the points (e_B, T_B), (e_C, T_C) and (e_D, T_D), i.e.

$$\begin{aligned} &T_B > T_C > T_D \qquad \text{or} \\ &T_B < T_C < T_D \end{aligned} \tag{3.17}$$

and

$$\begin{aligned} &e_B > e_C > e_D \qquad \text{or} \\ &e_B < e_C < e_D \end{aligned} \tag{3.18}$$

If they are not in sequential order (a rare occurrence) the Profile BREB computations cease at this point and the data is flagged for exclusion from subsequent analysis.

5. Calculate a 2σ confidence ellipse[23] for each of the $(e_A, T_A) \ldots (e_E, T_E)$ points by solving:

$$1 = \frac{(e - e_i)^2}{(\delta e)^2} + \frac{(T - T_i)^2}{(\delta T_i)^2} \tag{3.19}$$

where $i = A \ldots E$, $\delta e = \pm 0.8$ [%] and $\delta T_i = 0.03 \pm 0.0005|T_i|$ [°C] (Table 3.1, p. 67). Examples of such confidence ellipses can be seen in Fig. 3.25 (p. 103) and Fig. 3.26 (p. 104).

6. Calculate a straight Line of Best Fit (LoBF) through the points

[23] A 2σ confidence ellipse is the two-dimensional analogue to the one-dimensional 2σ confidence interval. The combination of uncertainties in two independent measurements (in this case, e and T) means that, on a two-dimensional plot of T vs. e, the 2σ uncertainty in the position of a point (e, T) is defined not by a rectangle but by an ellipse (Cook & Weisberg 1994).

(e_B, T_B), (e_C, T_C) and (e_D, T_D) by Taylor (1997):

$$T = a_0 + a_1\, e \tag{3.20}$$

where

$$a_0 = \frac{\sum {e_i}^2 \sum T_i - \sum e_i \sum e_i T_i}{n \sum {e_i}^2 - \left(\sum e_i\right)^2} \tag{3.21}$$

$$a_1 = \frac{n \sum e_i T_i - \sum e_i \sum T_i}{n \sum {e_i}^2 - \left(\sum e_i\right)^2} \tag{3.22}$$

and n is the number of points the LoBF is being fitted to (in this case, three).

7. Check if the LoBF intersects with the confidence ellipses at the points (e_B, T_B), (e_C, T_C) and (e_D, T_D). If not, the Profile BREB calculations cease at this point and these data are flagged for exclusion from subsequent analysis (this was rare). The intersection is calculated by the simultaneous solution of Eqn. 3.19 and Eqn. 3.20 which yields a quadratic function. At each (e, T) point there will be at least one point of intersection between Eqn. 3.19 and Eqn. 3.20 if and only if the discriminant, Dx, of the quadratic function is greater than or equal to zero, i.e.

$$\begin{aligned} Dx = {} & \left[2a_0a_1(\delta e)^2 - 2a_1T_i(\delta e)^2 - 2(\delta T_i)^2 e_i\right]^2 \\ & - 4\left[a_1^2(\delta e)^2 + (\delta T_i)^2\right]\left[a_0^2(\delta e)^2 \right. \\ & - 2a_0(\delta e)^2 T_i + (\delta e)^2 {T_i}^2 \\ & \left. - (\delta e)^2(\delta T_i)^2 + (\delta T_i)^2 {e_i}^2\right] \\ \geq {} & 0 \end{aligned} \tag{3.23}$$

8. Check, by the same process as above, whether the LoBF through points (e_B, T_B), (e_C, T_C) and (e_D, T_D) also intersects with the ellipses at points (e_A, T_A) and/or (e_E, T_E). If it does not then the LoBF remains unchanged. If it intersects with the ellipse at either (e_A, T_A) or (e_E, T_E), or both, then the LoBF is recalculated to

incorporate (e_A, T_A) and/or (e_E, T_E).

Two examples of LoBF fitting by Profile BREB are given in Fig. 3.25 (p. 103) and Fig. 3.26 (p. 104).

9. The slope of the LoBF is given by the equation for a_1, i.e. Eqn. 3.22 (p. 100).

10. Calculate the Bowen ratio, β

$$\beta = \frac{c_P\, P}{M_{ratio}\, \lambda} a_1 \tag{3.24}$$

where c_P is the specific heat capacity of air, taken to be a constant $1010\,\mathrm{J\,kg^{-1}K^{-1}}$, M_{ratio} is the molecular mass ratio of water vapour to air, taken to be 0.622, and λ is the latent heat of vapourisation of water (when $-5\,^{\circ}\mathrm{C} < T < 45\,^{\circ}\mathrm{C}$) in $\mathrm{J\,kg^{-1}}$, approximated by:

$$\lambda \approx 1000\left(2500.9 - 2.4007\,T + 0.0007\,T^2\right) \tag{3.25}$$

11. Calculate available energy flux, ϕ, by

$$R_N = SW_{downwelling} + LW_{downwelling} - SW_{upwelling} - LW_{upwelling} \tag{3.26}$$

$$G = \begin{cases} -0.1|R_N| & \text{if} \quad SW_{downwelling} > 0\,\mathrm{Wm^{-2}} \\ 0.5|R_N| & \text{if} \quad SW_{downwelling} \leq 0\,\mathrm{Wm^{-2}} \end{cases} \tag{3.27}$$

$$\phi = R_N + G \tag{3.28}$$

where all variables have units of $\mathrm{Wm^{-2}}$.[24] SW and LW are the shortwave and longwave components of radiation, respectively.

12. Calculate E_{BREB} $[\mathrm{mm\,s^{-1}}]$ by

$$E_{BREB} = \frac{\phi}{\lambda\,(1+\beta)} \qquad \text{for } \beta \neq -1 \tag{3.29}$$

[24]This is an approximation for G following Allen et al. (1998). See § 3.2.6 (p. 79).

E_{BREB} would then be multiplied by 240 to give the 4 min equivalent of E_{BREB}.

3.3.3.3 Uncertainty Calculations for Profile BREB

Measurements from twelve different sensors were required to calculate E_{BREB}. Each one of those sensors had it's own 2σ measurement uncertainty (or 'error'), specified by its manufacturer or on a calibration certificate. These measurement uncertainties propagated through the modelling to give a final 95 % confidence interval (CI)[25] for the final calculated E_{BREB}.

The process of calculating the propagation of error through the Profile BREB model is described in Appendix H (p. 379).

3.3.4 Quality Assurance for Profile BREB

Quality assurance for the Profile BREB system was based on

- careful selection and deployment of recently calibrated, accurate and precise sensors (whose measurement uncertainties were well understood);
- ensuring that the air the temperature and humidity sensors were measuring was representative of the surrounding environment by having well ventilated radiation shields whose own materials did not appreciably rise in temperature above the ambient temperature;
- selection of field sites that provided optimal conditions for Profile BREB; and
- application of the LoBF sub-algorithm at all modelling instances. The sub-algorithm enabled the identification and removal of questionable data points before β was computed.

[25] The terms 'confidence interval' and 'margin of error' are used interchangeably. Also, 2σ (referring to 2 standard deviations) and 95 % CI are used interchangeably.

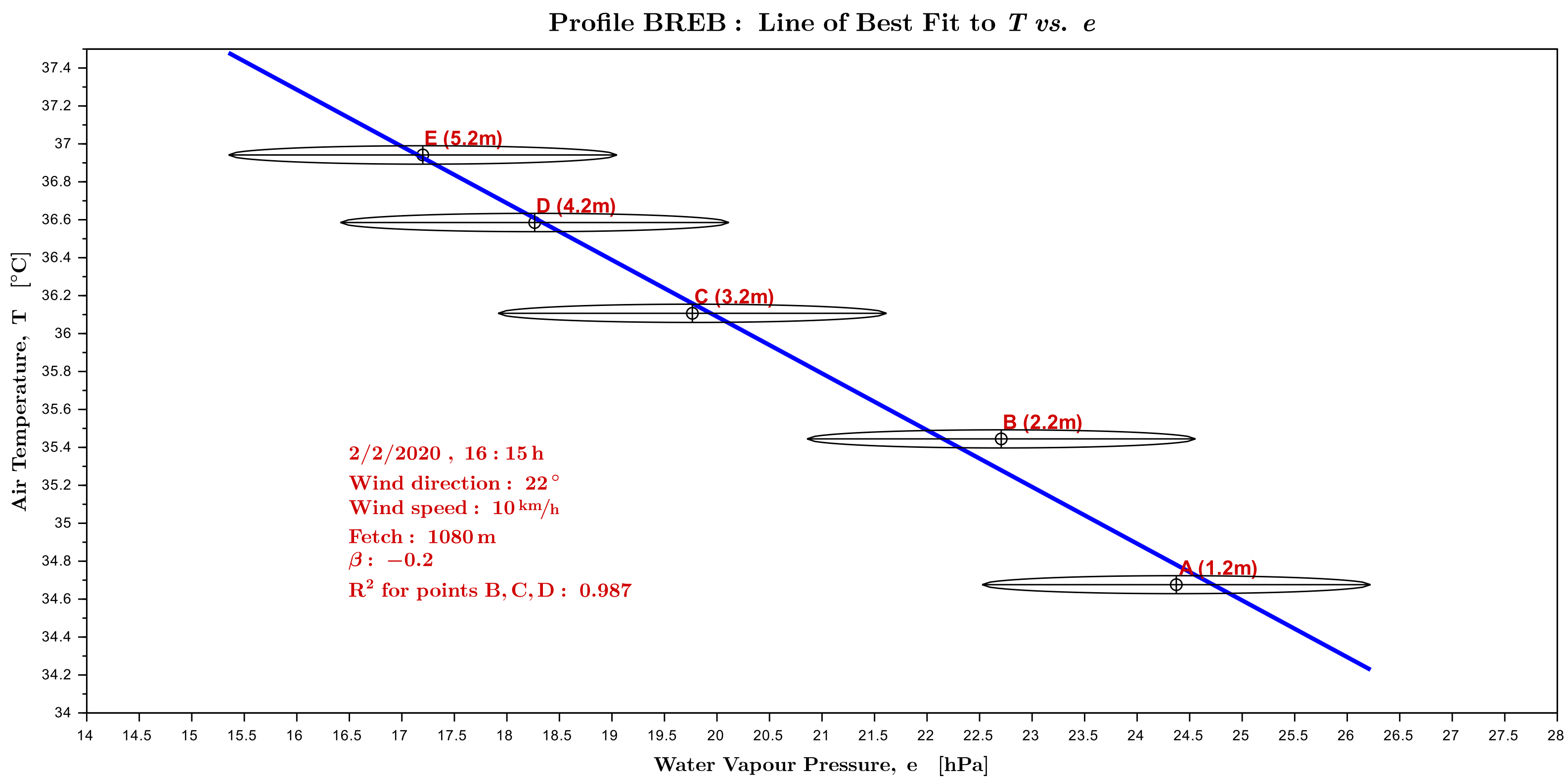

Figure 3.25: An example of confidence ellipses at each point and of fitting a least-squares Line of Best Fit (LoBF) through the points. The ellipses are the two-dimensional confidence ‘intervals’ due to the measurement uncertainties in both T and e (Cook & Weisberg 1994). In this example the LoBF through (e_B, T_B), (e_C, T_C) and (e_D, T_D) also intersected the ellipses at (e_A, T_A) and (e_E, T_E) and so the LoBF was recalculated to include all five points.

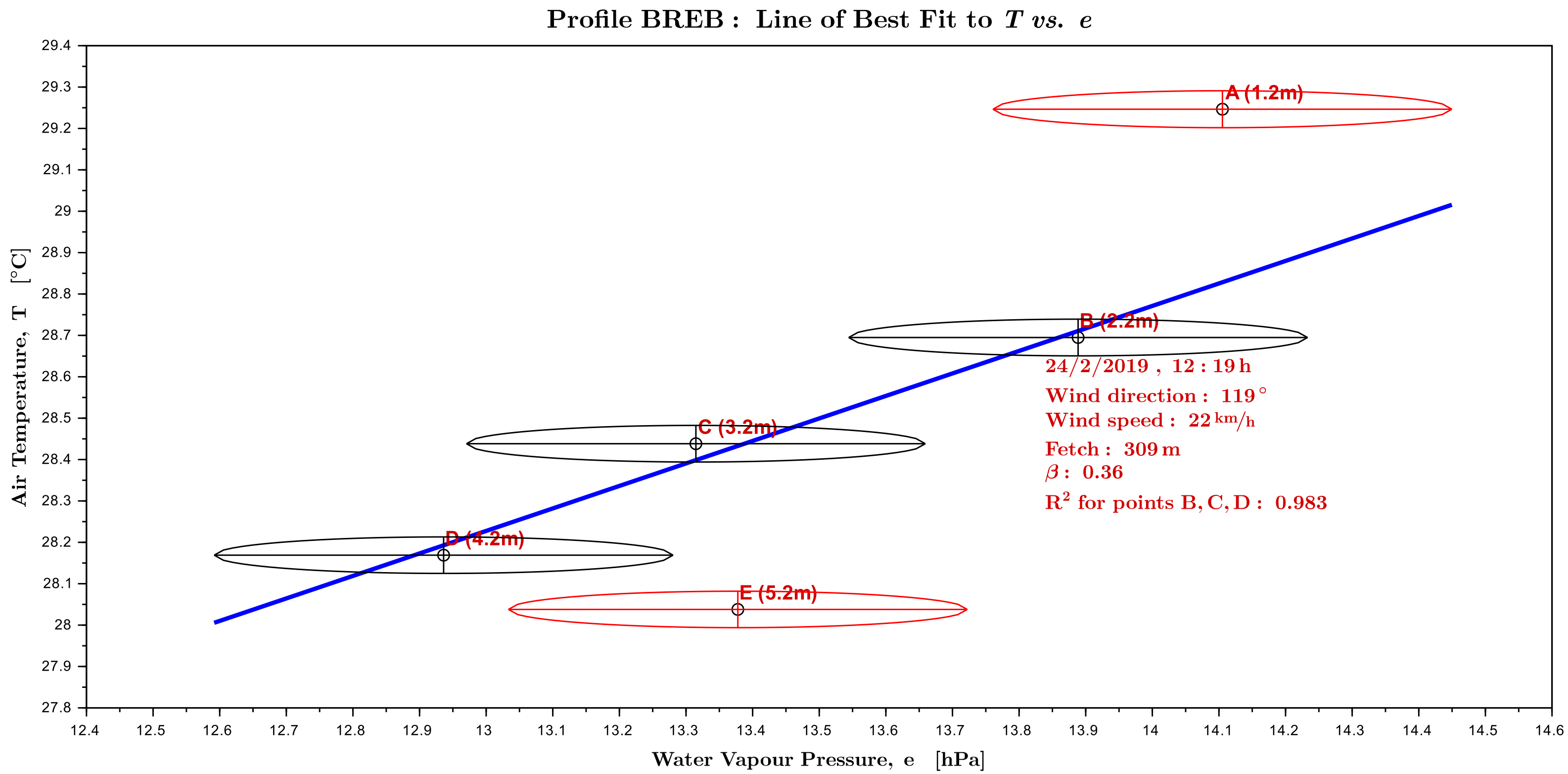

Figure 3.26: An example of confidence ellipses at each point and of fitting a least-squares Line of Best Fit (LoBF) through the points. The ellipses are the two-dimensional confidence 'intervals' due to the measurement uncertainties in both T and e (Cook & Weisberg 1994). In this example the LoBF through (e_B, T_B), (e_C, T_C) and (e_D, T_D) did not also intersect either of the ellipses at (e_A, T_A) and (e_E, T_E) and so the LoBF was only based on points (e_B, T_B), (e_C, T_C) and (e_D, T_D).

3.4 GPSTIC System

3.4.1 Theoretical Basis of the GPSTIC Model

GPSTIC was an application of the STIC model, which has been introduced in § 2.1 (p. 16). The derivation of STIC is detailed in Mallick et al. (2014, 2015a), the end result being the following set of four STIC closure equations:

$$g_B = \frac{\phi}{\rho\, c_P \left(T_0 - T + \frac{e_0 - e}{\gamma}\right)} \tag{3.30}$$

$$g_S = g_B \left(\frac{e_0 - e}{e_0^* - e_0}\right) \tag{3.31}$$

$$T_0 = T + \left(\frac{e_0 - e}{\gamma}\right)\left(\frac{1 - \Lambda}{\Lambda}\right) \tag{3.32}$$

$$\Lambda = \frac{2\, s\, \alpha_{PT}}{2\, s + 2\, \gamma + \gamma\, \frac{g_B}{g_S}\, (1 + M)} \tag{3.33}$$

where

$$M = \frac{s_1}{s_2}\, \frac{T_{SD} - T_D}{T_S - T_D} \tag{3.34}$$

$$T_{SD} = \frac{e_S^* - e - s_3 T_S + s_1 T_D}{s_1 - s_3} \tag{3.35}$$

s is the slope of the tangent to the saturation water vapour pressure curve vs. air temperature at T and the slopes s_1 and s_3 are as defined in Fig. 3.27 (p. 106) and they cannot be determined directly because the point (T_{SD}, e_S) cannot be measured. Mallick et al. (2015a) instead suggested an approximation of s_1 and s_3 by using the slopes at (T_D, e) and (T_S, e_S^*), respectively. Mallick did not specify how those slopes were determined; in this research they have been calculated by taking the first derivative of the Buck equation (Buck 1981, 1996), i.e. $\frac{de^*}{dT}$:

$$e^* = 6.1121 \exp\left[\left(18.678 - \frac{T}{234.5}\right)\left(\frac{T}{257.14 + T}\right)\right] \tag{3.36}$$

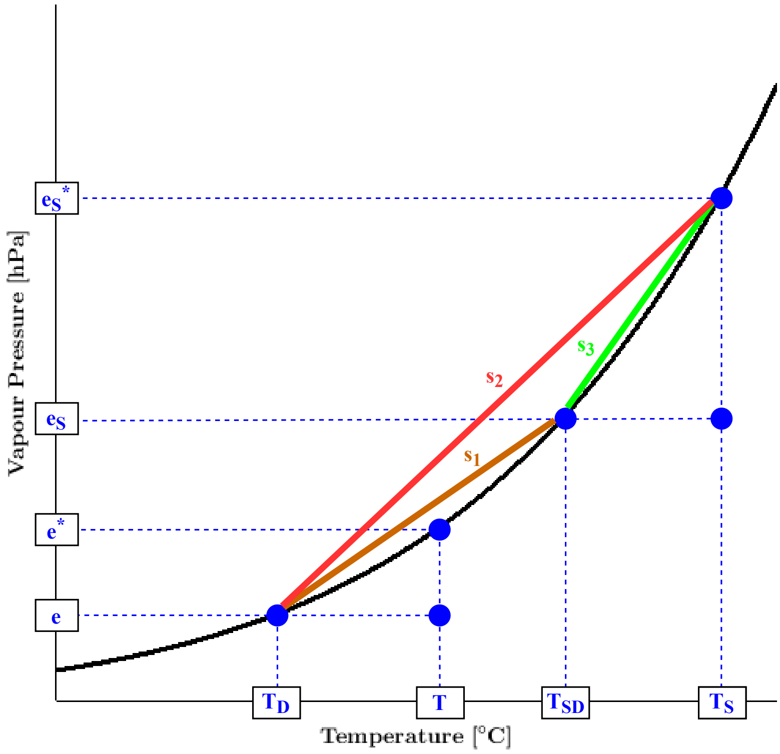

Figure 3.27: A saturation vapour pressure curve as an exponential function of temperature calculated by the Buck equation (Buck 1981, 1996). The relationships between dewpoint temperature (T_D), ambient temperature (T), dewpoint temperature at the leaf surface (T_{SD}) and leaf surface temperature (T_S) with the ambient vapour pressure (e), ambient saturation vapour pressure (e^*), vapour pressure at the leaf surface (e_S) and saturation vapour pressure at the leaf surface (e_S^*) have been reproduced from Mallick et al. (2014, 2015a). s_1, s_2 and s_3 are the slopes of the chords between various points on the curve.

$$\therefore \frac{de^*}{dT} = 6.1121 \left[\frac{-T}{234.5\,(T + 257.14)} + \frac{18.678 - \frac{T}{234.5}}{T + 257.14} - \frac{T\left(18.678 - \frac{T}{234.5}\right)}{(T + 257.14)^2} \right] \exp\left[\frac{T\left(18.678 - \frac{T}{234.5}\right)}{T + 257.14} \right] \tag{3.37}$$

The four STIC closure equations are not independent and they can be reformulated (Appendix I, p. 391) as a single, implicitly defined function for aerodynamic surface temperature, T_0 [°C], which is responsible for transferring the sensible heat flux:

$$T_0 = T + 6.1121 \left(\frac{X_1\, X_2 + X_3}{X_4} \right) \tag{3.38}$$

where

$$X_1 = 2M\, (s + \gamma - s\, \alpha_{PT}) \tag{3.39}$$

$$X_2 = \exp\left[\left(18.678 - \frac{T_0}{234.5} \right) \left(\frac{T_0}{257.14 + T_0} \right) \right] - e \tag{3.40}$$

$$X_3 = \gamma\, (1 + M) \tag{3.41}$$

$$X_4 = 2\, s\, \gamma\, \alpha_{PT} \tag{3.42}$$

Solving Eqn. 3.38 (by numerical methods) allowed e_0, g_B and g_S to be calculated and thus the PM equation, in the form

$$\lambda E = \frac{s\, \phi + \rho\, c_P\, g_B\, (e^* - e)}{s + \gamma \left(1 + \frac{g_B}{g_S} \right)} \tag{3.43}$$

could then be solved without resorting to reference crop conductances or crop coefficients.

As introduced in § 2.1 (p. 16), STIC, as conceived and applied by Mallick et al., was an RS model for which some or all of the required input data were remotely sensed (usually from space-satellites). GPSTIC, by contrast, is a novel application of STIC using only data from sensors that are proximal (i.e. situated near) to the ground. Unlike STIC, the intended purpose of GPSTIC is modelling of E at the field scale; crop water management and real-time irrigation decision making are potential applications that readily come to mind.

3.4.2 Physical Design of the GPSTIC System

The physical design requirements for the GPSTIC system were very simple:

1. T and RH were to be measured inside a radiation shield that was

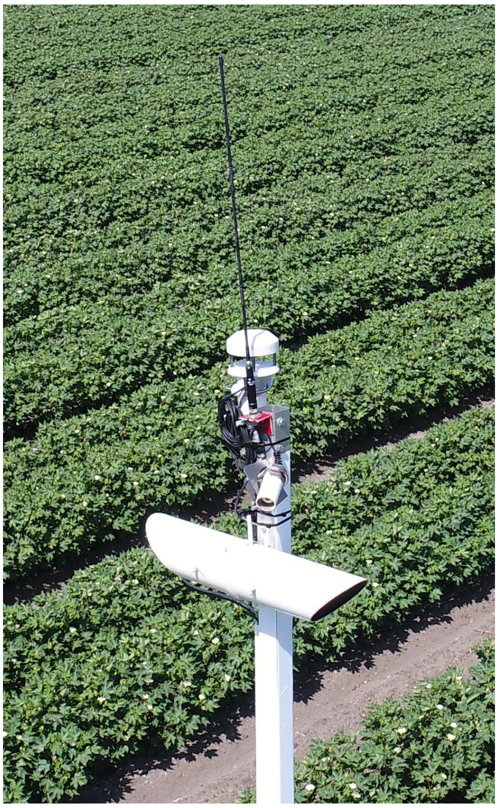

Figure 3.28: Photograph from a drone of the infrared radiometer near the top of the mast, between the two-dimensional sonic anemometer and the radiation shield. It was used to provide surface temperature data for GPSTIC.

located close to the crop; and

2. A composite surface temperature, T_S, of the soil and crop was to be measured using an infrared radiometer (IRR) from a sufficient height that the area viewed by the sensor was representative of the field.

By design all of GPSTIC's sensors were shared in common with Profile BREB except for the Apogee SI-411 IRR. This meant that differences in the modelling results between GPSTIC and Profile BREB were due to the computational algorithms and not due to differences in the input data. Furthermore, this commonality of sensors was entirely appropriate because the sensors themselves were not under evaluation.

3.4.2.1 Sensor Installation and Configuration

GPSTIC had five essential sensors: one RTD, one hygrometer, one net radiometer, one barometer, and one infrared radiometer. The first four of these were shared in common with the Profile BREB system.

The 4-wire Pt100 RTD and the Michell HS3 capacitive hygrometer used by GPSTIC were housed inside the lowest radiation shield (§ 3.3.2.2, p. 91), i.e. height 'A' in Profile BREB's vertical array.

From its position near the top of the 5.5 m tall mast the Apogee SI-411 IRR had a field-of-view of 57 m^2. It was oriented toward the northeast (i.e. bearing 45°) and 45° below the horizontal (Fig. 3.28, p. 108).

Every sensor was logged once every 60 s and then averaged over 4 min intervals by the same data logger as was used by Profile BREB. The power supply for the sensors and data logger was the same as that used by the Profile BREB system.

More details about each of the sensors are given in § 3.2 (p. 66).

3.4.3 An Algorithm for GPSTIC

GPSTIC has a relatively simple algorithm which is detailed step-by-step in § 3.4.3.1 (below) and the flow diagram in Fig. 3.29 (pp. 110 - 111).

3.4.3.1 Computing E_{GPSTIC}

This GPSTIC algorithm to compute E_{GPSTIC} was repeated every 60 s:

1. Measure and log T [°C] and RH [%], as close as practical to the crop canopy. Also measure and log R_N [Wm^{-2}], P [hPa], and T_S [°C].

2. Every 4 min calculate the 4 min averages for T, RH, R_N, P and T_S. These averaged values are used in subsequent calculations.

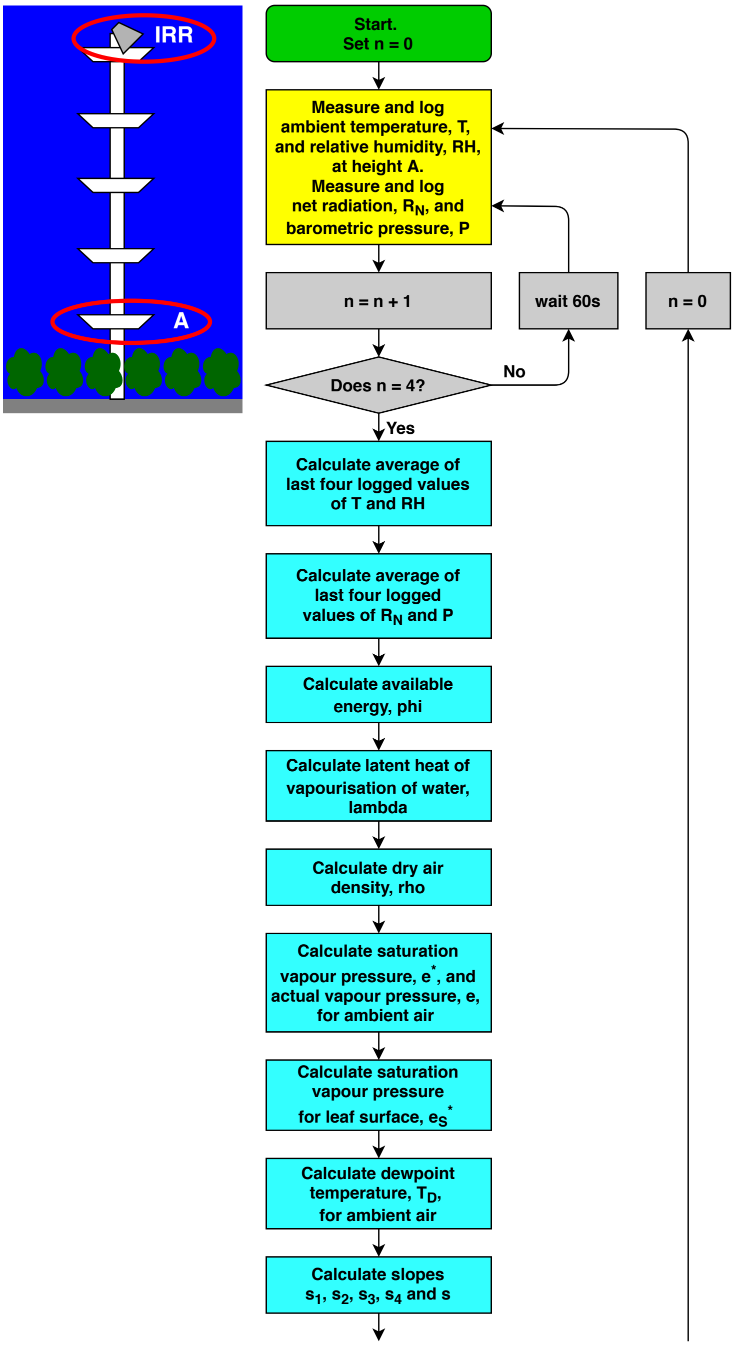

Figure 3.29: Flow diagram of the algorithm to compute GPSTIC (continued on following page). The illustration at top left shows the Profile BREB mast upon which the GPSTIC's IRR sensor was also mounted (at the top). The measurements of T and RH used for GPSTIC were from inside radiation shield 'A'.

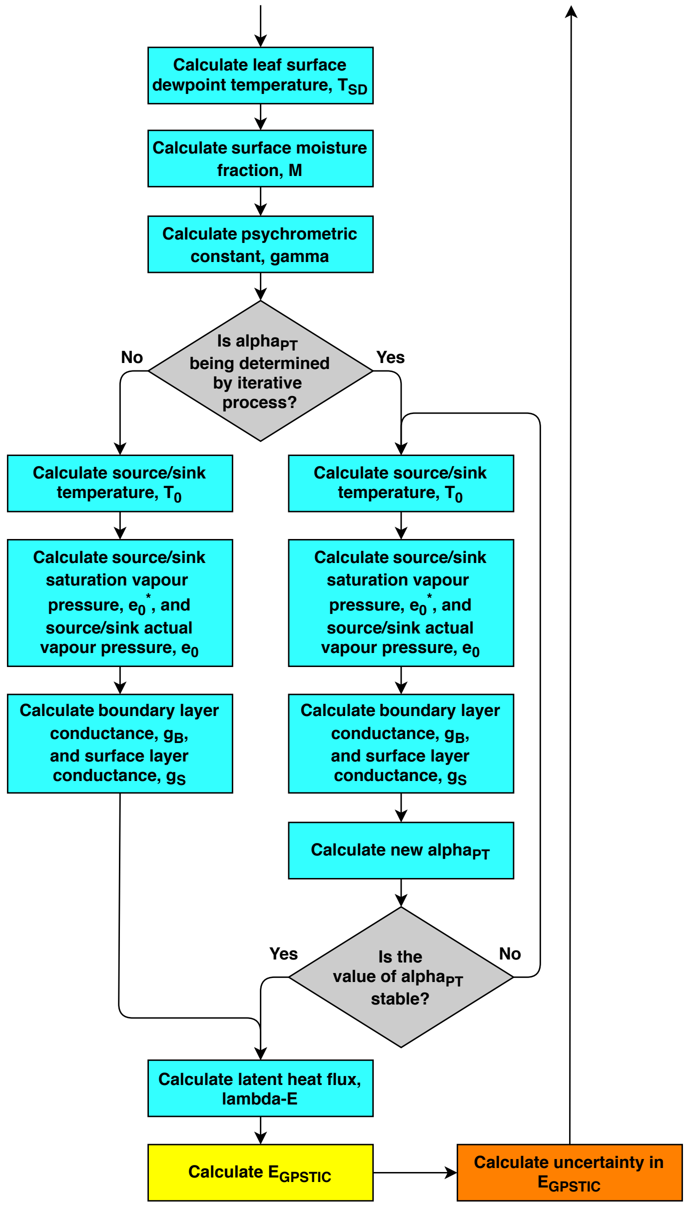

Figure 3.29: Flow diagram (continuing from previous page) of the algorithm to compute GPSTIC.

3. Calculate ϕ by

$$\begin{aligned} R_N = {} & SW_{downwelling} + LW_{downwelling} \\ & - SW_{upwelling} - LW_{upwelling} \end{aligned} \tag{3.44}$$

$$G = \begin{cases} -0.1|R_N| & \text{if} \quad SW_{downwelling} > 0\,\mathrm{Wm}^{-2} \\ 0.5|R_N| & \text{if} \quad SW_{downwelling} \leq 0\,\mathrm{Wm}^{-2} \end{cases} \tag{3.45}$$

$$\phi = R_N + G \tag{3.46}$$

where all variables have units of Wm^{-2}.[26]

4. Calculate the saturation vapour pressure e^* [hPa] and actual vapour pressure e [hPa] of the ambient air by the Buck Equation (Buck 1981, 1996):

$$e^* = 6.1121 \exp\left[\left(18.678 - \frac{T}{234.5}\right)\left(\frac{T}{257.14 + T}\right)\right] \tag{3.47}$$

$$e = e^* \left(\frac{RH}{100}\right) \tag{3.48}$$

5. Calculate the saturation vapour pressure against the leaf/soil's surface, e_S^* [hPa] by the Buck Equation:

$$e_S^* = 6.1121 \exp\left[\left(18.678 - \frac{T_S}{234.5}\right)\left(\frac{T_S}{257.14 + T_S}\right)\right] \tag{3.49}$$

6. Calculate the dry air density, ρ [$\mathrm{kg\,m^{-3}}$]:

$$\rho \approx 1.292 - 0.0047\,T + 0.00002\,T^2 \tag{3.50}$$

7. Calculate the dewpoint temperature of the ambient air, T_D [°C]:

$$T_D = \frac{116.91 + 237.3 \ln\left(\frac{e}{10}\right)}{16.78 - \ln\left(\frac{e}{10}\right)} \tag{3.51}$$

[26] This is an approximation for G following Allen et al. (1998). See § 3.2.6 (p. 79).

where the ambient vapour pressure e has units of hPa and $\ln(\cdot)$ is the natural logarithm.

8. Calculate the slopes s_1, s_2, s_3, and s [hPa °C^{-1}]:

$$\begin{aligned} s_1 = 6.1121 &\left[\frac{-T_D}{234.5\,(T_D + 257.14)} + \frac{18.678 - \frac{T_D}{234.5}}{T_D + 257.14} \right. \\ &\left. - \frac{T_D\left(18.678 - \frac{T_D}{234.5}\right)}{(T_D + 257.14)^2} \right] \exp\left[\frac{T_D\left(18.678 - \frac{T_D}{234.5}\right)}{T_D + 257.14} \right] \end{aligned} \tag{3.52}$$

$$s_2 = \frac{e_S^* - e}{T_S - T_D} \qquad \text{from Fig. 3.27 (p. 106)} \tag{3.53}$$

$$\begin{aligned} s_3 = 6.1121 &\left[\frac{-T_S}{234.5\,(T_S + 257.14)} + \frac{18.678 - \frac{T_S}{234.5}}{T_S + 257.14} \right. \\ &\left. - \frac{T_S\left(18.678 - \frac{T_S}{234.5}\right)}{(T_S + 257.14)^2} \right] \exp\left[\frac{T_S\left(18.678 - \frac{T_S}{234.5}\right)}{T_S + 257.14} \right] \end{aligned} \tag{3.54}$$

$$\begin{aligned} s = 6.1121 &\left[\frac{-T}{234.5\,(T + 257.14)} + \frac{18.678 - \frac{T}{234.5}}{T + 257.14} \right. \\ &\left. - \frac{T\left(18.678 - \frac{T}{234.5}\right)}{(T + 257.14)^2} \right] \exp\left[\frac{T\left(18.678 - \frac{T}{234.5}\right)}{T + 257.14} \right] \end{aligned} \tag{3.55}$$

9. Calculate the dewpoint temperature against the leaf surface, T_{SD} [°C]:

$$T_{SD} = \frac{e_S^* - e - s_3 T_S + s_1 T_D}{s_1 - s_3} \tag{3.56}$$

10. Calculate the surface moisture fraction, M:

$$M = \frac{s_1}{s_2} \frac{T_{SD} - T_D}{T_S - T_D} \tag{3.57}$$

11. Calculate the psychrometric constant, γ [hPa °C^{-1}]:

$$\gamma = \frac{c_P\, P}{M_{ratio}\, \lambda} \tag{3.58}$$

where P has units of hPa, c_P is taken to be a constant 1010 J kg^{-1}K^{-1}, M_{ratio} is taken to be 0.622, and λ [J kg^{-1}] is estimated by:

$$\lambda \approx 1000 \left(2500.9 - 2.4007\, T + 0.0007\, T^2\right) \tag{3.59}$$

when $-5\,°\mathrm{C} < T < 45\,°\mathrm{C}$.

12. Select a value for the Priestley-Taylor advection parameter, α_{PT} (default value is 1.26).

13. Solve the implicitly defined source/sink temperature, T_0 [°C]:

$$\begin{aligned} \text{Let} \quad X_1 &= 2M\,(s + \gamma - s\,\alpha_{PT}) \\ X_2 &= \exp\left[\left(18.678 - \frac{T_0}{234.5}\right)\left(\frac{T_0}{257.14 + T_0}\right)\right] - e \\ X_3 &= \gamma\,(1 + M) \\ X_4 &= 2\,s\,\gamma\,\alpha_{PT} \\ \text{Then} \quad T_0 &= T + 6.1121\left(\frac{X_1\,X_2 + X_3}{X_4}\right) \end{aligned} \tag{3.60}$$

14. Calculate the source/sink saturation vapour pressure e_0^* [hPa], and source/sink actual vapour pressure e_0 [hPa], by the Buck Equation:

$$e_0^* = 6.1121\,\exp\left[\left(18.678 - \frac{T_0}{234.5}\right)\left(\frac{T_0}{257.14 + T_0}\right)\right] \tag{3.61}$$

$$e_0 = e(1 - M) + e_0^*\,M \tag{3.62}$$

where Eqn. 3.62 is from Eqn. 18 in Mallick et al. (2015a).

15. Calculate the boundary layer conductance g_B [m s^{-1}], and stomatal/surface conductance g_S [m s^{-1}]:

$$g_B = \frac{\phi}{\rho\,c_P\left(T_0 - T + \frac{e_0 - e}{\gamma}\right)} \tag{3.63}$$

$$g_S = g_B\left(\frac{e_0 - e}{e_0^* - e_0}\right) \tag{3.64}$$

16. If α_{PT} is to be determined by an internal, iterative optimisation process then at this point calculate the new α_{*PT*} (if not, then skip to Step 17):

$$\alpha_{*PT*} = \frac{s+\gamma}{s+\gamma+\gamma\left(\frac{g_B}{g_S}\right)} + \frac{\rho\, c_p\, g_B\,(e^* - e)\,(s+\gamma)}{s^2\,\phi + s\,\gamma\,\phi + s\,\gamma\,\phi\left(\frac{g_B}{g_S}\right)} \tag{3.65}$$

Return to Step 13 with this new value for α_{PT} and repeat until the value of α_{PT} is stable.

17. Calculate E_{GPSTIC} [$\mathrm{mm\,s^{-1}}$] using the PM equation:

$$E_{GPSTIC} = \frac{s\,\phi + \rho\, c_P\, g_B\,(e^* - e)}{\lambda\left[s+\gamma\left(1+\frac{g_B}{g_S}\right)\right]} \tag{3.66}$$

As for Profile BREB, E_{GPSTIC} would then be multiplied by 240 to give the 4 min equivalent of E_{GPSTIC}.

3.4.3.2 Uncertainty Calculations for GPSTIC

Measurements from five different sensors were required to calculate E_{GPSTIC}. Each one of those sensors had it's own 2σ measurement uncertainty (or 'error'), specified by its manufacturer or on a calibration certificate. These measurement uncertainties propagated through the modelling to give a final 95 % CI for the calculated E_{GPSTIC}.

The process of calculating the propagation of error through the GPSTIC model is described in Appendix H (p. 379).

3.4.3.3 Concluding Remarks about the GPSTIC System

GPSTIC was an application of the STIC model. Descriptions in the literature of how the STIC model had been previously implemented were lacking in many helpful details. Nevertheless, an algorithm and computer code for the GPSTIC system were formed and ended up being quite concise. It is conceivable that the GPSTIC algorithm could be even be re-coded to execute within an intelligent data logger or even by a low-cost microprocessor. This was outside the scope of this research but could be an interesting path of future development for GPSTIC.

3.5 Chapter Conclusion

The GPSTIC and Profile BREB systems were custom developed for the purposes of this research, including algorithm development and writing the computer code; acquisition and programming of sensors; design and construction of physical structures; testing and debugging; and field deployment and data collection.

A Profile BREB system was developed as no EC system was available for this research. The Profile BREB system shared key sensors with the GPSTIC system which meant that differences in the modelling results could be ascribed to the models' algorithms and not confounded by differences in input data. The Profile BREB system also had some significant practical advantages, particularly that it had far lower electrical power requirements and that it would be much easier for farm's workers to remove from the field if so needed.

Certainly every effort was made to ensure the best possible performance by both GPSTIC and Profile BREB. This was an important factor for the quality of the modelling results that are presented in Chapters 4 and 5.

Chapter 4

RESULTS

Chapter 4 presents the environmental data that were measured during the three Data Sets, and the non-analysed results for the GPSTIC and Profile BREB modelling. All analyses are subsequently presented in Chapter 5 (p. 201).

4.1 Introduction

Field data were collected during the Australian summers of 2018/19 and 2019/20. There were three separate periods of data collection:

Data Set One (DS1) 165 consecutive hours of measurements from 18th to 25th February, 2019, at Field 14.

Data Set Two (DS2) 311 consecutive hours from 22nd October to 4th

November, 2019, at Field 16.

Data Set Three (DS3) 116 consecutive hours from 31$^{\text{st}}$ January to 5$^{\text{th}}$ February, 2020, at Field 16.

All environmental variables were measured and logged every 60 s. Upon return from the field, the data were then averaged in 4 min intervals before being used in the Profile BREB and GPSTIC modelling.

Two modelling scenarios were used in this research: the All Data scenario included *all* 4 min intervals except those instances that produced impossible results (associated with $\beta \approx -1$). A more restricted Selected Data modelling scenario included only the 4 min intervals that satisfied the following two conditions:

1. Bowen ratio, β, did not lie inside the range $-1.25 < \beta < -0.75$; and

2. The Profile BREB's LoBF through the (e, T) pairs at heights 'B', 'C' and 'D' had an $R^2 \geq 0.90$.

The reason for the first Selected Data criterion was that, historically, $-1.25 < \beta < -0.75$ has been regarded as being problematic for BREB systems. A recommendation by Tanner (1988) and Cellier and Olioso (1993) had been to automatically exclude instances when $-1.25 < \beta < -0.75$ from the modelling. The reason for the second criterion was to see if restricting the modelling to instances when the Profile BREB had an exceptionally good quality regression fit made any difference to the relative performance of GPSTIC and Profile BREB. (It turns out that it made little difference.)

Whenever any Profile BREB results were rejected (e.g. when $\beta \approx -1$, or under the Selected Data criteria) the corresponding GPSTIC results for the same 4 min interval were also rejected — even if there was no issue with the GPSTIC data — thereby allowing a fair comparison of the two models to be made.

4.2 Data Set One (DS1)

Data Set One (DS1) comprised 165 consecutive hours of measurements over the period 18th to 25th February, 2019. A description of the field site for DS1 is given in § 3.1.1 (p. 57).

4.2.1 Weather Conditions During DS1

Figures 4.1 - 4.5 (pp. 120 - 124) present the weather data during DS1 that were most relevant for the Profile BREB and GPSTIC modelling. Additional weather data for DS1 are presented in Appendix O (p. 427).

Much of Australia was in drought during DS1. Ambient air temperatures (Fig. 4.1, p. 120) were 35 - 38 °C during the day (overnight minimum approx. 20 °C), which was relatively mild compared to the preceding week when temperatures had been 43 - 47 °C. These warm conditions along with persistently low vapour pressures (Fig. 4.2, p. 121) and high solar radiation (Fig. 124, p. 124) caused high vapour pressure deficits and strong evaporative drivers.

There was no rainfall during DS1. Fig. 4.1 (p. 120) suggests that T and T_S did not fall to dewpoint. However, light mist above the canopy and a light dew on the canopy leaves were observed in the field overnight on the 18th and 24th February (the author was not at the field site on the other nights). Furthermore, the observations of light canopy mist and light dew deposition were consistent with the Profile BREB and GPSTIC modelling, both of which produced small negative numbers (approx. $-0.5\,\mathrm{mm\,night}^{-1}$) for E overnight. An explanation of the apparent inconsistency between Fig. 4.1 and the observed/modelled conditions is that the value of RH was probably higher at the leaf surfaces than at 0.2 m above the crop (the height at which ambient RH was measured). Consequently it is possible that $T_S < T_D$ on the leaf surface.[1]

[1] Indeed, the phenomenon of e, T and T_D differing between the ambient environment and near-leaf-surface environment formed part of the theoretical basis of the STIC model.

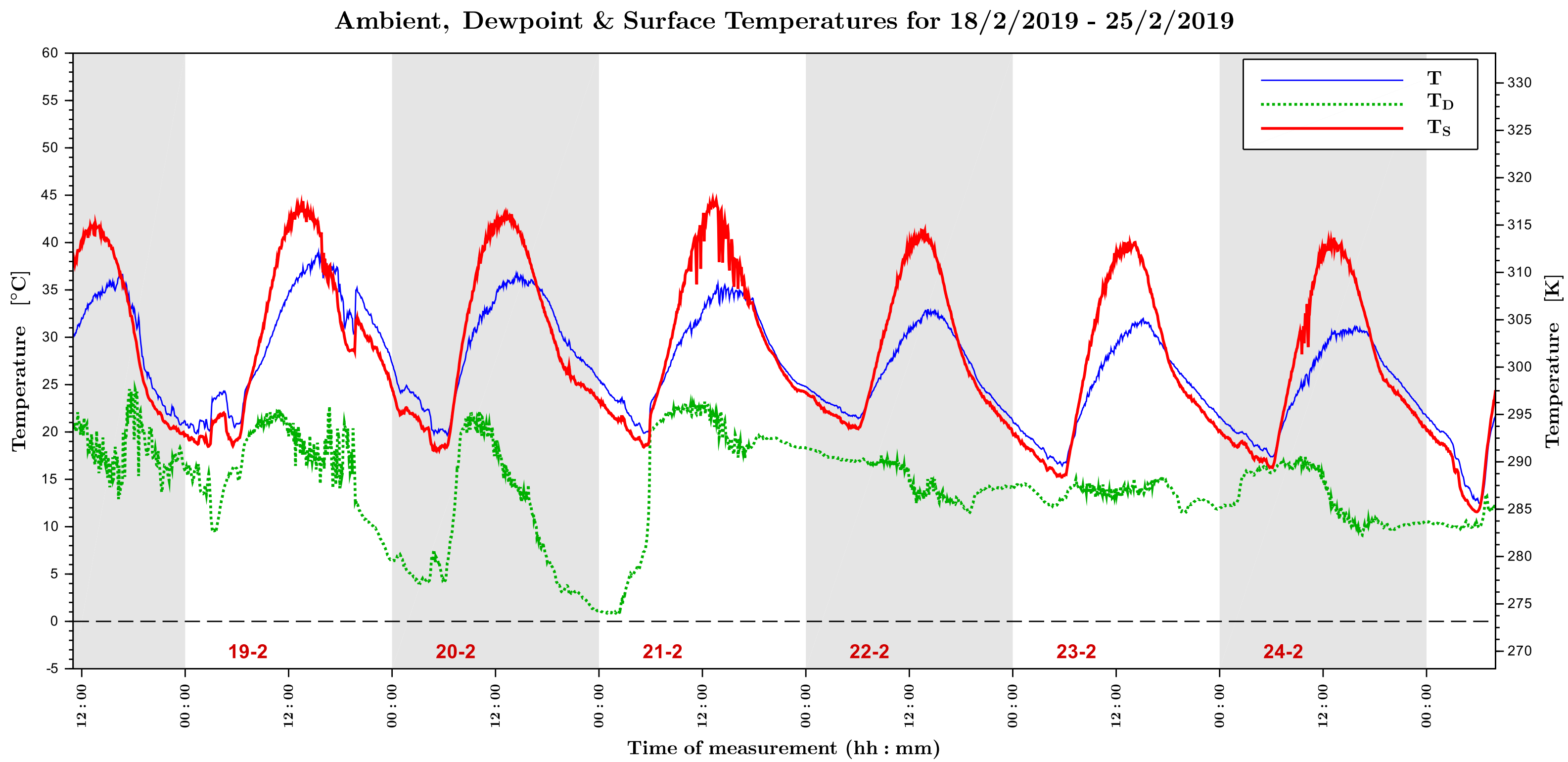

Figure 4.1: Temperatures in Field 14 during DS1. Ambient temperatures (T) and dewpoint temperatures (T_D) were measured 0.2 m above the crop canopy; surface temperatures (T_S) were measured using an infrared radiometer at 5.4 m above the ground, i.e. 4.4 m above the crop (with a visible surface area of 57 m^2).

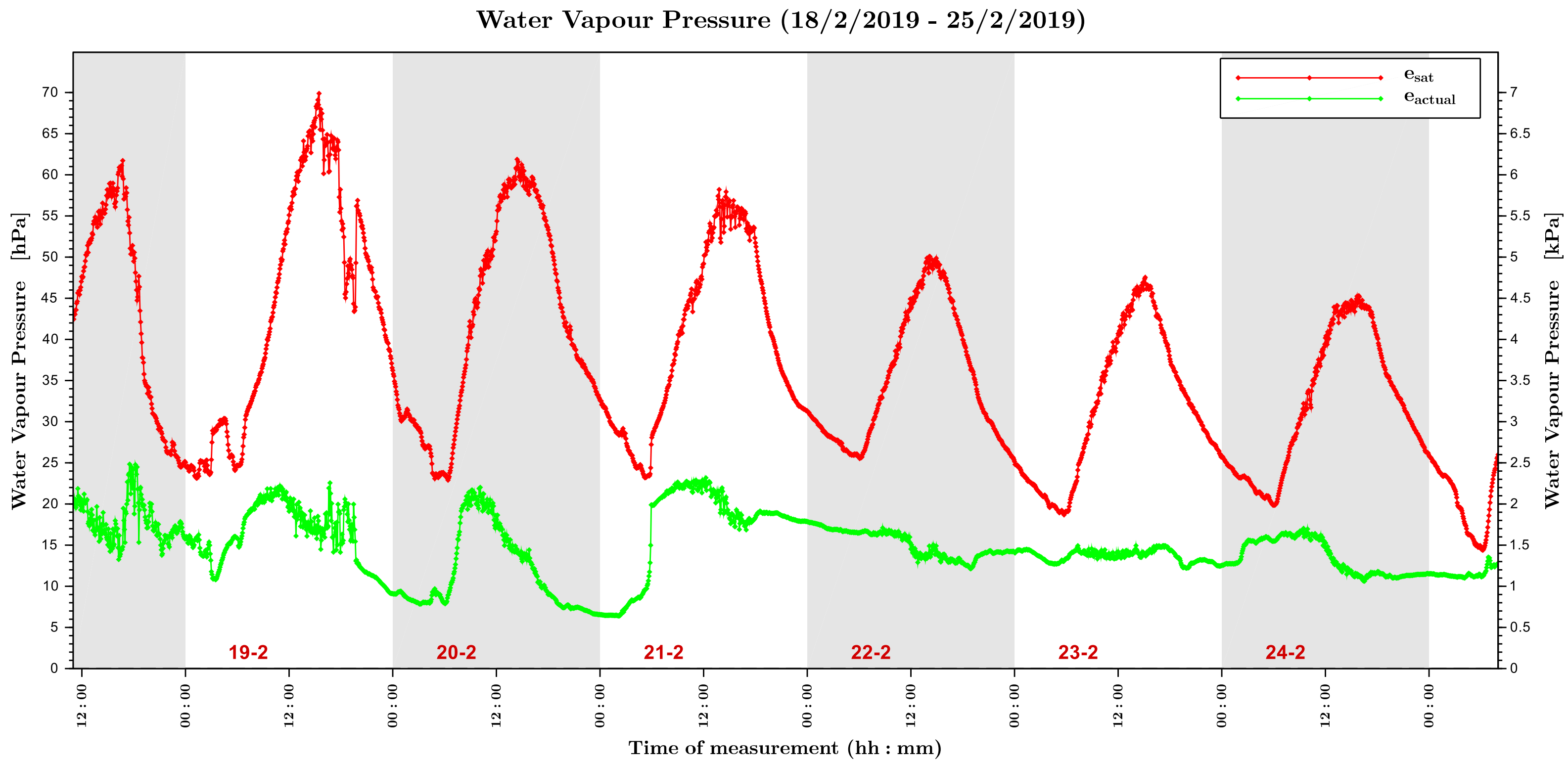

Figure 4.2: Saturation vapour pressure and actual vapour pressure, in Field 14 during DS1, as measured 0.2 m above the crop canopy. Saturation vapour pressure was calculated using the Buck Equation (Eqn. 3.15, p. 96).

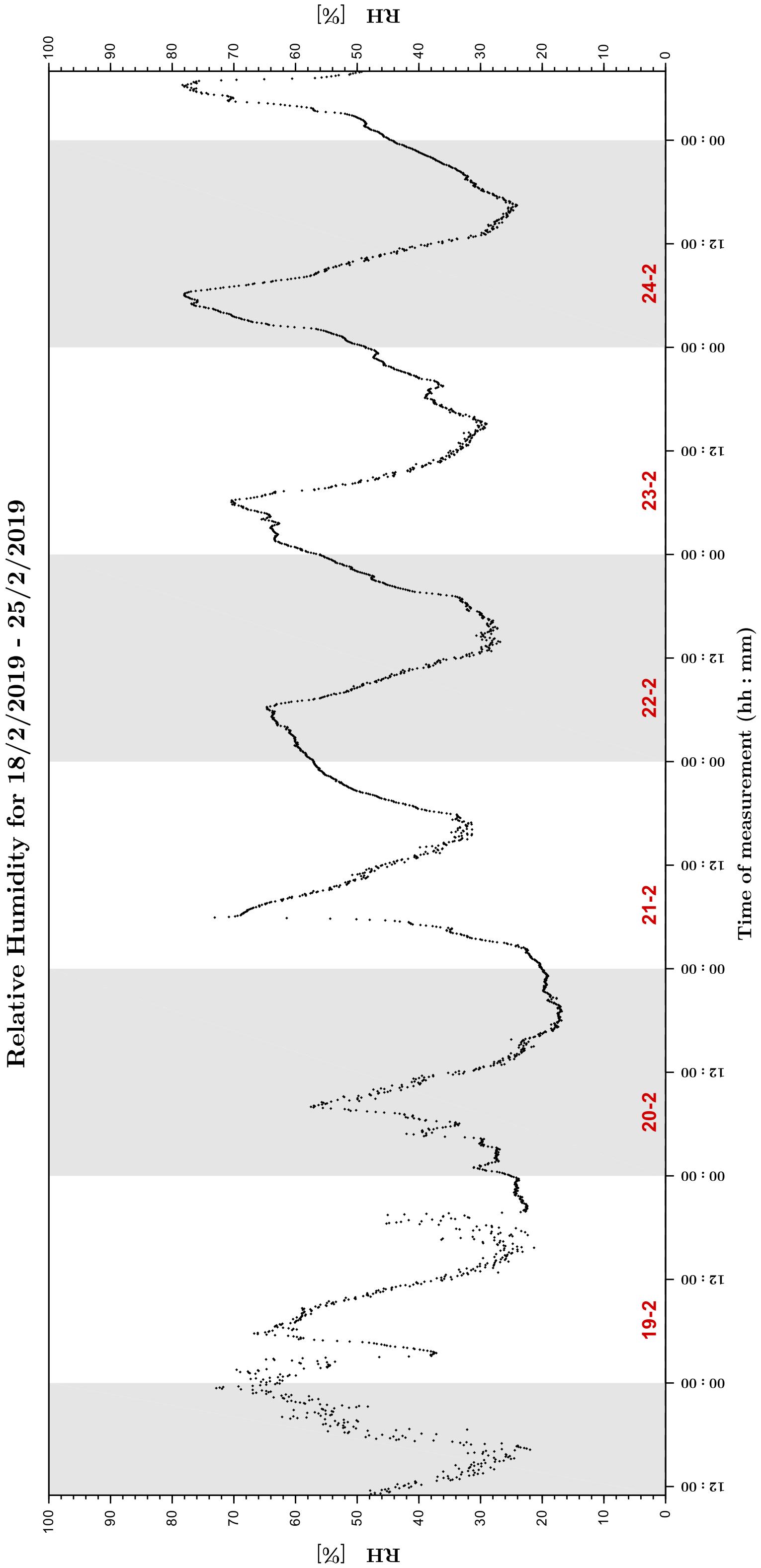

Figure 4.3: Relative humidity in Field 14 during DS1, as measured 0.2 m above the crop canopy.

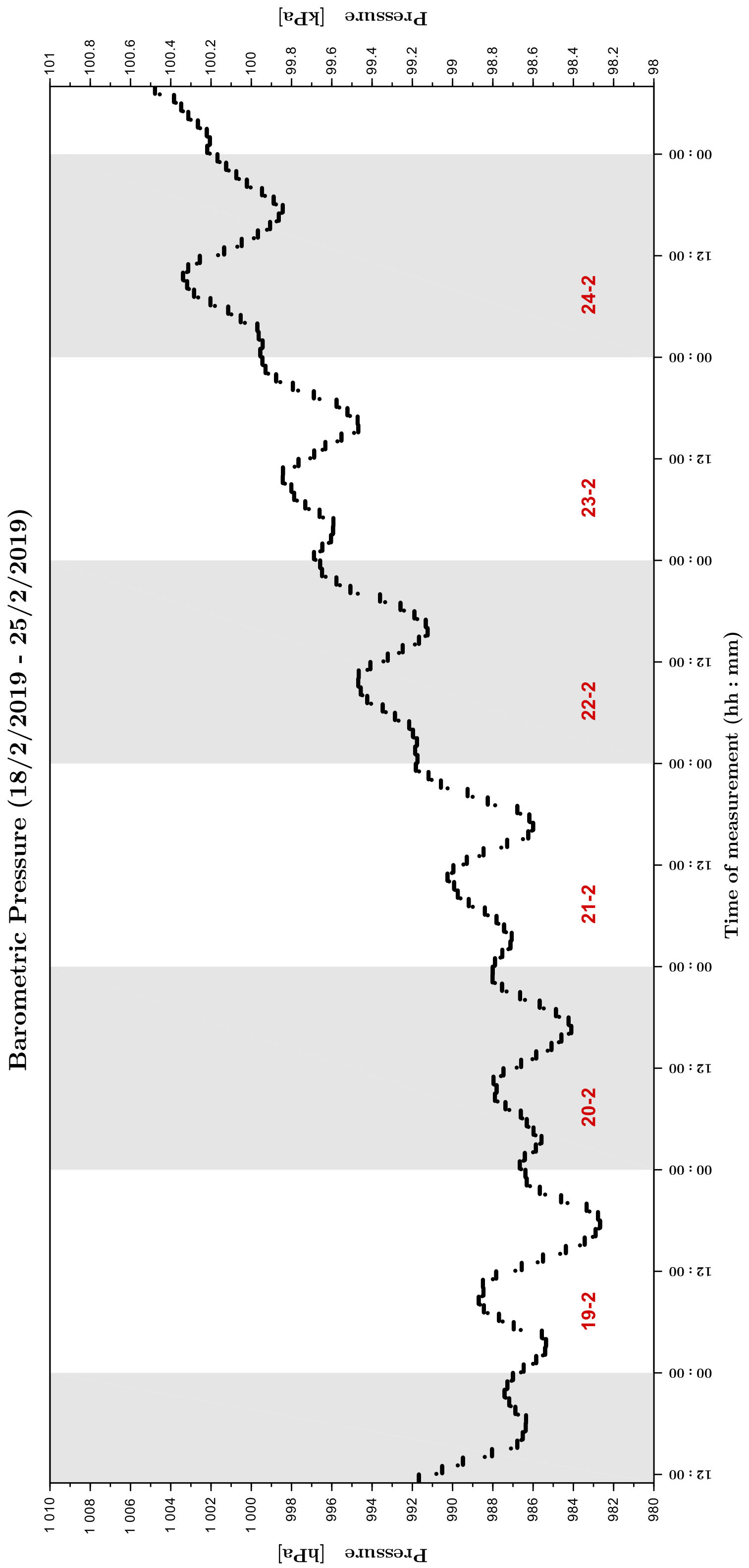

Figure 4.4: DS1: barometric pressure, P [hPa], measured hourly at 1.6 m above the ground (171 m above sea level).

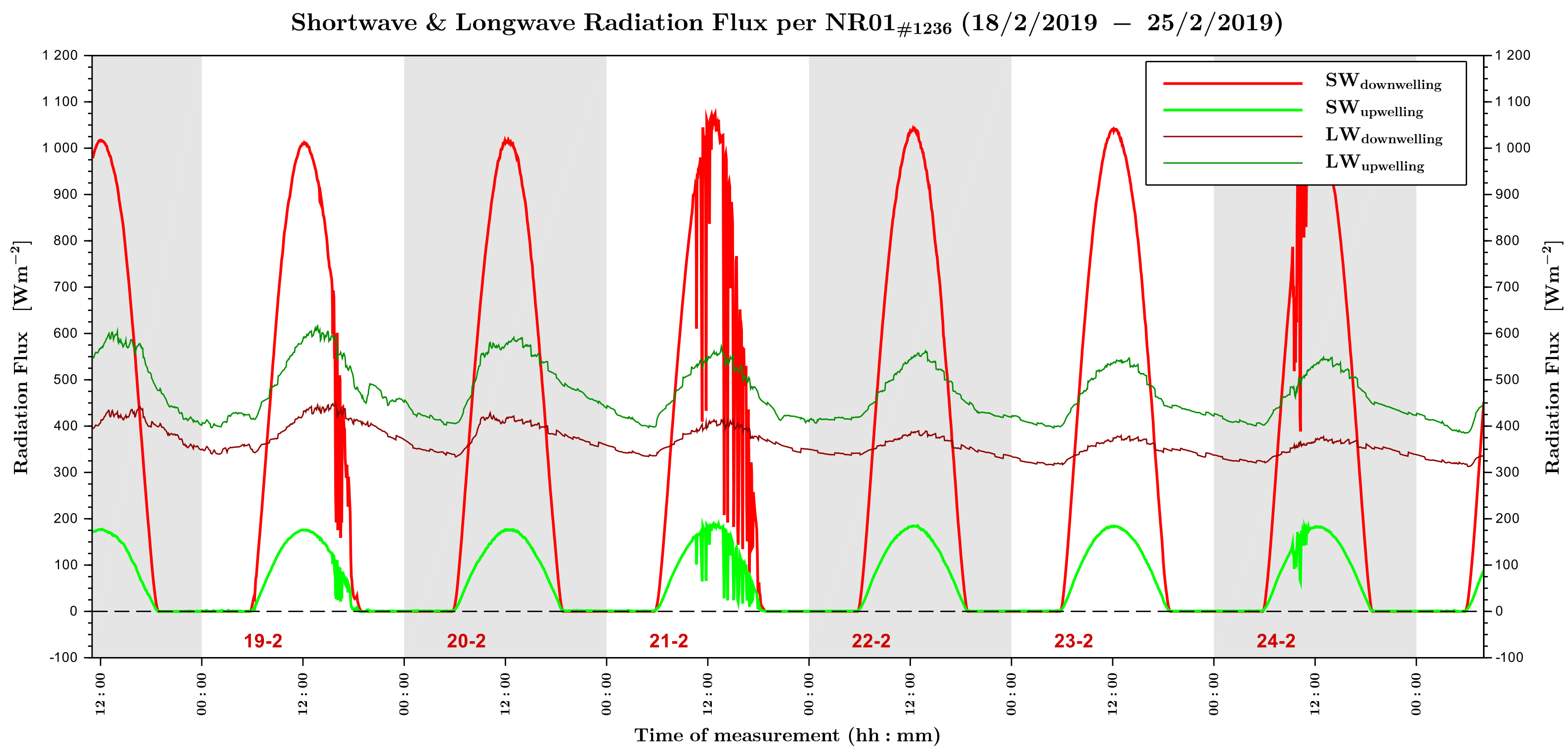

Figure 4.5: Downwelling and upwelling radiation (shortwave and longwave) in Field 14 during DS1. These data have already been adjusted per § 4.2.1.1 (p. 125) and Appendix F (p. 363).

4.2.1.1 Adjustments to DS1 Radiation Data

Some discussion of the adjustments that were retrospectively applied to the longwave radiation data from DS1 is warranted. (The radiation data from DS2 and DS3 did not require any adjustments.)

Two NR01 net radiometers were used during DS1 (serial numbers #1830 and #1236). $NR01_{\#1830}$ was newer and had been professionally re-calibrated in July 2019 with the intention that it would be used as the primary net radiometer for Profile BREB and GPSTIC. $NR01_{\#1236}$ was deployed alongside $NR01_{\#1830}$ as a back-up — this was just as well because some of the $NR01_{\#1830}$ cables were damaged by wildlife early in DS1. However, the data from the uncalibrated $NR01_{\#1236}$ needed to be 'calibrated' which was later done with reference to the $NR01_{\#1830}$.

Adjustments to Longwave Radiation: DS1 longwave radiation data from the uncalibrated $NR01_{\#1236}$ were adjusted after DS2 as described in Appendix F (p. 363). Fig. F.4 (p. 368) and Fig. F.7 (p. 371) show that both the downwelling and upwelling longwave radiation data (4.5 - 40 µm) required significant adjustment, the outcomes of which are shown in Fig. 4.6 (p. 127).

The *adjusted* longwave radiation data during DS1 were in the following ranges:

$$312 \leqslant LW_{downwelling} \leqslant 450 \quad [\mathrm{Wm^{-2}}] \tag{4.1}$$

$$385 \leqslant LW_{upwelling} \leqslant 616 \quad [\mathrm{Wm^{-2}}] \tag{4.2}$$

The temperatures at which these values of longwave radiation are emitted were calculated by

$$T = \left(\frac{LW}{\epsilon\,\alpha}\right)^{\frac{1}{4}} - 273.15 \quad [^\circ\mathrm{C}] \tag{4.3}$$

where the Stefan-Boltzmann constant, α, equals $5.6704 \times 10^{-8}\,\mathrm{Wm^{-2}K^{-4}}$ and ϵ is the surface emissivity. Fig. 4.7 (p. 128) compares T_S as measured by the IRR with that calculated by Eqn. 4.3 using the adjusted $LW_{upwelling}$ data. Their close alignment suggests that the adjustment process for the $LW_{upwelling}$ data was appropriate. Fig. 4.8 (p. 129) shows that approx. 95 % of measured T_S per the adjusted $NR01_{\#1236}$ were within 20 % of the T_S per the IRR.

Adjustments to Shortwave Radiation: It was unnecessary to make adjustments to the shortwave radiation data. For DS1 the shortwave radiation (0.285 - 3.00 µm) measurements were in the ranges

$$0 \leqslant SW_{downwelling} \leqslant 1074 \quad [\mathrm{Wm}^{-2}] \tag{4.4}$$

$$0 \leqslant SW_{upwelling} \leqslant 189 \quad [\mathrm{Wm}^{-2}] \tag{4.5}$$

The range of $SW_{downwelling}$ was consistent with modelled estimates of ‘clear-sky’ shortwave radiation for DS1[2] (Appendix L, p. 409), i.e. 975 - 1023 Wm^{-2}.

[2]There was additional uncertainty in the clear-sky models in Appendix L (p. 409) because the values of some modelling variables had to be estimated. The clear-sky models estimated $SW_{downwelling}$ to be approx. 975 - 1023 Wm^{-2} when $\tau_a = 0.2$, $\tau_m = 0.3$, $K_t = 0.95$, $N = 39$, $S_0 = 1367\,\mathrm{Wm}^{-2}$ and $e = 2\,\mathrm{kPa}$.

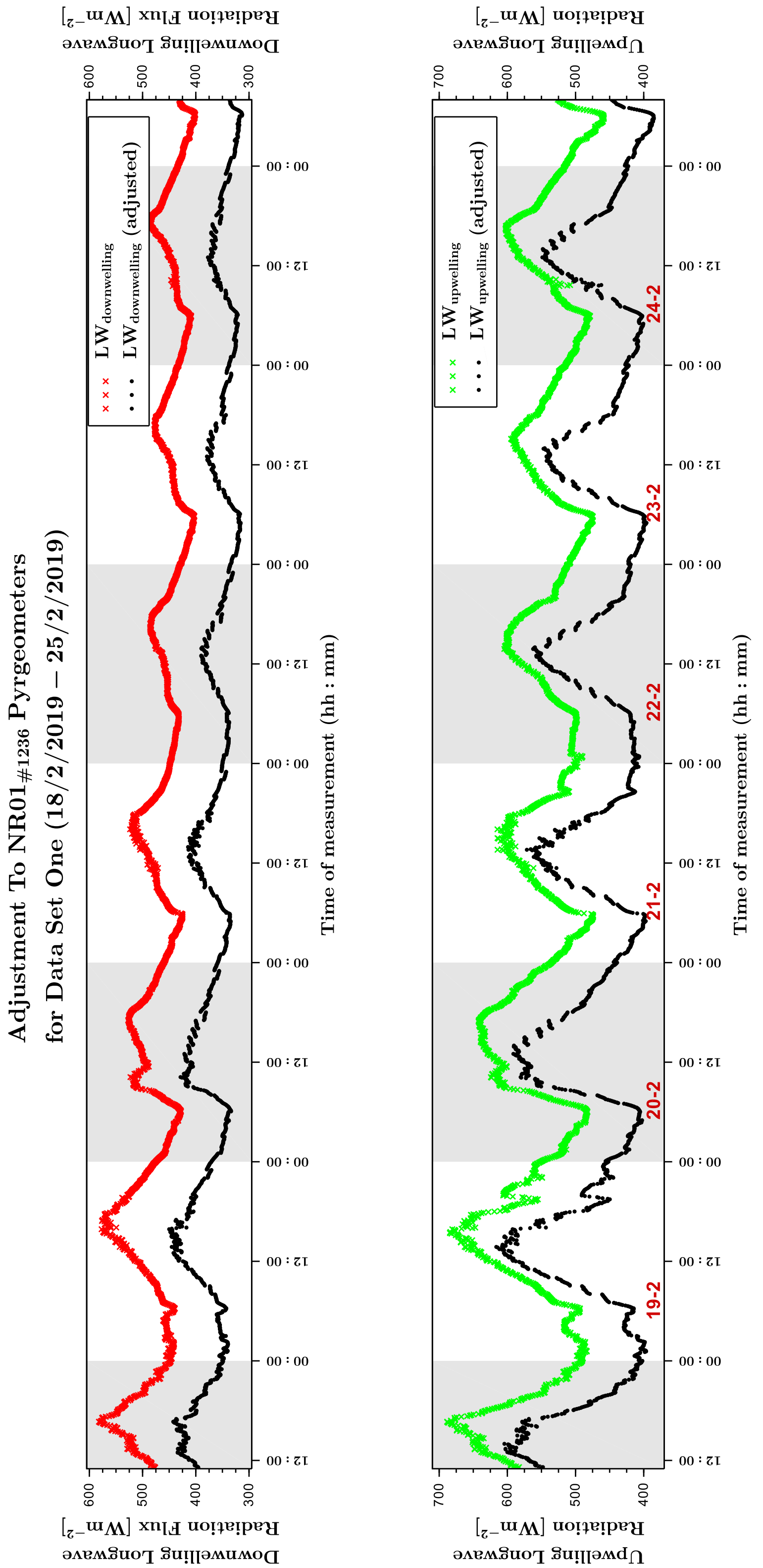

Figure 4.6: Longwave radiation from NR01$_{\#1236}$ in Field 14 during DS1, before and after being adjusted according to Appendix F (p. 363). The adjustment factors were determined after DS2 when it was possible to compare the longwave radiation data from the uncalibrated NR01$_{\#1236}$ with the calibrated NR01$_{\#1830}$.

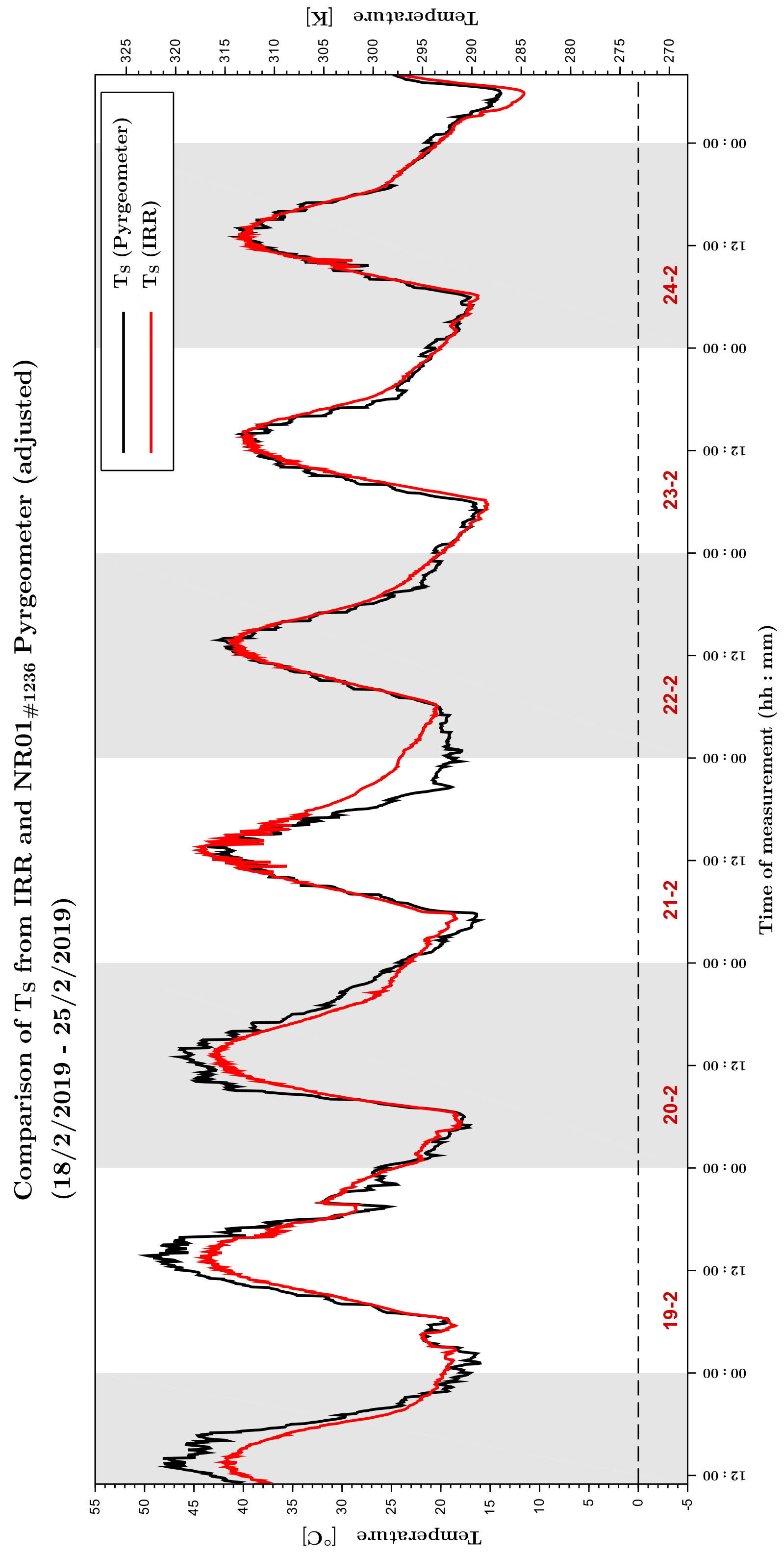

Figure 4.7: Comparison of T_S as determined by the IRR with that derived from the (adjusted) NR01$_{\#1236}$ downward facing pyrgeometer in Field 14 during DS1.

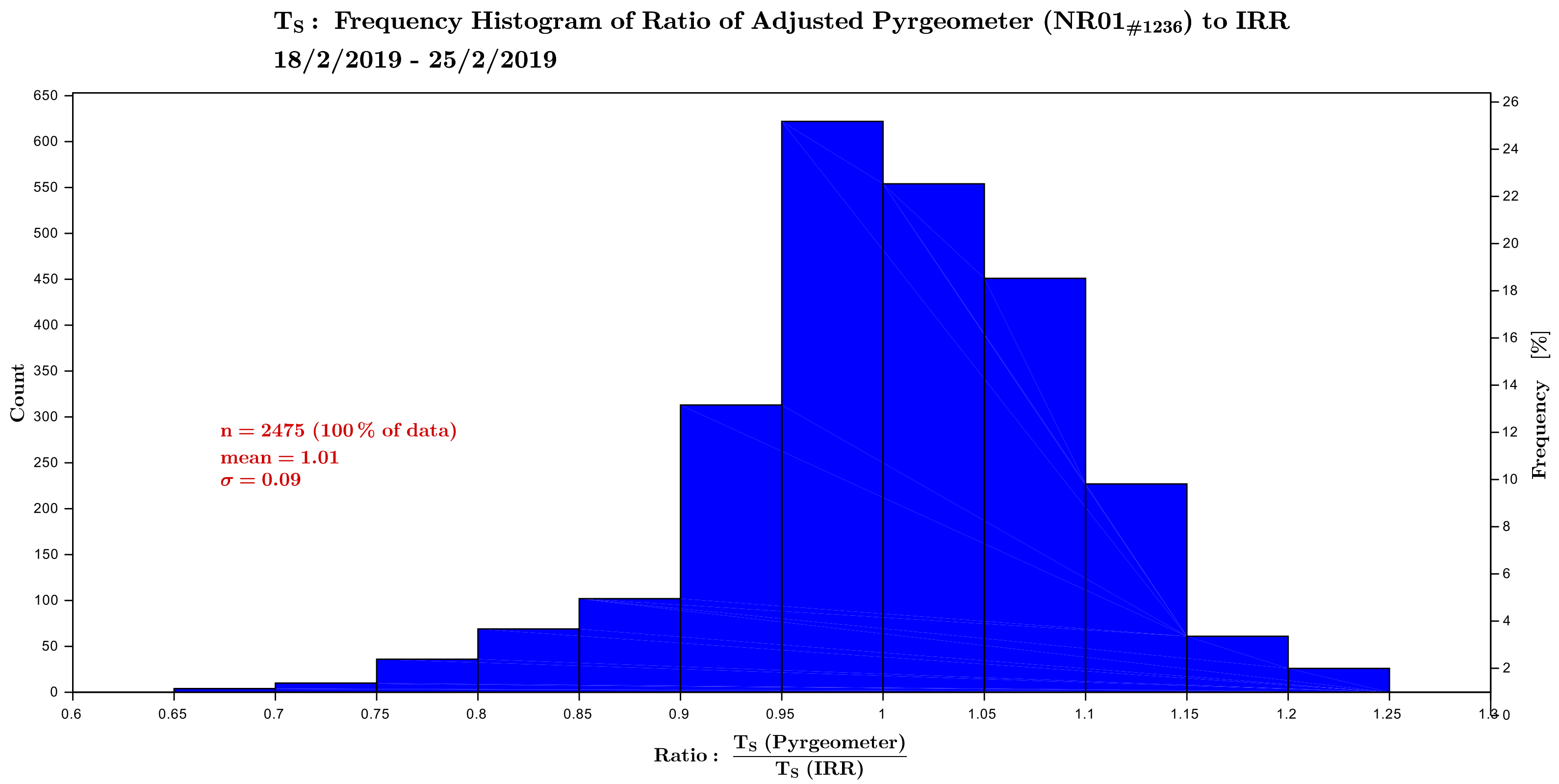

Figure 4.8: Frequency histogram of the ratio of T_S as determined by the IRR to T_S derived from the (adjusted) $NR01_{\#1236}$ downward facing pyrgeometer in Field 14 during DS1.

4.2.2 Results for Profile BREB During DS1

Figure 4.9: Photograph of the 5.5 m tall Profile BREB mast, showing the top four (of five) radiation shields that contained the capacitive hygrometers and RTDs. The shields are 1.0 m apart.

The Profile BREB system (Fig. 4.9, p. 130) operated continuously for 165 hours during DS1.

Fig. 4.10 (p. 131) and Fig. 4.11 (p. 132) provide two examples from DS1 of the LoBF sub-algorithm (§ 3.3.3.1, p. 95) 'in action'. At every time step all pairs of (e, T) data were evaluated for their suitability to be included in the LoBF.

Fig. 4.12 (p. 133) shows all values of β as determined by Profile BREB. During DS1 only 2 % of all data were inside the range $-1.25 < \beta < -0.75$ and these mainly occurred around sunrise. Significantly, not every dawn or dusk period featured β in this range. A large proportion of those 2 % had $\beta \approx -1$ and Fig. 4.13 (p. 134) confirms that these instances were the cause of the extreme values of E_{BREB}.

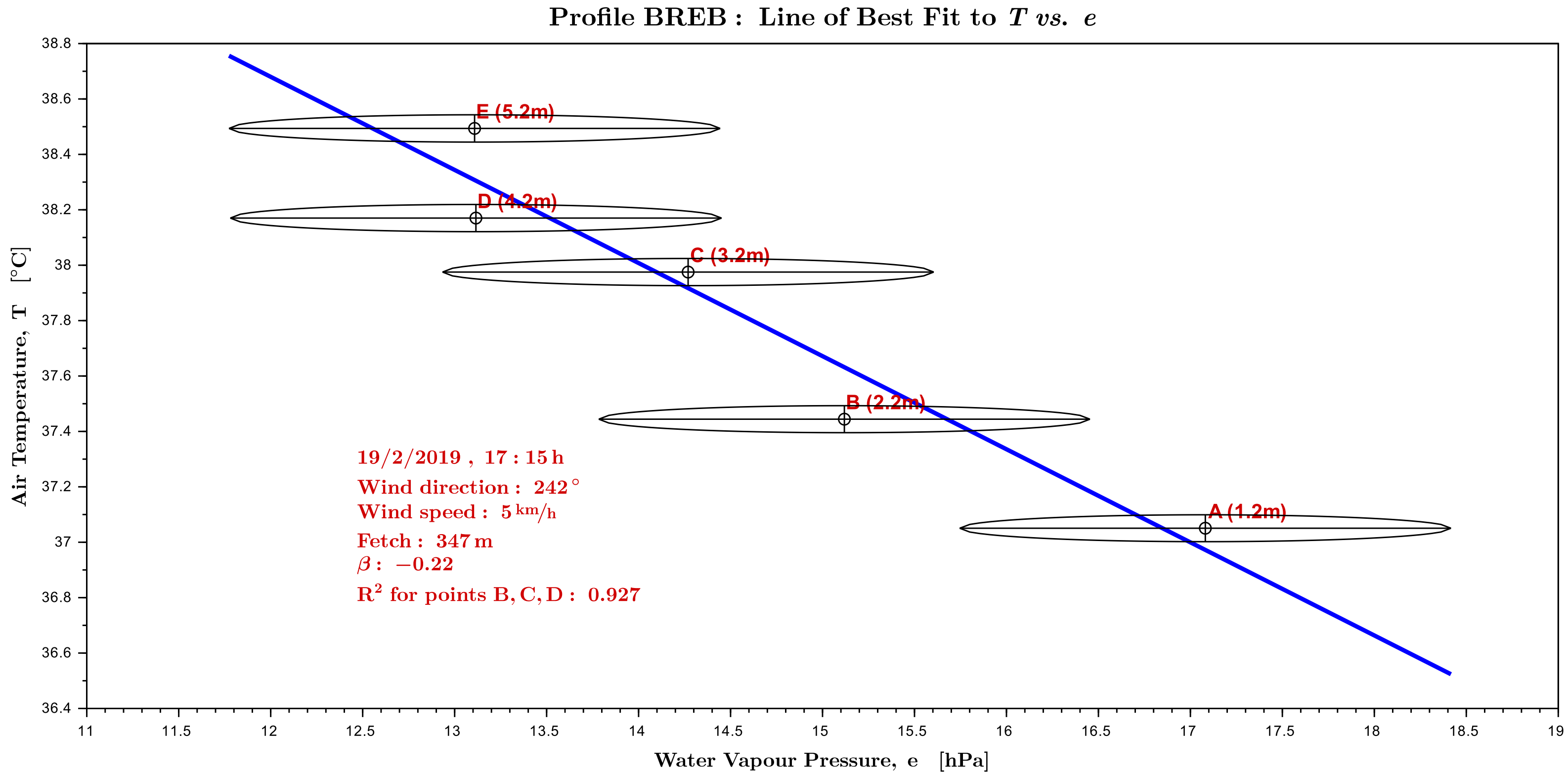

Figure 4.10: DS1: example from 19th February, 2019, at 17:15 h, of the LoBF sub-algorithm (§ 3.3.3.1, p. 95) in action. In this particular case, all five points were suitable for line fitting. The ellipses show the 95 % confidence extents based on the measurement uncertainties in e and T.

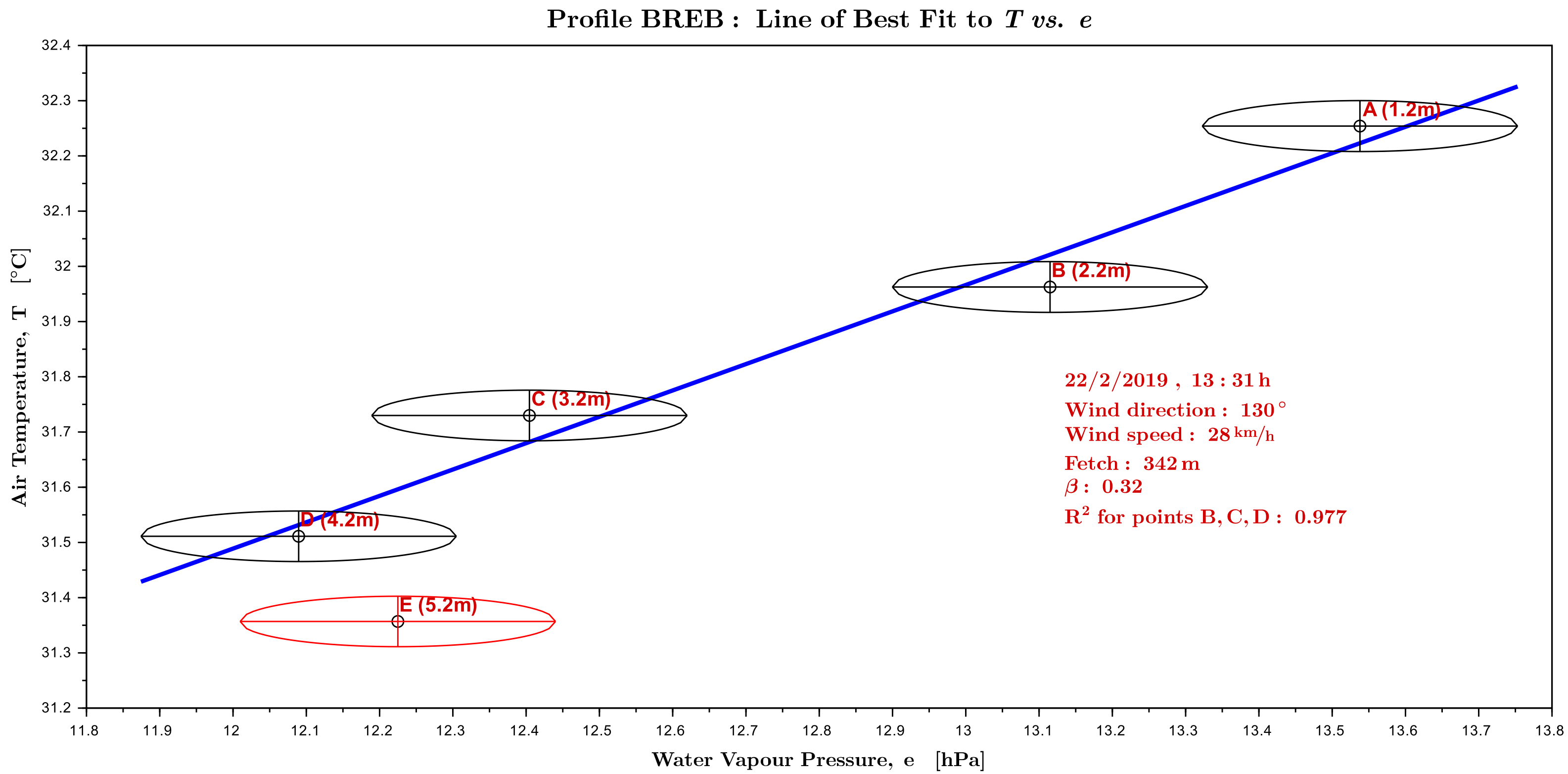

Figure 4.11: DS1: example from 22nd February, 2019, at 13:31 h, of the LoBF sub-algorithm (§ 3.3.3.1, p. 95) in action. In this particular case, the point at height 'E' was rejected from the line-fitting process because the regressed line did not intersect with its ellipse. The ellipses show the 95 % confidence extents based on the measurement uncertainties in e and T.

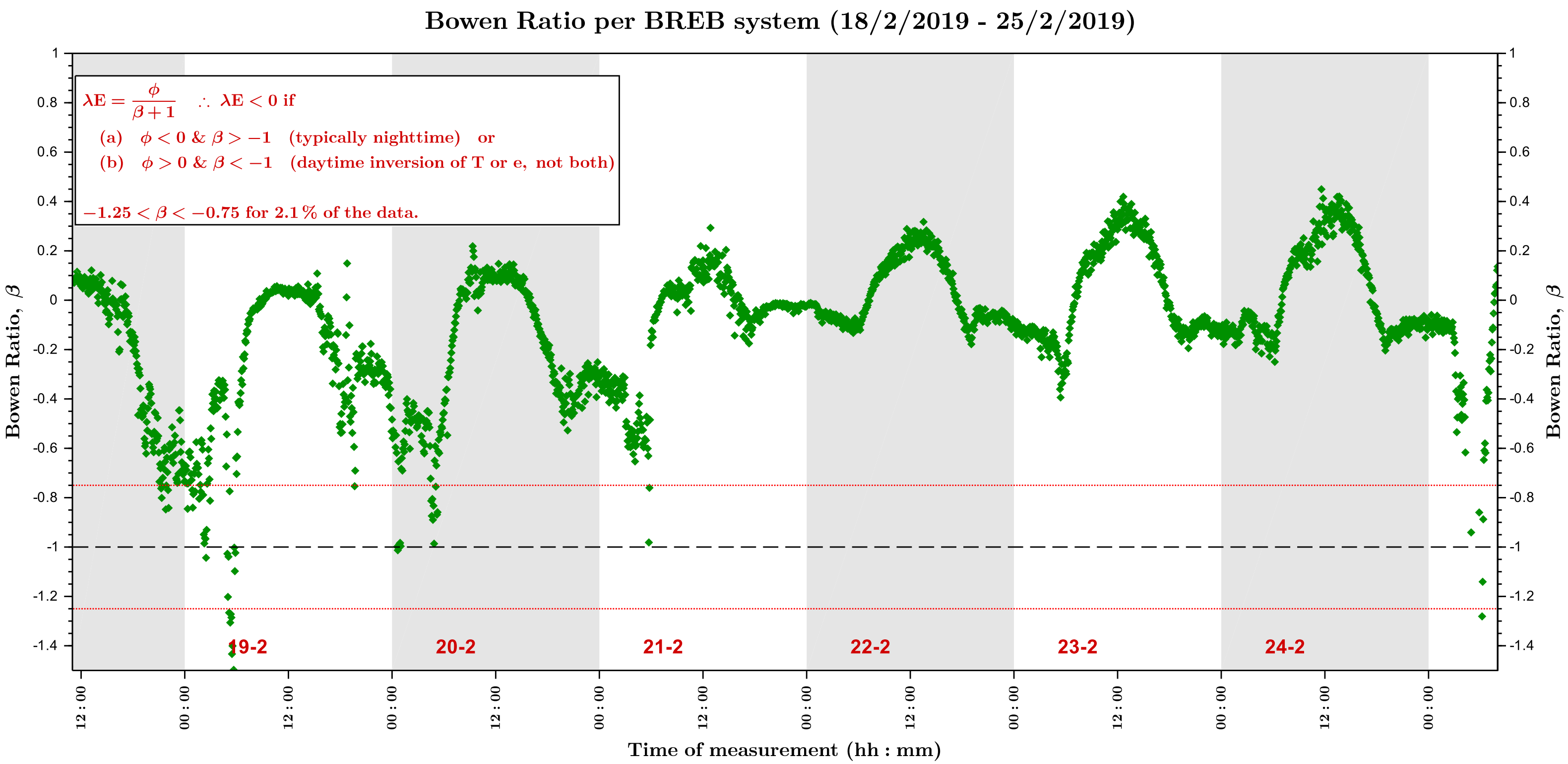

Figure 4.12: DS1: values for Bowen ratio, β, as determined by Profile BREB. The red lines mark $\beta = -0.75$ and $\beta = -1.25$, and the black dashed line marks $\beta = -1$.

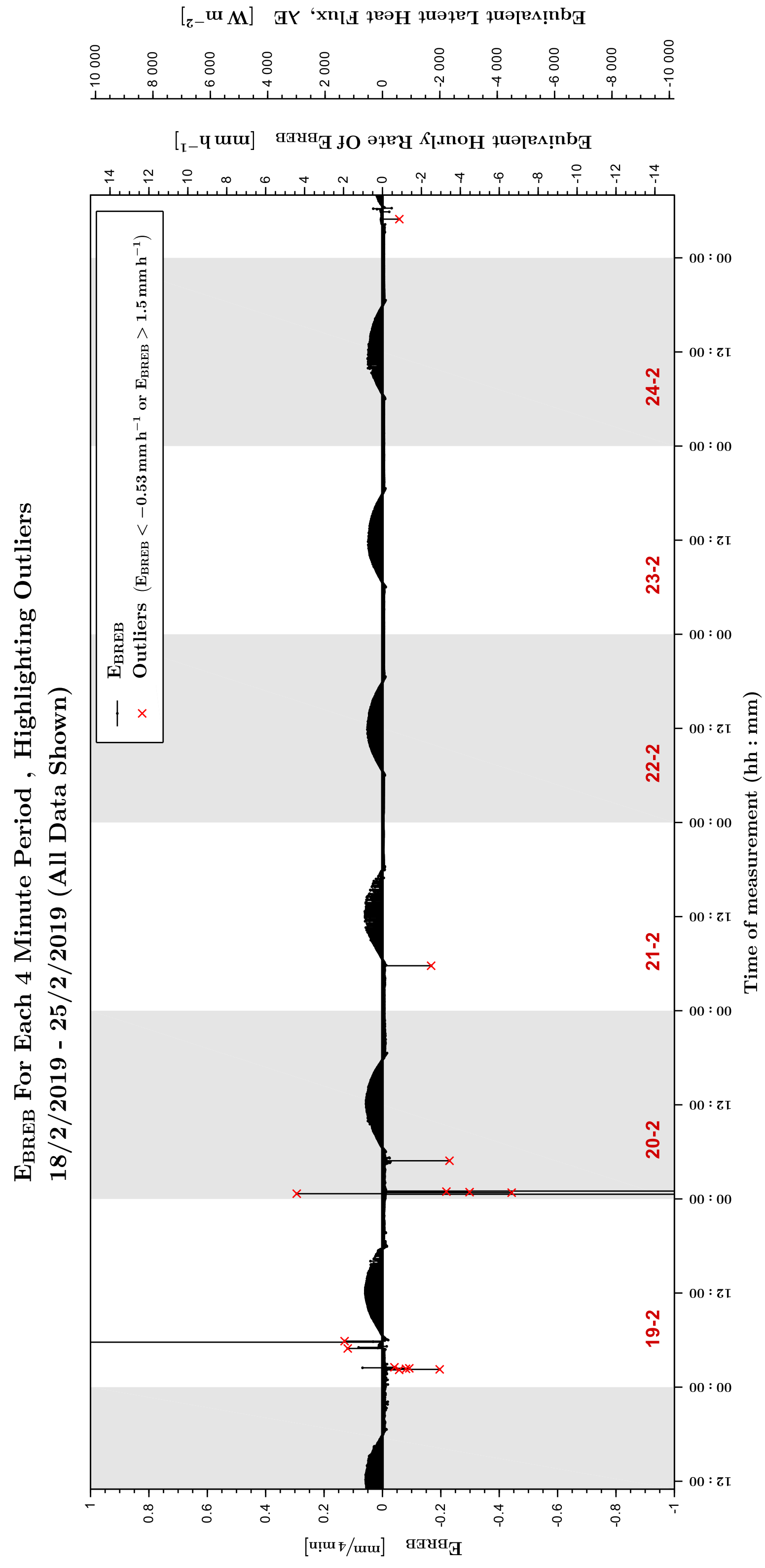

Figure 4.13: DS1: outliers in E_{BREB} that were impossibly large and had to be removed from subsequent analysis. Comparison with Fig. 4.12 (p. 133) shows that most of these values are associated with $\beta \approx -1$.

A change in the weather occurred on the 21st February[3] at around the same time as values of β abruptly increased. β then tended to increase thereafter, albeit very slowly. Two observations are made:

1. The recently irrigated soil was (apparently) able to adequately supply the plants with water during DS1. The low values of β indicate that the surface energy flux balance was dominated by λE, which could only happen in the presence of plentiful evapotranspiration. It was also observed (Fig. 4.1, p. 120) that the gap between T_S and T increased only slightly as the days progressed, despite ongoing high levels of insolation, i.e. evapotranspiration remained adequate for evaporative cooling. Likewise, β increased only slightly over the same period, i.e. λE decreased only slightly during this time since ϕ was essentially constant over this time (Fig. O.1, p. 428).

2. The small increase in β over DS1 was to be expected. Ongoing leaf transpiration and soil evaporation increases the soil water tension, ψ, making it more difficult to maintain adequate transpiration. This was observed in the slowly growing gap between T_S and T and in the rise of β as the days progressed, the latter phenomenon reflecting a growing share of the energy flux balance apportioned to H rather than λE.[4]

Fig. 4.15 (p. 137) presents the results for E_{BREB} for DS1. Fig. 4.16 (p. 138) presents the same results but with the 95 % CI (the orange-coloured bars) for each calculated value of E_{BREB}. The magnitude of the 95 % CI was impacted by the time of day and the environmental conditions at the field. The histogram in Fig. 4.17 (p. 139) shows the frequency distribution of E_{BREB} values during DS1. Most values of E_{BREB}

[3]From the weather data earlier in this chapter it can be seen that there were changes to cloud cover, P, e and RH.

[4]This does not contradict the first observation. The $T_S - T$ temperature gap and β were increasing, but slowly. That they didn't increase faster was due to the capacity of the soil to replenish water to the root-zone and the soil surface from deeper in the profile such that transpiration and evaporation could (nearly) be maintained at a constant rate.

fell in the following ranges:

$$\begin{array}{rrcl}
\text{Daytime (53 \% of data)} & 0 < E_{BREB} < & 0.90 & [\mathrm{mm\,h^{-1}}] \\
\text{Nighttime (47 \% of data)} & -0.15 < E_{BREB} < & -0.05 & [\mathrm{mm\,h^{-1}}]
\end{array}$$

Figure 4.14: Photograph from a drone, facing southwest, of Profile BREB in Field 14, February 2019. The sonic anemometer, infrared radiometric thermometer (for GPSTIC) and the datalogger's 3G antenna are at the top of the mast.

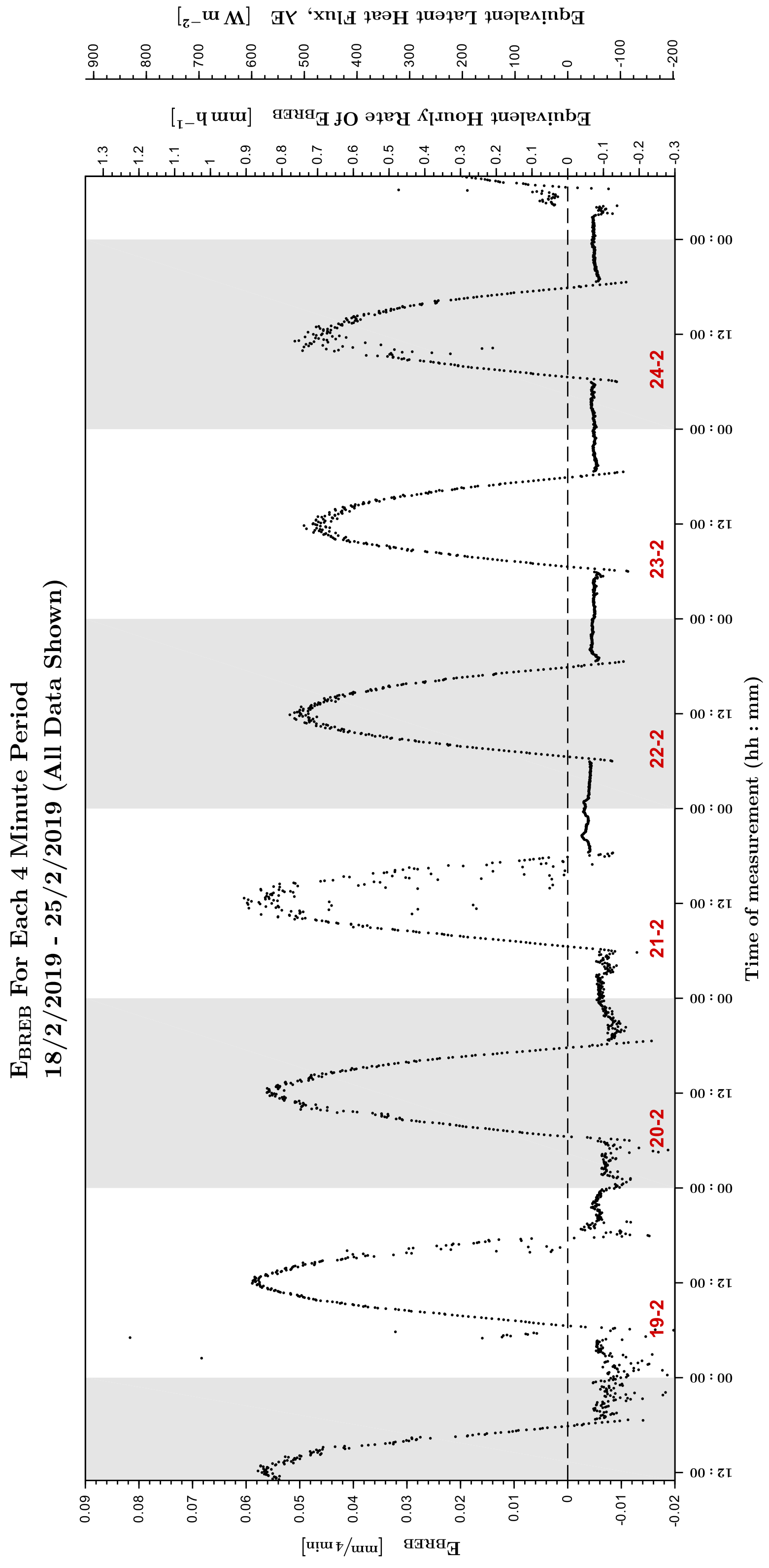

Figure 4.15: DS1: all modelled values for evapotranspiration per Profile BREB, i.e. E_{BREB}.

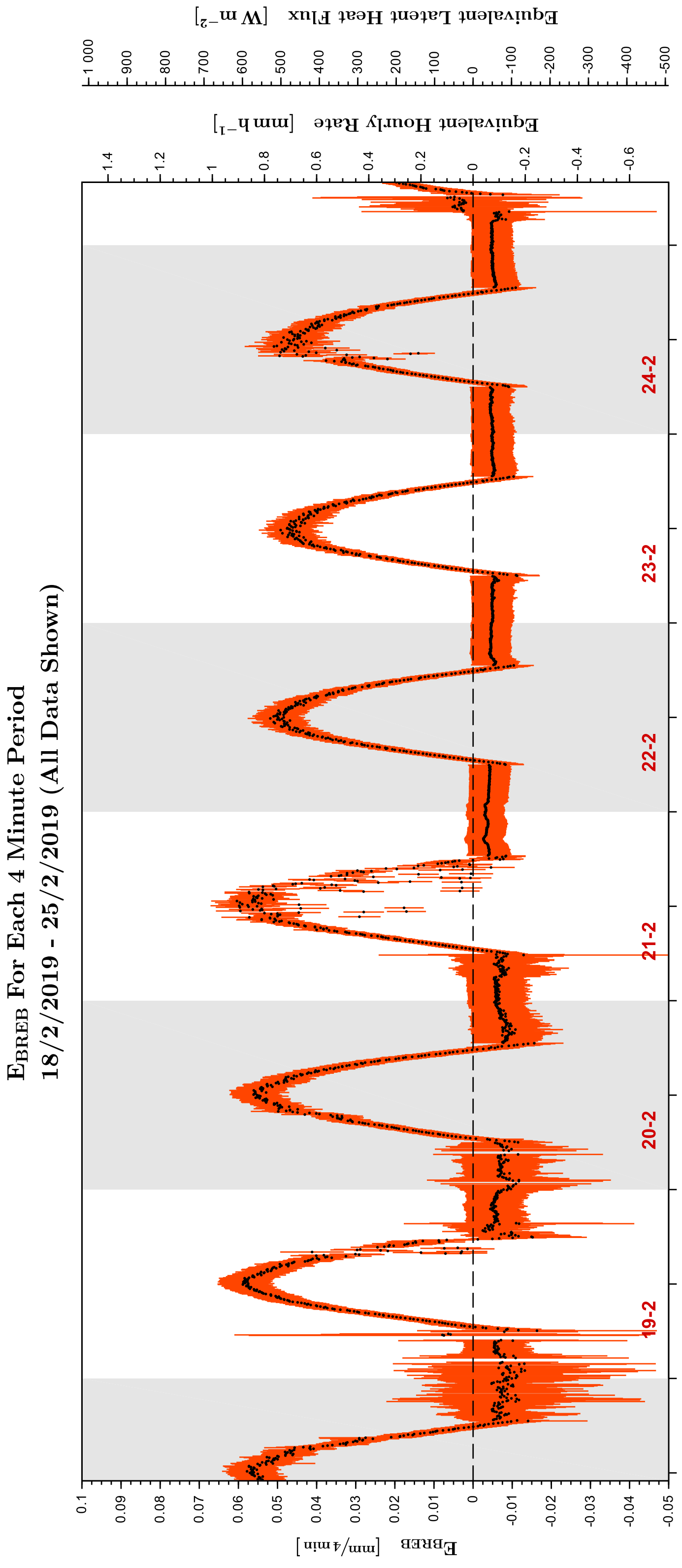

Figure 4.16: DS1: all modelled values for evapotranspiration per Profile BREB, i.e. E_{BREB}. The orange coloured error bars indicate the 95 % CI for each calculated value of E_{BREB}.

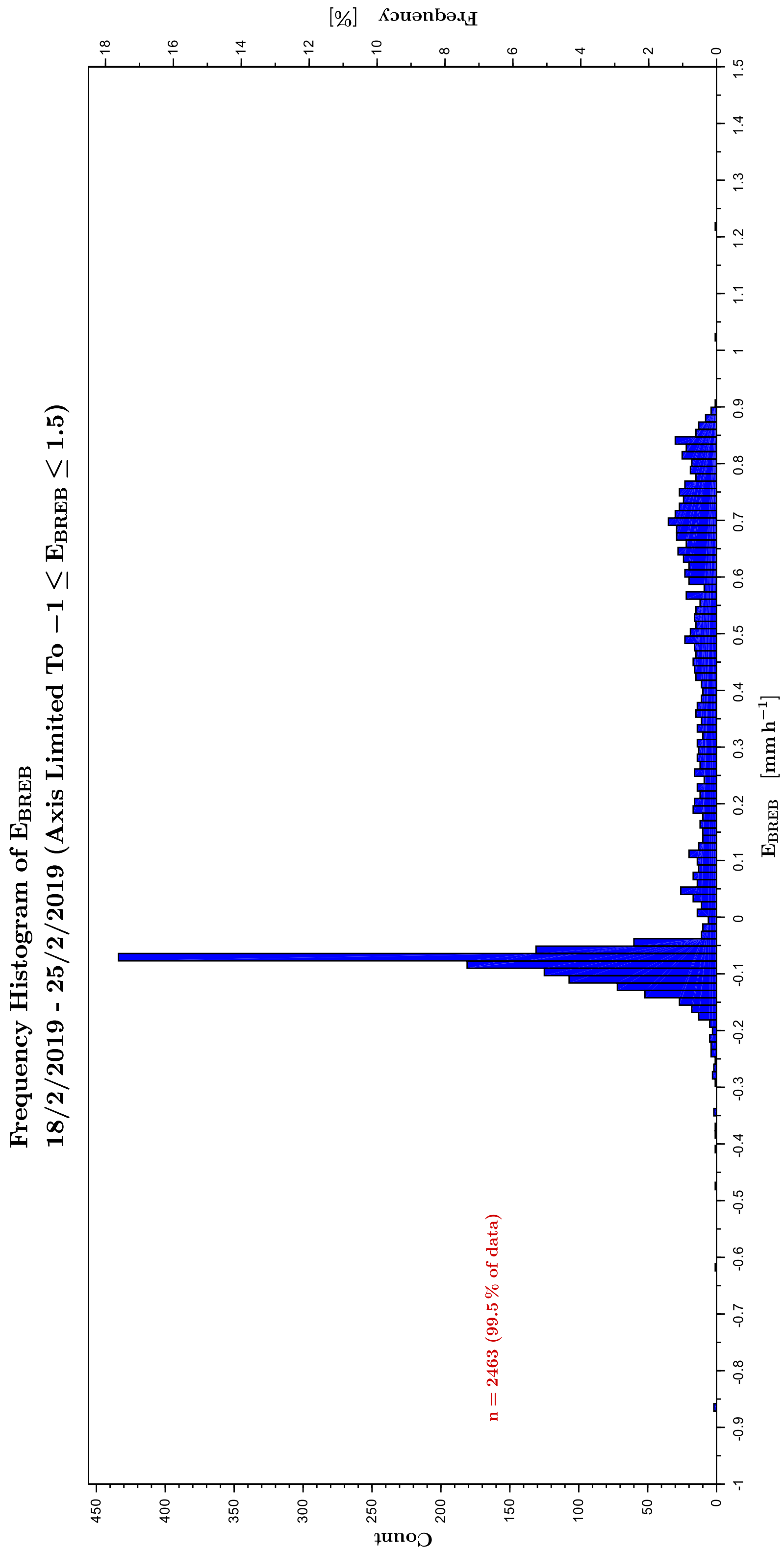

Figure 4.17: DS1: frequency histogram showing the distribution of E_{BREB}.

4.2.3 Results for GPSTIC During DS1

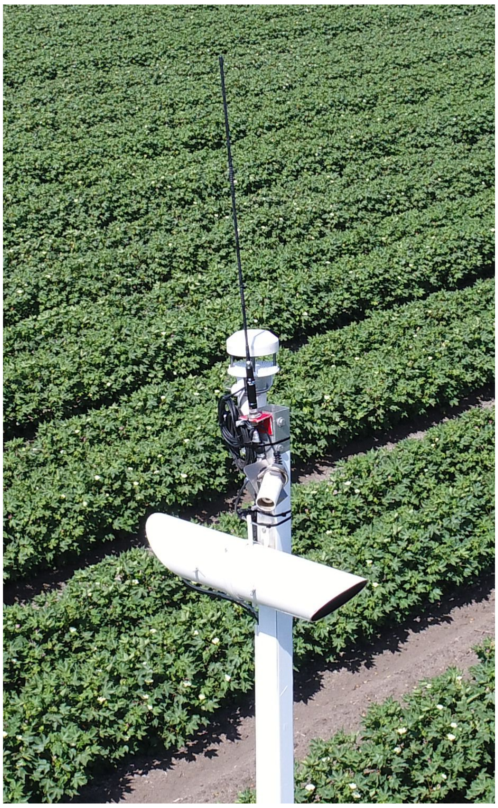

Figure 4.18: Photograph from a drone, February 2019, facing southwest, of the Apogee SI-411 infrared radiometer (IRR), visible just above the radiation shield. It was aimed at 45° below the horizontal and pointed toward a bearing of 45°. From the height of 5.5 m the area of ground visible to the sensor was 57 m^2.

GPSTIC was calculated at the same instances as Profile BREB to allow a like-with-like comparison of the two models. The input data to the GPSTIC model were the very same as used by Profile BREB, i.e. the same sensors supplied identical data to each of the models. The one exception was the SI-411 IRR that was used exclusively by GPSTIC. The commonality of sensors was deliberate in the design of the experiment so as to remove the confounding influence of using different sensors for different models.

α_{PT} was the single user-selected variable in GPSTIC (Profile BREB had no user-selected variables). The GPSTIC modelling was repeated for a range of values of α_{PT} between 0.95 and 1.50, including $\alpha_{PT} = 1.26$ (Mallick et al. 2014) and the internal iterative optimisation process for α_{*PT*}.[5]

Just as was done for E_{BREB}, example plots of E_{GPSTIC} vs. time are given (Fig. 4.19, p. 142 and Fig. 4.20, p. 143), the latter showing the 95 % CI for each modelled value of E_{GPSTIC}. A frequency histogram showing the spread of the results from GPSTIC is given in Fig. 4.21 (p. 144). These plots are for when a value of $\alpha_{PT} = 1.05$ was used in the modelling (which is shown in § 5.2.1, p. 218 to be the optimum value for α_{PT} for DS1). For $\alpha_{PT} = 1.05$ most values of E_{GPSTIC} fell in the following ranges:

Daytime (53 % of data)	$0 < E_{GPSTIC} < 0.85$	$[\mathrm{mm\,h^{-1}}]$
Nighttime (47 % of data)	$-0.1 < E_{GPSTIC} < 0$	$[\mathrm{mm\,h^{-1}}]$

Comparing Fig. 4.19 (p. 142) with Fig. 4.15 (p. 137) E_{GPSTIC} exhibited less scatter than E_{BREB} regardless of the time of day and GPSTIC did not produce any extreme outliers. The range of values of E_{GPSTIC} tended to be slightly narrower than for E_{BREB}.

The 95 % CI of E_{GPSTIC} were narrower and more consistent over time compared to those of E_{BREB}.[6]

These comparisons between E_{GPSTIC} and E_{BREB} held true regardless of the value of α_{PT}. The influence of the α_{PT} was to effectively shift the range of values of E_{GPSTIC} up or down as α_{PT} was made larger or smaller, respectively. A sensitivity analysis of the GPSTIC variables (Appendix G, p. 375) showed that E_{GPSTIC} was approximately proportional to α_{PT}. This relationship can be seen in Table 5.4 (p. 218).

[5] The internal iterative optimisation process for selecting α_{*PT*} developed in Mallick et al. (2015a) was included in the GPSTIC algorithm at Step 16 (p. 115). It later became apparent, however, that for GPSTIC there was no overall improvement in the modelling results by using α_{*PT*}.

[6] The difference in CI between the models was due to how measurement errors were propagated through the models and reflected that under some atmospheric conditions the sizes of the Profile BREB CI increased markedly.

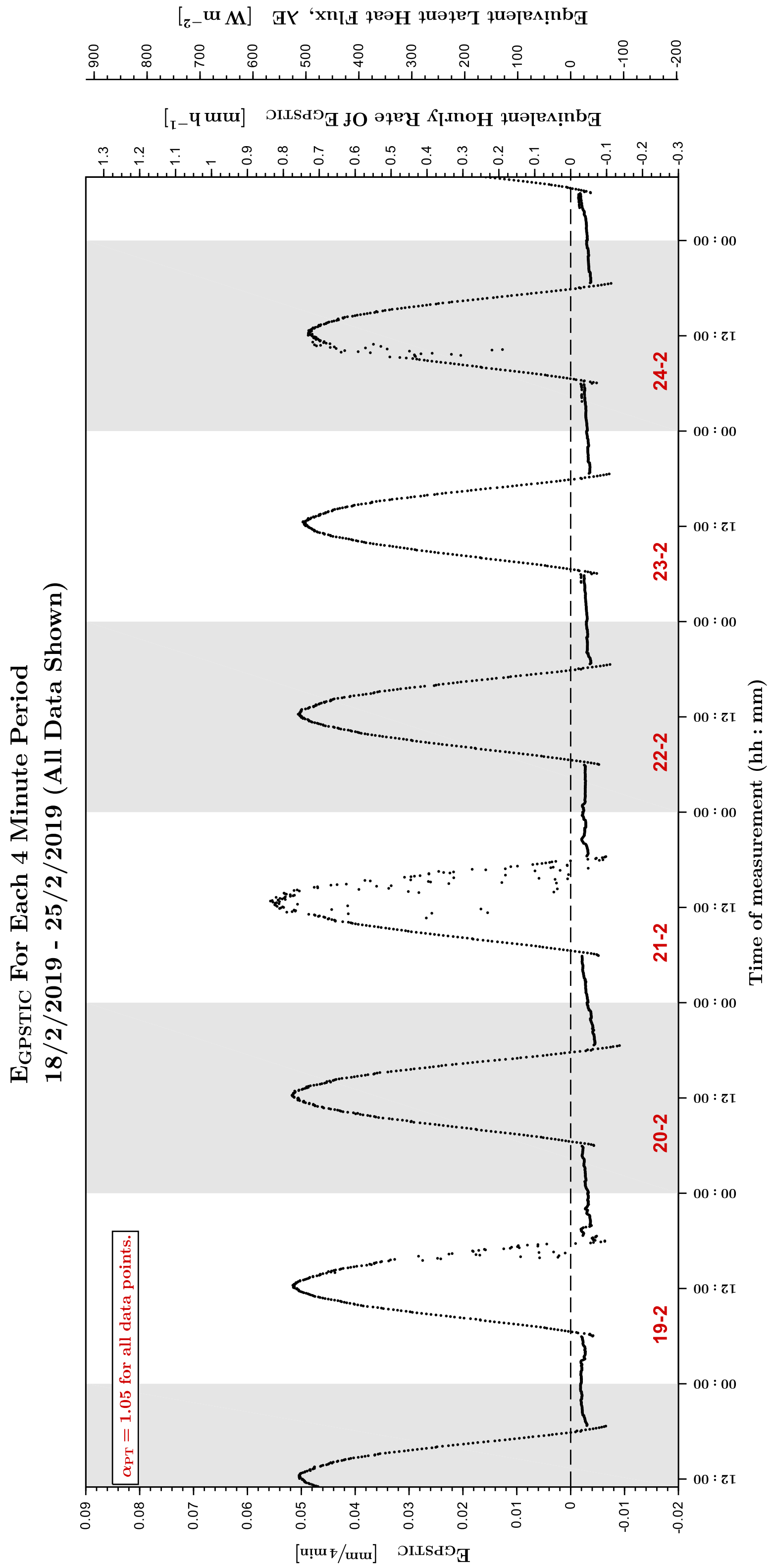

Figure 4.19: DS1: all modelled values for evapotranspiration per GPSTIC, i.e. E_{GPSTIC}, when $\alpha_{PT} = 1.05$.

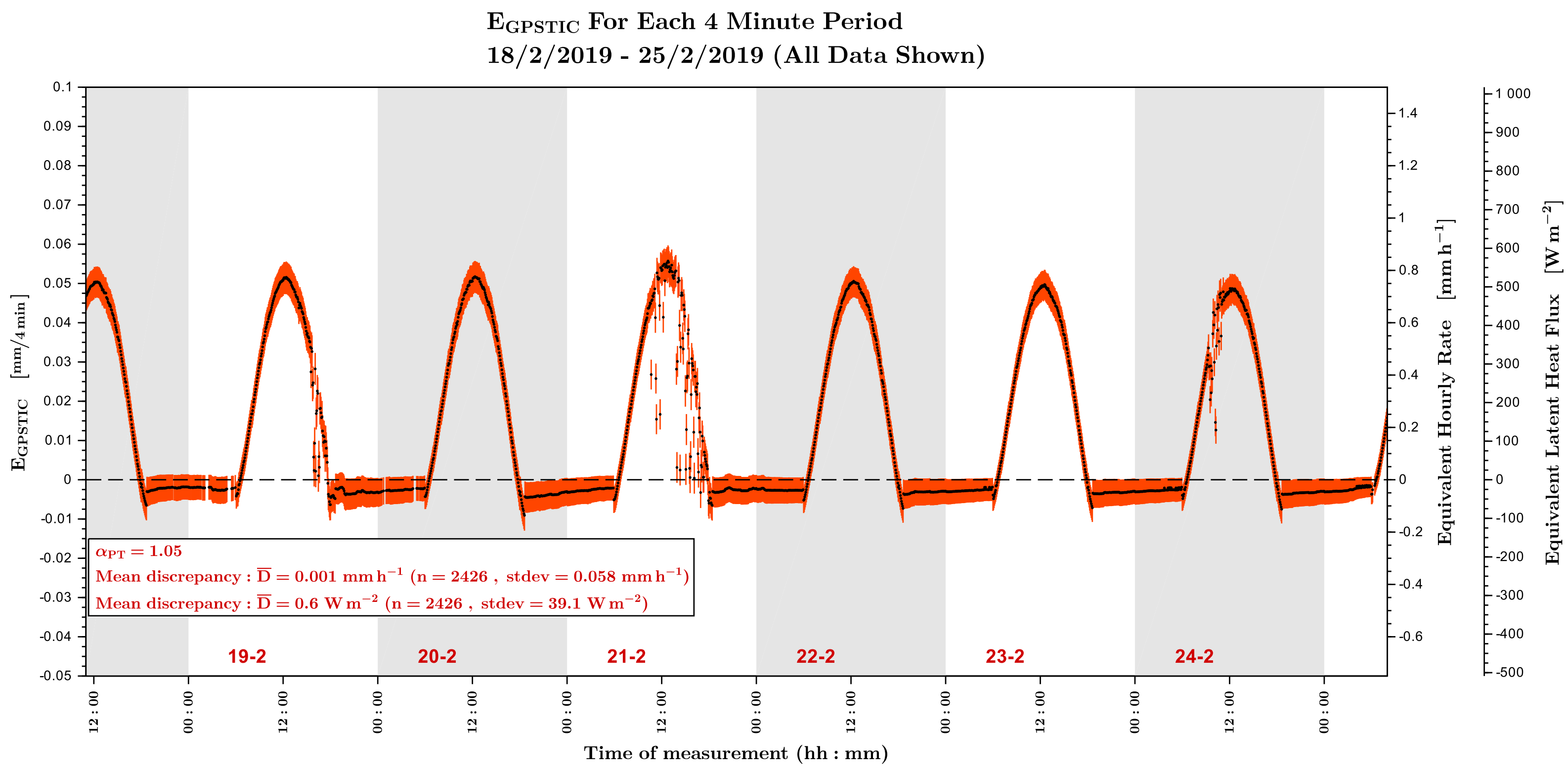

Figure 4.20: DS1: all modelled values for evapotranspiration per GPSTIC, i.e. E_{GPSTIC}, when $\alpha_{PT} = 1.05$. The orange coloured error bars indicate the 95 % CI for each calculated value of E_{GPSTIC}.

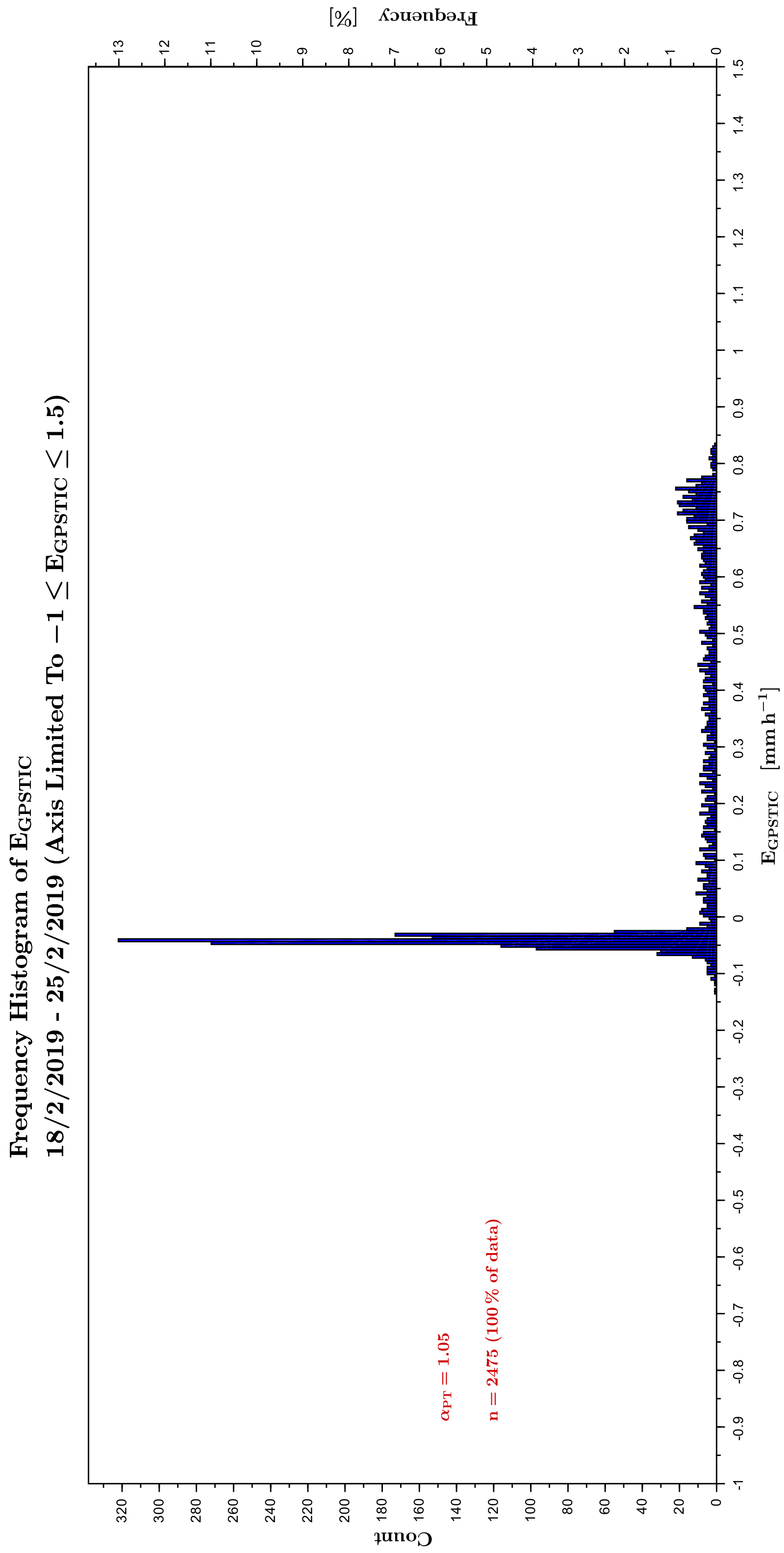

Figure 4.21: DS1: frequency histogram showing the distribution of E_{GPSTIC}, when $\alpha_{PT} = 1.05$.

4.3 Data Set Two (DS2)

Data Set Two (DS2) comprised 311 consecutive hours of measurements over the period 22nd October to 4th November, 2019. A description of the field site for DS2 is given in § 3.1.2 (p. 60).

4.3.1 Weather Conditions During DS2

Figures 4.22 - 4.26 (pp. 146 - 150) present the weather data during DS2 that were most relevant for Profile BREB and GPSTIC. Additional weather data for DS2 are presented in Appendix P (p. 437).

During DS2 Australia was in the midst of a severe drought and the winter months of 2019 preceding DS2 had been exceptionally dry and warm. The disastrous bushfires of the 2019 - 2020 summer were yet to begin in earnest but already a faint smudge of smoke from distant fires was visible around the horizon at sunrise and sunset.

T was approx. 30 - 34 °C during the day with overnight minimums of 10 - 20 °C (Fig. 4.22, p. 146) which was typical for that time of the year. T and RH were measured at 1.2 m above the bare soil (the height of the lowest radiation shield). Vapour pressures (Fig. 4.23, p. 147) were generally low and T_D dropped below −5 °C on the 27th and 28th February, reflecting the very arid conditions prior to and during DS2.

Field 16 was irrigated to field capacity by furrow irrigation on the 23rd October. There were also some light showers of rain during DS2: 0.2 mm of rain fell on the 26th October and 15.0 mm of rain fell on the 3rd November. Light mist above the bare soil was observed overnight on the 23rd October and 4th November (the only nights that the author was present at the field site) but it was difficult to determine whether any dew was deposited on the bare soil.

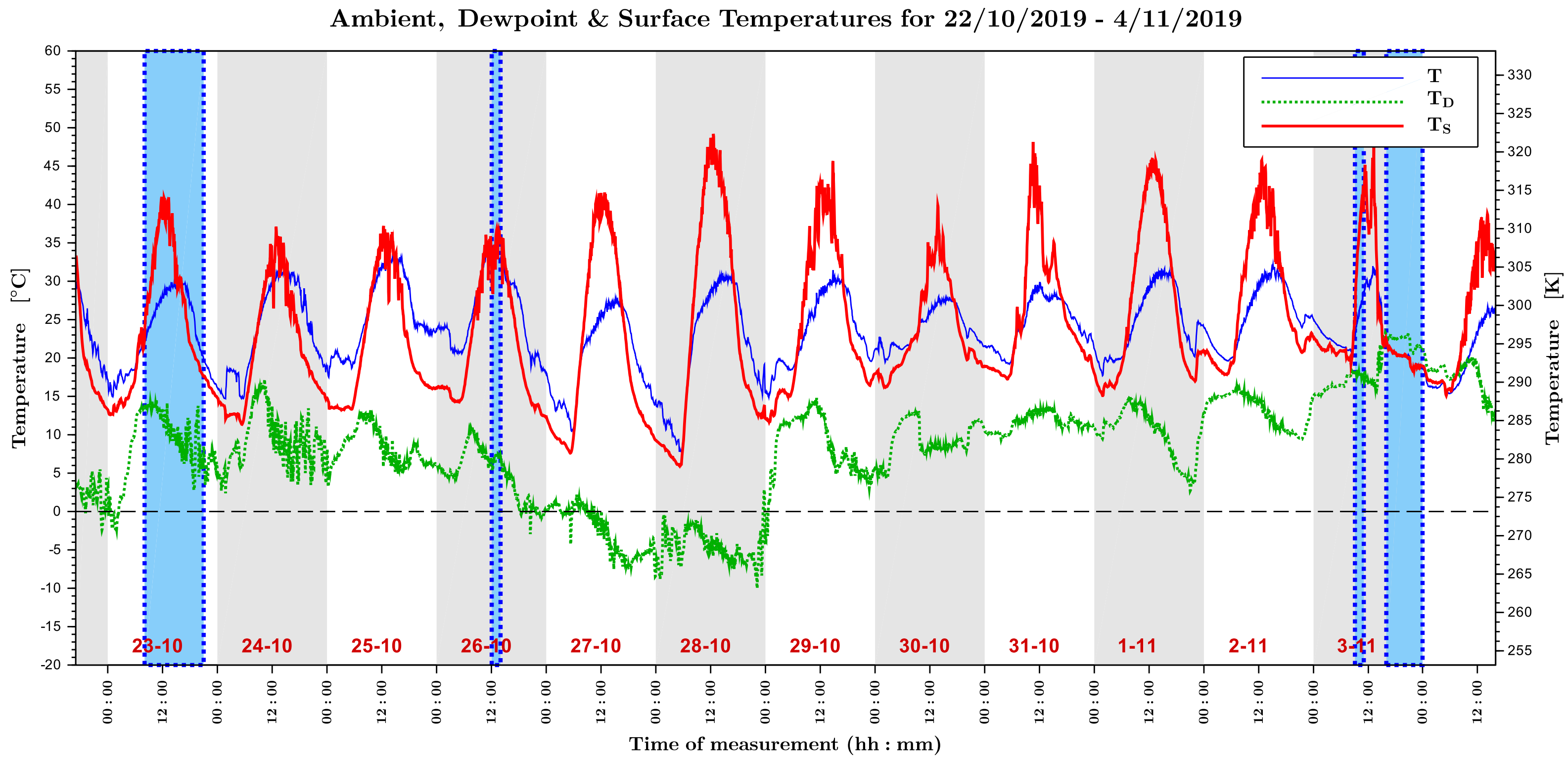

Figure 4.22: Temperatures in Field 16 during DS2. Ambient temperatures (T) and dewpoint temperatures (T_D) were measured 1.2 m above the bare soil; surface temperatures (T_S) were measured using an infrared radiometer at 5.4 m above the soil (with a visible surface area of 57 m^2). The shaded blue rectangles indicate when irrigation (23rd October) or rainfall occurred.

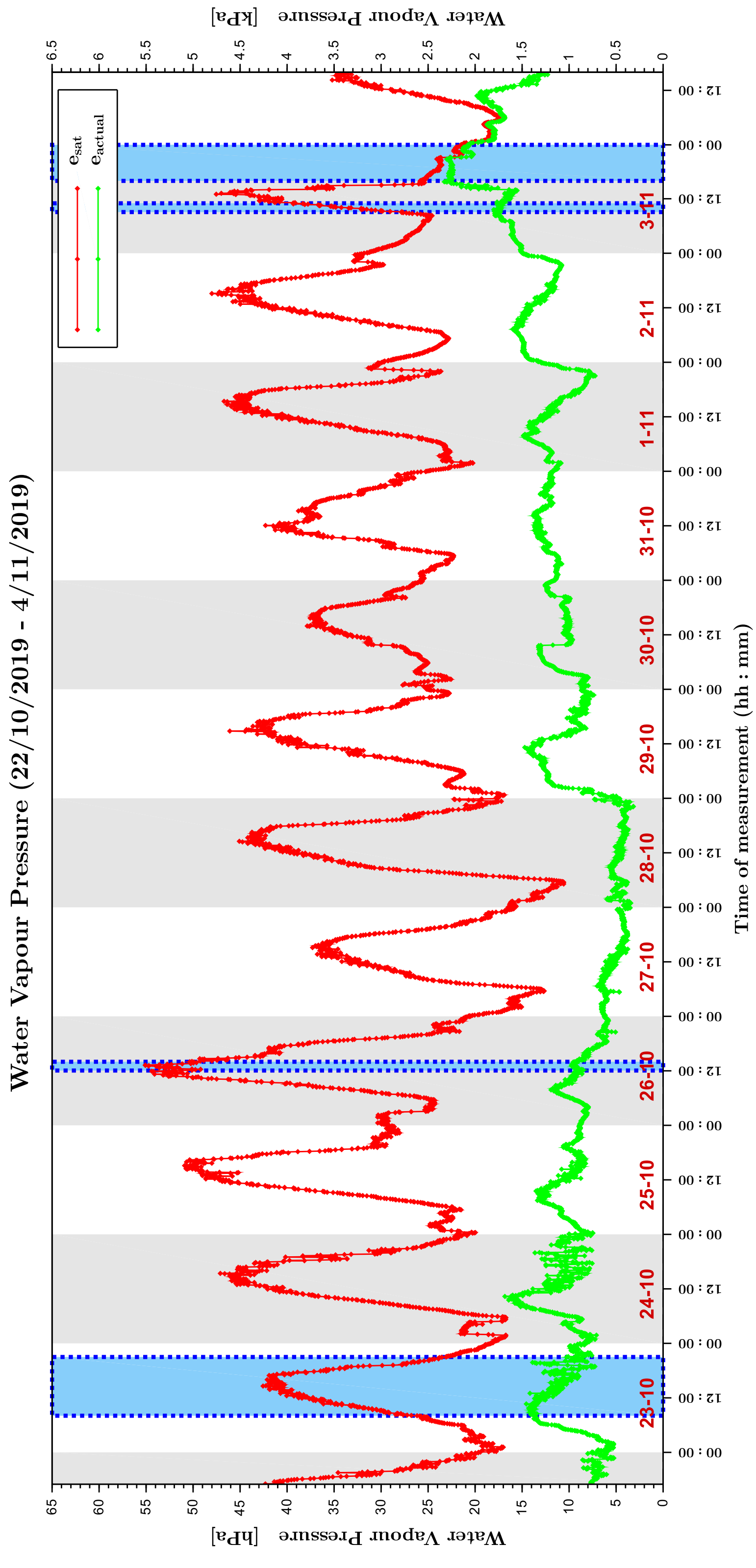

Figure 4.23: Saturation vapour pressure and actual vapour pressure, in Field 16 during DS2, as measured 1.2 m above the bare soil. Saturation vapour pressure was calculated using the Buck Equation (Eqn. 3.15, p. 96). The shaded blue rectangles indicate when irrigation (23rd October) or rainfall occurred.

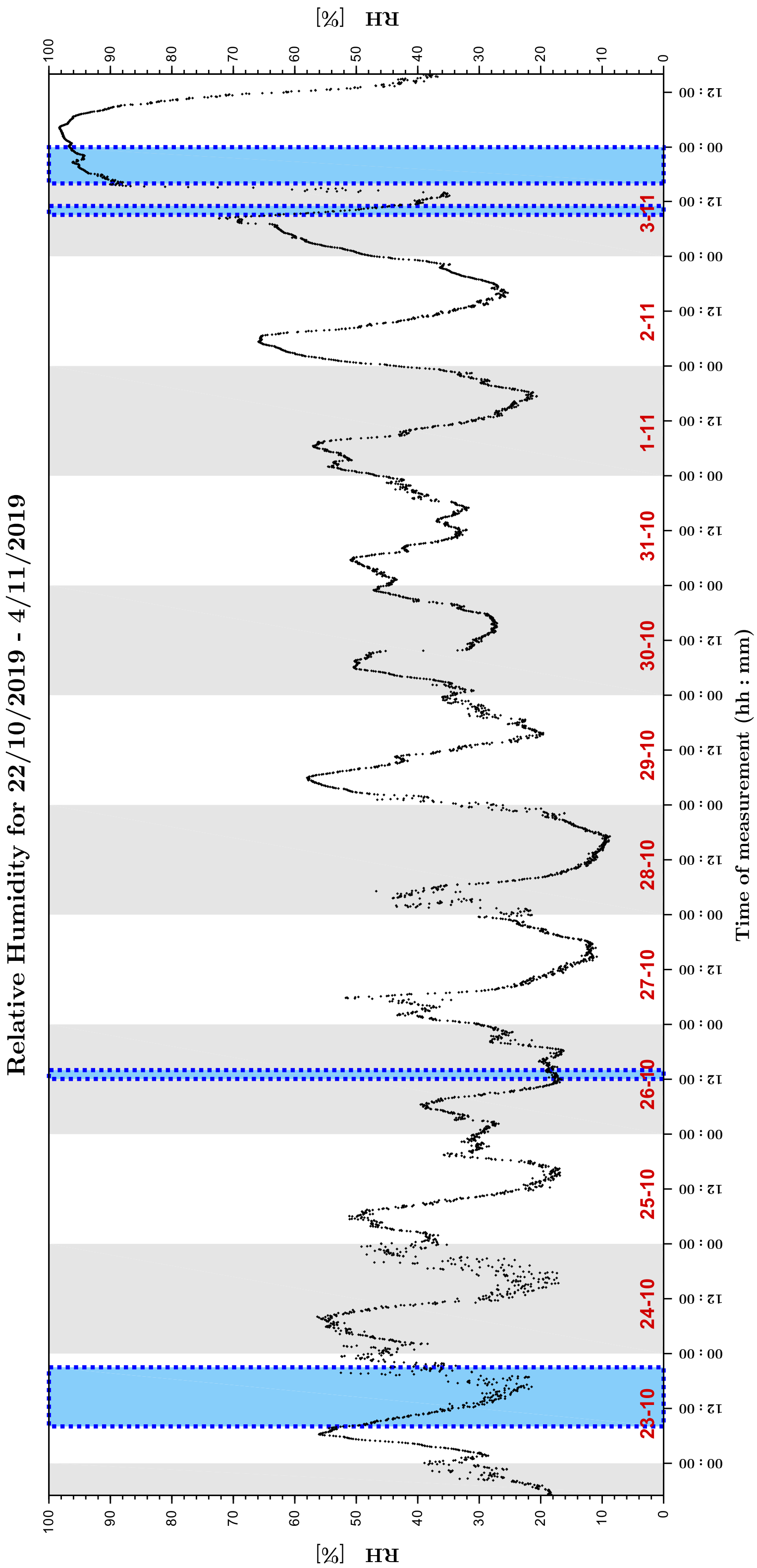

Figure 4.24: Relative humidity in Field 16 during DS2, as measured 1.2 m above the bare soil. The shaded blue rectangles indicate when irrigation (23rd October) or rainfall occurred.

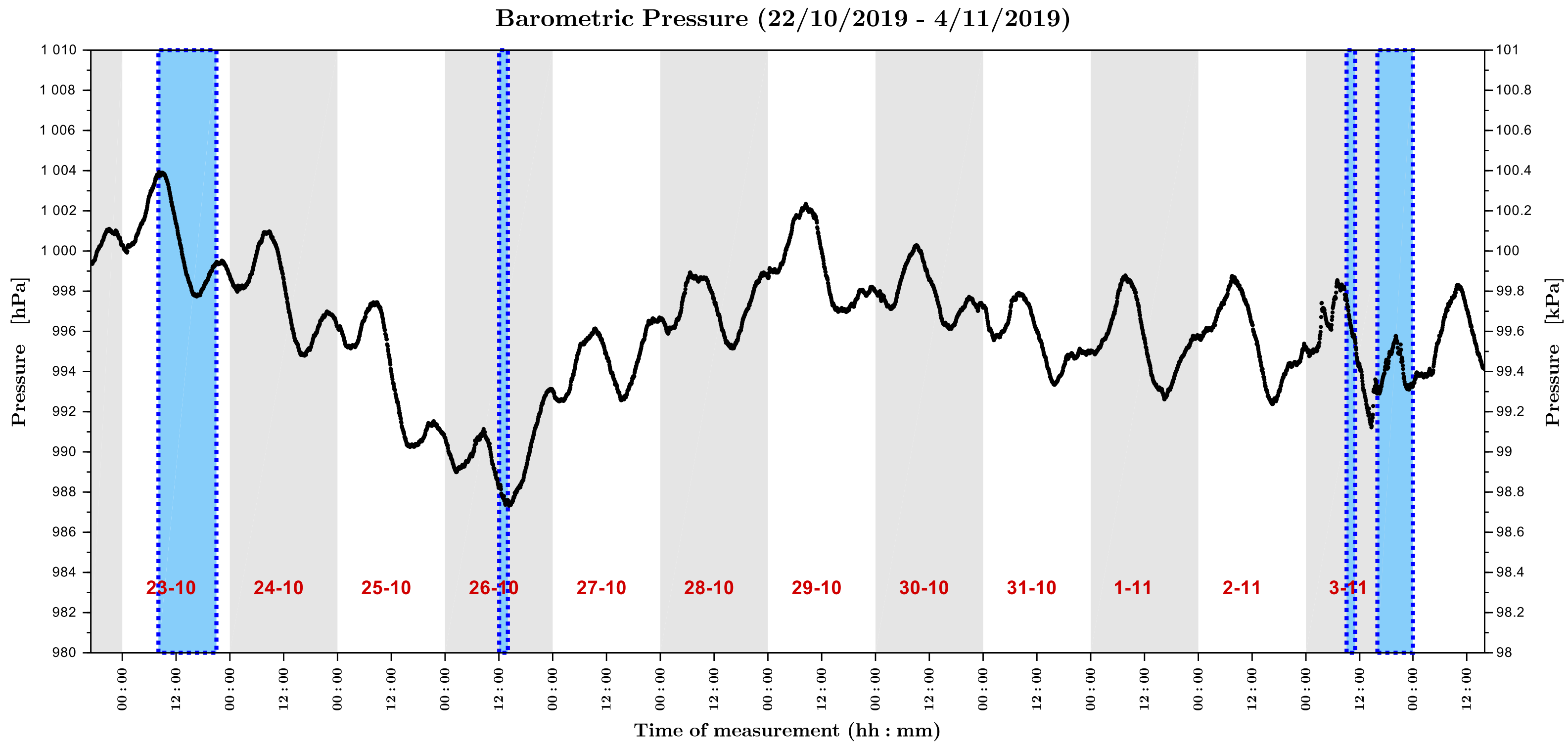

Figure 4.25: DS2: barometric pressure, P [hPa], measured every 60 s at 1.6 m above the soil surface (171 m above sea level). The shaded blue rectangles indicate when irrigation (23rd October) or rainfall occurred.

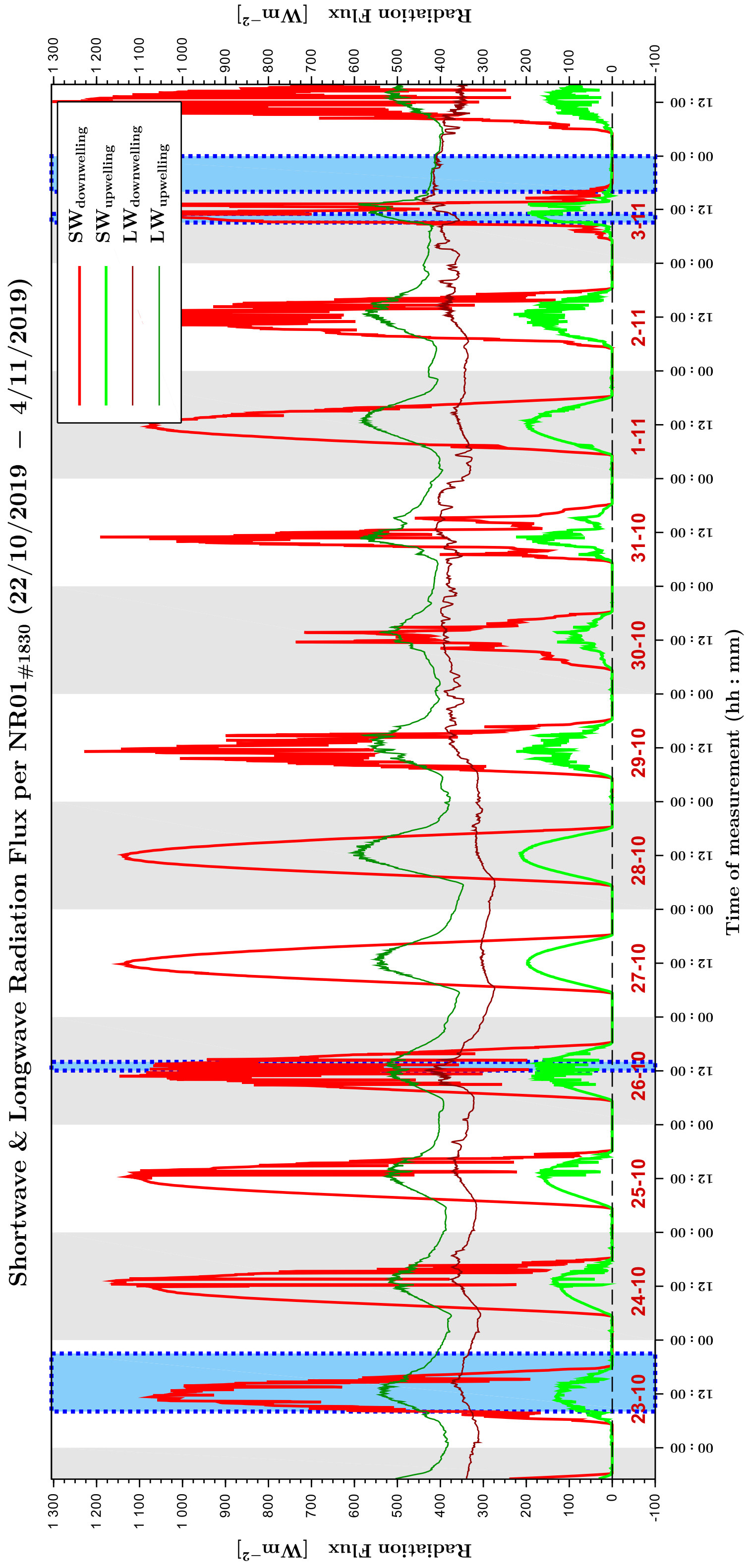

Figure 4.26: Downwelling and upwelling radiation (shortwave and longwave) in Field 16 during DS2. The net radiometer was a Hukseflux NR01 (#1830). The shaded blue rectangles indicate when irrigation (23rd October) or rainfall occurred.

Two NR01 net radiometers (serial numbers #1830 and #1236) were used during DS2 and both operated without any problems. Only the radiation data from the laboratory-calibrated $\mathrm{NR01}_{\#1830}$ were used for GPSTIC and Profile BREB.

4.3.1.1 DS2 Shortwave Radiation Data

The shortwave radiation (0.285 - 3.00 µm) measurements were in the range

$$0 \leqslant SW_{downwelling} \leqslant 1303 \quad [\mathrm{Wm^{-2}}] \tag{4.6}$$

$$0 \leqslant SW_{upwelling} \quad \leqslant \quad 230 \quad [\mathrm{Wm^{-2}}] \tag{4.7}$$

At first glance the maximum value for $SW_{downwelling}$ may appear too high, especially since the 'clear-sky' models (Appendix L, p. 409) predict shortwave radiation to be approx. 950 - 1040 $\mathrm{Wm^{-2}}$. However, the following points are relevant:

- The highest values of $SW_{downwelling}$ all occurred on days with broken cloud and so the estimates produced by the *clear-sky* models were not necessarily valid.

- Fig. 4.26 (p. 150) shows that most maximums of $SW_{downwelling}$ during DS2 were approx. 1100 - 1150 $\mathrm{Wm^{-2}}$, i.e. the maximum value of $SW_{downwelling} = 1303\,\mathrm{Wm^{-2}}$ in Eqn. 4.6 was not representative of the data.

- $\mathrm{NR01}_{\#1236}$ measured $SW_{downwelling} = 1285\,\mathrm{Wm^{-2}}$ at the same instance that $\mathrm{NR01}_{\#1830}$ measured $SW_{downwelling} = 1303\,\mathrm{Wm^{-2}}$. This is only a 1.4 % difference between the two pyranometers, i.e. well within the ± 3 % measurement uncertainty of the pyranometers.

- Vignola et al. (2016) reported that scattered clouds (that do not obstruct direct beam irradiance of the pyranometer) can cause measured $SW_{downwelling}$ to exceed clear-sky shortwave radiation by up to 10 % due to reflections off the clouds. Hukseflux (2017) stated that reflection against large cumulus clouds (Fig. 4.27, p. 152) can cause measurements of $SW_{downwelling}$ to be even in excess of the solar constant.[7]

Thus it can be concluded that the shortwave radiation measurements, whilst high, are not unreasonable.

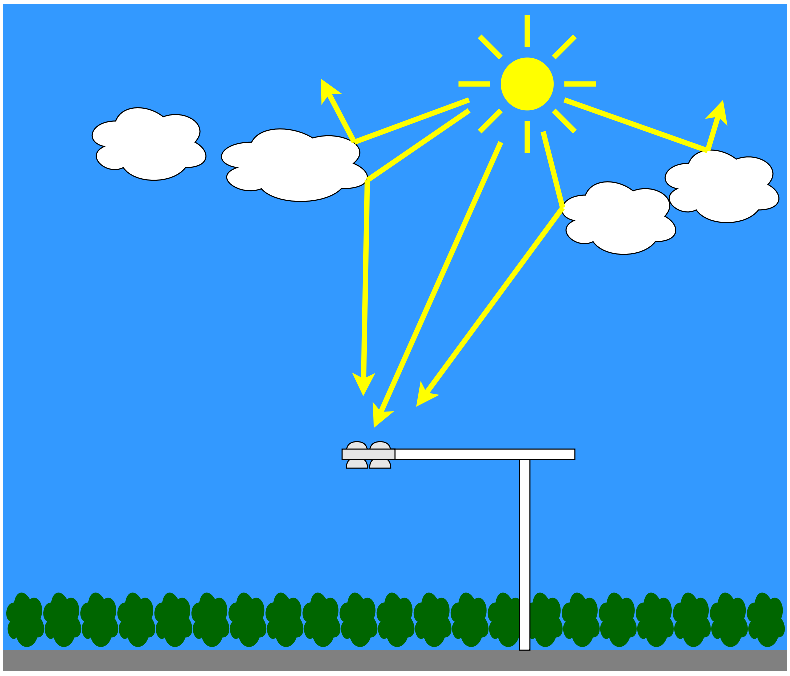

Figure 4.27: Illustration of the enhancement effect (by reflection) of broken clouds on a point measurement of downwelling shortwave radiation. Under such conditions it is possible that $SW_{downwelling}$ can exceed the solar constant (Hukseflux 2017).

[7]The solar constant is taken to be $S_0 = 1367\,\mathrm{W m^{-2}}$

4.3.1.2 DS2 Longwave Radiation Data

During DS2 the longwave radiation (4.5 - 40 µm) measurements were in the following ranges:

$$273 \leqslant LW_{downwelling} \leqslant 443 \quad [\mathrm{Wm}^{-2}] \tag{4.8}$$

$$346 \leqslant LW_{upwelling} \leqslant 606 \quad [\mathrm{Wm}^{-2}] \tag{4.9}$$

A method to evaluate the appropriateness of the longwave radiation data in Fig. 4.26 (p. 150) is to compare T_S as calculated by Eqn. 4.3 (p. 125) using the NR01$_{\#1830}$ upwelling longwave radiation data with the T_S measured by the IRR (Fig. 4.28, p. 154). The conformity of the two plots of terrestrial temperature is readily apparent (and further reflected in Fig. 4.29, p. 155) and thus the appropriateness of the upwelling longwave radiation data for DS2 is affirmed.

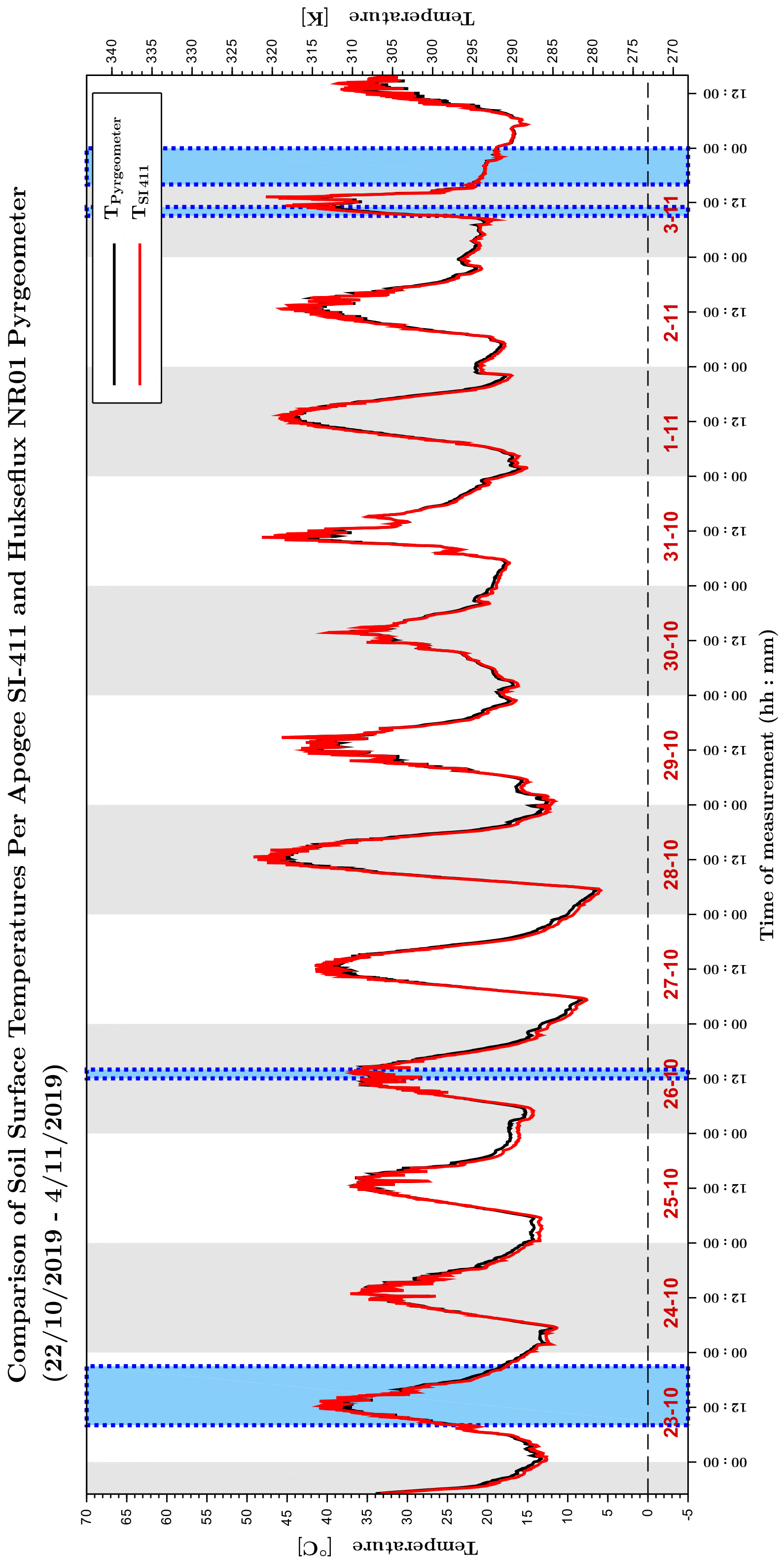

Figure 4.28: Comparison of T_S as determined by the IRR with that derived from the $NR01_{\#1830}$ downward facing pyrgeometer in Field 16 during DS2. The shaded blue rectangles indicate when irrigation (23^{rd} October) or rainfall occurred.

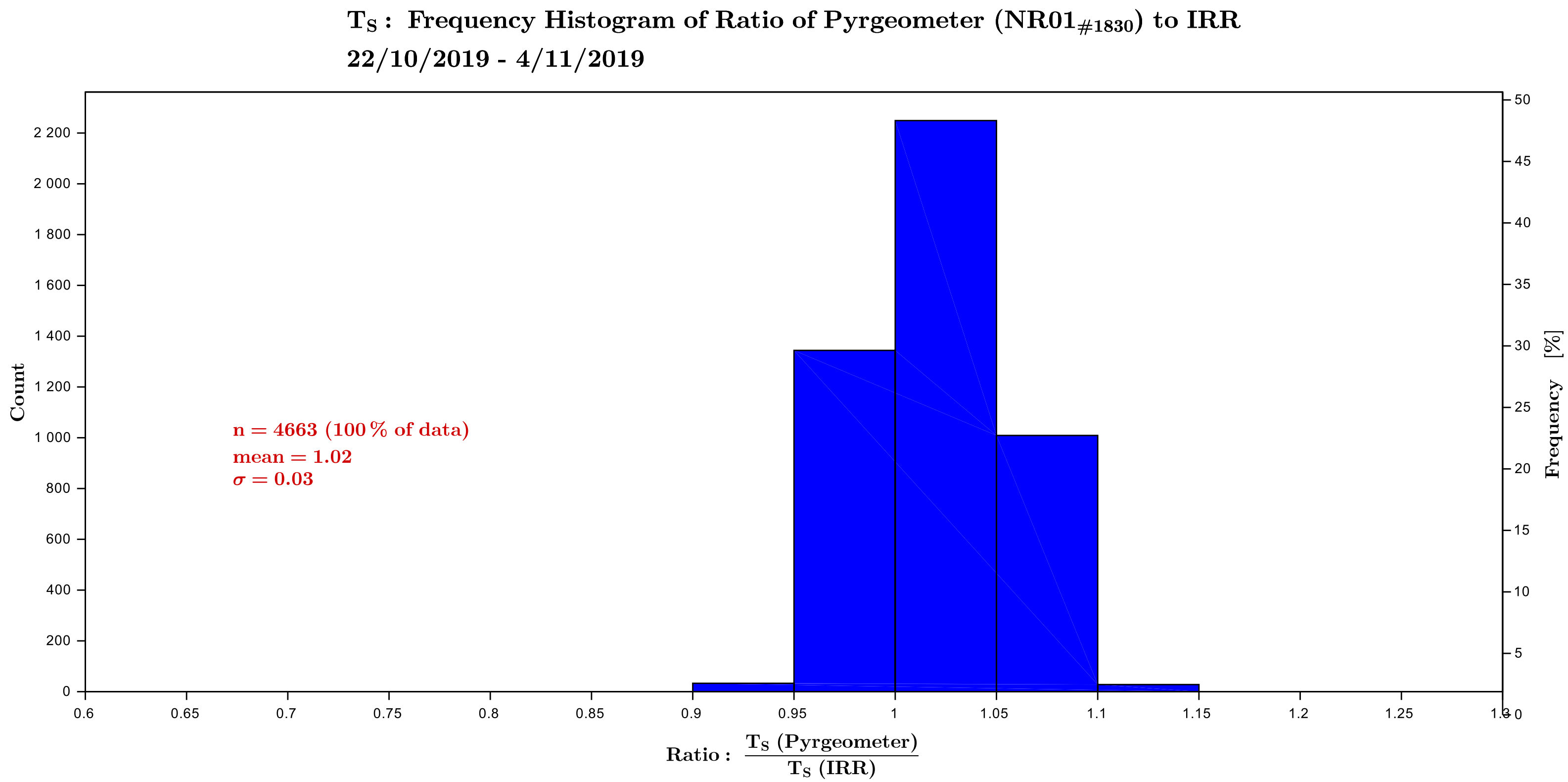

Figure 4.29: Frequency histogram of the ratio of T_S as determined by T_S derived from the $NR01_{\#1830}$ downward facing pyrgeometer to the IRR in Field 16 during DS2.

4.3.2 Results for Profile BREB During DS2

Profile BREB operated continuously above the bare soil for all 311 hours during DS2, making measurements every 60 s throughout the entire period. Fig. 4.30 (p. 156) and Fig. 4.31 (p. 157) show photographs of the Profile BREB system in Field 16 during DS2.

Profile BREB performed well despite the fact that its lowest sensors were 1.2 m above the bare soil (a consequence of being designed to operate above a fully grown cotton crop). Fig. 4.32 (p. 158) and Fig. 4.33 (p. 159) provide two examples from DS2 of the LoBF sub-algorithm in action. Fig. 4.34 (p. 160) provides a further example that demonstrates the ability of Profile BREB's algorithm to screen out (rare) occurrences where pairs of (e, T) would plot in a straight line but were found to be out of order, i.e. there wasn't a monotonically increasing or decreasing atmosphere profile of T or e.

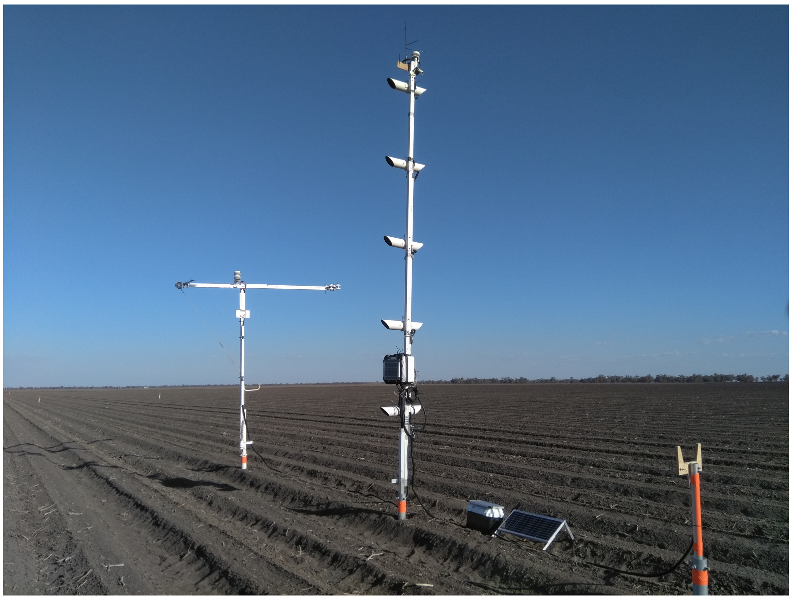

Figure 4.30: Photograph, looking east down the furrows, taken 22$^{\text{nd}}$ October 2019 (one day after planting and just prior to irrigation), of the Profile BREB mast with net radiometers in the background.

Figure 4.31: Photograph, facing south, of the Profile BREB / GPSTIC structure in Field 16, taken October 2019. The logger box is between the first and second radiation shields and has a solar panel on its front surface to power an extractor fan to help keep the box's interior temperature close to ambient temperatures. Without the fan the box's internal temperature was observed to rise above 60 °C.

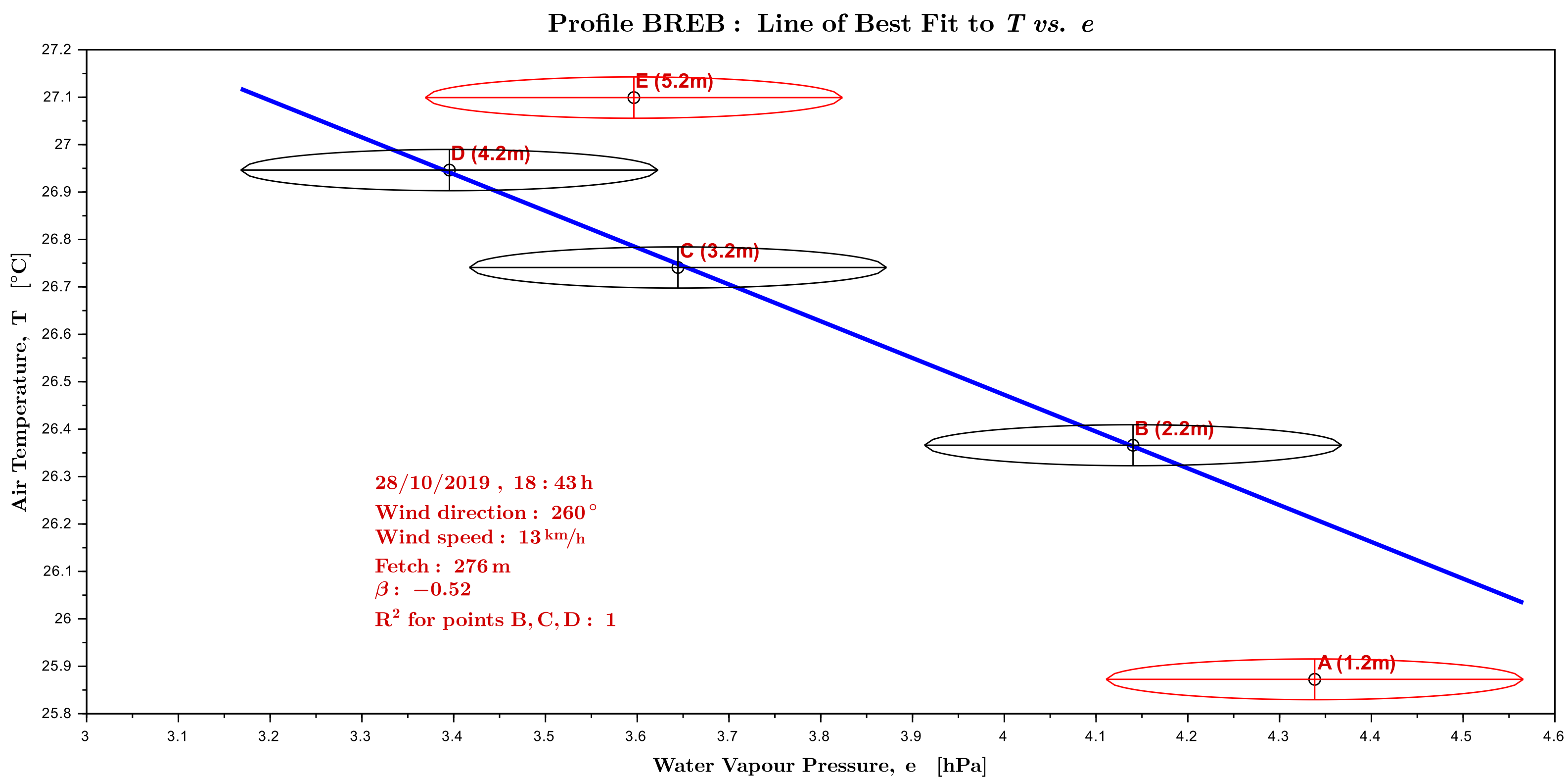

Figure 4.32: DS2: example from 28th October, 2019, at 18:43 h (five days after irrigation), of the LoBF sub-algorithm in action. The high quality fit ($R^2 = 1$) was possible by identifying that the lowest and highest (e, T) pairs should be excluded from the β calculations because they were too far removed from the LoBF. The ellipses show the 95 % confidence extents based on the measurement uncertainties in e and T.

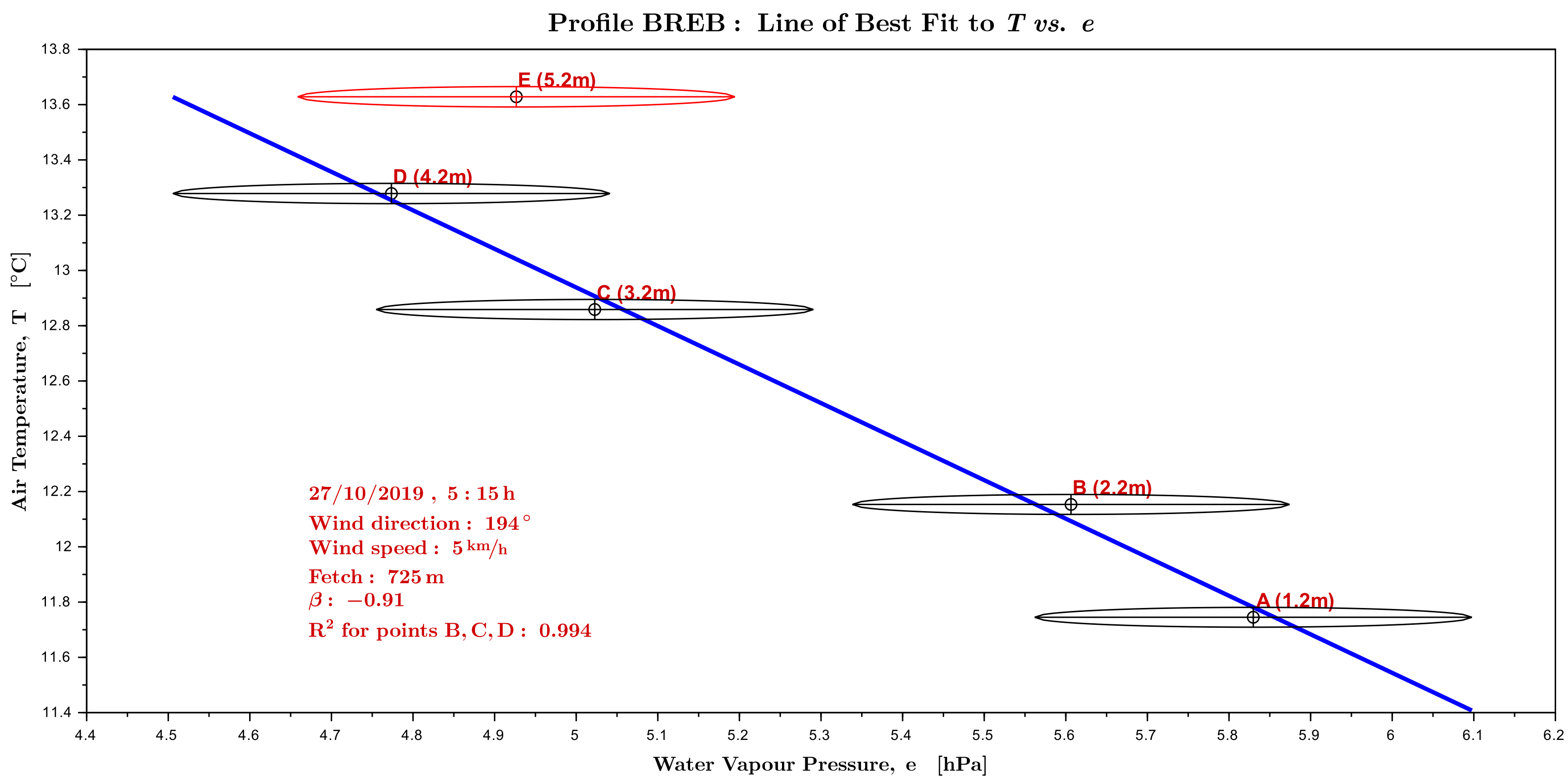

Figure 4.33: DS2: example from 27th October, 2019, at 05:15 h (four days after irrigation) of the LoBF sub-algorithm in action. The pair of (e, T) data at height 'E' was rejected from the line-fitting process because the regressed line did not intersect with its ellipse. The ellipses show the 95 % confidence extents based on the measurement uncertainties in e and T.

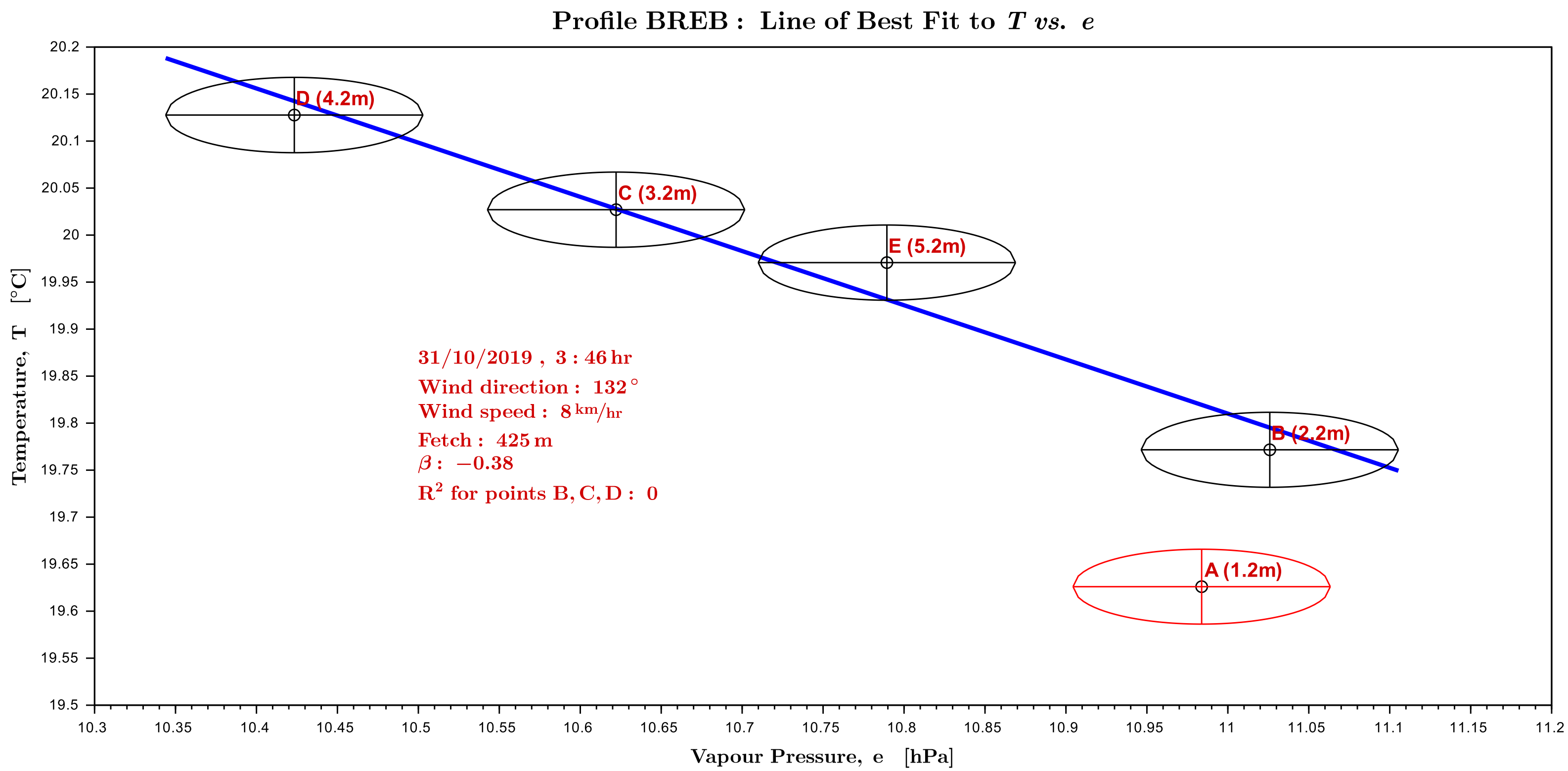

Figure 4.34: DS2: example of a rejected Profile BREB LoBF despite an apparently good straight-line-fit to the data. The plotted points ‘A’, ‘B’, ‘C’, ‘D’ and ‘E’ were not ordered correctly in the profile (they should have been ordered A-B-C-D-E or E-D-C-B-A) and so R^2 for this set of data was set to 0 (to flag it for subsequent removal).

Fig. 4.35 (p. 162) shows all values of β determined by Profile BREB during DS2. 5.0 % of all data were inside the range $-1.25 < \beta < -0.75$ and they mainly occurred around dawn/dusk. A relatively small proportion of those 5.0 % were very close to $\beta = -1$ and Fig. 4.36 (p. 163) shows that these β values were the cause of the extreme values of E_{BREB}.

For three days following irrigation β was close to zero during the day as there was plenty of free water on the warm soil surface. Then, as the soil dried, β slowly increased but remained less than 1, i.e. λE was always greater than H. The reason this was possible during DS2, despite negligible plant transpiration, was because the heavy-clay Vertosol soil in Field 16 was efficient at transporting water to the surface from deeper in the soil profile.[8] A plot of volumetric water content vs. time in Field 16 during DS2 is given in Fig. 4.37 (p. 164); it shows that within two to three days of the 23rd October irrigation water was already being drawn to the surface even from 500 mm depth. The warm temperatures, high solar radiation and low vapour pressures ensured that water that was drawn to the surface was readily evaporated.

[8] The matrix pull of the heavy-clay soil was strong and easily able to overcome the gravity force and the hydraulic resistance that opposed movement of water to the soil surface.

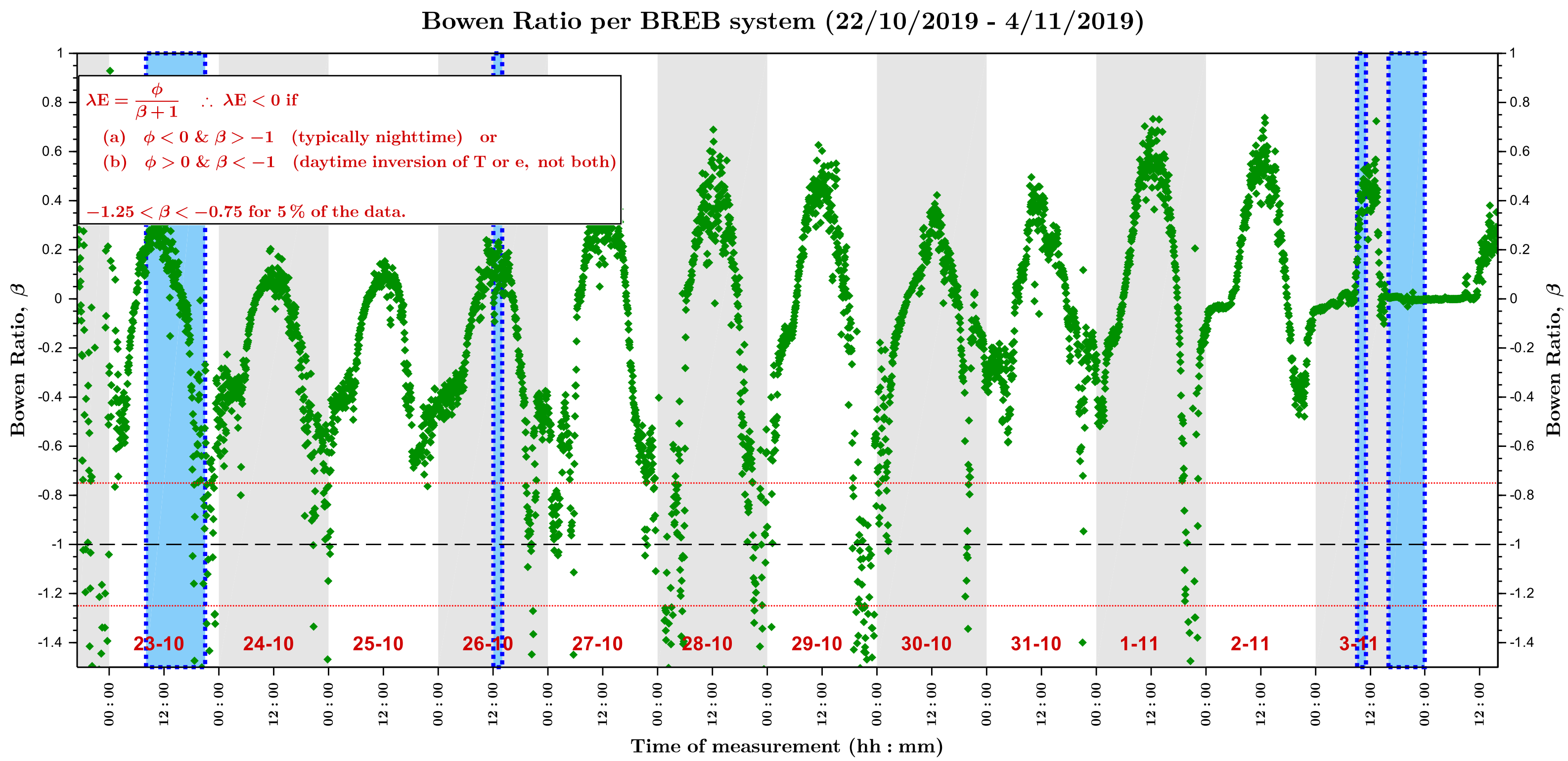

Figure 4.35: DS2: values for Bowen ratio, β as determined by Profile BREB. The red lines indicate $\beta = -0.75$ and $\beta = -1.25$, and the black dashed line indicate $\beta = -1$. The shaded blue rectangles indicate when irrigation (23$^{\text{rd}}$ October) or rainfall occurred.

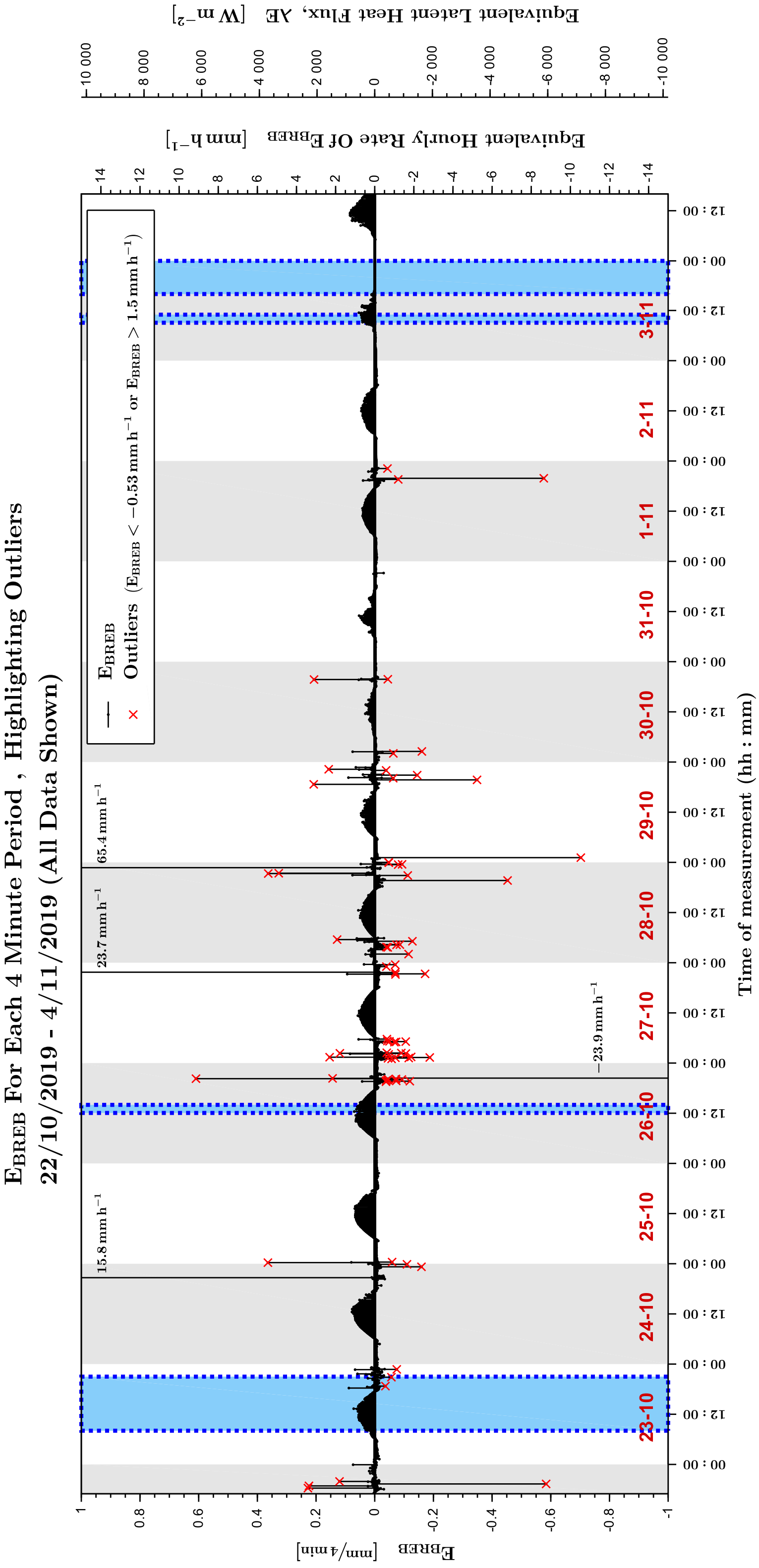

Figure 4.36: DS2: outliers in E_{BREB} that were impossibly large and had to be removed from subsequent analysis. Comparison with Fig. 4.35 (p. 162) shows that most of these values are associated with $\beta \approx -1$. The shaded blue rectangles indicate when irrigation (23rd October) or rainfall occurred.

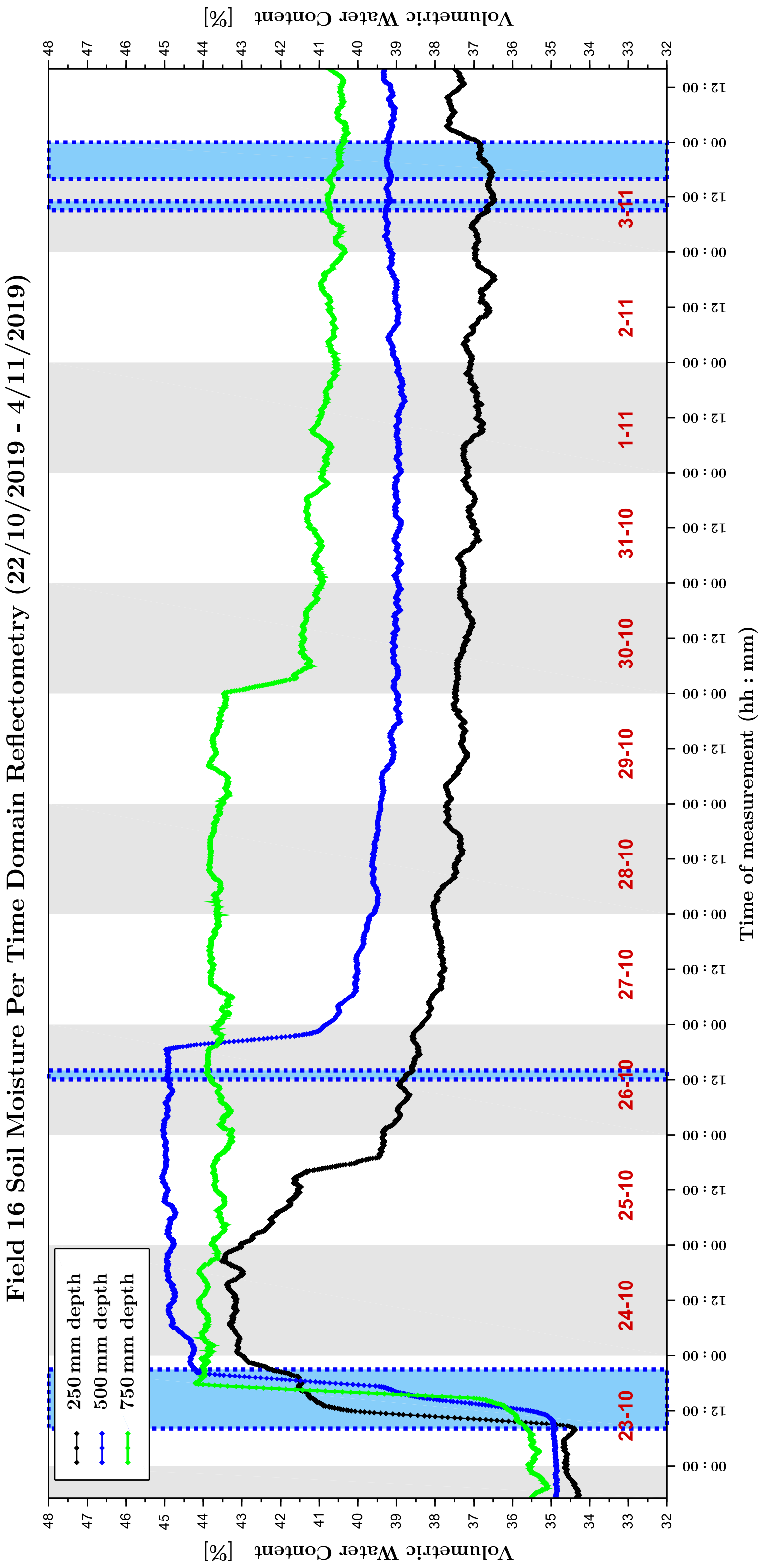

Figure 4.37: DS2: soil moisture data according to Time Domain Reflectometry (TDR) sensors buried at 250 mm, 500 mm and 750 mm depths in Field 16. The shaded blue rectangles indicate when irrigation (23^{rd} October) or rainfall occurred.

Figure 4.38: Photograph from a drone, facing northwest, of the author standing beneath the 5.5 m tall Profile BREB system in Field 16, November 2019. The seedlings are several centimetres tall.

Fig. 4.39 (p. 166) presents the results for E_{BREB} for DS2. Fig. 4.40 (p. 167) presents the same results but also includes the 95 % CI (the orange-coloured bars) for each calculated value of E_{BREB}. The histogram in Fig. 4.41 (p. 168) shows the frequency distribution of E_{BREB} values during DS2. Most values of E_{BREB} fell in the following ranges:

$$\text{Daytime (53\% of data)} \qquad 0 < E_{BREB} < 1.20 \qquad [\mathrm{mm\,h^{-1}}]$$
$$\text{Nighttime (47\% of data)} \qquad -0.50 < E_{BREB} < 0 \qquad [\mathrm{mm\,h^{-1}}]$$

As expected, the rate of E_{BREB} peaked following the 23$^{\text{rd}}$ October irrigation event and then slowly declined until the rain events on the 3$^{\text{rd}}$ November.

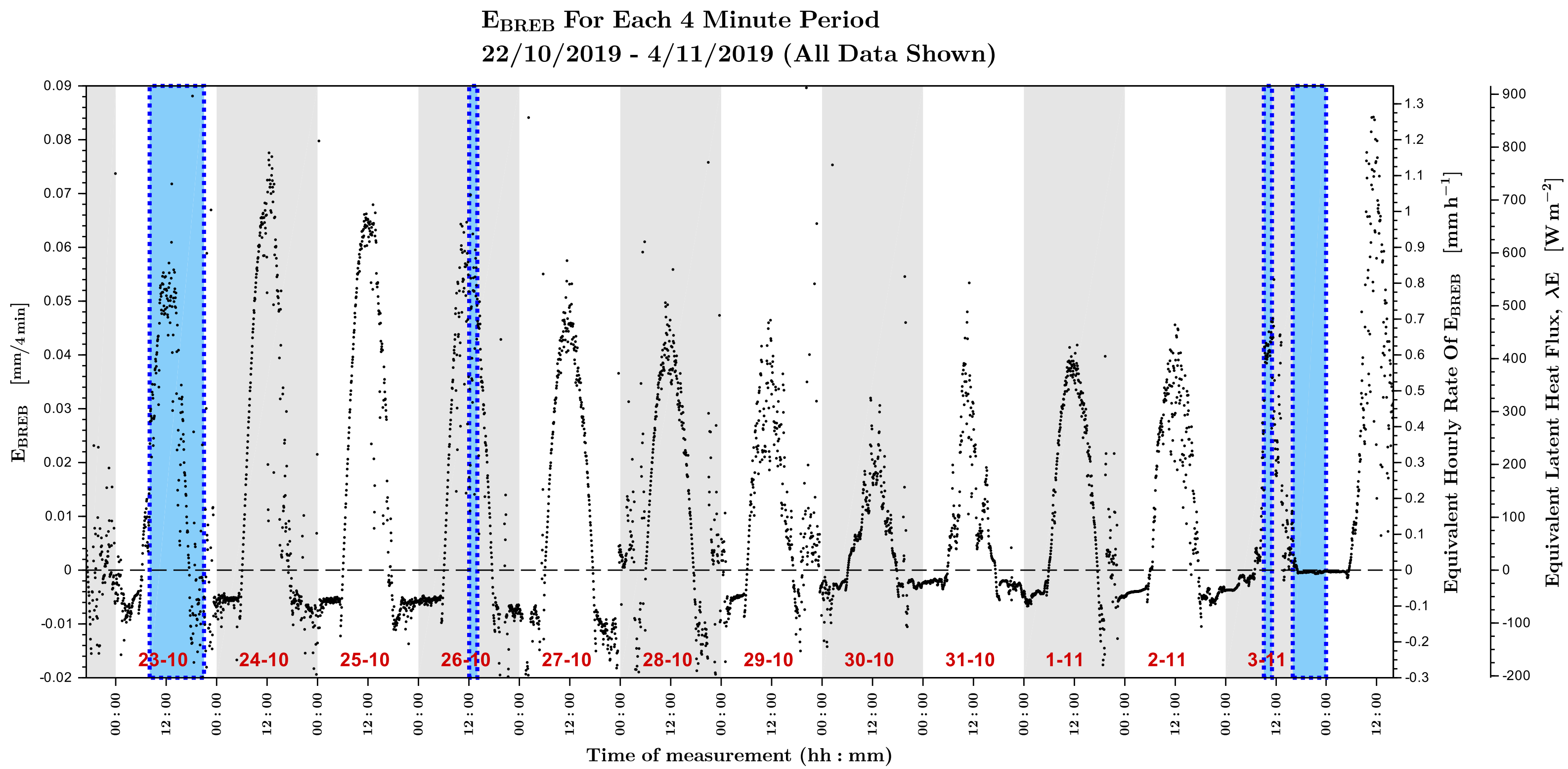

Figure 4.39: DS2: all modelled values for evapotranspiration per Profile BREB, i.e. E_{BREB}. The shaded blue rectangles indicate when irrigation (23rd October) or rainfall occurred.

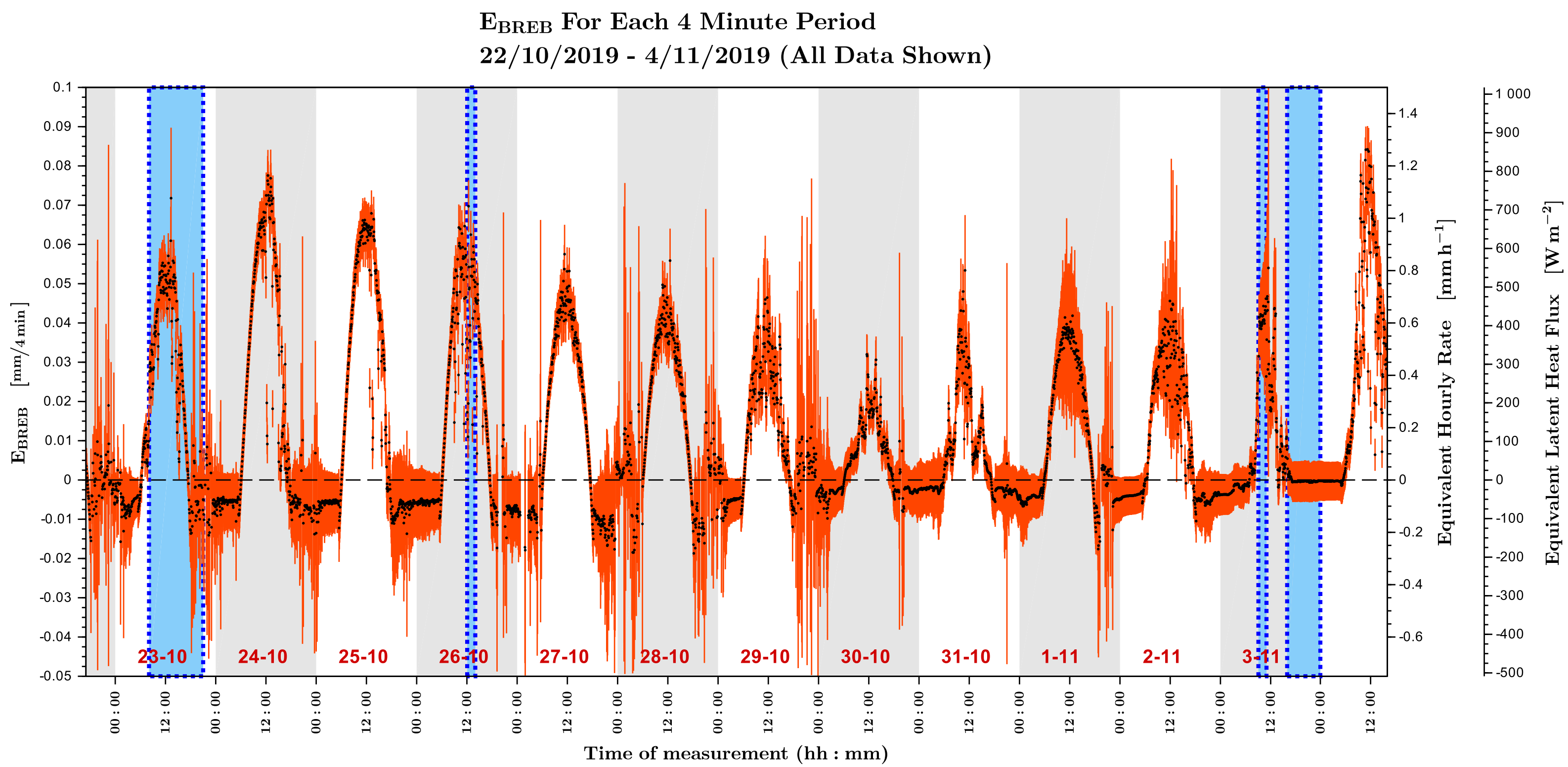

Figure 4.40: DS2: all modelled values for evapotranspiration per Profile BREB, i.e. E_{BREB}. The orange coloured error bars indicate the 95 % CI for each calculated value of E_{BREB}. The shaded blue rectangles indicate when irrigation (23^{rd} October) or rainfall occurred.

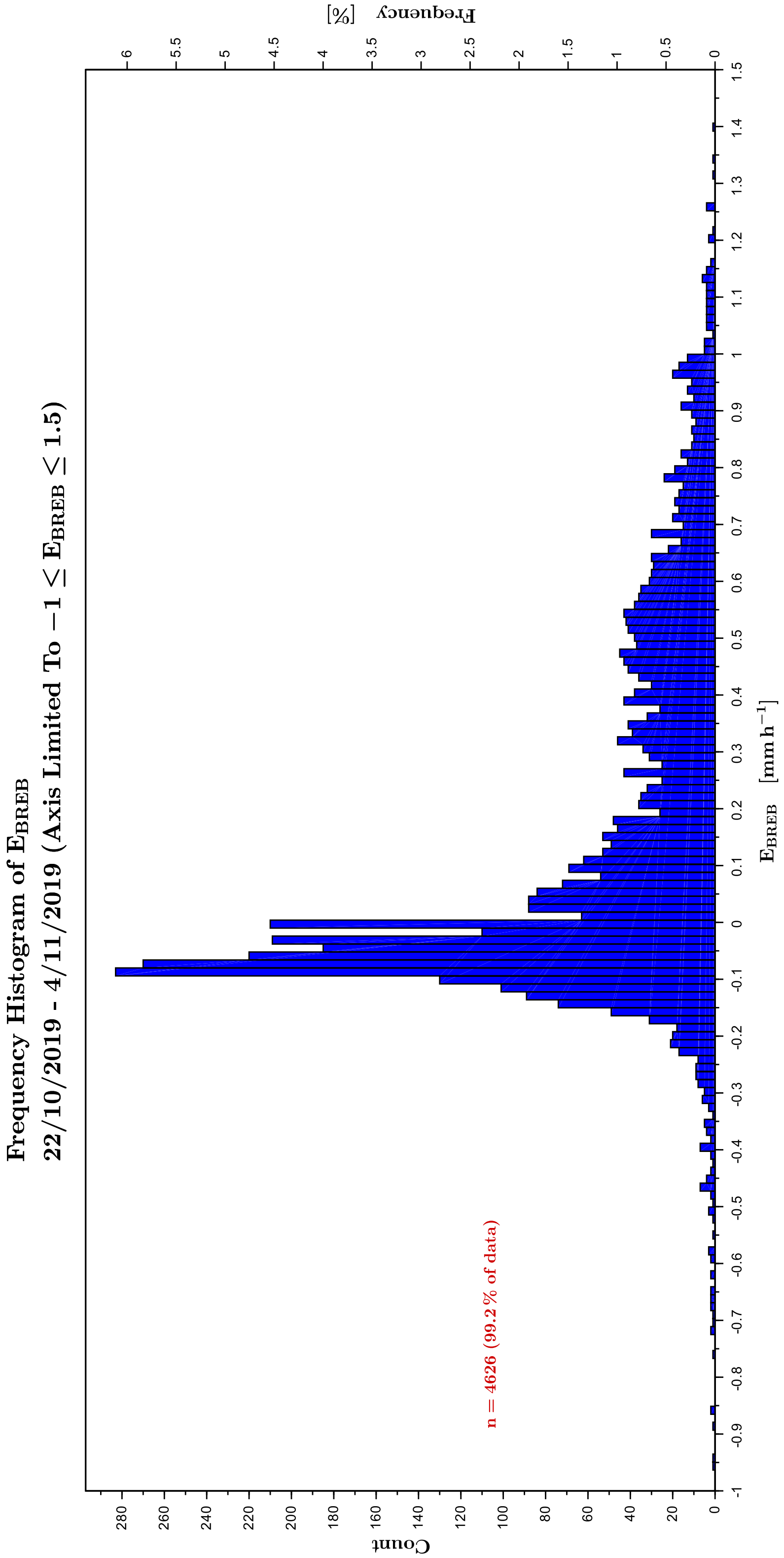

Figure 4.41: DS2: frequency histogram showing the distribution of E_{BREB}.

4.3.3 Results for GPSTIC During DS2

GPSTIC was calculated at the same instances as Profile BREB to allow a like-with-like comparison of the two models. The input data to the GPSTIC model were the very same as used by Profile BREB, i.e. the same sensors supplied identical data to each of the models.

The GPSTIC modelling was repeated for a range of values of α_{PT} between 0.95 and 1.50, including $\alpha_{PT} = 1.26$ (Mallick et al. 2014) and α_{*PT*} (Mallick et al. 2015a).

Plots of E_{GPSTIC} vs. time when $\alpha_{PT} = 1.05$ are given in Fig. 4.42 (p. 170) and Fig. 4.43 (p. 171), the latter showing the 95 % CI for each modelled value of E_{GPSTIC}. A frequency histogram showing the spread of values of E_{GPSTIC} is given in Fig. 4.44 (p. 172).[9]

Most values of E_{GPSTIC} fell in the following ranges:

$$\begin{array}{llll} \text{Daytime (56\% of data)} & 0 & < E_{GPSTIC} < 0.95 & [\mathrm{mm\,h^{-1}}] \\ \text{Nighttime (44\% of data)} & -0.13 & < E_{GPSTIC} < 0 & [\mathrm{mm\,h^{-1}}] \end{array}$$

Comparing Fig. 4.42 (p. 170) with Fig. 4.39 (p. 166) shows that E_{GPSTIC} again exhibited less scatter than E_{BREB} regardless of the time of day and GPSTIC did not produce any extreme outliers. The range of values of E_{GPSTIC} tended to be slightly narrower than for E_{BREB}.

The 95 % CI of E_{GPSTIC} were narrower and more consistent over time compared to those of E_{BREB} throughout DS2.

[9] It is shown in § 5.2.2 (p. 230) that $\alpha_{PT} = 1.05$ produced the best results for GPSTIC during DS2, as was the case during DS1.

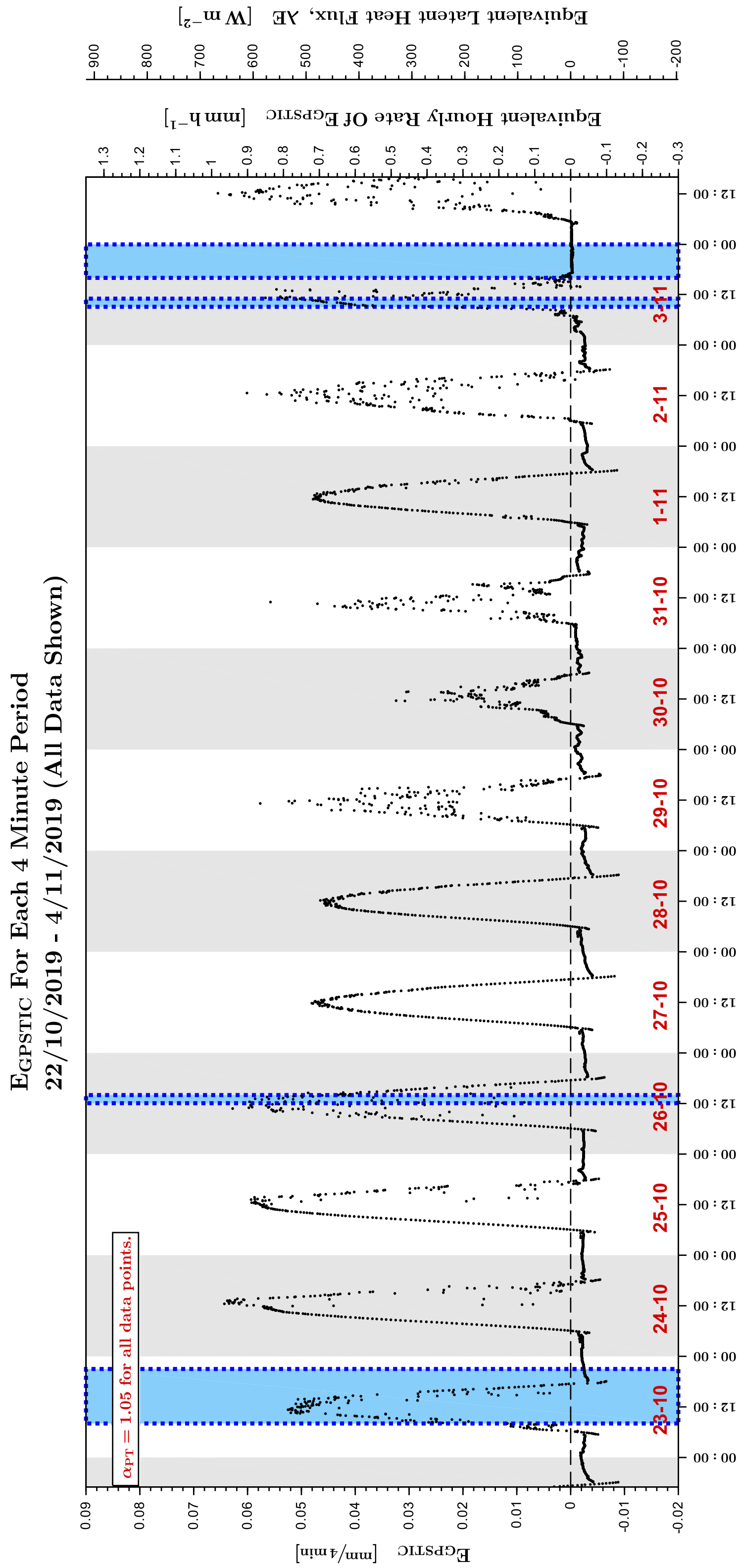

Figure 4.42: DS2: all modelled values for evapotranspiration per GPSTIC, i.e. E_{GPSTIC}, when $\alpha_{PT} = 1.05$. The shaded blue rectangles indicate when irrigation (23[rd] October) or rainfall occurred.

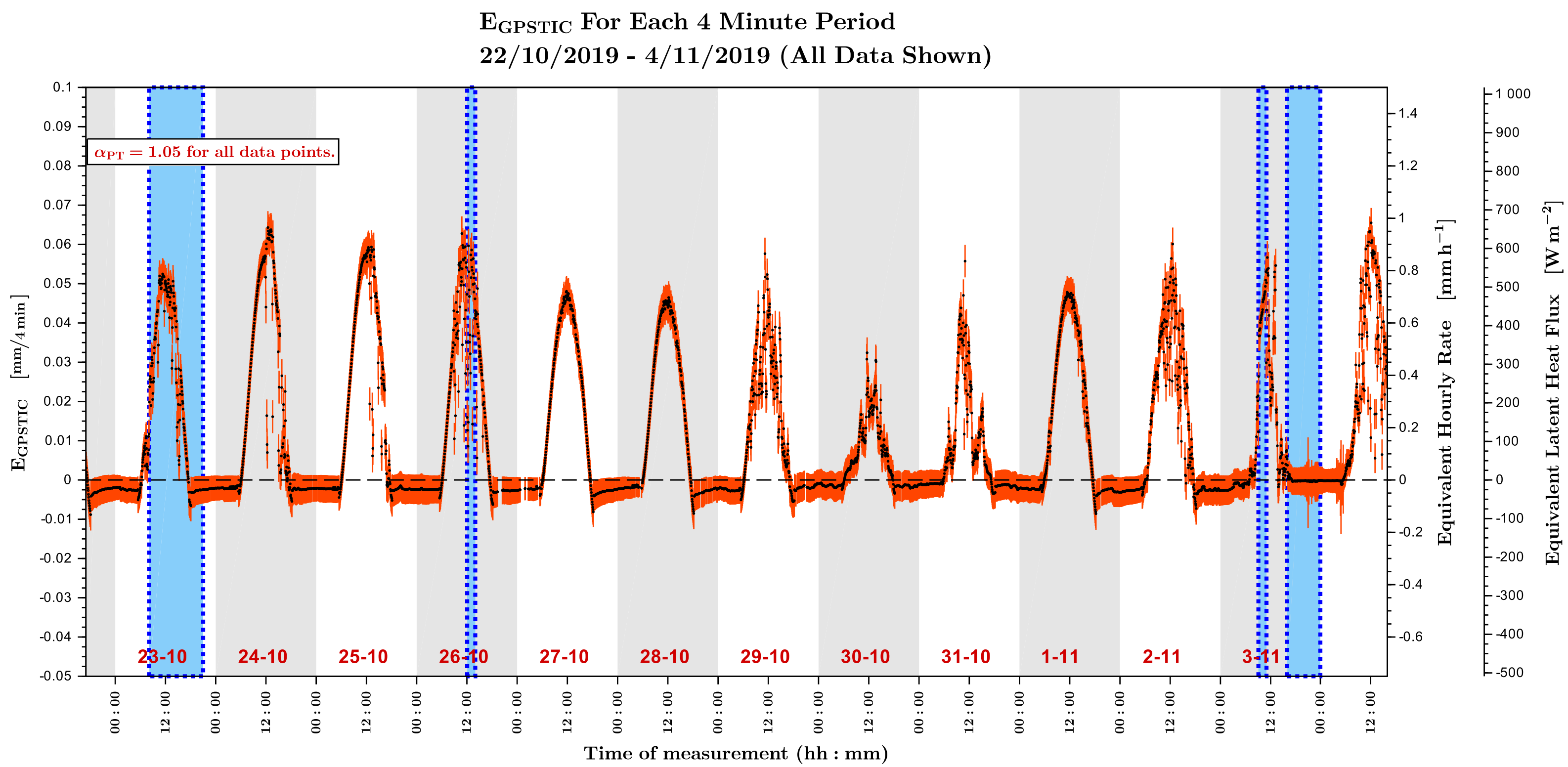

Figure 4.43: DS2: all modelled values for evapotranspiration per GPSTIC, i.e. E_{GPSTIC}, when $\alpha_{PT} = 1.05$. The orange coloured error bars indicate the 95 % CI for each calculated value of E_{GPSTIC}. The shaded blue rectangles indicate when irrigation (23rd October) or rainfall occurred.

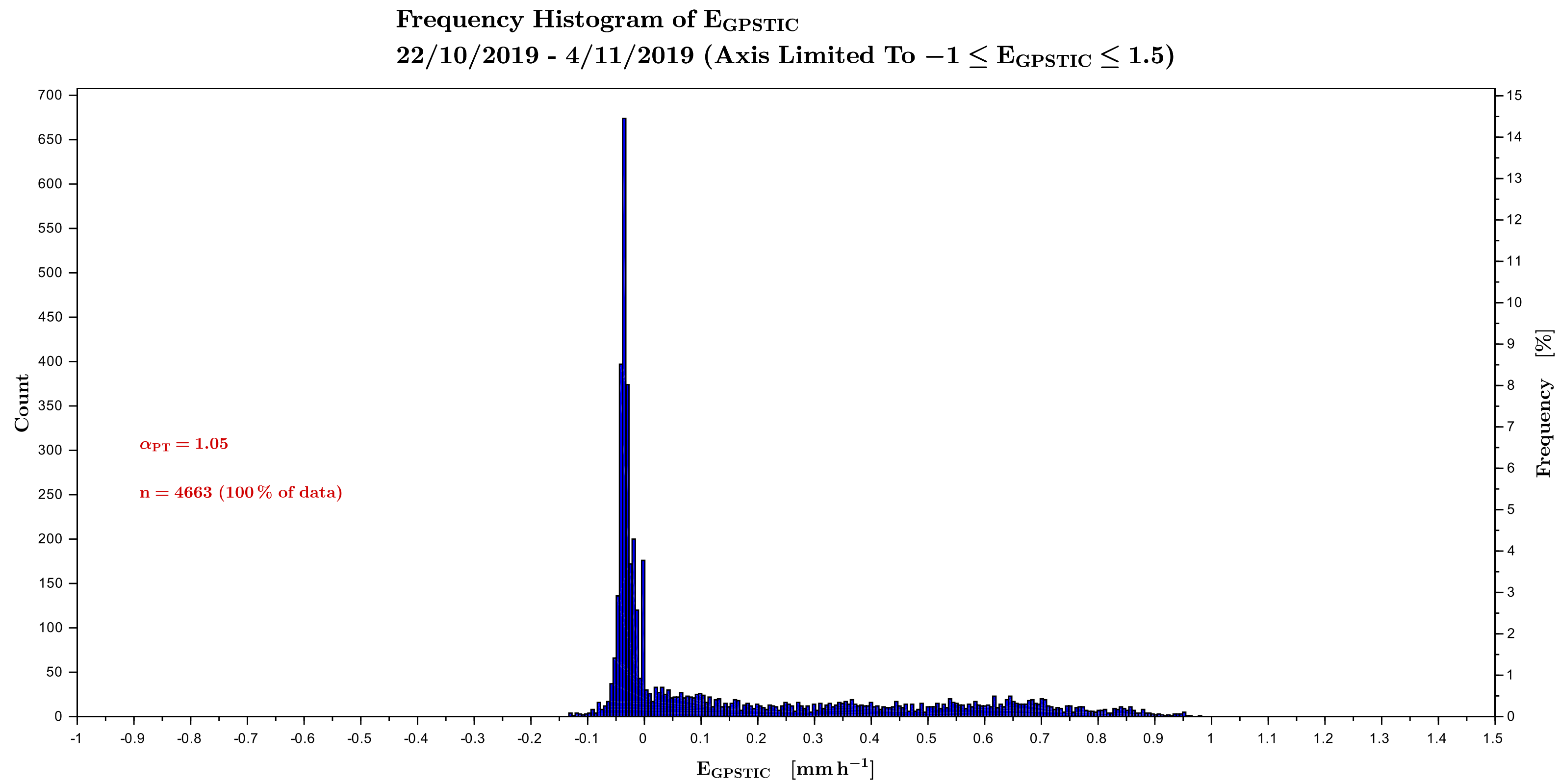

Figure 4.44: DS2: frequency histogram showing the distribution of E_{GPSTIC} when $\alpha_{PT} = 1.05$.

4.4 Data Set Three (DS3)

Figure 4.45: Photograph facing eastwards, taken 5th February 2020, of the Profile BREB / GPSTIC structures in Field 16. The cotton crop had a height of approx. 1.0 - 1.2 m which meant that it had reached the lowest radiation shield. The 20 W solar panel (near the left side of the photo) was positioned 20 m away from the tall mast.

Data Set Three (DS3) comprised 116 consecutive hours of measurements over the period 31st January to 5th February, 2020. The field site was the very same location in Field 16 as for DS2 (§ 3.1.2, p. 60). The cotton crop had grown to a height of approx. 1.0 - 1.2 m with a lush, well watered, full canopy coverage.

4.4.1 Weather Conditions During DS3

Figures 4.46 - 4.50 (pp. 175 - 179) present the relevant weather data for DS3. Additional weather data are provided in Appendix Q (p. 447).

During DS3 the eastern states of Australia were still in severe drought and were experiencing severe bushfires. However, there were no large fires in the vicinity of the current field site and the air quality was relatively good.

Up until February 2020 the summer had been very dry and warm. During DS3 the conditions were slightly cooler and more humid than the preceding couple of months. Approx. 250 mm of drought-breaking rain started on the 7th February, two days after DS3 was completed.

Plots of ambient T and RH (shown in Fig. 4.46, p. 175 and Fig. 4.47, p. 176) were made using data from the sensors in the second lowest radiation shield (height 'B' – see inset figure on p. 97) which was 2.2 m above the ground, i.e. 1.0 m above the canopy. This was because the lowest radiation shield, at 1.2 m above the ground (height 'A'), was at the same height as the growing crop and it was possible that free air movement through the shield could have been obstructed by canopy leaves. The data used for GPSTIC were also measured by the same sensors in radiation shield 'B' at 1.0 m above the crop.

During DS3 the maximum T ranged between 21 - 38 °C during the day (overnight minimums of 14 - 27 °C) which was mild for this time of the year. RH and T_D tended to be higher throughout DS3 than DS1 and DS2. Overnight mist and plenty of dew on the canopy were observed on 31st January and 4th February.

The mean wind speed at 5.5 m above the ground was 10.8 km h^{-1}. Minimum fetch distance was 260 m (fetch-to-height ratio = 65) and 66 % of the data for DS3 had a fetch-to-height ratio ≥ 100 (Fig. Q.5, p. 452).

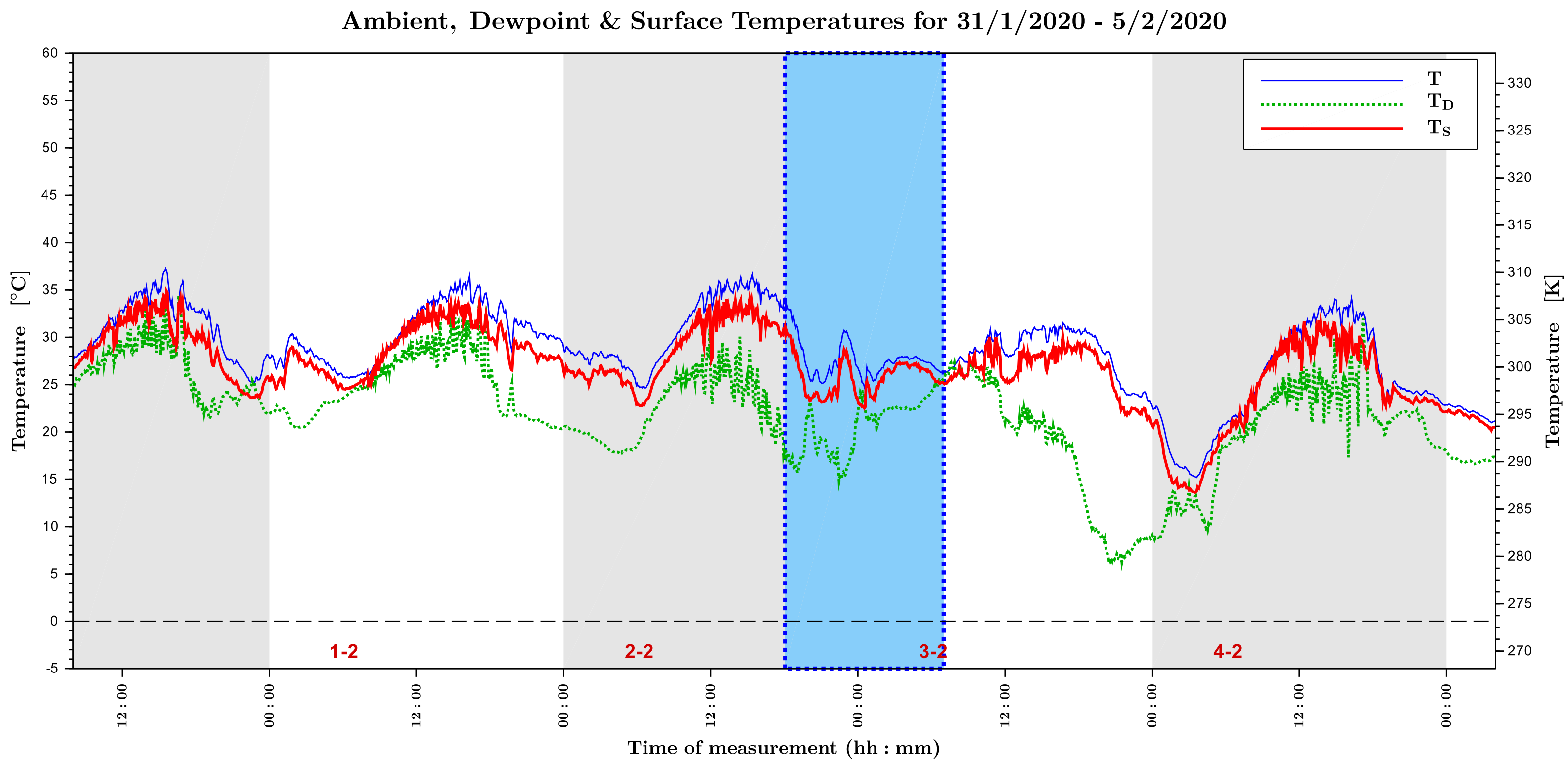

Figure 4.46: Temperatures in Field 16 during DS3. Ambient temperatures (T) and dewpoint temperatures (T_D) were measured 2.2 m above the ground (approx. 1.0 m above the crop); surface temperatures (T_S) were measured using an IRR at 5.4 m above the ground (with a visible surface area of 57 m^2). The shaded blue rectangle indicates when the irrigation on the 2nd February occurred.

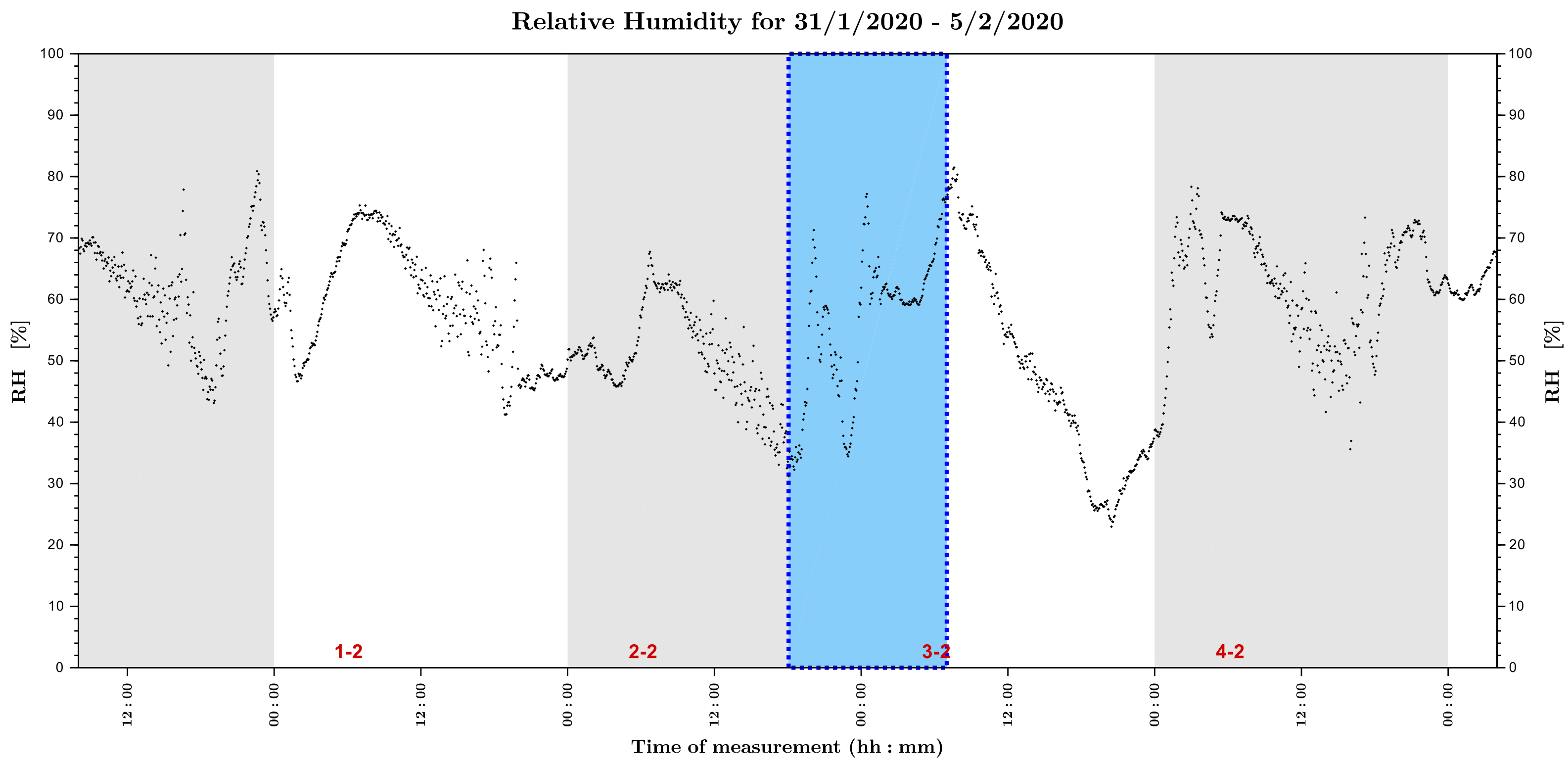

Figure 4.47: Relative humidity in Field 16 during DS3, as measured 2.2 m above the ground (approx. 1.0 m above the crop). The shaded blue rectangle indicates when the irrigation on the 2nd February occurred.

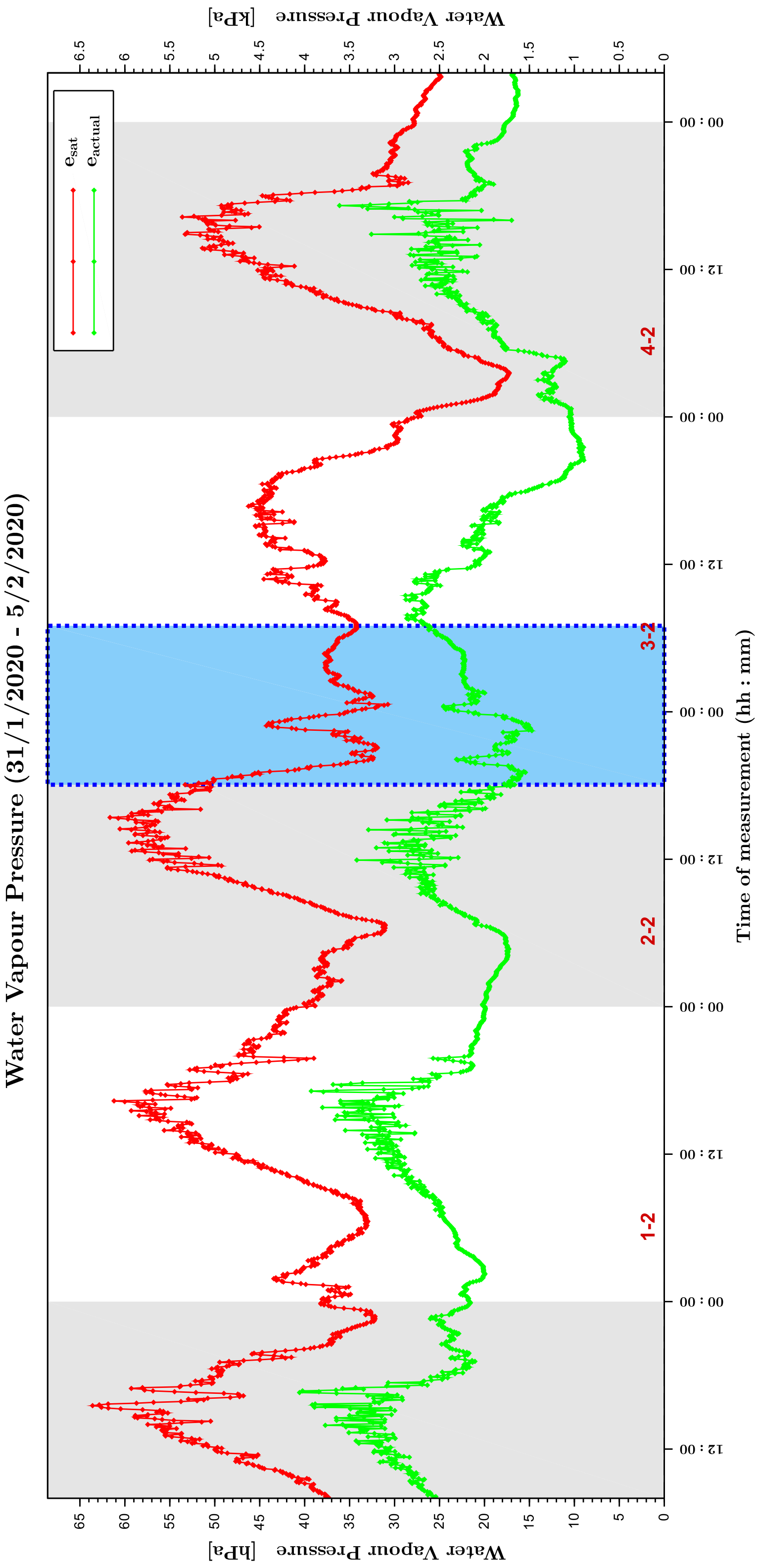

Figure 4.48: Saturation vapour pressure and actual vapour pressure in Field 16 during DS3, as measured 2.2 m above the ground (approx. 1.0 m above the crop). Saturation vapour pressure was calculated using the Buck Equation (Eqn. 3.15, p. 96). The shaded blue rectangle indicates when the irrigation on the 2[nd] February occurred.

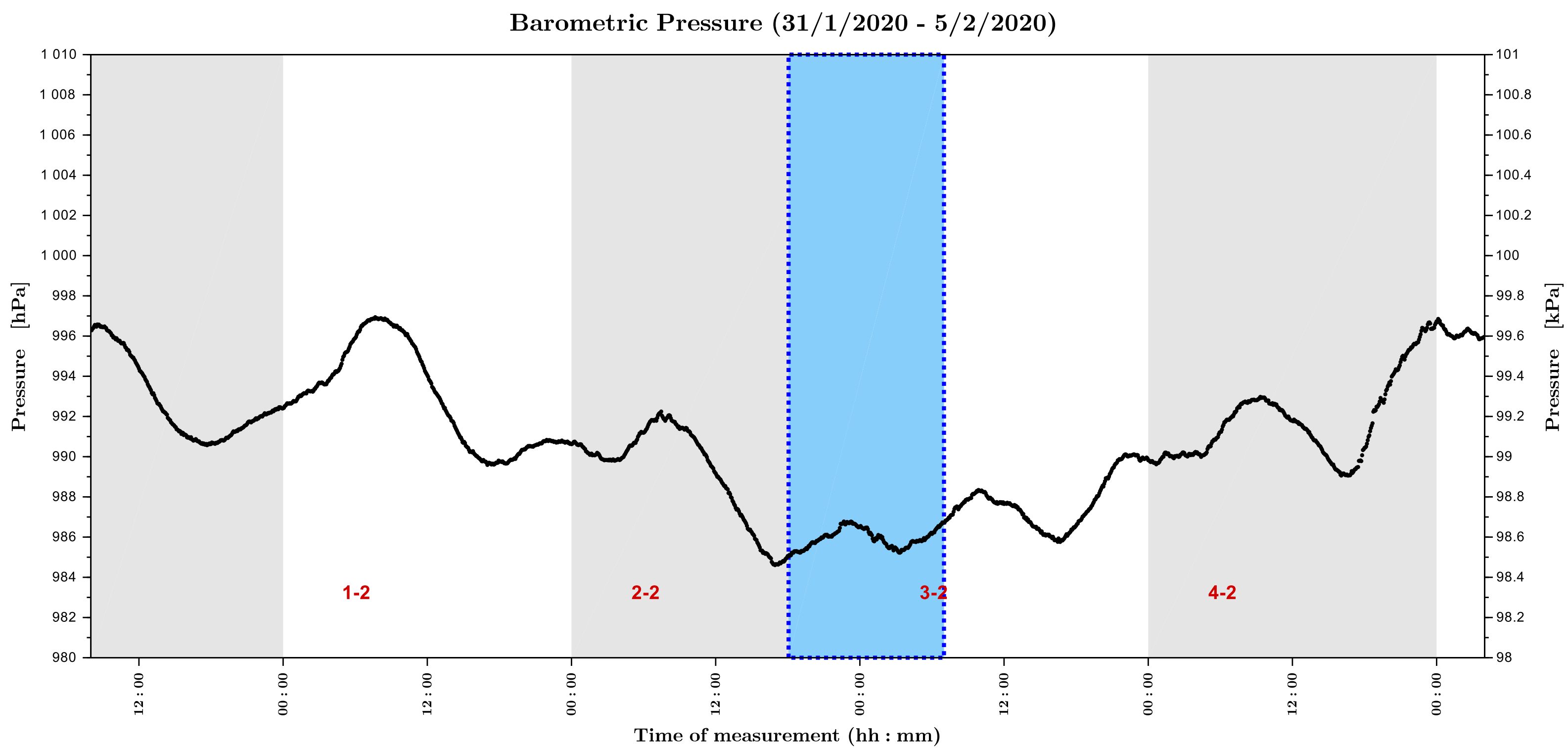

Figure 4.49: DS3: barometric pressure, P [hPa], measured every 60 s at 1.6 m above the ground (171 m above sea level). The shaded blue rectangle indicates when the irrigation on the 2nd February occurred.

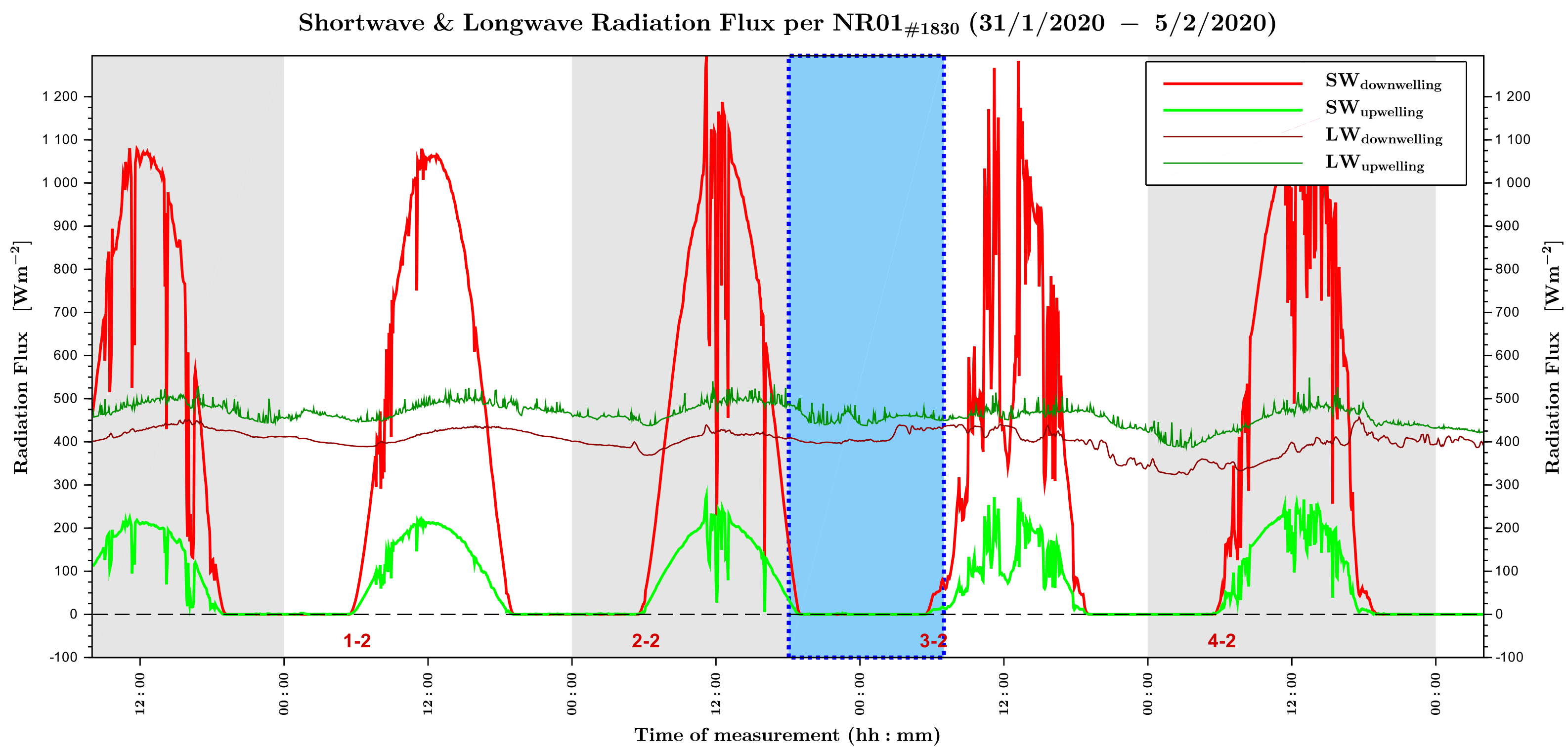

Figure 4.50: Downwelling and upwelling radiation (shortwave and longwave) in Field 16 during DS3. The net radiometer was a Hukseflux NR01 (serial number #1830). The shaded blue rectangle indicates when the irrigation on the 2nd February occurred.

Net radiometers $NR01_{\#1830}$ and $NR01_{\#1236}$ were set up in Field 16 at 3.0 m above the ground (approx. 1.8 - 2.0 m above the canopy). $NR01_{\#1236}$ was damaged by wildlife early in DS3 but this was of little consequence to the modelling as the laboratory-calibrated $NR01_{\#1830}$ was designated as the primary net radiometer.

Figure 4.51: Photograph of the NR01 net radiometers 1.8 m above the crop canopy, with the Profile BREB array of radiation shields in the background, taken 5th February, 2020. The canopy had closed and no soil was visible from above.

4.4.1.1 DS3 Shortwave Radiation Data

The shortwave radiation (0.285 - 3.00 µm) measurements were in the range

$$0 \leqslant SW_{downwelling} \leqslant 1293 \quad [\mathrm{Wm^{-2}}] \tag{4.10}$$

$$0 \leqslant SW_{upwelling} \leqslant 275 \quad [\mathrm{Wm^{-2}}] \tag{4.11}$$

As was the case during DS2, the maximum value for $SW_{downwelling}$ during DS3 initially appears too high given that the ‘clear-sky’ models (Appendix L, p. 409) estimate that downwelling shortwave radiation should be approx. 980 - 1040 $\mathrm{Wm^{-2}}$. However, for the same reasons as laid out on p. 151, the maximum value of $SW_{downwelling}$ was deemed to be acceptable and the shortwave radiation in Fig. 4.50 (p. 179) was assumed to be correct. Unfortunately the $\mathrm{NR01}_{\#1236}$ was damaged and unavailable to corroborate the radiation data during DS3.

4.4.1.2 DS3 Longwave Radiation Data

During DS3 the longwave radiation (4.5 - 40 µm) measurements were in the following ranges:

$$324 \leqslant LW_{downwelling} \leqslant 457 \quad [\mathrm{Wm^{-2}}] \tag{4.12}$$

$$387 \leqslant LW_{upwelling} \leqslant 549 \quad [\mathrm{Wm^{-2}}] \tag{4.13}$$

Eqn. 4.3 (p. 125) was used to calculate the pyrgeometer-derived T_S for DS3. These were compared to the IRR-measured T_S in Fig. 4.52 (p. 182). The two plots of T_S were observed to be mostly similar in magnitude and Fig. 4.53 (p. 183) shows that approx. 95 % of the pyrgeometer-derived T_S were within 10 % of the IRR-measured T_S. There was, however, a 'jaggedness' in the DS3 data that was not observed during DS1 or DS2 and it is interesting that the jaggedness occurred for *both* the IRR and the downward-facing pyrgeometer (but not the upward-facing pyrgeometer).[10] The uncertainty of the jaggedness notwithstanding, the performance of the IRR and the pyrgeometer were sufficiently close that the longwave radiation data were accepted as reasonable.

[10]The cause of the 'jaggedness' of the plotted data was unknown. The two sensors were quite independent of each other (the IRR was a digital SDI-12 sensor, the NR01 was a passive analogue sensor, and each had its own channels in the data logger) and there were no strong sources of electronic noise close to the cables. Furthermore, the two pyranometers and the upward-facing pyrgeometer did not exhibit the same jaggedness.

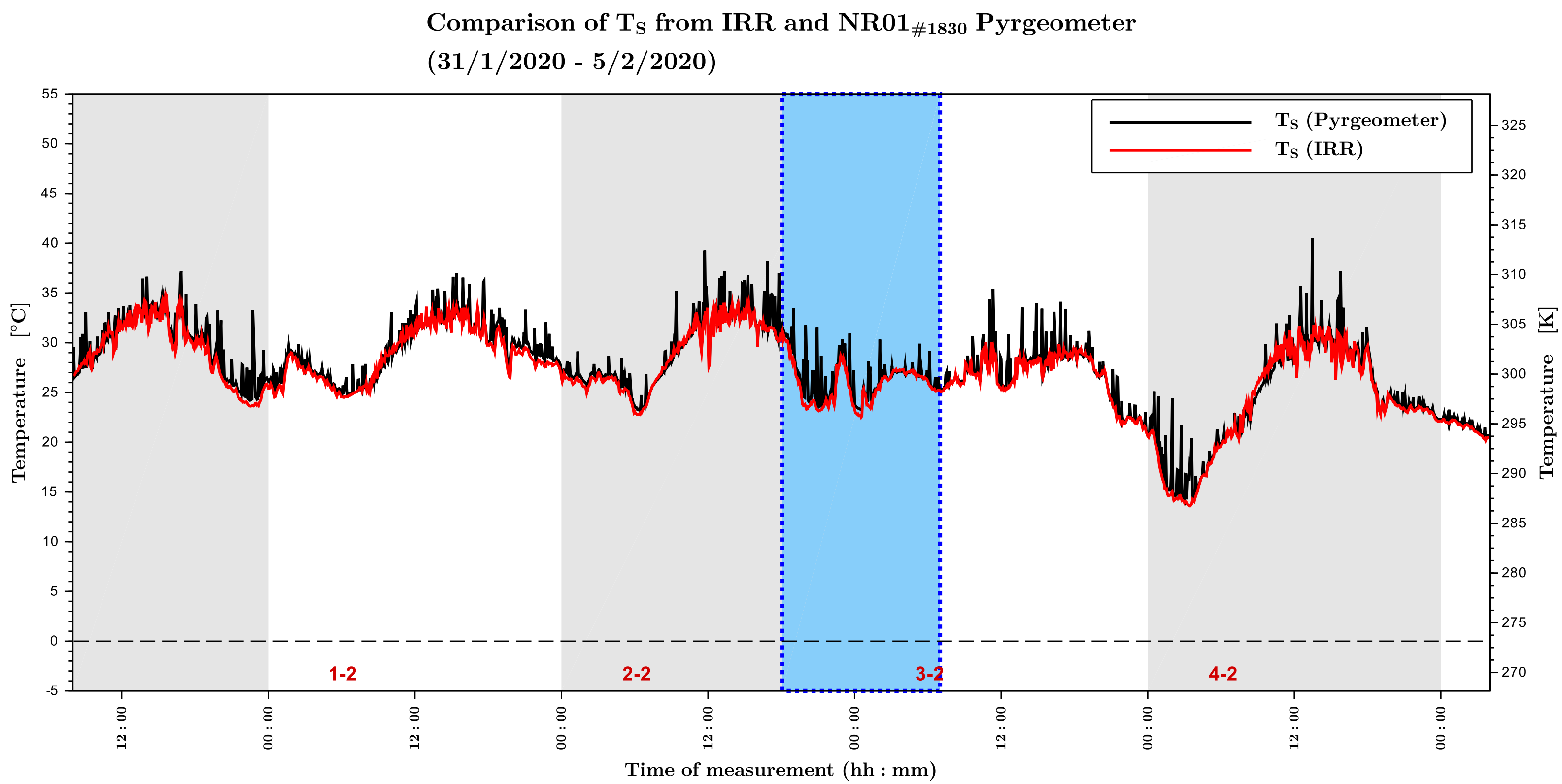

Figure 4.52: Comparison of T_S as determined by the IRR with that derived from the $NR01_{\#1830}$ downward facing pyrgeometer in Field 16 during DS3. The shaded blue rectangle indicates when the furrow-irrigation on the 2nd February occurred (this occurred beneath the fully-closed canopy).

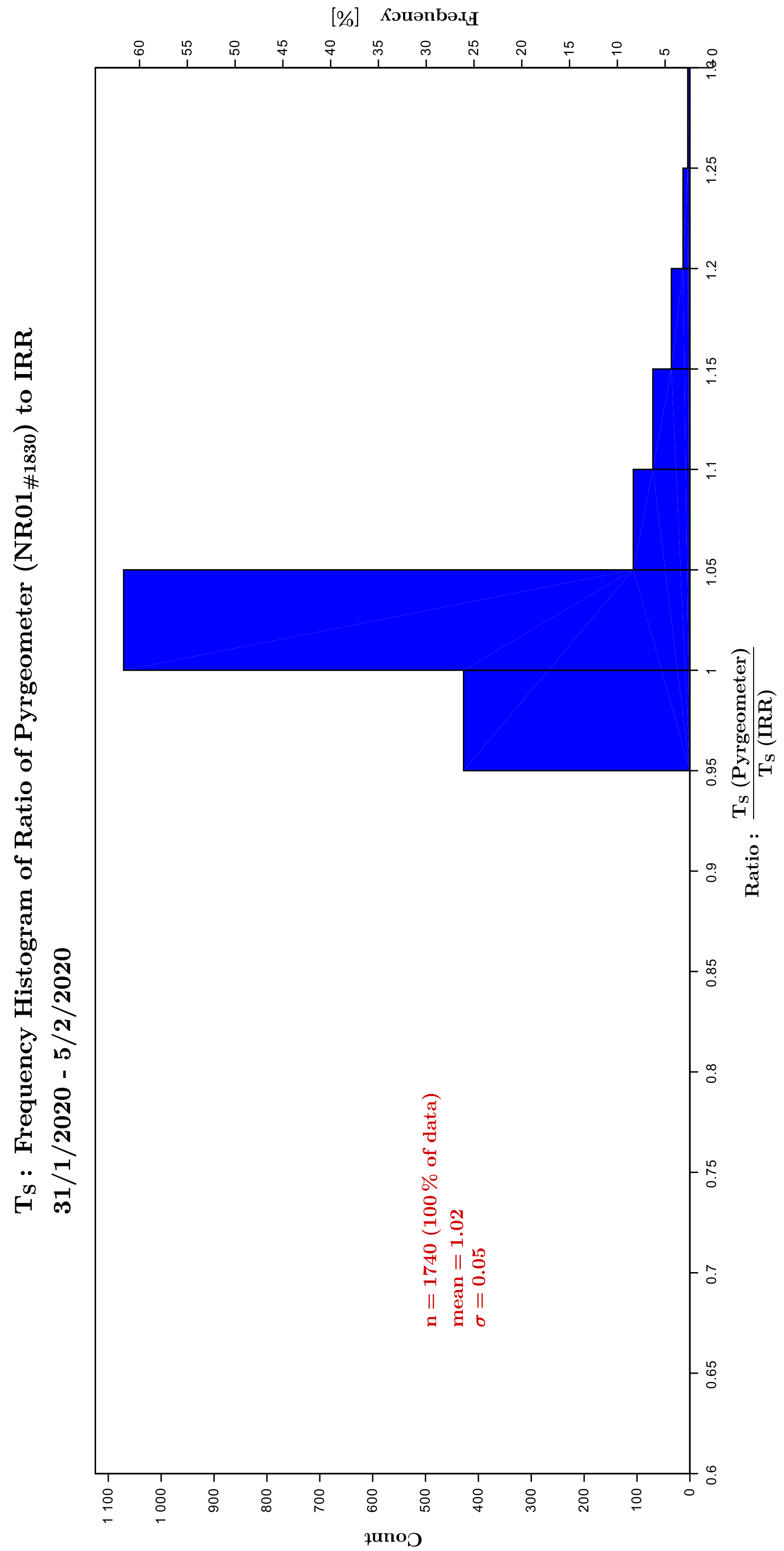

Figure 4.53: Frequency histogram of the ratio of T_S as determined by T_S derived from the NR01$_{\#1830}$ downward facing pyrgeometer to the IRR in Field 16 during DS3.

4.4.2 Results for Profile BREB During DS3

Figure 4.54: Photograph of the Profile BREB system taken on the 5th February, 2020, facing north. The cotton canopy had grown as high as the lowest radiation shield by this date.

The Profile BREB system operated above the fully-closed canopy (Fig. 4.54, p. 184) for all 116 hours during DS3, making measurements every 60 s throughout the entire period.

Fig. 4.55 (p. 186), Fig. 4.56 (p. 187) and Fig. 4.57 (p. 188) provide three examples from DS3 of the LoBF sub-algorithm in action. During DS1 and DS2 it was normally the case that the (e, T) pair at either height 'A' or height 'E' had to be rejected. During DS3, however, a near-perfect linear fit to all five data pairs was a surprisingly frequent occurrence (exemplified by Fig. 4.55).

Fig. 4.58 (p. 189) shows all values of β as determined by Profile BREB. During DS3, 10.6 % of all data were inside the range $-1.25 < \beta < -0.75$ and these mainly occurred around dawn/dusk, although a good number also occurred overnight on 2nd - 3rd February while the irrigation was underway. (Regarding the latter, it was possible that the cooling soil and crop and the warm irrigation water were providing different drivers when it came to evaporation. The warm water was driving positive evaporation, and the cooling ambient temperature and cooling canopy surface were driving negative evaporation. Thus the situation came to resemble dawn/dusk and β ended up hovering between -1.25 and -0.75.)

Comparison with Fig. 4.59 (p. 190) shows that these values of $\beta \approx -1$ corresponded to the outlier values of E_{BREB} in Fig. 4.58.

Fig. 4.60 (p. 191) presents the results for E_{BREB} for DS3. Fig. 4.61 (p. 192) presents the same results but also includes the 95 % CI (the orange-coloured error bars) for each calculated value of E_{BREB}. The histogram in Fig. 4.62 (p. 193) shows the frequency distribution of E_{BREB} values during DS3. Most values of E_{BREB} fell in the following ranges:

Daytime (57 % of data)	$0 < E_{BREB} < 1.30$	$[\mathrm{mm\,h^{-1}}]$
Nighttime (43 % of data)	$-0.95 < E_{BREB} < 0$	$[\mathrm{mm\,h^{-1}}]$

It can be seen that there was a greater incidence of $E_{BREB} < -0.5\,\mathrm{mm\,h^{-1}}$ than was the case for either DS1 or DS2 (albeit still only a fraction of a percentage of instances).

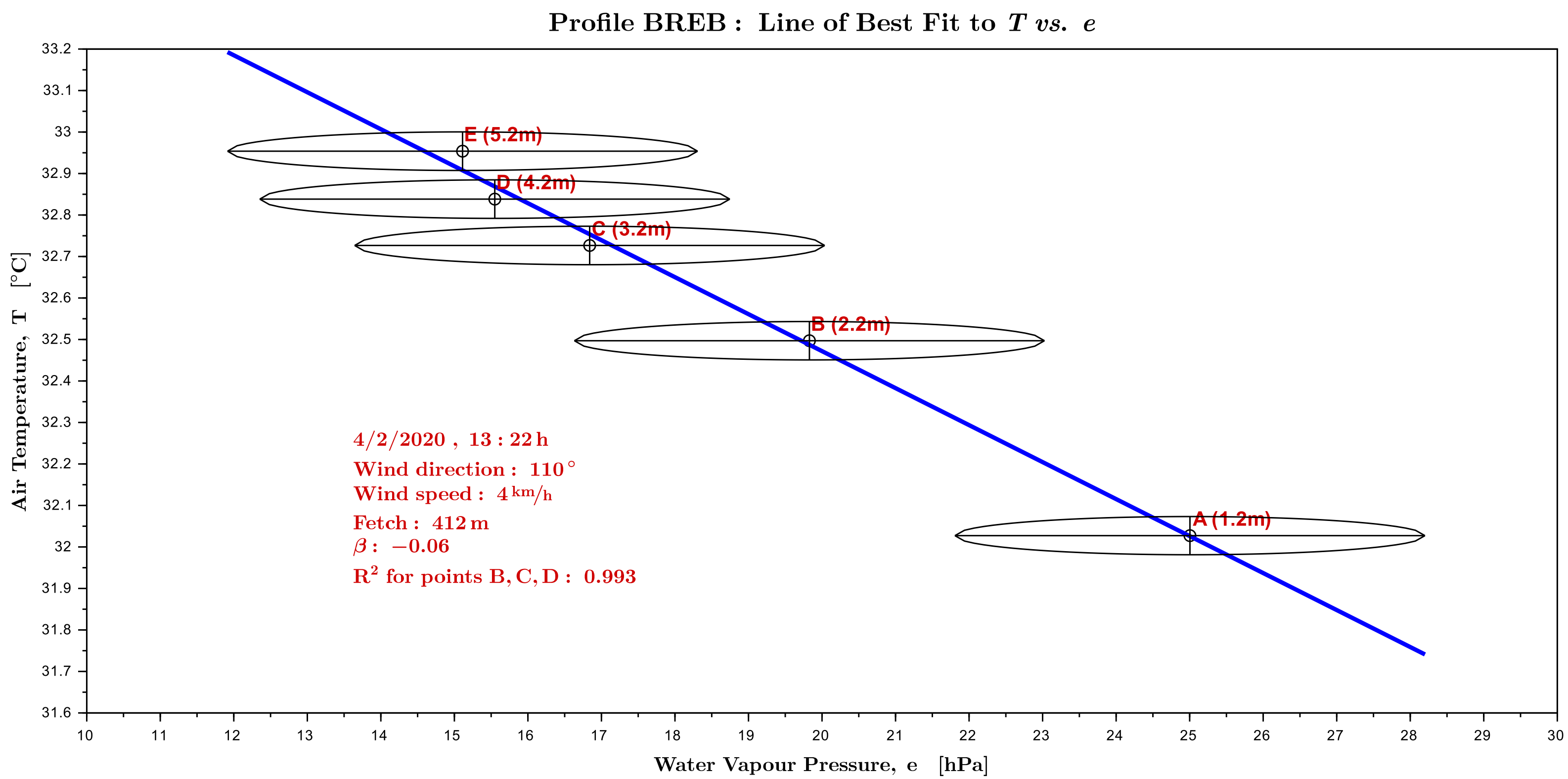

Figure 4.55: Example of fitting the LoBF to the Profile BREB data for the 4th February, 2020, at 13:22 h (two days after irrigation). This example shows a good LoBF through all five (e, T) pairs. The larger spacing between points 'A' and 'B' than points 'D' and 'E' shows that the temperature and humidity gradients are greater when close to the canopy.

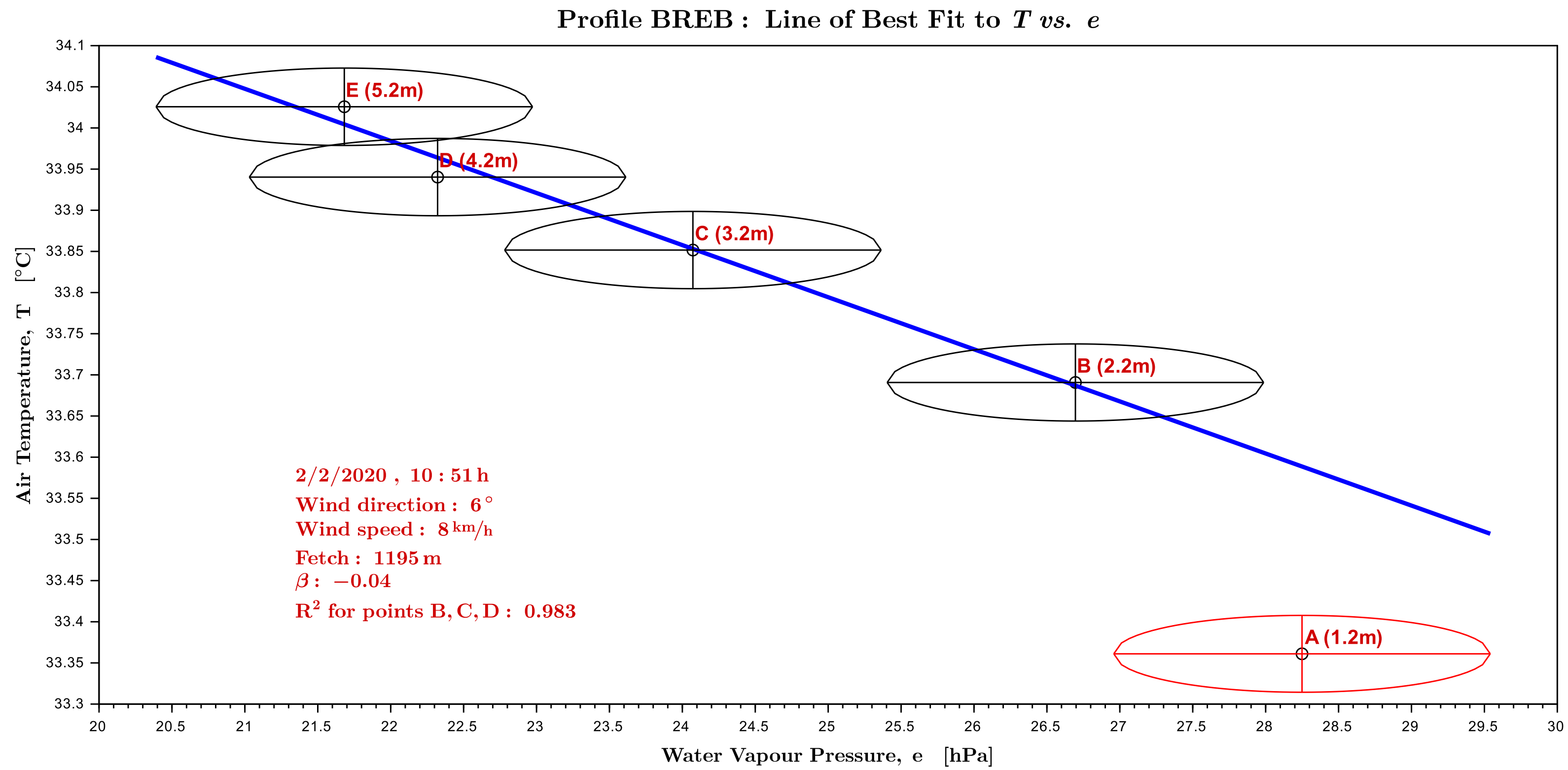

Figure 4.56: Example of fitting the LoBF to the Profile BREB data for the 2nd February, 2020, at 10:51 h. This example shows a good LoBF through the upper four (e, T) pairs, with the lowest (e, T) pair at height ‘A’ being rejected since it was out of line with the others.

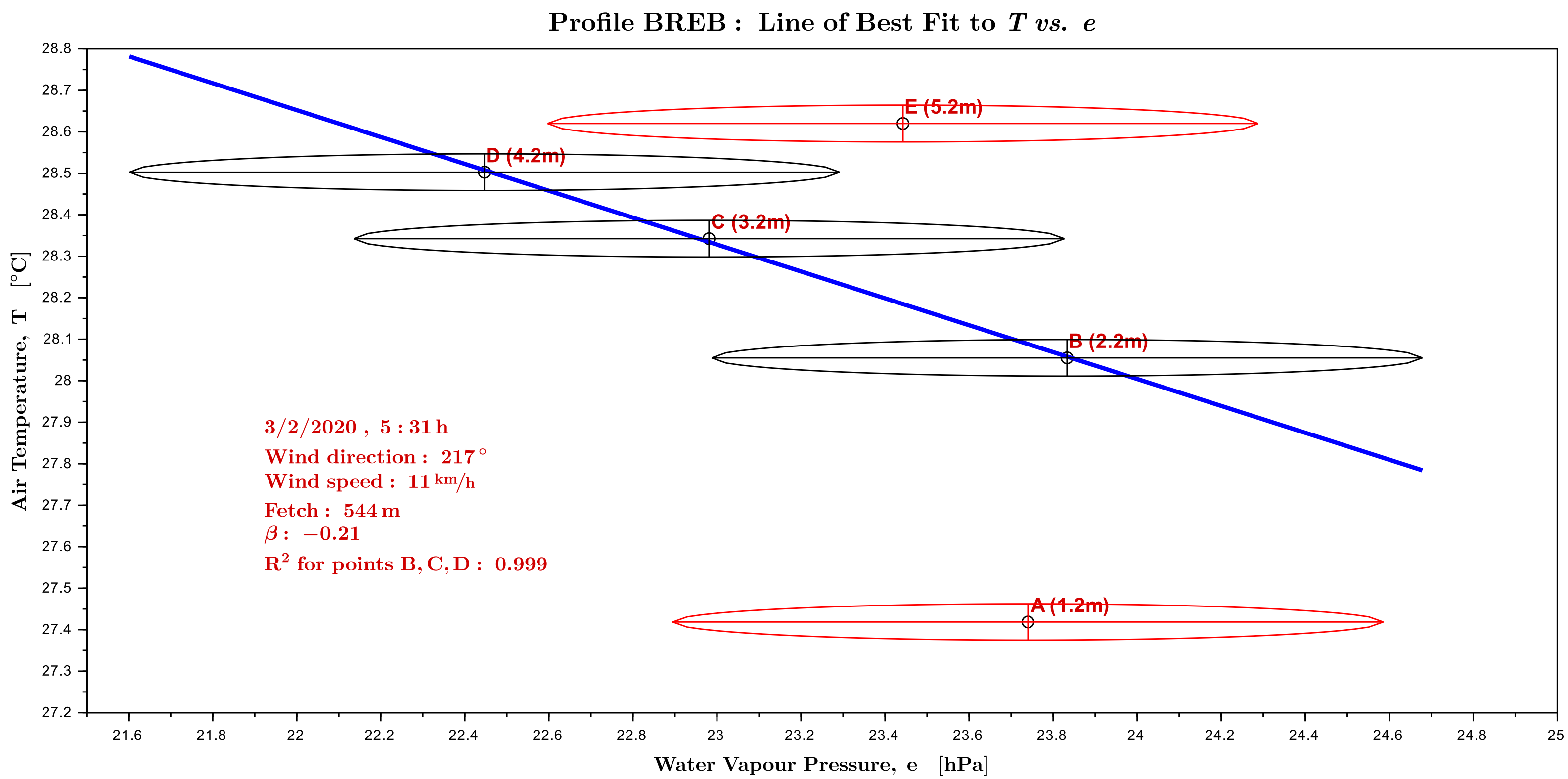

Figure 4.57: Example from 3rd February, 2020, at 05:31 h which was just prior to sunrise. A furrow irrigation had commenced at 18:00 h the previous day and was still running at the time of this measurement. Heights 'A' (closest to crop) and 'E' were rejected in this instance.

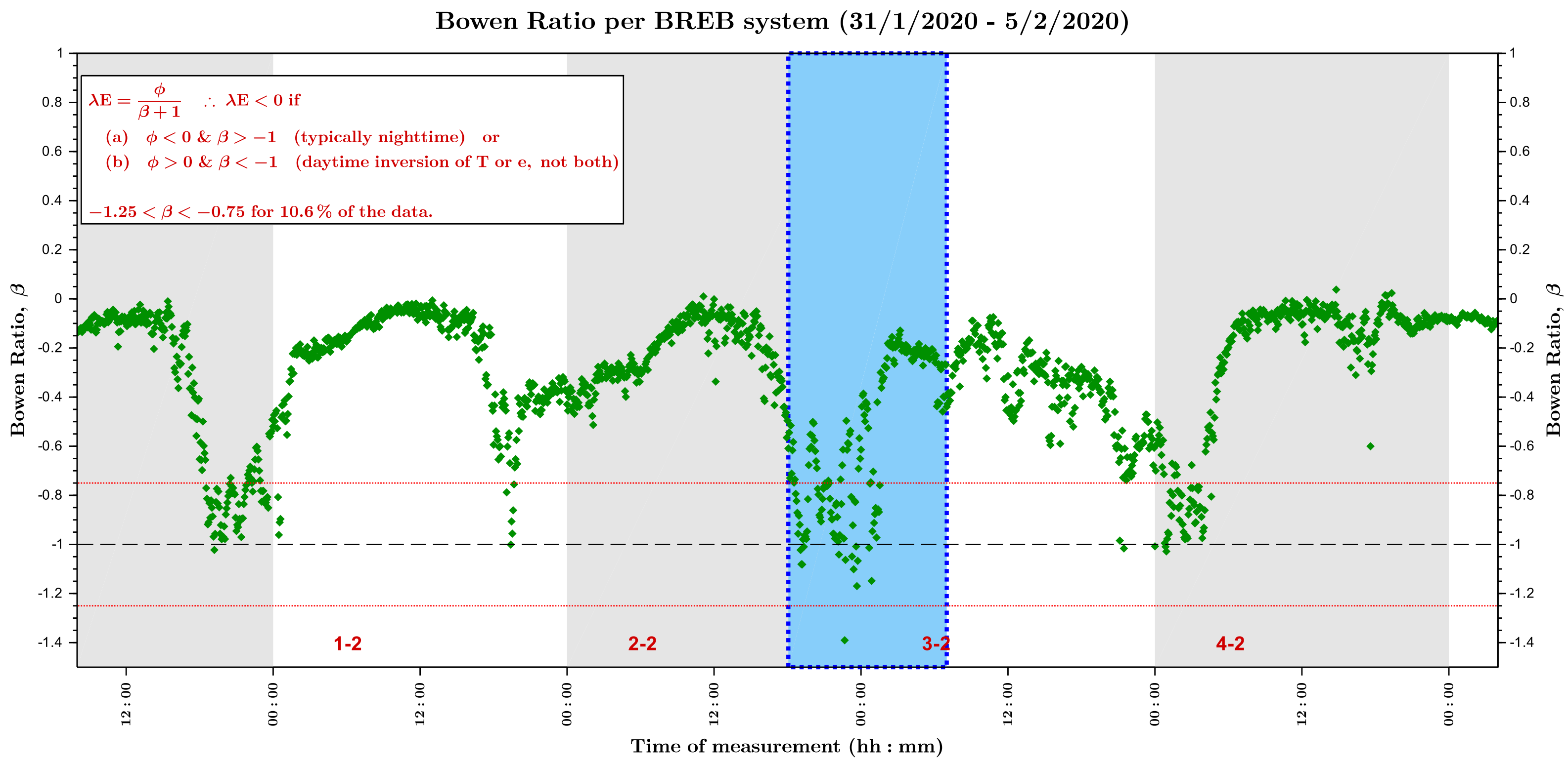

Figure 4.58: DS3: all values for Bowen ratio, β as determined by Profile BREB. The red lines mark $\beta = -0.75$ and $\beta = -1.25$, and the black dashed line marks $\beta = -1$. The shaded blue rectangle indicates when irrigation occurred on 2nd February.

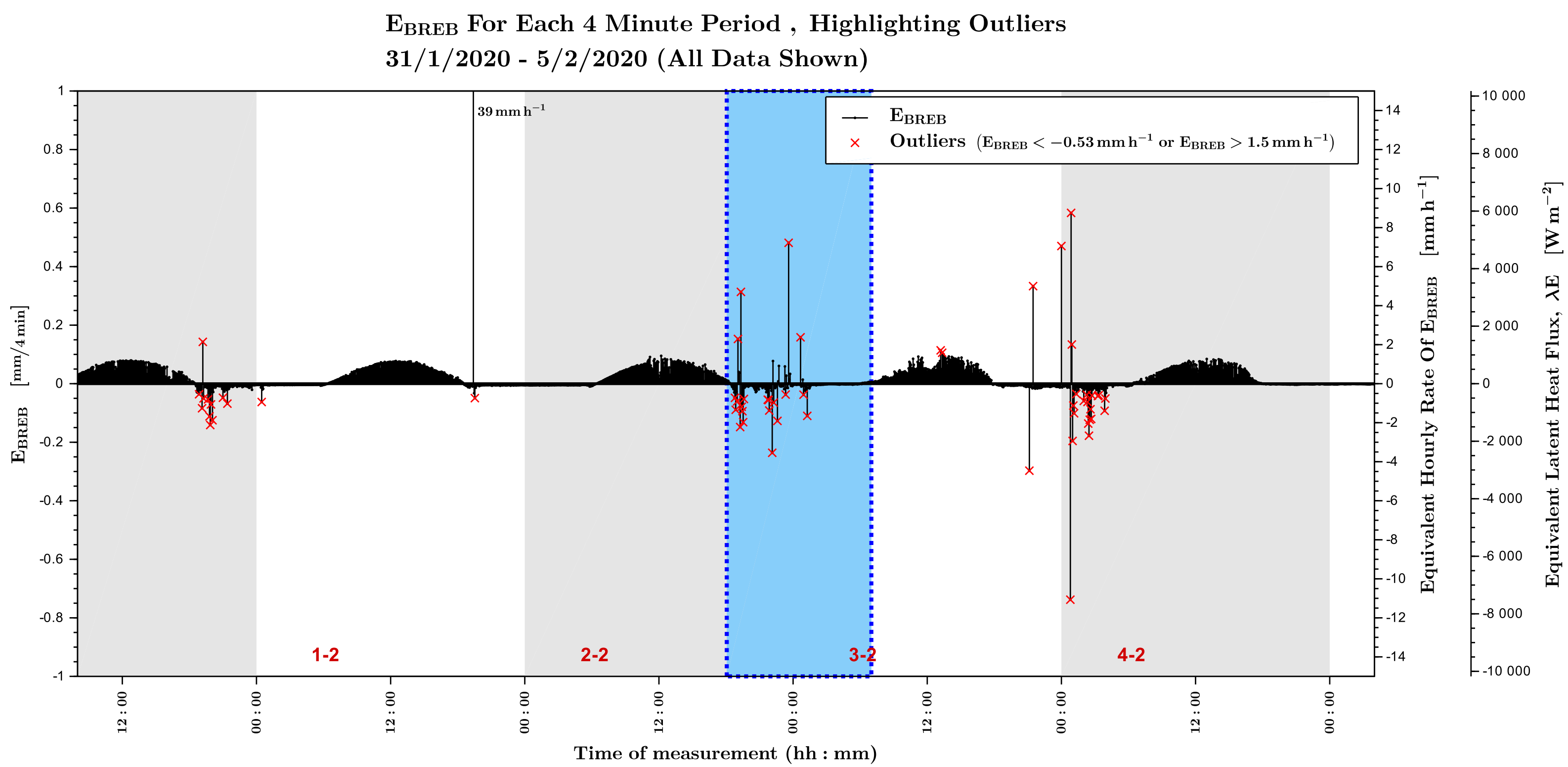

Figure 4.59: DS3: outliers in E_{BREB} that were impossibly large and had to be removed from subsequent analysis. Comparison with Fig. 4.58 (p. 189) shows that most of these values are associated with $\beta \approx -1$. The shaded blue rectangle indicates when irrigation occurred on 2nd February.

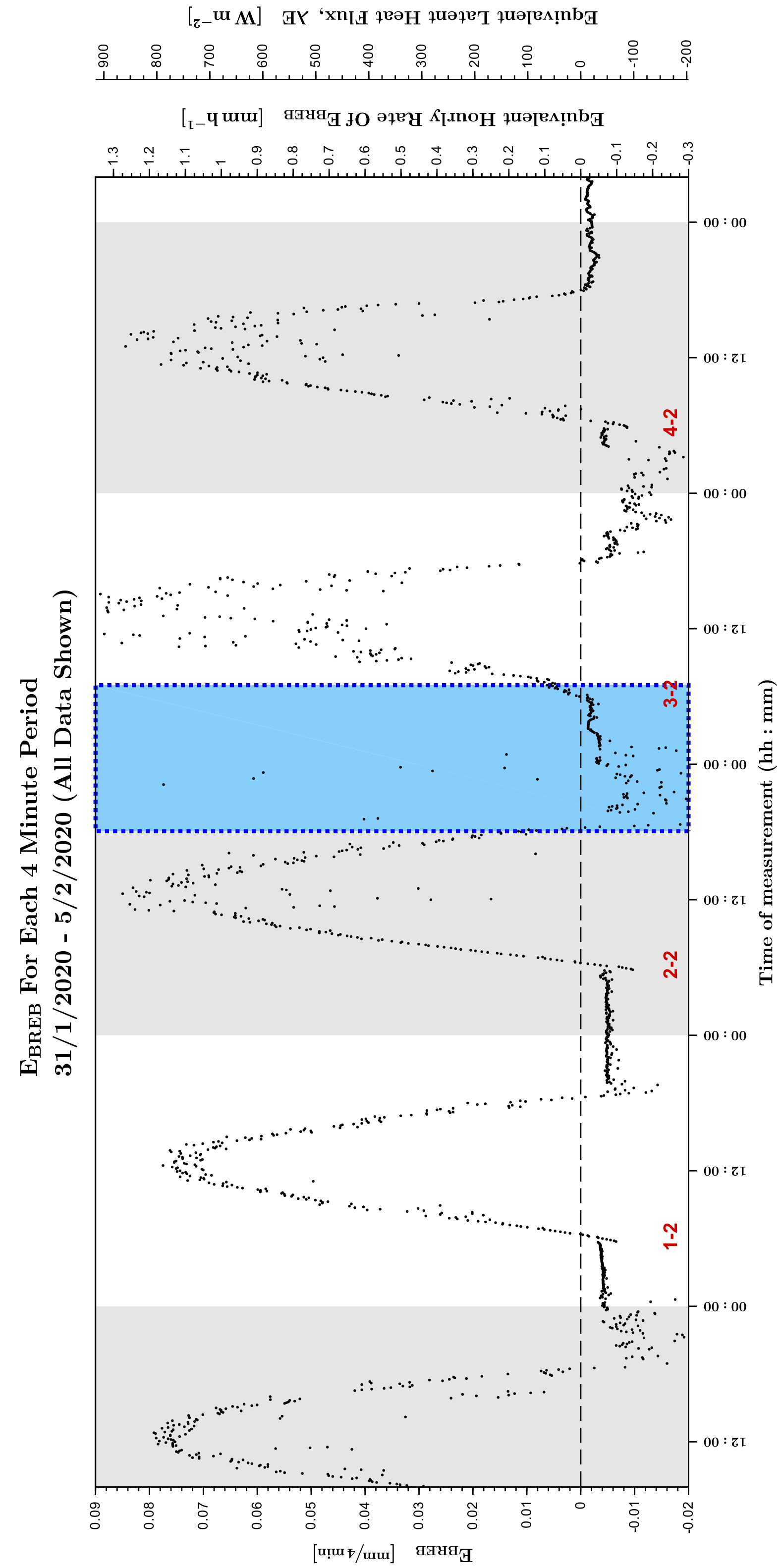

Figure 4.60: DS3: all modelled values for evapotranspiration per Profile BREB, i.e. E_{BREB}. The shaded blue rectangle indicates when irrigation occurred on 2nd February.

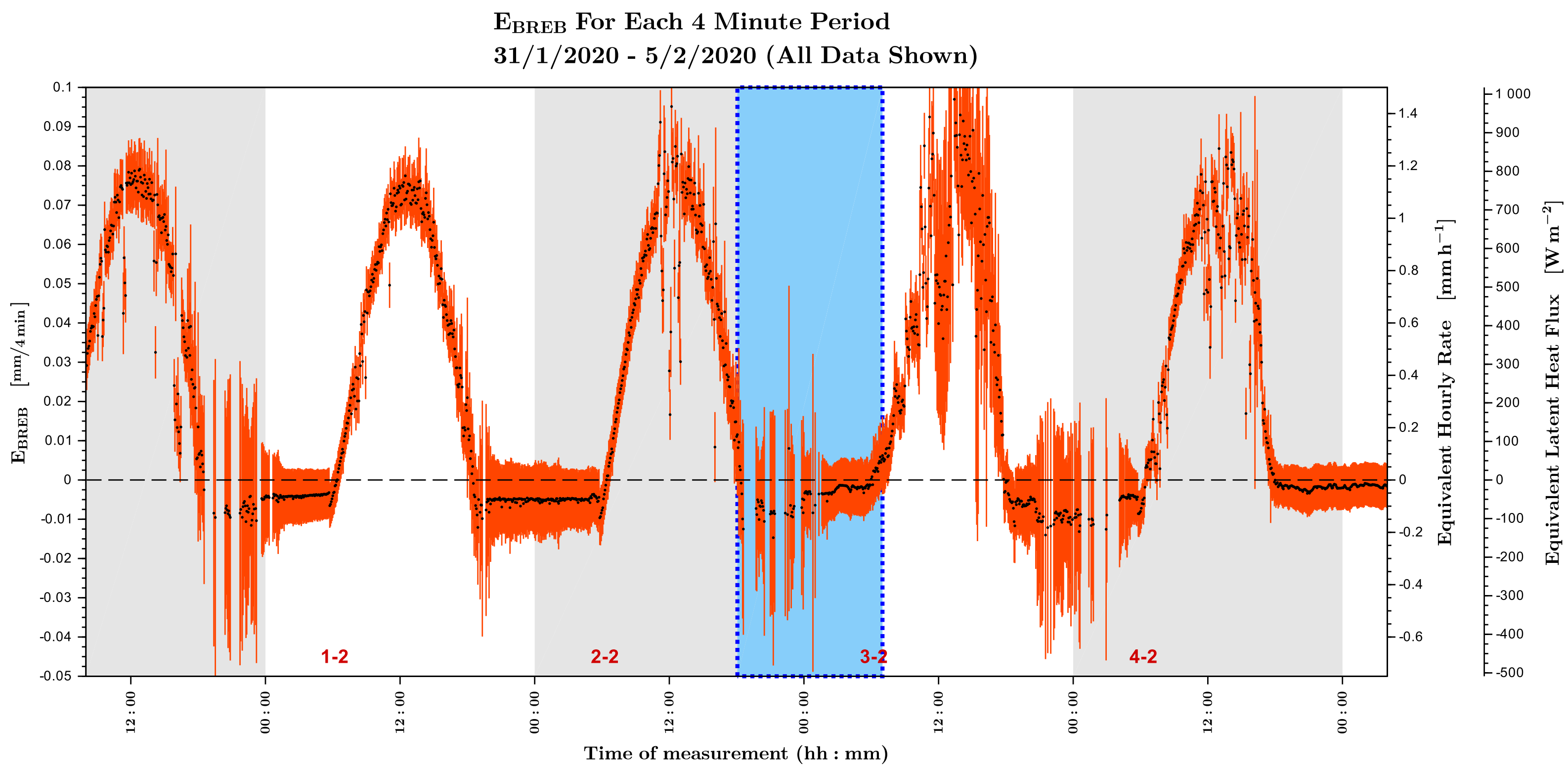

Figure 4.61: DS3: all modelled values for evapotranspiration per Profile BREB, i.e. E_{BREB}. The orange-coloured error bars indicate the 95 % CI for each calculated value of E_{BREB}. The shaded blue rectangle indicates when irrigation occurred on 2nd February.

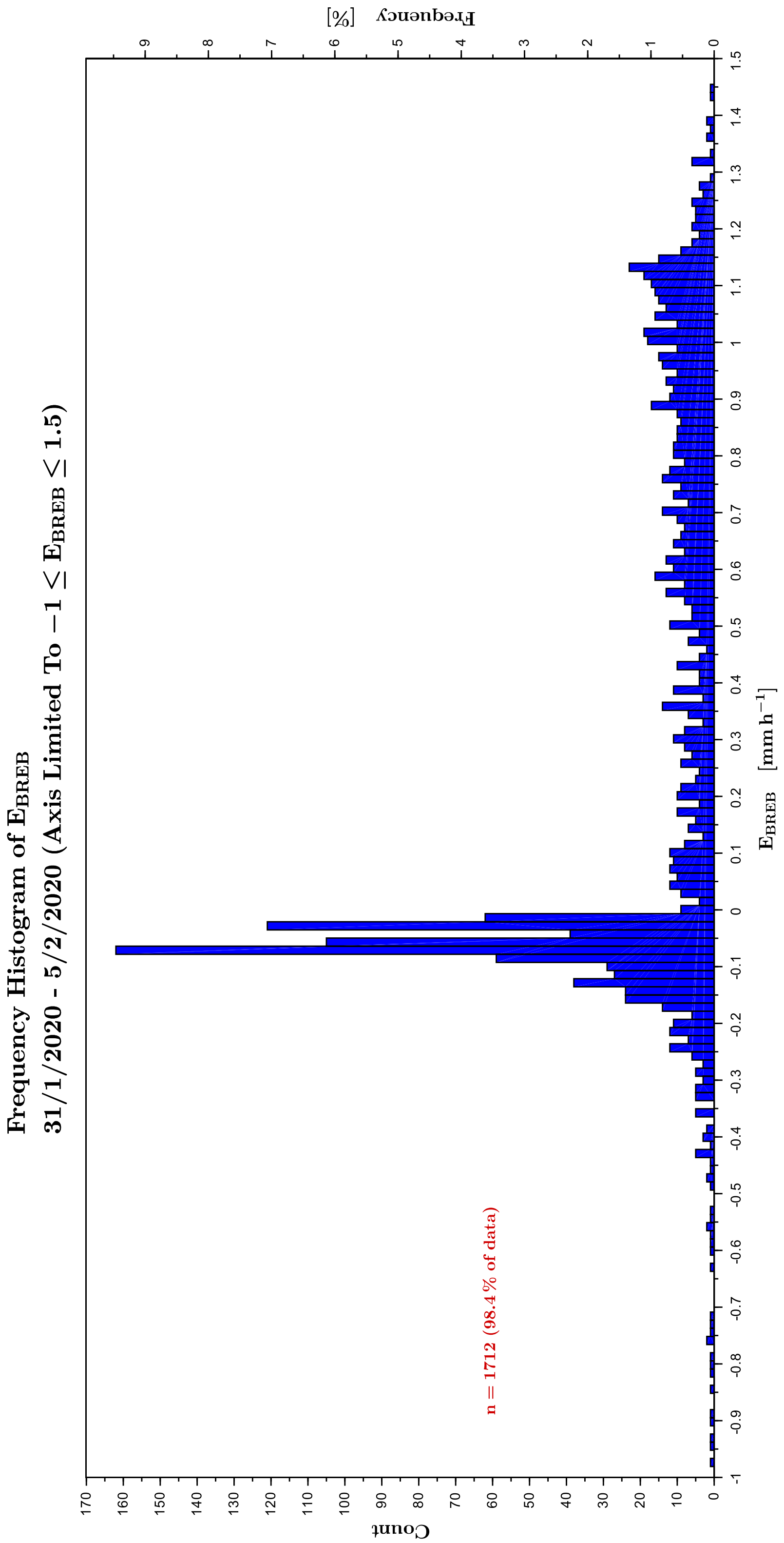

Figure 4.62: DS3: frequency histogram showing the distribution of E_{BREB}.

4.4.3 Results for GPSTIC During DS3

GPSTIC was calculated at the same instances as Profile BREB to allow a like-with-like comparison of the two models. The GPSTIC modelling was repeated for a range of values of α_{PT} between 0.95 and 1.50, including $\alpha_{PT} = 1.26$ and α_{*PT*}.

Figure 4.63: Photograph, facing southeast, of the top of the Profile BREB structure showing the GPSTIC's IRR just above the radiation shield, and below the two-dimensional sonic anemometer and antenna.

Plots of E_{GPSTIC} vs. time for $\alpha_{PT} = 1.42$ are given in Fig. 4.64 (p. 196) and Fig. 4.65 (p. 197), the latter showing the 95 % CI for each modelled value of E_{GPSTIC}. A frequency histogram showing the spread of values of E_{GPSTIC} is given in Fig. 4.66 (p. 198).[11]

[11] $\alpha_{PT} = 1.42$ is shown in § 5.2.3, p. 242 to produce the best results for GPSTIC during DS3, which was much higher than during DS1 and DS2.

During DS3 most values of E_{GPSTIC} were in the following ranges:

$$\begin{array}{lrcl} \text{Daytime (57\,\% of data)} & 0 & < E_{GPSTIC} < 1.35 & [\mathrm{mm\,h^{-1}}] \\ \text{Nighttime (43\,\% of data)} & -0.13 & < E_{GPSTIC} < 0 & [\mathrm{mm\,h^{-1}}] \end{array}$$

As was observed for DS1 and DS2, E_{GPSTIC} exhibited less scatter than E_{BREB} regardless of the time of day and GPSTIC did not produce any extreme outliers. The range of values of E_{GPSTIC} tended to be slightly narrower than for E_{BREB}.

The 95 % CI of E_{GPSTIC} were narrower and more consistent over time compared to those of E_{BREB} throughout DS3.

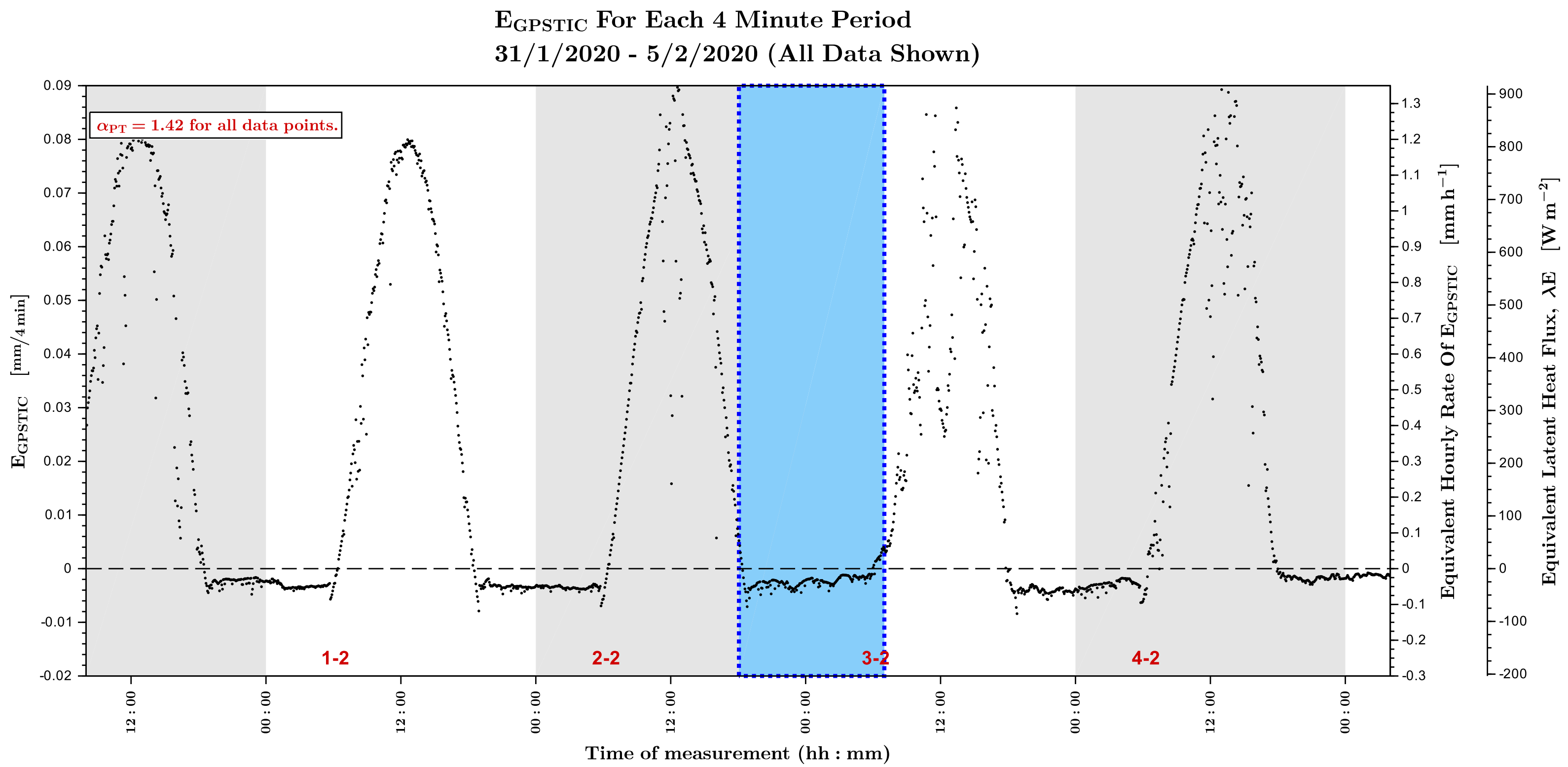

Figure 4.64: DS3: all modelled values for evapotranspiration per GPSTIC, i.e. E_{GPSTIC}, with $\alpha_{PT} = 1.42$. The shaded blue rectangle indicates when the irrigation on the 2nd February occurred.

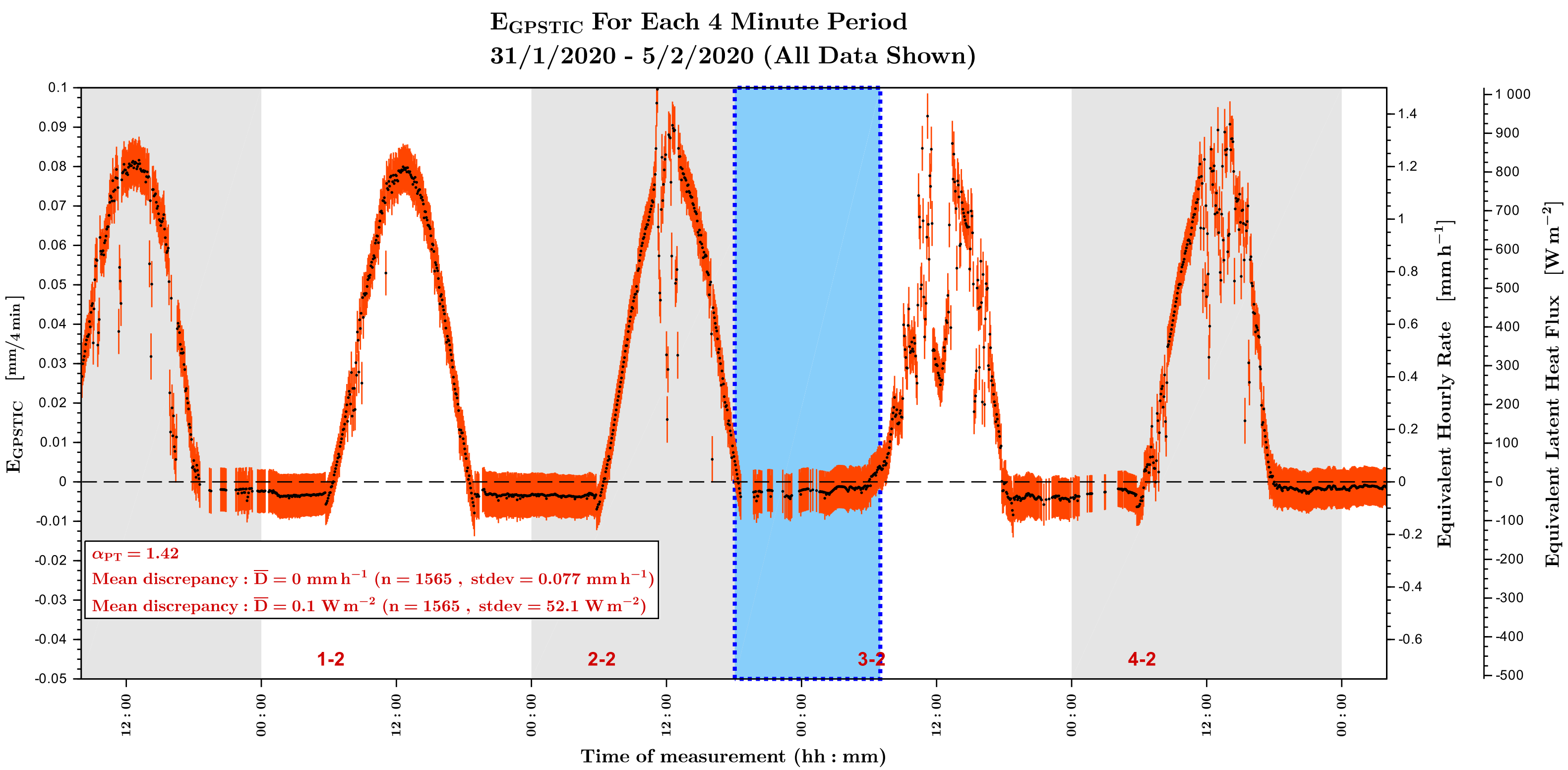

Figure 4.65: DS3: all modelled values for evapotranspiration per GPSTIC, i.e. E_{GPSTIC}, with $\alpha_{PT} = 1.42$. The orange coloured error bars indicate the 95 % CI for each calculated value of E_{GPSTIC}. The shaded blue rectangle indicates when the irrigation on the 2nd February occurred.

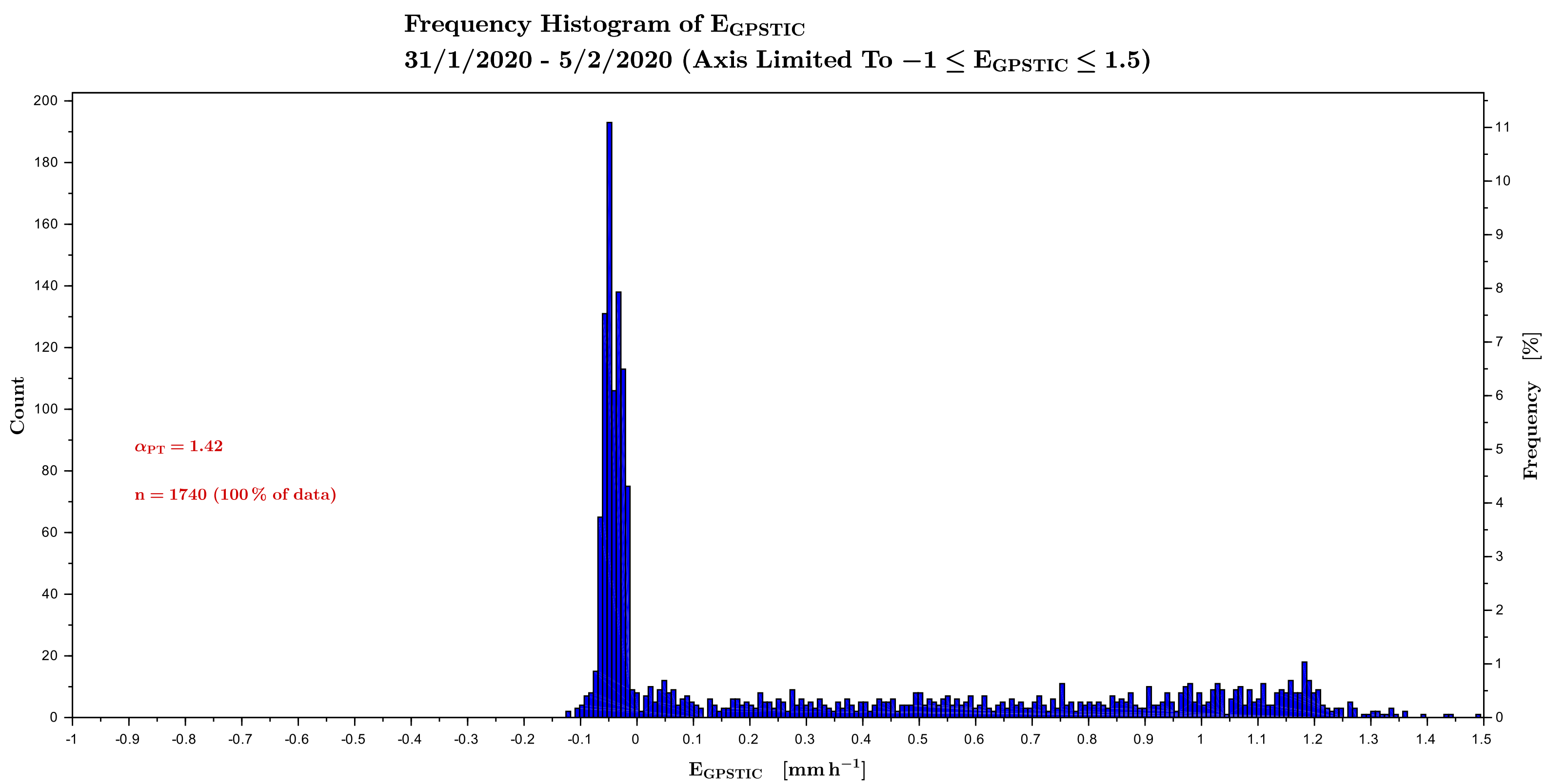

Figure 4.66: DS3: frequency histogram showing the distribution of E_{GPSTIC} with $\alpha_{PT} = 1.42$ over the period 31st January to 5th February, 2020.

4.5 Chapter Summary

This chapter has presented the environmental data that were used as inputs in the evapotranspiration modelling by GPSTIC and Profile BREB. The weather conditions were largely shaped by the severe ongoing drought that was afflicting much of eastern Australia during 2019 and 2020. Thus the measurements of environmental variables did not vary significantly across the three Data Sets. What did change significantly was the crop status within the field. During DS1 approx. one third of the field was bare soil (due to the single-skip planting configuration), and the cotton crop was approx. 0.9 - 1.0 m tall. During DS2 the crop seedlings had only just emerged and the soil was essentially bare. During DS3 the 1.0 - 1.2 m tall cotton crop had a fully-closed canopy with no exposed soil.

This chapter also presented, without analysis, the results of the evapotranspiration modelling. The GPSTIC and Profile BREB systems operated continuously, day and night, during each of the three Data Sets for a collective total of 592 hours of data. In all, 8880 modelled values of E were created by each of GPSTIC and Profile BREB.

The analyses and comparisons of these modelling results follow in Chapter 5.

This page intentionally left blank.

Chapter 5

ANALYSIS

This chapter reports on the evaluation of GPSTIC against the benchmark Profile BREB that was performed using linear regression and discrepancy analyses.[1] The latter were particularly useful for achieving the primary research aim of this thesis (§ 1.5, p. 6) where it was necessary to demonstrate that the mean daily discrepancy between GPSTIC and Profile BREB was less than $\pm 1\,\mathrm{mm\,day^{-1}}$.

5.1 Regression Analyses

Linear regressions of E_{GPSTIC} against E_{BREB} for different values of α_{PT} were performed for DS1, DS2 and DS3 in turn. The plots presented are for the best performing values of α_{PT} (in terms of closeness to the 1:1

[1]Discrepancy analyses were based on the methods of Taylor (1997).

line), as highlighted in the tables of regression equations.

There was significant scatter in the data when $E < 0\,\mathrm{mm\,h^{-1}}$ and it was unhelpful to include these data in the linear regressions. Consequently the regressions were fitted only to the data where

$$\begin{aligned} E_{GPSTIC} &> 0\,\mathrm{mm\,h^{-1}} \\ \text{and} \qquad E_{BREB} &> 0\,\mathrm{mm\,h^{-1}} \end{aligned}$$

On the plots this corresponds to the plotted points in the upper-right quadrant (comprising 46 %, 47 % and 50 % of the data for DS1, DS2 and DS3, respectively).

The effect of this was that nighttime evapotranspiration (which has a relatively small contribution to total accumulated evapotranspiration) was not included in the regressions. **This limitation on the data included in the regression analyses accounts for the *small* difference in outcomes between the regression and discrepancy analyses.**

5.1.1 Regression Analysis for DS1

E_{GPSTIC} was regressed against E_{BREB} for seven different values of α_{PT} for each of the All Data and Selected Data scenarios in DS1. A summary of the regression results is provided in Table 5.1 (p. 203) where it can be seen that an α_{PT} around 1.05 to 1.10 gave the closest agreement between GPSTIC and Profile BREB. Conversely, both the traditional α_{PT} of 1.26 and the iteratively-optimised α_{*PT*} (Mallick et al. 2015a)[2] performed relatively poorly under the conditions of DS1. But even these 'worst-performing' versions of GPSTIC were within 20 % of Profile BREB.

In Table 5.1 the regression slopes were considerably less when using the iteratively-optimised α_{*PT*}. This finding reflects the fact that the

[2]The iteratively-optimised α_{*PT*} had been introduced by Mallick et al. (2015a) to avoid the use of the commonly used $\alpha_{PT} = 1.26$ in the STIC model. The same iterative process was included as an option at Step 16 (p. 115) in the GPSTIC algorithm, the results of which have been tabulated in Table 5.1.

Table 5.1: Linear regression equations for E_{GPSTIC} vs. E_{BREB} for DS1 (18^{th} to 25^{th} February, 2019) for different values for α_{PT}. Only the data where $E_{GPSTIC} > 0\,\mathrm{mm\,h^{-1}}$ and $E_{BREB} > 0\,\mathrm{mm\,h^{-1}}$ were regressed. The regressions closest to the 1:1 line are highlighted.

DS1 – All Data[a]

α_{PT}	Linear Regression Equation ($\mathrm{mm\,h^{-1}}$)	R^2
1.00	$E_{GPSTIC} = 0.92E_{BREB} - 0.002$	0.962
1.05	$E_{GPSTIC} = 0.97E_{BREB} - 0.002$	0.964
1.10	$E_{GPSTIC} = 1.02E_{BREB} - 0.002$	0.964
1.15	$E_{GPSTIC} = 1.07E_{BREB} - 0.002$	0.964
1.20	$E_{GPSTIC} = 1.12E_{BREB} - 0.002$	0.964
1.26	$E_{GPSTIC} = 1.17E_{BREB} - 0.002$	0.964
α_{*PT*}[b]	$E_{GPSTIC} = 0.79E_{BREB} - 0.001$	0.980

DS1 – Selected Data[a]

α_{PT}	Linear Regression Equation ($\mathrm{mm\,h^{-1}}$)	R^2
1.00	$E_{GPSTIC} = 0.93E_{BREB} - 0.002$	0.962
1.05	$E_{GPSTIC} = 0.98E_{BREB} - 0.001$	0.960
1.10	$E_{GPSTIC} = 1.03E_{BREB} - 0.001$	0.960
1.15	$E_{GPSTIC} = 1.08E_{BREB} - 0.001$	0.960
1.20	$E_{GPSTIC} = 1.13E_{BREB} - 0.001$	0.960
1.26	$E_{GPSTIC} = 1.19E_{BREB} - 0.001$	0.960
α_{*PT*}	$E_{GPSTIC} = 0.79E_{BREB} - 0.001$	0.980

[a] All Data scenario excluded extreme outliers (1.9 % excluded). Selected Data excluded $-1.25 < \beta < -0.75$ and $R^2 < 0.90$ in Profile BREB line-of-best-fit (49.9 % excluded).

[b] Iterative process for optimisation of α_{PT} per Mallick et al. (2015a), denoted as α_{*PT*}.

iterative process consistently produced values for α_{*PT*} around 0.85 - 0.95 (discussed in § 6.4.2, p. 280, especially Fig. 6.1, p. 282 and Fig. 6.2, p. 283) which was consistent with the results reported in Mallick et al. (2015a). However, unlike the STIC model which saw improved results with the use of α_{*PT*}, GPSTIC's estimates of E tended to be poor when using α_{*PT*}.

Regression plots of E_{GPSTIC} vs. E_{BREB} are given in Fig. 5.1 (p. 205) and Fig. 5.3 (p. 207) for the highlighted values of α_{PT} in Table 5.1, i.e. $\alpha_{PT} = 1.10$ (All Data modelling) and $\alpha_{PT} = 1.05$ (Selected Data modelling), respectively.

Fig. 5.1 highlights the nighttime data (not included in the regression). It is also observed that 2.3 % of daytime data are also present in the lower left quadrant and all of these occurred within 65 min of sunrise or sunset (cf. Fig. 5.2, p. 206).

Fig. 5.3 highlights the data that were excluded in the Selected Data scenario. The effect of the data exclusion on the regression outcomes or the coefficient of determination was negligible; there was no benefit during DS1 from automatically excluding data according to the Selected Data criteria (p. 118).

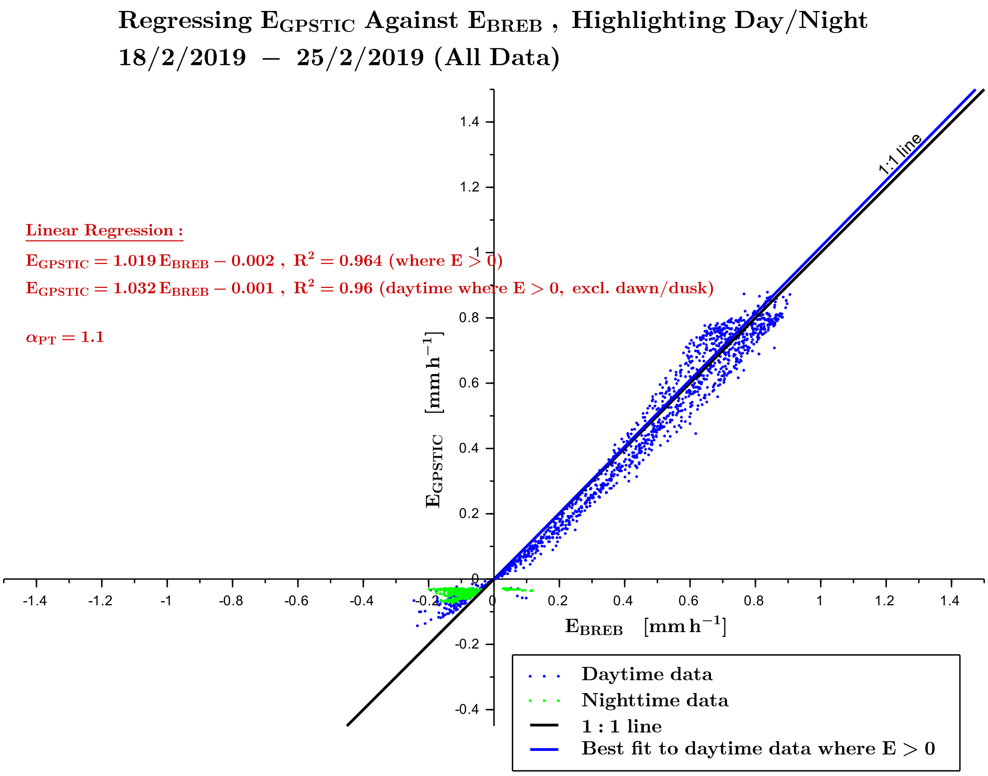

Figure 5.1: DS1: scatter plot and linear regression of E_{GPSTIC} vs. E_{BREB} when $\alpha_{PT} = 1.10$, all data plotted. Nighttime data are highlighted in green. The regression was for data where $E_{GPSTIC} > 0\,\mathrm{mm\,h^{-1}}$ and $E_{BREB} > 0\,\mathrm{mm\,h^{-1}}$.

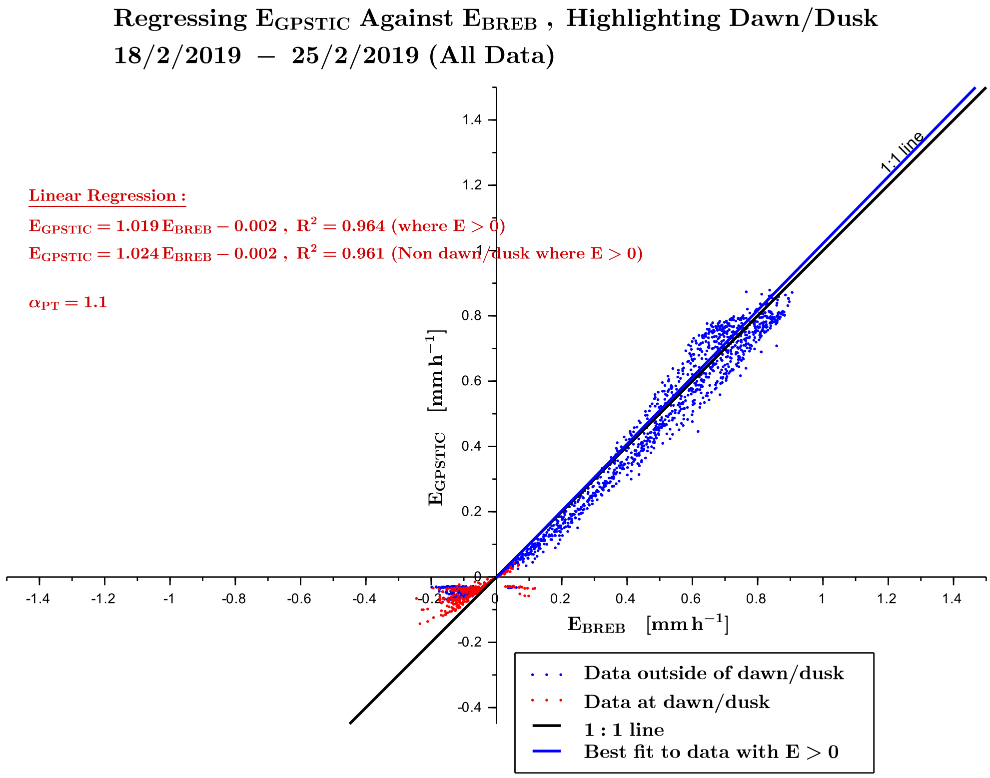

Figure 5.2: DS1: scatter plot and linear regression of E_{GPSTIC} vs. E_{BREB} when $\alpha_{PT} = 1.10$, all data plotted. Data within 65 min of dawn or dusk are highlighted in red. The regression equations are for data where $E_{GPSTIC} > 0\,\mathrm{mm\,h^{-1}}$ and $E_{BREB} > 0\,\mathrm{mm\,h^{-1}}$.

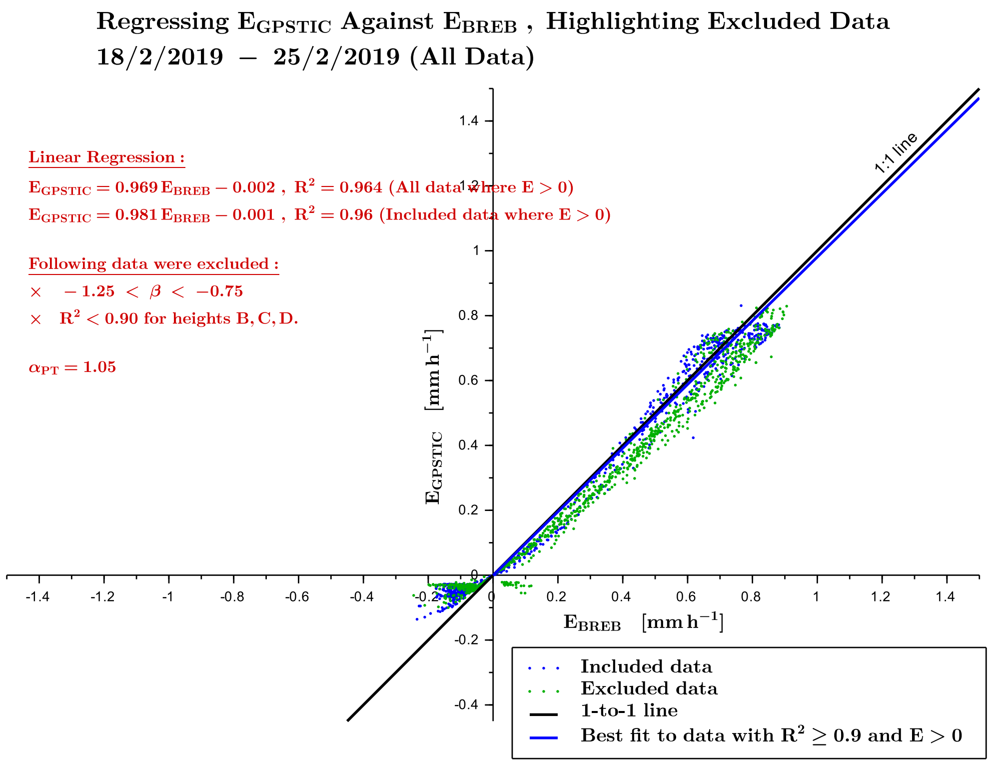

Figure 5.3: DSI: scatter plot and linear regression of E_{GPSTIC} vs. E_{BREB} when $\alpha_{PT} = 1.05$, all data plotted. The regression was for data where $E_{GPSTIC} > 0\,\mathrm{mm\,h^{-1}}$ and $E_{BREB} > 0\,\mathrm{mm\,h^{-1}}$. Data that were excluded in the Selected Data scenario are highlighted in green.

5.1.2 Regression Analysis for DS2

The regression analysis follows the same pattern as for DS1. E_{GPSTIC} was regressed against E_{BREB} for seven different values of α_{PT} for each of the All Data and Selected Data scenarios in DS2. A summary of the regression results is provided in Table 5.2 (p. 209) where it can be seen that selecting an α_{PT} between 1.10 and 1.20 gave a good agreement between GPSTIC and Profile BREB.

Regression plots of E_{GPSTIC} vs. E_{BREB} are given in Fig. 5.4 (p. 210) and Fig. 5.5 (p. 211) for the highlighted values of α_{PT} in Table 5.2, i.e. $\alpha_{PT} = 1.15$ (All Data) and $\alpha_{PT} = 1.10$ (Selected Data), respectively.

(Again, the regression slopes in Table 5.2 when using α_{*PT*} were considerably less than the other tabulated values. See comments on p. 202.)

Fig. 5.4 highlights the nighttime data. 6.2 % of the daytime data had negative evaporation; this was true across all values of α_{PT} and all of these data occurred within 65 min of sunrise or sunset.

Fig. 5.5 highlights the (e, T) points that were excluded in the Selected Data scenario. As was the case in DS1, there was negligible benefit (in terms of the quality of regression) by excluding these data.

Table 5.2: Linear regression equations for E_{GPSTIC} vs. E_{BREB} for DS2 (22$^{\text{nd}}$ October to 4$^{\text{th}}$ November, 2019) for different values for α_{PT}. Only the data where $E_{GPSTIC} > 0\,\text{mm}\,\text{h}^{-1}$ and $E_{BREB} > 0\,\text{mm}\,\text{h}^{-1}$ were regressed. The regressions closest to the 1:1 line have been highlighted.

DS2 – All Data[a]

α_{PT}	Linear Regression Equation ($\text{mm}\,\text{h}^{-1}$)	R^2
1.00	$E_{GPSTIC} = 0.86E_{BREB} + 0.001$	0.91
1.05	$E_{GPSTIC} = 0.91E_{BREB} + 0.001$	0.92
1.10	$E_{GPSTIC} = 0.95E_{BREB} + 0.001$	0.92
1.15	$E_{GPSTIC} = 1.00E_{BREB} + 0.001$	0.92
1.20	$E_{GPSTIC} = 1.04E_{BREB} + 0.001$	0.92
1.26	$E_{GPSTIC} = 1.09E_{BREB} + 0.001$	0.92
α_{*PT*}[b]	$E_{GPSTIC} = 0.70E_{BREB} + 0.001$	0.94

DS2 – Selected Data[a]

α_{PT}	Linear Regression Equation ($\text{mm}\,\text{h}^{-1}$)	R^2
0.95	$E_{GPSTIC} = 0.82E_{BREB} + 0.002$	0.90
1.00	$E_{GPSTIC} = 0.88E_{BREB} + 0.002$	0.91
1.05	$E_{GPSTIC} = 0.93E_{BREB} + 0.001$	0.92
1.10	$E_{GPSTIC} = 0.98E_{BREB} + 0.001$	0.92
1.15	$E_{GPSTIC} = 1.03E_{BREB} + 0.001$	0.92
1.26	$E_{GPSTIC} = 1.13E_{BREB} + 0.001$	0.92
α_{*PT*}	$E_{GPSTIC} = 0.72E_{BREB} + 0.001$	0.92

[a] All Data scenario excluded outliers (5.8 % excluded). Selected Data excluded $-1.25 < \beta < -0.75$ and $R^2 < 0.90$ in Profile BREB LoBF (49.6 % excluded).
[b] Iterative process for optimisation of α_{PT} per Mallick et al. (2015a), denoted as α_{*PT*}.

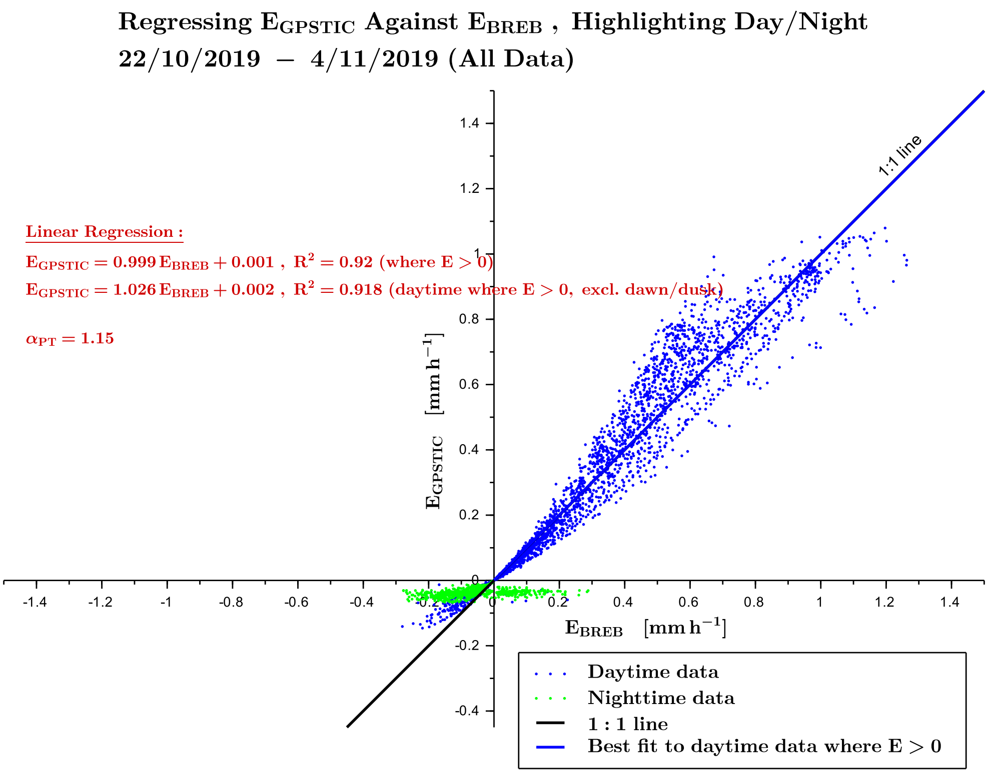

Figure 5.4: DS2: scatter plot and linear regression of E_{GPSTIC} vs. E_{BREB} when $\alpha_{PT} = 1.15$, all data plotted. Nighttime data are highlighted in green. The regression equations are for data where $E_{GPSTIC} > 0\,\mathrm{mm\,h^{-1}}$ and $E_{BREB} > 0\,\mathrm{mm\,h^{-1}}$.

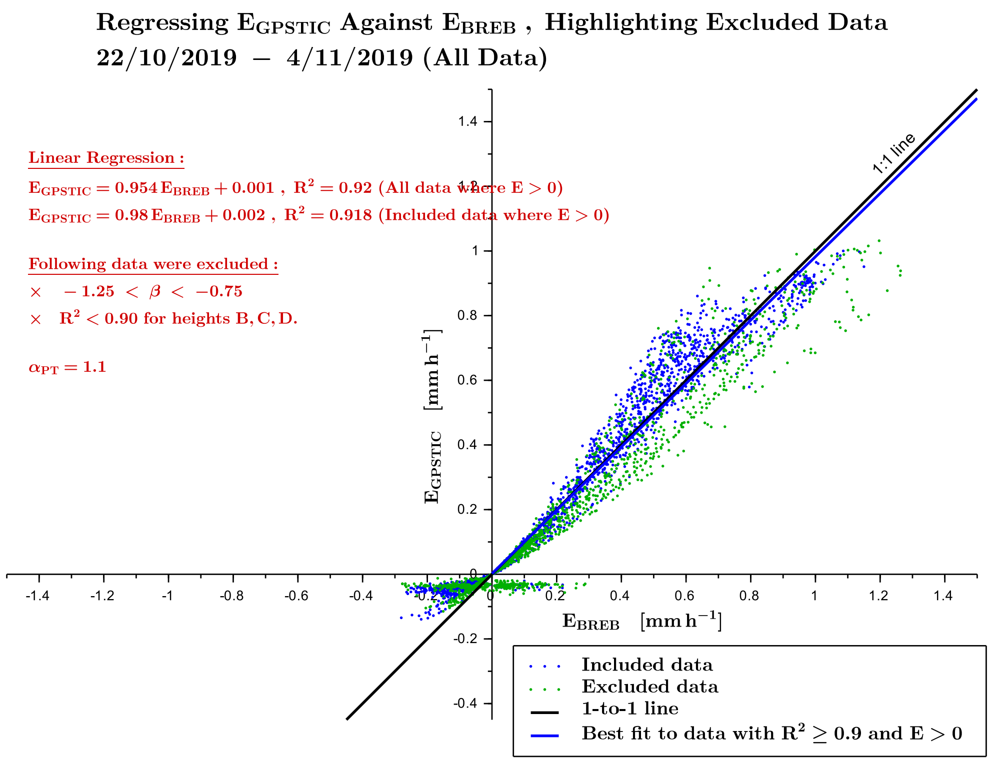

Figure 5.5: DS2: scatter plot and linear regression of E_{GPSTIC} vs. E_{BREB} when $\alpha_{PT} = 1.10$, all data plotted. Data that were excluded in the Selected Data scenario are highlighted in green. The regression equations are for data where $E_{GPSTIC} > 0\,\mathrm{mm\,h^{-1}}$ and $E_{BREB} > 0\,\mathrm{mm\,h^{-1}}$.

5.1.3 Regression Analysis for DS3

Again, the regression analysis for DS3 follows the same pattern as for DS1. E_{GPSTIC} was regressed against E_{BREB} for seven different values of α_{PT} for each of the All Data and Selected Data scenarios in DS3. A summary of the regression results is provided in Table 5.3 (p. 213) where it can be seen that, in contrast to DS1 and DS2, selecting an α_{PT} between 1.35 and 1.45 gave a good agreement between GPSTIC and Profile BREB. In the discrepancy analyses (§ 5.2.3, p. 242) α_{PT} between 1.35 and 1.45 also gave a good agreement between the GPSTIC and Profile BREB models during DS3.

(Again, as per comments on p. 202, the regression slopes in Table 5.3 when using α_{*PT*} were considerably less than the other tabulated values.)

Regression plots of E_{GPSTIC} vs. E_{BREB} are given in Fig. 5.6 (p. 214) and Fig. 5.7 (p. 215) for the highlighted values of α_{PT} in Table 5.3, i.e. $\alpha_{PT} = 1.35$ for both the All Data and Selected Data scenarios.

Fig. 5.6 highlights the nighttime data. 2.9 % of the daytime data had negative evapotranspiration and all of these occurred within 65 min of sunrise or sunset.

Fig. 5.7 highlights the (e, T) points that were excluded in the Selected Data scenario. The coefficient of determination was only slightly improved by doing so ($R^2 = 0.97$ vs. $R^2 = 0.94$); otherwise there was negligible benefit to excluding so much data (47.1 % of data) on the basis of $-1.25 < \beta < -0.75$ or $R^2 < 0.90$ for the LoBF through (e_B, T_B), (e_C, T_C) and (e_D, T_D) in Profile BREB.

Table 5.3: Linear regression equations for E_{GPSTIC} vs. E_{BREB} for DS3 (31st January to 5th February, 2020) for different values for α_{PT}. Only the data where $E_{GPSTIC} > 0\,\mathrm{mm\,h^{-1}}$ and $E_{BREB} > 0\,\mathrm{mm\,h^{-1}}$ were regressed. The regressions closest to the 1:1 line have been highlighted.

DS3 – All Data[a]

α_{PT}	Linear Regression Equation ($\mathrm{mm\,h^{-1}}$)	R^2
1.10	$E_{GPSTIC} = 0.80E_{BREB} - 0.002$	0.94
1.26	$E_{GPSTIC} = 0.92E_{BREB} - 0.003$	0.94
1.35	$E_{GPSTIC} = 0.99E_{BREB} - 0.003$	0.94
1.40	$E_{GPSTIC} = 1.02E_{BREB} - 0.003$	0.94
1.42	$E_{GPSTIC} = 1.03E_{BREB} - 0.003$	0.94
1.50	$E_{GPSTIC} = 1.09E_{BREB} - 0.003$	0.94
α_{*PT*}[b]	$E_{GPSTIC} = 0.68E_{BREB} - 0.002$	0.94

DS3 – Selected Data[a]

α_{PT}	Linear Regression Equation ($\mathrm{mm\,h^{-1}}$)	R^2
1.10	$E_{GPSTIC} = 0.82E_{BREB} - 0.002$	0.97
1.26	$E_{GPSTIC} = 0.94E_{BREB} - 0.002$	0.97
1.35	$E_{GPSTIC} = 1.01E_{BREB} - 0.003$	0.97
1.40	$E_{GPSTIC} = 1.04E_{BREB} - 0.003$	0.97
1.42	$E_{GPSTIC} = 1.06E_{BREB} - 0.003$	0.97
1.50	$E_{GPSTIC} = 1.11E_{BREB} - 0.003$	0.97
α_{*PT*}	$E_{GPSTIC} = 0.70E_{BREB} - 0.002$	0.97

[a] All Data scenario excluded outliers (10.0 % excluded). Selected Data excluded $-1.25 < \beta < -0.75$ and $R^2 < 0.90$ in Profile BREB line-of-best-fit (47.1 % excluded).

[b] Iterative process for optimisation of α_{PT} per Mallick et al. (2015a), denoted as α_{*PT*}.

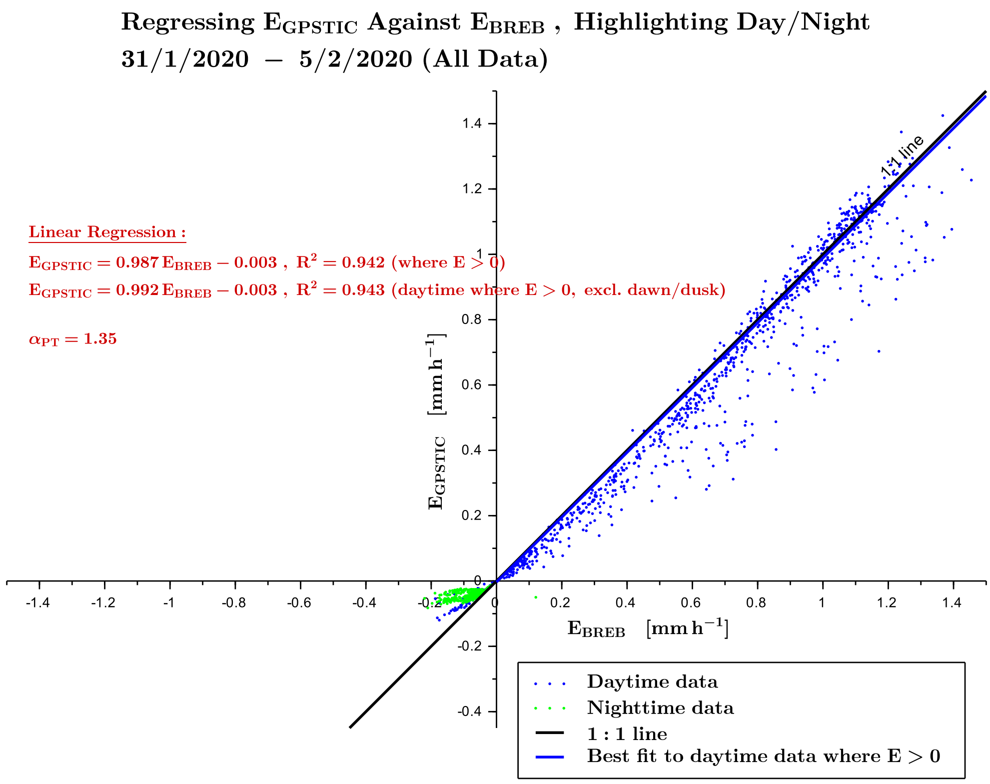

Figure 5.6: DS3: scatter plot and linear regression of E_{GPSTIC} vs. E_{BREB} when $\alpha_{PT} = 1.35$, all data plotted. Nighttime data are highlighted in green. The regression equations are for data where $E_{GPSTIC} > 0\,\mathrm{mm\,h^{-1}}$ and $E_{BREB} > 0\,\mathrm{mm\,h^{-1}}$.

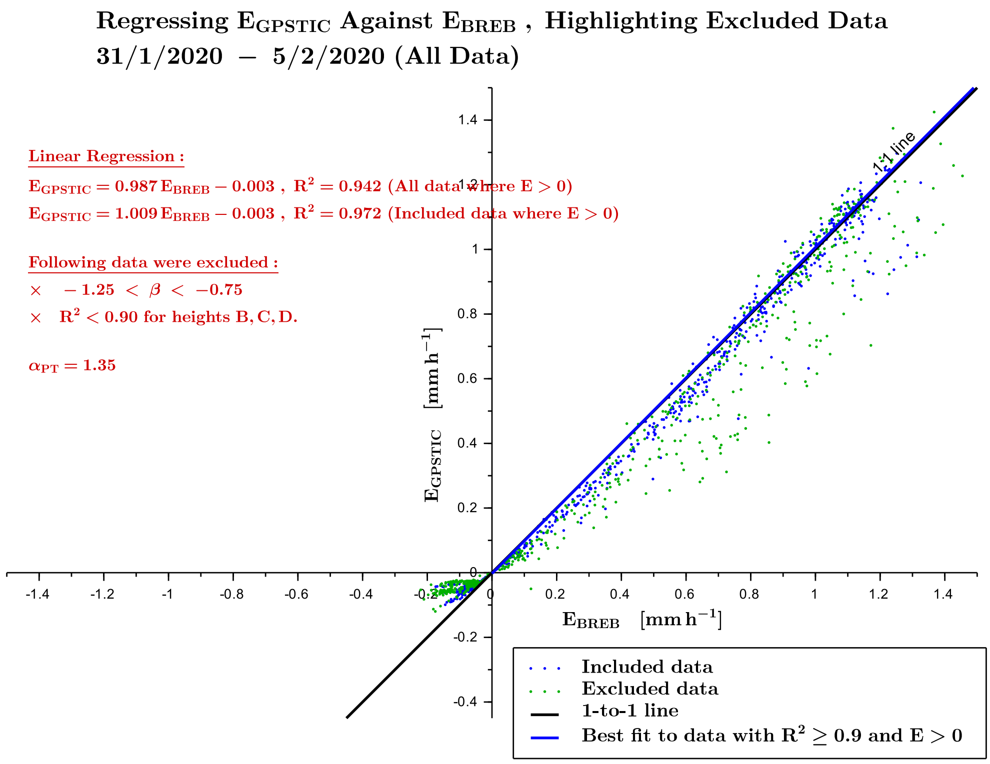

Figure 5.7: DS3: scatter plot and linear regression of E_{GPSTIC} vs. E_{BREB} when $\alpha_{PT} = 1.35$. All data are plotted but data that were not included in the Selected Data scenario (i.e. where $-1.25 < \beta < -0.75$ or $R^2 < 0.90$ for the LoBF through the data points (e_B, T_B), (e_C, T_C) and (e_D, T_D)) are highlighted in green. The regression equations are for data where $E_{GPSTIC} > 0\,\mathrm{mm\,h^{-1}}$ and $E_{BREB} > 0\,\mathrm{mm\,h^{-1}}$.

5.2 Discrepancy Analyses

The discrepancy analyses quantified the difference, or 'discrepancy', between the modelling results from GPSTIC and Profile BREB. The discrepancy, D, was defined as:

$$D = E_{GPSTIC} - E_{BREB} \tag{5.1}$$

The primary research aim could then be written as:

$$\text{if} \qquad \overline{D}_{daily} = \frac{\sum E_{GPSTIC} - \sum E_{BREB}}{\left(\frac{Y}{24\,\mathrm{h\,day^{-1}}}\right)} \tag{5.2}$$

$$\text{then} \qquad \left|\overline{D}_{daily}\right| \overset{?}{<} 1\,\mathrm{mm\,day^{-1}} \tag{5.3}$$

where $\overline{D}_{daily}$ was the mean daily discrepancy [mm day^{-1}], Y was the number of hours in the Data Set, and $\sum E_{GPSTIC}$ and $\sum E_{BREB}$ were the total accumulations of E [mm] for the Data Set. $\sum E_{GPSTIC}$ and $\sum E_{BREB}$ had to be calculated for the very same time intervals.

The primary rationale for the discrepancy analyses was to determine whether the daily cumulative discrepancy between GPSTIC and Profile BREB was within ± 1 mm day^{-1} (to achieve the primary research aim of the present research).

The optimal outcome would be that $\overline{D}_{daily} = 0$ mm. However, it would be unlikely that the discrepancy between the GPSTIC and Profile BREB models would actually be zero. The question as to whether the non-zero discrepancy between the two models was significant was evaluated — following Taylor (1997) — using the 95 % CI of the discrepancy. If the expected 'zero line', shown as the dashed line at $D = 0$ mm in the discrepancy plots, was consistently included within these 95 % CI bounds then it could be concluded that there was no significant discrepancy between GPSTIC and Profile BREB.

Thus the final column of Table 5.4 (p. 218), Table 5.5 (p. 230) and Table 5.6 (p. 242) shows the associated total accumulated uncertainties

δD_{total}, or 'total margins of error', in the calculated values of D_{total}. These were used to plot the 95 % CI 'error bars' in the discrepancy plots. The uncertainties in total discrepancy, δD_{total}, were calculated by

$$\delta D_{total} = \delta D^{(+)}_{total} + \left|\delta D^{(-)}_{total}\right| \tag{5.4}$$

where $\left|\delta D^{(-)}_{total}\right|$ denotes the absolute value of $\delta D^{(-)}_{total}$ and

$$\delta D^{(+)}_{total} = \sum_{i=1}^{n} \delta E_{BREB}{}^{(+)}\big|_n + \sum_{i=1}^{n} \delta E_{GPSTIC}{}^{(+)}\big|_n \tag{5.5}$$

$$\delta D^{(-)}_{total} = \sum_{i=1}^{n} \delta E_{BREB}{}^{(-)}\big|_n + \sum_{i=1}^{n} \delta E_{GPSTIC}{}^{(-)}\big|_n \tag{5.6}$$

where $\delta E_{BREB}{}^{(+)}\big|_n$ and $\delta E_{BREB}{}^{(-)}\big|_n$ were the upper and lower extents, respectively, of the 95 % CI for E_{BREB} for the n^{th} 4 min interval in the Data Set (and likewise for E_{GPSTIC}). Or, simply, the modelling uncertainty associated with each individual 4 min interval accumulated into an overall uncertainty for the Data Set.

This is not to say that the true value of D_{total} was equally likely at any point within the range $(D_{total} - \delta D_{total}, D_{total} + \delta D_{total})$; rather, the range simply indicated that there was a 95 % chance — given the measurement uncertainties inherent in the sensors — that the true value for D_{total} would lie somewhere inside of this range (and most likely to be close to the calculated value of D_{total}). Appendix H (p. 379) provides further background and explanation on how the modelling uncertainties were calculated.

In § 5.2 each of DS1, DS2 and DS3 are analysed in turn. The 4 min[3] discrepancies between GPSTIC and Profile BREB are analysed first followed by analyses of the accumulated discrepancies. The latter are particularly useful because of the clarity they provide as to the extent and significance of difference between the two models.

[3]The 4 min discrepancies are subscripted as 'inst' (for 'instantaneous') in the following sections, e.g. $\overline{D}_{inst}$.

5.2.1 Discrepancy Analysis for DS1

Table 5.4 (p. 218) summarises the modelling results for DS1 wherein the total accumulated E_{BREB}, total accumulated E_{GPSTIC} (for various α_{PT}), and the total accumulated discrepancy D are shown.

Table 5.4: Daily and total accumulated E_{BREB} and E_{GPSTIC} for the 165 hours of DS1 (18th to 25th February, 2019) with 95 % CI. The final column shows the final accumulated discrepancy D (where $D = E_{GPSTIC} - E_{BREB}$). The value of α_{PT} producing the smallest accumulated D has been highlighted.

DS1 – All Data[a]

E_{BREB} Total (mm)	E_{BREB} Mean Daily (mm/day)	α_{PT}	E_{GPSTIC} Total (mm)	E_{GPSTIC} Mean Daily (mm/day)	D Total (mm)
31.1 ±15.9	4.4	1.00	29.5 ± 7.8	4.2	−1.6 ±17.7
		1.05	31.2 ± 8.2	4.5	0.1 ±17.9
		1.10	32.8 ± 8.7	4.7	1.7 ±18.1
		1.15	34.3 ± 9.1	4.9	3.2 ±18.3
		1.20	35.9 ± 9.5	5.1	4.8 ±18.5
		1.26	37.6 ±10.0	5.4	6.5 ±18.8
		α_{*PT*}[b]	25.5 ± 8.8	3.6	−5.6 ±18.2

DS1 – Selected Data[a]

E_{BREB} Total (mm)	E_{BREB} Mean Daily (mm/day)	α_{PT}	E_{GPSTIC} Total (mm)	E_{GPSTIC} Mean Daily (mm/day)	D Total (mm)
10.9 ±8.4	1.6	0.90	9.8 ±3.9	1.4	−1.1 ±9.3
		0.95	11.2 ±3.8	1.6	0.3 ±9.2
		1.00	12.0 ±4.0	1.7	1.1 ±9.3
		1.10	13.3 ±4.4	1.9	2.4 ±9.5
		1.15	13.9 ±4.7	1.8	3.0 ±9.6
		1.26	15.3 ±5.1	2.2	4.4 ±9.8
		α_{*PT*}	10.1 ±4.3	1.4	−0.8 ±9.4

[a] All Data scenario excluded extreme outliers (1.9 % excluded). Selected Data excluded $-1.25 < \beta < -0.75$ and $R^2 < 0.90$ for the Profile BREB LoBF (49.9 % excluded).

[b] Iterative process for optimisation of α_{PT} per Mallick et al. (2015a), denoted α_{*PT*}

5.2.1.1 4 min Discrepancies During DS1

Plots of the 4 min discrepancies between GPSTIC and Profile BREB are shown in Fig. 5.8 (p. 220) and Fig. 5.9 (p. 221). These plots are for the highlighted values of α_{PT} in Table 5.4 (p. 218).

The mean daily discrepancy can be calculated from the final column of Table 5.4 (which presents the accumulated discrepancies after 165 hours, or 6.875 days, of DS1). In so doing it becomes apparent that $\left|\overline{D}_{daily}\right| < 1\,\mathrm{mm\,day^{-1}}$ for all tabulated values of α_{PT}.

With reference to Fig. 5.10 (p. 222) the mean 4 min discrepancy, $\overline{D}_{inst}$, between GPSTIC (with $\alpha_{PT} = 1.05$) and Profile BREB for the All Data scenario during DS1 was:

$$\overline{D}_{inst} = 0.0\,{}^{\mathrm{mm}}/_{4\,\mathrm{min}} \quad (\sigma = 0.0038\,{}^{\mathrm{mm}}/_{4\,\mathrm{min}}) \tag{5.7}$$

$$\equiv 0.0\,\mathrm{mm\,h^{-1}} \quad \left(\sigma = 0.057\,\mathrm{mm\,h^{-1}}\right) \tag{5.8}$$

or in terms of energy fluxes:

$$\overline{D}_{inst} = 0.2\,\mathrm{Wm^{-2}} \quad \left(\sigma = 38.5\,\mathrm{Wm^{-2}}\right) \tag{5.9}$$

The equivalent mean daily discrepancy was:

$$\begin{aligned}\overline{D}_{daily} &\approx 0.01\,\mathrm{mm\,day^{-1}} \\ &< 1\,\mathrm{mm\,day^{-1}}\end{aligned} \tag{5.10}$$

Therefore, following sustained, continuous measurement over 165 hours during DS1 the primary research question (Eqn. 5.3, p. 216) was answered in the affirmative.

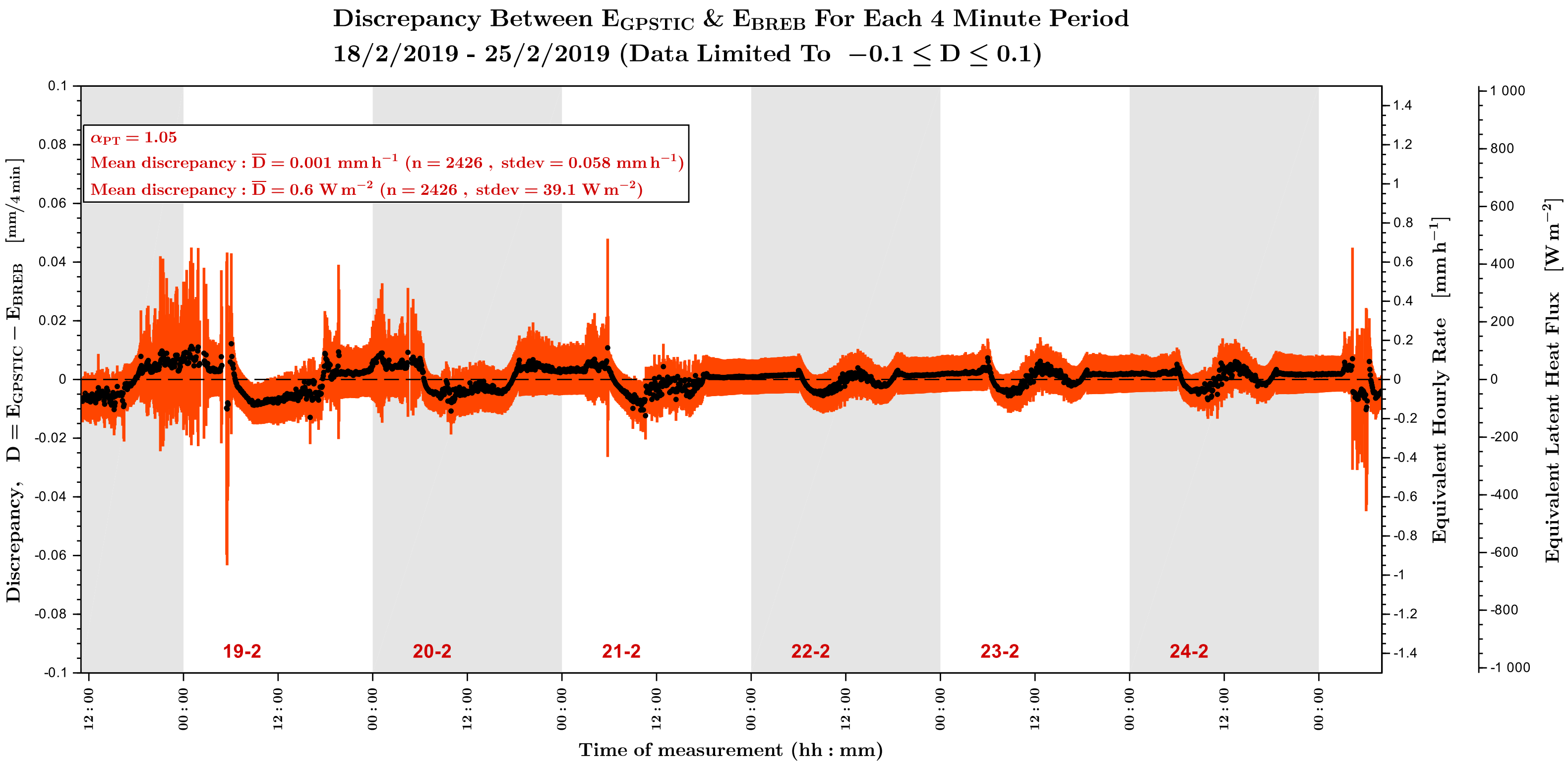

Figure 5.8: DS1: 4 min discrepancy between E_{GPSTIC} and E_{BREB} when $\alpha_{PT} = 1.05$. The 1.9 % of data not plotted lie outside the range $-0.53 < E_{BREB} < 1.5\,\mathrm{mm\,h^{-1}}$. The orange coloured bars indicate the 95 % CI.

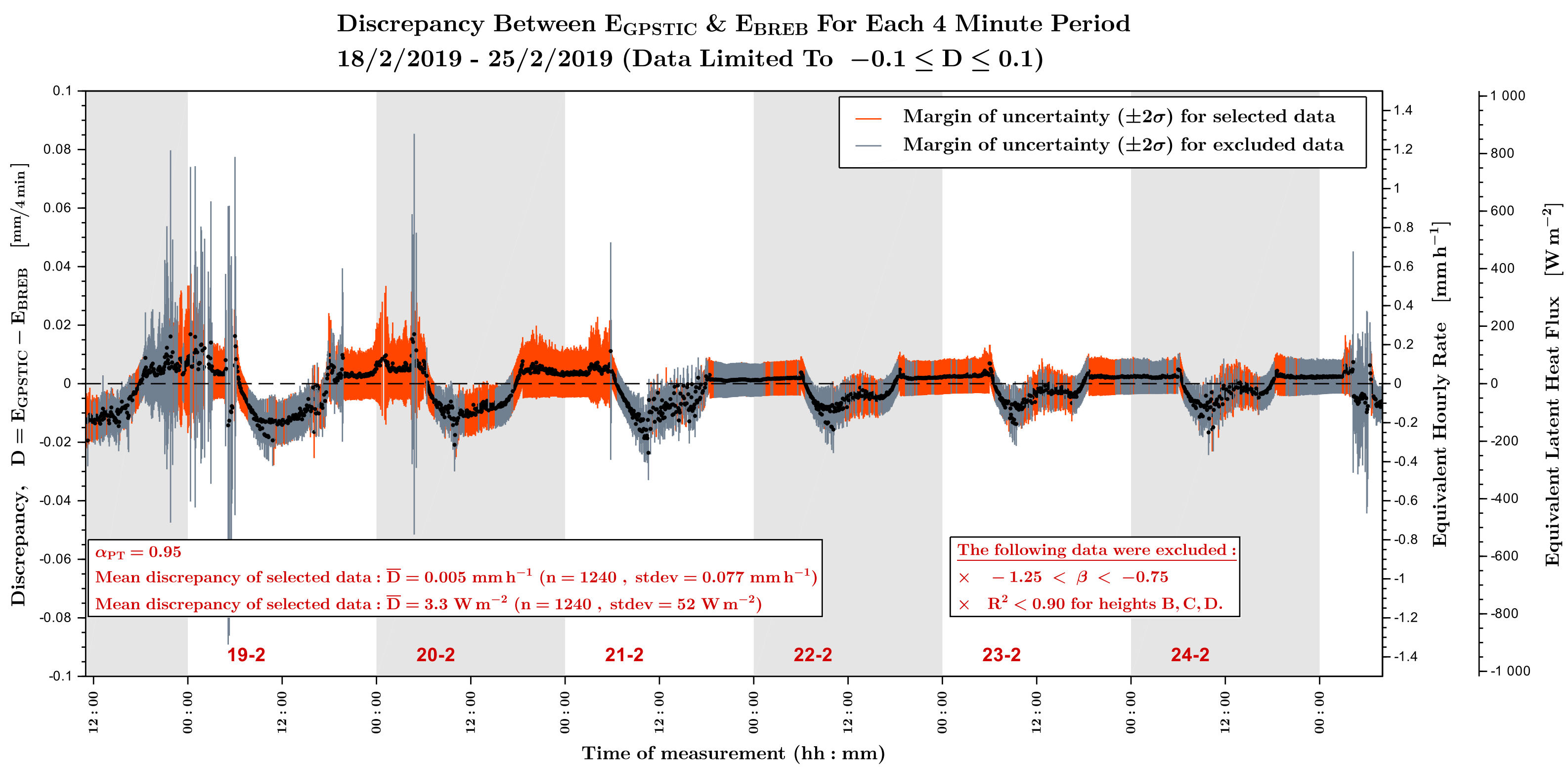

Figure 5.9: DS1: 4 min discrepancy between E_{GPSTIC} and E_{BREB} when $\alpha_{PT} = 0.95$, all data plotted but excluded data are distinguished. The orange-coloured and grey-coloured bars indicate the 95 % CI for the Selected Data and excluded data respectively.

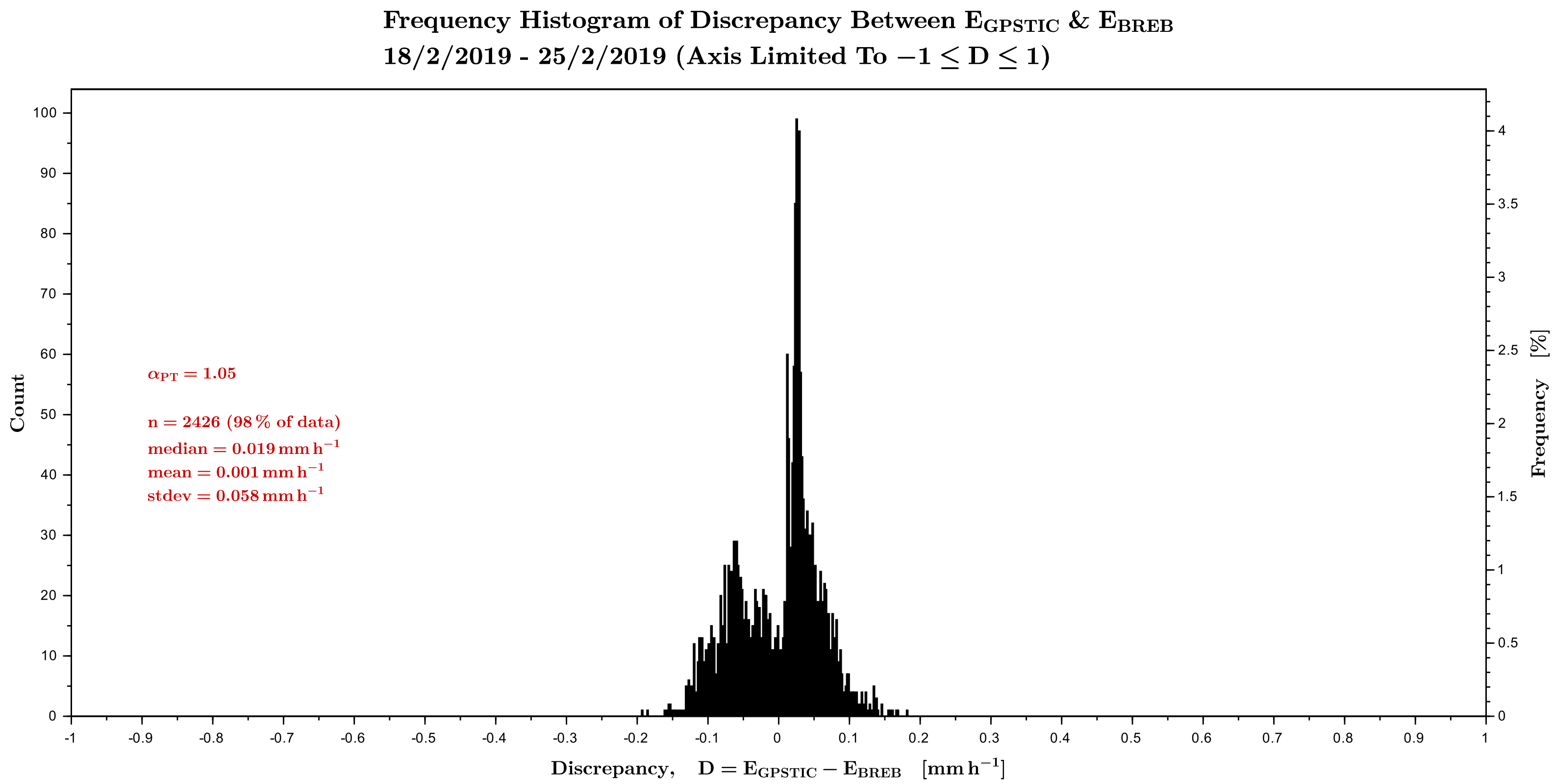

Figure 5.10: DS1: frequency histogram of the 4 min discrepancies between E_{GPSTIC} and E_{BREB} when $\alpha_{PT} = 1.05$. The 1.9 % of data not included in the histogram lie outside the range $-0.53 < E_{BREB} < 1.5\,\mathrm{mm\,h^{-1}}$.

5.2.1.2 Cumulative Discrepancy for DS1

Plots of the total accumulated E_{BREB} and E_{GPSTIC}, and the discrepancy between them, for the 165 hours of DS1 are shown in Fig. 5.11 (p. 224) and Fig. 5.12 (p. 225). These plots are based on the results in Table 5.4 (p. 218). The GPSTIC data corresponding to these same time periods were also rejected to allow a fair comparison of the models. The accumulated values of evapotranspiration in Fig. 5.12a (p. 225) and in Table 5.4 (p. 218) were small because so much data were rejected in the Selected Data scenario.

Several observations can be made from these plots (and Table 5.4, p. 218):

1. The requirement that $\left|\overline{D}_{daily}\right| < 1\,\text{mm}\,\text{day}^{-1}$ was met for all tabulated values of α_{PT} (calculated by Eqn. 5.2, p. 216).

2. For the All Data scenario the best outcome was achieved when $\alpha_{PT} = 1.05$. In this case the total accumulated discrepancy over 165 hours was only 0.1 mm, or $\overline{D}_{daily} = 0.01\,\text{mm}\,\text{day}^{-1}$. α_{*PT*} produced relatively poor results.

3. For the Selected Data scenario the best outcome was achieved when $\alpha_{PT} = 0.95$. In this case the total accumulated discrepancy over 165 hours was only 0.3 mm, or $\overline{D}_{daily} = 0.04\,\text{mm}\,\text{day}^{-1}$. In contrast to the All Data scenario, α_{*PT*} also produced good results. The 95 % CI ranges were approx. half of those of the All Data scenario, i.e. there was less uncertainty in the Selected Data results.

4. In Fig. 5.11b (p. 224) and Fig. 5.12b (p. 225) the 'zero line' (i.e. $D = 0\,\text{mm}$) was comfortably within the 95 % CI and, for most of the tabulated values of α_{PT}, it would have been comfortably within a 1σ (68 %) CI.

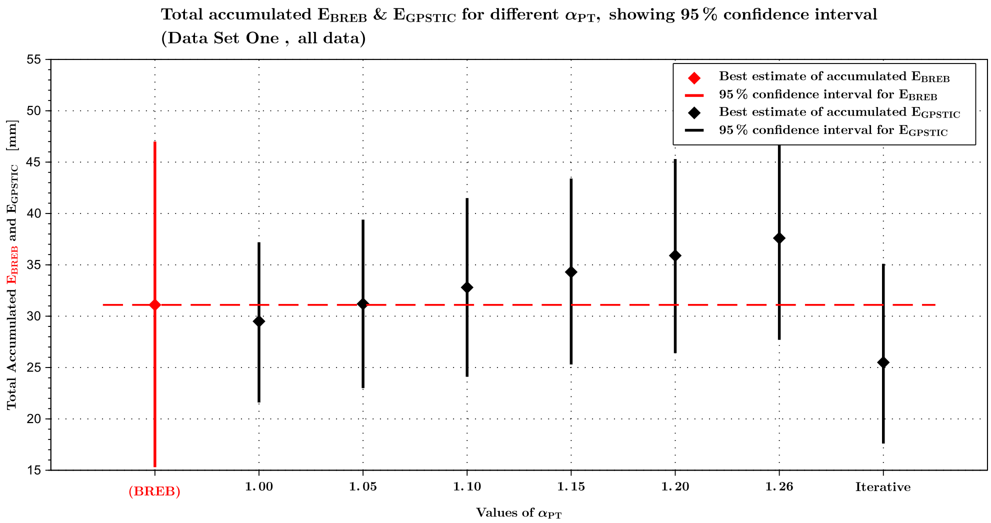

(a) Total accumulated E_{BREB} and E_{GPSTIC} after 165 hours during DS1.

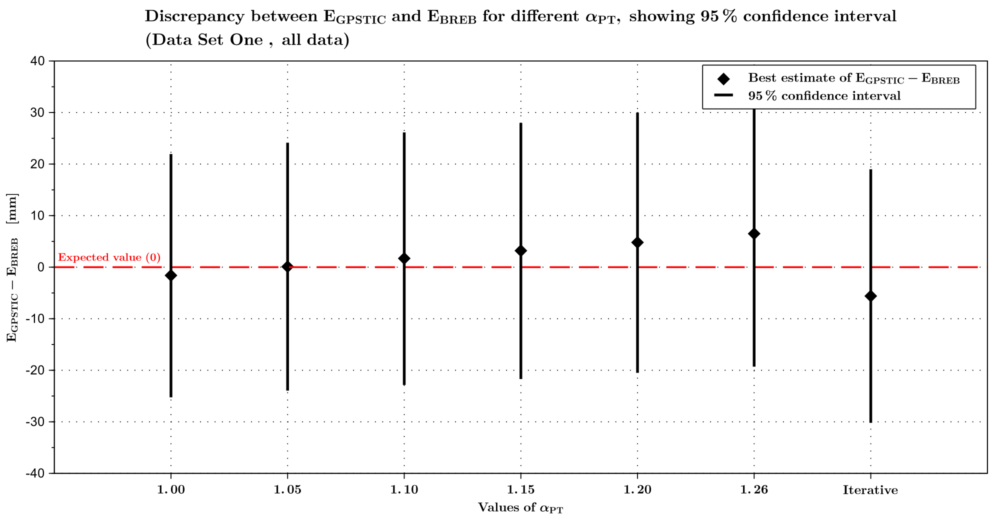

(b) Total accumulated discrepancy between E_{GPSTIC} and E_{BREB} after 165 hours during DS1.

Figure 5.11: Plotting the DS1 results from Table 5.4 (p. 218) for the All Data scenario. Plot (a) compares the total accumulated E_{GPSTIC} (for various values for α_{PT}) with the total accumulated E_{BREB}. Plot (b) compares the discrepancy between the total accumulated E_{GPSTIC} (for various values for α_{PT}) and the total accumulated E_{BREB}. The 95 % CI were determined by the propagation of the sensors' measurement uncertainties through the modelling (see Appendix H, p. 379).

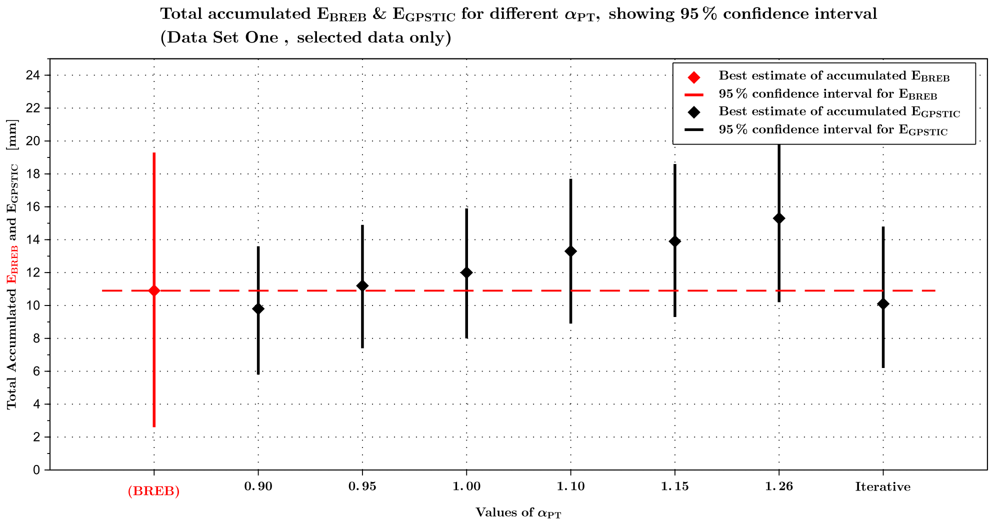

(a) Total accumulated E_{BREB} and E_{GPSTIC} after 165 hours during DS1.

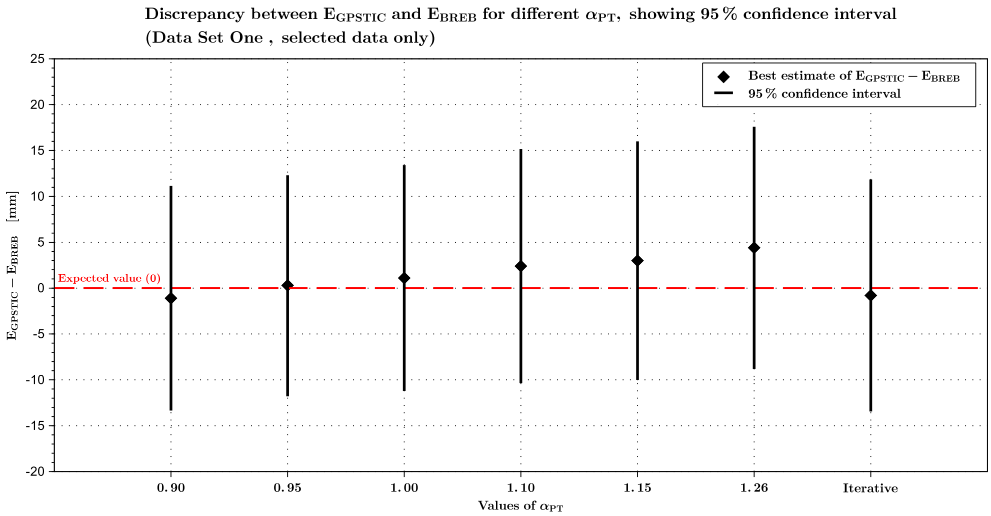

(b) Total accumulated discrepancy between E_{GPSTIC} and E_{BREB} after 165 hours during DS1.

Figure 5.12: Plotting the DS1 results from Table 5.4 (p. 218) for the Selected Data scenario, i.e. when the Profile BREB LoBF had an $R^2 > 0.90$ and when $\beta < -1.25$ or $\beta > -0.75$. The 95 % CI were determined by the propagation of the sensors' measurement uncertainties through the modelling (see Appendix H, p. 379).

5.2.1.3 Alignment of E_{GPSTIC} and E_{BREB} at $\alpha_{PT} = 1.05$

At this point attention is drawn to the DS1 results for the All Data scenario with $\alpha_{PT} = 1.05$ where $\overline{D}_{daily} \approx 0.01\,\mathrm{mm\,day^{-1}}$. Fig. 5.13 (p. 227) shows how closely GPSTIC and Profile BREB aligned with one another throughout DS1, even in the context of a discontinuous crop canopy. This was despite the fact that minimal screening of the Profile BREB data had been done (1.9 % of data were not included in the analysis simply because they were outside the range $-0.53 < E_{BREB} < 1.5\,\mathrm{mm\,h^{-1}}$.[4])

The persistent close alignment between GPSTIC and Profile BREB shown in Fig. 5.13 is strongly suggestive that *both* models were operating correctly over the 165 hours of DS1. The reasoning behind this assertion follows thus: GPSTIC (using $\alpha_{PT} = 1.05$) and Profile BREB exhibited near-identical alignment with each other for 2475 modelled values of E over 165 hours. Their near-identical alignment was due to either (a) both systems correctly modelling the same E over the entire period of DS1, or (b) both systems were incorrectly modelling E over the entire period of DS1 but doing so in an identical fashion. But option (b) is highly improbable because the GPSTIC and Profile BREB systems were quite independent of each other (see argument for independence in § 6.2.3, p. 273). Also, GPSTIC and Profile BREB both responded appropriately and similarly to changes in the environment. The logical and reasonable conclusion, then, is to accept that both GPSTIC and Profile BREB were operating correctly during DS1.[5]

[4] The rationale for this range is that E_{BREB} would not be expected to exceed this range under standard field conditions. All of the instances when E_{BREB} did exceed this range were associated with $\beta \approx -1$.

[5] And also, by the same argument, during DS2 and DS3.

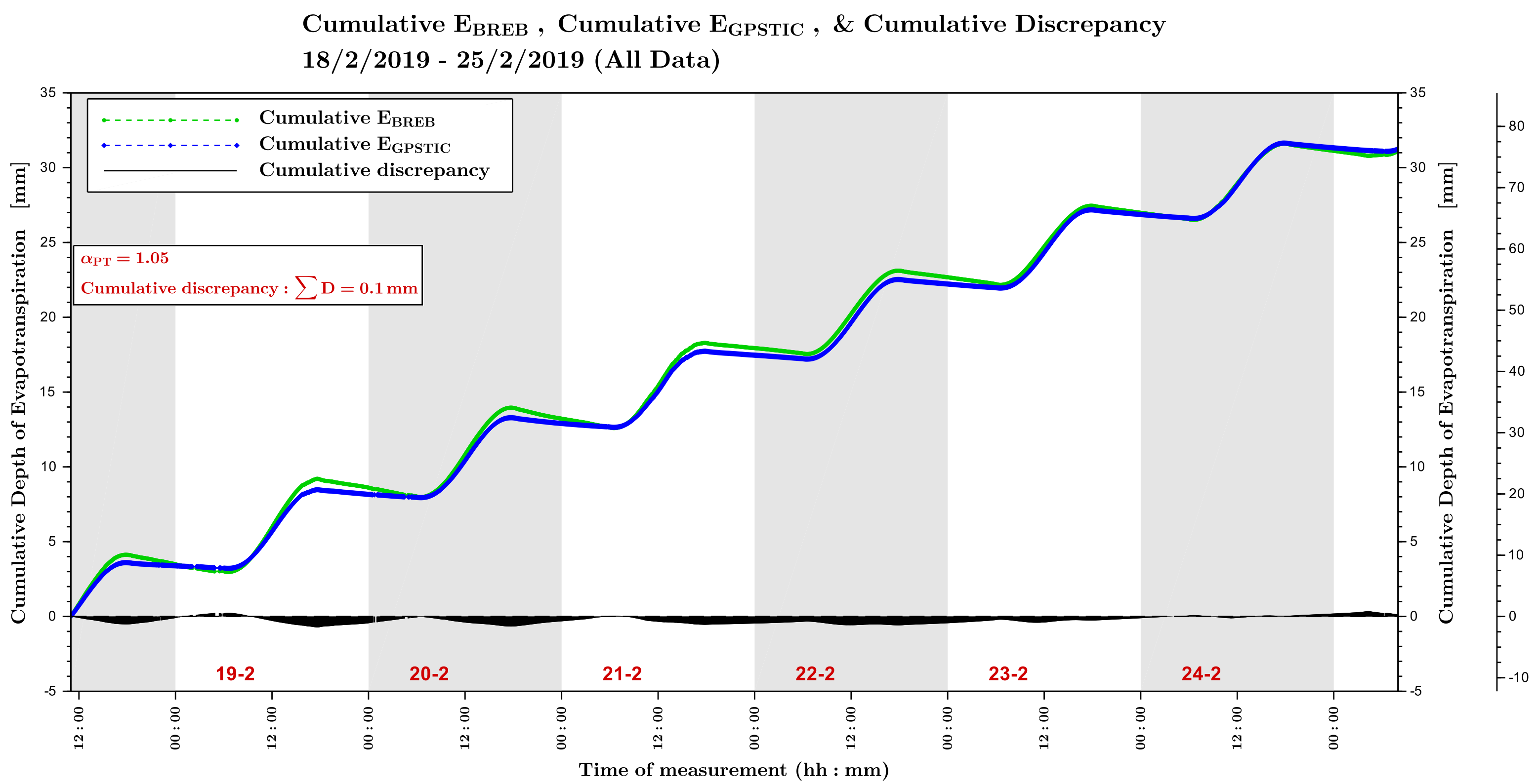

Figure 5.13: DS1: cumulative E_{GPSTIC} and E_{BREB} over time for the duration of DS1 when $\alpha_{PT} = 1.05$, all results plotted. Significantly, the plots aligned closely for the whole of DS1, not just the final values.

5.2.1.4 Paired t-Tests

Two-tailed t-tests were performed for the paired DS1 4 min values for E_{GPSTIC} and E_{BREB} following De Veaux et al. (2009). If n is the number of 4 min samples for each of E_{GPSTIC} and E_{BREB} during DS1 then

$$n = 2475 \tag{5.11}$$

The mean difference, $\bar{d}$, and standard deviation of the differences, σ_d, of the paired samples are (to 5 significant figures)

$$\begin{aligned} \bar{d} &= \frac{\sum_{i=1}^{n} \left[(E_{GPSTIC})_i - (E_{BREB})_i \right]}{n} \\ &= 0.001\,602\,9 \ {}^{\mathrm{mm}}/_{4\,\mathrm{min}} \end{aligned} \tag{5.12}$$

$$\begin{aligned} \sigma_d &= \sqrt{\frac{\sum_{i=1}^{n} \left(d_i - \bar{d} \right)^2}{n-1}} \\ &= 0.064\,247 \ {}^{\mathrm{mm}}/_{4\,\mathrm{min}} \end{aligned} \tag{5.13}$$

The standard error of the mean difference, $SE_{\bar{d}}$, is

$$\begin{aligned} SE_{\bar{d}} &= \frac{\sigma_d}{\sqrt{n}} \\ &= 0.001\,291\,4 \ {}^{\mathrm{mm}}/_{4\,\mathrm{min}} \end{aligned} \tag{5.14}$$

Because the paired samples are independent of each other, the number of degrees of freedom, DoF, is given by

$$\begin{aligned} DoF &= (n_{\mathrm{GPSTIC}} - 1) + (n_{\mathrm{BREB}} - 1) \\ &= 4948 \end{aligned} \tag{5.15}$$

If the null hypothesis is that there is no difference between E_{GPSTIC} and E_{BREB}, the two-tailed t value is given by

$$\begin{aligned} t_{DoF} &= \frac{\bar{d} - 0}{SE_{\bar{d}}} \qquad (5.16) \\ \therefore\ t_{4948} &= 1.241 \end{aligned}$$

from which the p-value is determined to be $p = 0.215$. This p-value is large and therefore the null hypothesis cannot be rejected. So even though there is an observed difference between the results of the two models, it cannot be concluded that the difference is not simply due to random chance. Furthermore, the 95 % Confidence Interval (CI_{95}) can be calculated by

$$\begin{aligned} CI_{95} &= \bar{d} \pm (t^{*}_{DoF} \times SE_{\bar{d}}) \qquad (5.17) \\ &= 0.0016029 \pm 0.002\,532\,4\ \mathrm{mm}/4\,\mathrm{min} \end{aligned}$$

where t^{*}_{DoF} is the critical t-value corresponding to the 95 % confidence level. Stated otherwise, we can be 95 % confident that during DS1 the true mean difference (to 3 significant figures) between E_{GPSTIC} and E_{BREB} was somewhere in the interval

$$-0.000930 \leq \bar{d} \leq 0.00414 \quad [\mathrm{mm}/4\,\mathrm{min}]$$

$$\text{or, equivalently,} \quad -0.0139 \leq \bar{d} \leq 0.0620 \quad [\mathrm{mm\,h^{-1}}]$$

5.2.2 Discrepancy Analysis for DS2

Table 5.5 (p. 230) summarises the modelling results for DS2 wherein the total accumulated E_{BREB}, total accumulated E_{GPSTIC} (for various α_{PT}), and the final accumulated discrepancies are shown.

Table 5.5: Daily and total accumulated E_{BREB} and E_{GPSTIC} for the 311 hours of DS2 (22nd October to 4th November, 2019), with 95 % CI. The final column shows the final accumulated discrepancy D (where $D = E_{GPSTIC} - E_{BREB}$). The α_{PT} producing the smallest discrepancies are highlighted.

DS2 – All Data[a]

E_{BREB}		E_{GPSTIC}			D
Total (mm)	Mean Daily (mm/day)	α_{PT}	Total (mm)	Mean Daily (mm/day)	Total (mm)
50.6 ±38.1	3.9	1.00	48.5 ±18.4	3.7	−2.1 ±42.3
		1.05	51.2 ±19.4	3.9	0.6 ±42.8
		1.10	53.8 ±20.3	4.1	3.2 ±43.2
		1.15	56.3 ±21.3	4.3	5.7 ±43.6
		1.20	58.8 ±22.2	4.5	8.2 ±44.1
		1.26	61.7 ±23.4	4.7	11.1 ±44.7
		α_{*PT*}[b]	39.1 ±19.6	3.0	−11.5 ±42.8

DS2 – Selected Data[a]

E_{BREB} Total (mm)	E_{BREB} Mean Daily (mm/day)	α_{PT}	E_{GPSTIC} Total (mm)	E_{GPSTIC} Mean Daily (mm/day)	D Total (mm)
27.9 ±21.3	2.1	0.90	25.3 ± 9.5	1.9	−2.6 ±23.3
		0.95	28.0 ± 9.3	2.2	0.1 ±23.2
		1.00	30.1 ± 9.8	2.3	2.2 ±23.4
		1.10	33.3 ±10.9	2.6	5.4 ±23.9
		1.15	34.9 ±11.5	2.7	7.0 ±24.2
		1.26	38.2 ±12.6	2.9	10.3 ±24.7
		α_{*PT*}	23.8 ±10.7	1.8	−4.1 ±23.8

[a] All Data scenario excluded outliers (5.8 % excluded). Selected Data excluded $-1.25 < \beta < -0.75$ and $R^2 < 0.90$ for the Profile BREB LoBF (49.6 % excluded).

[b] Iterative process for optimisation of α_{PT} per Mallick et al. (2015a), denoted α_{*PT*}

5.2.2.1 4 min Discrepancy During DS2

Plots of the 4 min discrepancies between GPSTIC and Profile BREB are shown in Fig. 5.14 (p. 232) and Fig. 5.15 (p. 233). These plots are for the highlighted values of α_{PT} in Table 5.5 (p. 230).

The mean daily discrepancy can be calculated from the final column of Table 5.5 (which presents the accumulated discrepancies after 311 hours, or 12.95 days, of DS2). As with DS1, $\left|\overline{D}_{daily}\right| < 1\,\mathrm{mm\,day^{-1}}$ for all tabulated values of α_{PT} in both the All Data and Selected Data scenarios.

With reference to Fig. 5.16 (p. 234) the mean 4 min discrepancy $\overline{D}_{inst}$ between GPSTIC (with $\alpha_{PT} = 1.05$) and Profile BREB for the All Data scenario during DS2 was:

$$\overline{D}_{inst} = 0.000\,13\,{}^{\mathrm{mm}}/_{4\,\mathrm{min}} \quad (\sigma = 0.0051\,{}^{\mathrm{mm}}/_{4\,\mathrm{min}}) \tag{5.18}$$

$$\equiv 0.002\,\mathrm{mm\,h^{-1}} \quad \left(\sigma = 0.076\,\mathrm{mm\,h^{-1}}\right) \tag{5.19}$$

or in terms of energy fluxes:

$$\overline{D}_{inst} = 1.5\,\mathrm{Wm^{-2}} \quad \left(\sigma = 51.3\,\mathrm{Wm^{-2}}\right) \tag{5.20}$$

The equivalent mean daily discrepancy was:

$$\begin{aligned}\overline{D}_{daily} &\approx 0.048\,\mathrm{mm\,day^{-1}} \\ &< 1\,\mathrm{mm\,day^{-1}}\end{aligned} \tag{5.21}$$

Again, **the primary research question (Eqn. 5.3, p. 216) was answered in the affirmative following sustained, continuous measurement over 311 hours during DS2.**

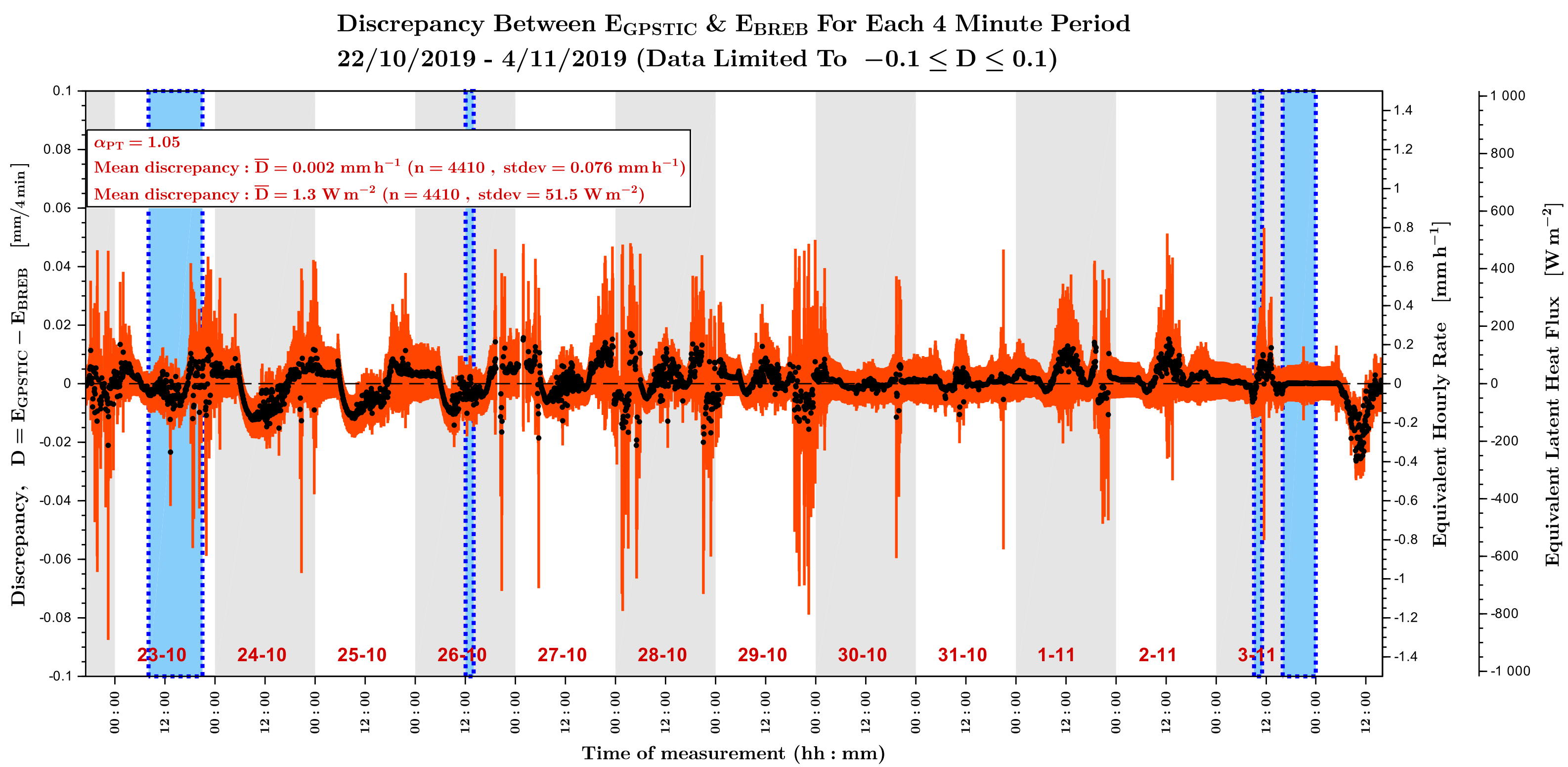

Figure 5.14: DS2: 4 min discrepancies between E_{GPSTIC} and E_{BREB} when $\alpha_{PT} = 1.05$. The 5.8 % of data not included lie outside the range $-0.53 < E_{BREB} < 1.5\,\mathrm{mm\,h^{-1}}$. The orange coloured bars indicate the 95 % CI. The shaded blue rectangles indicate when irrigation (23rd October) or rainfall occurred.

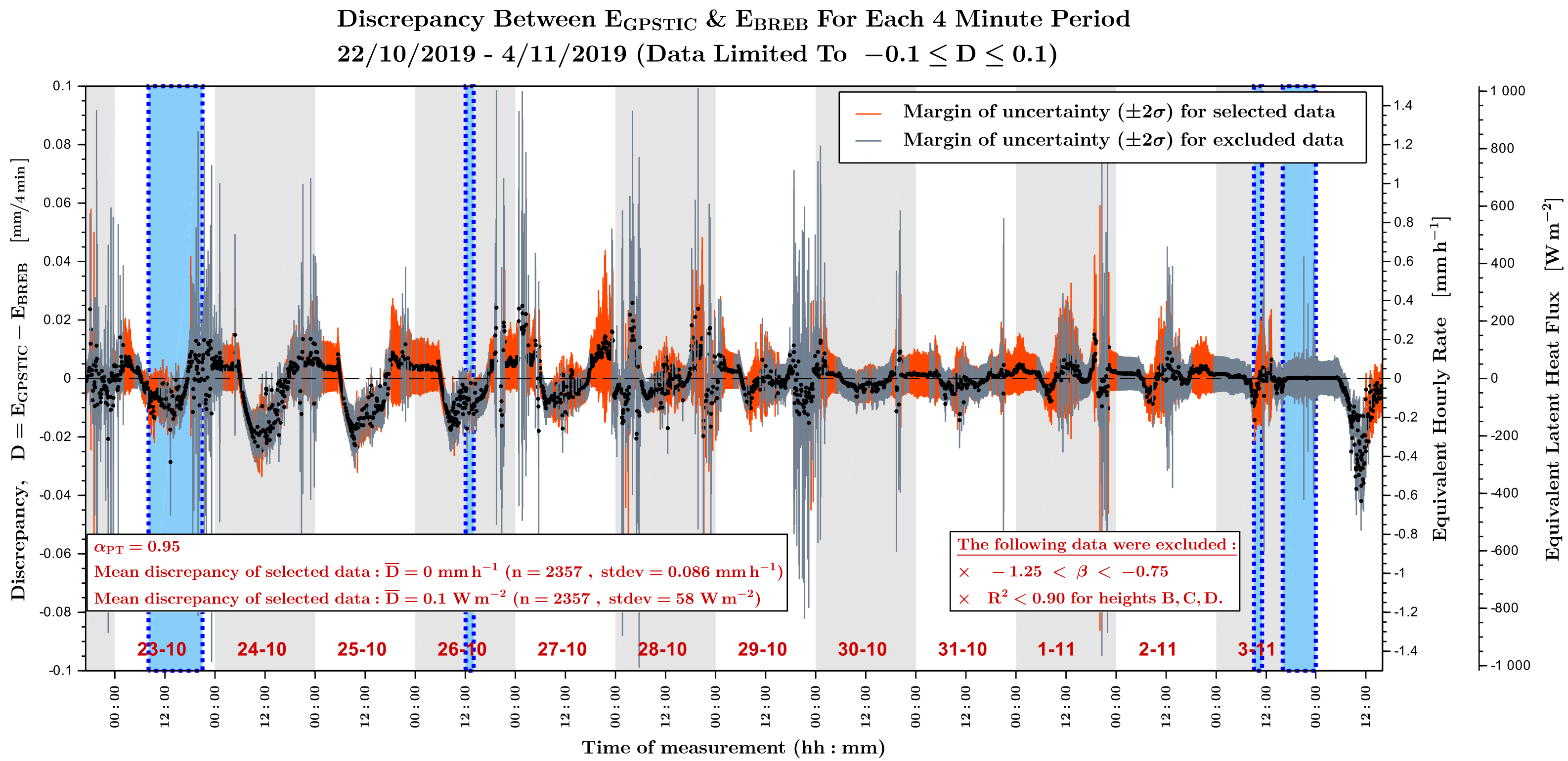

Figure 5.15: DS2: 4 min discrepancies between E_{GPSTIC} and E_{BREB} when $\alpha_{PT} = 0.95$. The 5.8 % of data not plotted lie outside the range $-0.53 < E_{BREB} < 1.5\,\mathrm{mm\,h^{-1}}$. The orange-coloured and grey-coloured bars indicate the 95 % CI for the data included and excluded in the Selected Data scenario respectively. The shaded blue rectangles indicate when irrigation (23$^{\mathrm{rd}}$ October) or rainfall occurred.

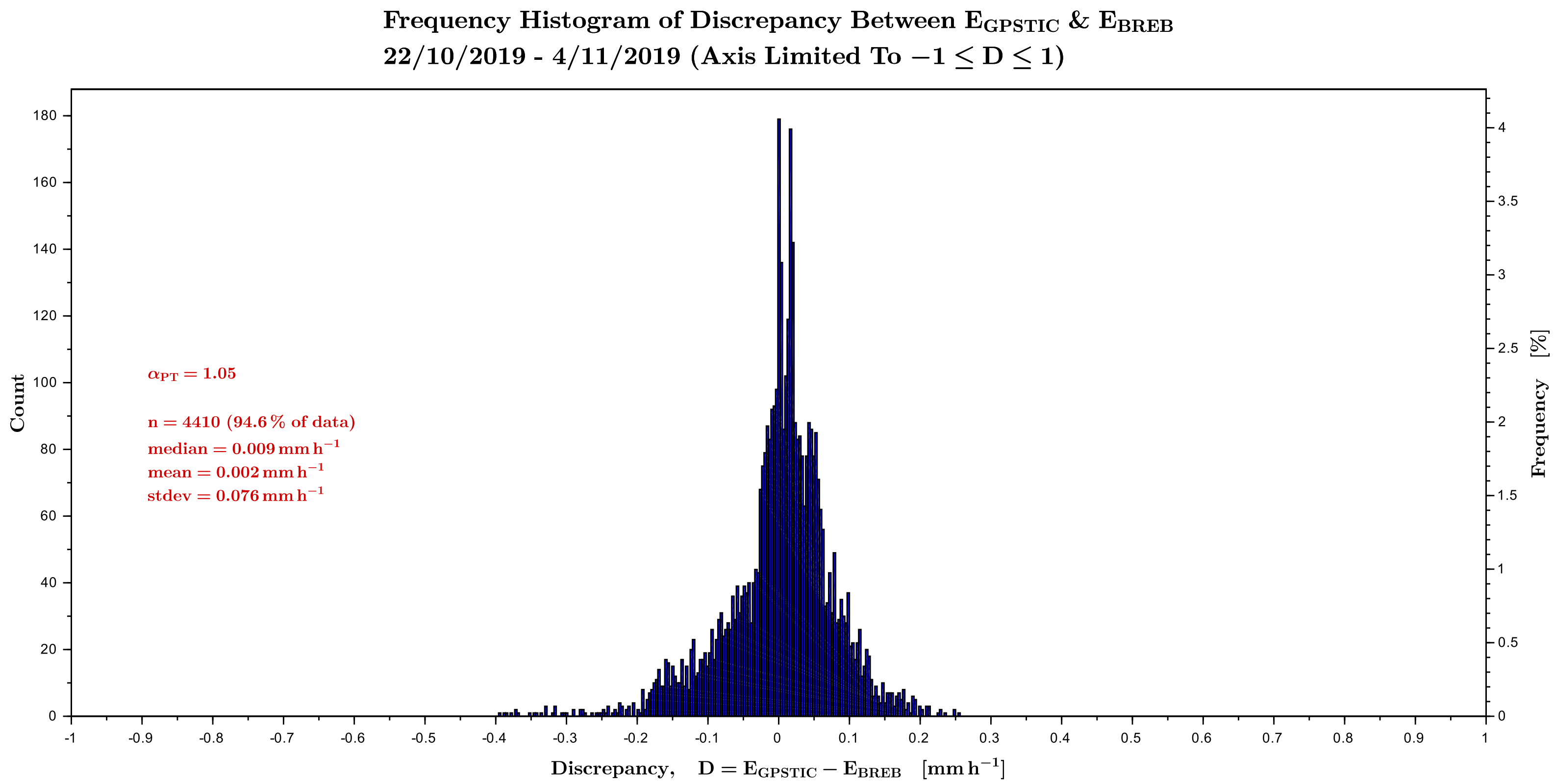

Figure 5.16: DS2: frequency histogram of the 4 min discrepancies between E_{GPSTIC} and E_{BREB} when $\alpha_{PT} = 1.05$. The 5.8 % of data not included in the histogram lie outside the range $-0.53 < E_{BREB} < 1.5\,\mathrm{mm\,h^{-1}}$.

5.2.2.2 Cumulative Discrepancy for DS2

Plots of the total accumulated E_{BREB} and E_{GPSTIC}, and the discrepancy between them, for the 311 hours of DS2 are shown in Fig. 5.17 (p. 236) and Fig. 5.18 (p. 237). These plots are based on the results in Table 5.5 (p. 230). The GPSTIC data corresponding to these same time periods were also rejected to allow a fair comparison of the models. The accumulated values of evapotranspiration in Fig. 5.18a (p. 237) and in Table 5.5 (p. 230) were small because so many data were rejected in the Selected Data scenario.

Several observations can be made from these plots (and Table 5.5, p. 230):

1. The requirement that $\left|\overline{D}_{daily}\right| < 1\,\text{mm day}^{-1}$ was met for all tabulated values of α_{PT} (calculated by Eqn. 5.2, p. 216), including α_{*PT*}.

2. For the All Data scenario the best outcome was achieved when $\alpha_{PT} = 1.05$ (as was the case with DS1). The total accumulated discrepancy over 311 hours was 0.6 mm, or $\overline{D}_{daily} = 0.048\,\text{mm day}^{-1}$. α_{*PT*} again produced relatively poor results for the All Data scenario but nonetheless still achieved $\left|\overline{D}_{daily}\right| = 0.9\,\text{mm day}^{-1}$ which was within requirements.

3. For the Selected Data scenario the best outcome was achieved when $\alpha_{PT} = 0.95$ (as for DS1) and, again, the size of the 95 % CI ranges were markedly reduced under this scenario. The total accumulated discrepancy over 311 hours was 0.1 mm, or $\overline{D}_{daily} = 0.008\,\text{mm day}^{-1}$. α_{*PT*} achieved $\left|\overline{D}_{daily}\right| = 0.3\,\text{mm day}^{-1}$ which was well within requirements.

4. In Fig. 5.17b (p. 236) and Fig. 5.18b (p. 237) the ‘zero line’ (i.e. $D = 0\,\text{mm}$) was comfortably well within the 95 % CI for all of the tabulated values of α_{PT}.

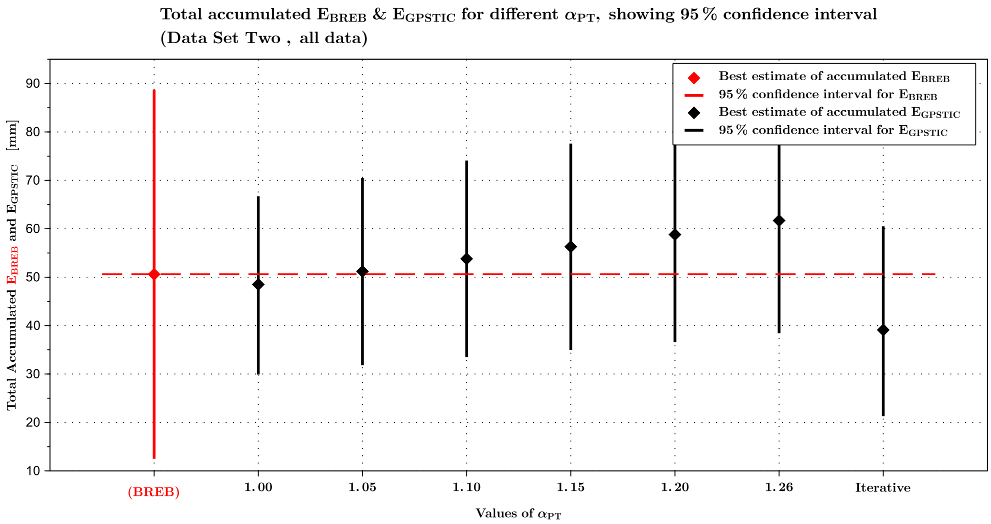

(a) Total accumulated E_{BREB} and E_{GPSTIC} after 311 hours during DS2.

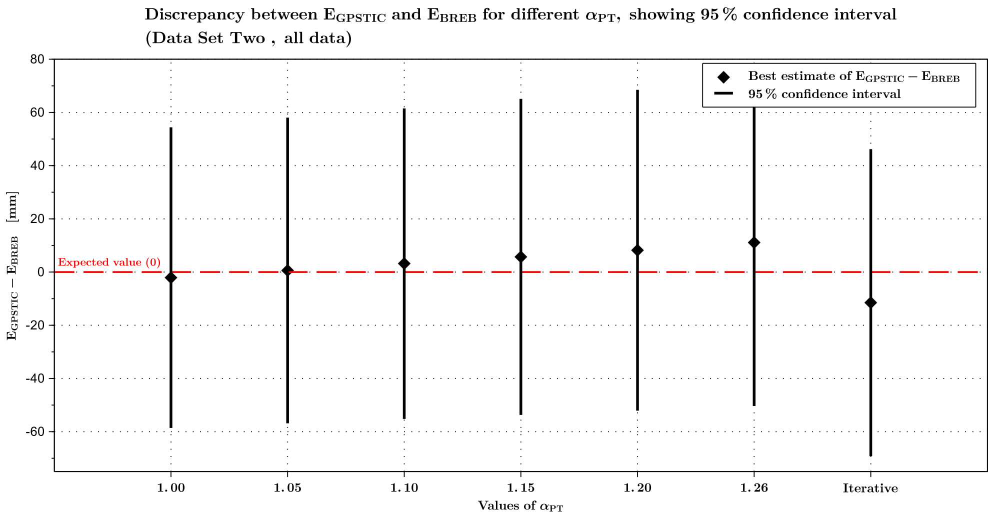

(b) Total accumulated discrepancy between E_{GPSTIC} and E_{BREB} after 311 hours during DS2.

Figure 5.17: Plotting the DS2 results from Table 5.5 (p. 230) for the All Data scenario. Plot (a) compares the total accumulated E_{GPSTIC} (for various values of α_{PT}) with the total accumulated E_{BREB}. Plot (b) compares the discrepancy between total accumulated E_{GPSTIC} (for various values of α_{PT}) and the total accumulated E_{BREB}. The 95 % CI were determined by the propagation of the sensors' measurement uncertainties through the modelling (see Appendix H, p. 379).

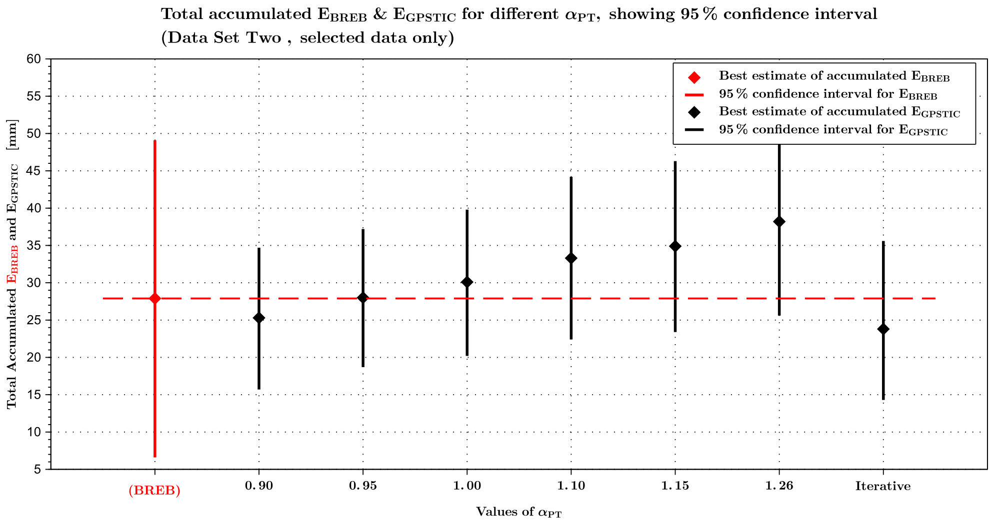

(a) Total accumulated E_{BREB} and E_{GPSTIC} after 311 hours during DS2.

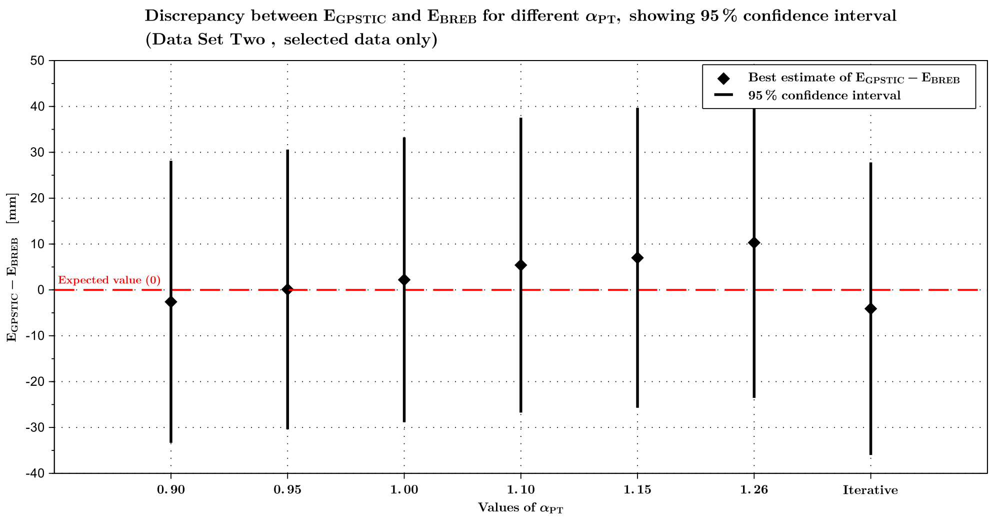

(b) Total accumulated discrepancy between E_{GPSTIC} and E_{BREB} after 311 hours during DS2.

Figure 5.18: Plotting the DS2 results from Table 5.5 (p. 230) for the Selected Data scenario, i.e. when the Profile BREB LoBF had an $R^2 > 0.90$ and when $\beta < -1.25$ or $\beta > -0.75$. The 95 % CI were determined by the propagation of the sensors' measurement uncertainties through the modelling (see Appendix H, p. 379).

5.2.2.3 Alignment of E_{GPSTIC} and E_{BREB} at $\alpha_{PT} = 1.05$

Attention is drawn to the DS2 results for the All Data scenario with $\alpha_{PT} = 1.05$ where $\overline{D}_{daily} = 0.048\,\text{mm}\,\text{day}^{-1}$. Fig. 5.19 (p. 239) shows a close alignment of GPSTIC and Profile BREB. The largest accumulated discrepancy between them was approx. 2 mm on the 3rd November. With the same reasons laid out for DS1 (§ 5.2.1.3, p. 226) it is argued that Profile BREB and GPSTIC were both operating appropriately and correctly over the 311 hours of DS2, i.e. with the caveat that such strong alignment between GPSTIC and Profile BREB was only seen when α_{PT} was selected to be in the range $1.00 < \alpha_{PT} < 1.10$.

The fields conditions during DS2 were markedly different to those encountered during DS1 and DS3. There was no transpiration and soil evaporation was the sole contributor to E. GPSTIC performed well under these conditions as shown by Fig. 5.19 (p. 239) which further strengthens the argument that GPSTIC is capable of equal performance to Profile BREB. Interestingly, even though field conditions during DS2 differed to those in DS1,[6] the best performance by GPSTIC (for the All Data scenario) was again when $\alpha_{PT} \approx 1.05$, as highlighted in Table 5.5 (p. 230), in contrast to DS3 where this was not the case.

[6]During DS1, approx. one third of the field was bare soil due to the single-skip planting configuration, e.g. Fig. 3.5a (p. 59) and Fig. 4.14 (p. 136). During DS2 100 % of the soil was directly insolated. During DS3 negligible soil was directly insolated because the canopy was fully-closed.

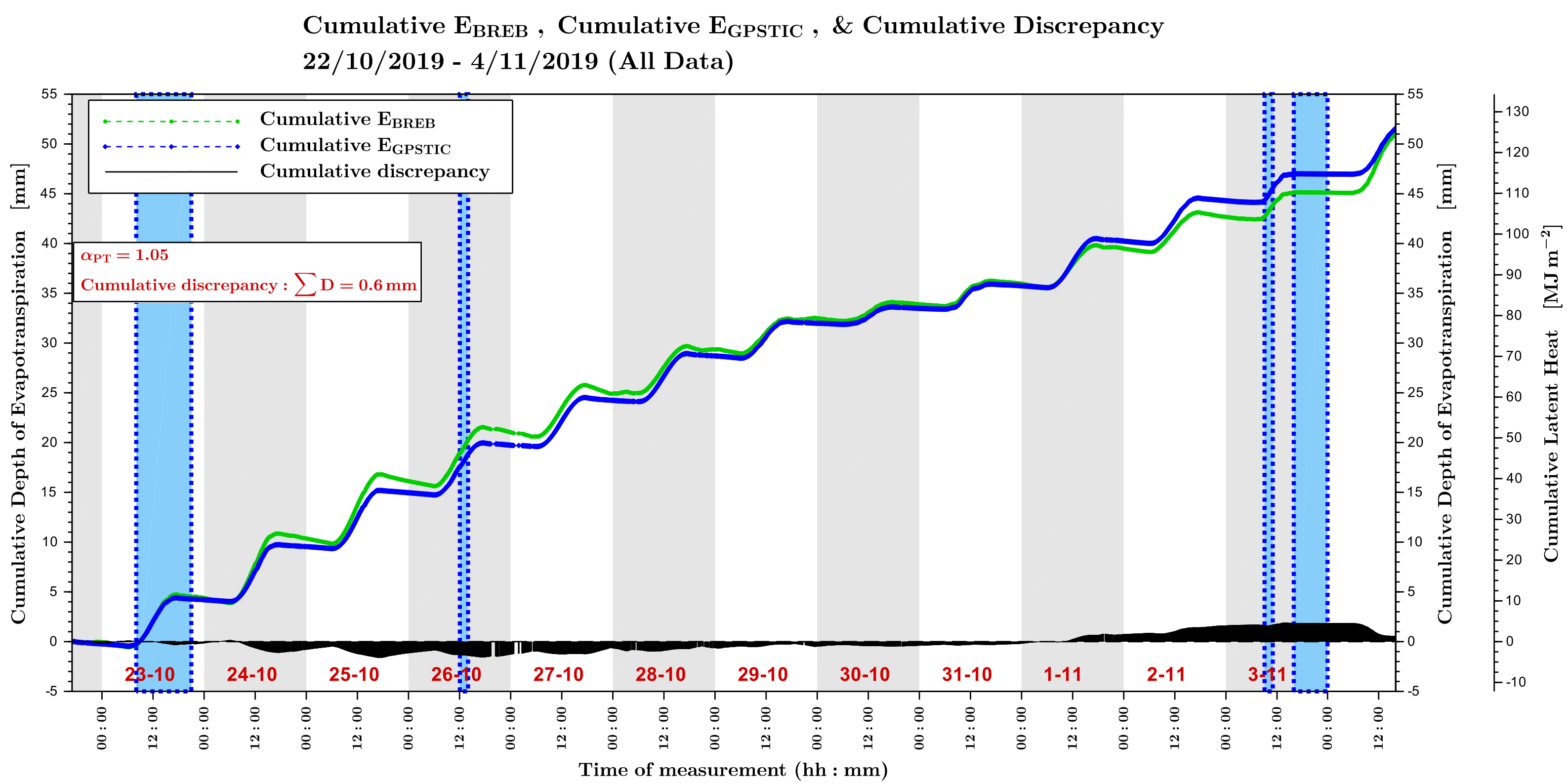

Figure 5.19: DS2: cumulative discrepancy between E_{GPSTIC} and E_{BREB} over time for the duration of DS2 when $\alpha_{PT} = 1.05$, all data plotted. Significantly, the plots aligned closely for the whole of DS2, at most having a 2 mm discrepancy between them (on the 3rd November). The shaded blue rectangles indicate when irrigation (23rd October) or rainfall occurred.

5.2.2.4 Paired t-Tests

Two-tailed t-tests were performed for the paired DS2 4 min values for E_{GPSTIC} and E_{BREB} following De Veaux et al. (2009). If n is the number of 4 min samples for each of E_{GPSTIC} and E_{BREB} during DS2 then

$$n = 4663 \tag{5.22}$$

The mean difference, $\bar{d}$, and standard deviation of the differences, σ_d, of the paired samples are (to 5 significant figures)

$$\begin{aligned} \bar{d} &= \frac{\sum_{i=1}^{n} \left[\left(E_{GPSTIC}\right)_i - \left(E_{BREB}\right)_i \right]}{n} \\ &= -0.000\,450\,40\ {}^{\mathrm{mm}}/_{4\,\mathrm{min}} \end{aligned} \tag{5.23}$$

$$\begin{aligned} \sigma_d &= \sqrt{\frac{\sum_{i=1}^{n} \left(d_i - \bar{d}\right)^2}{n-1}} \\ &= 0.078\,076\ {}^{\mathrm{mm}}/_{4\,\mathrm{min}} \end{aligned} \tag{5.24}$$

The standard error of the mean difference, $SE_{\bar{d}}$, is

$$\begin{aligned} SE_{\bar{d}} &= \frac{\sigma_d}{\sqrt{n}} \\ &= 0.001\,143\,4\ {}^{\mathrm{mm}}/_{4\,\mathrm{min}} \end{aligned} \tag{5.25}$$

Because the paired samples are independent of each other, the number of degrees of freedom, DoF, is given by

$$\begin{aligned} DoF &= (n_{\mathrm{GPSTIC}} - 1) + (n_{\mathrm{BREB}} - 1) \\ &= 9324 \end{aligned} \tag{5.26}$$

If the null hypothesis is that there is no difference between E_{GPSTIC} and E_{BREB}, the two-tailed t value is given by

$$\begin{aligned} t_{DoF} &= \frac{\bar{d} - 0}{SE_{\bar{d}}} \\ \therefore\ t_{9324} &= 0.394 \end{aligned} \tag{5.27}$$

from which the p-value is determined to be $p = 0.694$. This p-value is large and therefore the null hypothesis cannot be rejected. So even though there is an observed difference between the results of the two models, it cannot be concluded that the difference is not simply due to random chance. Furthermore, the 95 % Confidence Interval (CI_{95}) can be calculated by

$$\begin{aligned} CI_{95} &= \bar{d} \pm (t^*_{DoF} \times SE_{\bar{d}}) \\ &= -0.00045040 \pm 0.002\,242\,0\ \mathrm{mm}/4\,\mathrm{min} \end{aligned} \tag{5.28}$$

where t^*_{DoF} is the critical t-value corresponding to the 95 % confidence level. Stated otherwise, we can be 95 % confident that during DS2 the true mean difference (to 3 significant figures) between E_{GPSTIC} and E_{BREB} was somewhere in the interval

$$\begin{aligned} -0.00270 \leq \bar{d} \leq 0.00179 \quad [\mathrm{mm}/4\,\mathrm{min}] \\ \text{or, equivalently,} \quad -0.0405 \leq \bar{d} \leq 0.0269 \quad \left[\mathrm{mm\,h^{-1}}\right] \end{aligned}$$

5.2.3 Discrepancy Analysis for DS3

Table 5.6 (p. 242) summarises the modelling results for DS3 wherein the total accumulated E_{BREB}, total accumulated E_{GPSTIC} (for various α_{PT}), and the total accumulated discrepancies are shown.

Table 5.6: Daily and total accumulated E_{BREB} and E_{GPSTIC} for the 116 hours of DS3 (31st January to 5th February, 2020), with 95 % CI. The final column shows the final accumulated discrepancy D (where $D = E_{GPSTIC} - E_{BREB}$). The α_{PT} that produced the smallest discrepancies are highlighted.

DS3 – All Data[a]

E_{BREB} Total (mm)	E_{BREB} Mean Daily (mm/day)	E_{GPSTIC} α_{PT}	E_{GPSTIC} Total (mm)	E_{GPSTIC} Mean Daily (mm/day)	D Total (mm)
37.6 ±18.1	6.3	1.10	29.2 ± 7.4	4.9	−8.4 ±19.6
		1.26	33.5 ± 8.5	5.6	−4.1 ±20.0
		1.35	35.8 ± 9.1	6.0	−1.8 ±20.3
		1.40	37.1 ± 9.4	6.2	−0.5 ±20.4
		1.42	37.6 ± 9.5	6.3	0.0 ±20.4
		1.50	39.6 ±10.0	6.6	2.0 ±20.7
		α_{*PT*}[b]	24.8 ± 7.7	4.1	−12.8 ±19.7

DS3 – Selected Data[a]

E_{BREB} Total (mm)	E_{BREB} Mean Daily (mm/day)	E_{GPSTIC} α_{PT}	E_{GPSTIC} Total (mm)	E_{GPSTIC} Mean Daily (mm/day)	D Total (mm)
18.6 ±8.2	3.1	1.10	14.8 ± 4.3	2.5	−3.8 ± 9.3
		1.26	17.0 ± 5.0	2.8	−1.6 ± 9.6
		1.35	18.2 ±5.3	3.0	−0.4 ± 9.8
		1.40	18.8 ±5.5	3.1	0.2 ± 9.9
		1.42	19.1 ±5.5	3.2	0.5 ± 9.9
		1.50	20.1 ±5.8	3.4	1.5 ±10.0
		α_{*PT*}	12.6 ±4.5	2.1	−6.0 ± 9.4

[a] All Data scenario excluded outliers (10.0 % of data excluded). Selected Data scenario excluded $-1.25 < \beta < -0.75$ and $R^2 < 0.90$ in Profile BREB LoBF (47.8 % excluded).

[b] Iterative process for optimisation of α_{PT} per Mallick et al. (2015a), denoted α_{*PT*}

Table 5.6 shows that the best performance of GPSTIC occurred at higher values of $\alpha_{PT} \approx 1.40$ compared to DS1 and DS2 where $\alpha_{PT} \approx 1.05$. This is consistent with the observation that there was a persistent daytime temperature inversion ($^{dT}/_{dz} > 0$) and $\beta < 0$, both of which reflected the more significant influence of advected sensible heat during DS3 (§ 5.3.2, p. 258).

5.2.3.1 4 min Discrepancy During DS3

Plots of the 4 min discrepancies between GPSTIC and Profile BREB are shown in Fig. 5.20 (p. 244) and Fig. 5.21 (p. 245). These plots are for the highlighted values of α_{PT} in Table 5.6 (p. 242).

The mean daily discrepancy can be calculated from the final column of Table 5.6 (which presents the accumulated discrepancies after 116 hours, or 4.8 days, of DS3). Unlike DS1 and DS2, not all tabulated values of $\left|\overline{D}_{daily}\right|$ were less than $1\,\mathrm{mm\,day^{-1}}$. In the All Data scenario the GPSTIC model showed too much discrepancy with Profile BREB when $\alpha_{PT} = 1.10$ and when α_{*PT*} was used. However, in the Selected Data scenario, there was closer alignment between GPSTIC and Profile BREB across all α_{PT} except when α_{*PT*} was used (where $\overline{D}_{daily} = 1.2\,\mathrm{mm\,day^{-1}}$).

With reference to Fig. 5.22 (p. 246) the mean 4 min discrepancy between GPSTIC (with $\alpha_{PT} = 1.42$) and Profile BREB for the All Data scenario during DS3 was:

$$\overline{D}_{inst} = 0.0\,^{\mathrm{mm}}/_{4\,\mathrm{min}} \quad (\sigma = 0.0051\,^{\mathrm{mm}}/_{4\,\mathrm{min}}) \tag{5.29}$$

$$\equiv 0.0\,\mathrm{mm\,h^{-1}} \quad \left(\sigma = 0.077\,\mathrm{mm\,h^{-1}}\right) \tag{5.30}$$

or in terms of energy fluxes:

$$\overline{D}_{inst} = 0.0\,\mathrm{Wm^{-2}} \quad \left(\sigma = 52.4\,\mathrm{Wm^{-2}}\right) \tag{5.31}$$

The equivalent mean daily discrepancy was:

$$\overline{D}_{daily} \approx 0.005\,\mathrm{mm\,day^{-1}} \tag{5.32}$$

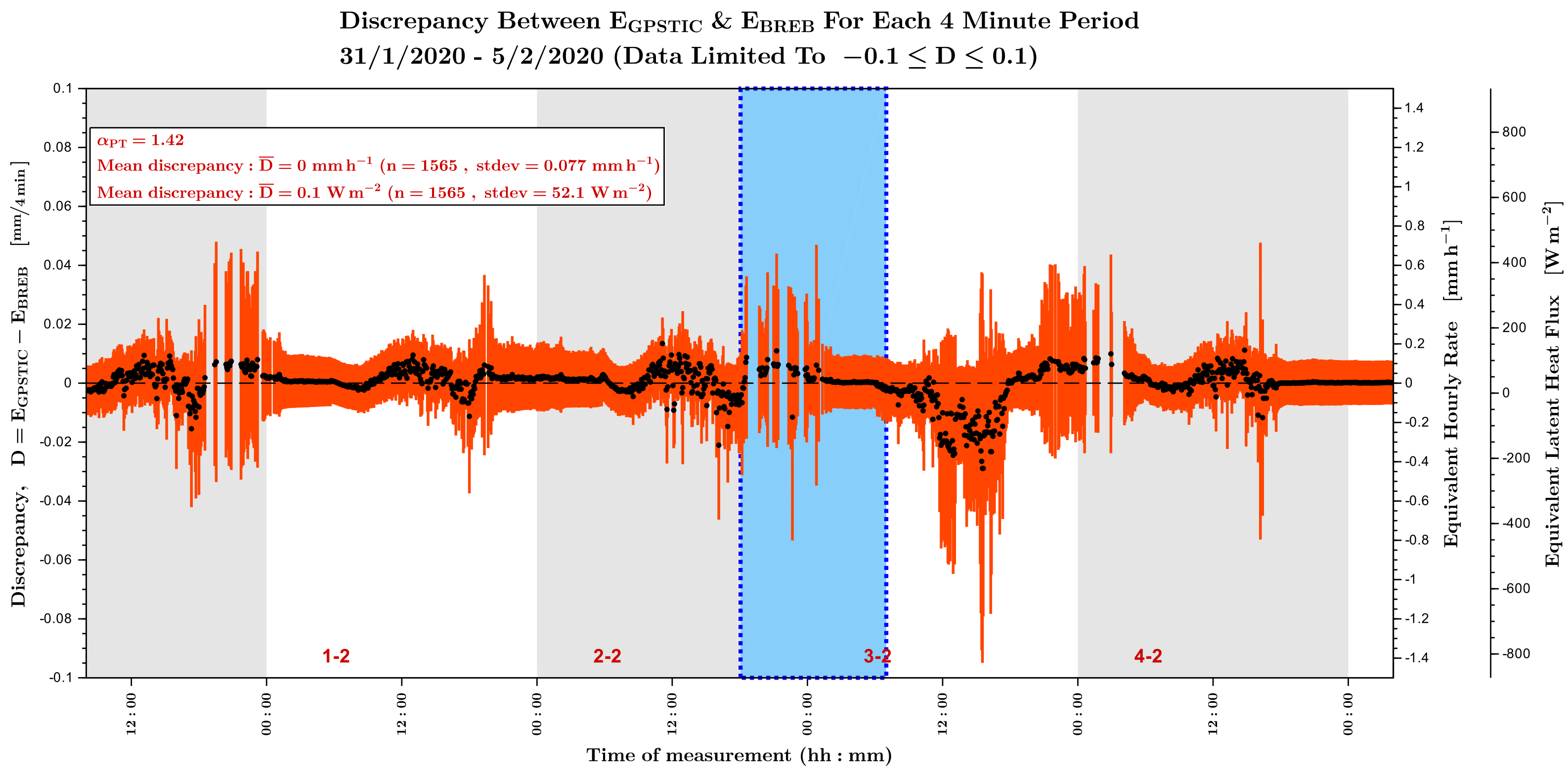

Figure 5.20: DS3: 4 min discrepancies between E_{GPSTIC} and E_{BREB} when $\alpha_{PT} = 1.42$. The 10.0 % of data not plotted lie outside the range $-0.53 < E_{BREB} < 1.5\,\mathrm{mm\,h^{-1}}$. The orange coloured bars indicate the 95 % CI. The shaded blue rectangle indicates when the irrigation on the 2nd February occurred.

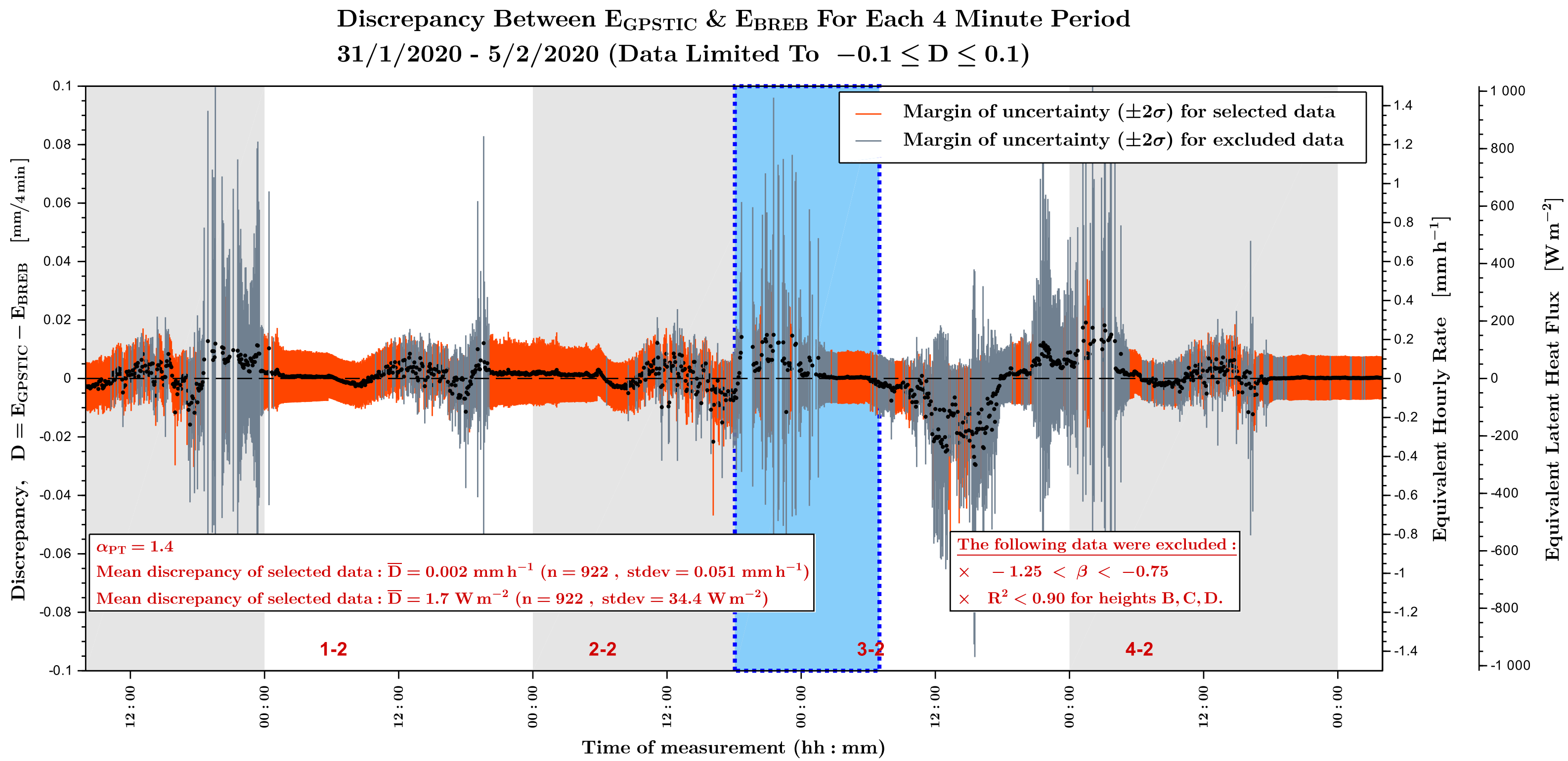

Figure 5.21: DS3: 4 min discrepancies between E_{GPSTIC} and E_{BREB} when $\alpha_{PT} = 1.40$. The 10.0 % of data not plotted lie outside the range $-0.53 < E_{BREB} < 1.5\,\mathrm{mm\,h^{-1}}$. The orange-coloured and grey-coloured bars indicate the 95 % CI for the data included and excluded in the Selected Data scenario respectively. The shaded blue rectangle indicates when the irrigation on the 2nd February occurred.

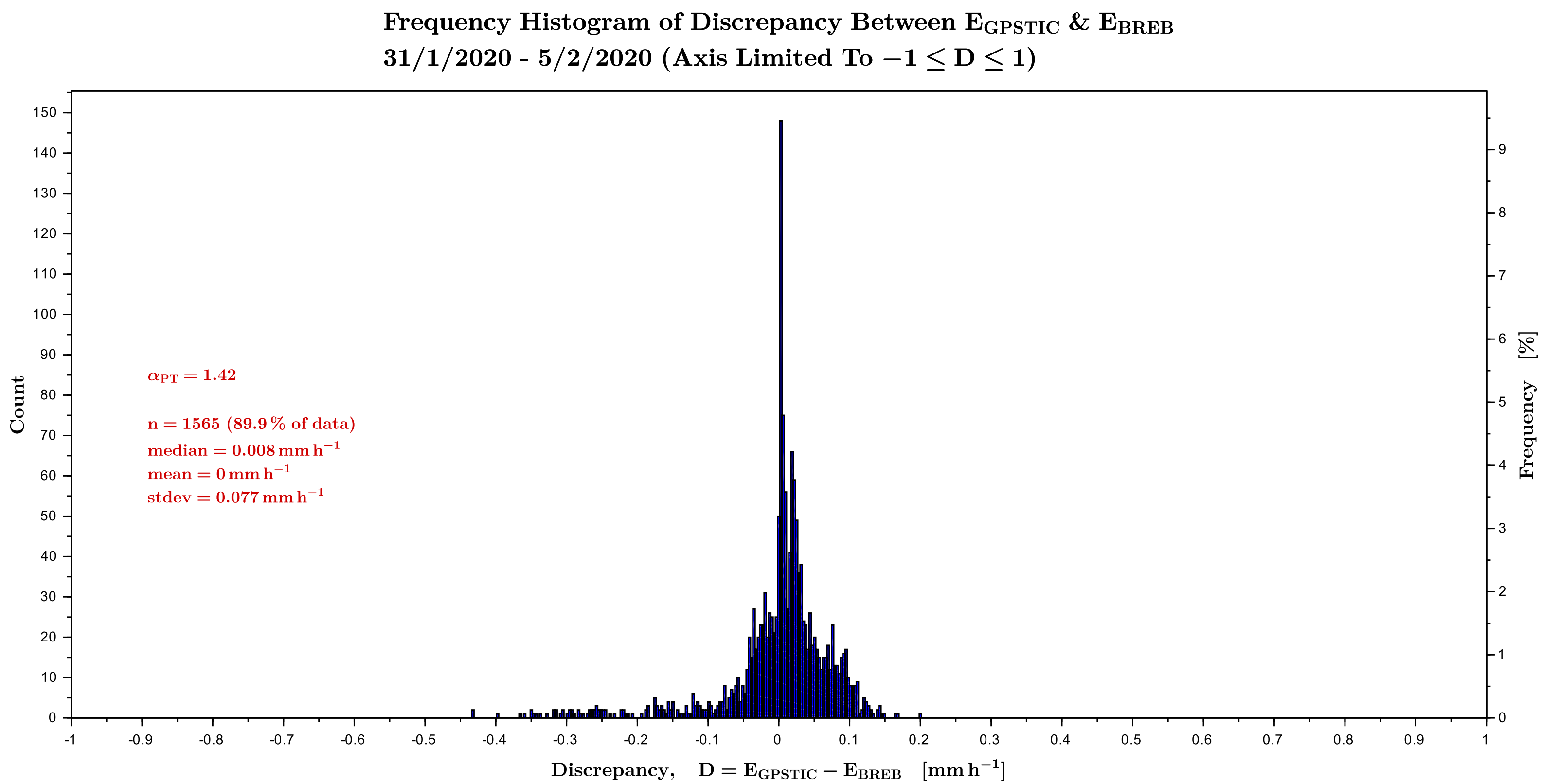

Figure 5.22: DS3: frequency histogram of the 4 min discrepancies between E_{GPSTIC} and E_{BREB} when $\alpha_{PT} = 1.42$. The 10.0 % of data not plotted lie outside the range $-0.53 < E_{BREB} < 1.5\,\mathrm{mm\,h^{-1}}$.

Again, as with DS1 and DS2 but this time over a fully-closed cotton canopy, **the primary research question (Eqn. 5.3, p. 216) was answered in the affirmative following sustained, continuous measurement over 116 hours during DS3.**

5.2.3.2 Cumulative Discrepancy for DS3

Plots of the total accumulated E_{BREB} and E_{GPSTIC}, and the discrepancy between them, for the 116 hours of DS3 are shown in Fig. 5.23 (p. 248) and Fig. 5.24 (p. 249). These plots are based on the results in Table 5.6 (p. 242). The GPSTIC data corresponding to these same time periods were also rejected to allow a fair comparison of the models. The accumulated values of evapotranspiration in Fig. 5.24a (p. 249) and in Table 5.6 (p. 242) were small because so many data were rejected in the Selected Data scenario.

Several observations can be made from these plots (and Table 5.6):

1. In the All Data scenario the requirement that $\left|\overline{D}_{daily}\right| < 1\,\text{mm}\,\text{day}^{-1}$ (calculated by Eqn. 5.2, p. 216) was met when $\alpha_{PT} \geq 1.26$. The best outcome was achieved when $\alpha_{PT} = 1.42$ where the total accumulated discrepancy over 116 hours was approx. 0.0 mm, or $\overline{D}_{daily} = 0.005\,\text{mm}\,\text{day}^{-1}$.

2. In the Selected Data scenario the requirement that $\left|\overline{D}_{daily}\right| < 1\,\text{mm}\,\text{day}^{-1}$ was met for all fixed values of α_{PT}. The best outcome was achieved when $\alpha_{PT} = 1.40$ where the total accumulated discrepancy over 116 hours was 0.2 mm, or $\overline{D}_{daily} = 0.04\,\text{mm}\,\text{day}^{-1}$.

3. Modelling GPSTIC with α_{*PT*} did not meet requirements in either of the All Data or Selected Data scenarios.

4. The discrepancy results of the Selected Data scenario had 95 % CI ranges that were about half of those of the All Data scenario, i.e. there was less uncertainty in the Selected Data results.

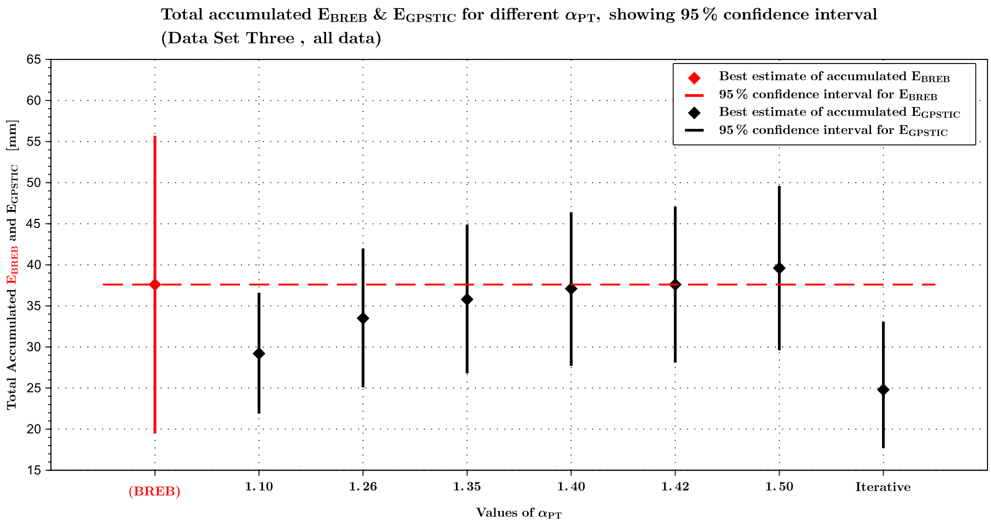

(a) Total accumulated E_{BREB} and E_{GPSTIC} after 116 hours during DS3.

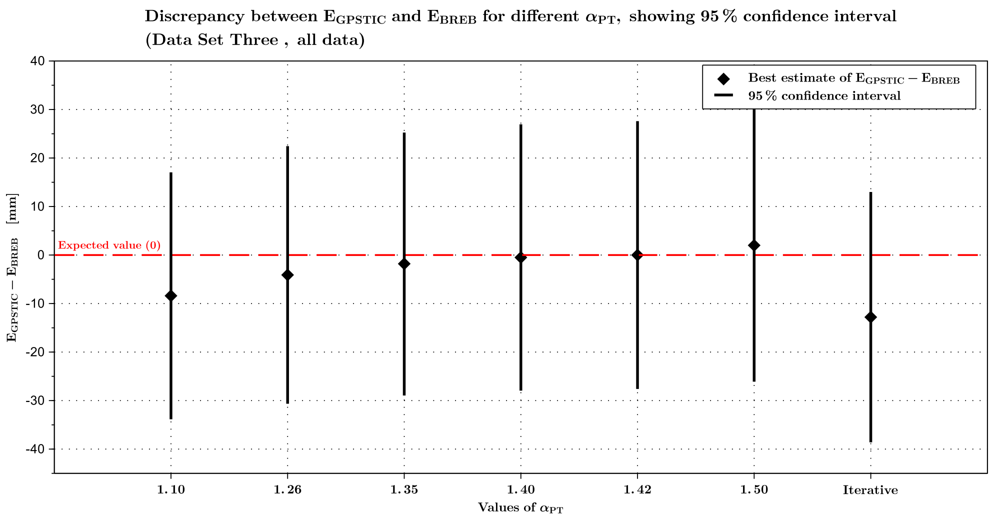

(b) Total accumulated discrepancy between E_{GPSTIC} and E_{BREB} after 116 hours during DS3.

Figure 5.23: Plotting the DS3 results from Table 5.6 (p. 242) for the All Data scenario. Plot (a) compares the total accumulated E_{GPSTIC} (for various values of α_{PT}) with the total accumulated E_{BREB}. Plot (b) compares the discrepancy between the total accumulated E_{GPSTIC} (for various values of α_{PT}) and the total accumulated E_{BREB}. The 95 % CI were determined by the propagation of the sensors' measurement uncertainties through the modelling (see Appendix H, p. 379).

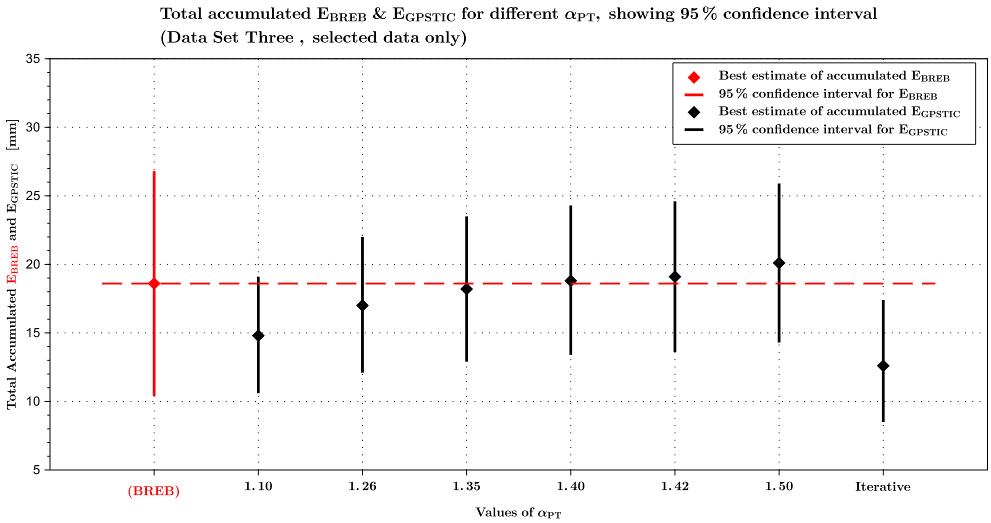

(a) Total accumulated E_{BREB} and E_{GPSTIC} after 116 hours during DS3.

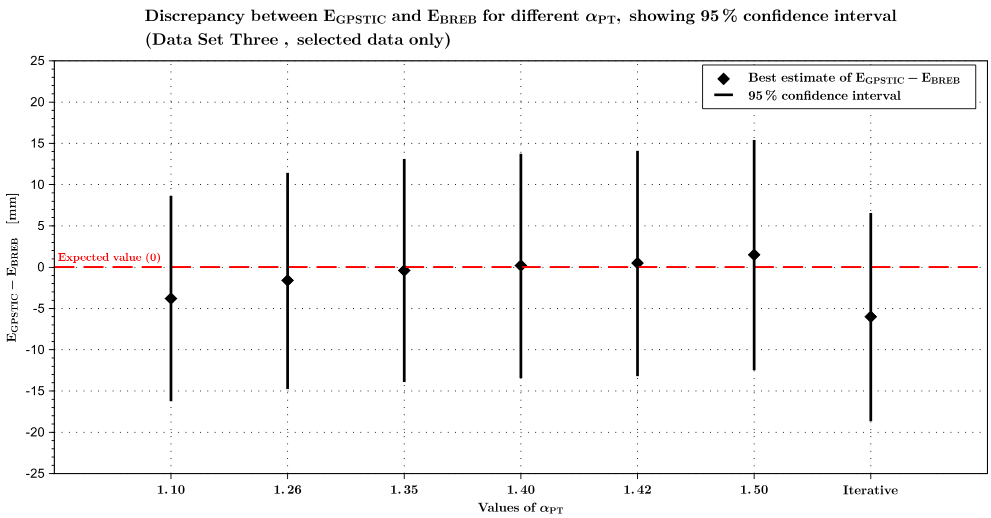

(b) Total accumulated discrepancy between E_{GPSTIC} and E_{BREB} after 116 hours during DS3.

Figure 5.24: Plotting the DS3 results from Table 5.6 (p. 242) for the Selected Data scenario, i.e. when the Profile BREB LoBF had an $R^2 > 0.90$ and when $\beta < -1.25$ or $\beta > -0.75$. The 95 % CI were determined by the propagation of the sensors' measurement uncertainties through the modelling (see Appendix H, p. 379).

5. In Fig. 248 (p. 248) and Fig. 249 (p. 249) the 'zero line' (i.e. $D = 0$ mm) was comfortably within the 95 % CI for all tabulated α_{PT}.

5.2.3.3 Alignment of E_{GPSTIC} and E_{BREB} at $\alpha_{PT} = 1.42$

Attention is drawn to the DS3 results for the All Data scenario with $\alpha_{PT} = 1.42$ where $\overline{D}_{daily} = 0.005\,\mathrm{mm\,day^{-1}}$. Fig. 5.25 (p. 251) shows a close alignment of GPSTIC and Profile BREB. For the reasons laid out in § 5.2.1.3 (p. 226) it is argued that Profile BREB and GPSTIC were both operating reliably and correctly over the 116 hours of DS3, i.e. with the caveat that such close alignment between GPSTIC and Profile BREB was only seen when α_{PT} was selected to be in the range $1.35 < \alpha_{PT} < 1.50$.

During DS3 the best performing values of α_{PT} were much larger than for DS1 and DS2 ($\alpha_{PT} \approx 1.40$ vs. $\alpha_{PT} \approx 1.05$). This is covered further in § 5.3.2 (p. 258).

Fig. 5.25 (p. 251) makes a compelling case that GPSTIC was capable of equal performance to Profile BREB over a fully closed canopy with no visible soil.

Fig. 5.26 (p. 252) is also included to show that excluding nighttime data from the modelling (Appendix K, p. 405) had little effect on the closeness of the alignment between GPSTIC and Profile BREB.

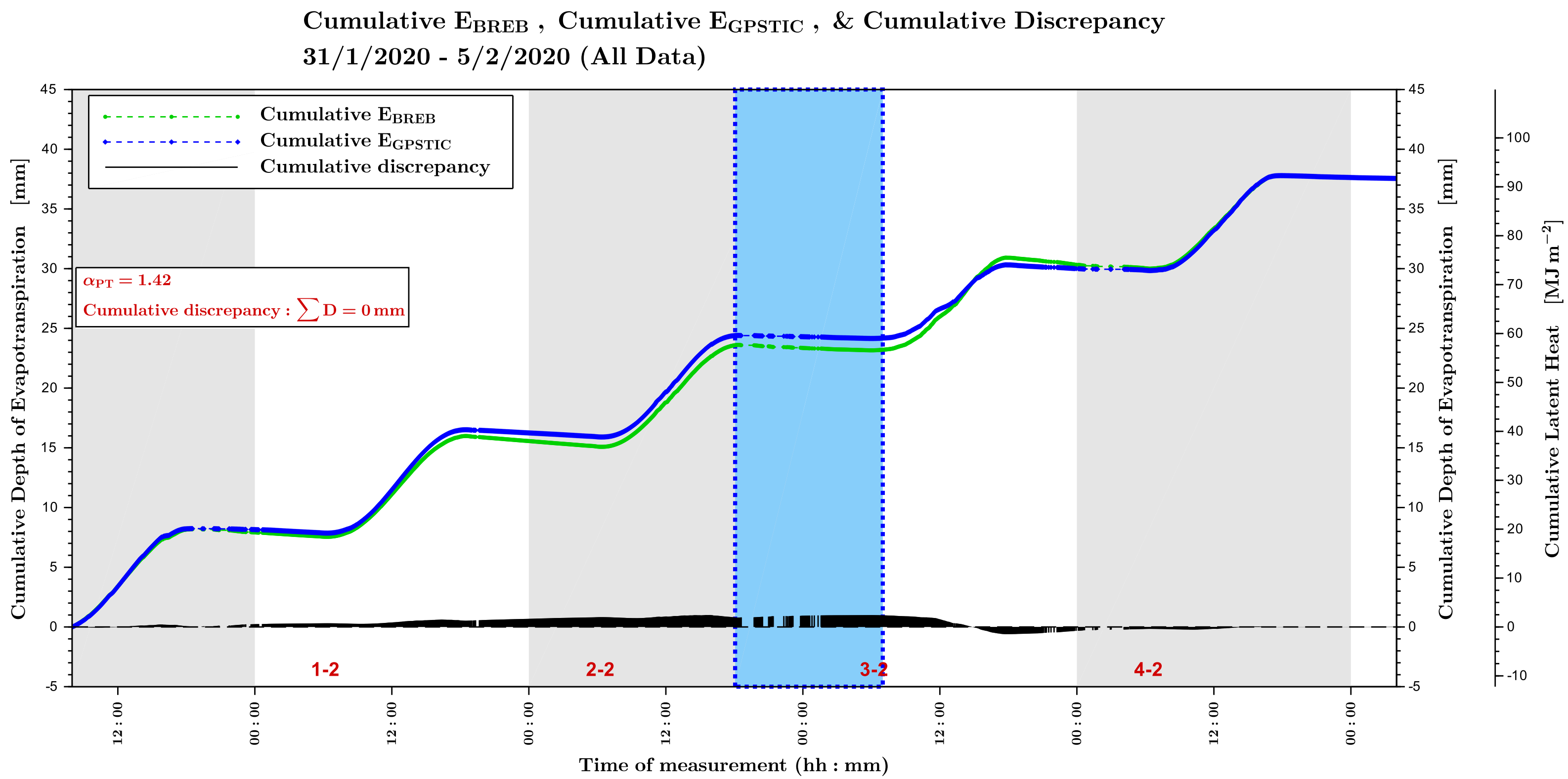

Figure 5.25: DS3: Cumulative E_{GPSTIC} and E_{BREB} vs. time and the cumulative discrepancy between them when $\alpha_{PT} = 1.42$, all data plotted. Significantly, the plots aligned closely for the whole of DS3, not just the final values. The shaded blue rectangle indicates when the irrigation on the 2nd February occurred.

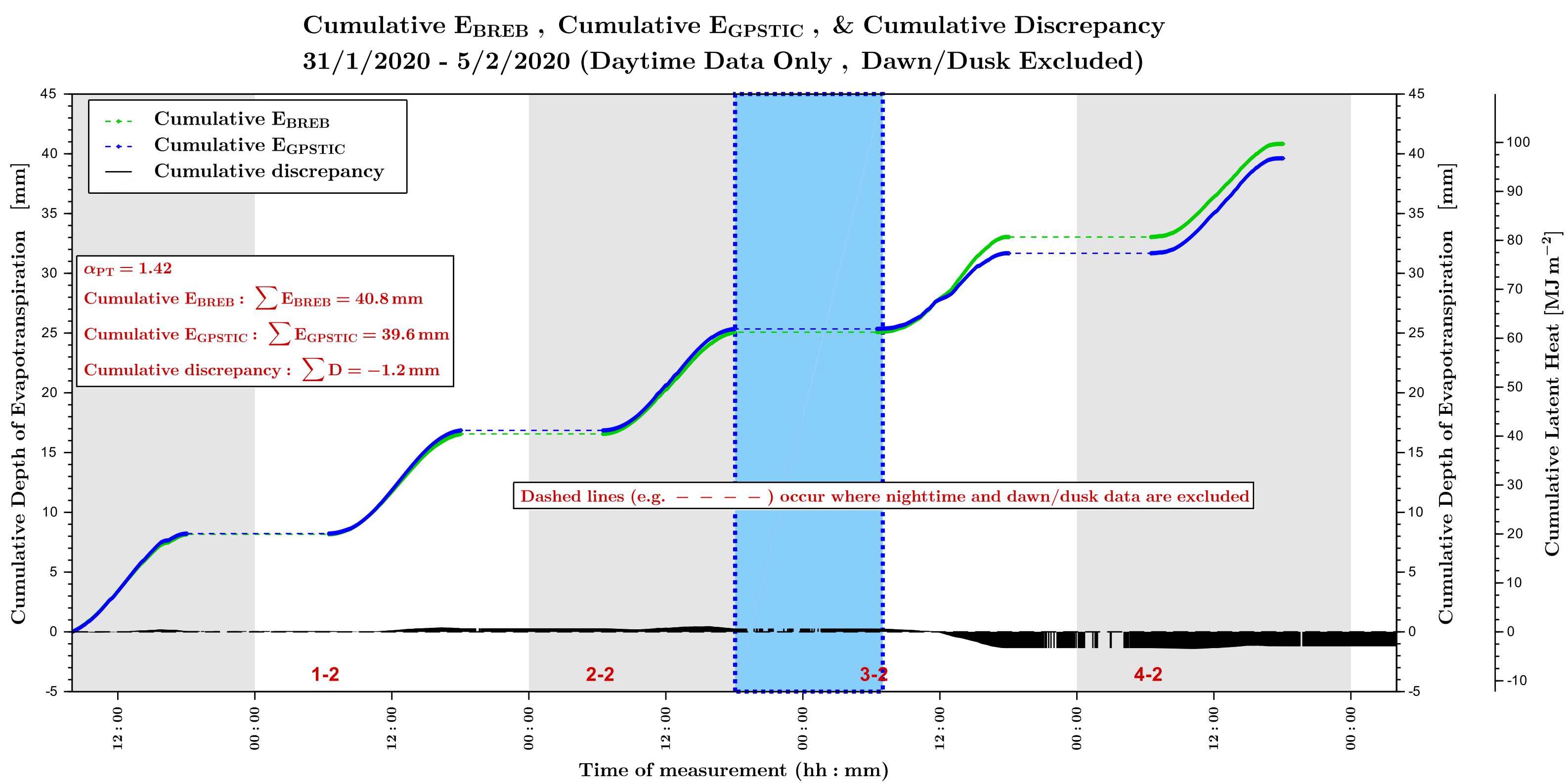

Figure 5.26: DS3: Cumulative E_{GPSTIC} and E_{BREB} vs. time and the cumulative discrepancy between them when $\alpha_{PT} = 1.42$, daytime data only. The shaded blue rectangle indicates when the irrigation on the 2nd February occurred.

5.2.3.4 Paired t-Tests

Two-tailed t-tests were performed for the paired DS3 4 min values for E_{GPSTIC} and E_{BREB} following De Veaux et al. (2009). If n is the number of 4 min samples for each of E_{GPSTIC} and E_{BREB} during DS2 then

$$n = 1740 \tag{5.33}$$

The mean difference, $\bar{d}$, and standard deviation of the differences, σ_d, of the paired samples are (to 5 significant figures)

$$\begin{aligned} \bar{d} &= \frac{\sum_{i=1}^{n} \left[(E_{GPSTIC})_i - (E_{BREB})_i \right]}{n} \\ &= 0.000\,297\,00\ {}^{\text{mm}}/_{4\,\text{min}} \end{aligned} \tag{5.34}$$

$$\begin{aligned} \sigma_d &= \sqrt{\frac{\sum_{i=1}^{n} \left(d_i - \bar{d}\right)^2}{n-1}} \\ &= 0.071\,932\ {}^{\text{mm}}/_{4\,\text{min}} \end{aligned} \tag{5.35}$$

The standard error of the mean difference, $SE_{\bar{d}}$, is

$$\begin{aligned} SE_{\bar{d}} &= \frac{\sigma_d}{\sqrt{n}} \\ &= 0.001\,724\,4\ {}^{\text{mm}}/_{4\,\text{min}} \end{aligned} \tag{5.36}$$

Because the paired samples are independent of each other, the number of degrees of freedom, DoF, is given by

$$\begin{aligned} DoF &= (n_{\text{GPSTIC}} - 1) + (n_{\text{BREB}} - 1) \\ &= 3478 \end{aligned} \tag{5.37}$$

If the null hypothesis is that there is no difference between E_{GPSTIC} and E_{BREB}, the two-tailed t value is given by

$$\begin{aligned} t_{DoF} &= \frac{\bar{d} - 0}{SE_{\bar{d}}} \qquad (5.38) \\ \therefore\ t_{3478} &= 0.172 \end{aligned}$$

from which the p-value is determined to be $p = 0.863$. This p-value is large and therefore the null hypothesis cannot be rejected. So even though there is an observed difference between the results of the two models, it cannot be concluded that the difference is not simply due to random chance. Furthermore, the 95 % Confidence Interval (CI_{95}) can be calculated by

$$\begin{aligned} CI_{95} &= \bar{d} \pm (t^{*}_{DoF} \times SE_{\bar{d}}) \qquad (5.39) \\ &= 0.00029700 \pm 0.003\,382\,0\ ^{\mathrm{mm}}/_{4\,\mathrm{min}} \end{aligned}$$

where t^{*}_{DoF} is the critical t-value corresponding to the 95 % confidence level. Stated otherwise, we can be 95 % confident that during DS3 the true mean difference (to 3 significant figures) between E_{GPSTIC} and E_{BREB} was somewhere in the interval

$$-0.00309 \leq \bar{d} \leq 0.00368 \quad \left[^{\mathrm{mm}}/_{4\,\mathrm{min}}\right]$$

$$\text{or, equivalently,} \quad -0.0464 \leq \bar{d} \leq 0.0552 \quad \left[\mathrm{mm\,h^{-1}}\right]$$

5.3 Comparison of the Data Sets

Table 5.7 (p. 256) and Table 5.8 (p. 257) provide a brief summary and comparison of the field conditions and modelling results across DS1, DS2 and DS3.

5.3.1 Differences in the Crop

The most significant difference between the three data sets was the status of the crop.

During DS1 the crop had a partially-closed canopy (due to the 'single-skip' planting configuration) and the plants were shorter and thinner than those in DS3. Thus T_S was a composite measurement of soil and canopy temperature and E comprised both soil evaporation and canopy transpiration.

During DS2 the cotton seed had just been planted and the seedlings were only a few centimetres tall by the end of DS2. The field essentially comprised bare, cultivated soil and so T_S was just a measure of soil's surface temperature. During DS2 the transpiration component of E was negligible.

During DS3 the crop had a lush, well-watered and fully-closed canopy that was approx. 20 % taller than the crop in DS1. No soil was visible from above and T_S was essentially a measure of canopy temperature. The shaded, humid environment near the soil surface (beneath the canopy) meant that the soil surface remained damp for much longer than DS1 and DS2. Thus during DS3 E was dominated by canopy transpiration.

Thus whilst all of the current research was conducted within the context of a broadacre, furrow-irrigated cotton crop, GPSTIC was still able to be evaluated under a variety of crop conditions.

Table 5.7: Comparison of field conditions for DS1, DS2 and DS3.

	DS1	DS2	DS3
Field status	125 days old cotton crop. 1.0 m tall, partial canopy (every 3rd planting row was bare). Furrow-irrigated to FC six days prior to DS1.	Cotton seed planted one day prior to DS2. Bare cultivated soil, formed into furrows. Irrigated to FC during DS2.	102 days old cotton crop, 1.0 - 1.2 m tall. Every row planted, fully closed canopy. Furrow-irrigated to FC during DS3.
Environmental conditions	Ongoing drought, no rainfall. Mostly clear sky. High solar radiation. RH = 20 - 80 % T = 15 - 38 °C T_D = 1 - 25 °C	Severe drought. Preceding winter very warm & dry. Broken cloud at times with high solar radiation. Increasing RH & 15 mm rain late in DS2. RH = 10 - 98 % T = 10 - 34 °C T_D = −5 - 15 °C	Severe drought but cooler & more humid than preceding weeks. Increasing broken cloud but still seeing high solar radiation. RH = 30 - 80 % T = 14 - 38 °C T_D = 5 - 33 °C

FC = Field Capacity. The heavy clay in Fields 14 and 16 had a FC of approx. 48 - 50 % VWC [$m^3\,m^{-3}$].

Table 5.8: Comparison of modelling results for DS1, DS2 and DS3. The stated uncertainties are 95 % (2σ) CI.

		DS1	DS2	DS3
Number of modelled values of E (including outliers)[a]		2475 values of E over 165 hours	4665 values of E over 311 hours	1740 values of E over 116 hours
Outliers rejected[b]		1.9 %	5.8 %	10.0 %
Daytime with $E < 0$[c]		14.1 %	16.2 %	14.0 %
Regression – typical R^2	All Data	0.96	0.92	0.94
	Select Data	0.96	0.92	0.97
Regression – best α_{PT}	All Data	1.10	1.15	1.35
	Select Data	1.05	1.10	1.35
E_{GPSTIC} with $\alpha_{PT} = 1.26$	Total	37.6 ± 10.0 mm	61.7 ± 23.4 mm	33.5 ± 8.5 mm
	Mean Daily	5.4 ± 1.5 mm day^{-1}	4.7 ± 1.8 mm day^{-1}	5.6 ± 1.8 mm day^{-1}
E_{GPSTIC} with best α_{PT}	Total	31.2 ± 8.2 mm	51.2 ± 19.4 mm	37.6 ± 9.5 mm
	Mean Daily	4.5 ± 1.2 mm day^{-1} ($\alpha_{PT} = 1.05$)	3.9 ± 1.5 mm day^{-1} ($\alpha_{PT} = 1.05$)	6.3 ± 2.0 mm day^{-1} ($\alpha_{PT} = 1.42$)
E_{BREB}	Total	31.1 ± 15.9 mm	50.6 ± 38.1 mm	37.6 ± 18.1 mm
	Mean Daily	4.4 ± 2.3 mm day^{-1}	3.9 ± 2.9 mm day^{-1}	6.3 ± 3.7 mm day^{-1}
Range of β		$-1.3 < \beta < 0.5$	$-1.4 < \beta < 0.7$	$-1.0 < \beta < 0$

[a] Data were measured every 60 s and averaged into 4 min blocks for use in the models. The numbers in this row are the number of 4 min blocks.

[b] Rejected when $E_{BREB} < -0.53$ mm h^{-1} or $E_{BREB} > 1.5$ mm h^{-1} (which occurred when $\beta \approx -1$).

[c] Proportion of all daytime data (i.e. when $SW_{downwelling} > 0$ Wm^{-2}) where $E < 0$ mm h^{-1}. Across all three data sets these points all occurred within 65 min of sunrise or sunset.

5.3.2 Differences in Modelling Results

The modelling results from DS1 and DS2 were remarkably similar despite the marked differences in the crop status. In each case GPSTIC showed the best performance when $1.05 \leq \alpha_{PT} \leq 1.15$ and the ranges of β were likewise very similar ($-1.3 < \beta < 0.5$ and $-1.4 < \beta < 0.7$, respectively).

The modelling results for DS3, however, had some significant differences:

1. Mean daily E was 43 % and 62 % higher than DS1 and DS2, respectively (which was as expected since the DS3 crop was planted at full density and well-watered).

2. α_{PT} was about 35 - 45 % higher during DS3 compared to DS1 and DS2, respectively.

3. $\beta < 0$ for almost all of DS3, including throughout the daytime (Fig. 4.58, p. 189).

Points (2) and (3) are significant because they stand as observational evidence that there was an inverse relationship between α_{PT} and β (having been determined separately by the GPSTIC and Profile BREB models, respectively). This inverse relationship had been mathematically predicted in Appendix I.2 (p. 396).

As an advective-heat parameter, α_{PT} would be expected to be larger when there was a net advection of heat[7] into the field (Davies & Allen 1973, Weiß & Menzel 2008). Approx. 30 % of the field received direct solar radiation during DS1, and nearly 100 % of the field received direct solar radiation during DS2 (there was slight shading of the southern face of the furrows). The dry soil surface[8] was hotter than the ambient temperature and became a potent in-field generator of H — enough to

[7] Given the the dryness of the surrounding drought-stricken landscape, this would be mostly advected H.

[8] Evaporation from the soil still occurred as water was drawn up from deeper in the soil profile. It was not enough, however, to keep the soil from heating well above ambient temperatures.

counter much of the advected H. Thus it was observed during DS1 and DS2 (where there were conditions of high soil insolation) that

1. ${}^{dT}/_{dz} < 0$ (e.g. Fig. 4.11, p. 132 at 13:31);

2. the Profile BREB system appropriately determined that β was greater than zero during the daytime (Fig. 4.12, p. 133 and Fig. 4.35, p. 162); and

3. the best value of α_{PT} in the GPSTIC model during DS1 and DS2 was found to be $\alpha_{PT} \approx 1.05$ — a relatively small value that reflected the low net advected H.

In contrast, the crop canopy was fully closed during DS3 and the area of directly insolated soil was negligible. Consequently the in-field generation of H was small (since more energy flux was apportioned to λE than H by the transpiring crop). Daytime temperature inversions where ${}^{dT}/_{dz} > 0$ (e.g. Fig. 4.55, p. 186) were generally present. This indicated that the lower air adjacent to the crop was cooler than the air higher above (which had been advected from the surrounding hot drought-stricken landscape) and so there was a pronounced net movement of H downwards toward the crop (by turbulent transfer). Thus it was appropriate that $\beta < 0$ during the day[9] (Fig. 4.58, p. 189). A higher value of $\alpha_{PT} \approx 1.4$ produced the best performance in GPSTIC — a contrasting outcome to DS1 and DS2 but entirely consistent with the stronger role of advected H during DS3. (This was also consistent with Appendix I.2, p. 396 which showed that α_{PT} and β are inversely related.)

Thus even within the limited context of this research, i.e. broadacre furrow-irrigated cotton, the three data sets have provided an opportunity to evaluate GPSTIC under a variety of field conditions. The patterns for

[9] β is often negative at nighttime, manifesting in a net downward movement of λE. (Nighttime negative E in this research is discussed in Appendix K, p. 405.) However, β can be negative during the daytime when the fluxes of H and λE are in opposite directions. Since λE is unlikely to be downward (because T and T_S are typically above T_D) then H must be directed downward.

best α_{PT} and β (as determined using GPSTIC and Profile BREB, respectively) were appropriate for the conditions and were a further indication that these models were functioning correctly.

5.4 Chapter Summary and Conclusion

The GPSTIC model was used to estimate E for each of 8880 4 min intervals of (averaged) data. These data were measured across three separate periods of fieldwork: DS1 (February 2019) featured a composite of cotton canopy and exposed soil that had been irrigated six days prior to data collection; DS2 (October - November 2019) featured bare soil that was irrigated during DS2; and DS3 (January - February 2020) featured a vigorously growing, fully-closed cotton canopy that was irrigated during DS3. All three Data Sets occurred within the context of a hot, drought-stricken landscape.

A co-located Profile BREB system provided a simultaneous estimate of E (as a benchmark) for each 4 min interval.

E_{GPSTIC} and E_{BREB} were compared on a 4 min interval-by-interval basis using regression analyses and 4 min discrepancy analyses. Whilst the two models rarely matched exactly, the regressions showed close to 1:1 correspondence with coefficients of determination around 0.92 - 0.96. Likewise, plots of the interval-by-interval discrepancies between the two models showed that the discrepancies were insignificant given the uncertainties in the modelling outputs (illustrated by the 95 % CI error bars) that were a consequence of the sensors' measurement uncertainties.

The cumulative discrepancy analyses presented in § 5.2 (p. 216) repeatedly demonstrated that GPSTIC was *capable* of meeting the requirement that $\left|\overline{D}_{daily}\right| < 1\,\mathrm{mm\,day}^{-1}$ (§ 1.5.2, p. 7) for all of the conditions encountered. Plotting the cumulative E_{GPSTIC} vs. time and E_{BREB} vs. time on the same axes showed that very close alignment between the two models was possible. This close alignment was not observed for just a small number of 4 min intervals; rather, it was observed over thousands of modelled values of E_{GPSTIC} and E_{BREB} where the cumulative discrepancy between the two models never exceeded more than a few millimetres depth of E.

The precise performance of the GPSTIC model was contingent upon which values for the α_{PT} advection parameter were chosen. It was observed in DS1 and DS2 that under daytime conditions where ${}^{dT}/_{dz} < 0$, $\beta > 0$ and net advected H was small then the best α_{PT} was approx. 1.05 - 1.10. In contrast, it was observed in DS3 that under daytime conditions where a temperature inversion was present (i.e. ${}^{dT}/_{dz} > 0$), $\beta < 0$ and net advected H was significant then the best α_{PT} was approx. 1.35 - 1.50. All of these observations were consistent with the mathematical deduction that α_{PT} should be inversely related to β (Appendix I.2, p. 396 and comments on p. 279).

Based on the outcomes of the analyses presented here, GPSTIC was not only capable of consistently estimating E within 1 mm day^{-1} of an independent Profile BREB system, it was also shown to be capable of matching Profile BREB extremely closely (i.e. within 0.05 mm day^{-1}) when an appropriate value for the α_{PT} advection parameter had been chosen.

Chapter 6

DISCUSSION

There were two key outcomes from this research:

1. The ability of the novel GPSTIC system to accurately estimate E was demonstrated (at least under the conditions evaluated).

2. The custom-built Profile BREB system (including its novel Line-of-Best-Fit algorithm) also demonstrated a robust performance.

This chapter reflects on the achievement of the Research Aims before discussing the performance of the GPSTIC and Profile BREB systems. After that, other matters of modelling uncertainty, the α_{PT} advection parameter, and data exclusion criteria are discussed before finally looking at the contributions and limitations of this research.

6.1 Achievement of the Research Aims

The primary aim of this research (§ 1.5, p. 6) was to answer the question 'Can the proposed model GPSTIC measure the cumulative evapotranspiration from a broadacre, irrigated cotton crop to within ± 1 mm day^{-1} of a benchmark measurement?', otherwise stated as:

$$\left|\overline{D}_{daily}\right| \overset{?}{<} 1\,\mathrm{mm\,day^{-1}} \qquad (6.1)$$

where $\overline{D}_{daily}$ is the mean daily discrepancy between E_{GPSTIC} and E_{BREB}.

For each of the three Data Sets the primary research aim has been answered in the affirmative. Indeed, GPSTIC was shown to be capable, across a variety of field conditions, of estimating E to a greater accuracy than that specified by Eqn. 6.1. With an appropriately selected value for the α_{PT} advection parameter,[1] E_{GPSTIC} would exhibit a consistently close alignment with E_{BREB} throughout an entire Data Set.

With regard to the secondary aim of this research, **a contribution to the body of knowledge about STIC has been made here**. This is in several respects:

1. This has been a wholly independent study of GPSTIC (and, by implication, of STIC).[2]

2. Unlike STIC, which relied on interpolating data between satellite revisits, the present research directly measured and logged accurate data every 60 s, day and night. This provided an opportunity to undertake a high-temporal-resolution evaluation of the STIC-based GPSTIC model. The quality of the evaluation was further

[1] A single value of α_{PT} was chosen for the entire duration of a Data Set. It was *not* the case that a different value of α_{PT} was chosen for each 4 min interval.

[2] It is stressed, however, that the present research does not, in fact, provide a *validation* of the STIC model. STIC was not designed by Mallick et al. to be implemented in the context or manner of the present research. That GPSTIC has performed well only *suggests* that STIC was correctly formulated.

improved by having GPSTIC co-located with the benchmark Profile BREB.

3. Unlike STIC, which was reliant upon the use of remote sensing, the GPSTIC system could operate and be evaluated under all weather and field conditions. Thus the present research presented an opportunity to evaluate a STIC-based model under conditions that would otherwise be problematic for remote sensing systems.

GPSTIC has been shown as capable of estimating E with similar accuracy as Profile BREB, which was accepted as an accurate representation of E in the field. By implication, then, the theory and model equations that form the basis of GPSTIC (i.e. those of STIC) were shown to be correct and effective.

However, it would be inappropriate to take this further and say that GPSTIC *validates* the original STIC model. GPSTIC was not applied in the same fashion as the original STIC model as intended by Mallick et al., i.e. using remotely-sensed data. Rather, it would be more appropriate to say that the results from GPSTIC can instil greater *confidence* in the RS-based STIC model.

Table 6.1 (p. 266) presents a summary of the values for mean daily discrepancy, $\overline{D}_{daily}$, between GPSTIC and Profile BREB for each of DS1, DS2 and DS3 (as calculated in Chapter 5). $\overline{D}_{daily}$ was close to zero for each of DS1, DS2 and DS3.

Table 6.1: Mean daily discrepancy, $\overline{D}_{daily}$, between E_{GPSTIC} and E_{BREB} during DS1, DS2 and DS3. Also tabulated is the mean 4 min discrepancy, $\overline{D}_{inst}$, in terms of λE. All data were included in the modelling except at the times when $E_{BREB} < -0.53\,\mathrm{mm\,h^{-1}}$ or $E_{BREB} > 1.5\,\mathrm{mm\,h^{-1}}$.

Data Set	n[a] [h]	$\overline{D}_{daily} \pm 2\sigma$ [mm day^{-1}]	$\overline{D}_{inst} \pm 2\sigma$ [Wm^{-2}]
DS1 ($\alpha_{PT} = 1.05$)	165	0.01±2.7	0.2±38.5
DS2 ($\alpha_{PT} = 1.05$)	311	0.05±3.6	1.5±51.3
DS3 ($\alpha_{PT} = 1.42$)	116	0.00±3.7	0.0±52.4

[a] 'n' is the number of consecutive hours used in the modelling.

A summary of the total accumulations of GPSTIC and Profile BREB, and the total discrepancy between them (as calculated in Chapter 5) is provided by Table 6.2 (p. 267). It can be seen that the accumulated E_{GPSTIC} never differed from the accumulated E_{BREB} by more than 1.2 % across DS1, DS2 or DS3.

Table 6.2: Total accumulated discrepancy, D, for the data sets DS1, DS2 and DS3 (where $D = E_{GPSTIC} - E_{BREB}$). All data were included in the modelling except at the times when $E_{BREB} < -0.53\,\mathrm{mm\,h^{-1}}$ or $E_{BREB} > 1.5\,\mathrm{mm\,h^{-1}}$.

	E_{GPSTIC}		E_{BREB}		D		
Data Set	Total [mm]	Mean Daily [$\mathrm{mm\,day^{-1}}$]	Total [mm]	Mean Daily [$\mathrm{mm\,day^{-1}}$]	Total [mm]	Total [%][a]	Mean Daily [$\mathrm{mm\,day^{-1}}$]
DS1 ($\alpha_{PT} = 1.05$)	31.2	4.5	31.1	4.4	0.1	0.3 %	0.01
DS2 ($\alpha_{PT} = 1.05$)	51.2	3.9	50.6	3.9	0.6	1.2 %	0.05
DS3 ($\alpha_{PT} = 1.42$)	37.6	3.1	37.6	3.1	0.0	0.0 %	0.00

[a] Calculated by

$$\text{Total Discrepancy [\%]} = \frac{(E_{GPSTIC})_{Total} - (E_{BREB})_{Total}}{(E_{BREB})_{Total}} \times 100$$

6.2 Performance Evaluation

For the purposes of this research *two* separate measurement systems were custom designed and constructed:

1. A novel GPSTIC system.
2. A Profile BREB system, against which the GPSTIC system was evaluated.

These systems were designed from the outset to complement each other in terms of having some sensors shared in common, and being able to make field measurements at the same frequency and at the same location.

6.2.1 Performance of GPSTIC

As previously described (§ 3.4, p. 105) the GPSTIC system comprised a suite of sensors and a programmable logging system, an algorithm — based around the STIC closure equations (Eqns. 3.30 - 3.33, p. 105), the Buck equation (Eqn. 3.47, p. 112), and the Penman-Monteith equation (Eqn. 3.66, p. 115) — and a computer script to execute the GPSTIC algorithm.

The original STIC had been shown in the literature to perform well (§ 2.1, p. 16) but this did not necessarily confer a guarantee that GPSTIC could perform likewise. GPSTIC had significant differences from STIC in terms of the spatial scales involved, the temporal resolution of measured data, and the nature of the sensing systems (i.e. direct measurements of ambient conditions vs. inference of ambient conditions from satellite-based radiation sensors).

Several analysis techniques were applied in Chapter 5 to the modelling results. Linear regressions of the 4 min results for E_{GPSTIC} vs. E_{BREB} had slopes close to unity and coefficients of determination around 0.92 - 0.96. These results are an improvement upon those reported in the literature for STIC, e.g. Mallick et al. (2016) reported $R^2 = 0.94$ for λE and $R^2 = 0.61$ for H over the Amazon rainforest, compared to EC;

Obringer et al. (2016) reported $R^2 = 0.84$ compared to EC over combined urban/rural settings; Mallick et al. (2018) reported $R^2 = 0.60 - 0.85$ at Australian semi-arid sites, compared to EC; and Bhattarai et al. (2019) reported $R^2 = 0.6$ over irrigated, high λE sites, compared to four two-height BREB systems. The latter is particularly striking given the similarity of circumstances with the present research. Furthermore, it would be expected that the high λE conditions would be ideal for the BREB systems that Bhattarai et al. used. However, Bhattarai et al. noted that the presence of cloud cover and the lack of ground-based meteorological data caused difficulties for the STIC model (a situation that GPSTIC avoided altogether by using ground-based sensing).

The lower coefficients of determination for STIC in the literature compared to GPSTIC in this research may be due to several factors:

1. STIC could only be implemented on clear-sky days when satellite overpasses occurred. This meant that significant interpolation of the data between suitable overpasses had be undertaken, introducing greater uncertainty into the STIC modelling. In contrast, data interpolation not required for the ground-based systems (i.e. GPSTIC, Profile BREB and EC systems).

2. STIC relied on inferring climatological variables from remotely-sensed radiometric data whereas EC, Profile BREB and GPSTIC were all able to directly measure climatological variables in the field.

3. The spatial resolution of data used by STIC in the literature was sometimes very large, e.g. Bhattarai et al. (2018) reported 1 km $\times$ 1 km pixel resolution for their radiometric data, and Obringer et al. (2016) reported 32 km pixel resolution. The EC flux towers against which STIC was compared in these studies likely had a much smaller footprint than these scales and this may have caused a mismatch of footprints and thus lower R^2 values. In contrast, GPSTIC and Profile BREB were co-located in the same field and would have been subject to the same flux footprint.

4. EC systems can experience problems with energy misclosure, acknowledged by Renner et al. (2019), and this may have contributed to the R^2 values for the STIC vs. EC studies.

It is also interesting to note that problems arose for STIC when remote systems were not able to accurately measure T_S. Mallick et al. (2015b, 2016) reported problems with modelled H due to emissivity errors in T_S, and Mallick et al. (2018) reported that STIC was more sensitive to T_S at semi-arid sites. Udelhoven et al. (2017) reported that the accuracy of T_S needed to be better than $\pm 1\,\mathrm{K}$. (The Apogee SI-411 used by GPSTIC was able to measure T_S to an accuracy of $\pm 0.18\,\mathrm{K}$.)

Analyses of 4 min discrepancies between E_{GPSTIC} and E_{BREB} showed that they were generally close to zero (but rarely equal to zero). However, the non-zero discrepancies were shown to be insignificant in light of the modelling uncertainties (illustrated by the 95 % CI error bars) that stemmed from the sensors' inherent measurement uncertainties.

After making 4 min comparisons of GPSTIC and Profile BREB, the approach of analyses shifted to compare them in terms of the cumulative totals of E_{GPSTIC} and E_{BREB}. The cumulative discrepancy analyses in § 5.2 (p. 216) repeatedly demonstrated that GPSTIC was not only capable of meeting the requirement that $\left|\overline{D}_{daily}\right| < 1\,\mathrm{mm\,day^{-1}}$ (under the field conditions encountered) but was capable of far greater accuracy. Table 6.2 (p. 267) showed that $\left|\overline{D}_{daily}\right| \leq 0.05\,\mathrm{mm\,day^{-1}}$ across all Data Sets (i.e. up to 1.2 % error between the GPSTIC and Profile BREB). Furthermore, plotting the cumulative E_{GPSTIC} vs. time and E_{BREB} vs. time on the same axes showed that extremely close alignment between GPSTIC and Profile BREB was possible. This close alignment was not just happenchance for just a small number of data points; rather, it was observed that for 8880 independently modelled values of E_{GPSTIC} and E_{BREB} (from 592 hours' worth of field data) the accumulated discrepancy between GPSTIC and Profile BREB never exceeded, at any time, more than a few millimetres depth of E.

Collectively, these findings demonstrate that GPSTIC can make accurate determinations of E in a broadacre cropping environment. This was extraordinary because GPSTIC required no crop- or field-specific information (except for an appropriately chosen α_{PT} advection parameter), no reference crop, and no complex instrumentation beyond a set of sensors to measure T, RH, T_S and R_N. Furthermore, the GPSTIC system appears to have maintained its performance across all diurnal hours and across a variety of field conditions.

6.2.2 Performance of Profile BREB

The implicit assumption behind the discussion thus far is that the benchmark Profile BREB against which GPSTIC has been compared was itself appropriate and adequately accurate. It is the author's view that not only was this the case but that it would be difficult to maintain a contrary position in light of the results presented in this thesis.

Indeed, it was not by chance that Profile BREB provided quality benchmark data. It was, in essence, an evolutionary development of the profile-type BREB systems that had been reported in the literature (§ 2.4.6, p. 43). The present Profile BREB had the additional advantage of incorporating more modern, precise sensors that were well suited to this very purpose.[3] In this research there were also the advantages of having large flat fields with extensive fetch in all directions; significant temperature and humidity gradients in the field; the ability to make frequent measurements;[4] and minimal in-field infrastructure requirements (thereby minimising disturbances to air flows). For example, the instrumentation and infrastructure requirements of the present Profile BREB were much less than the profile systems of Sinclair et al. (1975), Lafleur et al. (1992) and Olejnik (1996), Olejnik et al. (2001*a*) which not only improved the practicality of the system (in terms of being able to be de-

[3]The 4-wire Pt100 RTDs (§ 3.2.1, p. 68) and the Michel Hygrosmart HS3 capacitive hygrometers (§ 3.2.2, p. 70) are particularly in mind here.

[4]Frequent measurements, i.e. every 60 s, were possible mainly because there was no sensor exchange mechanism or air-aspiration system (such as used by Olejnik et al. (2001*b*) in their profile-type BREB system).

ployed into an annually cropped field with ongoing agronomic activities), but also the frequency of measurement that was possible.

Furthermore, the novel LoBF sub-algorithm improved the accuracy of β by providing an automated, objective process (based on the sensors' inherent measurement uncertainties) for evaluating the suitability of (e, T) data points for the LoBF linear regression. It was thus possible to produce line-fittings to each of the 8880 sets of multi-height data in a similar fashion to Sinclair et al. (1975) — see Fig. 2.7 (p. 45).

In the literature, some authors, e.g. Spittlehouse and Black (1980) and Angus and Watts (1984), expressed their reservations about the ability of profile BREB methods to be able to handle low-gradient conditions (despite Blad and Rosenberg (1974) and Sinclair et al. (1975) having shown otherwise). In this research the Profile BREB system showed itself as capable of performing well under low-gradient conditions. This was partly due to the use of modern, accurate sensors that were unavailable to Spittlehouse and Black, and Angus and Watts. However, the Profile BREB algorithm created for this research was also a contributor to this capability in that it could identify any data that should be excluded from the line-fitting process.[5] The Profile BREB system also obviated any need to pre-emptively exclude data on the basis of the time-of-day or when $-1.25 < \beta < -0.75$ (Ohmura 1982, Perez et al. 1999, Savage et al. 2009) — a valuable characteristic of the profile approach that was particularly demonstrated in the work of Sinclair et al. (1975). The consequence was that, for this research, a greater proportion of the Profile BREB data could be retained for the analysis.

In this discussion of Profile BREB's performance it is also worth highlighting that the Profile BREB system was able to determine β every 60 s, without requirement for any quiet non-measurement periods. This is in contrast with the ubiquitous two-height BREB system designed by Tanner et al. (1987) which is typically reported to operate with a 66 % duty cycle (i.e. no measurements are made for a third of the time while air

[5] Sinclair et al. (1975) also used this process, albeit applied manually.

exchange is underway).[6] Even the profile design of Sinclair et al. (1975) had to include periodic non-measurement periods because their system used an air-aspiration system (like Tanner et al.). The fact that Profile BREB's sensors did not require exchange both reduced the mechanical complexity and power demands of the system, but also helped to ensure the continuity and completeness of the measured data.

The quality of the results from Profile BREB largely speaks for itself. For example, the plots in Fig. 5.13 (p. 227), Fig. 5.19 (p. 239) and Fig. 5.25 (p. 251) showed a consistent close alignment between GPSTIC and Profile BREB over thousands of modelled values of E. Logically, only one of two following statements could have been true:

1. Both systems were *correctly* modelling E.

2. Both systems were *incorrectly* modelling E, but doing so in an almost identical fashion.

If Profile BREB and GPSTIC were independent of one another (see § 6.2.3 below) then statement (2) is simply too improbable to accept.

It was by this reasoning that it was deemed that the estimates of E from Profile BREB were, in fact, appropriate and adequately accurate throughout each of DS1, DS2 and DS3.

6.2.3 Independence of GPSTIC and Profile BREB

The argument that the results from Profile BREB could be accepted as appropriate and adequately accurate (made in the previous section) was contingent upon GPSTIC and Profile BREB actually being independent of each other.

By design, GPSTIC and Profile BREB shared some sensors and a data logger in common. This feature was desired because having identical input data supplied to the GPSTIC and Profile BREB models meant that

[6] Appendix A.4, p. 334 makes a case that for the system designed by Tanner et al. (1987) the 66 % duty cycle is inadequate to ensure that the 'old' air is sufficiently replaced by the 'new' air. Nevertheless, the 66 % duty cycle is common practice.

differences in the results could be ascribed to the models themselves, rather than to differences in the input data. Thus with respect to how the environmental variables were *measured*, GPSTIC and Profile BREB were not independent.

But the claim that GPSTIC and Profile BREB were independent of each other was not made with respect to the measurement of the data. Rather, the claim of independence pertained to what each model *did* with the data.

GPSTIC and Profile BREB each had their own computational algorithm. These algorithms were based on different theoretical foundations and assumptions, and neither theory was dependent upon or made any reference to the other. The algorithms also had very different approaches to solve for λE. GPSTIC relied on radiometric measurements of T_S in order to solve the 'STIC closure equations' (Eqns. 3.30 - 3.33, p. 105), whereas Profile BREB relied on precise, direct measurements of T and e at a multitude of points above an evaporating surface in order to determine β. And finally, there was no interaction between the GPSTIC and Profile BREB algorithms, and neither relied upon or was influenced by the output of the other.

Thus GPSTIC and Profile BREB were, indeed, quite independent of each other in terms of how they computed λE.

6.3 Uncertainty in the Modelling

One of the practices adopted in this thesis has been to report the modelling uncertainties with the modelling results. These were the consequence of the sensors' inherent measurement uncertainties being propagated through the modelling (as described in Appendix H, p. 379).

The principal motivation for reporting the modelling uncertainties primarily came from the need to determine whether non-zero discrepancies between E_{GPSTIC} and E_{BREB} were significant. It was deemed that if the horizontal line $D = 0$ passed through the 95 % CI error bars (e.g. Fig. 5.8, p. 220 and Fig. 5.11b, p. 224) then there was not a significant discrepancy between the outputs of the two models — especially if $D = 0$ was near the centre of the 95 % CI error bars.

A secondary motivation stemmed from the fact that the 2σ confidence ellipses, which were central to the novel Profile BREB LoBF sub-algorithm, were formed using the temperature and humidity sensors' measurement uncertainties. How these sensor uncertainties propagated into modelling uncertainty was an interesting consideration in the development of the Profile BREB system (and confirmed the value of using sensors with lower measurement uncertainties).

The modelling uncertainties presented in this research were often unflattering. As an example, the best result for the GPSTIC model during DS1 was shown in Table 5.4 (p. 218) to be $E_{GPSTIC} = 31.2 \pm 8.2\,\text{mm}$ which meant that the best result had a relative uncertainty of $\pm 26\,\%$. But two comments are warranted at this point. Firstly, this reflects the decision to use a 2σ or 95 % CI criterion. This is standard instrumentation practice (and so sensors' uncertainties are often cited as 95 % CI) but is quite harsh in the context of environmental measurements and atmospheric science where 1σ may be more appropriate. And secondly, these modelling uncertainties are not as bad as they appear. Continuing the above example, while we can have 95 % confidence that the 'true' value for accumulated E_{GPSTIC} was *somewhere* within the range 23.0 - 39.4 mm, it would most likely have been close to the modelled value of 31.2 mm. Indeed, for the true value to actually be as low as 23.0 mm or as high as 39.4 mm when the modelled value was 31.2 mm would be a very unlikely event.

The uncertainties associated with the discrepancies were even less flattering. However, these are easily misunderstood and so an explanation by example will be given — again from Table 5.4 (p. 218):

$$\begin{array}{ll} \text{If} & E_{GPSTIC} = 31.2 \pm 8.2\,\text{mm} \\ \text{and} & E_{BREB} = 31.1 \pm 15.9\,\text{mm} \end{array}$$

Then the discrepancy, D, between the two models would be

$$\begin{aligned} D &= 31.2 - 31.1 \\ &= 0.1\,\text{mm} \end{aligned}$$

The uncertainty in the discrepancy (δD) would be found by summing in quadrature the uncertainty for each model

$$\begin{aligned} \delta D &= \sqrt{(\delta E_{GPSTIC})^2 + (\delta E_{BREB})^2} \\ &= \sqrt{8.2^2 + 15.9^2} \\ &= 17.9\,\text{mm} \end{aligned}$$

Thus the discrepancy between the models could finally be written as

$$D = 0.1 \pm 17.9\,\text{mm}$$

Here the (absolute) uncertainty of ±17.9 mm looks very large in comparison to the value of D but such is the nature of discrepancy analyses where D is expected to be close to zero. Also, it is clearly pointless to report the *relative* uncertainty when D is expected to be close to zero.

6.4 The $\boldsymbol{\alpha_{PT}}$ Advection Parameter

The GPSTIC model provided the choice to manually enter a value for the α_{PT} advection parameter or to use an internal iterative optimisation algorithm — following Mallick et al. (2015a) — to determine its value. Interestingly, the values of α_{PT} that produced the best performance by GPSTIC in this research did not replicate the experiences of Mallick et al. (2014, 2015a). Furthermore, the use of the iteratively-optimised α_{*PT*}[7] invariably produced poor results for GPSTIC in this research, again in contrast to the findings of Mallick et al.

The following sections will discuss, in turn, the use of the manually-entered α_{PT} and the iteratively-optimised α_{*PT*} in relation to GPSTIC.

6.4.1 Manually-Entered $\boldsymbol{\alpha_{PT}}$

The approach of manually entering α_{PT} (where a single fixed value of α_{PT} was used for the entire Data Set) worked extremely well for GPSTIC across all three Data Sets and across all 24 of the diurnal hours (including the usually troublesome dawn/dusk periods and overnight). The analyses in § 5.1 (p. 201) and § 5.2 (p. 216) demonstrated that, with a carefully selected value of α_{PT}, GPSTIC could consistently maintain very close alignment with Profile BREB.

Two key differences between GPSTIC and STIC (with respect to a manually-entered α_{PT}) were observed:

1. Mallick et al. (2014) reported that λE was relatively insensitive to the value of the user-selectable α_{PT} advection parameter when $1.00 < \alpha_{PT} < 1.50$ in the STIC model. In contrast, the performance of GPSTIC was quite sensitive to the selected value of α_{PT}. This can be seen in the Regression Analysis Tables 5.1 (p. 203), 5.2 (p. 209), 5.3 (p. 213)), and the Discrepancy Analysis Tables 5.4

[7]In this thesis the notation α_{*PT*} is used to indicate that the value of α_{PT} was determined by the internal optimisation process first described in Mallick et al. (2015a).

(p. 218), 5.5 (p. 230), 5.6 (p. 242) where step changes in E_{GPSTIC} were essentially proportional to the step changes in α_{PT}.

2. As a consequence of (1), GPSTIC was trialled across a range of values for α_{PT} between 0.9 and 1.5 to determine which gave the best alignment with Profile BREB.[8] In so doing, the best value for α_{PT} was found to be approx. 1.05 in DS1 and DS2, and approx. 1.42 in DS3. This is in contrast to STIC where a fixed value of $\alpha_{PT} = 1.26$ was considered adequate and appropriate across all field sites.

Table 6.3: Summary of results when a fixed value of $\alpha_{PT} = 1.26$ was used in the GPSTIC modelling. The evaluation criterion for GPSTIC was that $\left|\overline{D}_{daily}\right| < 1\,\mathrm{mm\,day^{-1}}$.

Data Set	$\left\|\overline{D}_{daily}\right\|$[a] [mm day^{-1}]	Error Using $\alpha_{PT} = 1.26$[b]
DS1	0.94	23 %
DS2	0.86	21 %
DS3	0.85	−11 %

[a] The mean daily discrepancy between GPSTIC and Profile BREB was

$$\left|\overline{D}_{daily}\right| = \left|\frac{\sum E_{GPSTIC} - \sum E_{BREB}}{\left(\frac{Y}{24\,\mathrm{h\,day^{-1}}}\right)}\right|$$

where Y was the number of hours in the data set.

[b] The percentage difference between the mean daily E_{GPSTIC} using $\alpha_{PT} = 1.26$ [mm day^{-1}] and the mean daily E_{BREB} [mm day^{-1}].

Table 6.3 (p. 278) shows that selecting a fixed value of $\alpha_{PT} = 1.26$ still gave acceptable results for GPSTIC across DS1, DS2 and DS3 in

[8] A single fixed value of α_{PT} was used for a whole Data Set. Thus it was the best *overall* alignment between GPSTIC and Profile BREB that was sought, not a separate optimisation for every 4 min interval of data and not an optimal alignment for the *final* cumulative totals of the two models.

terms of satisfying the evaluation criterion that $\left|\overline{D}_{daily}\right| < 1\,\mathrm{mm\,day^{-1}}$. However, these did not reflect GPSTIC's best performance and it can be seen that the error in mean daily E_{GPSTIC} (with respect to mean daily E_{BREB}) that resulted from using $\alpha_{PT} = 1.26$ in DS1, DS2 and DS3 was 23 %, 21 % and −11 %, respectively. These errors were larger than those reported when STIC was modelled with $\alpha_{PT} = 1.26$ (11 - 15 % error in Mallick et al. (2014) and 5 - 13 % error in Mallick et al. (2015a)). Possible reasons for the difference in results between GPSTIC and STIC when using a fixed $\alpha_{PT} = 1.26$ would include:

1. Differences in the models' algorithms *per se*.

2. Differences in the data collection methods (i.e. ground-proximal, directly sensed measurements of ambient conditions vs. inference of ambient conditions from space-based remotely-sensed radiation data).

3. Differences in the spatiotemporal scales and resolutions involved.

4. Differences in the environmental conditions between this research (i.e. a single, irrigated cropping field within a hot, drought-stricken landscape) and environmental conditions evaluated by STIC (usually composite landscapes due to the scales involved).

Based on the results of this research, α_{PT} should not be regarded as fixed across the course of a cropping season (especially for annual crops). DS2 and DS3 were at opposite ends of the 2019/20 season in Field 16 and featured similar weather conditions, however the surface cover in Field 16 had changed dramatically in the intervening time. Whereas DS2 had essentially bare soil (with seedlings just emerging), DS3 had a fully-grown crop with a completely closed canopy. The daytime temperature profiles ($^{dT}/_{dz}$) had changed from predominantly negative to positive, and daytime values for β had changed from predominantly positive to negative. Meanwhile, the values of α_{PT} that produced the best performance by GPSTIC changed from $\alpha_{PT} \approx 1.05$ in DS2 to $\alpha_{PT} \approx 1.42$ in DS3. All of these changes reflect the changing significance of advected sensible heat[9] and are consistent with Appendix I.2 (p. 396) which shows, mathematically, that α_{PT} and β are inversely related. Accordingly, in the context of an annually cropped field whose surface cover is changing, it is inappropriate to use a single fixed value of α_{PT} for the entire duration of a growing season.[10]

(It is also acknowledged that at the large spatial scales that STIC was employed, i.e. grids in the order of kilometres across, a fixed value of $\alpha_{PT} = 1.26$ may indeed have been appropriate. STIC was generally not being used to evaluate single fields; rather, it was often used to estimate E over wide, composite landscapes.)[11]

6.4.2 Internal Iterative Optimisation of α_{*PT*}

GPSTIC contained an option to determine α_{*PT*} using an internal iterative optimisation process. This was the same as described in Mallick et al. (2015a) and the optimisation was performed for every 4 min interval of data. Fig. 6.1 (p. 282) gives four example plots from DS1 that show how GPSTIC's optimisation algorithm converged on a value of α_{*PT*}. These were quite similar to Fig. 2.2 (p. 26) that was presented by Mallick et al. (2015a) as an example of their iterative process. Fig. 6.2 (p. 283) shows a plot of the 2475 values of α_{*PT*} determined for DS1. Comparable plots for DS2 and DS3 are presented in Appendix M (p. 415) where it can be seen that α_{*PT*} was likewise around 0.8 - 0.9.

Two observations regarding the values of GPSTIC's α_{*PT*} are readily made: Firstly, their value did not substantially change between the Data

[9]Since the weather and the surrounding landscape did not change significantly in the intervening time, it was the changing extent of crop cover that caused the changes to the *net* advected sensible heat.

[10]Being an advection parameter there are other factors that would influence the value of α_{PT}, such as the nature of surface cover in the surrounding landscape, the moisture availability in the surrounding landscape and in the field, and the stability of the atmosphere.

[11]This was due, in part, to Mallick et al.'s interest in and emphasis on large-scale modelling. It was sometimes also due to the pixel resolution limitations of the satellite-based RS sensors.

Sets despite the fact that the temperature profiles, Bowen ratios and extent of surface coverage all changed substantially. And secondly, the values of α_{*PT*} were consistently much smaller than the best performing fixed values of α_{PT}. Table 6.4 (p. 284) shows that the performance of GPSTIC was poor when using α_{*PT*} values, especially for DS3. Indeed, $\left|\overline{D}_{daily}\right|$ was no better when GPSTIC used α_{*PT*} than when it used a fixed value of $\alpha_{PT} = 1.26$ (cf. Table 6.3, p. 278).

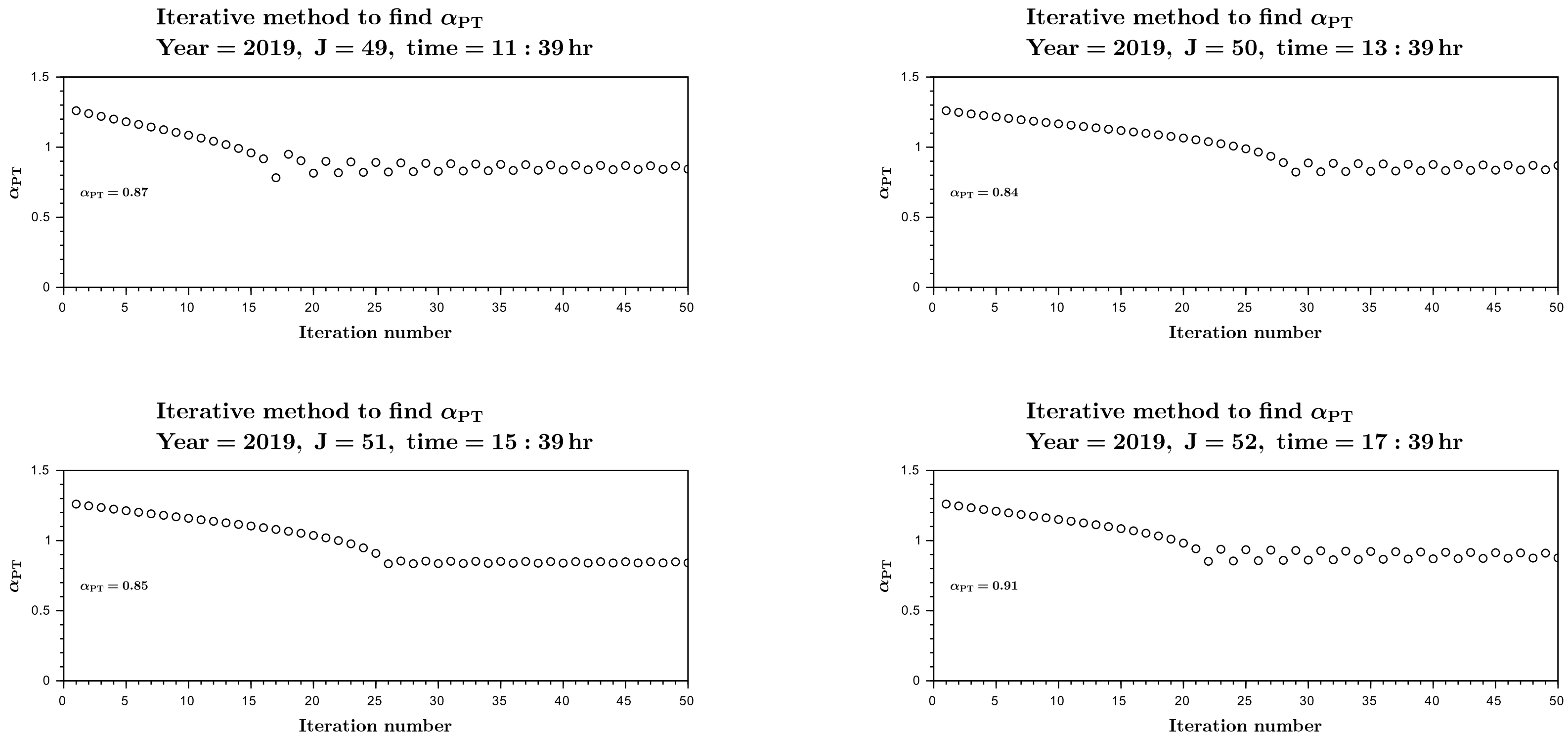

Figure 6.1: GPSTIC: four example plots from DS1 showing the progressive optimisation of α_{*PT*} using the internal iterative process, following the procedure of Mallick et al. (2015a). The end results are similar to Fig. 2.2 (p. 26) although the convergence in GPSTIC's optimisation process appears to have taken more iterations.

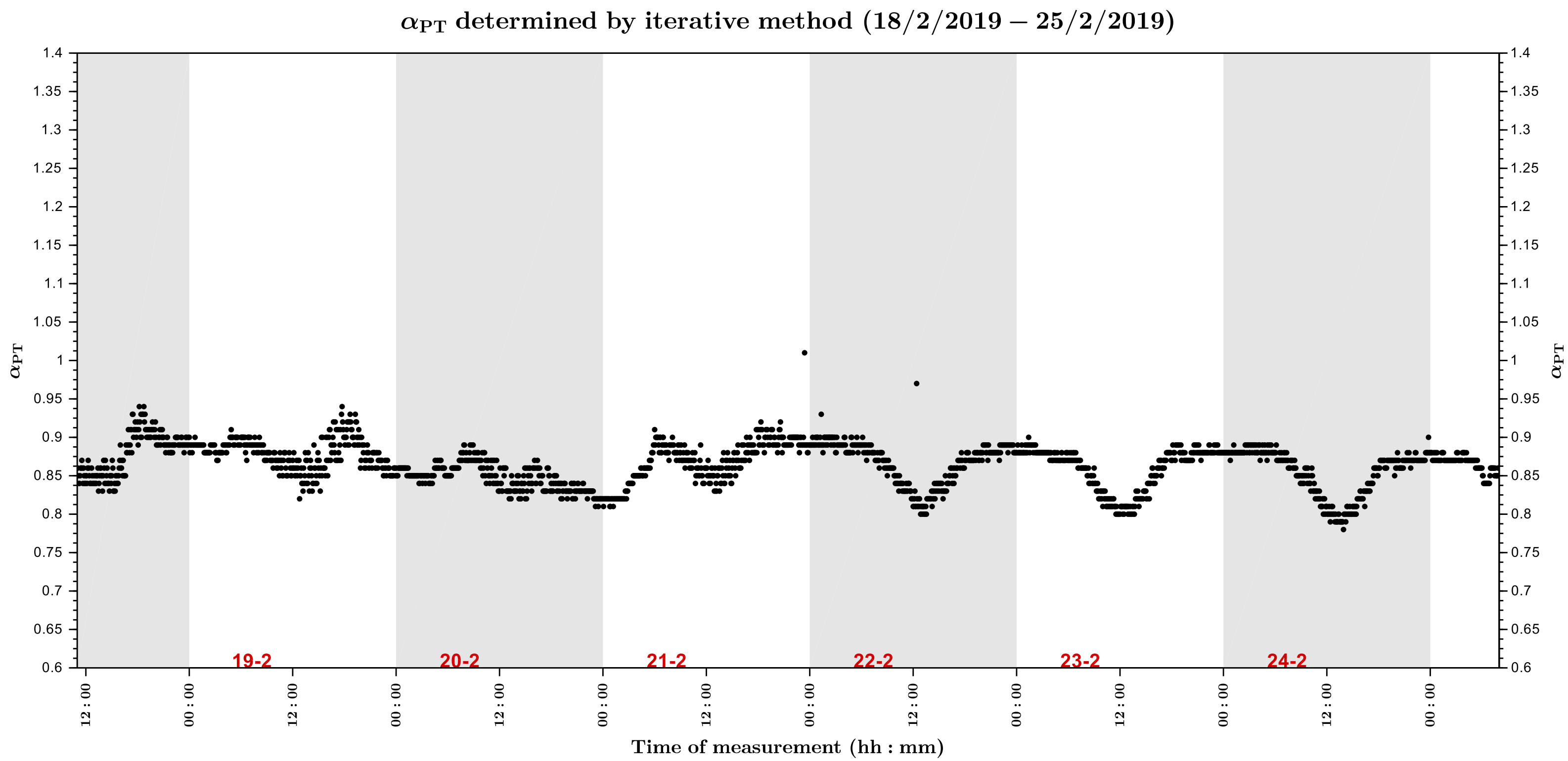

Figure 6.2: GPSTIC: a plot of all 2475 of the optimised values for α_{*PT*} during DS1 as determined by the internal iterative process. The determination of optimal α_{*PT*} was performed for every 4 min interval of data. Comparable plots for DS2 and DS3 are presented in Appendix M (p. 415).

Table 6.4: Comparison across DS1, DS2 and DS3 of total accumulated E_{GPSTIC} and E_{BREB} when E_{GPSTIC} was modelled using the iterative optimisation process for α_{*PT*} (Step 16, p. 115 in the GPSTIC algorithm).

Data Set	Accumulated Totals		Model Discrepancies	
	E_{GPSTIC} [mm]	E_{BREB} [mm]	Percentage	$\lvert \overline{D}_{daily} \rvert$ [mm day^{-1}]
DS1	25.5	31.1	-18 %	0.81
DS2	39.1	50.6	-23 %	0.88
DS3	24.8	37.6	-34 %	2.65

So why were the results for GPSTIC relatively poor when using α_{*PT*} and why were the values of α_{*PT*} in Fig. 6.2 (p. 283) so small? It is unlikely to be due to an error in the GPSTIC algorithm (or computer program) because Mallick et al. (2015a) also reported that the iterative optimisation process produced values for α_{PT} around 0.80 - 0.90. Perhaps, instead, the algebraic derivation of α_{*PT*} (used at Step 16, p. 115 in the GPSTIC algorithm) was flawed? This was more plausible because STIC and GPSTIC were using the very same equation to compute α_{*PT*}.[12] Mallick et al. (2015a) did not detail how they had derived their equation for α_{*PT*} but a possible derivation has been included in Appendix I.3 (p. 397).[13] This derivation shows that there was, in fact, no error in Eqn. 25 in Mallick et al. (2015a), which is identical to Eqn. I.32 (p. 398), and so it can be concluded that there were no problems with the equations themselves.

It is possible that the problem lies further back in the idea of equating the λE of Priestley and Taylor (1972) with the λE of Monteith (1965), i.e. the step of equating Eqn. I.28 with Eqn. I.30 in Appendix I.3 (p. 397). Those two models were based upon different assumptions and, importantly, they were intended to operate at vastly different scales.

[12]This was Eqn. 25 (p. 10) in Mallick et al. (2015a)

[13]Only Eqn. I.29, Eqn. I.30 and Eqn. I.32 were provided by Mallick et al. (2015a); the other equations were left to the reader to figure out.

This may also explain why α_{*PT*} worked for STIC and not GPSTIC. Just like the Priestley-Taylor model (§ 2.2, p. 23), STIC was intended to operate at very large scales. It is possible then that the equating of Priestley-Taylor's λE with Penman-Monteith's λE (to derive an equation for α_{*PT*}) was justifiable in the context of STIC but not for GPSTIC given the very small spatial scales at which GPSTIC is intended to operate.

6.4.3 Concluding Remarks About $\boldsymbol{\alpha_{PT}}$

Strictly speaking, the aim of this research was not to quantify or characterise the α_{PT} advection parameter *per se*. Furthermore, the process by which α_{PT} has been determined in this research reduces the ability to generalise the results to other crops, climates, topographies, etc.

For present purposes it was sufficient to identify that fixed values of $\alpha_{PT} = 1.05$ produced the best results for GPSTIC in each of DS1 and DS2, and likewise $\alpha_{PT} = 1.42$ in DS3. The 'best' values of α_{PT} were observed to be consistent with the advection conditions (which were manifested in the patterns of ${}^{dT}/_{dz}$ and β). Mathematically it was predicted that α_{PT} and β should be inversely related (Appendix I.2, p. 396) and this was observed in this research.

It was a significant, incidental finding of this research that the 'best' values for α_{PT} differed to those reported by Mallick et al. (2014), that GPSTIC was more sensitive to α_{PT} than was STIC, and that the internal iterative process to optimise α_{*PT*} following Mallick et al. (2015a) produced better results for STIC than GPSTIC. An investigation into the reasons for each of these was outside the scope of this research. These are recommended for future work (§ 7.2, p. 295), an undertaking that will likely require trialling GPSTIC across a variety of crops, climates, topographies, etc. to be able to fully understand and specify α_{PT} as a quantitative function of another environmental variable(s).

6.5 Data Exclusion Criteria

Measurements of 18 different environment variables[14] were made every 60 s for a total of 592 hours across the three Data Sets. These were averaged in 4 min intervals to give 8880 time steps of (averaged) data.

6.5.1 All Data and Selected Data Scenarios

The 'All Data' modelling scenarios included all 8880 time steps of data except those instances when the magnitude of E_{BREB} was unreasonably large, i.e. when $E_{BREB} < -0.53\,\mathrm{mm\,h^{-1}}$ or $E_{BREB} > 1.5\,\mathrm{mm\,h^{-1}}$.

The reason behind these particular values (i.e. $-0.53\,\mathrm{mm\,h^{-1}}$ and $1.5\,\mathrm{mm\,h^{-1}}$) was because they were the hourly equivalents of $-0.035\,{}^{\mathrm{mm}}/_{4\,\mathrm{min}}$ and $0.100\,{}^{\mathrm{mm}}/_{4\,\mathrm{min}}$, respectively. These 4 min values were selected because they enabled the identification of *most* of the obvious outlier results, e.g. Fig. 4.13 (p. 134). Generally the outliers were associated with $\beta \approx -1$. (Interestingly, DS3 had an unusually high number of instances where $\beta \approx -1$, many of which did not occur around dawn or dusk but during the overnight irrigation event.) The excluded outliers amounted to 1.9 %, 5.8 % and 10.0 % of the data in DS1, DS2 and DS3, respectively, and they had to be removed as the magnitudes of E_{BREB} could become impossibly large and could greatly distort the Profile BREB results — especially the cumulative totals.[15]

The 'Selected Data' modelling scenarios excluded all instances when $-1.25 < \beta < -0.75$ in keeping with the recommendations of Tanner (1988) and Cellier and Olioso (1993). These instances generally occurred around dawn or dusk and have tended to be problematic for BREB systems in the past. A further exclusion was applied to any instance where $R^2 < 0.90$ for the regression in the Profile BREB LoBF. This was mainly to limit the modelling results to only those instances when there was a

[14] The measured variables were T_S, P, $W_{direction}$, W_{speed}, $T_A \ldots T_E$ (ambient temperature at heights A - E), $RH_A \ldots RH_E$ (relative humidity at heights A - E), $SW_{downwelling}$, $SW_{upwelling}$, $LW_{downwelling}$, $LW_{upwelling}$.

[15] Fig. 4.13 (p. 134), Fig. 4.36 (p. 163) and Fig. 4.59 (p. 190) show when $\beta \approx -1$ and their relationship with the outlier results.

very high quality regression. Generally, application of the 'Selected Data' exclusion criteria resulted in approx. half of the data being excluded from the modelling.

There was no clear improvement in the modelling results as a result of applying the Selected Data exclusion criteria. It would appear that not all data associated with $-1.25 < \beta < -0.75$ were problematic after all, and the LoBF sub-algorithm appears to have effectively dealt with the problematic instances anyway. Thus it was unnecessary (with Profile BREB) to pre-emptively exclude data where $-1.25 < \beta < -0.75$.

Most of the excluded data under the Selected Data scenario were because of the $R^2 < 0.90$ exclusion criterion. It appears that while the modelling uncertainties were slightly improved by applying this criterion, the overall modelling results (in terms of the closeness of alignment between GPSTIC and Profile BREB) were not appreciably improved.

Modelling with 'All Data' was the preferred scenario because it meant that no data were pre-emptively removed, thereby allowing GPSTIC and Profile BREB to be compared across all diurnal hours and across all field conditions encountered. Additionally, there was minimal screening of the data so as to remain above any accusation that problematic field data were conveniently removed so as to improve the modelling results.

6.5.2 Choice of Fieldwork Periods

There were three periods of data collection for this research and the full date range of all three were included in the modelling and are presented in this thesis. Since this research was undertaken at a commercial farm (and not a dedicated research facility) the fieldwork dates were dictated largely by practical concerns such as not having the Profile BREB system in the field when inter-row soil cultivation had to occur; coordinating travel to the field site (a 13 hour return trip) with other activities; and working around disruptive events such as major bushfires (which closed highway access to the field site) and State border closures due to the Covid-19 pandemic. That is, field work happened when it could (and not according to dates when it might have been perceived to be advantageous for the modelling).

6.6 Contributions of this Research

There have been several contributions of this research:

1. The GPSTIC model has been proposed, developed and evaluated as a novel application of STIC. This research has affirmed it as an efficacious and reliable model for estimating E at the scale of a single cropping field. GPSTIC could also be of interest to researchers and agriculturalists for the following reasons:

    (a) It is a relatively inexpensive and (practically) simple system compared with other micro-meteorological systems. It is also less likely to obstruct agronomic activities in a commercial cropping environment than other in-field micro-meteorological systems. (This also relates back to the original rationale for GPSTIC — § 1.2 (p. 2) — as having the potential 'to facilitate the real-time estimations of E at a field or sub-field scale for the purpose of agricultural irrigation and water management'.)

    (b) It does not rely on calculating an ET_0 from a reference crop. The concept of a reference crop, particularly as described by Allen et al. (1998), was an effective approach to work around the issue of unknown aerodynamic and stomatal conductances (which are generally difficult to measure) in the PM equation. The drawback of the FAO-56 approach, however, is that becomes necessary for an agriculturalist to maintain a reference crop — a practice that, anecdotally at least, is rarely done correctly outside of research environments. GPSTIC obviates any requirement for a reference crop.

    (c) It does not require prior knowledge of crop specific parameters.

(d) It is potentially capable of operating *continuously* and in real-time under all weather conditions. It was shown to be capable of operating under all of the conditions encountered during this research, including high ambient temperatures.

2. A 'modern' Profile BREB was developed for this research involving new, accurate field sensors and a novel algorithm that was effective at assessing which measured data should be included in the modelling. The popularisation of EC, historical limitations on sensor capabilities, and limitations inherent in the two-height BREB systems (that have become the default form of BREB) appear to have reduced the level of interest in BREB methods in recent decades. Perhaps the performance of the Profile BREB system during this research may help to invigorate further interest in, and re-imagining of, the profile approaches to BREB.

3. The STIC model had been shown in the literature to perform well — using remotely sensed data — across a variety of contexts and biomes. It has not, however, had a lot of uptake by researchers outside of those directly involved with its development. This research provides an independent affirmation of the STIC model (albeit using ground-proximal instead of remotely sensed data) thereby giving further credence to the STIC model. Also, this research may help to increase STIC's exposure — especially to researchers who do not ordinarily follow developments in the Remote Sensing discipline.

And, finally, a less fundamental contribution but valid nevertheless:

4. This research offered an opportunity to use some new precision environmental sensors that exemplify a newer generation of sensors. Recent sensor developments have potential to enhance field evapotranspiration research (including through techniques such as Profile BREB and GPSTIC) that had hitherto been hampered by costly, high maintenance and/or relatively inaccurate sensors. The

Michell HS3 hygrometers and the 4-wire Pt100 RTD sensors, in particular, performed well in the field during this research.

6.7 Limitations of the Research

The purpose of this research was only to evaluate whether GPSTIC *could* perform as well as a benchmark Profile BREB system. The answer is that this was the case, but an important caveat in this answer is that GPSTIC was only evaluated under a very limited range of field conditions. Thus a limitation of this research is that the results cannot automatically be generalised to other field or crop situations.

In particular it is noted that across DS1, DS2 and DS3 there was always a sufficient supply of water from the soil profile to sustain evaporation and/or transpiration (because of recent or contemporaneous irrigations). Given the important role that T_S plays in the GPSTIC model it is unclear whether GPSTIC's performance would necessarily differ when faced with more water-limited conditions.

(At this point, two counter arguments are made in response: firstly, the original STIC model has been shown to perform well across a wide variety of biomes and landscapes, thereby increasing the likelihood — but by no means guaranteeing — that GPSTIC could do likewise. And secondly, there were no crop-specific or field-specific parameters, besides the α_{PT} advection parameter, in the GPSTIC model. This was reflected in the fact that GPSTIC performed equally well whether the field featured an incomplete cotton canopy (DS1), only bare soil (DS2), or a fully-closed cotton canopy (DS3). This suggests that the GPSTIC model's solid performance was not contingent on the particular field conditions encountered in this research.)

Another limitation of this research is that it was decided not to thoroughly investigate and characterise the α_{PT} advection parameter. There were several reasons for this decision: firstly, it was not necessary in order to achieve the Research Aims; secondly, it was not within the Scope of this research to do so; and thirdly, even if it were included within the

Research Scope it was unlikely that it could even be done within the timeframe and resources of this PhD. Indeed, a thorough investigation would necessarily involve evaluating the relationship of α_{PT} vis-à-vis GPSTIC under a variety of in-field and extra-field conditions, in a variety of climates and across a variety of seasons — the possible combinations could become very large!

Instead, it was simply observed that when the net advected heat into the field was relatively small — manifested by daytime temperature profiles where ${}^{dT}/_{dz} < 0$ and daytime $\beta > 0$ — then the value for α_{PT} that produced the best agreement between GPSTIC and Profile BREB was also small, i.e. around 1.05 - 1.10. Alternatively, when net advected heat into the field was relatively large — manifested by inverse temperature profiles where ${}^{dT}/_{dz} > 0$ and $\beta < 0$ during the daytime — then the best value for α_{PT} was also relatively large, i.e. around 1.40 - 1.50. These were consistent with the concept of α_{PT} being an *advection* parameter.

Nevertheless, it is recognised that not having a process to more precisely predict which α_{PT} to use with a given set of field conditions is a limitation on the practicality of the GPSTIC model.

This page intentionally left blank.

Chapter 7

CONCLUSION

At the outset of this research it was unclear whether a GPSTIC system would even work, let alone be capable of performing equally to a Profile BREB system. No attempt at applying the STIC model to field-scale or sub-field-scale applications using only ground-proximal sensors (i.e. without remote sensing) had been reported in the literature.

The GPSTIC system was conceived, designed and assembled for this research. The Profile BREB system was also custom developed for this research. Both systems demonstrated their reliability over a total of 592 hours of operations in fairly hot field environments and were shown to provide quality modelling results throughout.

7.1 Achievement of Research Aims

The original context and motivation for this research was to further the capability of measuring and monitoring crop water use with a view to improving agricultural water management. GPSTIC — a novel application of the STIC model — was proposed for this purpose. It was envisaged that GPSTIC might (eventually) be able to provide relatively low-cost, real-time measurements and monitoring of E at a field scale since it was not reliant upon any remote sensing sources of data.

Given this context, and given the uncertainties in other variables associated with irrigation management – such as unknown deep drainage, unknown field runoff, spatially variable rainfall, and uncertain applied irrigation depths – it was deemed sufficient to evaluate whether GPSTIC could estimate E to within ±1 mm day^{-1} of an accurate benchmark.

This research has repeatedly, and with no exceptions, shown that GPSTIC was capable of meeting this standard.

Furthermore, it was demonstrated that, with an appropriately selected α_{PT}, GPSTIC could estimate E to within ±0.05 mm day^{-1} of the benchmark. It was possible to achieve consistent close alignment with the Profile BREB system; indeed, when cumulative totals of GPSTIC and Profile BREB were compared, the greatest discrepancy at any point in this research was only 1.2 %.

A Profile BREB system was developed to serve as the benchmark (meeting Research Objective 2 on p. 7). This system was capable of determining the Bowen ratio at each and every minute of the 24 hour day. Its sensors and algorithm proved to be reliable and efficient, especially in that the line-fitting algorithm obviated the need for manual inspection of the data. The system also met requirements for low electrical power requirements (thereby reducing the size of solar infrastructure) and that it could be installed and removed from the field with minimal disassembly.

This research affirmed the efficacy of the GPSTIC model. These results also imply that the original STIC closure equations used by Mallick et al. (2014), upon which GPSTIC was based, were correctly conceived and formulated. Strictly speaking, however, it cannot be claimed that this research proves or validates the original STIC model, as Mallick et al. applied it. This was because GPSTIC was not supplied with the remotely-sensed forms of data or at the spatiotemporal scales that STIC was intended for. Nevertheless, the positive outcomes for GPSTIC go a long way toward providing an independent affirmation of STIC.

7.2 Suggested Future Work

Several limitations of this research were noted in § 6.7 (p. 290) and these are the obvious starting points for future work.

1. GPSTIC needs to be evaluated (against a benchmark) under a greater variety of field conditions. Its performance over different crops, natural vegetation, topographies, field scales, climatic regimes, etc. should be investigated. *If* GPSTIC performs as well as it did in this research, and as well as STIC has been reported in the literature, then it has potential to be a significant practical tool for measuring and monitoring E.

2. A thorough investigation should be undertaken of the relationship of the α_{PT} advection parameter vis-à-vis the GPSTIC model and the environmental conditions so as to help improve the practicality of the GPSTIC model. It would make sense to do this concurrently with Item (1).

3. The effectiveness of the Profile BREB system indicates that further development of this system is warranted.

And of lower status,

4. An investigation into how nighttime negative E in an irrigated cropping environment might be accurately apportioned to dew and to mist, and how much mist is blown from the field, would improve the accuracy of water balance modelling for irrigation management.

5. The GPSTIC system developed in this research consisted of high quality research-grade sensors. To make the GPSTIC system more suitable for adoption by agriculturalists it should be investigated whether GPSTIC can still make acceptable estimates of E with less costly, lower quality industrial grade (or consumer grade?) sensors and logging systems.

REFERENCES

Abu-Hamdeh, N. H., 2003. 'Thermal properties of soils as affected by density and water content', *Biosystems Engineering* **86**(1), 97–102.

Ait Hssaine, B., Merlin, O., Ezzahar, J., Ojha, N., Er-Raki, S. & Khabba, S., 2020. 'An evapotranspiration model self-calibrated from remotely sensed surface soil moisture, land surface temperature and vegetation cover fraction: application to disaggregated SMOS and MODIS data.', *Hydrology & Earth System Sciences* **24**(4).

Allen, R. G., Pereira, L. S., Raes, D., Smith, M. et al., 1998. 'Crop Evapotranspiration - Guidelines for computing crop water requirements-FAO Irrigation and Drainage Paper 56', *FAO, Rome* **300**(9), D05109.

Allen, R. G., Tasumi, M. & Trezza, R., 2007. 'Satellite-based energy balance for mapping evapotranspiration with internalized calibration (METRIC) — model', *Journal of Irrigation and Drainage Engineering* **133**(4), 380–394.

Allen, R. G., Walter, I. A., Elliott, R. L., Howell, T. A., Itenfisu, D., Jensen, M. E. & Snyder, R. L., 2005. The ASCE Standardized Reference Evapotranspiration Equation, American Society of Civil Engineers.

Aminzadeh, M. & Or, D., 2014. 'Energy partitioning dynamics of drying terrestrial surfaces', *Journal of Hydrology* **519**, 1257–1270.

Anderson, M., Norman, J., Diak, G., Kustas, W. & Mecikalski, J., 1997. 'A two-source time-integrated model for estimating surface fluxes using thermal infrared remote sensing', *Remote Sensing of the Environment* **60**, 195–216.

Angus, D. & Watts, P., 1984. 'Evapotranspiration — how good is the Bowen ratio method?', *Agricultural Water Management* **8**(1-3), 133–150.

Apogee, 2018. 'Infrared Radiometer Owner's Manual', https://www.apogeeinstruments.com/content/SI-400-manual.pdf.

Aschonitis, V., Demertzi, K., Papamichail, D., Colombani, N. & Mastrocicco, M., 2015. 'Revisiting the Priestley-Taylor method for the assessment of reference crop evapotranspiration in Italy', *Italian Journal of Agrometeorology* **20**(2), 5–18.

ASTM International, 2015. 'ASTM G183-15: Standard practice for field use of pyranometers, pyrheliometers and UV radiometers'. **URL:** *https://www.astm.org/Standards/G183.htm*

Baik, J. & Choi, M., 2015. 'Evaluation of remotely sensed actual evapotranspiration products from COMS and MODIS at two different flux tower sites in Korea', *International Journal of Remote Sensing* **36**(1), 375–402.

Ball, J. T., Woodrow, I. E. & Berry, J. A., 1987. A model predicting stomatal conductance and its contribution to the control of photosynthesis under different environmental conditions, *in* 'Progress in Photosynthesis Research', Springer, pp. 221–224.

Barton, I., 1979. 'A parameterization of the evaporation from nonsaturated surfaces', *Journal of Applied Meteorology* **18**(1), 43–47.

Bastiaanssen, W. G., Menenti, M., Feddes, R. & Holtslag, A., 1998. 'A remote sensing surface energy balance algorithm for land (SEBAL). 1. Formulation', *Journal of Hydrology* **212**, 198–212.

Bateni, S., Entekhabi, D., Margulis, S., Castelli, F. & Kergoat, L., 2014. 'Coupled estimation of surface heat fluxes and vegetation dynamics from remotely sensed land surface temperature and fraction of photosynthetically active radiation', *Water Resources Research* **50**(11), 8420–8440.

Bhattarai, N., Mallick, K., Brunsell, N. A., Sun, G. & Jain, M., 2018. 'Regional evapotranspiration from image-based implementation of the Surface Temperature Initiated Closure (STIC1. 2) model and its validation across an aridity gradient in the conterminous United States', *Hydrology and Earth System Sciences* **22**(4), 2311–2341.

Bhattarai, N., Mallick, K., Stuart, J., Vishwakarma, B. D., Niraula, R., Sen, S. & Jain, M., 2019. 'An automated multi-model evapotranspiration mapping framework using remotely sensed and reanalysis data', *Remote Sensing of Environment* **229**, 69–92.

Bhattarai, N., Quackenbush, L. J., Im, J. & Shaw, S. B., 2017. 'A new optimized algorithm for automating endmember pixel selection in the SEBAL and METRIC models', *Remote Sensing of Environment* **196**, 178–192.

Biscoe, P. V., Scott, R. & Monteith, J., 1975. 'Barley and its environment. iii. carbon budget of the stand', *Journal of Applied Ecology* pp. 269–293.

Black, T. A., 1979. 'Evapotranspiration from Douglas fir stands exposed to soil water deficits', *Water Resources Research* **15**(1), 164–170.

Blad, B. L. & Rosenberg, N. J., 1974. 'Lysimetric calibration of the Bowen ratio-energy balance method for evapotranspiration estimation in the Central Great Plains', *Journal of Applied Meteorology* **13**(2), 227–236.

Blonquist, J., Norman, J. & Bugbee, B., 2009. 'Automated measurement of canopy stomatal conductance based on infrared temperature', *Agricultural and Forest Meteorology* **149**(12), 2183–2197.

Boegh, E., Soegaard, H. & Thomsen, A., 2002. 'Evaluating evapotranspiration rates and surface conditions using Landsat TM to estimate atmospheric resistance and surface resistance', *Remote Sensing of Environment* **79**(2-3), 329–343.

Bouchet, R., 1963. 'Evapotranspiration reelle et potentielle, signification climatique', *International Association of Science and Hydrology* **62**(6), 134–142.

Bowen, I. S., 1926. 'The ratio of heat losses by conduction and by evaporation from any water surface', *Physical Review* **27**(6), 779.

Brockamp, B. & Wenner, H., 1963. 'Verdunstungsmessungen auf den Steiner See bei Münster', *Dt Gewässerkundl Mitt* **7**, 149–154.

Brutsaert, W., 1982. Energy Budget and Related Methods, *in* 'Evaporation into the Atmosphere', Springer, pp. 209–230.

Brutsaert, W. & Stricker, H., 1979. 'An advection-aridity approach to estimate actual regional evapotranspiration', *Water Resources Research* **15**(2), 443–450.

Buck, A., 1996. 'Model Cr-1a Hygrometer with Autofill Operating Manual', *Buck Research Instruments LLC: Aurora, CO, USA* . **URL:** *http://www.hygrometers.com/wp-content/uploads/CR-1A-users-manual-2009-12.pdf*

Buck, A. L., 1981. 'New equations for computing vapor pressure and enhancement factor', *Journal of Applied Meteorology* **20**(12), 1527–1532.

Campbell, A., 1973. 'The effect of stability on evaporation rates measured by the energy balance method', *Agricultural Meteorology* **11**, 261–267.

Campbell Scientific, 2005. 'Bowen Ratio Instrumentation: Instruction Manual 9/05', http://s.campbellsci.com/documents/au/manuals/bowen.pdf.

Carlson, T. N., Capehart, W. J. & Gillies, R. R., 1995. 'A new look at the simplified method for remote sensing of daily evapotranspiration', *Remote Sensing of Environment* **54**(2), 161–167.

Castellvi, F., Stockle, C., Perez, P. & Ibanez, M., 2001. 'Comparison of methods for applying the Priestley-Taylor equation at a regional scale', *Hydrological Processes* **15**(9), 1609–1620.

Cellier, P. & Brunet, Y., 1992. 'Flux-gradient relationships above tall plant canopies', *Agricultural and Forest Meteorology* **58**(1-2), 93–117.

Cellier, P. & Olioso, A., 1993. 'A simple system for automated long-term Bowen ratio measurement', *Agricultural and Forest Meteorology* **66**(1-2), 81–92.

Cleugh, H. A., Leuning, R., Mu, Q. & Running, S. W., 2007. 'Regional evaporation estimates from flux tower and MODIS satellite data', *Remote Sensing of Environment* **106**(3), 285–304.

Comunian, A., Giudici, M., Landoni, L. & Pugnaghi, S., 2018. 'Improving Bowen-ratio estimates of evaporation using a rejection criterion and multiple-point statistics', *Journal of Hydrology* **563**, 43–50.

Cook, R. D. & Weisberg, S., 1994. *An Introduction To Regression Graphics*, Wiley Series In Probability And Mathematical Statistics, John Wiley & Sons, New York.

Courault, D., Seguin, B. & Olioso, A., 2005. 'Review on estimation of evapotranspiration from remote sensing data: From empirical to numerical modeling approaches', *Irrigation and Drainage Systems* **19**(3-4), 223–249.

Cummings, N. W. & Richardson, B., 1927. ‘Evaporation from lakes’, *Physical Review* **30**(4), 527.

Davies, J. & Allen, C., 1973. ‘Equilibrium, potential and actual evaporation from cropped surfaces in southern Ontario’, *Journal of Applied Meteorology* **12**(4), 649–657.

De Bruin, H. & Holtslag, A., 1982. ‘A simple parameterization of the surface fluxes of sensible and latent heat during daytime compared with the Penman-Monteith concept’, *Journal of Applied Meteorology* **21**(11), 1610–1621.

De Veaux, R. D., Velleman, P. F. & Bock, D. E., 2009. *Intro Stats, 3rd Ed.*, Pearson Boston:.

Denmead, O. & McIlroy, I., 1970. ‘Measurements of non-potential evaporation from wheat’, *Agricultural Meteorology* **7**, 285–302.

Dhungel, R., Allen, R. G., Trezza, R. & Robison, C. W., 2014. ‘Comparison of latent heat flux using aerodynamic methods and using the Penman–Monteith method with satellite-based surface energy balance’, *Remote Sensing* **6**(9), 8844–8877.

Dicken, U., Cohen, S. & Tanny, J., 2013. ‘Examination of the Bowen ratio energy balance technique for evapotranspiration estimates in screenhouses’, *Biosystems Engineering* **114**(4), 397–405.

Dyer, A., 1965. ‘Discussion on change of terrain roughness and the wind profile by HA Panofsky and AA Townsend’, *QJR Meteorol. Soc.* **91**, 241.

Dyer, A., 1967. ‘The turbulent transport of heat and water vapour in an unstable atmosphere’, *Quarterly Journal of the Royal Meteorological Society* **93**(398), 501–508.

Dyer, A. & Hicks, B., 1970. ‘Flux-gradient relationships in the constant flux layer’, *Quarterly Journal of the Royal Meteorological Society* **96**(410), 715–721.

Eichinger, W. E., Parlange, M. B. & Stricker, H., 1996. 'On the concept of equilibrium evaporation and the value of the Priestley-Taylor coefficient', *Water Resources Research* **32**(1), 161–164.

Erell, E., Leal, V. & Maldonado, E., 2005. 'Measurement of air temperature in the presence of a large radiant flux: an assessment of passively ventilated thermometer screens', *Boundary-Layer Meteorology* **114**(1), 205–231.

Escarabajal-Henarejos, D., Fernández-Pacheco, D., Molina-Martínez, J., Martínez-Molina, L. & Ruiz-Canales, A., 2015. 'Selection of device to determine temperature gradients for estimating evapotranspiration using energy balance method', *Agricultural Water Management* **151**, 136–147.

Euser, T., Luxemburg, W., Everson, C., Mengistu, M., Clulow, A. & Bastiaanssen, W., 2014. 'A new method to measure bowen ratios using high-resolution vertical dry and wet bulb temperature profiles', *Hydrology and Earth System Sciences* **18**(6), 2021–2032.

Fick, A., 1855. 'Ueber diffusion', *Annalen der Physik* **170**(1), 59–86.

Flint, A. L. & Childs, S. W., 1991. 'Use of the Priestley-Taylor evaporation equation for soil water limited conditions in a small forest clearcut', *Agricultural and Forest Meteorology* **56**(3-4), 247–260.

Fritschen, L. J., 1965. 'Accuracy of evapotranspiration determinations by the Bowen ratio method', *Hydrological Sciences Journal* **10**(2), 38–48.

Fritschen, L. & Simpson, J., 1982. An automatic system for measuring Bowen ratio gradients using platinum resistance elements, *in* '6th Symposium on Temperature; Its Measurement and Control in Science and Industry. March', Vol. 14, p. 18.

Fu, P. & Weng, Q., 2016. 'Consistent land surface temperature data generation from irregularly spaced Landsat imagery', *Remote Sensing of Environment* **184**, 175–187.

Fu, P., Xie, Y., Weng, Q., Myint, S., Meacham-Hensold, K. & Bernacchi, C., 2019. 'A physical model-based method for retrieving urban land surface temperatures under cloudy conditions', *Remote Sensing of Environment* **230**, 111191.

Gan, G. & Liu, Y., 2020. 'Inferring transpiration from evapotranspiration: A transpiration indicator using the Priestley-Taylor coefficient of wet environment', *Ecological Indicators* **110**, 105853.

Gao, Z., Bian, L. & Liu, S., 2005. 'Flux measurements in the near surface layer over a non-uniform crop surface in China', *Hydrology and Earth System Sciences Discussions* **2**(3), 1067–1085.

Garratt, J. & Hicks, B., 1973. 'Momentum, heat and water vapour transfer to and from natural and artificial surfaces', *Quarterly Journal of the Royal Meteorological Society* **99**(422), 680–687.

Gerhards, M., Schlerf, M., Mallick, K. & Udelhoven, T., 2019. 'Challenges and future perspectives of multi-/hyperspectral thermal infrared remote sensing for crop water-stress detection: A review', *Remote Sensing* **11**(10), 1240.

Giles, D., Black, T. & Spittlehouse, D., 1985. 'Determination of growing season soil water deficits on a forested slope using water balance analysis', *Canadian Journal of Forest Research* **15**(1), 107–114.

Gillies, R., Kustas, W. & Humes, K., 1997. 'A verification of the 'triangle' method for obtaining surface soil water content and energy fluxes from remote measurements of the Normalized Difference Vegetation Index (NDVI) and surface radiant temperature', *International Journal of Remote Sensing* **18**(15), 3145–3166.

Hanks, R., Allen, L. & Gardner, H., 1971. 'Advection and evapotranspiration of wide-row sorghum in the Central Great Plains 1', *Agronomy Journal* **63**(4), 520–527.

He, X., Xu, T., Bateni, S. M., Ek, M., Liu, S. & Chen, F., 2020. 'Mapping regional evapotranspiration in cloudy skies via variational assimilation of all-weather land surface temperature observations', *Journal of Hydrology* p. 124790.

He, X., Xu, T., Bateni, S. M., Neale, C. M., Auligne, T., Liu, S., Wang, K., Mao, K. & Yao, Y., 2018. 'Evaluation of the weak constraint data assimilation approach for estimating turbulent heat fluxes at six sites', *Remote Sensing* **10**(12), 1994.

He, X., Xu, T., Bateni, S. M., Neale, C. M., Liu, S., Auligne, T., Wang, K. & Zhu, S., 2019. 'Mapping regional turbulent heat fluxes via assimilation of MODIS land surface temperature data into an ensemble Kalman smoother framework', *Earth and Space Science* **6**(12), 2423–2442.

Heilman, J. L., Brittin, C. L. & Neale, C. M. U., 1989. 'Fetch requirements for Bowen ratio measurements of latent and sensible heat fluxes', *Agricultural and Forest Meteorology* **44**(3-4), 261–273.

Heinemann, A., Hoogenboom, G. & De Faria, R., 2002. 'Determination of spatial water requirements at county and regional levels using crop models and GIS: An example for the State of Parana, Brazil', *Agricultural Water Management* **52**(3), 177–196.

Hillel, D., 1971. *Soil and Water: Physical Principles and Processes*, Academic Press.

Hsieh, C.-I., Katul, G. & Chi, T.-w., 2000. 'An approximate analytical model for footprint estimation of scalar fluxes in thermally stratified atmospheric flows', *Advances in Water Resources* **23**(7), 765–772.

Hua, D., Hao, X., Zhang, Y. & Qin, J., 2020. 'Uncertainty assessment of potential evapotranspiration in arid areas, as estimated by the Penman-Monteith method', *Journal of Arid Land* **12**, 166–180.

Huband, N. & Monteith, J., 1986. 'Radiative surface temperature and energy balance of a wheat canopy', *Boundary-Layer Meteorology* **36**(1-2), 1–17.

Hukseflux, 2016. 'User Manual HFP01SC v1624', https://www.hukseflux.com/sites/default/files/product_manual/HFP01SC_manual_v1624.pc

Hukseflux, 2017. 'User Manual NR01,RA01 v1710', https://www.hukseflux.com/sites/default/files/product_manual/NR01_RA01_manual_v1710.

Huschke, R. E. et al., 1959. 'Glossary of meteorology'.

Huwald, H., Higgins, C. W., Boldi, M.-O., Bou-Zeid, E., Lehning, M. & Parlange, M. B., 2009. 'Albedo effect on radiative errors in air temperature measurements', *Water Resources Research* **45**(8).

Irmak, S., 2010. 'Nebraska water and energy flux measurement, modeling, and research network (NEBFLUX)', *Transactions of the ASABE* **53**(4), 1097–1115.

Irmak, S., Kilic, A. & Chatterjee, S., 2014b. 'On the equality assumption of latent and sensible heat energy transfer coefficients of the Bowen ratio theory for evapotranspiration estimations: Another look at the potential causes of inequalities', *Climate* **2**(3), 181–205.

Irmak, S., Skaggs, K. E. & Chatterjee, S., 2014a. 'A review of the Bowen ratio surface energy balance method for quantifying evapotranspiration and other energy fluxes', *Transactions of the ASABE* **57**(6), 1657–1674.

Isbell, R., 2016. *The Australian Ssoil Classification*, CSIRO Publishing.

Islam, T., Hulley, G. C., Malakar, N. K., Radocinski, R. G., Guillevic, P. C. & Hook, S. J., 2017. 'A physics-based algorithm for the simultaneous retrieval of land surface temperature and emissivity from VIIRS thermal infrared data', *IEEE Transactions on Geoscience and Remote Sensing* **55**(1), 563–576.

Jacobs, W. C., 1942. 'On the energy exchange between sea and atmosphere', *J. mar. Res* **5**(1), 37.

Jacobs, W. C., 1943. 'Sources of atmospheric heat and moisture over the North Pacific and North Atlantic Oceans', *Annals of the New York Academy of Sciences* **44**(1), 19–40.

Jarvis, P., 1976. 'The interpretation of the variations in leaf water potential and stomatal conductance found in canopies in the field', *Philosophical Transactions of the Royal Society of London. B, Biological Sciences* **273**(927), 593–610.

Jiang, L. & Islam, S., 2001. 'Estimation of surface evaporation map over southern Great Plains using remote sensing data', *Water Resources Research* **37**(2), 329–340.

Jones, H. G., 2013. *Plants and Microclimate: A quantitative approach to environmental plant physiology*, Cambridge University Press.

Jung, M., Reichstein, M. & Bondeau, A., 2009. 'Towards global empirical upscaling of FLUXNET eddy covariance observations: validation of a model tree ensemble approach using a biosphere model'.

Jung, M., Reichstein, M., Ciais, P., Seneviratne, S. I., Sheffield, J., Goulden, M. L., Bonan, G., Cescatti, A., Chen, J., De Jeu, R. et al., 2010. 'Recent decline in the global land evapotranspiration trend due to limited moisture supply', *Nature* **467**(7318), 951–954.

Jury, W. & Tanner, C., 1975. 'Advection modification of the Priestley and Taylor evapotranspiration formula 1', *Agronomy Journal* **67**(6), 840–842.

Kalma, J. & Jupp, D., 1990. 'Estimating evaporation from pasture using infrared thermometry: evaluation of a one-layer resistance model', *Agricultural and Forest Meteorology* **51**(3-4), 223–246.

Katul, G., Goltz, S. M., Hsieh, C.-I., Cheng, Y., Mowry, F. & Sigmon, J., 1995. 'Estimation of surface heat and momentum fluxes using the flux-variance method above uniform and non-uniform terrain', *Boundary-Layer Meteorology* **74**(3), 237–260.

Kelliher, F. M., Leuning, R., Raupach, M. & Schulze, E.-D., 1995. 'Maximum conductances for evaporation from global vegetation types', *Agricultural and Forest Meteorology* **73**(1-2), 1–16.

Kustas, W. & Norman, J., 1996. 'Use of remote sensing for evapotranspiration monitoring over land surfaces', *Hydrological Sciences Journal* **41**(4), 495–516.

Kustas, W. P., 1990. 'Estimates of evapotranspiration with a one-and two-layer model of heat transfer over partial canopy cover', *Journal of Applied Meteorology* **29**(8), 704–715.

Kustas, W. P. & Norman, J. M., 1999. 'Evaluation of soil and vegetation heat flux predictions using a simple two-source model with radiometric temperatures for partial canopy cover', *Agricultural and Forest Meteorology* **94**(1), 13–29.

Lafleur, P. M., Rouse, W. R. & Carlson, D. W., 1992. 'Energy balance differences and hydrologic impacts across the northern treeline', *International Journal of Climatology* **12**(2), 193–203.

Lang, A., McNaughton, K., Fazu, C., Bradley, E. F. & Ohtaki, E., 1983a. 'Inequality of eddy transfer coefficients for vertical transport of sensible and latent heats during advective inversions', *Boundary-Layer Meteorology* **25**(1), 25–41.

Lang, A., McNaughton, K., Fazu, C., Bradley, E. F. & Ohtaki, E., 1983b. 'An experimental appraisal of the terms in the heat and moisture flux equations for local advection', *Boundary-Layer Meteorology* **25**(1), 89–102.

Lawrence, M. G., 2005. 'The relationship between relative humidity and the dewpoint temperature in moist air: A simple conversion and applications', *Bulletin of the American Meteorological Society* **86**(2), 225–234.

Leclerc, M. & Thurtell, G., 1990. 'Footprint prediction of scalar fluxes using a Markovian analysis', *Boundary-Layer Meteorology* **52**(3), 247–258.

Lenters, J. D., Kratz, T. K. & Bowser, C. J., 2005. 'Effects of climate variability on lake evaporation: Results from a long-term energy budget study of Sparkling Lake, northern Wisconsin (USA)', *Journal of Hydrology* **308**(1-4), 168–195.

Lettau, H. & Davidson, B., 1957. Exploring the atmosphere's first mile, Symposium Publications Division, Pergamon Press.

Leuning, R., 1995. 'A critical appraisal of a combined stomatal-photosynthesis model for C3 plants', *Plant, Cell & Environment* **18**(4), 339–355.

Leuning, R., Zhang, Y., Rajaud, A., Cleugh, H. & Tu, K., 2008. 'A simple surface conductance model to estimate regional evaporation using MODIS leaf area index and the Penman-Monteith equation', *Water Resources Research* **44**(10).

Lewis, J., 1995. 'The story behind the Bowen ratio', *Bulletin of the American Meteorological Society* **76**(12), 2433–2443.

Lhomme, J.-P., 1997. 'A theoretical basis for the Priestley-Taylor coefficient', *Boundary-Layer Meteorology* **82**(2), 179–191.

Li, Z.-L., Tang, R., Wan, Z., Bi, Y., Zhou, C., Tang, B., Yan, G. & Zhang, X., 2009. 'A review of current methodologies for regional evapotranspiration estimation from remotely sensed data', *Sensors* **9**(5), 3801–3853.

Lindroth, A. & Halldin, S., 1990. 'Gradient measurements with fixed and reversing temperature and humidity sensors above a thin forest', *Agricultural and Forest Meteorology* **53**(1-2), 81–103.

Liou, Y.-A., Le, M. S. & Chien, H., 2018. 'Normalized difference latent heat index for remote sensing of land surface energy fluxes', *IEEE Transactions on Geoscience and Remote Sensing* **57**(3), 1423–1433.

Liu, B. Y. & Jordan, R. C., 1960. 'The interrelationship and characteristic distribution of direct, diffuse and total solar radiation', *Solar Energy* **4**(3), 1–19.

Long, D., Longuevergne, L. & Scanlon, B. R., 2014. 'Uncertainty in evapotranspiration from land surface modeling, remote sensing, and GRACE satellites', *Water Resources Research* **50**(2), 1131–1151.

Ma, N., Zhang, Y., Szilagyi, J., Guo, Y., Zhai, J. & Gao, H., 2015. 'Evaluating the complementary relationship of evapotranspiration in the alpine steppe of the Tibetan Plateau', *Water Resources Research* **51**(2), 1069–1083.

Ma, Y., Liu, S., Song, L., Xu, Z., Liu, Y., Xu, T. & Zhu, Z., 2018. 'Estimation of daily evapotranspiration and irrigation water efficiency at a Landsat-like scale for an arid irrigation area using multi-source remote sensing data', *Remote Sensing of Environment* **216**, 715–734.

Mahato, S. & Pal, S., 2019. 'Influence of land surface parameters on the spatio-seasonal land surface temperature regime in rural West Bengal, India', *Advances in Space Research* **63**(1), 172–189.

Malek, E. & Bingham, G. E., 1993. 'Comparison of the Bowen ratio-energy balance and the water balance methods for the measurement of evapotranspiration', *Journal of Hydrology* **146**, 209–220.

Malek, E., Bingham, G. E. & McCurdy, G. D., 1990. 'Evapotranspiration from the margin and moist playa of a closed desert valley', *Journal of Hydrology* **120**(1-4), 15–34.

Mallick, K., Boegh, E., Trebs, I., Alfieri, J. G., Kustas, W. P., Prueger, J. H., Niyogi, D., Das, N., Drewry, D. T. & Hoffmann, L., 2015a. 'Reintroducing radiometric surface temperature into the Penman-Monteith formulation', *Water Resources Research* **51**(8), 6214–6243.

Mallick, K., Jarvis, A., Fisher, J. B., Tu, K. P., Boegh, E. & Niyogi, D., 2013. 'Latent heat flux and canopy conductance based on Penman–Monteith, Priestley–Taylor equation, and Bouchets complementary hypothesis', *Journal of Hydrometeorology* **14**(2), 419–442.

Mallick, K., Jarvis, A. J., Boegh, E., Fisher, J. B., Drewry, D. T., Tu, K. P., Hook, S. J., Hulley, G., Ardö, J. & Beringer, J., 2014. 'A surface temperature initiated closure (STIC) for surface energy balance fluxes', *Remote Sensing of Environment* **141**, 243–261.

Mallick, K., Jarvis, A., Wohlfahrt, G., Kiely, G., Hirano, T., Miyata, A., Yamamoto, S. & Hoffmann, L., 2015b. 'Components of near-surface energy balance derived from satellite soundings–Part 1: Noontime net available energy', *Biogeosciences* **12**(2), 433–451.

Mallick, K., Toivonen, E., Trebs, I., Boegh, E., Cleverly, J., Eamus, D., Koivusalo, H., Drewry, D., Arndt, S. K., Griebel, A. et al., 2018. 'Bridging Thermal Infrared Sensing and Physically-Based Evapotranspiration Modeling: From Theoretical Implementation to Validation Across an Aridity Gradient in Australian Ecosystems', *Water Resources Research* **54**(5), 3409–3435.

Mallick, K., Trebs, I., Boegh, E., Giustarini, L., Schlerf, M., Drewry, D. T., Hoffmann, L., Randow, C. v., Kruijt, B., Araùjo, A. et al., 2016. 'Canopy-scale biophysical controls of transpiration and evaporation in the Amazon Basin', *Hydrology and Earth System Sciences* **20**(10), 4237–4264.

McAneney, K. & Itier, B., 1996. 'Operational limits to the Priestley-Taylor formula', *Irrigation Science* **17**(1), 37–43.

McAneney, K. J., Green, A. E. & Astill, M. S., 1995. 'Large-aperture scintillometry: the homogeneous case', *Agricultural and Forest Meteorology* **76**(3-4), 149–162.

McEwen, G. F., 1937. *Some Energy Relations Between The Sea Surface And The Atmosphere*, Yale University.

McIlroy, I., 1971. 'An instrument for continuous recording of natural evaporation', *Agricultural Meteorology* **9**, 93–100.

McMahon, T., Peel, M., Lowe, L., Srikanthan, R., McVicar, T. et al., 2013. 'Estimating actual, potential, reference crop and pan evaporation using standard meteorological data: a pragmatic synthesis', *Hydrology and Earth System Sciences* **17**(4), 1331–1363.

McNaughton, K. & Black, T. A., 1973. 'A study of evapotranspiration from a Douglas fir forest using the energy balance approach', *Water Resources Research* **9**(6), 1579–1590.

McNeil, D. D. & Shuttleworth, W. J., 1975. 'Comparative measurements of the energy fluxes over a pine forest', *Boundary-Layer Meteorology* **9**(3), 297–313.

McShane, R. R., Driscoll, K. P. & Sando, R., 2017. 'A review of surface energy balance models for estimating actual evapotranspiration with remote sensing at high spatiotemporal resolution over large extents', *Scientific Investigations Report 2017–5087. Reston, VA: US Geological Survey* .

Meijninger, W. M. L., Green, A. E., Hartogensis, O. K., Kohsiek, W., Hoedjes, J. C. B., Zuurbier, R. M. & De Bruin, H. A. R., 2002.

'Determination of area-averaged water vapour fluxes with large aperture and radio wave scintillometers over a heterogeneous surface – Flevoland field experiment', *Boundary-Layer Meteorology* **105**(1), 63–83.

Miao, X., Zhang, Y., Zhang, J. & Zhou, X., 2019. 'Temperature and emissivity smoothing separation with nonlinear relation of brightness temperature and emissivity for thermal infrared sensors', *Remote Sensing* **11**(24), 2959.

Michel, D., Philipona, R., Ruckstuhl, C., Vogt, R. & Vuilleumier, L., 2008. 'Performance and uncertainty of CNR1 net radiometers during a one-year field comparison', *Journal of Atmospheric and Oceanic Technology* **25**(3), 442–451.

Michell Instruments, 2017. *Hygrosmart HS3 Advanced RH & Temperature Probe User's Manual*, 97516 Issue 5 edn.

Millar, G., McGarry, D., Gardner, E. & Gunawardena, A., 2006. 'Deep drainage and irrigation management'.

Miralles, D., Holmes, T., De Jeu, R., Gash, J., Meesters, A. & Dolman, A., 2011. 'Global land-surface evaporation estimated from satellite-based observations', *Hydrology and Earth System Sciences* **15**(2), 453.

Moges, S., Katambara, Z. & Bashar, K., 2003. 'Decision support system for estimation of potential evapotranspiration in Pangani Basin', *Physics and Chemistry of the Earth, Parts A/B/C* **28**(20-27), 927–934.

Monin, A. & Obukhov, A., 1954. 'Basic laws of turbulent mixing in the surface layer of the atmosphere', *Contributions by the Geophysical Institute of the Academy of Sciences USSR* **151**(163), e187.

Monteith, J. L., 1965. Evaporation and environment. the state and movement of water in living organisms., *in* 'Symposia of the Society for Experimental Biology', Vol. 19, p. 4.

Monteith, J. L., 1973. *Principles of Environmental Physics*, Edward Arnold London.

Monteith, J. L., 1981. 'Evaporation and surface temperature', *Quarterly Journal of the Royal Meteorological Society* **107**(451), 1–27.

Monteith, J. L. & Unsworth, M., 2013. *Principles of Environmental Physics: Plants, Animals, and the Atmosphere*, Academic Press.

Morari, F. & Giardini, L., 2001. 'Estimating evapotranspiration in the Padova Botanical Garden', *Irrigation Science* **20**(3), 127–137.

Morton, F. I., 1965. 'Potential evaporation and river basin evaporation', *Journal of the Hydraulics Division* **91**(6), 67–97.

Mu, Q., Heinsch, F. A., Zhao, M. & Running, S. W., 2007. 'Development of a global evapotranspiration algorithm based on MODIS and global meteorology data', *Remote Sensing of Environment* **111**(4), 519–536.

Mu, Q., Zhao, M. & Running, S. W., 2011. 'Improvements to a MODIS global terrestrial evapotranspiration algorithm', *Remote Sensing of Environment* **115**(8), 1781–1800.

Mukammal, E. & Neumann, H., 1977. 'Application of the Priestley-Taylor evaporation model to assess the influence of soil moisture on the evaporation from a large weighing lysimeter and class A pan', *Boundary-Layer Meteorology* **12**(2), 243–256.

Munro, D. & Oke, T., 1975. 'Aerodynamic boundary-layer adjustment over a crop in neutral stability', *Boundary-Layer Meteorology* **9**(1), 53–61.

Nakamura, R. & Mahrt, L., 2005. 'Air temperature measurement errors in naturally ventilated radiation shields', *Journal of Atmospheric and Oceanic Technology* **22**(7), 1046–1058.

Nie, D., Kanemasu, E., Fritschen, L., Weaver, H., Smith, E., Verma, S., Field, R., Kustas, W. & Stewart, J., 1992. 'An intercomparison of surface energy flux measurement systems used during FIFE 1987', *Journal of Geophysical Research: Atmospheres* **97**(D17), 18715–18724.

Nishida, K., Nemani, R. R., Glassy, J. M. & Running, S. W., 2003. 'Development of an evapotranspiration index from Aqua/MODIS for monitoring surface moisture status', *IEEE Transactions on Geoscience and Remote Sensing* **41**(2), 493–501.

Norman, J., Anderson, M., Kustas, W., French, A., Mecikalski, J., Torn, R., Diak, G., Schmugge, T. & Tanner, B., 2003. 'Remote sensing of surface energy fluxes at 10m pixel resolutions', *Water Resources Research* **39**(8).

Norman, J., Kustas, W. & Humes, K., 1995. 'A two-source approach for estimating soil and vegetation energy fluxes in observations of directional radiometric surface temperature', *Agricultural and Forest Meteorology* **77**, 263–293.

Obringer, R., Zhang, X., Mallick, K., Alemohammad, S. & Niyogi, D., 2016. 'Assessing urban droughts in a smart city framework', *International Archives of the Photogrammetry, Remote Sensing & Spatial Information Sciences* **41**.

Ochsner, T. E., Sauer, T. J. & Horton, R., 2006. 'Field tests of the soil heat flux plate method and some alternatives', *Agronomy Journal* **98**(4), 1005.

O'Dell, D. B., Sauer, T. J., Hicks, B. B., Lambert, D. M., Smith, D. R., Bruns, W., Basson, A., Marake, M. V., Walker, F., Wilcox Jr, M. D.

et al., 2014. 'Bowen ratio energy balance measurement of carbon dioxide (CO2) fluxes of no-till and conventional tillage agriculture in Lesotho', *Open Journal of Soil Science* .

Ohmura, A., 1982. 'Objective criteria for rejecting data for Bowen ratio flux calculations', *Journal of Applied Meteorology* **21**(4), 595–598.

Olejnik, J., 1996. 'Catchment scale modelling of heat and water balance structure under present and future climatic conditions', *Roczniki Akademii Rolniczej w Poznaniu* **268**.

Olejnik, J., Eulenstein, F., Kêdziora, A. & Werner, A., 2001*a*. 'Comparison of daily evapotranspiration rates obtained from water balance model and modified Bowen's ratio method', *International Agrophysics* **15**(1), 37–50.

Olejnik, J., Eulenstein, F., Kedziora, A. & Werner, A., 2001*b*. 'Evaluation of a water balance model using data for bare soil and crop surfaces in Middle Europe', *Agricultural and Forest Meteorology* **106**(2), 105–116.

Omega, 2019. 'What is the difference between a 2, 3 and 4 wire RTD?', https://www.omega.com/en-us/resources/rtd-2-3-4-wire-connections.

Oswald, C. J. & Rouse, W. R., 2004. 'Thermal characteristics and energy balance of various-size Canadian Shield lakes in the Mackenzie River Basin', *Journal of Hydrometeorology* **5**(1), 129–144.

Panofsky, H. A. & Townsend, A., 1964. 'Change of terrain roughness and the wind profile', *Quarterly Journal of the Royal Meteorological Society* **90**(384), 147–155.

Pasquier, C., Bourennane, H., Cousin, I., Séger, M., Dabas, M., Thiesson, J. & Tabbagh, J., 2016. 'Comparison between thermal airborne remote sensing, multi-depth electrical resistivity profiling, and soil mapping: an example from Beauce (Loiret, France)', *Near Surface Geophysics* **14**(4), 345–356.

Payero, J., Neale, C., Wright, J. & Allen, R., 2003. 'Guidelines for validating bowen ratio data', *Transactions of the ASAE* **46**(4), 1051.

Peacock, C. E. & Hess, T. M., 2004. 'Estimating evapotranspiration from a reed bed using the Bowen ratio energy balance method', *Hydrological Processes* **18**(2), 247–260.

Penman, H. L., 1946. 'Some aspects of evaporation in nature', *Scientific Journal of the Royal College of Sciences* **16**, 117–129.

Penman, H. L., 1948. Natural evaporation from open water, bare soil and grass, *in* 'Proceedings of the Royal Society of London A: Mathematical, Physical and Engineering Sciences', Vol. 193, The Royal Society, pp. 120–145.

Pereira, A. R., 2004. 'The Priestley–Taylor parameter and the decoupling factor for estimating reference evapotranspiration', *Agricultural and Forest Meteorology* **125**(3-4), 305–313.

Perez, P., Castellvi, F., Ibanez, M. & Rosell, J., 1999. 'Assessment of reliability of Bowen ratio method for partitioning fluxes', *Agricultural and Forest Meteorology* **97**(3), 141–150.

Poznikova, G., Trnka, M., Fischer, M., Orsag, M. & Zalud, Z., 2012. 'Applicability of Bowen Ratio Energy Balance method in fetch limited conditions', *MendelNet* .

Price, J. C., 1990. 'Using spatial context in satellite data to infer regional scale evapotranspiration', *IEEE Transactions on Geoscience and Remote Sensing* **28**(5), 940–948.

Priestley, C., 1959. 'Turbulent transfer in the lower atmosphere'.

Priestley, C. & Taylor, R., 1972. 'On the assessment of surface heat flux and evaporation using large-scale parameters', *Monthly Weather Review* **100**(2), 81–92.

Pruitt, W., 1963. 'Application of several energy balance and aerodynamic evaporation equations under a wide range of stability', *Final Report to USAEPG on Contract No. DA-36-039-SC80334* pp. 107–124.

Pruitt, W. & Aston, M. J., 1963. 'Atmospheric and surface factors affecting evapotranspiration', *Final Report to USAEPG on Contract No. DA-36-039-SC80334* **80334**, 69–105.

Renner, M., Brenner, C., Mallick, K., Wizemann, H.-D., Conte, L., Trebs, I., Wei, J., Wulfmeyer, V., Schulz, K. & Kleidon, A., 2019. 'Using phase lags to evaluate model biases in simulating the diurnal cycle of evapotranspiration', *Hydrology and Earth System Sciences* **23**(1), 515–535.

Revfeim, K. & Jordan, R., 1976. 'Precision of evaporation measurements using the Bowen ratio', *Boundary-Layer Meteorology* **10**(2), 97–111.

Rider, N., 1954. 'Eddy diffusion of momentum, water vapour, and heat near the ground', *Philosophical Transactions of the Royal Society of London, A* **246**(918), 481–501.

Rider, N. & Robinson, G., 1951. 'A study of the transfer of heat and water vapour above a surface of short grass', *Quarterly Journal of the Royal Meteorological Society* **77**(333), 375–401.

Ringrose-Voase, A. & Nadelko, A., 2011. 'Quantifying deep drainage in an irrigated cotton landscape', *Final Report for Cotton Research and Development Corporation, Project CRC125/Cotton Catchment Communities Cooperative Research Centre Project* **1**, 12.

Roerink, G., Su, Z. & Menenti, M., 2000. 'S-SEBI: A simple remote sensing algorithm to estimate the surface energy balance', *Physics and Chemistry of the Earth, Part B: Hydrology, Oceans and Atmosphere* **25**(2), 147–157.

Rosenberg, N. J., Blad, B. L. & Verma, S. B., 1983. *Microclimate: the biological environment*, John Wiley & Sons.

Ryu, Y., Baldocchi, D. D., Kobayashi, H., van Ingen, C., Li, J., Black, T. A., Beringer, J., Van Gorsel, E., Knohl, A., Law, B. E. et al., 2011. 'Integration of MODIS land and atmosphere products with a coupled-process model to estimate gross primary productivity and evapotranspiration from 1 km to global scales', *Global Biogeochemical Cycles* **25**(4).

Sánchez, J. M., French, A. N., Mira, M., Hunsaker, D. J., Thorp, K. R., Valor, E. & Caselles, V., 2011. 'Thermal infrared emissivity dependence on soil moisture in field conditions', *IEEE Transactions on Geoscience and Remote Sensing* **49**(11), 4652–4659.

Savage, M. J., 2009. 'Estimation of evaporation using a dual-beam surface layer scintillometer and component energy balance measurements', *Agricultural and Forest Meteorology* **149**(3-4), 501–517.

Savage, M. J., 2010. 'Field evaluation of polymer capacitive humidity sensors for Bowen ratio energy balance flux measurements', *Sensors* **10**(8), 7748–7771.

Savage, M. J., Everson, C. S. & Metelerkamp, B. R., 2009. 'Bowen ratio evaporation measurement in a remote montane grassland: Data integrity and fluxes', *Journal of Hydrology* **376**(1-2), 249–260.

Schellenberg, R., 2002. 'The trouble with humidity: The hidden challenge of RH calibration', *Retrieved March 2017* **10**, 2014.

Schilperoort, B., Coenders-Gerrits, M., Luxemburg, W., Rodríguez, C. J., Vaca, C. C. & Savenije, H., 2018. 'Using distributed temperature sensing for Bowen ratio evaporation measurements', *Hydrology and Earth System Sciences* **22**(1), 819.

Schilperoort, B., Coenders-Gerrits, M., van Iersel, T., Jiménez Rodríguez, C., Luxemburg, W., Cisneros Vaca, C. & Ucer, M., 2017. Using Distributed Temperature Sensing for evaporation measurements: background, verification, and future applications., *in* 'EGU General Assembly Conference Abstracts', Vol. 19, p. 10577.

Schmid, H., 1994. 'Source areas for scalars and scalar fluxes', *Boundary-Layer Meteorology* **67**(3), 293–318.

Schmidt, W., 1915. 'Radiation and evaporation from an open water surface, a contribution to the heat budget of the world oceans and to the water budget of the earth', *Annals of Hydrological and Maritime Meteorology* **43**, 111–124.

Schuepp, P. H., Leclerc, M. Y., MacPherson, J. I. & Desjardins, R. L., 1990. 'Footprint prediction of scalar fluxes from analytical solutions of the diffusion equation', *Boundary-Layer Meteorology* **50**(1-4), 355–373.

Schymanski, S. J. & Or, D., 2017. 'Leaf-scale experiments reveal an important omission in the Penman-Monteith equation', *Hydrology and Earth System Sciences* **21**(2), 685.

Sexstone, G. A., Clow, D. W., Stannard, D. I. & Fassnacht, S. R., 2016. 'Comparison of methods for quantifying surface sublimation over seasonally snow-covered terrain', *Hydrological Processes* **30**(19), 3373–3389.

Sheffield, J., Wood, E. F. & Munoz-Arriola, F., 2010. 'Long-term regional estimates of evapotranspiration for Mexico based on downscaled ISCCP data', *Journal of Hydrometeorology* **11**(2), 253–275.

Shuttleworth, W. J., 2007. 'Putting the "vap" into evaporation', *Hydrology and Earth System Sciences* **11**(1), 210–244.

Shuttleworth, W. J. & Calder, I. R., 1979. 'Has the Priestley-Taylor equation any relevance to forest evaporation?', *Journal of Applied Meteorology* **18**(5), 639–646.

Sinclair, T., Allen, L. & Lemon, E., 1975. 'An analysis of errors in the calculation of energy flux densities above vegetation by a Bowen-ratio profile method', *Boundary-Layer Meteorology* **8**(2), 129–139.

Singh, R. K. & Irmak, A., 2011. 'Treatment of anchor pixels in the METRIC model for improved estimation of sensible and latent heat fluxes', *Hydrological sciences journal* **56**(5), 895–906.

Slatyer, R. O., McIlroy, I. C. et al., 1961. 'Practical microclimatology, with special reference to the water factor in soil-plant atmosphere relationships.', *Practical microclimatology.* .

Spittlehouse, D. & Black, T., 1980. 'Evaluation of the Bowen ratio/energy balance method for determining forest evapotranspiration', *Atmosphere-Ocean* **18**(2), 98–116.

Stannard, D. I., 1997. 'A theoretically based determination of Bowen-ratio fetch requirements', *Boundary-Layer Meteorology* **83**(3), 375–406.

Stewart, J. B., 1988. 'Modelling surface conductance of pine forest', *Agricultural and Forest meteorology* **43**(1), 19–35.

Stewart, R. B. & Rouse, W. R., 1977. 'Substantiation of the Priestley and Taylor parameter α= 1.26 for potential evaporation in high latitudes', *Journal of Applied Meteorology* **16**(6), 649–650.

Su, Z., 2002. 'The Surface Energy Balance System (SEBS) for estimation of turbulent heat fluxes', *Hydrology and Earth System Sciences* **6**(1), 85–99.

Sumner, D. & Jacobs, J., 2005. 'Utility of Penman-Monteith, Priestley-Taylor, reference evapotranspiration, and pan evaporation methods to estimate pasture evapotranspiration', *Journal of Hydrology* **308**(1), 81–104.

Sun, Z., Wang, Q., Matsushita, B., Fukushima, T., Ouyang, Z. & Watanabe, M., 2009. 'Development of a simple remote sensing evapotranspiration model (Sim-ReSET): algorithm and model test', *Journal of Hydrology* **376**(3-4), 476–485.

Suomi, V., 1957. 'Double-psychrometer lift apparatus', *Exploring the Atmosphere's First Mile* **1**, 183–187.

Sverdrup, H., 1943. 'On the ratio between heat conduction from the sea surface and heat used for evaporation', *Annals of the New York Academy of Sciences* **44**(1), 81–88.

Swinbank, W. & Dyer, A., 1967. 'An experimental study in micro-meteorology', *Quarterly Journal of the Royal Meteorological Society* **93**(398), 494–500.

Tabari, H. & Talaee, P. H., 2011. 'Local calibration of the Hargreaves and Priestley-Taylor equations for estimating reference evapotranspiration in arid and cold climates of Iran based on the Penman-Monteith model', *Journal of Hydrologic Engineering* **16**(10), 837–845.

Tajfar, E., Bateni, S., Lakshmi, V. & Ek, M., 2020. 'Estimation of surface heat fluxes via variational assimilation of land surface temperature, air temperature and specific humidity into a coupled land surface-atmospheric boundary layer model', *Journal of Hydrology* **583**, 124577.

Tajfar, E., Bateni, S. M., Heggy, E. & Xu, T., 2020. 'Feasibility of estimating turbulent heat fluxes via variational assimilation of reference-level air temperature and specific humidity observations', *Remote Sensing* **12**(7), 1065.

Tang, Q., Peterson, S., Cuenca, R. H., Hagimoto, Y. & Lettenmaier, D. P., 2009. 'Satellite-based near-real-time estimation of irrigated crop water consumption', *Journal of Geophysical Research: Atmospheres* **114**(D5).

Tanner, B. D., 1988. Use requirements for Bowen ratio and eddy correlation determination of evapotranspiration, *in* 'Planning now for irrigation and drainage in the 21st century', ASCE, pp. 605–616.

Tanner, B., Greene, J. & Bingham, G., 1987. 'A Bowen ratio design for long term measurements', *American Society of Agricultural Engineers* .

Tanner, C., 1960. 'Energy balance approach to evapotranspiration from crops 1', *Soil Science Society of America Journal* **24**(1), 1–9.

Tanner, C. & Pelton, W., 1960. 'Potential evapotranspiration estimates by the approximate energy balance method of Penman', *Journal of Geophysical Research* **65**(10), 3391–3413.

Tarara, J. M. & Hoheisel, G.-A., 2007. 'Low-cost shielding to minimize radiation errors of temperature sensors in the field', *HortScience* **42**(6), 1372–1379.

Tateishi, R. & Ahn, C., 1996. 'Mapping evapotranspiration and water balance for global land surfaces', *ISPRS Journal of Photogrammetry and Remote Sensing* **51**(4), 209–215.

Taylor, G. I., 1938. 'The Spectrum of Turbulence', *Proceedings of the Royal Society of London. Series A-Mathematical and Physical Sciences* **164**(919), 476–490.

Taylor, J., 1997. *Introduction to Error Analysis, The Study of Uncertainties in Physical Measurements, Second Edition*, 2nd edn, University Science Books.

Tetens, O., 1930. 'Uber einige meteorologische begriffe', *Zeitschrift fur Geophysik* **6**, 297–309.

Thornthwaite, C. W. & Holzman, B., 1942. *Measurement of evaporation from land and water surfaces*, number 817, US Department of Agriculture.

Tian, J., Song, S. & He, H., 2019. 'The relationship between soil emissivity and soil reflectance under the effects of soil water content', *Physics and Chemistry of the Earth, Parts A/B/C* **110**, 133–137.

Tomlinson, S., 1996. Comparison of Bowen-ratio, eddy-correlation, and weighing-lysimeter evapotranspiration for two sparse-canopy sites in eastern Washington, Technical report, US Dept. of the Interior, US Geological Survey; US Geological Survey, Branch of Information Services.

Udelhoven, T., Schlerf, M., Segl, K., Mallick, K., Bossung, C., Retzlaff, R., Rock, G., Fischer, P., Müller, A., Storch, T. et al., 2017. 'A satellite-based imaging instrumentation concept for hyperspectral thermal remote sensing', *Sensors* **17**(7), 1542.

Unland, H. E., Houser, P. R., Shuttleworth, W. J. & Yang, Z.-L., 1996. 'Surface flux measurement and modeling at a semi-arid Sonoran Desert site', *Agricultural and Forest Meteorology* **82**(1-4), 119–153.

Unsworth, M. H. & Monteith, J., 1972. 'Aerosol and solar radiation in Britain', *Quarterly Journal of the Royal Meteorological Society* **98**(418), 778–797.

Utset, A., Farre, I., Martınez-Cob, A. & Cavero, J., 2004. 'Comparing Penman–Monteith and Priestley–Taylor approaches as reference-evapotranspiration inputs for modeling maize water-use under Mediterranean conditions', *Agricultural Water Management* **66**(3), 205–219.

van Iersel, T., Coenders-Gerrits, A. & Schilperoort, B., 2016. 'Verifying the BR-DTS method with hand measurements executed with the PT-100 and the Eddy Covariance method'.

Verma, M., Fisher, J. B., Mallick, K., Ryu, Y., Kobayashi, H., Guillaume, A., Moore, G., Ramakrishnan, L., Hendrix, V., Wolf, S. et al., 2016. 'Global surface net-radiation at 5 km from MODIS Terra', *Remote Sensing* **8**(9), 739.

Verma, S. B., Rosenberg, N. J. & Blad, B. L., 1978. 'Turbulent exchange coefficients for sensible heat and water vapor under advective conditions', *Journal of Applied Meteorology* **17**(3), 330–338.

Vignola, F., Michalsky, J. & Stoffel, T., 2016. *Solar and Infrared Radiation Measurements*, CRC Press.

Wagle, P., Bhattarai, N., Gowda, P. H. & Kakani, V. G., 2017. 'Performance of five surface energy balance models for estimating daily evapotranspiration in high biomass sorghum', *ISPRS Journal of Photogrammetry and Remote Sensing* **128**, 192–203.

Wan, Z., Zhang, K., Xue, X., Hong, Z., Hong, Y. & Gourley, J. J., 2015. 'Water balance-based actual evapotranspiration reconstruction from ground and satellite observations over the conterminous United States', *Water Resources Research* **51**(8), 6485–6499.

Wang, K., Li, Z. & Cribb, M., 2006. 'Estimation of evaporative fraction from a combination of day and night land surface temperatures and NDVI: A new method to determine the Priestley–Taylor parameter', *Remote Sensing of Environment* **102**(3-4), 293–305.

Weiß, M. & Menzel, L., 2008. 'A global comparison of four potential evapotranspiration equations and their relevance to stream flow modelling in semi-arid environments.', *Advances in Geosciences* **18**.

Wight, J. R., Hanson, C. L. & Wright, J. L., 1993. 'Comparing Bowen ratio-energy balance systems for measuring ET', *http://eprints.nwisrl.ars.usda.gov/858/1/808.pdf* .

WMO, 1983. *Measurement of Radiation*, Guide to Meteorological Instruments and Methods of Observation, 7th Ed., WMO - No.8, World Meteorological Organisation, Geneva.

Xu, C.-Y. & Singh, V., 1998. 'Dependence of evaporation on meteorological variables at different time-scales and intercomparison of estimation methods', *Hydrological Processes* **12**(3), 429–442.

Xu, J., Peng, S., Ding, J., Wei, Q. & Yu, Y., 2013. 'Evaluation and calibration of simple methods for daily reference evapotranspiration estimation in humid East China', *Archives of Agronomy and Soil Science* **59**(6), 845–858.

Xu, T., He, X., Bateni, S. M., Auligne, T., Liu, S., Xu, Z., Zhou, J. & Mao, K., 2019. 'Mapping regional turbulent heat fluxes via variational assimilation of land surface temperature data from polar orbiting satellites', *Remote Sensing of Environment* **221**, 444–461.

Yadav, M. & Saxena, G., 1973. 'Effect of compaction and moisture content on specific heat and thermal capacity of soils', *Journal of the Indian Society of Soil Science* **21**(2), 129–132.

Yagci, A. L., Santanello, J. A., Jones, J. W. & Barr, J., 2017. 'Estimating evaporative fraction from readily obtainable variables in mangrove forests of the Everglades, USA', *International Journal of Remote Sensing* **38**(14), 3981–4007.

Yang, Y., Qiu, J., Su, H., Bai, Q., Liu, S., Li, L., Yu, Y. & Huang, Y., 2017. 'A one-source approach for estimating land surface heat fluxes using remotely sensed land surface temperature', *Remote Sensing* **9**(1), 43.

Yeh, G.-T. & Brutsaert, W., 1971. 'A solution for simultaneous turbulent heat and vapour transfer between a water surface and the atmosphere', *Boundary-Layer Meteorology* **2**(1), 64–82.

Zeng, Z., Piao, S., Lin, X., Yin, G., Peng, S., Ciais, P. & Myneni, R. B., 2012. ‘Global evapotranspiration over the past three decades: estimation based on the water balance equation combined with empirical models’, *Environmental Research Letters* **7**(1), 014026.

Zhang, K., Kimball, J. S., Mu, Q., Jones, L. A., Goetz, S. J. & Running, S. W., 2009. ‘Satellite based analysis of northern ET trends and associated changes in the regional water balance from 1983 to 2005’, *Journal of Hydrology* **379**(1-2), 92–110.

Zhang, K., Kimball, J. S., Nemani, R. R. & Running, S. W., 2010. ‘A continuous satellite-derived global record of land surface evapotranspiration from 1983 to 2006’, *Water Resources Research* **46**(9).

Zhang, K., Kimball, J. S., Nemani, R. R., Running, S. W., Hong, Y., Gourley, J. J. & Yu, Z., 2015. ‘Vegetation greening and climate change promote multidecadal rises of global land evapotranspiration’, *Scientific Reports* **5**, 15956.

Zhang, K., Kimball, J. S. & Running, S. W., 2016. ‘A review of remote sensing based actual evapotranspiration estimation’, *Wiley Interdisciplinary Reviews: Water* **3**(6), 834–853.

Zhang, M., Wang, B., Cleverly, J., Liu, D. L., Feng, P., Zhang, H., Huete, A., Yang, X. & Yu, Q., 2020. ‘Creating new near-surface air temperature datasets to understand elevation-dependent warming in the Tibetan Plateau’, *Remote Sensing* **12**(11), 1722.

Zhao, W. L., Qiu, G. Y., Xiong, Y. J., Paw U, K. T., Gentine, P. & Chen, B. Y., 2020. ‘Uncertainties caused by resistances in evapotranspiration estimation using high-density eddy covariance measurements’, *Journal of Hydrometeorology* **21**(6), 1349–1365.

Zhu, W., Jia, S. & Lv, A., 2017. ‘A universal Ts-VI triangle method for the continuous retrieval of evaporative fraction from MODIS products’, *Journal of Geophysical Research: Atmospheres* .

Zhuang, Q., Wang, H. & Xu, Y., 2020. 'Comparison of Remote Sensing based multi-source ET models over cropland in a semi-humid region of China', *Atmosphere* **11**(4), 325.

Zhuang, Q., Wu, B., Yan, N., Zhu, W. & Xing, Q., 2016. 'A method for sensible heat flux model parameterization based on radiometric surface temperature and environmental factors without involving the parameter KB- 1', *International Journal of Applied Earth Observation and Geoinformation* **47**, 50–59.

APPENDICES

Appendix A

ADDITIONAL REVIEW OF BREB

A.1 Early Developments of BREB

Around the period of the late 19th to early 20th centuries there was a growing interest in determining the rates of evaporation and energy transfer from the world's oceans and lakes. Schmidt (1915) made what was probably the first attempt to estimate evaporation as a residual of an energy budget. To do so he introduced a ratio, R:

$$R = \frac{H}{\lambda E} \tag{A.1}$$

where the original symbols for the flux terms have been changed to be consistent with those used in this thesis. Combining Eqn. A.1 into the one-dimensional energy balance equation Schmidt provided a way to estimate an ocean's evaporation rate:

$$E = \frac{\phi}{\lambda\,(1 + R)} \tag{A.2}$$

However, just how to determine an appropriate value of R remained a contentious issue until Bowen (1926). Bowen had applied Fick's Law (Fick 1855) for molecular diffusion to water vapour and sensible heat over an open water surface to determine the value of R. Fortuitously, his work has also proven applicable to the turbulent flow regime the diffusivities in the molecular and turbulent transport regimes are of very similar magnitude (Lewis 1995). Bowen had observed that the molecular diffusion coefficients for water vapour and heat energy

> ...differ only by a few percent (a relationship predicted by the kinetic theory). This leads one to expect that heat losses by evaporation and diffusion, and by conduction will follow the same laws and will be affected in the same way by convection.

This allowed Bowen to make significant simplifying assumptions that led to an expression for R:

$$R = \frac{c_p\,P}{\epsilon}\,\frac{(T_2 - T_1)}{\lambda(T_2)\,e_2 - \lambda(T_1)\,e_1} \tag{A.3}$$

$$\approx \frac{c_p\,P}{\epsilon\,\lambda\left(\bar{T}\right)}\,\frac{(T_2 - T_1)}{(e_2 - e_1)} \tag{A.4}$$

The most significant assumption that Bowen made was that the diffusivities of λE and H (denoted by κ_W and κ_H, respectively) are equal. This was a major simplification because κ_W and κ_H are generally unknown and difficult to measure.

Thus Bowen had derived a way to determine Schmidt's ratio, which became known as the Bowen ratio following Sverdrup (1943), and the use of β replaced R following Penman (1946). The ratio was regarded as a constant until McEwen (1937) showed it to vary in space and time, and Lettau and Davidson (1957) showed it to vary between $-\infty$ and $+\infty$, usually twice per day.[1]

An attractive feature of Bowen's process for determining the Ratio was that it only required the collection of 'easily measurable quantities'

[1] $\beta > 1$ means that sensible heat is greater than latent heat, usually observed under dry conditions. Expected values are (approx.) $\beta > 10$ in deserts, $0.4 < \beta < 0.8$ in forests and dry grasslands, $\beta < 0.4$ in freely transpiring well-watered crops, and $\beta < 0.1$ over open water surfaces.

(Bowen 1926), namely air temperature, vapour pressure and air pressure. However, Bowen's process only achieved prominence following Jacobs (1942) and Jacobs (1943) where the Ratio was determined to make estimates of energy flux exchanges over the Pacific and Atlantic Oceans. Penman (1946) showed the Ratio R (subsequently β) could be applied over land surfaces. However, wider use of Bowen's process had to wait until the latter half of the 20$^{\text{th}}$ century when field instruments of adequate sensitivity and accuracy were developed.

A.2 Applications of BREB

Early use of BREB was for estimating E from large water bodies such as oceans and lakes (Bowen 1926, Cummings & Richardson 1927, Lenters et al. 2005). Since Penman (1946) it has also been applied in homogeneous agricultural cropping fields (Fritschen 1965, Blad & Rosenberg 1974, Irmak et al. 2014b), heterogeneous wetlands (Peacock & Hess 2004), forests (McNeil & Shuttleworth 1975, Spittlehouse & Black 1980, Lindroth & Halldin 1990), snow (Sexstone et al. 2016), deserts (Malek et al. 1990, Unland et al. 1996), on hillslopes (Nie et al. 1992) and even inside large screenhouses (Dicken et al. 2013).

A.3 Standard Approach to Calculate β

The standard (i.e. two-height) approach to calculate E_{BREB} from the Bowen Ratio, β, is as follows:

$$E_{BREB} = \frac{\phi}{\lambda\,(1+\beta)} \tag{A.5}$$

where

$$\phi = R_N + G \tag{A.6}$$

$$\beta = \frac{c_P\,P}{M_{ratio}}\,\frac{(T_2 - T_1)}{\lambda(T_2)\,e_2 - \lambda(T_1)\,e_1} \tag{A.7}$$

as per Bowen (1926). Eqn. A.7 can be approximated by

$$\beta = \frac{c_P\, P}{M_{ratio}\, \lambda\left(\overline{T}\right)} \frac{(T_2 - T_1)}{(e_2 - e_1)} \tag{A.8}$$

where c_P is the specific heat capacity of air, M_{ratio} is the molecular mass ratio of water vapour to air, and $\lambda\left(\overline{T}\right)$ is the latent heat of vapourisation of water at the mean of temperatures T_1 and T_2.

The latter term of Eqn. A.8 is the slope of the line between (e_1, T_1) and (e_2, T_2) on a T vs. e plot. It is standard practice, then, to implement the BREB method by measuring e and T at only two heights above a surface. However, because even identical sensors are rarely identical in performance, and because fine gradients of e and T are often involved,[2] it becomes necessary to repeatedly alternate the positions of the sensors to cancel out any systematic, persistent biases between the sensors.

Importantly, the two-height approach to BREB provides no way to know whether the sensors are correctly located within the IBL. Adequacy of fetch, appropriate sensor heights and their separation, and sensor settling times are thus important issues for BREB researchers.

A.4 Two-height BREB Systems

The popularisation of the two-height exchange systems (whether by mechanical exchange of sensors or by aspirating air from alternate heights) is often attributed to Tanner (1960) although Tanner and Tanner et al. (1987) acknowledged that Suomi (1957) had already been using a two-height exchange system. The alternating two-height approach has become the default approach to implementing BREB and its proponents have been unequivocal in their view as to the necessity of an alternating exchange system. Irmak et al. (2014a) stated that:

> …it has been proven (Fritschen 1965, Fritschen & Simpson 1982) that exchanging the air temperature and humidity

[2] The 'gradients' of e and T are ${}^{\Delta e}/_{\Delta z}$ and ${}^{\Delta T}/_{\Delta z}$, where z is height.

> sensor positions periodically and calculating the averages between consecutive periods is an essential part of the BREB method and must be done to remove sensor biases and obtain true gradients and accurate β and flux results ...Attempting to obtain true gradients continuously without exchanging the sensor positions is futile. The biases between the sensors have several sources, are not constant, and can only be seen when sensors have been exchanged.

Similarly, Spittlehouse and Black (1980) stated:

> The success of the Bowen ratio energy balance method in reliably measuring evapotranspiration is related to three factors: first, the periodic reversal of symmetrically constructed psychrometers in order to remove systematic measurement errors; second, the differential measurement of temperature over a distance of at least 3 m [3] ...Such a system is significantly more accurate than profile Bowen ratio systems especially those using absolute rather than differential temperature measurement.

However, Spittlehouse and Black (1980) did note that under some circumstances the biases do not cancel out, particularly when biases are position dependent. Revfeim and Jordan (1976) observed that there are not always significant accuracy benefits from aspirating air to a common sensor. Olejnik et al. (2001*b*) and Payero et al. (2003) – citing Angus and Watts (1984), Tanner (1988), and Heilman et al. (1989) – raised what might be the most concerning objection to the two-height BREB approaches: How does the operator of a two-height BREB system know if their measurements have been taken within the internal boundary layer (IBL)? (The answer is they don't.)

[3] Notably, very few two-height BREB systems in the literature had vertical separations of sensors greater than 1.5 m. This is in contrast to Profile BREB systems that often had vertical spans up to 4 m.

There is recourse to rules-of-thumb to guide placement of sensors so that they are (hopefully) within the IBL. However, the effects of such practices are three-fold. Firstly, there can be a false confidence in the quality of the calculated β.[4] Secondly, it constrains the use of BREB to situations where there is very large fetch. Heilman et al. (1989) attempted to refute the need for large fetch but did not give a satisfactory explanation as to how they knew their two-height BREB systems were inside the IBL. And thirdly, the operator cannot place their lower instruments close to the canopy because they might inadvertently (and undetectably) end up inside the surface roughness layer, i.e. below the IBL. This last point is significant because the temperature and humidity gradients are often greatest close to the canopy. Stannard (1997) wrote that the vertical separation between the lower sensors and the canopy should be minimised because this will reduce the accuracy and precision requirements of the sensors.

Another difficulty with the alternating two-height approaches is the need to allow time for stabilisation of the sensors to their new environment after they have exchanged positions (or time for newly aspirated air to flush out the 'old' air from the previous inlet height). Generally this requires a quiet period where no measurements are made following exchange. For example, Cellier and Olioso (1993) excluded measurements for 45 s following sensor exchange, and Tanner et al. (1987) excluded measurements for 40 s. However, this is not always done properly. Fritschen (1965), for example, reported time constants of 5 - 7 min for his thermocouples and dew probes but exchanged the sensor positions every 15 min, and Tanner et al. (1987) indicated that the time constant, τ, of their aspirated two-height BREB system was 5 min. It can be seen in Fig. A.1 (p. 337) that if $\tau = 5$ min it should take 15 min to achieve 95 % equalisation with the outside air. This should be a 'quiet' non-measurement period yet Tanner et al. reported that, after switching air inlets, 40 s quiet time was observed, then 80 s worth of measurements made, then

[4]This is especially concerning because BREB cannot be cross-checked by an energy closure analysis.

air inlets were switched to repeat the cycle.[5]

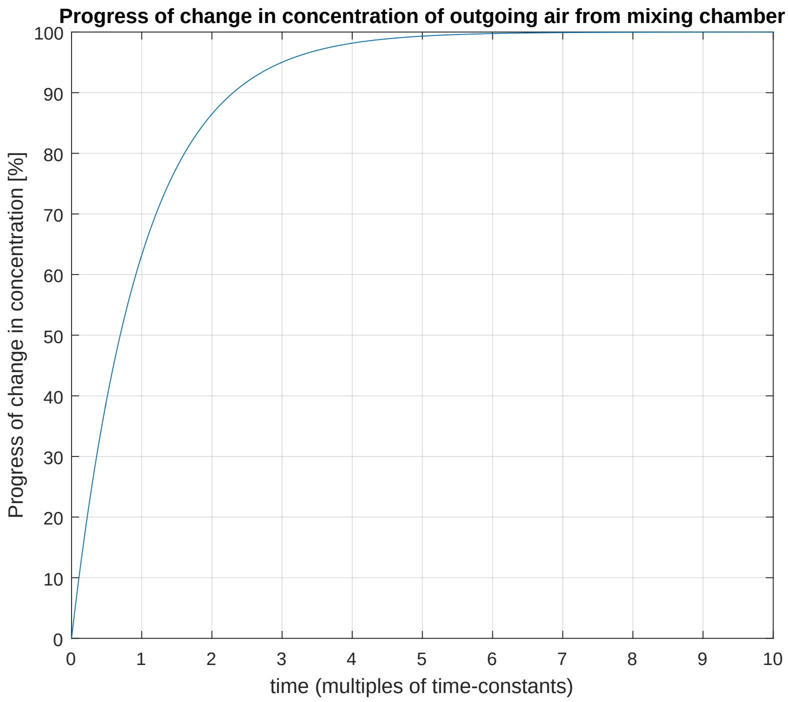

Figure A.1: Modelling the change in a concentration (e.g. of water vapour) inside a mixing chamber after a step-change in the concentration outside the chamber, if the air is being continuously aspirated through the mixing chamber. The modelled equation is $c_{out} = c_0 \exp\left(\frac{-t}{\tau}\right) + c_{in}\left[1 - \exp\left(\frac{-t}{\tau}\right)\right]$ where c_{out} is the concentration of the outflow [qty vol^{-1}], c_0 is the concentration prior to the step change [qty vol^{-1}], c_{in} is the incoming concentration [qty vol^{-1}], τ is the system time constant [s] where $\tau = \frac{\text{system volume}}{\text{flow rate}}$, and t is time [s]. Assumptions: rate of inflow equals rate of outflow; air is uniformly mixed inside chamber; step-change occurs at time $t = 0$.

There are other difficulties associated with two-height BREB systems such as air leaks in aspirated systems, alterations to heat and/or mois-

[5]Furthermore, the chromel-constantan thermocouples used by Tanner et al. have an absolute tolerance of $\pm 1.5\,^{\circ}$C for Class 1 sensors. Whilst it was the temperature *difference* that Tanner et al. were measuring, hence their use of differential voltage, not all of the tolerance was necessarily due to sensor offset error.

ture of aspirated air between the inlet and the measurement chamber,[6] mechanical complexity, and power requirements (especially if running vacuum pumps).

[6]Many aspirated systems, e.g. Campbell Scientific (2005), will thus measure T at the air inlets. This does, however, recall the original problem where two temperature sensors may have systematic biases between them. But it is, nevertheless, a practical compromise since T is easier to measure accurately than humidity.

Appendix B

PAPERS CITING MALLICK ET AL. (2014,2015)

Below is an annotated list of papers, in addition to those already mentioned in § 2.1 (p. 16), that cite the STIC model or Mallick et al. (2014, 2015a):

(1) Aminzadeh and Or (2014) noted that Mallick et al. (2014) proposed the use of the Priestley-Taylor α_{PT} to account for drying power of air in the PM equation.

(2) Bateni et al. (2014) stated that most approaches for retrieving surface heat flux fit into one of five categories; they categorised the model created by Mallick et al. (2014) as a combination method that incorporates land surface temperature data into the PM equation to eliminate the need to specify surface to atmosphere conductance terms, i.e. g_S and g_B.

(3) Dhungel et al. (2014) noted that Mallick et al. (2014) had demonstrated a method to physically integrate the radiometric surface temperature into the PM equation for estimating terrestrial surface energy balance fluxes. They also noted the difficulties inherent in the PM equation that result from eliminating the T_S term.

(4) Baik and Choi (2015) cited Mallick et al. (2014) reporting that stomatal conductances are non-stationary due to scale dependence and spatio-temporal heterogeneity.

(5) Ma et al. (2015) noted that Mallick et al. (2014) had demonstrated that E estimated using the complementary-relationship of Bouchet (1963) and Morton (1965) is realistic when compared with EC based approaches.

(6) Mallick et al. (2015b) cited Mallick et al. (2014) when noting that λE is almost always specified in terms of available energy flux, ϕ.

(7) Wan et al. (2015) cited Mallick et al. (2014) when stating that evaporation and transpiration processes occur simultaneously and are difficult to separate.

(8) Fu and Weng (2016) cited Mallick et al. (2014) when stating that land surface temperature data from satellite thermal infrared imagery is a crucial variable used for modelling surface energy fluxes.

(9) Pasquier et al. (2016) cited Mallick et al. (2014) saying that plant temperature is governed by its evapotranspiration and this predominant term of the heat exchange can consequently be assessed.

(10) Verma et al. (2016), co-authored by Mallick, cited Mallick et al. (2014), with other papers, stating that surface net-radiation is critical in the global energy and water cycle because 'it couples the land surface to the lower atmosphere and exerts a dominant control on the terrestrial hydrological cycle.'

(11) Zhuang et al. (2016) noted that Mallick et al. (2014) had used an alternative equation for λE following Boegh et al. (2002).

(12) Bhattarai et al. (2017) cited Mallick et al. (2014) saying that T_S is the primary variable in most remote sensing surface energy balance models and that it must be used correctly to reduce uncertainties in λE and H.

(13) Islam et al. (2017) noted that Mallick et al. (2014) performed a sensitivity analysis of surface energy balance fluxes to uncertainties in land surface temperatures using a thermal-based E model.

(14) Schymanski and Or (2017) noted, citing Mallick et al. (2013) and Mallick et al. (2016), that accounting for radiative and surface temperatures of leaves and canopies are among the challenges of upscaling from leaf-scale models to canopy-scale. They also referred the reader to Mallick et al. (2014) for clarification regarding the assumption Penman (1948) had made to eliminate T_S of the leaf from his model.

(15) Udelhoven et al. (2017) briefly described the technique of Mallick et al. (2014) to physically integrate T_S into the PM equation to estimate surface energy balance fluxes. Furthermore, it was noted that empirical parameterisation of aerodynamic and canopy conductances are not required.

(16) Wagle et al. (2017) simply noted that Mallick et al. (2014) had developed a relatively complex Surface Energy Balance model.

(17) Yagci et al. (2017) noted that Mallick et al. (2014) had expressed that biased sampling of T_S, e.g. from undetected pixel-wide or subpixel clouds, could degrade the STIC model's performance.

(18) Yang et al. (2017) noted that Mallick et al. (2014) had proposed a new method named STIC which integrates land surface temperature into the PM equation for estimating terrestrial surface energy balance fluxes.

(19) Zhu et al. (2017) cited Mallick et al. (2014) reporting the uncertainties associated with the complex solution of aerodynamic and stomatal resistances.

(20) He et al. (2018) noted that the STIC method of Mallick et al. (2013, 2014) estimates turbulent heat fluxes by integrating land surface temperature into the PM equation.

(21) Ma et al. (2018) noted that Mallick et al. (2014, 2015a, 2016) also observed a systematic overestimation of E by in arid and semi-arid regions. They also attributed the observed very high levels of λE at well-irrigated fields covered by vegetables to strong horizontal advection of dry and warm air from adjacent areas.

(22) Fu et al. (2019) cited Mallick et al. (2014) among others when saying that land surface temperature is one of the most important parameters in understanding land surface water and carbon cycles and energy fluxes from local to global scales.

(23) Gerhards et al. (2019), co-authored by Mallick, was a review paper of thermal infrared remote sensing for crop water-stress detection. STIC was described as a physically-based non-parametric and calibration-free approach to E estimation.

(24) He et al. (2019) listed a number of methods developed to estimate turbulent heat fluxes from remotely sensed land surface temperature data, including Mallick et al. (2013) and Mallick et al. (2014).

(25) Liou et al. (2018) cited Mallick et al. (2014) as one of a number of approaches that integrates ground observations and remotely sensed data to estimate the energy exchange between land surface and atmosphere.

(26) Mahoto and Pal (2019) cited Mallick et al. (2014) when saying that land surface temperature data extracted from the satellite thermal infrared imagery is used for modelling surface energy fluxes.

(27) Miao et al. (2019) listed Mallick et al. (2014), among others, saying that thermal infrared data can be used to estimate land surface temperature which is a key variable in hydrological applications.

(28) Xu et al. (2019) listed Mallick et al. (2013) and Mallick et al. (2014) as incorporating land surface temperature observations into the PM equation.

(29) Ait Hssaine et al. (2020) listed Mallick et al. (2014, 2015a, 2016, 2018) as being a PM-based model using land surface temperature data.

(30) Gan and Liu (2020) listed Mallick et al. (2014) as an example of using Remote Sensing land surface temperature to estimate E without parameterising surface resistance.

(31) He et al. (2020) listeds Mallick et al. (2013) and Mallick et al. (2014) as examples of PM methods that incorporated Remote Sensing.

(32) Hua et al. (2020) cited Mallick et al. (2014) saying that ground parameter data for the PM model can be obtained accurately by Remote Sensing.

(33) Taifar, Bateni, Heggy and Xu 2020 and Taifar, Bateni, Lakshmi and Ek (2020) listed Mallick et al. (2013) and Mallick et al. (2014) as examples of combination methods that incorporated land surface temperature into the PM model.

(34) Zhang et al. (2020) included Mallick et al. (2014) in a list of papers that use remotely sensed land surface temperature in modelling of surface energy balance.

(35) Zhao et al. (2020) noted that the PM equation can only be used when exact values of resistances are known and that there are no methods to accurately determine aerodynamic resistances. They pointed out a number of models that avoid the problem of resistance parameterisation including Mallick et al. (2014).

(36) Zhuang et al. (2020) cited Mallick et al. (2014) saying that the ambient air temperature next to a crop is responsible for the transfer of heat from the surface to the atmosphere, and this temperature can be significantly different to T_S.

Appendix C

CALIBRATION CERTIFICATES

This page intentionally left blank.

apogee
INSTRUMENTS
721 West 1800 North
Logan, UT 84321

Certificate of Calibration
Apogee Instruments Infrared Radiometer
SI-400 and MI-200 Series

Calibration Overview		
Model/Serial Number	:	**SI-411_2452**
Calibration Date	:	11-Aug-2017
Recommended Recalibration Date	:	11-Aug-2019
Mean of Differences from Target	:	-0.001 °C
Target Temperature Uncertainty (95% confidence) from -30 to 65°C	:	**0.121 °C**
Maximum Difference from Target	:	0.179 °C
Minimum Difference from Target	:	-0.133 °C
Maximum Detector Response	:	1.396 mV
Minimum Detector Response	:	-0.819 mV
Average Output Sensitivity	:	67.039 μV / °C

Coefficient Correction Errors

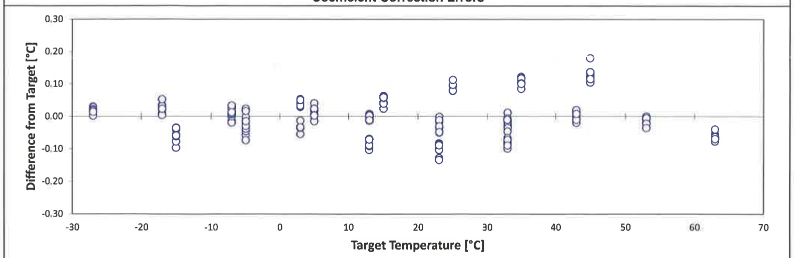

Calibration Procedure

An Infrared Radiometer (IRR) combines a thermopile detector and a National Institute of Standards and Technology (NIST) traceable thermistor to measure a mV response proportional to the thermal radiation balance between the target temperature and the thermopile temperature (sensor body temperature). IRRs are placed in a temperature controlled housing, which is thermally insulated from a blackbody cone. The housing, pointed at a blackbody cone, is temperature cycled through various sensor body set-points. The blackbody cone temperature (measured with NIST traceable thermistors) is likewise cycled through multiple temperature set-points relative to each sensor body temperature set-point. A linear fit is used to model each sensor body set-point with the respective blackbody cone set-points versus the thermopile signal at those set-points. The slopes and y-intercepts of all linear fits corresponding to each sensor body temperature are then fit to a second order polynomial in order to adequately interpolate between the calibrated set-points. These two sets of second order polynomial coefficients represent the custom calibration coefficients as given above.

Traceability

All thermistors are measured for accuracy in a constant temperature bath that is directly traceable to the NIST. The overall measurement system uncertainty for all the bath and measurement allowances combined for error is typically less than 0.1°C and completely traceable to National Standards.

Technical Manager : Jacob Bingham Date : 11-Aug-2017

Please keep this document for your records

Website: www.apogeeinstruments.com E-mail: techsupport@apogeeinstruments.com Ph: (435)792-4700 Fax: (435)787-8268

Figure C.1: Calibration certificate for Apogee SI-411 IRR.

Middleton Solar

CALIBRATION CERTIFICATE

4-Component Net Radiometer

Date of issue	25th Jul. 2018	
Certificate Number	C5250	
Instrument Serial No.	1830	
Instrument Manufacturer	Hukseflux	
Instrument Model	NR01	
Sensitivity, top SW sensor	SR01#2780 = 15.26	$\mu V/W.m^{-2}$
Sensitivity, bottom SW sensor	SR01#2781 = 14.65	$\mu V/W.m^{-2}$
Sensitivity, top LW sensor	IR01#2757 = 11.72	$\mu V/W.m^{-2}$
Sensitivity, bottom LW sensor	IR01#2758 = 11.48	$\mu V/W.m^{-2}$
Reference sensor, SW	EQ08-S #4901	
Reference sensor, LW	PG01 #7001	
SW Calibration uncertainty, U_{95}	3%	
LW Calibration uncertainty, U_{95}	8%	

Comments:

Approved Signatory ____________

Procedure: calibrated outdoors by comparison to a reference Pyranometer for Short Wave (SW), and to a reference Pyrgeometer for Long Wave (LW), with the sun as a source for SW, and the night sky as a source for LW. Reference instruments traceable to the World Radiometric Reference (for SW), and to the World Infrared Standard Group (for LW), via master reference instruments.

Annual calibration is recommended.

Middleton Solar, Australia.

www.middletonsolar.com

817052DSC

Figure C.2: Calibration certificate for Hukseflux NR01 net radiometer.

MICHELL Instruments

Certificate of Conformity

Certificate of Conformity No.	10000519
Product Description	HS3 Probe
Product Order Code	HS3-P+B2+C1+D1+E8+F1
Product Model Serial No.	PAA000486
Sales Order No.	26877
Line No.	1
Configured Probe Functional Test Completed	15 June 2017

Calibration Certificate

Interchangeable Sensor Order	HS3-S
Interchangeable Sensor Serial	SAA000773
Interchangeable Sensor Cal Date	15 June 2017

The above mentioned item has been calibrated at the following points in the Michell Instruments Humidity Calibration Laboratory against the below Test Equipment traceable to the defined National Standard.

Reference Humidity %RH	Observed Humidity %RH	Difference %RH	Permissible Difference %RH
15.01	15.05	0.04	+0.8/-0.8
29.92	30.24	0.32	+0.8/-0.8
49.89	50.32	0.43	+0.8/-0.8
69.80	70.15	0.35	+0.8/-0.8
90.15	90.14	-0.01	+0.8/-0.8

Reference Temperature °C	Observed Temperature °C	Difference °C	Permissible Difference °C
23.17	23.23	0.06	+0.2/-0.2

Calibration Reference Equipment

Type	Serial Number	Calibration Date	Certificate No.
Humidity Generator	GENHR01	02/04/16	4469MBW2016
Humidity Reference	ETALTD04	21/09/15	H1528031C
Electrical Reference	MNUM5708	28/02/17	C07E170381
Temperature Reference	ETALTS02	11/04/16	TE4001

The uncertainties are based on a standard uncertainty multiplied by a coverage factor k=2, providing a level of confidence of approximately 95%.

Michell Instruments certify that the above equipment has been designed, manufactured, tested and inspected in full accordance with our quality assurance procedures and conforms to the requirements of the contract/purchase order.

Name Frank Lauwerijssen **Quality Technician**

Michell Instruments Benelux B.V. Krombraak 11, Oosterhout, 4906 CR, The Netherlands
www.michell.com

Figure C.3: Calibration certificate for Michell Hygrosmart HS3 temperature and humidity probe (#PAA000486).

Certificate of Conformity

MICHELL Instruments

Certificate No	22826		
Product Description	HS3-P		
Product Order Code	HS3-P-B2-C1-D1-E8-F1		
Product Model Serial No.	PAA001278		
Sales Order No.	30686		
Customer	AMS Instrumentation & Cal.	**Customer Order No.**	00013877

Calibration Certificate

Interchangeable Sensor Order	
Interchangeable Sensor Serial	SAA002056
Interchangeable Sensor Cal Date	01-06-2018

The above mentioned item has been calibrated at the following points in the Michell Instruments Humidity Calibration Laboratory against the below Test Equipment traceable to the National Standard.

Reference %RH	Sensor %RH digital reading	Difference %RH digital	Sensor RH Volt reading	Difference %RH Volt reading	Permissible Difference %RH
15.60	15.67	+0.07	0.16	-0.04	+0.8/-0.8
30.50	30.87	+0.37	0.31	+0.26	+0.8/-0.8
50.53	51.06	+0.53	0.51	+0.48	+0.8/-0.8
70.50	71.15	+0.65	0.71	+0.61	+0.8/-0.8
90.86	91.16	+0.30	0.91	+0.28	+0.8/-0.8

Reference Temperature °C	Sensor T digital reading °C	Difference °C digital	Sensor T Volt reading	Difference T Volt reading	Permissible Difference °C
23.31	23.28	-0.03	0.54	-0.04	+0.5/-0.5

Calibration Reference Equipment

Type	Instrument	Serial No.	Certificate No.
Humidity Generator	Thunder Scientific 2500	215400-392	--
Humidity Reference	DP30	--	H1720265E
Temperature Reference	I300	C72001	TF3001
Voltage Reference	Keithley	0801435	C07E170383

Michell Instruments certify that the above equipment has been designed, manufactured, tested and inspected in full accordance with our quality assurance procedures and conforms to the requirements of the contract/purchase order.

Name Rob Schoonen Quality Technician

Michell Instruments BV Krombraak 11, 4906 CR Oosterhout, The Netherlands

Figure C.4: Calibration certificate for Michell Hygrosmart HS3 temperature and humidity probe (#PAA001278).

MICHELL Instruments

Certificate of Conformity

Certificate No	22827		
Product Description	HS3-P		
Product Order Code	HS3-P-B2-C1-D1-E8-F1		
Product Model Serial No.	PAA001054		
Sales Order No.	30686		
Customer	AMS Instrumentation & Cal.	**Customer Order No.**	00013877

Calibration Certificate

Interchangeable Sensor Order	
Interchangeable Sensor Serial	SAA002107
Interchangeable Sensor Cal Date	01-06-2018

The above mentioned item has been calibrated at the following points in the Michell Instruments Humidity Calibration Laboratory against the below Test Equipment traceable to the National Standard.

Reference %RH	Sensor %RH digital reading	Difference %RH digital	Sensor RH Volt reading	Difference %RH Volt reading	Permissible Difference %RH
15.60	15.66	+0.06	0.16	-0.01	+0.8/-0.8
30.50	30.73	+0.23	0.31	+0.22	+0.8/-0.8
50.53	50.85	+0.32	0.51	+0.31	+0.8/-0.8
70.50	70.93	+0.43	0.71	+0.44	+0.8/-0.8
90.86	91.01	+0.15	0.91	+0.15	+0.8/-0.8

Reference Temperature °C	Sensor T digital reading °C	Difference °C digital	Sensor T Volt reading	Difference T Volt reading	Permissible Difference °C
23.31	23.29	-0.02	0.54	-0.04	+0.5/-0.5

Calibration Reference Equipment

Type	Instrument	Serial No.	Certificate No.
Humidity Generator	Thunder Scientific 2500	215400-392	--
Humidity Reference	DP30	--	H1720265E
Temperature Reference	I300	C72001	TF3001
Voltage Reference	Keithley	0801435	C07E170383

Michell Instruments certify that the above equipment has been designed, manufactured, tested and inspected in full accordance with our quality assurance procedures and conforms to the requirements of the contract/purchase order.

Name Rob Schoonen Quality Technician

Michell Instruments BV Krombraak 11, 4906 CR Oosterhout, The Netherlands

Figure C.5: Calibration certificate for Michell Hygrosmart HS3 temperature and humidity probe (#PAA001054).

MICHELL Instruments

Certificate of Conformity

Certificate No	22828		
Product Description	HS3-P		
Product Order Code	HS3-P-B2-C1-D1-E8-F1		
Product Model Serial No.	PAA001047		
Sales Order No.	30686		
Customer	AMS Instrumentation & Cal.	**Customer Order No.**	00013877

Calibration Certificate

Interchangeable Sensor Order	
Interchangeable Sensor Serial	SAA002117
Interchangeable Sensor Cal Date	01-06-2018

The above mentioned item has been calibrated at the following points in the Michell Instruments Humidity Calibration Laboratory against the below Test Equipment traceable to the National Standard.

Reference %RH	Sensor %RH digital reading	Difference %RH digital	Sensor RH Volt reading	Difference %RH Volt reading	Permissible Difference %RH
15.60	15.60	+0.00	0.15	-0.11	+0.8/-0.8
30.50	30.77	+0.27	0.31	+0.25	+0.8/-0.8
50.53	50.99	+0.46	0.51	+0.48	+0.8/-0.8
70.50	71.01	+0.51	0.71	+0.50	+0.8/-0.8
90.86	90.80	-0.06	0.91	-0.06	+0.8/-0.8

Reference Temperature °C	Sensor T digital reading °C	Difference °C digital	Sensor T Volt reading	Difference T Volt reading	Permissible Difference °C
23.31	23.32	+0.01	0.54	+0.00	+0.5/-0.5

Calibration Reference Equipment

Type	Instrument	Serial No.	Certificate No.
Humidity Generator	Thunder Scientific 2500	215400-392	--
Humidity Reference	DP30	--	H1720265E
Temperature Reference	I300	C72001	TF3001
Voltage Reference	Keithley	0801435	C07E170383

Michell Instruments certify that the above equipment has been designed, manufactured, tested and inspected in full accordance with our quality assurance procedures and conforms to the requirements of the contract/purchase order.

Name Rob Schoonen Quality Technician

Michell Instruments BV Krombraak 11, 4906 CR Oosterhout, The Netherlands

Figure C.6: Calibration certificate for Michell Hygrosmart HS3 temperature and humidity probe (#PAA001047).

MICHELL Instruments

Certificate of Conformity

Certificate No	22825		
Product Description	HS3-P		
Product Order Code	HS3-P-B2-C1-D1-E8-F1		
Product Model Serial No.	PAA001320		
Sales Order No.	30686		
Customer	AMS Instrumentation & Cal.	**Customer Order No.**	00013877

Calibration Certificate

Interchangeable Sensor Order	
Interchangeable Sensor Serial	SAA002029
Interchangeable Sensor Cal Date	01-06-2018

The above mentioned item has been calibrated at the following points in the Michell Instruments Humidity Calibration Laboratory against the below Test Equipment traceable to the National Standard.

Reference %RH	Sensor %RH digital reading	Difference %RH digital	Sensor RH Volt reading	Difference %RH Volt reading	Permissible Difference %RH
15.60	15.64	+0.04	0.16	-0.06	+0.8/-0.8
30.50	30.79	+0.29	0.31	+0.26	+0.8/-0.8
50.53	50.97	+0.44	0.51	+0.46	+0.8/-0.8
70.50	71.09	+0.59	0.71	+0.57	+0.8/-0.8
90.86	91.09	+0.23	0.91	+0.22	+0.8/-0.8

Reference Temperature °C	Sensor T digital reading °C	Difference °C digital	Sensor T Volt reading	Difference T Volt reading	Permissible Difference °C
23.31	23.29	-0.02	0.54	-0.01	+0.5/-0.5

Calibration Reference Equipment

Type	Instrument	Serial No.	Certificate No.
Humidity Generator	Thunder Scientific 2500	215400-392	--
Humidity Reference	DP30	--	H1720265E
Temperature Reference	I300	C72001	TF3001
Voltage Reference	Keithley	0801435	C07E170383

Michell Instruments certify that the above equipment has been designed, manufactured, tested and inspected in full accordance with our quality assurance procedures and conforms to the requirements of the contract/purchase order.

Name Rob Schoonen Quality Technician

Michell Instruments BV Krombraak 11, 4906 CR Oosterhout, The Netherlands

Figure C.7: Calibration certificate for Michell Hygrosmart HS3 temperature and humidity probe (#PAA001320).

TC Ltd, Units 1-6, Brimington Rd North, Chesterfield, S41 9BE, United Kingdom
Email: callab@tc.co.uk - Web: www.tc.co.uk
Tel: 01895 252222 - Fax: 01895 273540

CERTIFICATE OF CALIBRATION

Date of Issue: 7th August 2017
Customer: NCEA
Address: Building 9, West St, Toowoomba, QLD
Order Number: EMAIL ORDER
Our Reference: 00020267
Date Received: 26th July 2017
Type: Pt100 3.0mm x 200mm
Serial Number: 04524/1A
Product Code: 16-1-3.0-4-200-CE4CL-R100-1/10-5 MTRS RP47
Platinum Resistance Thermometer
Ambient Temp: 20°C +/- 2°C

Approved Signatory
L R Walker
K M Donaldson

KDonaldson

Certificate Number : 17-0387-1A

Calibration Procedure: The thermometer was calibrated by comparison with two reference resistance thermometers. The calibration took place in a Venus dry block. All measurements are traceable to recognised national standards. The resistance outputs were measured on a precision digital multimeter. All tests were carried out in a controlled environment using devices having known and traceable values. The temperature measurements are traceable to ITS-90. The thermometer resistances were converted using IEC60751:2008. Both the National Association of Testing Authorities and the United Kingdom Accreditation Service are signatories to the International Mutual Recognition Arrangement. Under the ILAC-MRA agreement measurements traceable to UKAS standards have an equivalent level of integrity as those traceable to NATA standards.

REFERENCE TEMPERATURE (°C)	MEASURED RESISTANCE (Ω)	EQUIVALENT IEC VALUE (°C)	ERROR (°C)	UNCERTAINTY (+/- °C)
-0.07	99.966	-0.09	-0.02	0.3
29.81	111.594	29.79	-0.02	0.3
59.72	123.129	59.71	-0.01	0.3

The PRT sensor was measured using a current of 1mA.
The depth of immersion of the test thermometer was 170mm

Calibration date: 5 August 2017

The reported expanded uncertainty is based on a standard uncertainty multiplied by a coverage factor of $k = 2$, providing a level of confidence of approximately 95%. The uncertainty evaluation has been carried out in accordance with UKAS requirements.

Note: It is the user's responsibility to determine the long-term drift and the uncertainty under the conditions of use

This certificate is issued in accordance with the laboratory accreditation requirements of the United Kingdom Accreditation Service. It provides traceability of measurement to the SI system of units and/or to units of measurement realised at the National Physical Laboratory or other recognised national metrology institutes. This certificate may not be reproduced other than in full, except with the prior written approval of the issuing laboratory.

Page 1 of 1 Authorised by: L Walker Date: Jul 2017 (GB) Issue 17/01

Figure C.8: Calibration certificate for TC Measurement & Control 1/10 DIN Pt100 RTD.

dataTaker

Page 1 of 1

Certificate of Traceable Calibration

Product Description

Model: DT85LM3-4
Serial: 111284

Kernel Assembly: AS1532D0 1926-010
Terminal Assembly: AS1546D0 1934-017
Firmware: 85 Version 9.20.8973

Calibration Details

Calibration Date: 2017/08/11 15:15:02
Test Location: Apptek, Unit 1, 2 Pinacle Street Brendale QLD 4500
Ambient Temperature: 25.2 °C
NATA Certified Reference: Fluke 8840A Serial 5141011
Calibration Reference: DT8x Tester JIG-274 Version 1.51.0033, Calibrated 2017/07/20 13:27:27

Calibration Results

The following table lists measurements performed against traceable references.

Range	Channel(options)	Reference	Actual Reading	Allowable Error[1]	Error	Status
+50 V	1+HV(GL50)	+10.0000 V	+10.0008	± 0.15 %	0.008 %	PASS
+3000 mV	1*V(GL3V)	+2500.3 mV	+2500.5	± 0.1 %	0.009 %	PASS
+300 mV	1+V(GL300MV)	+249.99 mV	+250.03	± 0.1 %	0.015 %	PASS
+30 mV	1-V(GL30MV)	+24.992 mV	+24.999	± 0.1 %	0.026 %	PASS
-50 V	1+HV(GL50)	-10.0000 V	-10.0008	± 0.15 %	0.008 %	PASS
-3000 mV	1*V(GL3V)	-2500.1 mV	-2500.5	± 0.1 %	0.017 %	PASS
-300 mV	1+V(GL300MV)	-249.98 mV	-250.00	± 0.1 %	0.007 %	PASS
-30 mV	1-V(GL30MV)	-25.001 mV	-25.000	± 0.1 %	-0.005 %	PASS
10 k Ω	1R(4W,I)	100.0000 Ω	100.006	± 0.2 %	0.006 %	PASS

[1] Allowable Error indicates the maximum allowable difference between the Reference and the Actual Reading, specified as a percentage of the Actual Reading, when the ambient temperature is between 5°C and 40°C.

The product covered by this certificate meets or exceeds the required performance specified by Thermo Fisher Scientific Australia Pty. Ltd.

The measurements performed to generate this certificate are traceable to Australian national standards of measurement.

This product has been manufactured under an ISO9001:2008 quality system.

file:///G:/dt80/reports/DT85LM3/html/DT85LM3-111284%2011-08-2017%203-15-0... 11/08/2017

Figure C.9: Calibration certificate for dataTaker DT85M data logger.

This page intentionally left blank.

Appendix D

AREA OF GROUND VISIBLE TO SI-411

The method to calculate the area visible to the Apogee SI-411 IRR (with circular aperture and a half field-of-view of $\alpha = 22°$) is detailed here.

The intersection of an oblique cone and a flat plane forms an ellipse. The variables in the following derivation are as illustrated in Fig. D.1 (p.358).

$$
\begin{aligned}
d_1 &= h\ \tan(\theta - \alpha) \\
d_2 &= h\ \tan(\theta) \\
d_3 &= h\ \tan(\theta + \alpha) \\
d_4 &= d_2 - d_1 \\
&= h\ \tan(\theta) - h\ \tan(\theta - \alpha) \\
d_5 &= d_3 - d_2 \\
&= h\ \tan(\theta + \alpha) - h\ \tan(\theta) \\
a &= d_4 + d_5
\end{aligned}
$$

$$
\underline{\text{Ellipse major axis}} \quad \boxed{a = \frac{h\ \tan(\theta + \alpha) - h\ \tan(\theta - \alpha)}{2}} \tag{D.1}
$$

$$
x = d_5 - a
$$

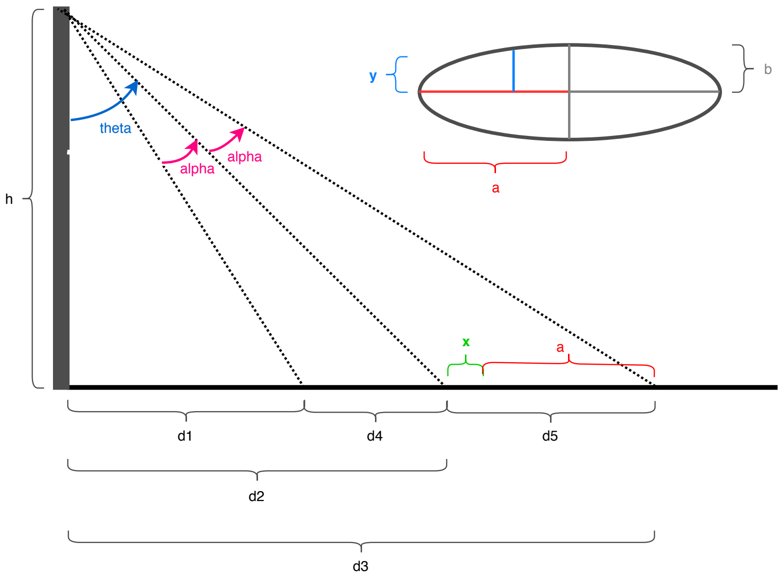

Figure D.1: Schematic diagram for derivation of equation to determine visible ground area by an Apogee SI-411.

$$= \frac{1}{2} h \tan(\theta + \alpha) - h \tan(\theta) + \frac{1}{2} h \tan(\theta - \alpha)$$

$$y = \frac{h}{\cos(\theta)} \tan(\alpha)$$

When centered at the Origin, an ellipse has the following Cartesian equation:

$$\underline{\text{Equation of ellipse}} \quad 1 = \frac{x^2}{a^2} + \frac{y^2}{b^2} \tag{D.2}$$

Making the minor axis, b, the subject:

$$\underline{\text{Ellipse minor axis}} \quad \boxed{b = \sqrt{\frac{y^2}{(1 - \frac{x^2}{a^2})}}} \tag{D.3}$$

$$\underline{\text{Area of ellipse}} \quad \boxed{A = \pi\, a\, b} \tag{D.4}$$

For the particular case of $\theta = 45°$, $\alpha = 22°$ and $h = 5.5\,\text{m}$, then $x = 2.15\,\text{m}$, $y = 3.14\,\text{m}$, $a = 5.31\,\text{m}$, $b = 3.44\,\text{m}$ and so $A = 57.3\,\text{m}^2$.

Appendix E

CALCULATING FETCH

Fetch is the upwind distance from the edge of a field (or from an abrupt change within a field) to a particular point in the field. Adequate fetch is necessary for a stable internal boundary layer to form, which is essential to the BREB, EC, and PM models (among others). What constitutes adequate fetch is not universally agreed upon, however, but a commonly used rule-of-thumb is that fetch:height ratios should be at least 100:1 (see § 2.4.2, p. 32). The surrounding terrain, relative heights of vegetation in and around the field, roughness of crop canopy, wind speed and atmospheric stability regime can all impact on adequacy of fetch.

Fetch was not a variable in either of the Profile BREB or GPSTIC models. It was calculated, nonetheless, to provide context for the modelling and the fetch results for DS1, DS2 and DS3 are presented in Appendices O (p. 427), P (p. 437) and Q (p. 447) respectively.

Here it is assumed that the field is rectangular. The size of the field, the position of interest within the field, the orientation of the field, and the direction from which the wind is coming are all required to be specified.

E.1 Algorithm to Calculate Fetch

With reference to Fig. E.1 (p. 361), let fb be the bearing (clockwise from grid north) of the long axis of a rectangular field, so that fb is strictly limited in either of the following ranges:

$$
\begin{aligned}
&0^\circ \leqslant fb \leqslant 90^\circ \\
\text{or} \qquad &270^\circ \leqslant fb \leqslant 359^\circ
\end{aligned}
$$

Let wb be the bearing (relative to grid north) of the wind's direction. Then rw is the bearing of the wind relative to the field if the field is rotated by fb° so that its long axis is aligned with grid north.

$$
\begin{aligned}
\text{If} \qquad & 0^\circ \leqslant fb \leqslant 90^\circ \\
& \text{then} \qquad rw = wb - fb \\
\text{Else if} \qquad & 270^\circ \leqslant fb \leqslant 359^\circ \\
& \text{then} \qquad rw = (360^\circ - fb) + wb
\end{aligned}
$$

If necessary, rw is corrected so that $0^\circ \leqslant rw \leqslant 359^\circ$.

If the wind crosses the boundary of the field over the long edge (e.g. Wind 1 in Fig E.1), then the fetch, f, is calculated by:

$$
\begin{aligned}
\text{if} \qquad & 0^\circ \leqslant rw \leqslant 90^\circ \\
& \text{then} \qquad f = \frac{x_1}{\sin rw} \\
\text{else if} \qquad & 90^\circ < rw \leqslant 180^\circ \\
& \text{then} \qquad f = \frac{x_1}{\sin(180^\circ - rw)} \\
\text{else if} \qquad & 180^\circ < rw \leqslant 270^\circ \\
& \text{then} \qquad f = \frac{x_2}{\sin(rw - 180^\circ)}
\end{aligned}
$$

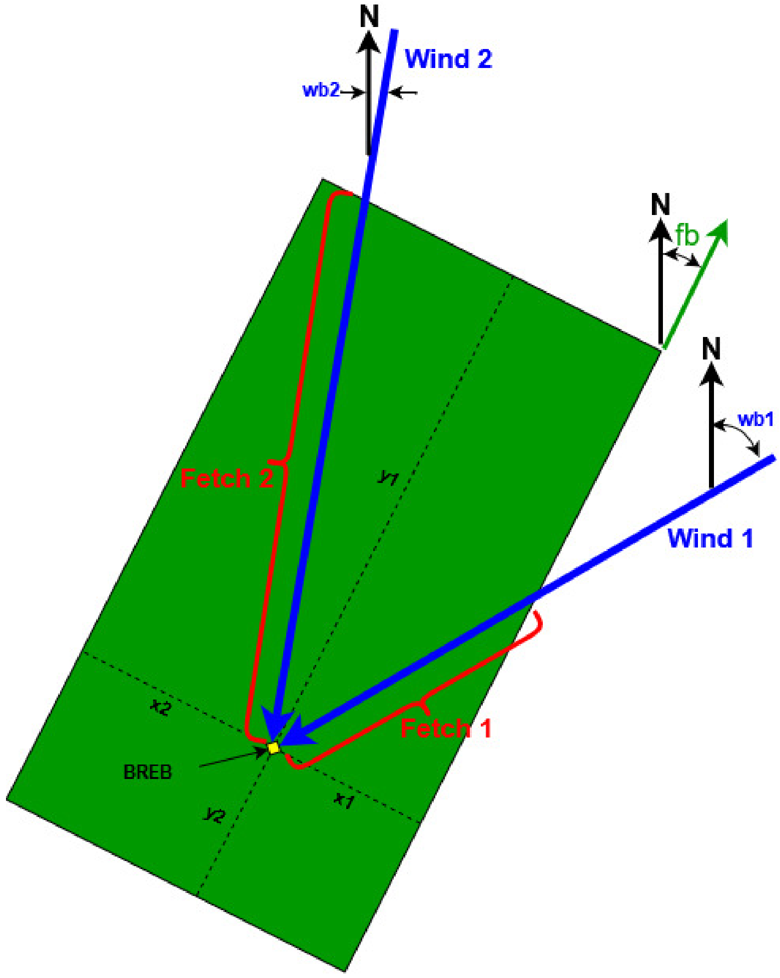

Figure E.1: Schematic diagram for fetch calculations. fb is the bearing of the long axis of the field, clockwise from grid north. wb_1 and wb_2 are the bearings of the wind relative to grid north. $Fetch_1$ and $Fetch_2$ are the fetch distances associated with $Wind_1$ and $Wind_2$.

$$
\begin{aligned}
\text{else if} \quad & 270^\circ < rw < 360^\circ \\
& \text{then} \qquad f = \frac{x_2}{\sin(360 - rw^\circ)}
\end{aligned}
$$

If the wind crosses the boundary of the field over the short edge (e.g. Wind 2 in Fig. E.1), then f is calculated by:

$$
\begin{aligned}
\text{if} \quad & 0^\circ \leqslant rw \leqslant 90^\circ \\
& \text{then} \qquad f = \frac{y_1}{\cos rw} \\
\text{else if} \quad & 90^\circ < rw \leqslant 180^\circ \\
& \text{then} \qquad f = \frac{y_2}{\cos(180^\circ - rw)} \\
\text{else if} \quad & 180^\circ < rw \leqslant 270^\circ \\
& \text{then} \qquad f = \frac{y_2}{\cos(rw - 180^\circ)} \\
\text{else if} \quad & 270^\circ < rw < 360^\circ \\
& \text{then} \qquad f = \frac{y_1}{\cos(360^\circ - rw)}
\end{aligned}
$$

Appendix F

ADJUSTING NR01$_{\#1236}$ DATA FROM DS1

Figure F.1: Photograph, taken February 2019, of the two NR01 net radiometers mounted at the end of the 2.5 m long horizontal arm of the EC structure, 2.0 m above the crop canopy. Both of the net radiometers were wired to the same DT85M data logger.

The Hukseflux NR01 net radiometer (serial number #1830) was the primary instrument for measuring shortwave and longwave radiation. It was professionally re-calibrated prior to DS1 (Fig. C.2, p. 348). A second NR01 (serial number #1236), positioned alongside NR01$_{\#1830}$ and logged simultaneously by the same data logger, was used as a back-up. The NR01$_{\#1236}$ was an older instrument than NR01$_{\#1830}$ and had spent significantly more time in the field. It was not expected that NR01$_{\#1236}$ would be required and so it had not been re-calibrated prior to this research (due to calibration costs).

However, the simultaneous use of two NR01 sensors proved fortunate. Early in DS1 some of the cables of NR01$_{\#1830}$ were damaged by wildlife, despite being housed inside protective split-conduit tubing.[1]

During DS2 both net radiometers operated alongside each other without malfunction or interference. By comparing the radiation data from the (uncalibrated) NR01$_{\#1236}$ to the NR01$_{\#1830}$ a set of adjustment factors to match the NR01$_{\#1236}$'s data to that of NR01$_{\#1830}$ was determined.

F.0.1 Adjustments to DS1 Shortwave Radiation

Fig. F.2 (p. 365) and Fig. F.3 (p. 366) show that there was little difference between NR01$_{\#1236}$ and NR01$_{\#1830}$ when it came to shortwave radiation (especially when allowing for the $\pm 3\,\%$ uncertainty in the shortwave measurements). Thus no adjustment to the shortwave radiation data from DS1 was undertaken.

[1]During DS3 the cables of the NR01$_{\#1236}$ were also damaged by wildlife (probably cockatoo parrots given the height at which cable damage occurred). This was of little consequence, however, because NR01$_{\#1830}$ was being used as the primary net radiometer.

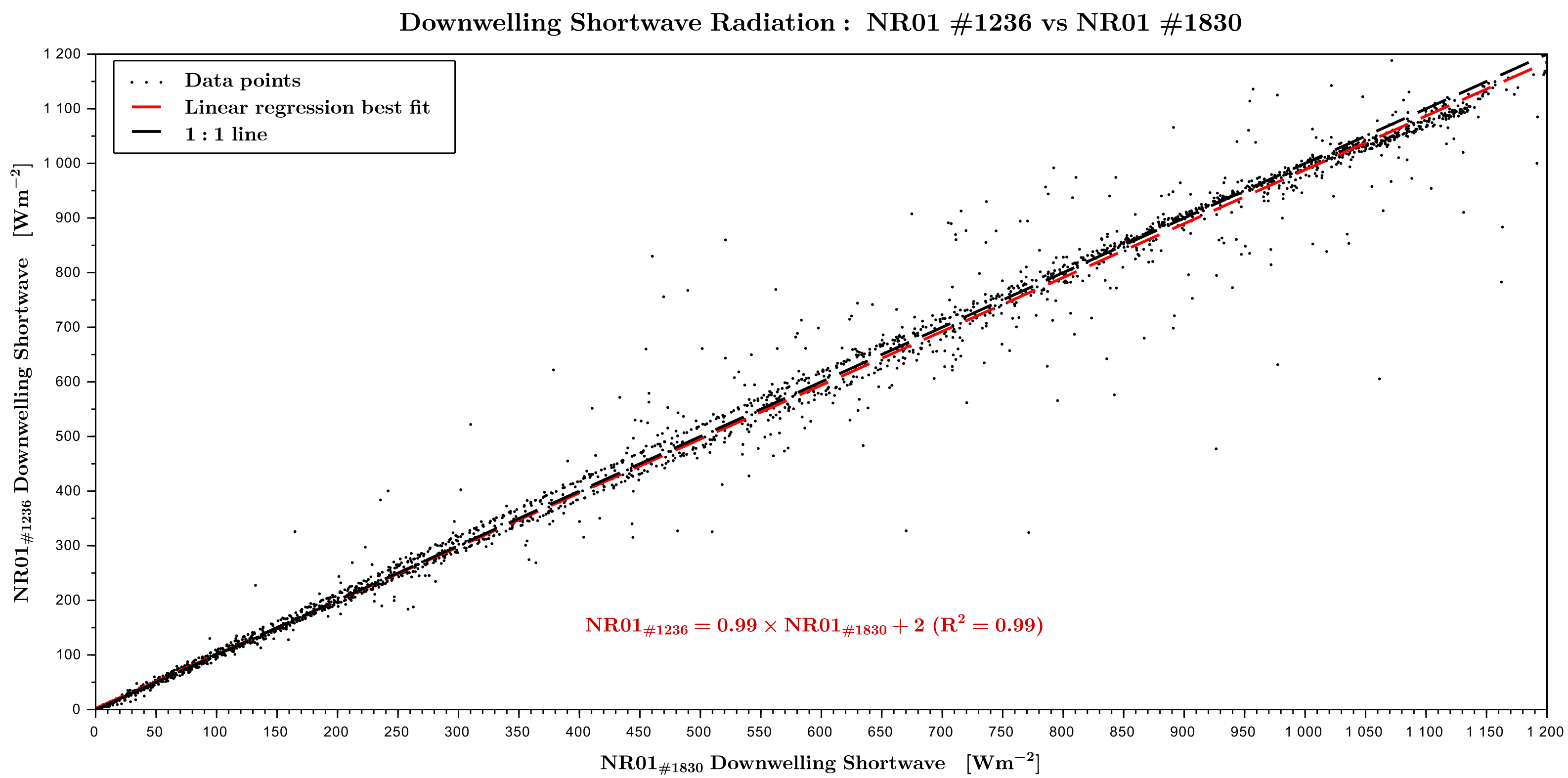

Figure F.2: Plotting $SW_{downwelling}$ from Hukseflux $NR01_{\#1236}$ against the laboratory-calibrated Hukseflux $NR01_{\#1830}$.

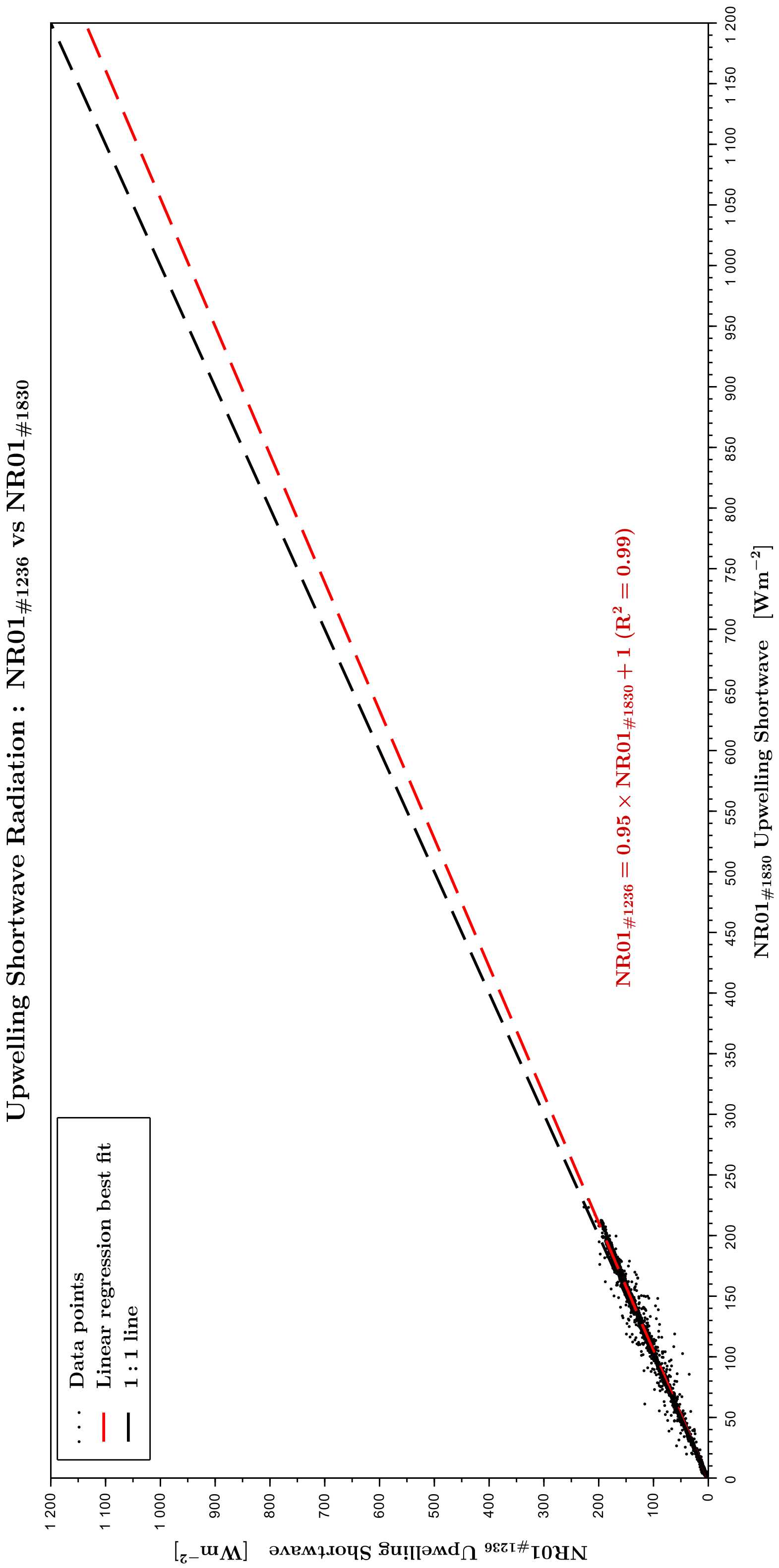

Figure F.3: Plotting $SW_{upwelling}$ from Hukseflux NR01$_{\#1236}$ against the laboratory-calibrated Hukseflux NR01$_{\#1830}$.

F.0.2 Adjustments to DS1 Longwave Radiation

Fig. F.4 (p. 368) and Fig. F.7 (p. 371) show that there was significant difference between $NR01_{\#1236}$ and $NR01_{\#1830}$ when it came to longwave radiation. Part of the difference will be due to the $\pm 8\,\%$ uncertainty in the longwave measurements (Fig. C.2, p. 348).

The scatter of the $NR01_{\#1236}$ vs. $NR01_{\#1830}$ longwave data meant that an adjustment to the $NR01_{\#1236}$ data using a linear regression process was inappropriate. Instead, the ratio of $NR01_{\#1236}$ to $NR01_{\#1830}$ for the downwelling and upwelling longwave data was calculated for every measured instance (Fig. F.5, p. 369 and Fig. F.8, p. 372, respectively). A mean ratio for each hour of the day was calculated, from which an adjustment factor to (retrospectively) apply to the $NR01_{\#1236}$ longwave data from DS1 was calculated:

$$\text{Hourly Adjustment Factor} = \frac{1}{\text{Hourly Mean Ratio}} \tag{F.1}$$

This is, clearly, a crude adjustment to the DS1 $NR01_{\#1236}$ longwave data but Fig. F.6 (p. 370) and Fig. F.9 (p. 373) show that the plotted data lie closer to the 1:1 line after the adjustment process.

Fig. 4.7 (p. 128) shows that after the adjustment process of the DS1 data there is mostly reasonable alignment between T_S as measured by the Apogee SI-411 infrared radiometer and that deduced from the downward facing pyrgeometer of the $NR01_{\#1236}$. This offers some support of the adjustment techniques used here.[2]

[2]The IRR and pyrgeometer have different spectral sensitivities, different fields of view and different angles of orientation. It would be expected that some differences in measured T_S will be observed.

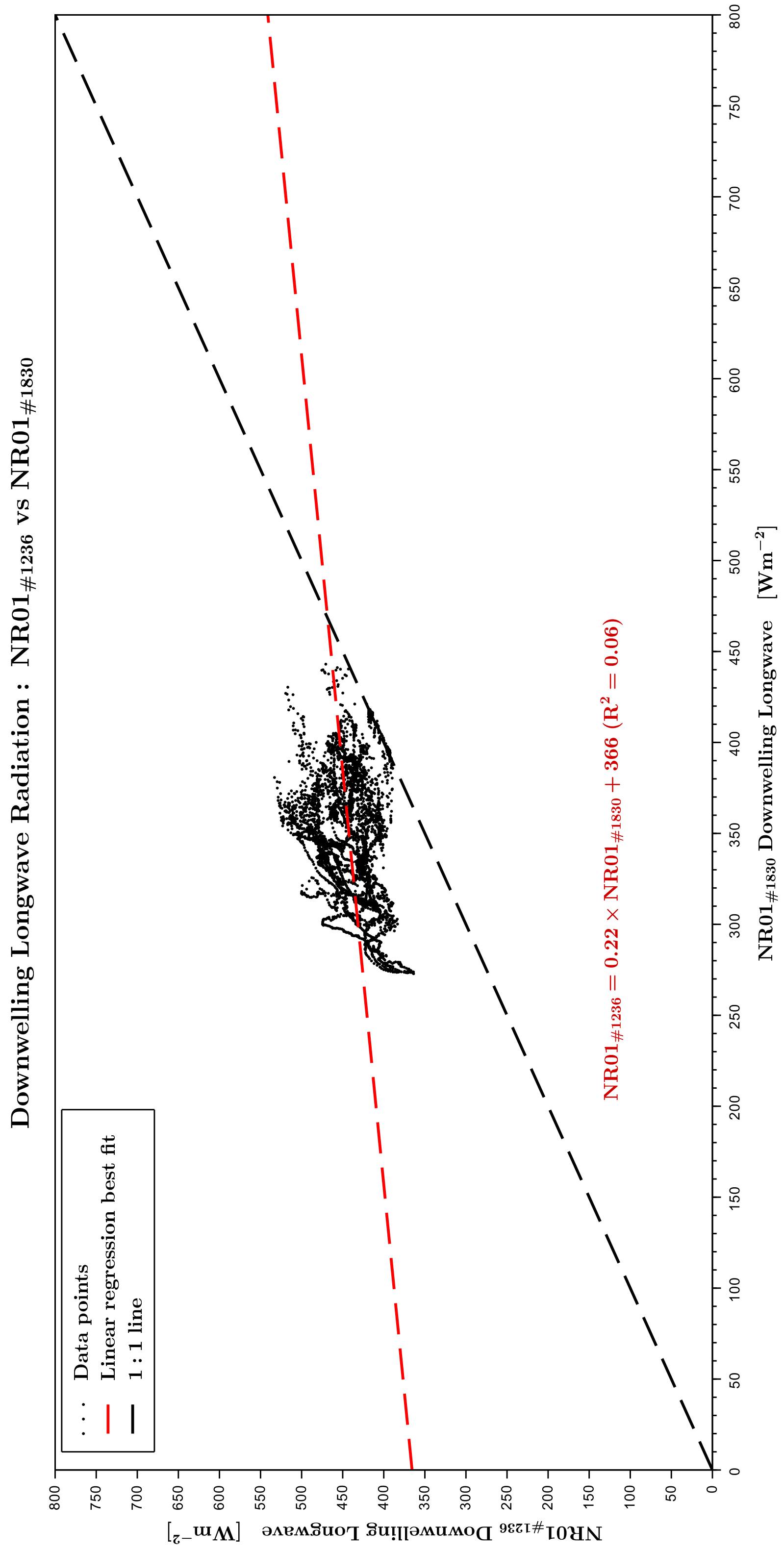

Figure F.4: Plotting $LW_{downwelling}$ from Hukseflux NR01$_{\#1236}$ against the laboratory-calibrated Hukseflux NR01$_{\#1830}$.

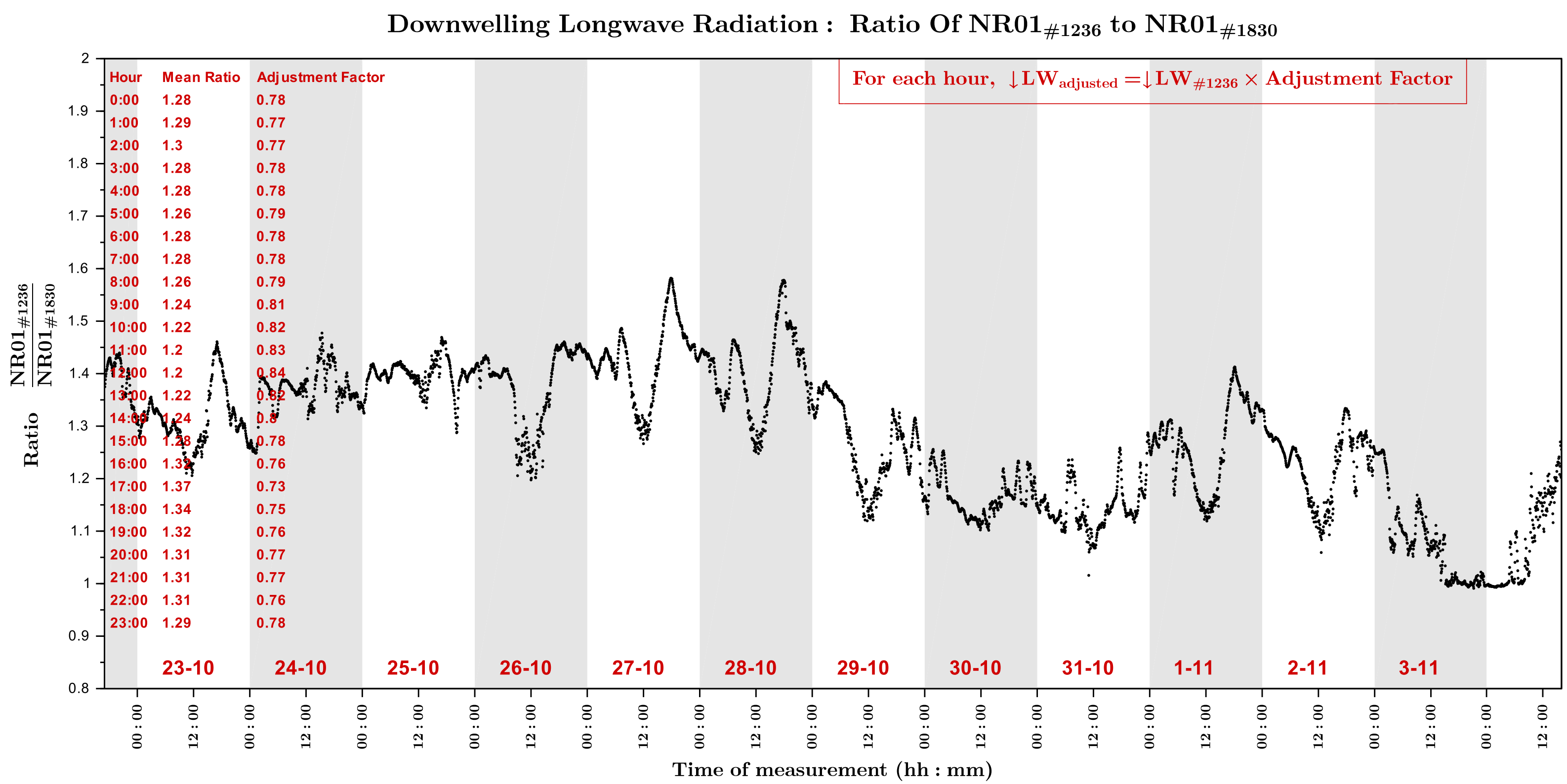

Figure F.5: Ratio of NR01$_{\#1236}$ to NR01$_{\#1830}$ for $LW_{downwelling}$. The mean ratio for each hour and the adjustment factor (to apply to the NR01$_{\#1236}$ $LW_{downwelling}$ data from DS1) are listed.

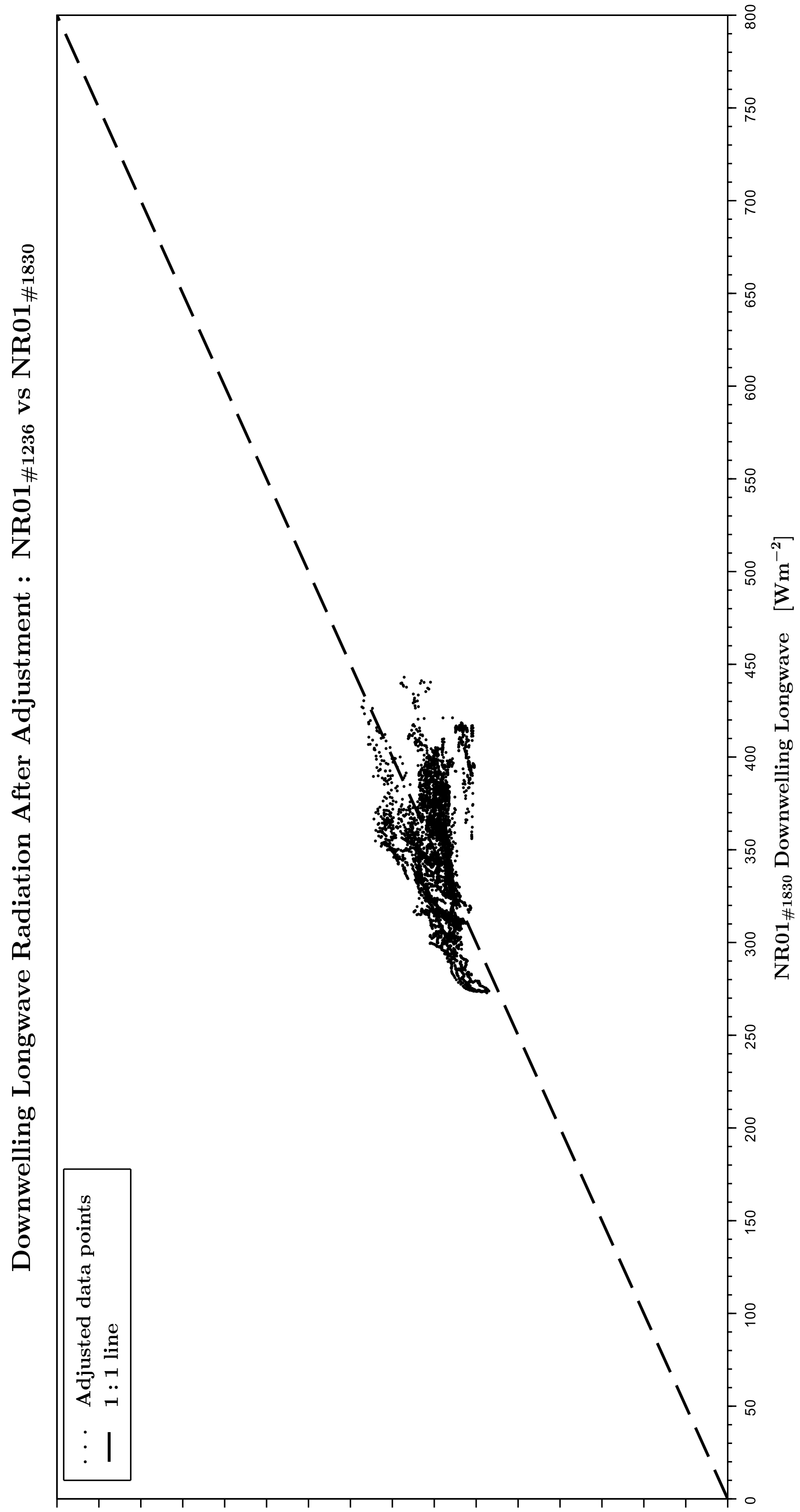

Figure F.6: Result of adjusting $LW_{downwelling}$ from Hukseflux NR01$_{\#1236}$ by applying hourly adjustment factors.

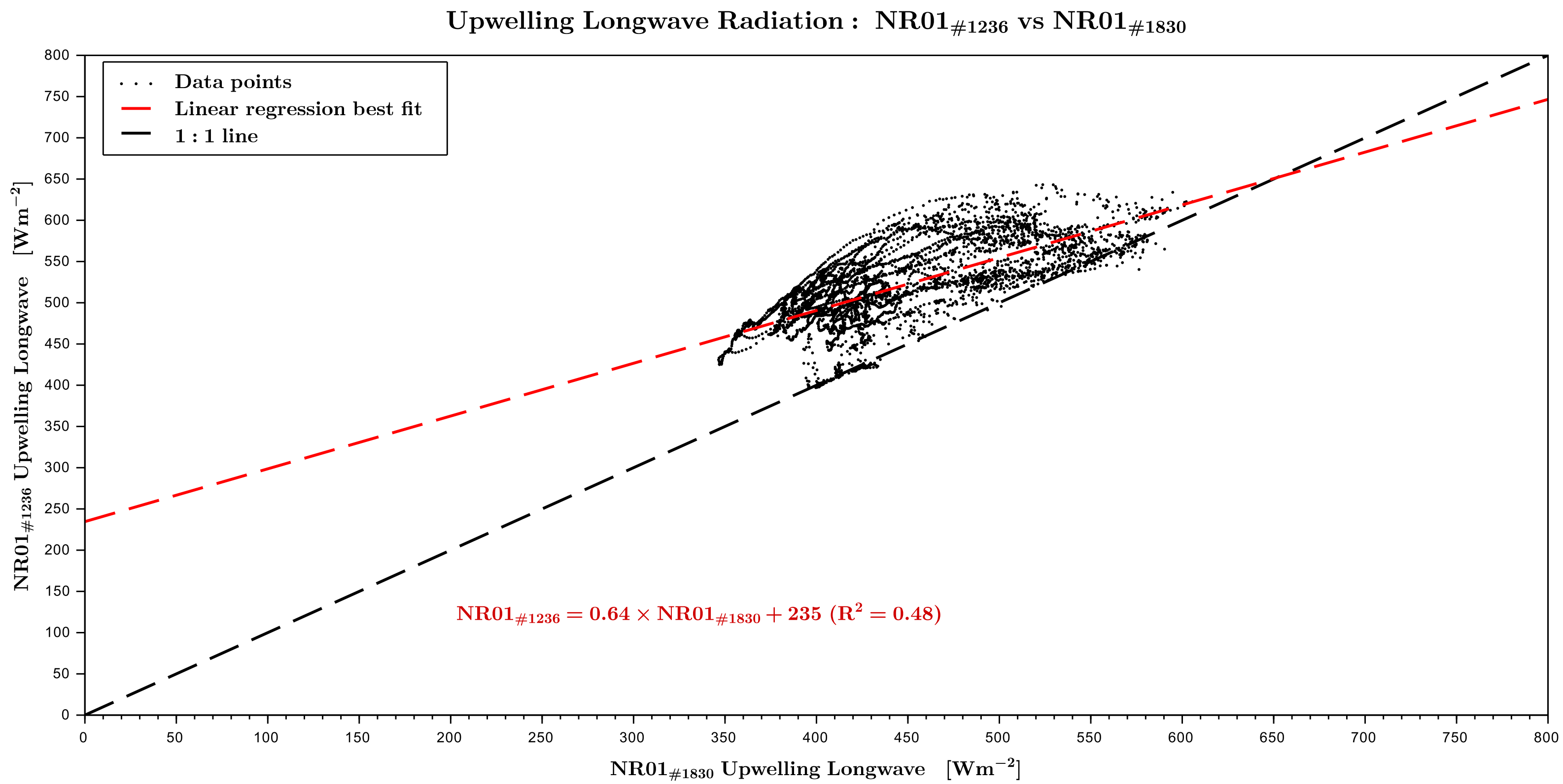

Figure F.7: Plotting $LW_{upwelling}$ from Hukseflux NR01$_{\#1236}$ against the laboratory-calibrated Hukseflux NR01$_{\#1830}$.

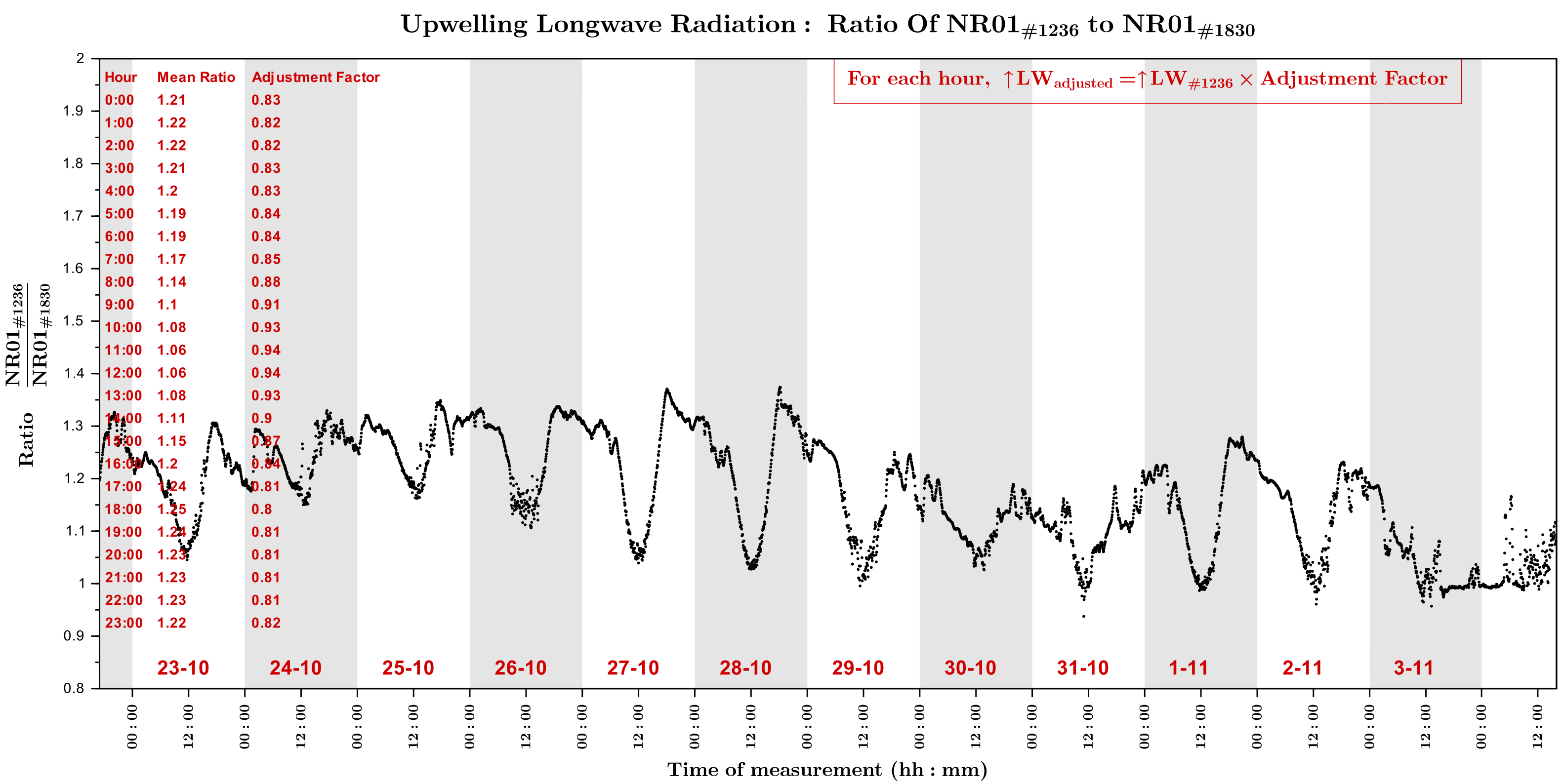

Figure F.8: Ratio of NR01$_{\#1236}$ to NR01$_{\#1830}$ for $LW_{upwelling}$. The mean ratio for each hour and the adjustment factor (to apply to the NR01$_{\#1236}$ $LW_{upwelling}$ data from DS1) are listed.

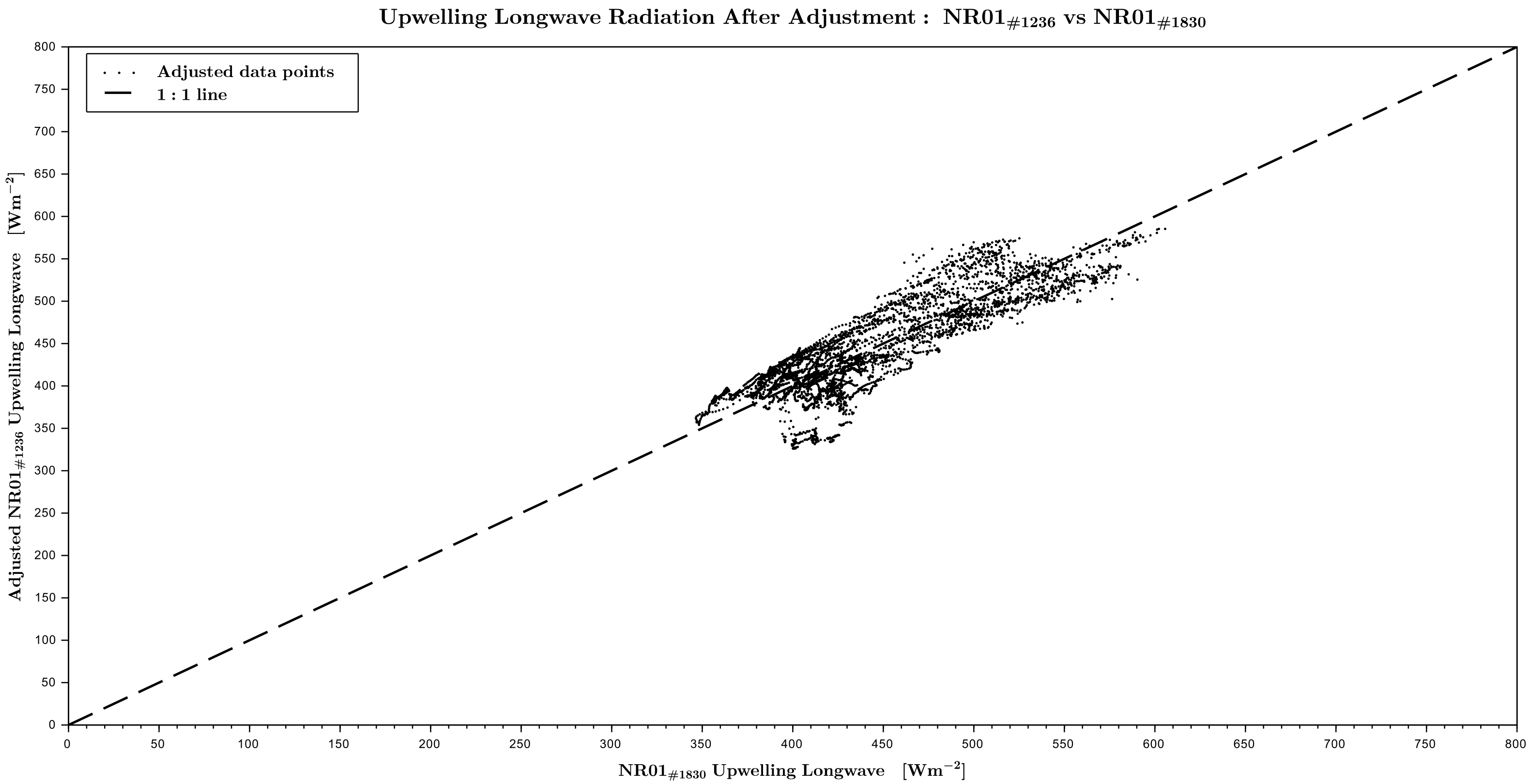

Figure F.9: Result of adjusting $LW_{upwelling}$ from Hukseflux NR01$_{\#1236}$ by applying hourly adjustment factors.

This page intentionally left blank.

Appendix G

SENSITIVITY ANALYSIS FOR GPSTIC

GPSTIC requires the following input variables:

- Ambient air temperature, T [°C]
- Radiometric surface temperature, T_S [°C]
- Relative humidity, RH [%]
- Available energy flux, ϕ [$\mathrm{Wm^{-2}}$]
- Barometric pressure, P [hPa]
- Priestley-Taylor alpha, α_{PT}

GPSTIC's sensitivity to each of the input variables was evaluated by varying one input variable at a time and observing the percentage change in the model's output, ΔE:

$$\Delta E = \left(\frac{E_1 - E_0}{E_0}\right) \times 100 \tag{G.1}$$

where E_0 and E_1 are un-varied and varied E, respectively.

Fig. G.1 (p. 376) shows the results when the input variables were scaled by factors between 0.75 and 1.25 (in increments of 0.05).

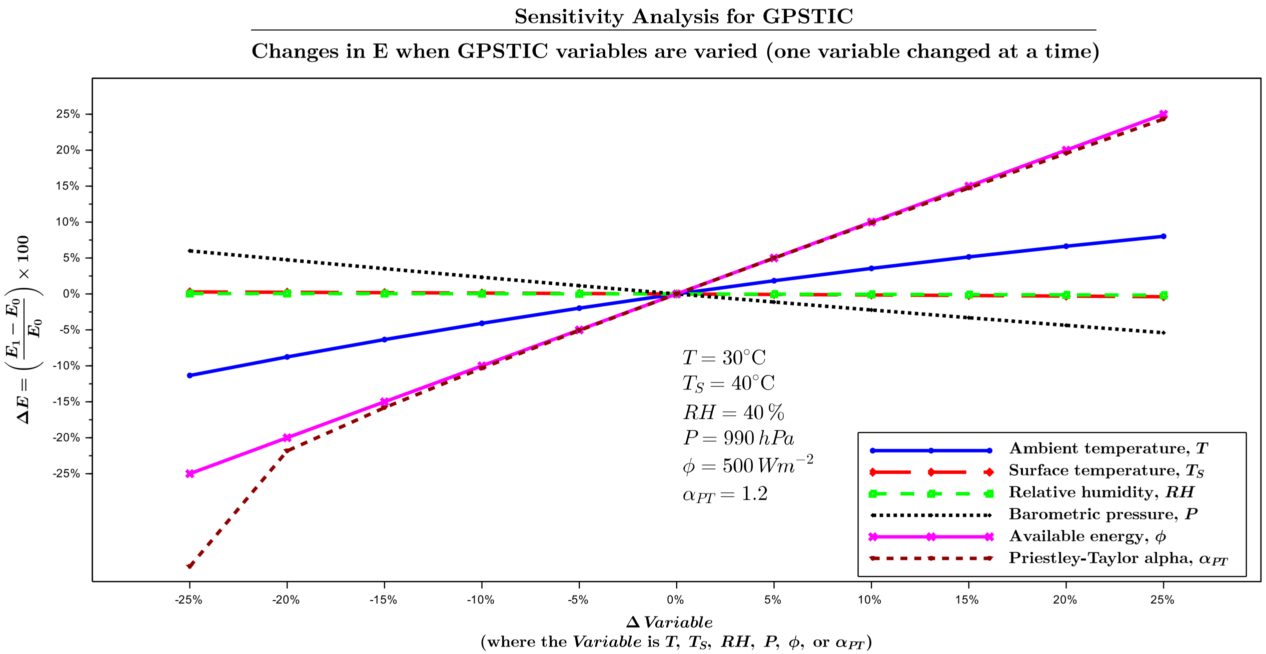

Figure G.1: Sensitivity analysis for the GPSTIC model. The individual input variables were changed by specified percentage amounts, one at a time. E_0 and E_1 are un-varied and varied values of E, respectively. The values of the (unchanged) variables used for the analysis are listed in the plot.

Fig. G.1 suggests that GPSTIC is quite insensitive to changes in T_S and RH and approximately proportional to ϕ and α_{PT}. The latter results are expected, but those regarding T_S and RH are not.

If these sensitivity results are correct then this suggests that there is scope for using lower cost, less accurate sensors for T_S and RH but not for ϕ (which is unfortunate because net radiometers are relatively expensive instruments).

The sensitivity of GPSTIC to changes in α_{PT} is reflected in the results in Tables 5.1 (p. 203), 5.2 (p. 209) and 5.3 (p. 213). The sensitivity of GPSTIC to α_{PT} is concerning because there are not yet any clear guidelines as to its selection (§ 2.2, p. 23).

But there is also a problem in the method of this sensitivity analysis: it does not allow for the interdependence of the variables on each other. Varying one will inevitably cause a change in others and it is unrealistic that one variable can be varied while the others remain unchanged.

The case of T_S is an interesting thought exercise. If T_S changes then it must be due to either:

(a) a change in ϕ and/or T, or

(b) impaired thermo-regulation by the plant or soil surface due to reduction of evapotranspiration (e.g. inadequate soil moisture, occluded xylem/stomata, or a saturated atmosphere).

But in the sensitivity analysis of T_S all other variables were held constant so Option (a) must be ruled out. Instead we might suspect a reduction in E as described by Option (b) to be the cause of a rising T_S. However, this would also cause a rise in T as more of ϕ is apportioned to sensible heat. But this is not allowed to happen (because we have stipulated that all other variables must remain constant) so effectively we have created an impossible scenario. It should not be surprising, then, if unexpected and questionable results come out of the sensitivity analysis.

This page intentionally left blank.

Appendix H

UNCERTAINTY ANALYSIS

Every sensor has an inherent measurement uncertainty that is usually specified by a manufacturer or on a calibration certificate as $\pm\,\delta x$ (absolute uncertainty) or $\pm\,x\,\%$ (relative uncertainty).

When the instrument manufacturer does not make explicitly clear otherwise, it is assumed in this thesis that reported sensor uncertainties are 2σ (or 95 % CI), as illustrated in Fig. H.1 (p. 379). This means that it can be expected that 95 % of measurements will be between $x - \delta x$ and $x + \delta x$ (but most measurements would be expected to be close to x).

Often 2σ standards are used in instrumentation sciences, and 1σ standards are used in environmental and atmospheric sciences. In this research, a very strict 2σ standard has been applied in all uncertainty analyses.

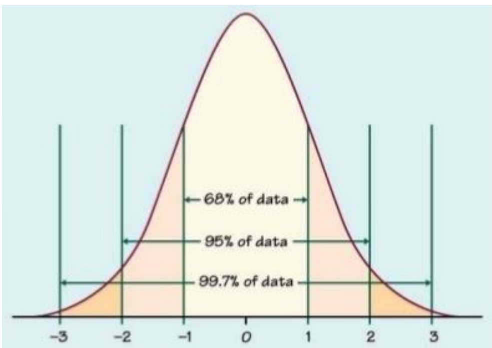

Figure H.1: Normal distribution plot showing 2σ (95 %) bounds.

H.1 Error Propagation

Error propagation is the analysis of the impact that measurement uncertainties have on a model's final outputs. The objective is to determine what range of outputs from a model will constitute the 95 % confidence interval given the uncertainty of the measurements that are being entered into the model.

H.1.1 Calculation of Error Propagation - Net Radiation (As An Example)

Error propagation can be calculated using analytical methods or numerical methods. Both methods have their merits and both are used in this thesis, although numerical methods predominate due to the complexity of the BREB and GPSTIC models.

The process of calculating the uncertainty in net radiation, δR_N, is given here as a simple example for both methods.

1. **Algebraic Methods for Calculating Error Propagation**

   The following principles for calculating error propagation using algebraic methods are taken from Taylor (1997):

   (a) When equation variables are added (or subtracted), then the absolute uncertainty of the sum (or difference) is calculated by the addition of the absolute uncertainties of each of the variables.

   $$\text{Let } s \text{ be the sum} \qquad s = x + y$$

   If the variables x and y are not independent, then

   $$\delta s = \delta x + \delta y \tag{H.1}$$

If the variables x and y are independent, then

$$\delta s = \sqrt{(\delta x)^2 + (\delta y)^2} \tag{H.2}$$

(b) When equation variables are multiplied (or divided), then the relative uncertainty of the product (or quotient) is calculated by the sum of the relative uncertainties.

e.g. Let p be the product $\qquad p = xy$

If the variables x and y are not independent, then

$$\frac{\delta p}{p} = \frac{\delta x}{x} + \frac{\delta y}{y} \tag{H.3}$$

If the variables x and y are independent, then

$$\frac{\delta p}{p} = \sqrt{\left(\frac{\delta x}{x}\right)^2 + \left(\frac{\delta y}{y}\right)^2} \tag{H.4}$$

(c) If the same variables appear in both the numerator and denominator then Equations H.1 - H.4 may significantly overestimate the error. This is because it is possible that errors in the numerator may, to some extent, cancel errors in the denominator, referred to as *compensating errors* (Taylor 1997). This problem is avoided by using the following rule for calculating uncertainty:

Let q be defined as $\qquad q = f\left(x_1, \ldots, x_i\right)$

Then if $x_1, \ldots, x_i$ are independent and random

$$\delta q = \sqrt{\left(\frac{\partial q}{\partial x_1}\delta x_1\right)^2 + \cdots + \left(\frac{\partial q}{\partial x_i}\delta x_i\right)^2} \tag{H.5}$$

where $\frac{\partial q}{\partial x_i}$ is the partial derivative of q with respect to x_i.

Eqn. H.5 can, in theory, be used in all circumstances. However, sometimes Equations H.1 - H.4 or numerical methods may be preferred to having to calculate the partial derivatives of a function.

Considering the net radiation example:[1]

$$\text{Let} \qquad R_N = SW_d + LW_d - SW_u - LW_u$$

Per the calibration certificate (p. 348) the 2σ relative uncertainties of the four sensors are:

$$\frac{\delta SW_d}{SW_d} = 3\,\%$$
$$\frac{\delta LW_d}{LW_d} = 8\,\%$$
$$\frac{\delta SW_u}{SW_u} = 3\,\%$$
$$\frac{\delta LW_u}{LW_u} = 8\,\%$$

Using some typical radiation values for the purposes of this example (as measured on 18$^{\text{th}}$ February, 2019):

$$SW_d = 857\,\mathrm{Wm^{-2}}$$

[1] For compactness $SW_{downwelling}$ is denoted SW_d and $LW_{upwelling}$ is denoted LW_u (etc.)

$$
\begin{aligned}
LW_d &= 548\,\mathrm{Wm}^{-2} \\
LW_u &= 644\,\mathrm{Wm}^{-2} \\
SW_u &= 148\,\mathrm{Wm}^{-2}
\end{aligned}
$$

The absolute uncertainty is then calculated as follows:

$$
\delta R_N = \sqrt{\left(\frac{\delta SW_d}{SW_d} SW_d\right)^2 + \left(\frac{\delta LW_d}{LW_d} LW_d\right)^2 + \left(\frac{\delta LW_u}{LW_u} LW_u\right)^2 + \left(\frac{\delta SW_u}{SW_u} SW_u\right)^2}
$$

where

$$
\begin{aligned}
\left(\frac{\delta SW_d}{SW_d} SW_d\right)^2 &= (0.03 \times 857)^2 \\
&= 661\,\mathrm{W}^2\mathrm{m}^{-4} \\
\left(\frac{\delta LW_d}{LW_d} LW_d\right)^2 &= (0.08 \times 548)^2 \\
&= 1922\,\mathrm{W}^2\mathrm{m}^{-4} \\
\left(\frac{\delta LW_u}{LW_u} LW_u\right)^2 &= (0.08 \times 644)^2 \\
&= 2654\,\mathrm{W}^2\mathrm{m}^{-4} \\
\left(\frac{\delta SW_u}{SW_u} SW_u\right)^2 &= (0.03 \times 148)^2 \\
&= 20\,\mathrm{W}^2\mathrm{m}^{-4} \\
\therefore\ \delta R_N &= \sqrt{661 + 1922 + 2654 + 20} \\
&= 73\,\mathrm{Wm}^{-2}
\end{aligned}
$$

While R_N is reported to equal $613\,\mathrm{Wm}^{-2}$ based on the sensors' measurements, it can more correctly be said that we have 95 % confidence that the true value for R_N lies in the range

$$
540\,\mathrm{Wm}^{-2} \leqslant R_N \leqslant 686\,\mathrm{Wm}^{-2} \tag{H.6}
$$

which effectively equates to a 11.9 % relative uncertainty in R_N overall.

If (say) the four sensors couldn't be considered to be independent then

$$\begin{aligned}\delta R_N &= \frac{\delta SW_d}{SW_d}SW_d + \frac{\delta LW_d}{LW_d}LW_d + \frac{\delta LW_u}{LW_u}LW_u + \frac{\delta SW_u}{SW_u}SW_u \\ &= (0.03 \times 857) + (0.08 \times 548) \\ &\quad + (0.08 \times 644) + (0.03 \times 148) \\ &= 126\,\mathrm{Wm}^{-2}\end{aligned}$$

In this case, it would be correctly said that one can have 95 % confidence that the true value for R_N lies somewhere in the range

$$487\,\mathrm{Wm}^{-2} \leqslant R_N \leqslant 739\,\mathrm{Wm}^{-2} \tag{H.7}$$

which effectively equates to a 20.6 % relative uncertainty overall. Thus the propagated error is markedly larger when measurements cannot be considered independent of each other.

2. **Numerical Method for Calculating Error Propagation**
   The numerical method for calculating the error propagation is to repeatedly re-calculate an equation using different combinations of the minimum and maximum values for the equation variables. In the present example for calculating R_N, the minimum and maximum values for the equation variables are discovered as follows:[2]

$$SW_{d_{(min)}} = SW_d - \frac{\delta SW_d}{SW_d}SW_d$$

[2]In this simple example it is obvious that the minimum value for R_N will be calculated by $R_N = SW_{d_{(min)}} - SW_{u_{(max)}} + LW_{d_{(min)}} - LW_{u_{(max)}}$ and the maximum value for R_N will be calculated by $R_N = SW_{d_{(max)}} - SW_{u_{(min)}} + LW_{d_{(max)}} - LW_{u_{(min)}}$. However, all combinations are presented here to show the process used when the solution is not obvious.

$$
\begin{aligned}
&= 857 - (0.03 \times 857) \\
&= 831\,\mathrm{Wm^{-2}} \\
SW_{d_{(max)}} &= SW_d + \frac{\delta SW_d}{SW_d} SW_d \\
&= 857 + (0.03 \times 857) \\
&= 883\,\mathrm{Wm^{-2}} \\
LW_{d_{(min)}} &= LW_d - \frac{\delta LW_d}{LW_d} LW_d \\
&= 548 - (0.08 \times 548) \\
&= 504\,\mathrm{Wm^{-2}} \\
LW_{d_{(max)}} &= LW_d + \frac{\delta LW_d}{LW_d} LW_d \\
&= 548 + (0.08 \times 548) \\
&= 592\,\mathrm{Wm^{-2}} \\
SW_{u_{(min)}} &= SW_u - \frac{\delta SW_u}{SW_u} SW_u \\
&= 148 - (0.03 \times 148) \\
&= 144\,\mathrm{Wm^{-2}} \\
SW_{u_{(max)}} &= SW_u + \frac{\delta SW_u}{SW_u} SW_u \\
&= 148 + (0.03 \times 148) \\
&= 152\,\mathrm{Wm^{-2}} \\
LW_{u_{(min)}} &= LW_u - \frac{\delta LW_u}{LW_u} LW_u \\
&= 644 - (0.08 \times 644) \\
&= 592\,\mathrm{Wm^{-2}} \\
LW_{u_{(max)}} &= LW_u + \frac{\delta LW_u}{LW_u} LW_u \\
&= 644 + (0.08 \times 644) \\
&= 696\,\mathrm{Wm^{-2}}
\end{aligned}
$$

There are 16 possible combinations of input variables ($SW_{d_{(max)}}$, $LW_{u_{(min)}}$ etc.) to calculate R_N. The minimum is given by:

$$\begin{aligned}
R_N &= SW_{d_{(min)}} - SW_{u_{(max)}} + LW_{d_{(min)}} - LW_{u_{(max)}} \\
&= 831 - 152 + 504 - 696 \\
&= 487\,\mathrm{Wm}^{-2} \quad \boxed{\text{MINIMUM VALUE}} \qquad \text{(H.8)} \\
R_N &= SW_{d_{(max)}} - SW_{u_{(min)}} + LW_{d_{(max)}} - LW_{u_{(min)}} \\
&= 883 - 144 + 592 - 592 \\
&= 739\,\mathrm{Wm}^{-2} \quad \boxed{\text{MAXIMUM VALUE}} \qquad \text{(H.9)}
\end{aligned}$$

We have 95 % confidence that the true value for R_N lies in the range

$$487\,\mathrm{Wm}^{-2} \leqslant R_N \leqslant 739\,\mathrm{Wm}^{-2} \qquad \text{(H.10)}$$

which effectively equates to a 20.5 % relative uncertainty in R_N overall.

Three conclusions regarding the calculation of error propagation by algebraic vs. numerical methods are made from the preceding example:

- When measurements are *not* independent, the algebraic and numerical methods will produce identical results (cf. Eqn. H.7, p. 384 and Eqn. H.10, p. 386).

- When measurements are independent, the algebraic method will produce a smaller uncertainty range because in the algebraic method the uncertainties can be added in quadrature (Taylor 1997).

- When a model (such as GPSTIC) contains large numbers of equations and variables; trigonometric, logarithmic, or exponential functions (etc.); implicitly-defined equations; and a requirement for iterative loops to converge on a solution then the algebraic methods can quickly become unwieldy and present significant opportunities for mistakes (and, crucially, no means by which to detect those mistakes), both during the formulation of equations and the subsequent coding. Thus, the numerical method may be the preferred option in such cases (even if this means forgoing the smaller propagated error that comes by adding in quadrature).

H.1.2 Error Propagation When Calculating LoBF by Linear Regression

Profile BREB requires multiple pairs of (e, T) to be simultaneously measured at different heights above a crop. A line-of-best-fit (LoBF) through these points is then calculated by linear regression and the slope of the LoBF, a_1, is used to calculate β (e.g. Fig. H.2, p. 390).

For this thesis, five pairs of measurements, denoted $(e_A, T_A) \ldots (e_E, T_E)$, were made simultaneously for every minute of the hour. Those values were then averaged in 4 min intervals and the LoBF and a_1 were thus calculated 15 times per hour. β and E_{BREB} were also calculated for every 4 min interval by the following equations:

$$a_1 = \frac{n \sum e_i T_i - \sum e_i \sum T_i}{n \sum {e_i}^2 - \left(\sum e_i\right)^2} \tag{H.11}$$

$$\beta = \frac{c_P\, P}{\lambda\, \epsilon}\, a_1 \tag{H.12}$$

$$E_{BREB} = \frac{\phi}{\lambda\,(1+\beta)}$$

$$\therefore E_{BREB} = \frac{\phi}{\lambda\left(1 + \frac{c_P\, P}{\lambda\, \epsilon}\, a_1\right)} \tag{H.13}$$

The uncertainties in the measurement of e and T propagate from Eqn. H.11 through to Eqn. H.13 to give an uncertainty in E_{BREB}, i.e. δE_{BREB}. Calculating this first required δa_1 which was best done by Eqn. H.5 (p. 382). There were 10 input variables for Eqn. H.11, i.e. $e_A, \ldots, e_E$ and $T_A, \ldots, T_E$ and so 10 partial derivatives were calculated. Eqn. H.11 (with $n = 5$) was expanded and terms collected so that the numerator,

G, and denominator, H, of a_1 were:

$$\begin{aligned}
G = 4\,&(e_A T_A + e_B T_B + e_C T_C + e_D T_D + e_E T_E) \\
&- e_A\,(T_B + T_C + T_D + T_E) \\
&- e_B\,(T_A + T_C + T_D + T_E) \\
&- e_C\,(T_A + T_B + T_D + T_E) \\
&- e_D\,(T_A + T_B + T_C + T_E) \\
&- e_E\,(T_A + T_B + T_C + T_D) \\
H = 4\,&\left({e_A}^2 + {e_B}^2 + {e_C}^2 + {e_D}^2 + {e_E}^2\right) \\
&- 2e_A\,(e_B + e_C + e_D + e_E) \\
&- 2e_B\,(e_C + e_D + e_E) \\
&- 2e_C\,(e_D + e_E) \\
&- 2e_D e_E
\end{aligned}$$

Then the partial derivatives are:

$$\begin{aligned}
\frac{\partial a_1}{\partial e_A} &= \frac{(4T_A - T_B - T_C - T_D - T_E)\,H - 2\,G\,(4e_A - e_B - e_C - e_D - e_E)}{H^2} \\
\frac{\partial a_1}{\partial e_B} &= \frac{(4T_B - T_A - T_C - T_D - T_E)\,H - 2\,G\,(4e_B - e_A - e_C - e_D - e_E)}{H^2} \\
&\vdots \\
\frac{\partial a_1}{\partial T_D} &= \frac{4e_D - e_A - e_B - e_C - e_E}{H} \\
\frac{\partial a_1}{\partial T_E} &= \frac{4e_E - e_A - e_B - e_C - e_D}{H}
\end{aligned}$$

The absolute uncertainty for a_1 is:

$$\delta a_1 = \sqrt{\left(\frac{\partial a_1}{\partial e_A}\delta e_A\right)^2 + \cdots + \left(\frac{\partial a_1}{\partial T_E}\delta T_E\right)^2} \tag{H.14}$$

and the absolute uncertainty in β is:

$$\delta\beta = \frac{c_P\,P}{\lambda\,\epsilon}\,\delta a_1 \tag{H.15}$$

Finally, by taking the partial derivatives of Eqn. H.13 (p. 387) and combining with Eqn. H.12 (p. 387) and Eqn. H.15 (p. 388), the absolute uncertainty in evapotranspiration, δE is:

$$\begin{aligned}
\frac{\partial E}{\partial \phi} &= \frac{1}{\lambda\,(1+\beta)} \\
\frac{\partial E}{\partial \beta} &= \frac{-\phi}{\lambda\,(1+\beta)^2} \\
\delta E &= \sqrt{\left(\frac{\partial E}{\partial \phi}\delta\phi\right)^2 + \left(\frac{\partial E}{\partial \beta}\delta\beta\right)^2} \\
\therefore\, \delta E &= \sqrt{\frac{(\delta\phi)^2}{\lambda^2\left(1+\frac{c_P\,P}{\lambda\,\epsilon}\,a_1\right)^2} + \frac{\phi^2\left(\frac{c_P\,P}{\lambda\,\epsilon}\,\delta a_1\right)^2}{\lambda^2\left(1+\frac{c_P\,P}{\lambda\,\epsilon}\,a_1\right)^4}}
\end{aligned} \tag{H.16}$$

The 95 % CI containing the correct value for E is:

$$(E - \delta E) \leqslant E \leqslant (E + \delta E) \tag{H.17}$$

where E is per Eqn. H.13 (p. 387) and δE is per Eqn. H.16 (p. 389).

These equations were coded in the Profile BREB Scilab code to compute the uncertainty in E_{BREB} for every 4 min interval. The uncertainty in GPSTIC was also computed in Scilab (for the same 4 min intervals) but using the numerical process described on p. 384 because the equations were more complex (e.g. implicitly-defined non-linear equations requiring iterative solution processes).

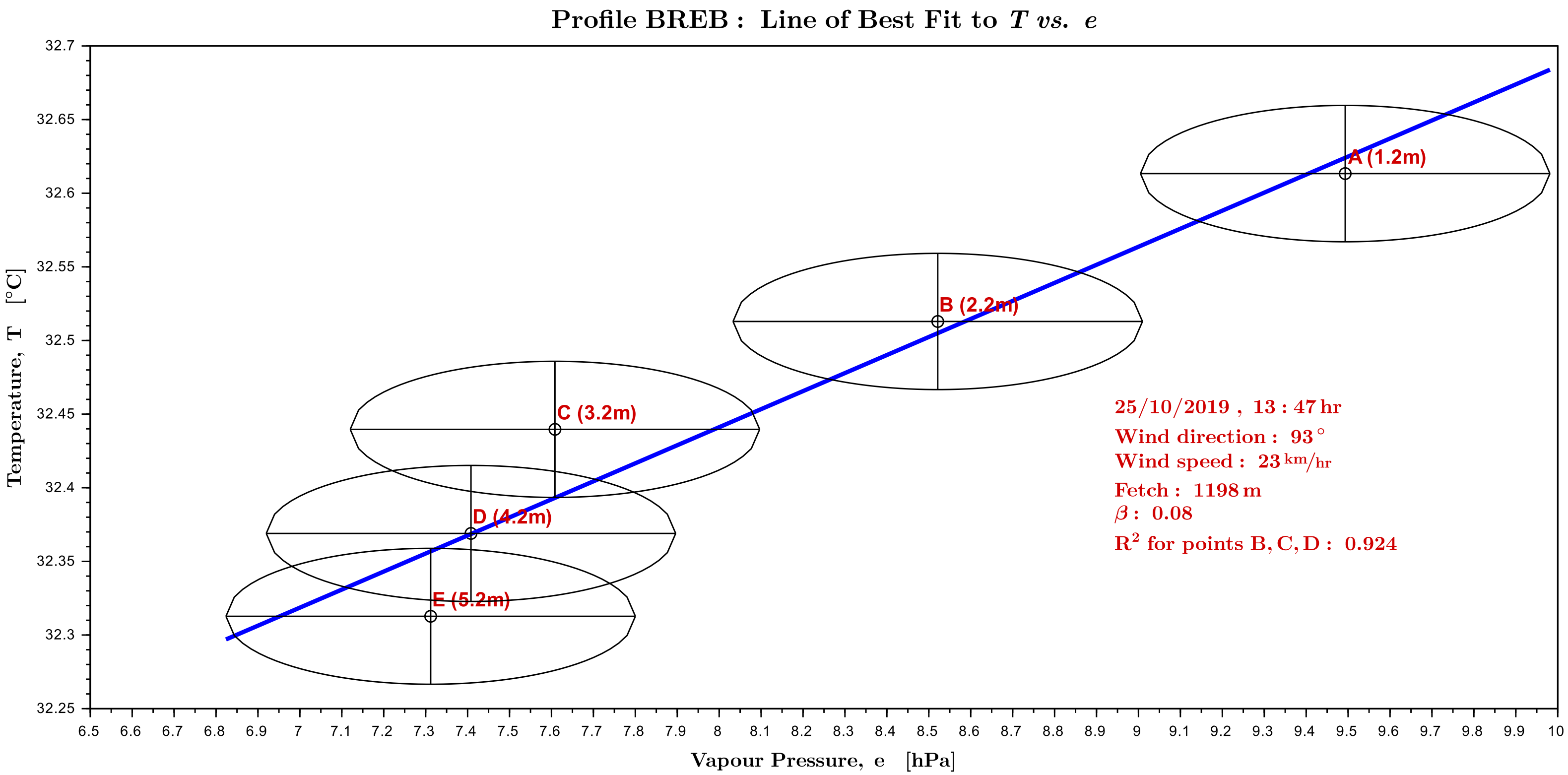

Figure H.2: Example of the LoBF sub-algorithm in action. The ellipses indicate the 95 % (2σ) confidence region for each plotted point which are the consequence of measurement uncertainty in each of e and T (Cook & Weisberg 1994).

Appendix I

ALGEBRAIC REWORKINGS AND DERIVATIONS

This appendix contains the step-by-step algebraic workings that were too voluminous for inclusion in the main body of the thesis.

The three sections of work are:

I.1 Reworking of STIC Closure Equations

Mallick et al. (2014) and Mallick et al. (2015a) presented the following four equations (I.1 to I.4) whose simultaneous solution yields values for aerodynamic conductivity, g_B, and stomatal conductivity, g_S.

$$g_B = \frac{\phi}{\rho c_p \left(T_0 - T_A + \frac{e_0 - e_A}{\gamma}\right)} \tag{I.1}$$

$$g_S = g_B \frac{e_0 - e_A}{{e_0}^* - e_0} \tag{I.2}$$

$$T_0 = T_A + \left(\frac{e_0 - e_A}{\gamma}\right)\left(\frac{1 - \Lambda}{\Lambda}\right) \tag{I.3}$$

$$\Lambda = \frac{2\alpha_{PT} s}{2s + 2\gamma + \gamma \frac{g_B}{g_S}(1 + M)} \tag{I.4}$$

These equations are not independent and can be combined to form a single implicitly-defined equation for T_0 (Eqn. I.11, p. 395). Solving for T_0 by numerical methods then allows the equations for g_B (Eqn. I.1) and g_S (Eqn. I.2) to be solved. The step-by-step algebraic manipulations to derive T_0 are laid out here (commencing overleaf):

$$
\begin{aligned}
g_S &= g_B \frac{e_0 - e_A}{{e_0}^* - e_0} \\
&= \frac{\phi}{\rho c_p \left(T_0 - T_A + \frac{e_0 - e_A}{\gamma}\right)} \frac{e_0 - e_A}{{e_0}^* - e_0} && \text{(I.5)} \\
\Lambda &= \frac{2\alpha_{PT} s}{2s + 2\gamma + \gamma \frac{g_B}{g_S} (1 + M)} \\
&= \frac{2\alpha_{PT} s}{2s + 2\gamma + \gamma \frac{\frac{\phi}{\rho c_p \left(T_0 - T_A + \frac{e_0 - e_A}{\gamma}\right)}}{\frac{\phi}{\rho c_p \left(T_0 - T_A + \frac{e_0 - e_A}{\gamma}\right)} \frac{e_0 - e_A}{{e_0}^* - e_0}} (1 + M)} \\
&= \frac{2\alpha_{PT} s}{2s + 2\gamma + \frac{\gamma (1+M) \phi}{\rho c_p \left[T_0 - T_A + \frac{e_0 - e_A}{\gamma}\right]} \frac{\rho c_p \left[T_0 - T_A + \frac{e_0 - e_A}{\gamma}\right]}{\phi \left(\frac{e_0 - e_A}{{e_0}^* - e_0}\right)}} \\
&= \frac{2\alpha_{PT} s}{2s + 2\gamma + \frac{\gamma (1+M)}{\left(\frac{e_0 - e_A}{{e_0}^* - e_0}\right)}} \\
&= \frac{2\alpha_{PT} s}{\frac{2s \left(\frac{e_0 - e_A}{{e_0}^* - e_0}\right) + 2\gamma \left(\frac{e_0 - e_A}{{e_0}^* - e_0}\right) + \gamma (1+M)}{\left(\frac{e_0 - e_A}{{e_0}^* - e_0}\right)}} \\
&= \frac{2\alpha_{PT} s \left(\frac{e_0 - e_A}{{e_0}^* - e_0}\right)}{2s \left(\frac{e_0 - e_A}{{e_0}^* - e_0}\right) + 2\gamma \left(\frac{e_0 - e_A}{{e_0}^* - e_0}\right) + \gamma (1 + M)} \\
&= \frac{\frac{2\alpha_{PT} s (e_0 - e_A)}{({e_0}^* - e_0)}}{\frac{2s (e_0 - e_A)}{{e_0}^* - e_0} + \frac{2\gamma (e_0 - e_A)}{{e_0}^* - e_0} + \frac{\gamma (1+M)({e_0}^* - e_0)}{{e_0}^* - e_0}} \\
&= \frac{2\alpha_{PT} s (e_0 - e_A)}{({e_0}^* - e_0)} \times \frac{({e_0}^* - e_0)}{2s (e_0 - e_A) + 2\gamma (e_0 - e_A) + \gamma (1 + M)} \\
&= \frac{2\alpha_{PT} s e_0 - 2\alpha_{PT} s e_A}{2s e_0 - 2s e_A + 2\gamma e_0 - 2\gamma e_A + \gamma + \gamma M} \\
&= \frac{2\alpha_{PT} s e_0 - 2\alpha_{PT} s e_A}{(2s + 2\gamma) e_0 - 2s e_A - 2\gamma e_A + \gamma + \gamma M} && \text{(I.6)}
\end{aligned}
$$

Substituting Λ into the equation for T_0:

$$
\begin{aligned}
T_0 &= T_A + \left(\frac{e_0 - e_A}{\gamma}\right)\left(\frac{1-\Lambda}{\Lambda}\right) \\
&= T_A + \left(\frac{e_0 - e_A}{\gamma}\right)\left(\frac{1 - \frac{2\alpha s e_0 - 2\alpha_{PT} s e_A}{(2s+2\gamma)e_0 - 2se_A - 2\gamma e_A + \gamma + \gamma M}}{\frac{2\alpha_{PT} s e_0 - 2\alpha_{PT} s e_A}{(2s+2\gamma)e_0 - 2se_A - 2\gamma e_A + \gamma + \gamma M}}\right) \\
&= T_A + \left(\frac{e_0 - e_A}{\gamma}\right)\left(\frac{(2s+2\gamma)\,e_0 - 2se_A - 2\gamma e_A + \gamma + \gamma M - 2\alpha_{PT} s e_0 + 2\alpha_{PT} s e_A}{(2s+2\gamma)\,e_0 - 2se_A - 2\gamma e_A + \gamma + \gamma M} \times \frac{(2s+2\gamma)\,e_0 - 2se_A - 2\gamma e_A + \gamma + \gamma M}{2\alpha_{PT} s e_0 - 2\alpha_{PT} s e_A}\right) \\
&= T_A + \left(\frac{e_0 - e_A}{\gamma}\right)\left(\frac{(2s+2\gamma)\,e_0 - 2se_A - 2\gamma e_a + \gamma + \gamma M - 2\alpha_{PT} s e_0 + 2\alpha_{PT} s e_A}{2\alpha_{PT} s e_0 - 2\alpha_{PT} s e_A}\right) \\
&= T_A + \left(\frac{e_0 - e_A}{\gamma}\right)\left(\frac{(2s+2\gamma-2\alpha s)\,e_0 + \gamma + \gamma M - (2s+2\gamma-2\alpha_{PT} s)\,e_A}{2\alpha_{PT} s e_0 - 2\alpha_{PT} s e_A}\right)
\end{aligned}
$$

e_0 is given by Mallick et al. (2015a) as

$$
e_0 = e_A\,(1-M) + M{e_0}^* \tag{I.7}
$$

Substituting into T_0:

$$
\begin{aligned}
T_0 &= T_A + \left(\frac{e_A\,(1-M) + M{e_0}^* - e_A}{\gamma}\right)\left(\frac{(2s+2\gamma-2\alpha_{PT} s)\,(e_A\,(1-M) + M{e_0}^*) + \gamma + \gamma M - (2s+2\gamma-2\alpha_{PT} s)\,e_A}{2\alpha_{PT} s\,(e_A\,(1-M) + M{e_0}^*) - 2\alpha_{PT} s e_A}\right) \\
&= T_A + \left(\frac{e_A - Me_A + M{e_0}^* - e_A}{\gamma}\right)\left(\frac{(2s+2\gamma-2\alpha_{PT} s)\,(e_A - Me_A + M{e_0}^*) + \gamma + \gamma M - 2se_A - 2\gamma e_A + 2\alpha_{PT} s e_A}{2\alpha_{PT} s\,(e_A - Me_A + M{e_0}^*) - 2\alpha_{PT} s e_A}\right)
\end{aligned}
$$

Expanding and collecting terms:

$$\begin{aligned}
T_0 &= T_A + \left(\frac{Me_0{}^* - Me_A}{\gamma}\right)\left(\frac{e_0{}^*\left(2sM + 2\gamma M - 2\alpha_{PT} sM\right) - 2sMe_A - 2s\gamma M + 2\alpha_{PT} sMe_A + \gamma + \gamma M}{2\alpha_{PT} sM\left(e_0{}^* - e_A\right)}\right) \\
&= T_A + \left(\frac{M\left(e_0{}^* - e_A\right)}{\gamma}\right)\left(\frac{2Me_A\left(\alpha_{PT} s - s - \gamma\right) - 2Me_0{}^*\left(\alpha_{PT} s - s - \gamma\right) + \gamma + \gamma M}{2\alpha_{PT} sM\left(e_0{}^* - e_A\right)}\right)
\end{aligned} \tag{I.8}$$

The general equation for saturated vapour pressure over an open water surface for $T > 0\,^\circ\mathrm{C}$ is (Buck 1981, 1996):

$$e^* = 0.61121 \exp\left[\left(18.678 - \frac{T}{234.5}\right)\left(\frac{T}{257.14 + T}\right)\right] \tag{I.9}$$

Thus $e_0{}^*$ is given by:

$$e_0{}^* = 0.61121 \exp\left[\left(18.678 - \frac{T_0}{234.5}\right)\left(\frac{T_0}{257.14 + T_0}\right)\right] \tag{I.10}$$

Substituting Eqn. I.10 into Eqn. I.8 and simplifying finally yields the implicitly defined equation for T_0:

$$T_0 = T_A + \left(\frac{2M\left(\alpha_{PT} s - s - \gamma\right)\left(e_A - 0.61121 \exp\left[\left(18.678 - \frac{T_0}{234.5}\right)\left(\frac{T_0}{257.14 + T_0}\right)\right]\right) + \gamma + \gamma M}{2\alpha_{PT} s\gamma}\right) \tag{I.11}$$

I.2 Relationship Between α_{PT} and β

The inverse relationship between the Priestley-Taylor α_{PT} advection parameter and the Bowen ratio β is demonstrated by the following. By definition,

$$\beta = \frac{H}{\lambda E} \tag{I.12}$$

$$\text{and} \quad \phi = R_N + G \tag{I.13}$$

$$\therefore \lambda E = \left[\frac{1}{1+\beta}\right] \phi \qquad (\beta \neq -1) \tag{I.14}$$

Combining the following three equations:

$$\Delta_{PT} = \frac{\lambda}{c_p}\frac{dq_s^*}{dT} \qquad \text{(from Eqn. 2.2, p. 24)}$$

$$\lambda E = \alpha_{PT}\frac{\Delta_{PT}}{1+\Delta_{PT}}\left(R_N + G\right) \qquad \text{(from Eqn. 2.3, p. 24)}$$

$$\frac{dq_s^*}{dT} = \frac{M_{ratio}}{P}\frac{de^*}{dT} \qquad \text{(from Eqn. I.25, p. 397)}$$

yields the following:

$$\lambda E = \alpha_{PT}\left[\frac{\frac{\lambda\, M_{ratio}}{c_P\, P}\left(\frac{de^*}{dT}\right)}{1+\frac{\lambda\, M_{ratio}}{c_P\, P}}\right]\left(R_N + G\right) \tag{I.15}$$

$$= \left[\alpha_{PT}\left(\frac{de^*}{dT}\right)\frac{\lambda\, M_{ratio}}{c_P\, P + \lambda\, M_{ratio}}\right]\phi \tag{I.16}$$

Equating Eqn. I.14 with Eqn. I.16:

$$\frac{1}{1+\beta} = \alpha_{PT}\left(\frac{de^*}{dT}\right)\frac{\lambda\, M_{ratio}}{c_P\, P + \lambda\, M_{ratio}} \qquad (\beta \neq -1) \tag{I.17}$$

Rearranging,

$$1 = \alpha_{PT}\left(1+\beta\right)\left[\frac{\lambda\, M_{ratio}}{c_P\, P + \lambda\, M_{ratio}}\right]\frac{de^*}{dT} \tag{I.18}$$

If C_1 and C_2 (two constants) are defined as

$$C_1 = \left[\frac{\lambda\, M_{ratio}}{c_P\, P + \lambda\, M_{ratio}}\right] \tag{I.19}$$

$$C_2 = \left.\frac{de^*}{dT}\right|_{\text{at } T=T_i} \tag{I.20}$$

where C_2 is a constant because $\frac{de^*}{dT}$ has a particular (constant) value when T has a particular value (i.e. $T = T_i$). Then Eqn. I.18 can be re-written as

$$\alpha_{PT} = \frac{1}{C_1 C_2}\frac{1}{(1+\beta)} \qquad (\beta \neq -1) \tag{I.21}$$

That is, for a given T,

$$\alpha_{PT} \propto \frac{1}{(1+\beta)} \qquad (\beta \neq -1) \tag{I.22}$$

and it is evident that α_{PT} and β are inversely related.

I.3 Deriving An Equation For $\boldsymbol{\alpha_{*PT*}}$

Eqn. I.32 can be derived by the following:

$$\text{Let} \quad q_s = \frac{m_{water\ vapour}}{m_{moist\ air}} \qquad (q_s \text{ is specific humidity}) \tag{I.23}$$

$$= \frac{M_{ratio}}{P} e^* \tag{I.24}$$

$$\frac{dq_s^*}{dT} = \frac{M_{ratio}}{P}\frac{de^*}{dT} \tag{I.25}$$

M_{ratio} is the molecular mass ratio of water vapour to dry air (≈ 0.622). $\frac{dq_s^*}{dT}$ is the slope of the saturated specific humidity curve and $\frac{de^*}{dT}$ is the slope of the saturation vapour pressure curve. $\frac{de^*}{dT}$ was s in the nomenclature of Mallick et al. (2015a) so

$$\frac{dq_s^*}{dT} = \frac{M_{ratio}\, s}{P} \tag{I.26}$$

$$\text{Let} \quad \Delta_{PT} = \frac{\lambda}{c_P}\frac{dq_s^*}{dT} \qquad \text{(from Eqn. 2.2, p. 24)}$$

$$= \frac{\lambda}{c_p}\frac{M_{ratio}\, s}{P} \tag{I.27}$$

$$\lambda E = \alpha_{PT}\,\frac{\Delta_{PT}}{1+\Delta_{PT}}\,\phi \qquad \text{(from Eqn. 2.3, p. 24)}$$

$$= \alpha_{PT}\,\frac{M_{ratio}\,\lambda\, s}{c_P\, P + M_{ratio}\,\lambda\, s}\,\phi \tag{I.28}$$

Let D_A, g_B and g_S denote the vapour pressure deficit, bulk aerodynamic conductance and bulk stomatal conductance, respectively. Then the Penman-Monteith equation is

$$\lambda E = \frac{s\,\phi + \rho c_P\, g_B\, D_A}{s+\gamma\left(1+\frac{g_B}{g_S}\right)} \tag{I.29}$$

$$= \frac{s\phi}{s+\gamma}\left[\frac{s+\gamma}{s+\gamma\left(1+\frac{g_B}{g_S}\right)} + \frac{\rho\, c_P\, g_B\, D_A\,(s+\gamma)}{s\,\phi\left\{s+\gamma\left(1+\frac{g_B}{g_S}\right)\right\}}\right] \tag{I.30}$$

$$\text{where} \quad \gamma = \frac{c_P\, P}{M_{ratio}\,\lambda} \tag{I.31}$$

Substituting Eqn. I.31 into the first term $\left(\frac{s\,\phi}{s+\gamma}\right)$ of Eqn. I.30 and then equating with Eqn. I.28 gives the following solution for α_{PT} (now denoted α_{*PT*})

$$\alpha_{*PT*} = \frac{s+\gamma}{s+\gamma\left(1+\frac{g_B}{g_S}\right)} + \frac{\rho\, c_P\, g_B\, D_A(s+\gamma)}{s\,\phi\left\{s+\gamma\left(1+\frac{g_B}{g_S}\right)\right\}} \tag{I.32}$$

Appendix J

SOIL MOISTURE DATA

TDR soil moisture sensors had been installed in Field 14 for the 2018/19 summer season. These sensors, installed at depths of 250 mm, 500 mm and 750 mm, were logged every 15 min throughout the season and the data are shown in Fig. J.2 (p. 401) and Fig. J.3 (p. 402).

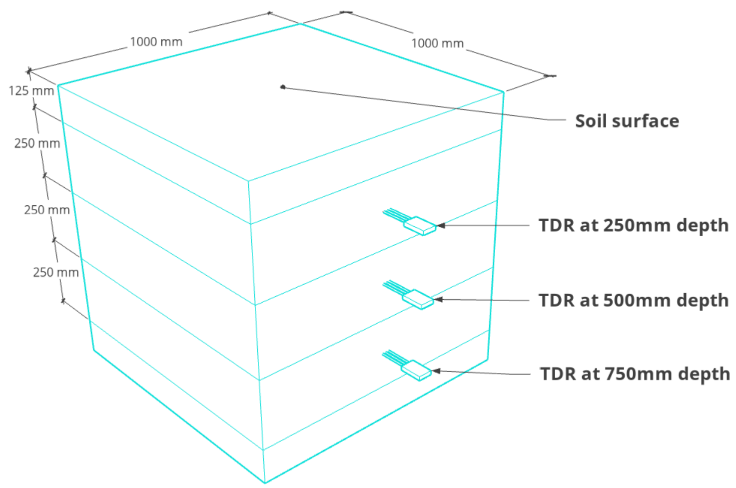

Figure J.1: An illustration of TDR soil moisture sensor positioning in each of three layers beneath the soil surface. The 125 mm surface layer has no sensor in it. The TDR sensors were installed by auguring an access hole and backfilling after installation.

Each of the three 250 mm deep soil layers (Fig. J.1, p. 399) had a

Table J.1: Comparison of soil water content by soil layer between 18th February, 2019, and 25th February, 2019. Data comes from Fig. J.3 (p. 402). θ = volumetric water content [%], θ^* = layer's water content [m^3].

	18-Feb-2019		25-Feb-2019	
Soil Layer [mm]	θ [%]	θ^* [m^3]	θ [%]	θ^* [m^3]
0 - 125	-	-	-	-
125 - 375	29.3	0.073	30.0	0.075
375 - 625	30.6	0.076	25.7	0.064
625 - 875	35.2	0.088	23.3	0.058

total volume of 0.250 m^3 (per m^2 of soil surface) whose volumetric water content, θ, was assumed to equal that reported by the TDR sensor at the centre of the layer. It was also assumed that the top 125 mm layer of soil was dry and contributing very little to E. The volume of water in each layer, θ^*, was found by:

$$\theta^*_{250} = \theta_{250} \times 0.250\,\mathrm{m}^3$$
$$\theta^*_{500} = \theta_{500} \times 0.250\,\mathrm{m}^3$$
$$\theta^*_{750} = \theta_{750} \times 0.250\,\mathrm{m}^3$$

where θ_{250} and θ^*_{250} are the volumetric water content [%] and the layer's water content [m^3] associated with the 250 mm TDR probe (etc.). Table J.1 (p. 400) presents the values for θ and θ^* in Field 14, as read from Fig. J.3 for 18th and 25th February, 2019.

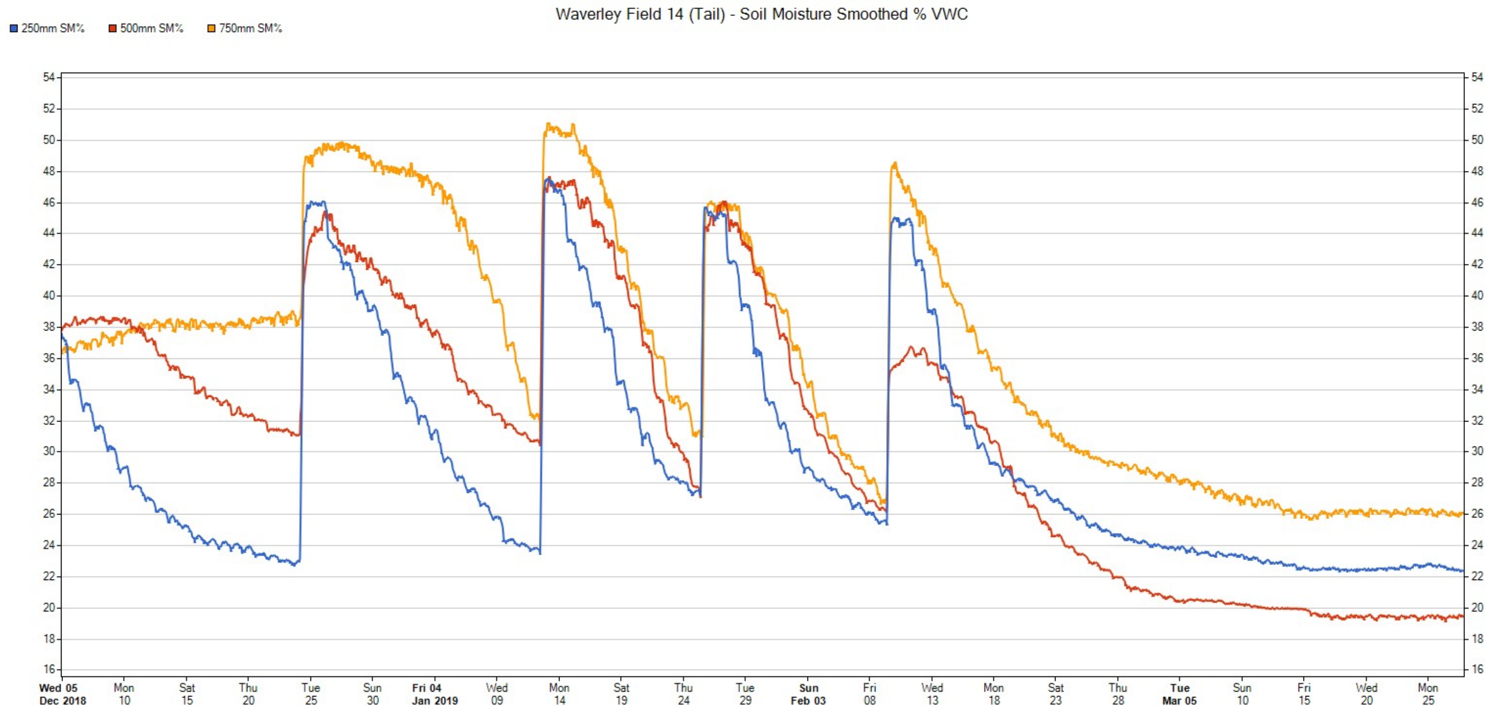

Figure J.2: Volumetric water content, θ, in Field 14 between December 2018 and March 2019, as measured with TDR sensors at depths of 250 mm, 500 mm and 750 mm. The spikes in moisture levels are due to irrigation events.

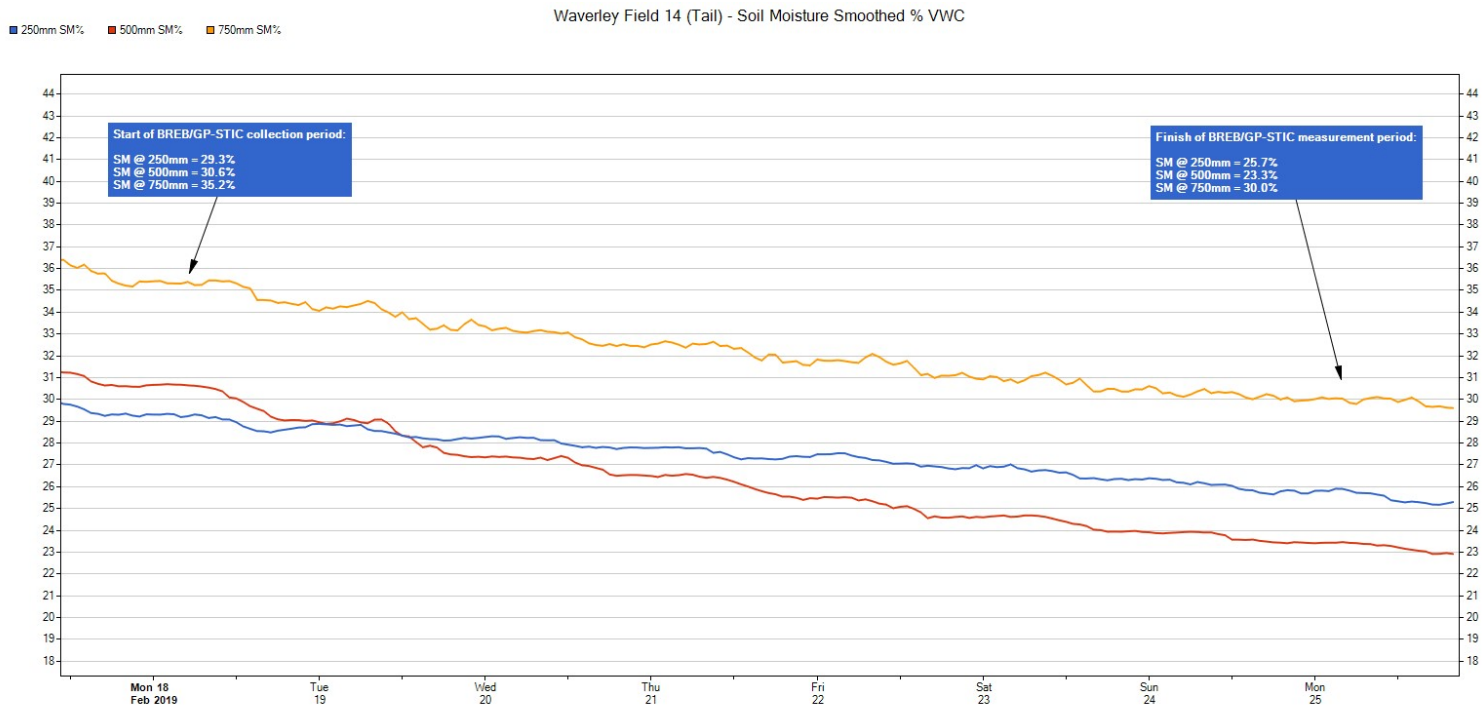

Figure J.3: Volumetric water content, θ in Field 14, as measured with TDR sensors at depths of 250 mm, 500 mm and 750 mm.

The change in the total soil water volume, ΔV, was found to be

$$\begin{aligned}\Delta V &\approx 0.198\,\mathrm{m}^3 - 0.238\,\mathrm{m}^3 \\ &\approx -0.040\,\mathrm{m}^3\end{aligned}$$

i.e. approximately 40 mm per square metre of field was removed from the top 1 m of soil. This differs from that calculated by Profile BREB (31.1 mm) and GPSTIC (31.1 mm) for DS1. Two explanations for this discrepancy are:

- Deep drainage of water from the soil profile was not accounted for by Profile BREB and GPSTIC. Deep drainage can be 0.5 - 1 mm day^{-1} (or more) in the vertosol soils (Millar et al. 2006, Ringrose-Voase & Nadelko 2011), especially if deeper layers of soil are dry and exert a matric pull on the water.
- Nighttime evapotranspiration – which was approx. -0.6 mm night^{-1} during DS1 – may not necessarily be returned to the soil. Night-time mist was observed to form over Field 14 and could be blown away from the field. If the surrounding landscape is arid then Profile BREB and GPSTIC (and other micro-meterological methods too) will be liable to underestimate water from the soil profile.

Deep drainage alone could account for the differences between ΔV and the GPSTIC / Profile BREB modelling. This also serves as a reminder that E modelling does not capture the full story of water losses from the soil profile, an important consideration if GPSTIC (or Profile BREB) are to be used as part of irrigation management.

This page intentionally left blank.

Appendix K

ACCOUNTING FOR NEGATIVE *E*

Given that

$$E = \frac{\phi}{\lambda\,(\beta + 1)} \tag{K.1}$$

then negative E occurred whenever

$$\text{(a)} \qquad \phi < 0 \quad \& \quad \beta > -1 \tag{K.2}$$

$$\text{or} \quad \text{(b)} \qquad \phi > 0 \quad \& \quad \beta < -1 \tag{K.3}$$

Case (a) mainly occurred at nighttime and accounted for the majority of negative E observed during this research.

However, Table 5.8 (p. 257) shows that 14.1 %, 16.2 % and 14.0 % of daytime data in DS1, DS2 and DS3, respectively, were also associated with negative E. This was observed equally for both Profile BREB and GPSTIC. These data were all identified as occurring within 65 min after sunrise or 65 min before sunset (e.g. compare Fig. 5.1, p. 205 with Fig. 5.2, p. 206).

It is interesting that during DS2 a greater proportion of daytime data (16.2 %) were associated with negative E. According to Case (b) this means there were more daytime instances of $\beta < -1$. Fig. 4.35

(p. 162) shows that this did not occur during the middle of the day; rather, these instances occurred more often during the hour before sunset. During this time the bare soil was no longer strongly insolated by the low-altitude sun but the (hot) soil surface was meanwhile radiating into cold space. Fig. 4.22 (p. 146) shows that prior to sunset T_S decreased sooner and faster than T. As the soil surface rapidly cooled (by radiation) the surrounding warm air transferred heat to the soil, itself cooling in the process, and so a pronounced daytime temperature inversion was formed.[1]

Returning to Case (a), Fig. 5.13 (p. 227), Fig. 5.19 (p. 239) and Fig. 5.25 (p. 251) all show that there was a *small* amount of negative E at nighttime. The average nighttime E was $-1.0\,\mathrm{mm\,night^{-1}}$, $-0.6\,\mathrm{mm\,night^{-1}}$ and $-0.5\,\mathrm{mm\,night^{-1}}$ during DS1, DS2 and DS3, respectively.

A negative E required that energy was released as the water vapour went through a phase change into water droplets. These droplets either remained suspended as mist above the soil or crop, or were deposited as dew on the soil or crop surface if $T_S < T_D$. Both phenomena were observed to occur overnight on the first and last nights of DS1 and DS3. Nighttime mist was likewise observed during DS2 but it was unclear whether dew deposition also occurred because it was difficult to see or feel dew on the bare soil.

How should the nighttime negative E be accounted for? If the negative E was deposited as dew then it remained in the field and was available to be 'burned off'[2] in the morning sun. This would present as an overnight decrease in the accumulated total of E because the water was truly returned to the field.

However, if the negative E remained suspended as mist then it was liable to be blown away from the field before the morning sun arrived. In this research the blown mist would not have been replaced by upwind

[1]This phenomenon was less pronounced during DS1 and DS3 because during the daytime the transpiring crop canopy did not become as hot as the bare soil surface. Also, the canopy partially or fully obstructed the view of space from the soil during DS1 and DS3.

[2]i.e. undergo a phase change from liquid water into water vapour.

mist (since there was no mist upwind of the field due to the extreme dryness of the surrounding drought-stricken landscape). The negative E, then, should not be added to the accumulations of E because the water was not returned to the field and was not available to be 'burned off' in the morning.[3]

How much of the nighttime negative E took the form of dew and how much took the form of mist was unknown. The plots of accumulated totals presented in this thesis have taken the approach to add the whole amount of negative E to the totals (as though all negative E took the form of dew). Thus the presented cumulative totals for E_{GPSTIC} and E_{BREB} should be understood as probable underestimates.

Of course, an alternative approach may have been to exclude all nighttime data from the modelling. Fig. 5.26 (p. 252) illustrates, as an example, the impact when the negative nighttime E in Fig. 5.25 (p. 251) was excluded from the accumulation. As expected, the total accumulation was slightly larger.

However, the nighttime-exclusion approach would have been unsatisfactory in two respects: firstly, it would have been equivalent to deeming all nighttime negative E to have taken the form of mist that was blown from the field. Any cumulative totals, then, would have been overestimates because clearly not all negative E was actually mist. And secondly, it was desired that GPSTIC be evaluated for as much of the available data as possible. To dismiss the nighttime data was to ignore nearly half of the available data.

[3]When the modelling is done over very large scales this may not be an issue because the blown mist may still be within the boundaries of the study area by the time morning arrives (and thus available to be 'burned off' in the morning sun). Clearly that is not the case in the present research.

This page intentionally left blank.

Appendix L

CLEAR SKY RADIATION CALCULATIONS

Two different models for clear-sky shortwave radiation are presented here. These were used to cross-check the measurements of the sky-facing NR01 pyranometer, i.e. $SW_{downwelling}$.

L.1 Monteith-Unsworth ('MU') Model

An estimate of shortwave solar radiation at solar noon on cloudless days can be made with the following equations which have been taken from Monteith and Unsworth (2013), Jones (2013) and Vignola et al. (2016).

The solar declination angle, δ_s, in radians, is calculated by

$$\begin{aligned}\delta_s = \sin^{-1}\left\{\sin\left(\frac{23.44\,\pi}{180}\right)\cos\left[\frac{\pi}{180}\left(\frac{360(N+10)}{365.24}\right.\right.\right. \\ \left.\left.\left.+\,0.0167\frac{360}{\pi}\sin\left(\frac{2\,\pi(N-2)}{365.24}\right)\right)\right]\right\}\end{aligned} \tag{L.1}$$

where N is the Julian date minus one. All trigonometric functions are calculated in radians. If *Latitude* is in degrees (positive degrees for South of the equator), then the solar zenith angle, θ_s, in radians, is calculated by

$$\theta_s = Latitude\left(\frac{\pi}{180}\right) - \delta_s \tag{L.2}$$

Eqn. L.2 is only true at solar noon, and θ_s is the complement of the solar altitude. If S_0 is the solar constant (assumed to be 1367 Wm^{-2}) then the extra-terrestrial radiation perpendicular to a horizontal plane on the earth's surface, ${S_p}^*$, in Wm^{-2}, is calculated by

$${S_p}^* = S_0\left[1 + 0.034\cos\left(2\pi\frac{N}{365.24}\right)\right]\cos\theta_s \tag{L.3}$$

${S_p}^*$ will be attenuated by molecular and aerosol scattering and absorption. The shortwave radiation at the earth's surface, perpendicular to a horizontal plane on the earth's surface, S_p, in Wm^{-2}, is given by

$$S_p = {S_p}^*\,\tau_r^m \tag{L.4}$$

where m is the optical path length and τ_r is the atmospheric transmissivity. m can be described as the ratio of the path length of the sunlight through the atmosphere to the height of the atmosphere (Fig. L.1, p. 411):

$$m = \left(\frac{P}{P_0}\right)\frac{1}{\cos\theta_s} \tag{L.5}$$

where P and P_0 are the barometric pressures at the location of interest and sea level, respectively. The first term $\left(\frac{P}{P_0}\right)$ provides an adjustment for locations that are higher than sea level. Liu and Jordan (1960), cited by Monteith and Unsworth (2013), observed that τ_r was usually about 0.45 to 0.75 on cloudless days. τ_r can be calculated by

$$\tau_r = e^{-(\tau_a + \tau_m)} \tag{L.6}$$

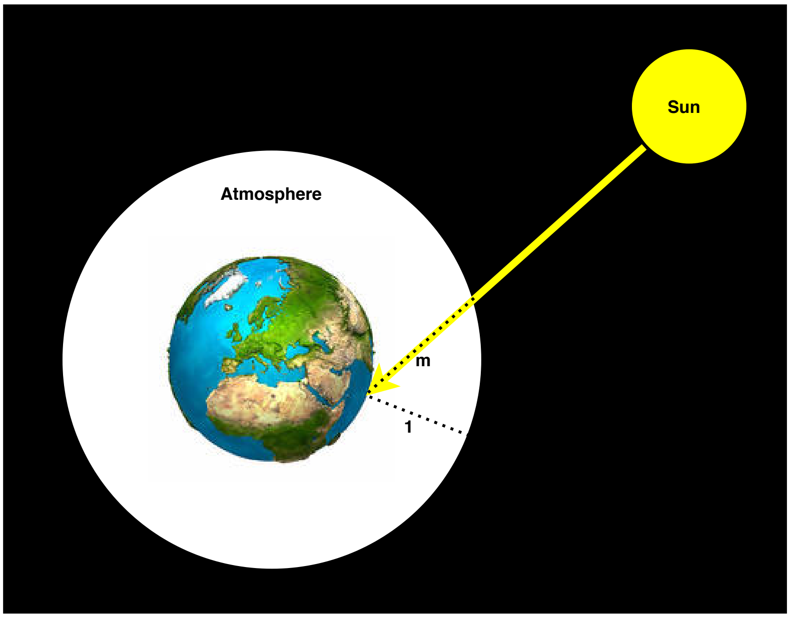

Figure L.1: Illustration (not to scale) showing that the optical path length, m, is the ratio of the transmission distance of sunlight through the atmosphere to the height of the atmosphere (which is taken as unity).

where τ_a is an aerosol extinction coefficient and τ_m is a molecular extinction coefficient. Liu and Jordan (1960) reported that a value of 0.3 is typically adopted for τ_m, and τ_a ranges between 0.05 for very clean dry air and 0.60 for very polluted air (Unsworth & Monteith 1972). Diffuse shortwave radiation, S_d, in Wm^{-2}, can be estimated by

$$S_d = 0.3\, S_0\, [1 - \tau_r^m]\, \cos\theta_s \tag{L.7}$$

where the 0.3 was empirically determined by Liu and Jordan (1960). Finally, the total shortwave irradiance, S_t, in Wm^{-2}, of a horizontal surface on the earth for a given *Latitude* and date is calculated by

$$S_t = S_p + S_d \tag{L.8}$$

L.2 EWRI-ASCE Model

Appendix D of Allen et al. (2005) outlined a simplified procedure for estimating clear-sky shortwave radiation at a point on the earth's surface. This is presented in a modified form here and, where relevant, variable names are kept the same as per Monteith and Unsworth (2013).

The solar zenith angle, θ_s, is calculated by

$$\begin{aligned}\theta_s = \cos^{-1}\Big[&\sin\left(\frac{\pi}{180}Latitude\right)\sin\delta_s + \ldots \\ &\cos\left(\frac{\pi}{180}Latitude\right)\cos\delta_s\cos\omega\Big]\end{aligned} \tag{L.9}$$

where *Latitude* is in degrees (negative degrees for South of the equator) and all trignonometric functions are working with radians. ω is the solar time angle. At solar noon $\omega = 0$ and Eqn. L.9 is then identical to Eqn. L.2 (p. 410). Alternatively, θ_s can be calculated by Eqn. L.1 and Eqn. L.2 (p. 409). Precipitable water in the atmosphere, W, in mm, is estimated by

$$W = 0.14\, e_{actual}\, P + 2.1 \tag{L.10}$$

where P is local barometric pressure, in kPa. A 'clearness index' for direct beam radiation, K_B, is estimated by

$$K_B = 0.98\, e^{\left[\frac{-0.00146\,P}{K_t\cos\theta_s} - 0.075\left(\frac{W}{\cos\theta_s}\right)^{0.4}\right]} \tag{L.11}$$

where K_t is a turbidity coefficient. This is a similar concept to τ_r in Eqn. L.6 (p. 410) but $K_t = 1.0$ for clean air and $0 \leq K_t \leq 0.5$ for very polluted air. A 'transmissivity index' for diffuse radiation, K_D, is estimated by

$$K_D = \begin{cases} 0.35 - 0.36\,K_B & \text{for } K_B \geq 0.15 \\ 0.18 + 0.82\,K_B & \text{for } K_B < 0.15 \end{cases} \tag{L.12}$$

If S_0 is the solar constant (assumed to be $1367\,\mathrm{Wm}^{-2}$) then the total solar irradiance at the earth's surface, S_t, in Wm^{-2}, is finally calculated by

$$S_t = (K_B + K_D)\, S_0 \tag{L.13}$$

L.3 Comparison

As an example, assuming clean air, i.e. $\tau_a \approx 0.2$, $\tau_m \approx 0.3$ and $K_t \approx 0.8$, and if $N = 39$ (i.e. 19^{th} February) and $Latitude = 30°$, then the MU and ASCE models estimate $S_t = 975\,\mathrm{Wm}^{-2}$ and $S_t = 1008\,\mathrm{Wm}^{-2}$, respectively — a difference of only 3.4 %.

This page intentionally left blank.

Appendix M

PLOTS OF α_{*PT*} FOR DS2 AND DS3

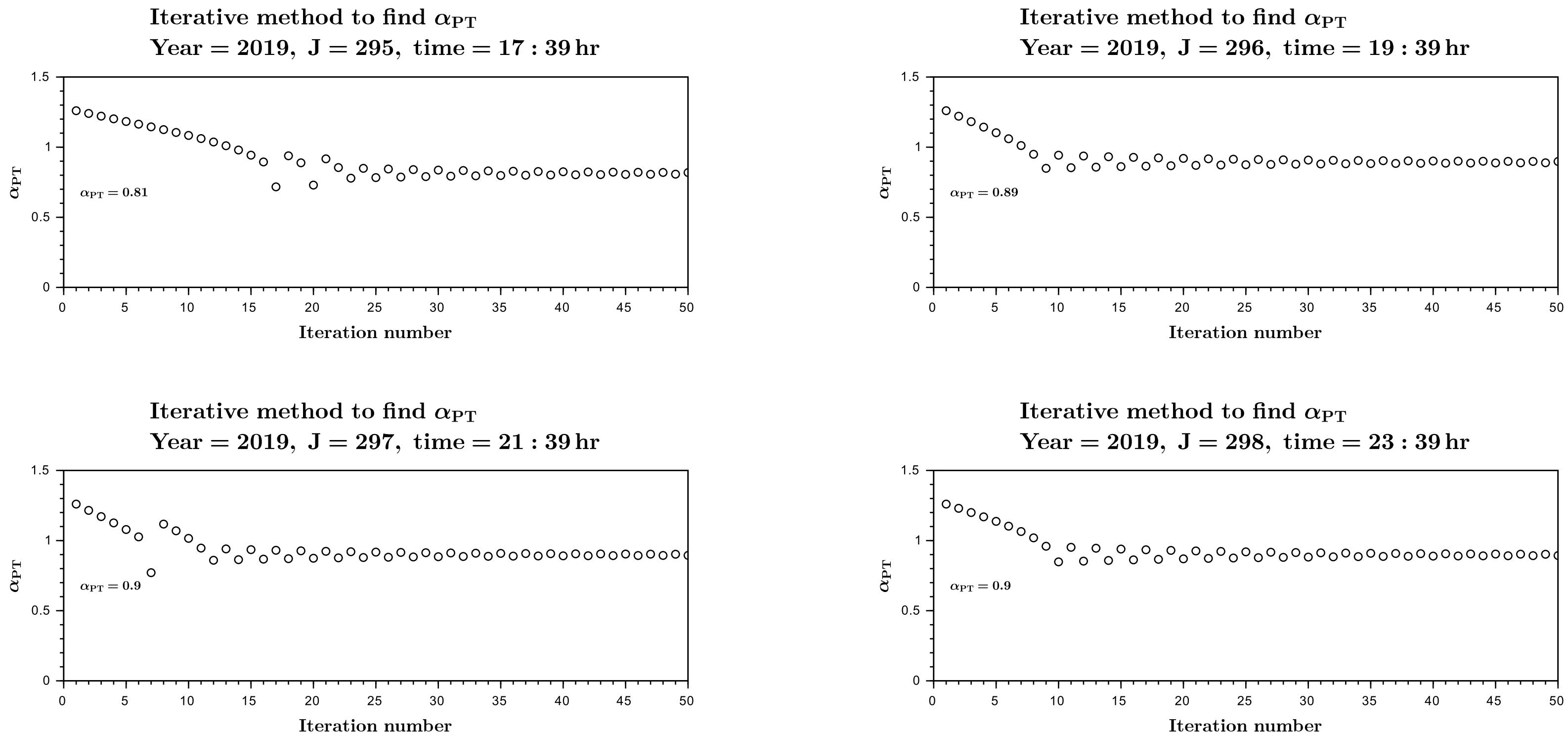

Figure M.1: GPSTIC: four example plots from DS2 showing the progressive optimisation of α_{*PT*} using the internal iterative process, following the procedure of Mallick et al. (2015a). The end results are similar to Fig. 2.2 (p. 26) although the convergence in GPSTIC's optimisation process appears to have taken more iterations.

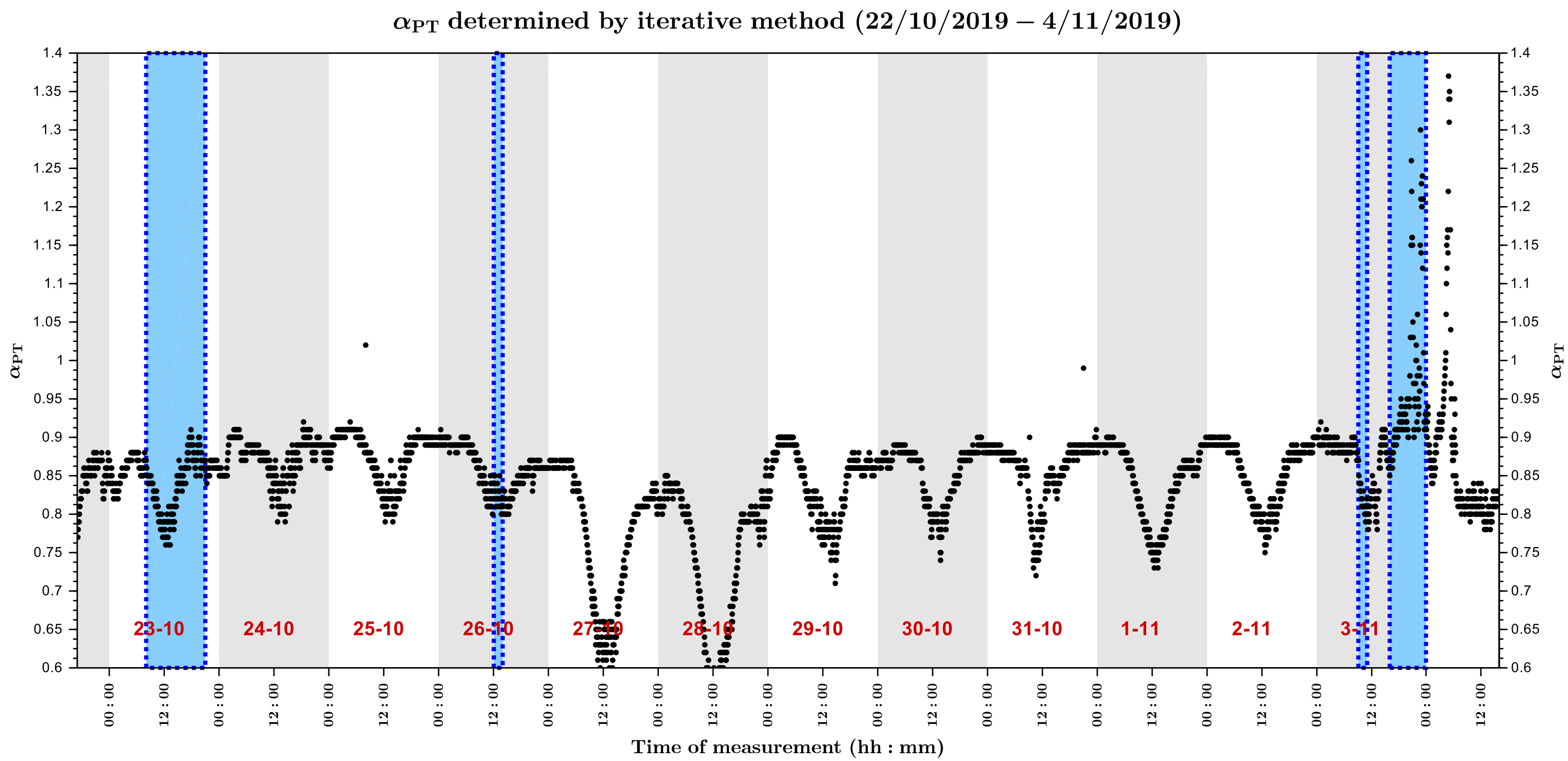

Figure M.2: GPSTIC: a plot of all 4665 of the optimised values for α_{*PT*} in DS2 as determined by the internal iterative process. The determination of optimal α_{*PT*} was performed for every 4 min interval of data. The shaded blue rectangles indicate when irrigation (23rd October) or rainfall occurred.

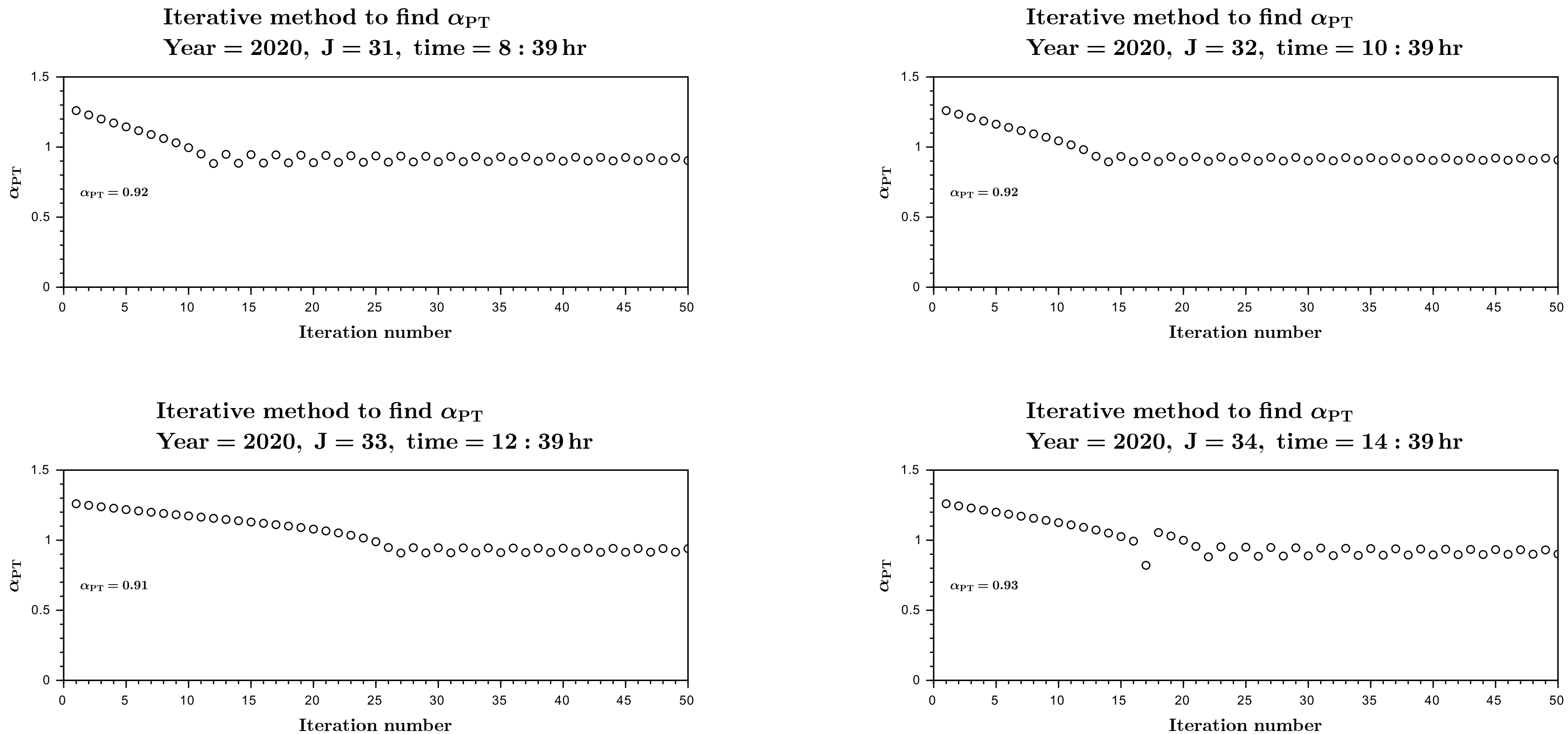

Figure M.3: GPSTIC: four example plots from DS3 showing the progressive optimisation of α_{*PT*} using the internal iterative process, following the procedure of Mallick et al. (2015a). The end results are similar to Fig. 2.2 (p. 26) although the convergence in GPSTIC's optimisation process appears to have taken more iterations.

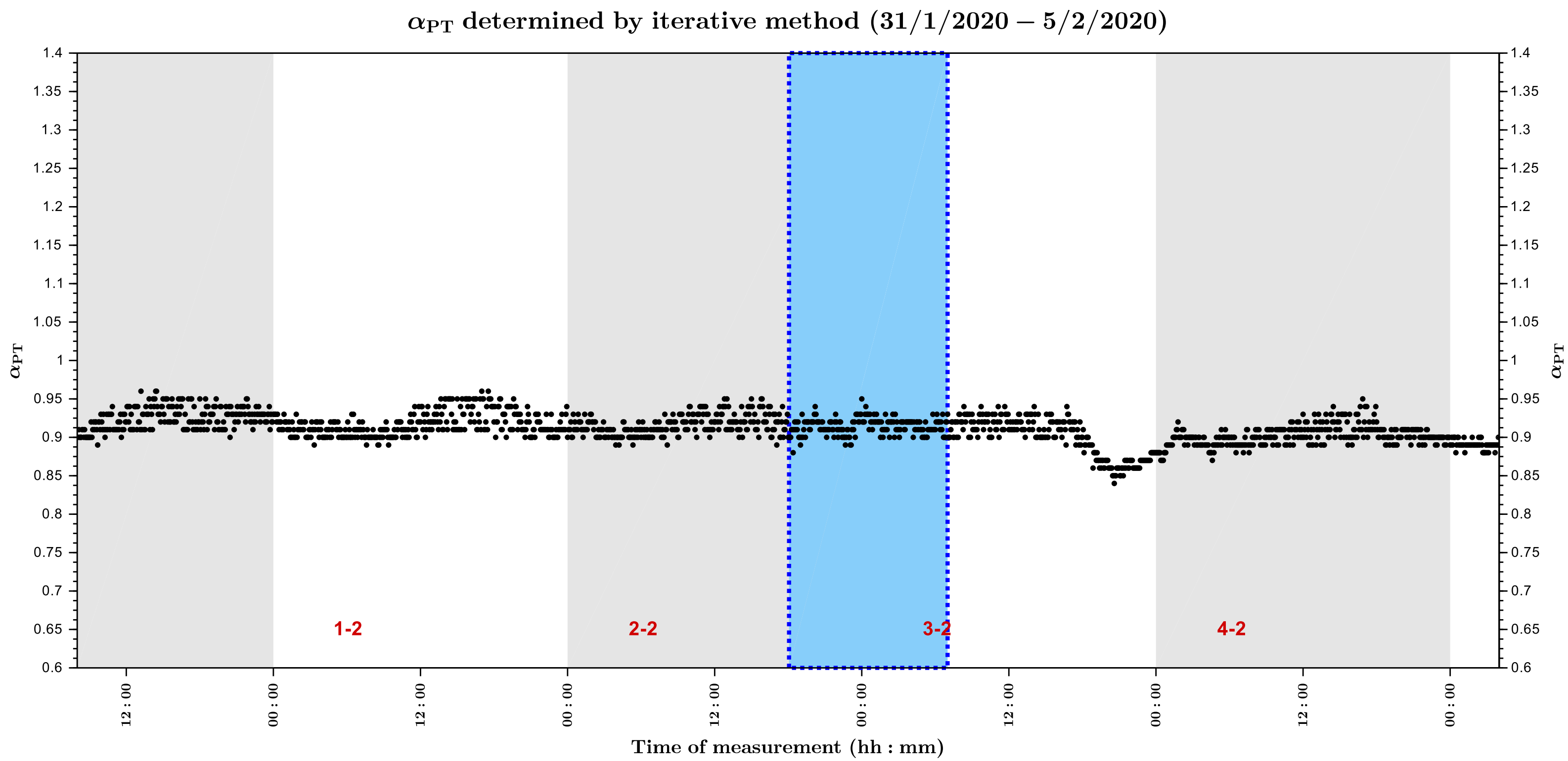

Figure M.4: GPSTIC: a plot of all 1740 of the optimised values for α_{*PT*} in DS3 as determined by the internal iterative process. The determination of optimal α_{*PT*} was performed for every 4 min interval of data. The shaded blue rectangle indicates when the irrigation on the 2$^{\text{nd}}$ February occurred.

This page intentionally left blank.

Appendix N

FLUX FOOTPRINT ANALYSIS

Flux footprint analysis for the Profile BREB system is undertaken here following the process outlined in Schuepp et al. (1990) and Gao et al. (2005).

A constant assumed wind speed, U [$\mathrm{m\,s^{-1}}$], defined as the average wind speed between the surface and the observation height above the zero plane displacement, z [m] (Schuepp et al. 1990, p. 360), can be calculated by

$$U = \frac{u_* \left[\ln\left(\frac{z-d}{z_0}\right) - 1 + \frac{z_0}{z-d}\right]}{k\left(1 - \frac{z_0}{z-d}\right)} \tag{N.1}$$

The relative contribution to vertical flux, f, as a function of x (the upwind distance from the measurement point) can be calculated by

$$f = \frac{U\left(z-d\right)}{u_* k x^2} e^{\left(\frac{-U(z-d)}{k u_* x}\right)} \tag{N.2}$$

where u_* is the friction velocity [m s^{-1}], d is the zero plane displacement height [m], z_0 is the roughness length governing momentum transfer [m], and k is the von Karman constant which is equal to 0.41. d and z_0 can be estimated (Allen et al. 1998) by

$$d = \frac{2}{3}h \tag{N.3}$$

$$z_0 = 0.1h \tag{N.4}$$

where h is the mean crop height [m]. u_* can be estimated by

$$u_* = \frac{k\left(u_{z_2} - u_{z_1}\right)}{\ln\left(\frac{z_2-d}{z_1-d}\right)} \tag{N.5}$$

The cumulative normalised contribution to the surface flux, C_f, can be calculated by

$$C_f = e^{\left(\frac{-U(z-d)}{ku_*x}\right)} \tag{N.6}$$

The mean wind speed during DS1, DS2 and DS3 was 5.2 m s^{-1}, 4.4 m s^{-1} and 3.6 m s^{-1}, respectively (from Fig. O.2, p. 429, Fig. P.2, p. 439 and Fig. Q.2, p. 449). This footprint modelling will conservatively be based upon the highest mean wind speed, i.e. $u_{z_2} = 5.2$ m s^{-1} at $z_2 = 5.5$ m, i.e. at the top of the Profile BREB mast where the anemometer was located. Since wind speed was only measured at one height by the Profile BREB, it is assumed (for modelling purposes) that $u_{z_1} = 1.0$ m s^{-1} at $z_1 = 1.0$ m, i.e. at crop height. Thus $u_* = 0.64$.[1] If values of $h = 1.0$ m and $z = 4.0$ m are also assumed then Fig. N.1 (p. 423) shows the relative and cumulative contributions to vertical flux as a function of distance from the Profile BREB.

Fig. O.5 (p. 432) and Fig. P.5 (p. 442) show that the minimum fetch during this research was 261 m. The cumulative footprint plot in Fig. N.1 (p. 423) shows that when the wind was in the direction of the minimum

[1]As it turns out, f and C_f are quite insensitive to u_*.

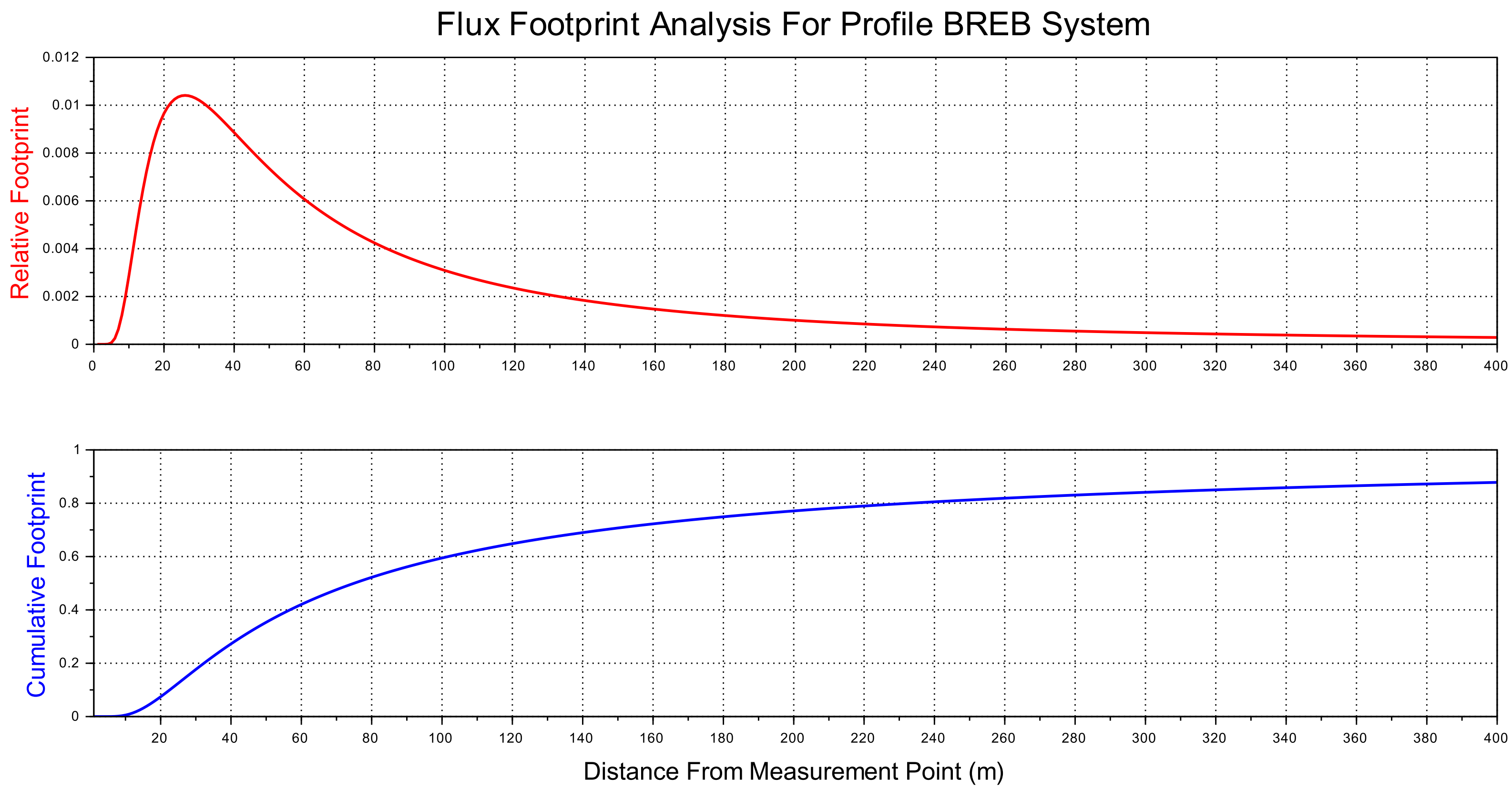

Figure N.1: Footprint analysis for the Profile BREB system assuming crop height is 1.0 m, Profile BREB height is 5.5 m above ground, wind speed is $5.2\,\mathrm{m\,s^{-1}}$, and friction velocity is $0.64\,\mathrm{m\,s^{-1}}$.

fetch, just over 80 % of the vertical flux was from inside the field itself. This is reasonably similar to Fig. 2.4 (p. 33) where Poznikova et al. (2012) reported that 85 - 95 % of flux came from the field at this range (based on a measurement height of 2 m), depending on the stability regime. It can also be seen that the strongest contribution to the flux measurement occurred around 20 - 60 m from the Profile BREB mast which was well in from the field's boundaries.

N.1 Scilab Code for Footprint Analysis

The following Scilab code was used to create Fig. N.1 (p. 423):

```
z = 4; // above crop height of Profile BREB [m]
h = 1.0; // height of crop [m]
z0 = 0.1*h; // momentum roughness length [m]
d = (2/3)*h; // zero plane displacement height [m]
k = 0.41; // von Karman constant
u = 5.2; // mean wind speed [m/s]
ustar = 0.64; // friction velocity [m/s]
x = 1:400; // distances from measurement point [m]

U = ustar*(log((z-d)/z0) - 1 + z0/(z-d))/ (k*(1 - z0/(z-d)));
f = U*(z-d)./(ustar.*k.*x.^2).*exp(-U.*(z-d)./(k.*ustar.*x));
Cf = exp(-U.*(z-d)./(k.*ustar.*x));
scf();
subplot(2,1,1)
    plot(x,f);
    ax1 = gca();
        tit = 'Flux Footprint Analysis For Profile BREB System';
        ax1.title.text = tit;
        ax1.title.font_size = 5;
        ylab = 'Relative Footprint';
        ax1.y_label.text = ylab;
```

```
        ax1.y_label.font_size = 4;
        ax1.y_label.font_color = 5;
        ax1.grid = [1,1];
        ax1.grid_style = [9,9];
    ln1 = gce();
        ln1.children.mark_mode = "on";
        ln1.children.line_style = 1;
        ln1.children.foreground = 5;
        ln1.children.thickness = 2;
        ln1.children.mark_mode = "off";
subplot(2,1,2)
    plot(x,Cf);
    xscale = [min(x),1,max(x),20]; // [min,step,max,display_step]
    yscale = [0,0.1,1,0.1];
    ax2 = gca();
        ax2.data_bounds = [xscale(1), yscale(1);xscale(3),yscale(3)];
        ax2.tight_limits = ["on","on"];
        xlab = 'Distance From Measurement Point (m)';
        ax2.x_label.text = xlab;
        ax2.x_label.font_size = 4;
        ylab = 'Cumulative Footprint';
        ax2.y_label.text = ylab;
        ax2.y_label.font_size = 4;
        ax2.y_label.font_color = 2;
        ax2.grid = [1,1];
        ax2.grid_style = [9,9];
   ln2 = gce();
        ln2.children.mark_mode = "on";
        ln2.children.line_style = 1;
        ln2.children.foreground = 2;
        ln2.children.thickness = 2;
        ln2.children.mark_mode = "off";
```

This page intentionally left blank.

Appendix O

ADDITIONAL WEATHER DATA FOR DS1

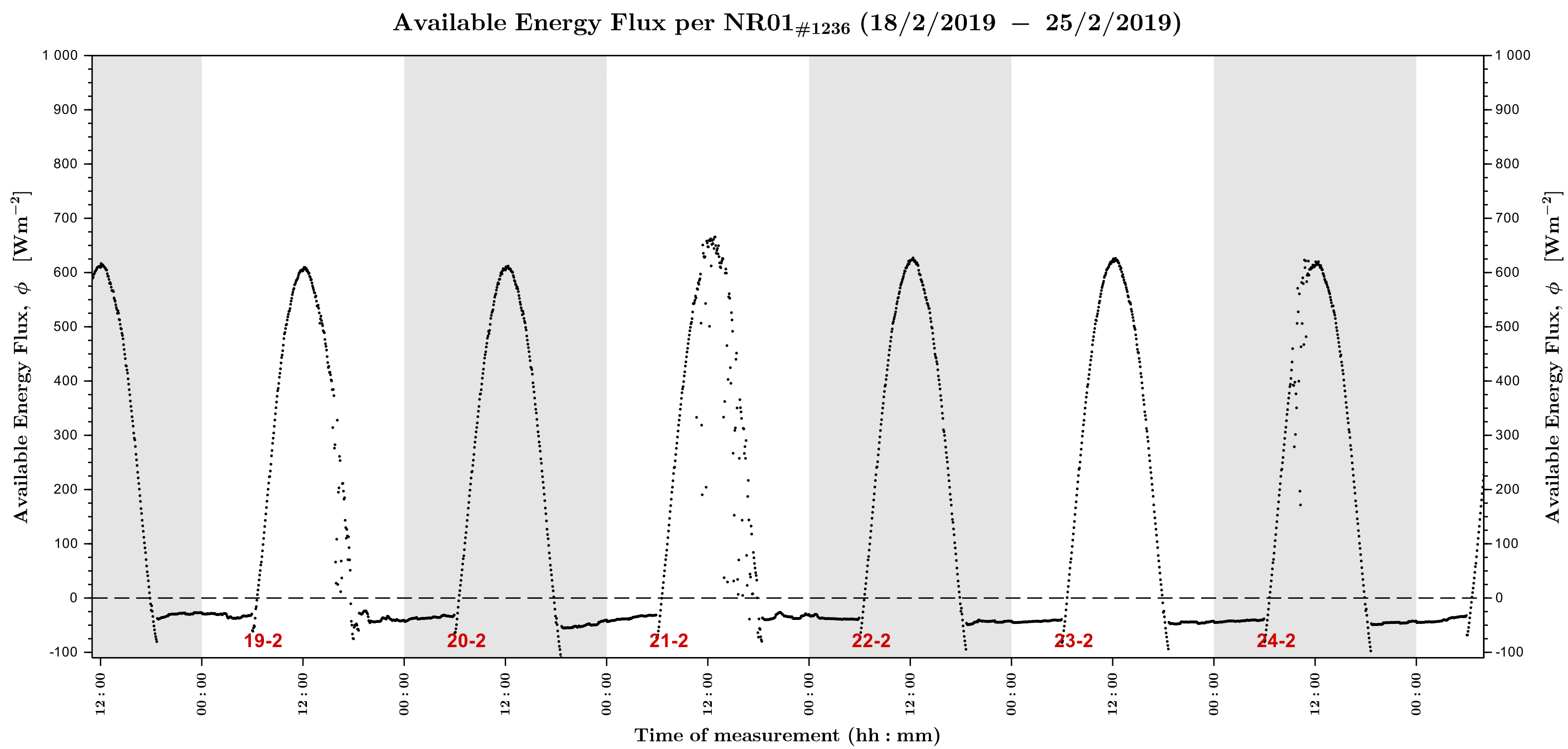

Figure O.1: DS1: available energy flux, ϕ [Wm^{-2}]. The available energy flux was calculated by $\phi = R_N + G$ (where flux directions are as defined in § 0.3, p. xxxiii).

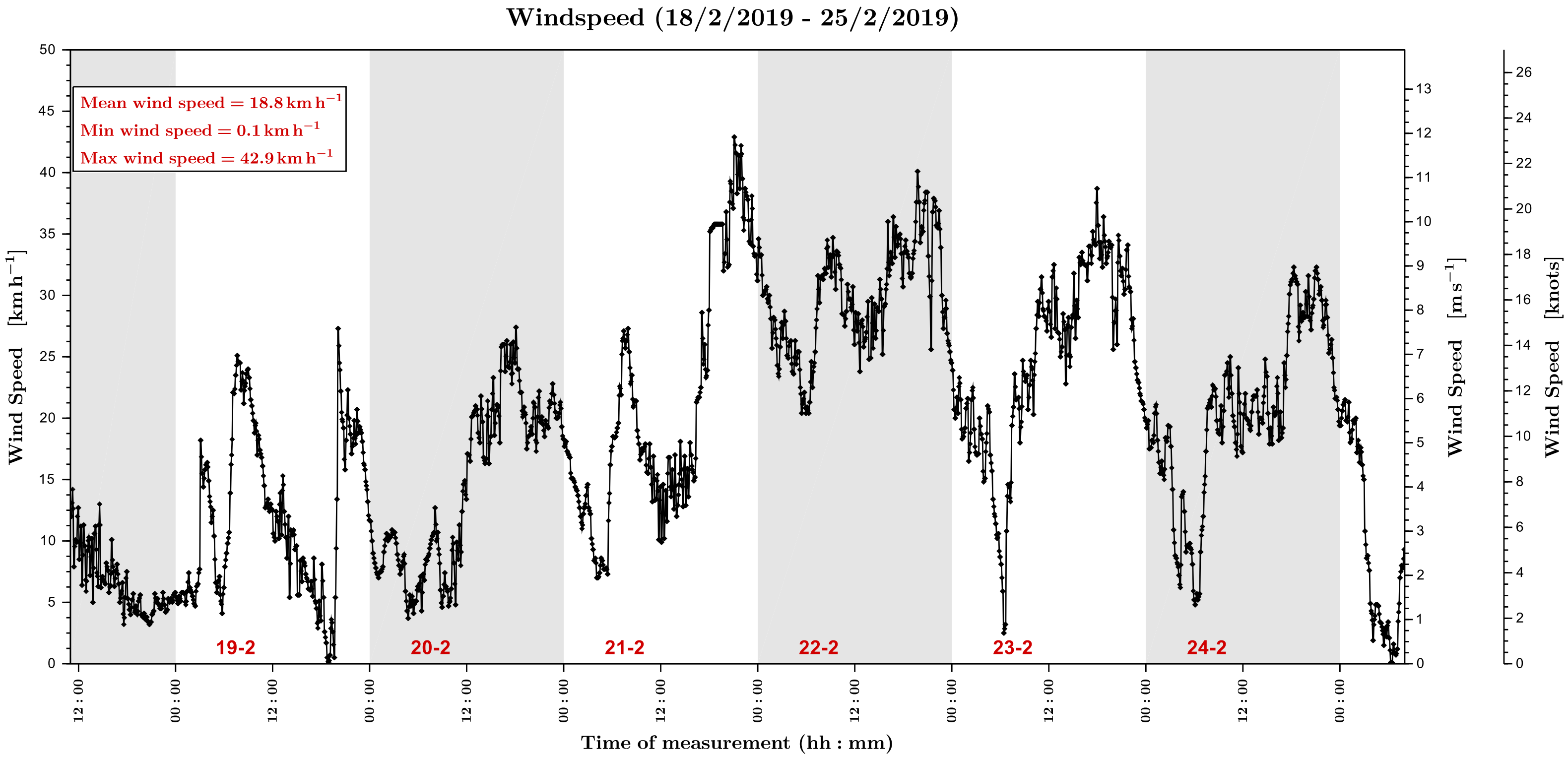

Figure O.2: DS1: wind speed, W_{sp} [km h^{-1}], as measured by a cup-anemometer at an automated weather station located 1.8 km from Field 14.

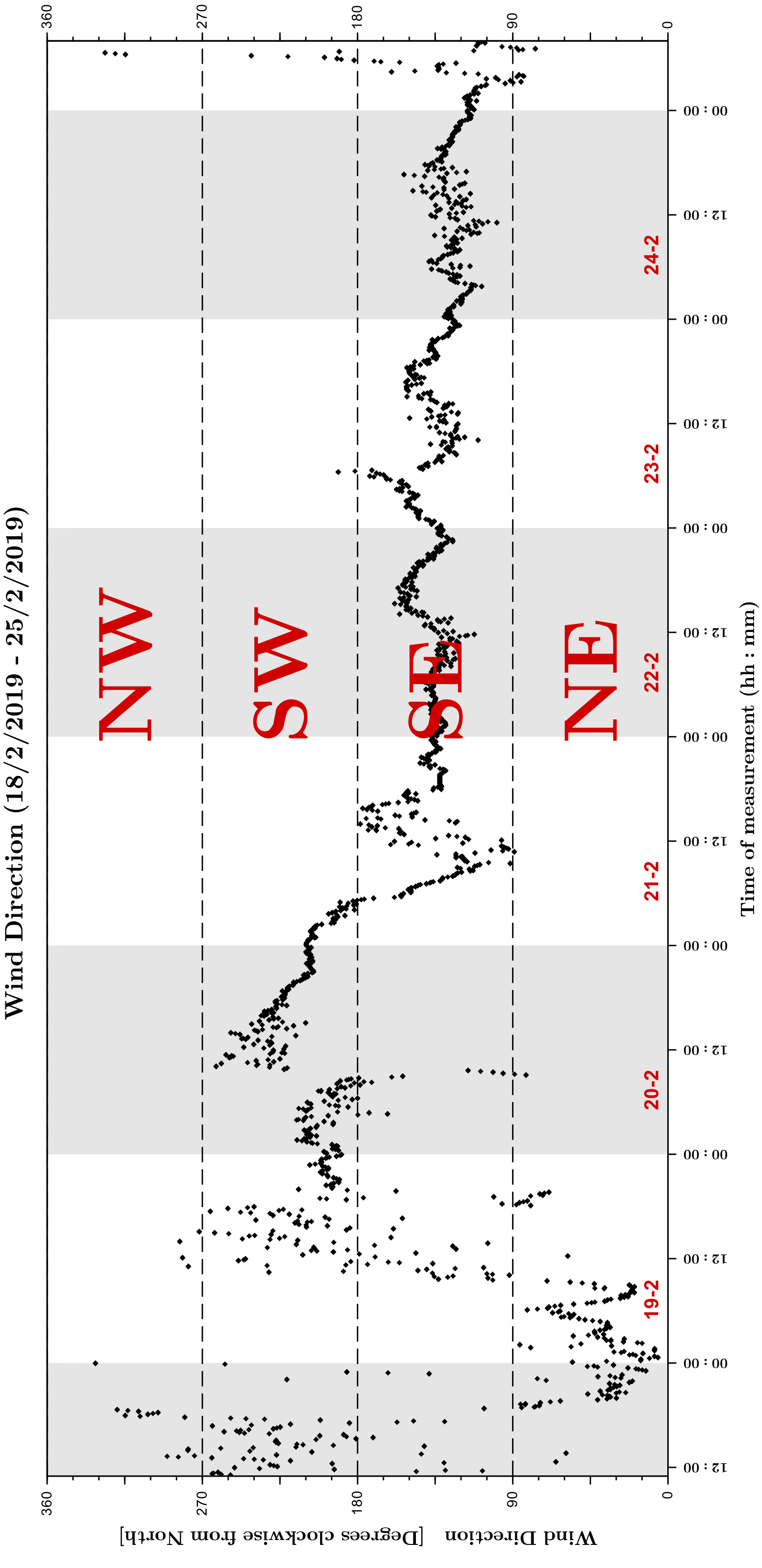

Figure O.3: DS1: wind direction, W_{dir} [°], relative to grid North, as measured by a wind-vane at an automated weather station located 1.8 km from Field 14.

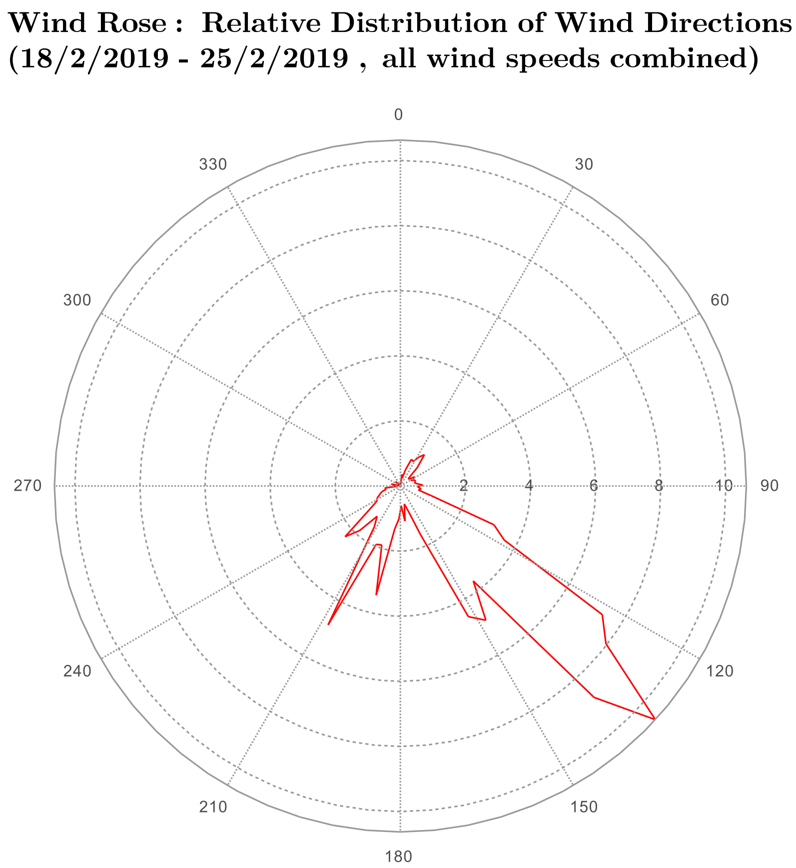

Figure O.4: DS1: windrose showing the relative proportion of time with a given wind direction, as measured by a wind-vane at an automated weather station located 1.8 km from Field 14.

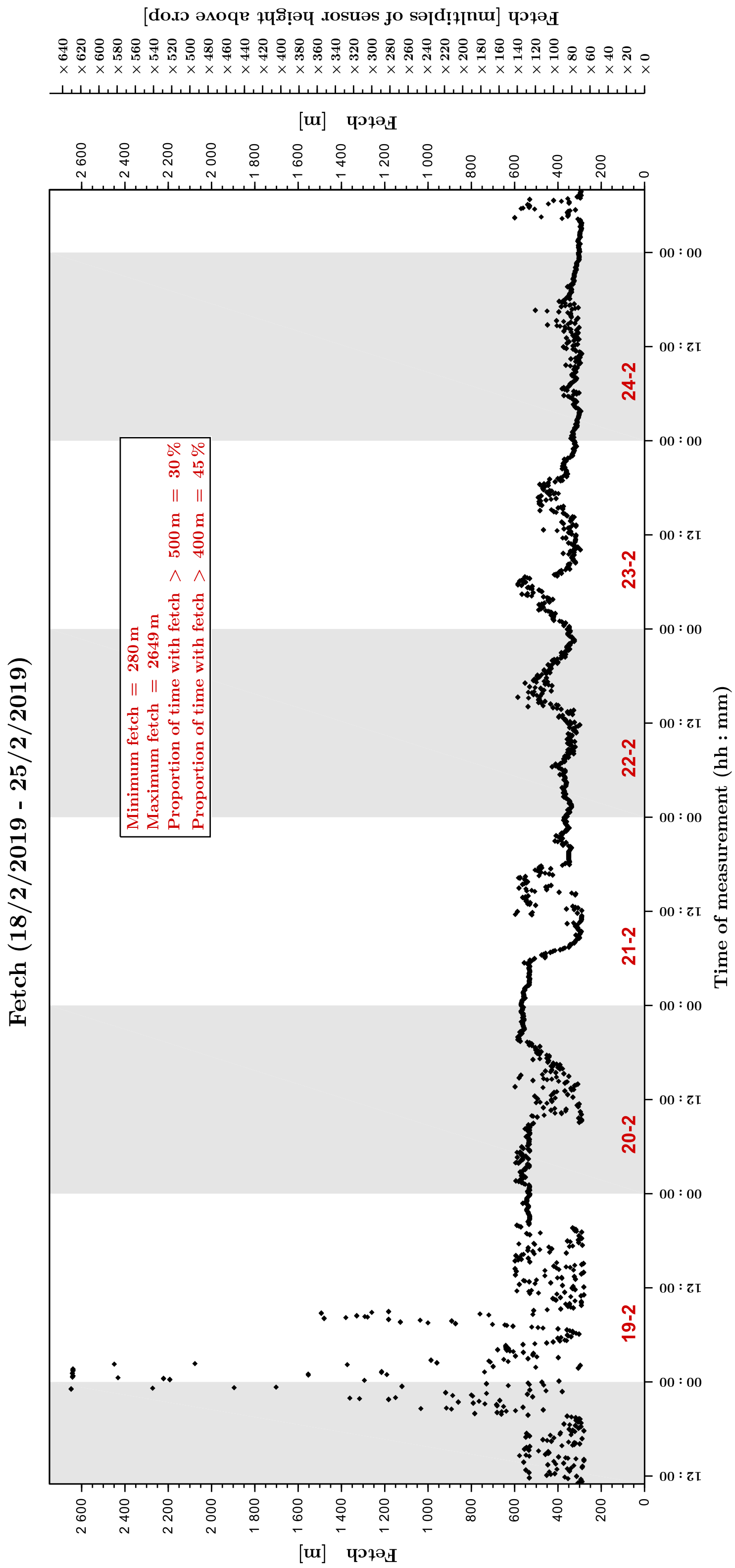

Figure O.5: DS1: fetch, f [m], where fetch was the upwind distance to the edge of the crop (see Appendix E, p. 359).

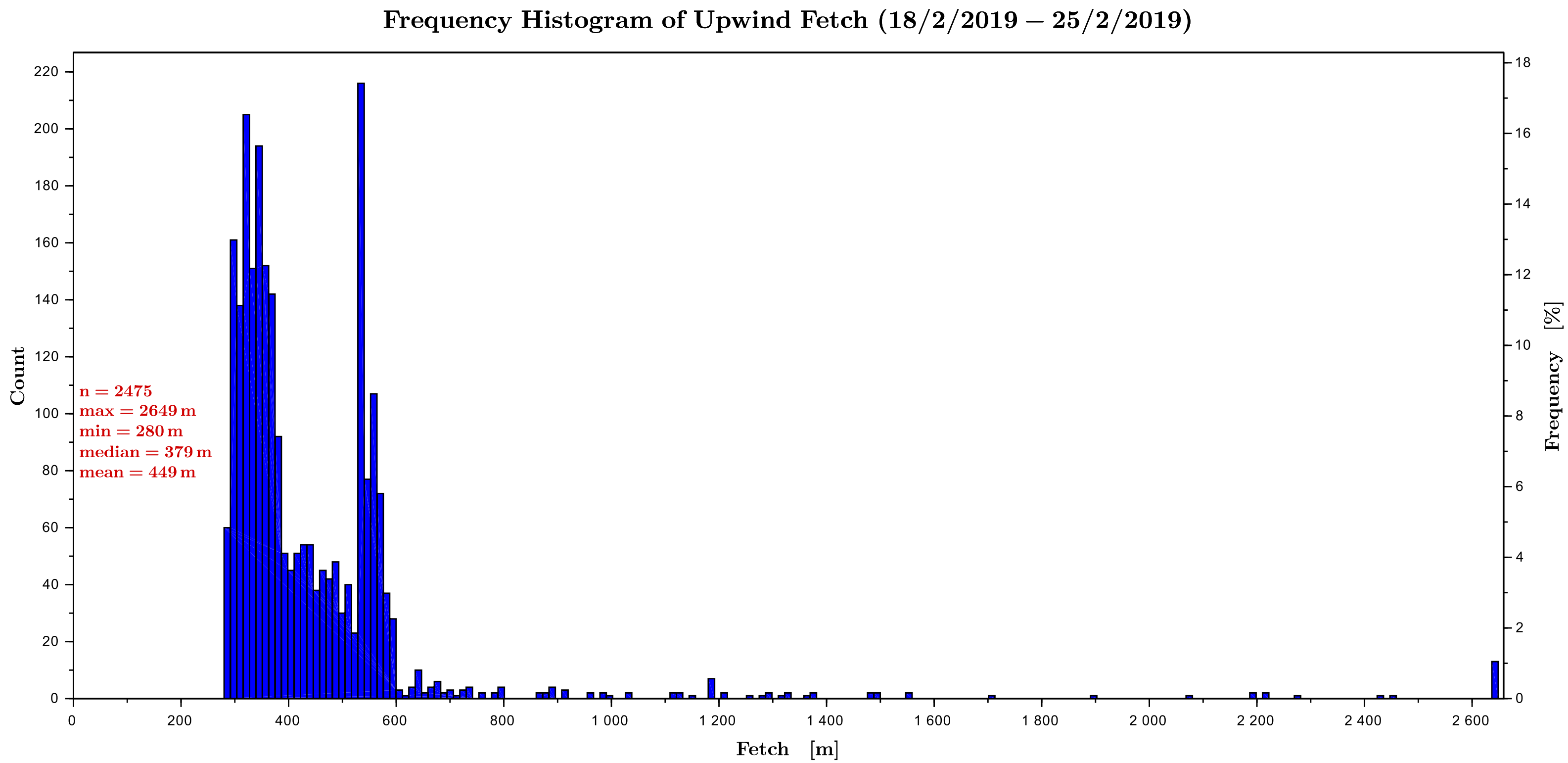

Figure O.6: DS1: distribution of fetch distances [m], where fetch was the upwind distance to the edge of the crop (see Appendix E, p. 359).

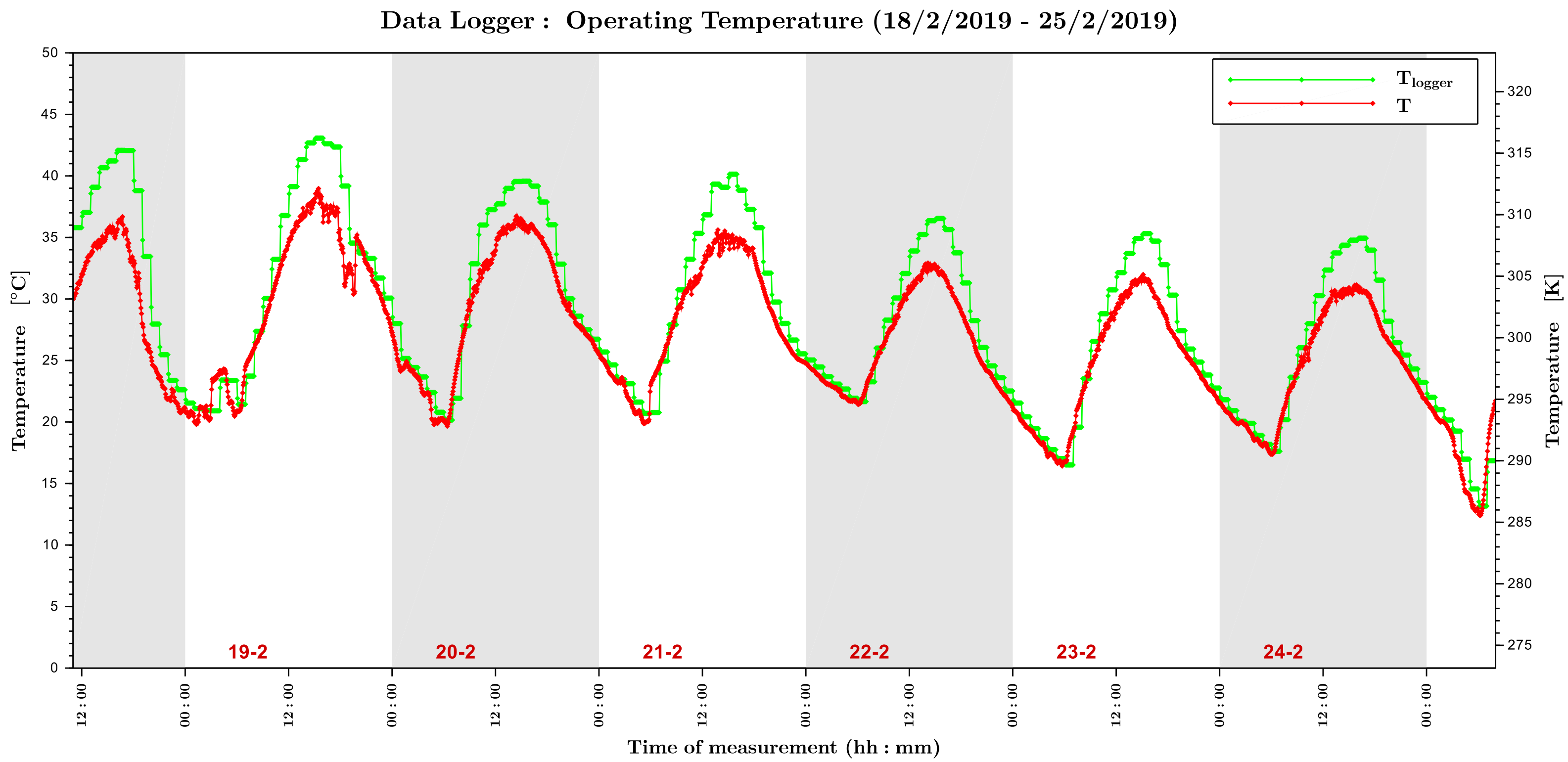

Figure O.7: DS1: temperature [°C] inside the logger's enclosure, measured hourly. The enclosure was actively vented to the surroundings by a fan.

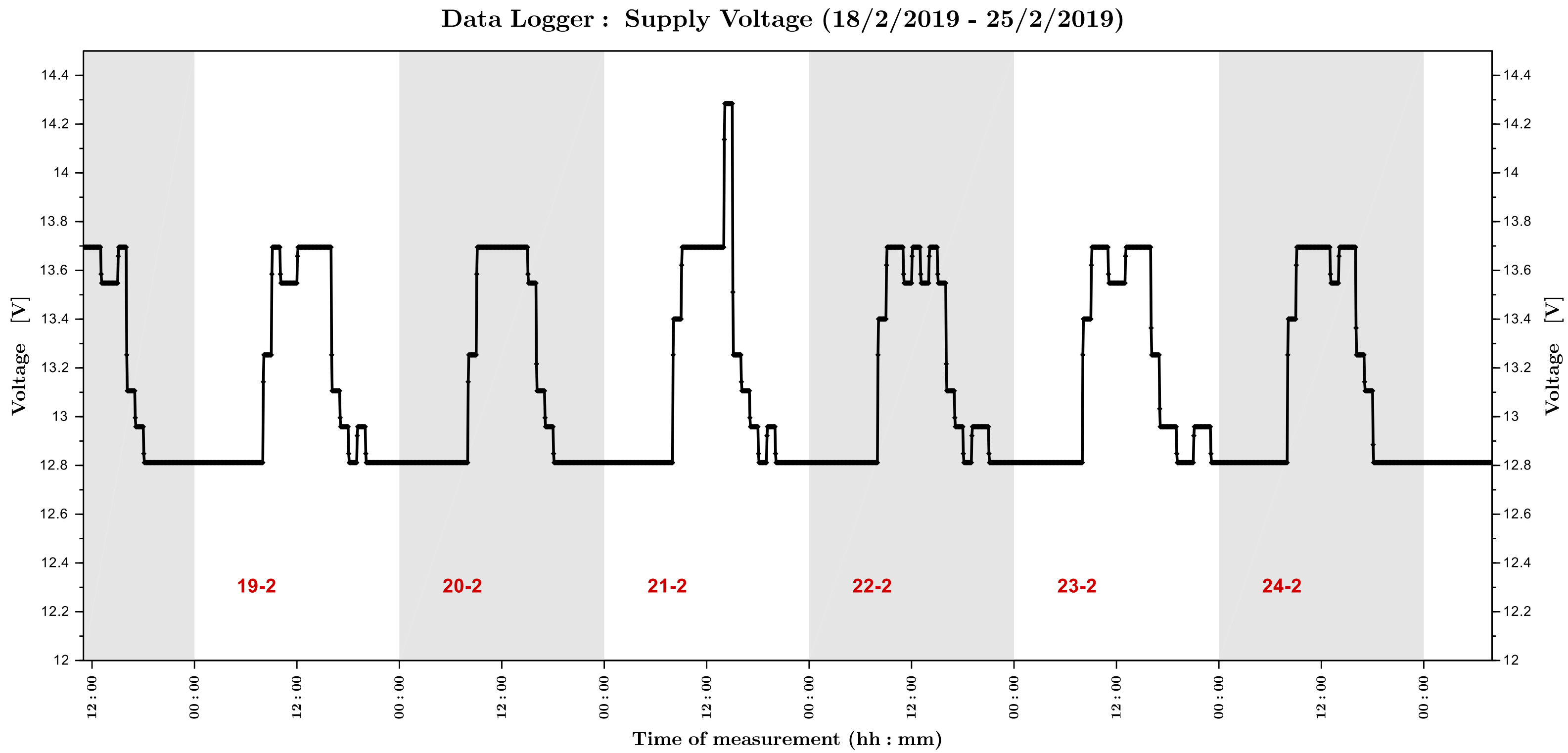

Figure O.8: DS1: logger's supply voltage [V] from a regulated 20 W solar panel and 12 V battery.

This page intentionally left blank.

Appendix P

ADDITIONAL WEATHER DATA FOR DS2

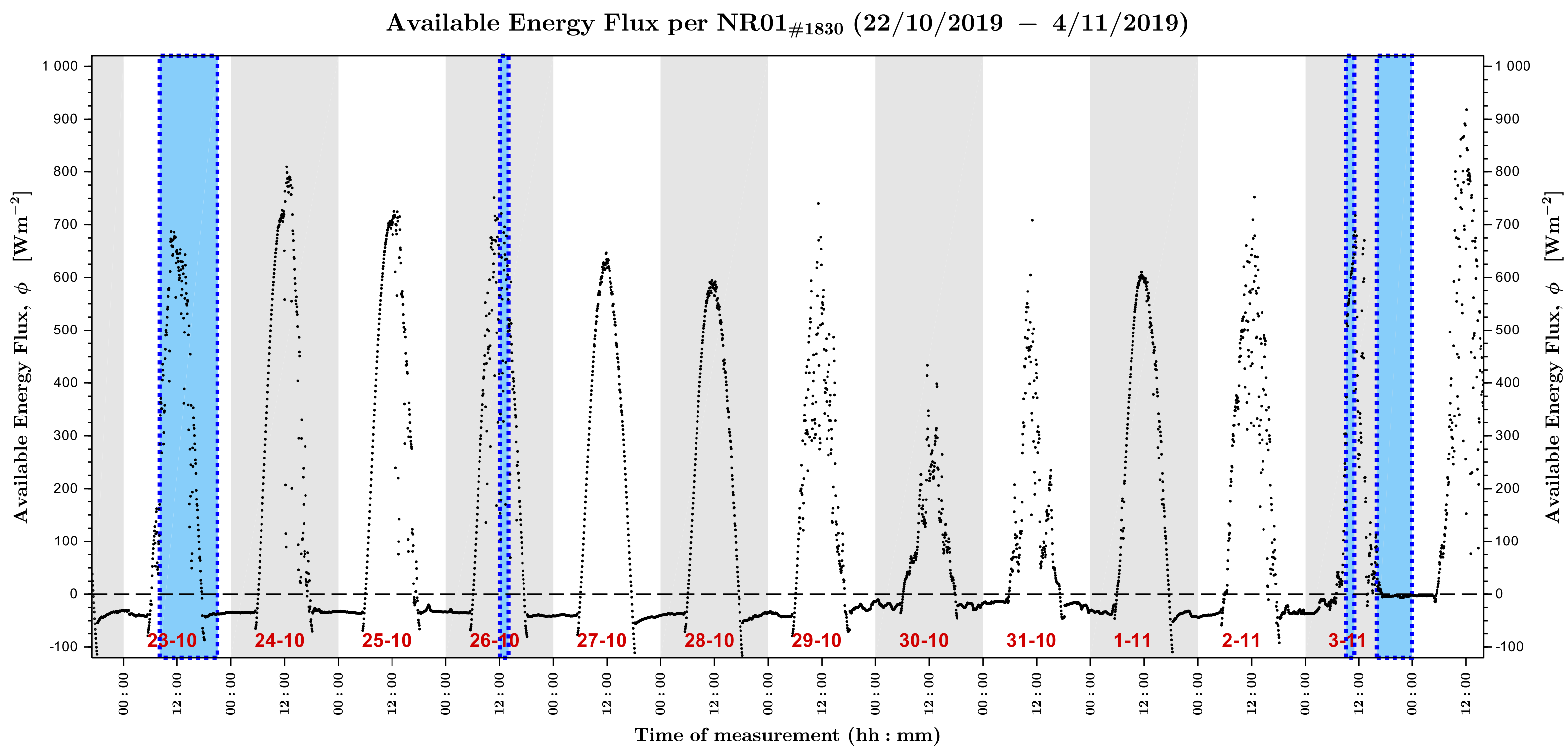

Figure P.1: DS2: available energy flux, ϕ [Wm^{-2}]. The available energy flux was calculated by $\phi = R_N + G$ (where flux directions are as defined in § 0.3, p. xxxiii). The shaded blue rectangles indicate when irrigation (23[rd] October) or rainfall occurred.

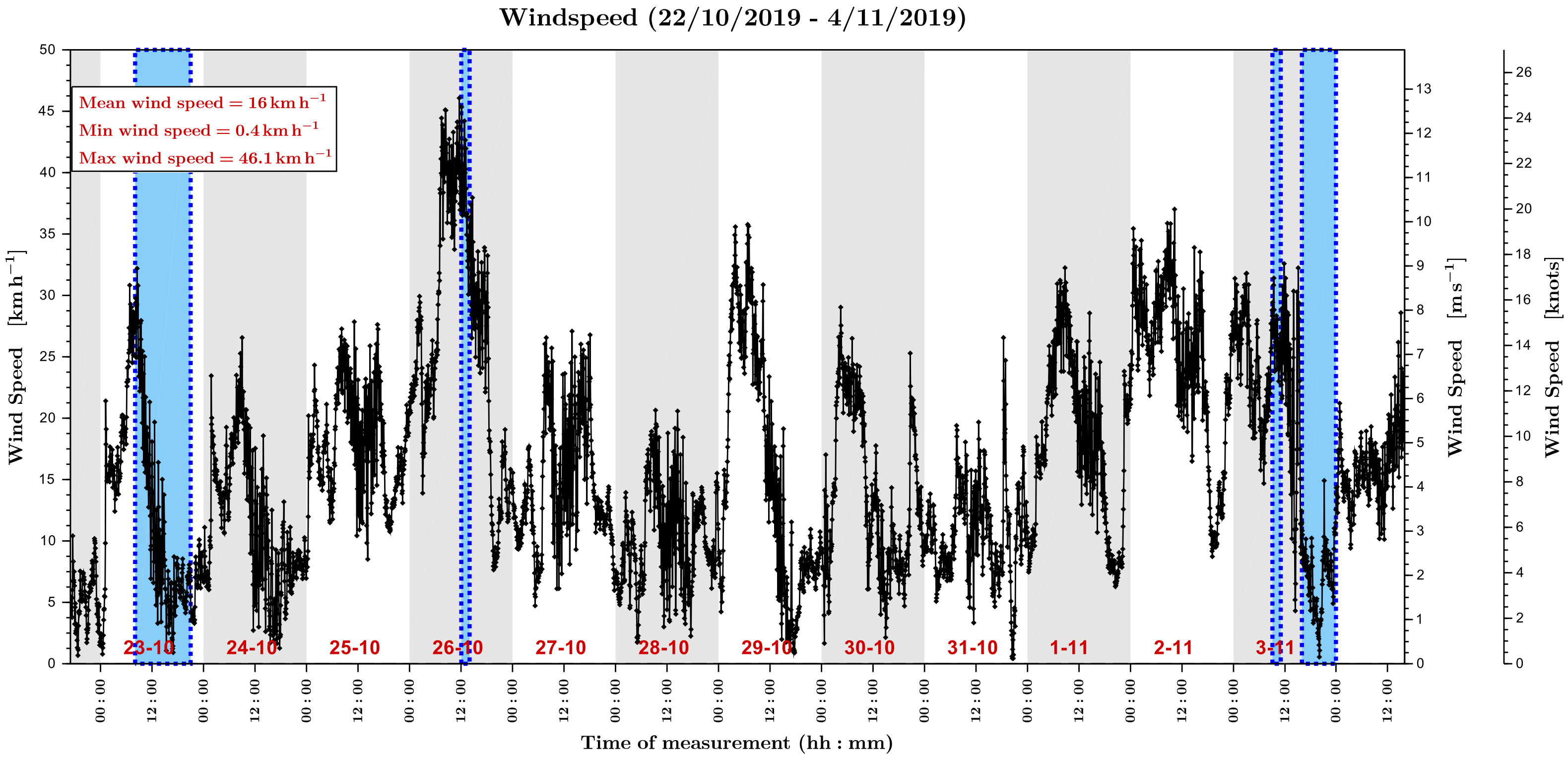

Figure P.2: DS2: wind speed, W_{sp} [km h^{-1}], as measured by a 2-dimensional sonic anemometer in Field 16 at 5.5 m above the ground. The shaded blue rectangles indicate when irrigation (23rd October) or rainfall occurred.

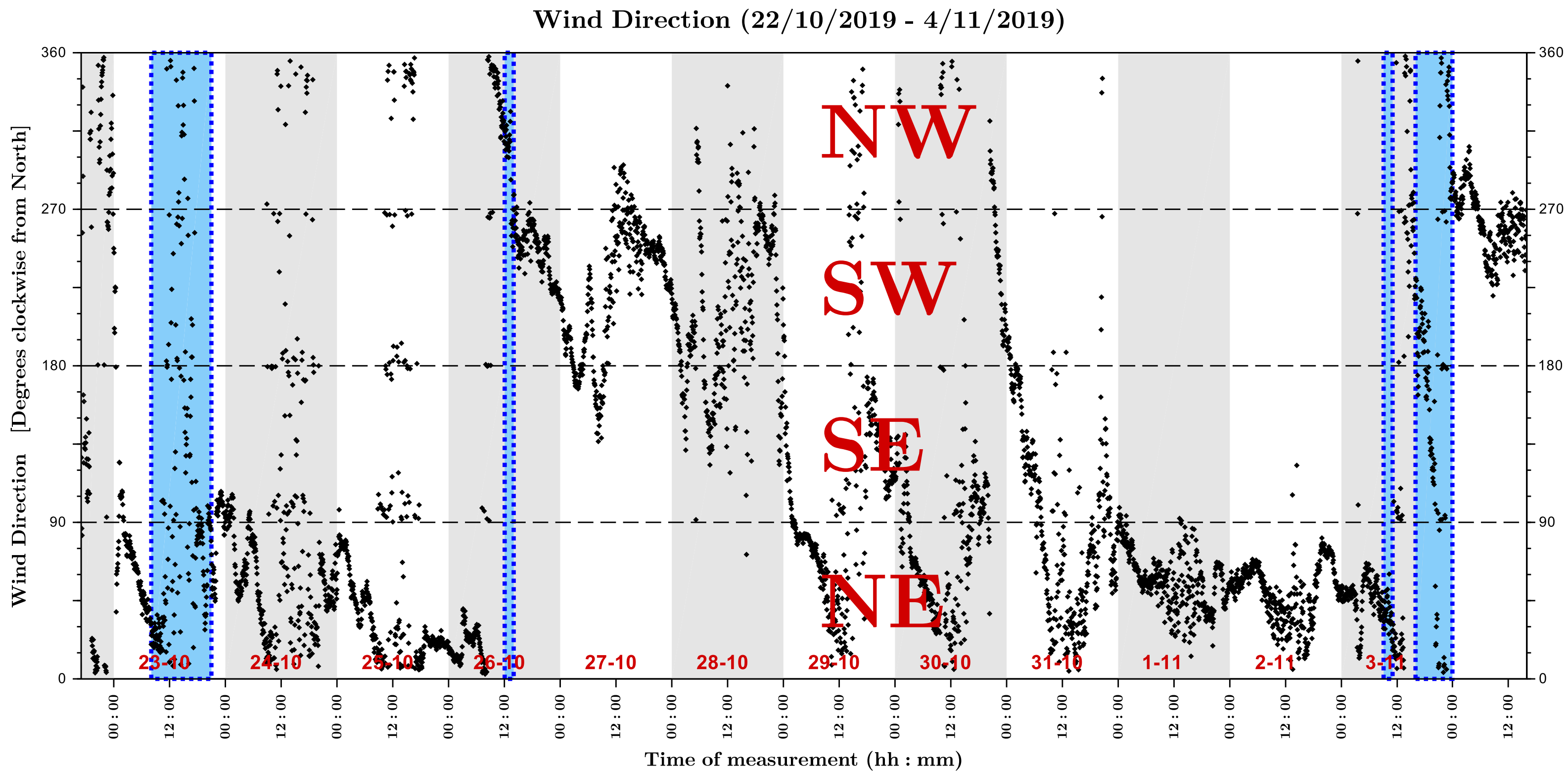

Figure P.3: DS2: wind direction, W_{dir} [°] relative to grid North, as measured by a 2-dimensional sonic anemometer in Field 16 at 5.5 m above the ground. The shaded blue rectangles indicate when irrigation (23rd October) or rainfall occurred.

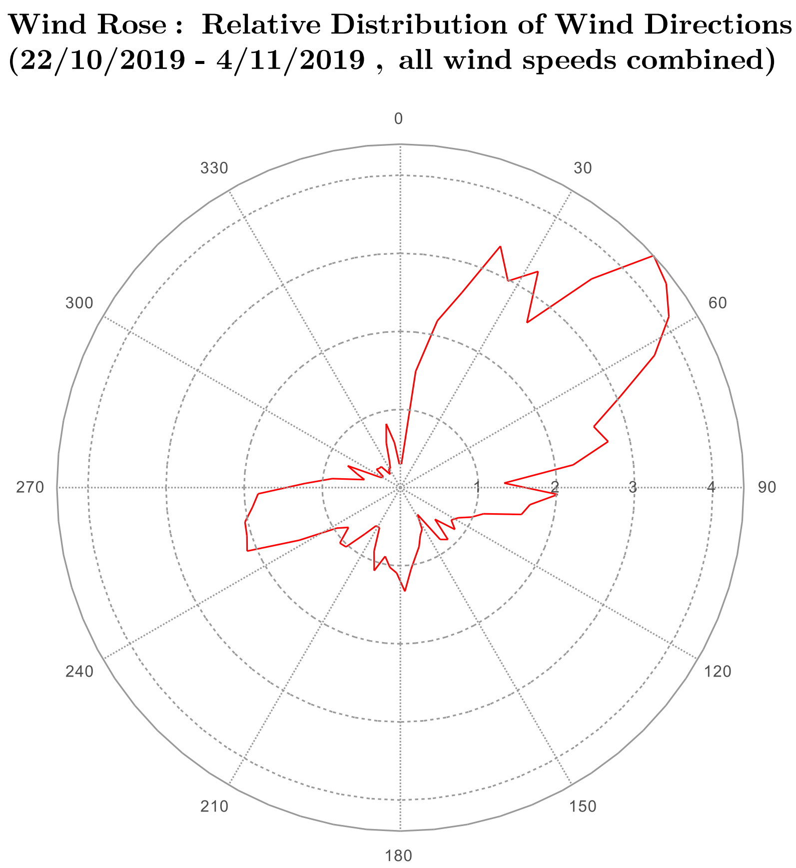

Figure P.4: DS2: windrose showing the relative proportion of time with a given wind direction, as measured by a 2-dimensional sonic anemometer in Field 16 at 5.5 m above the ground.

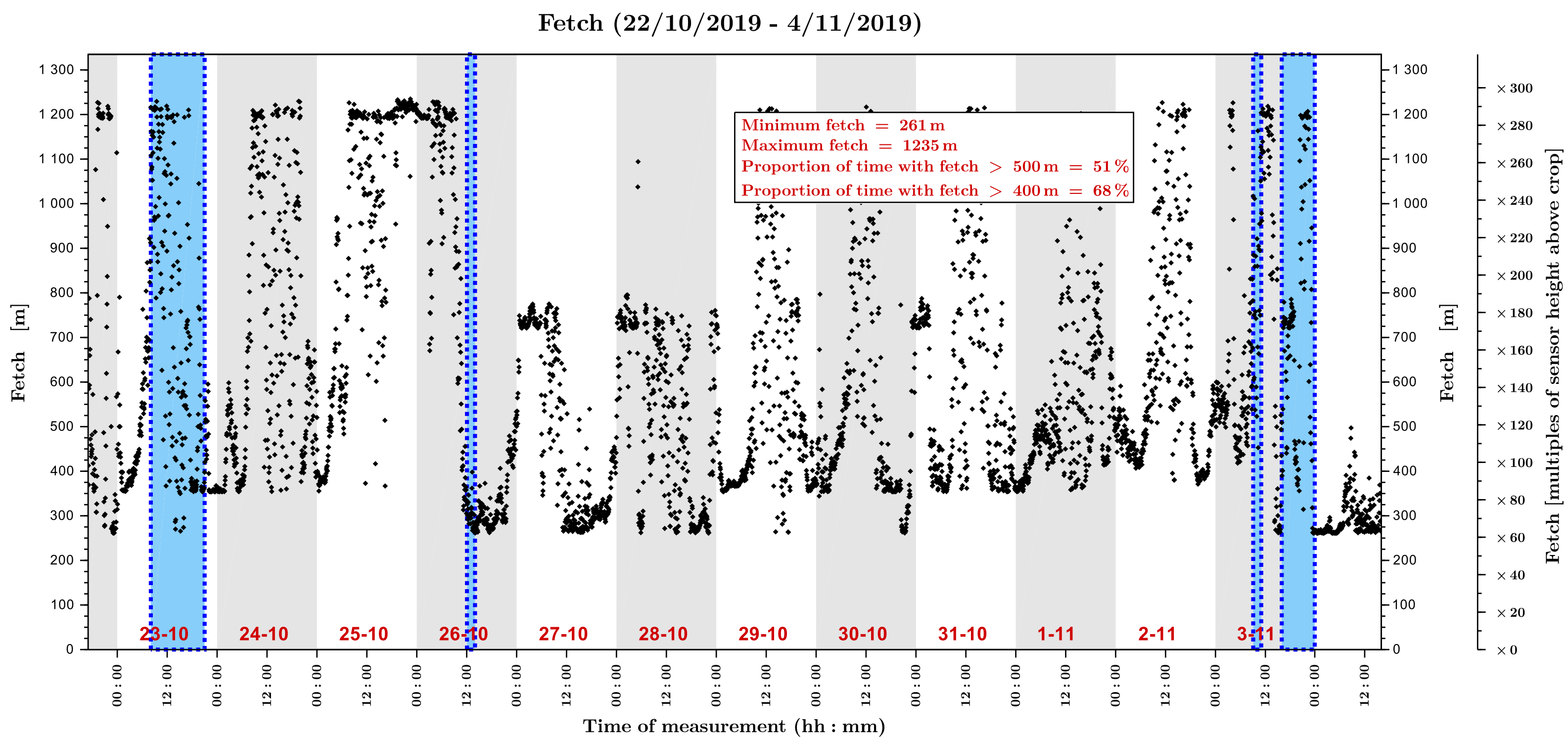

Figure P.5: DS2: fetch, f [m], where fetch was the upwind distance to the edge of the crop (see Appendix E, p. 359). The shaded blue rectangles indicate when irrigation (23[rd] October) or rainfall occurred.

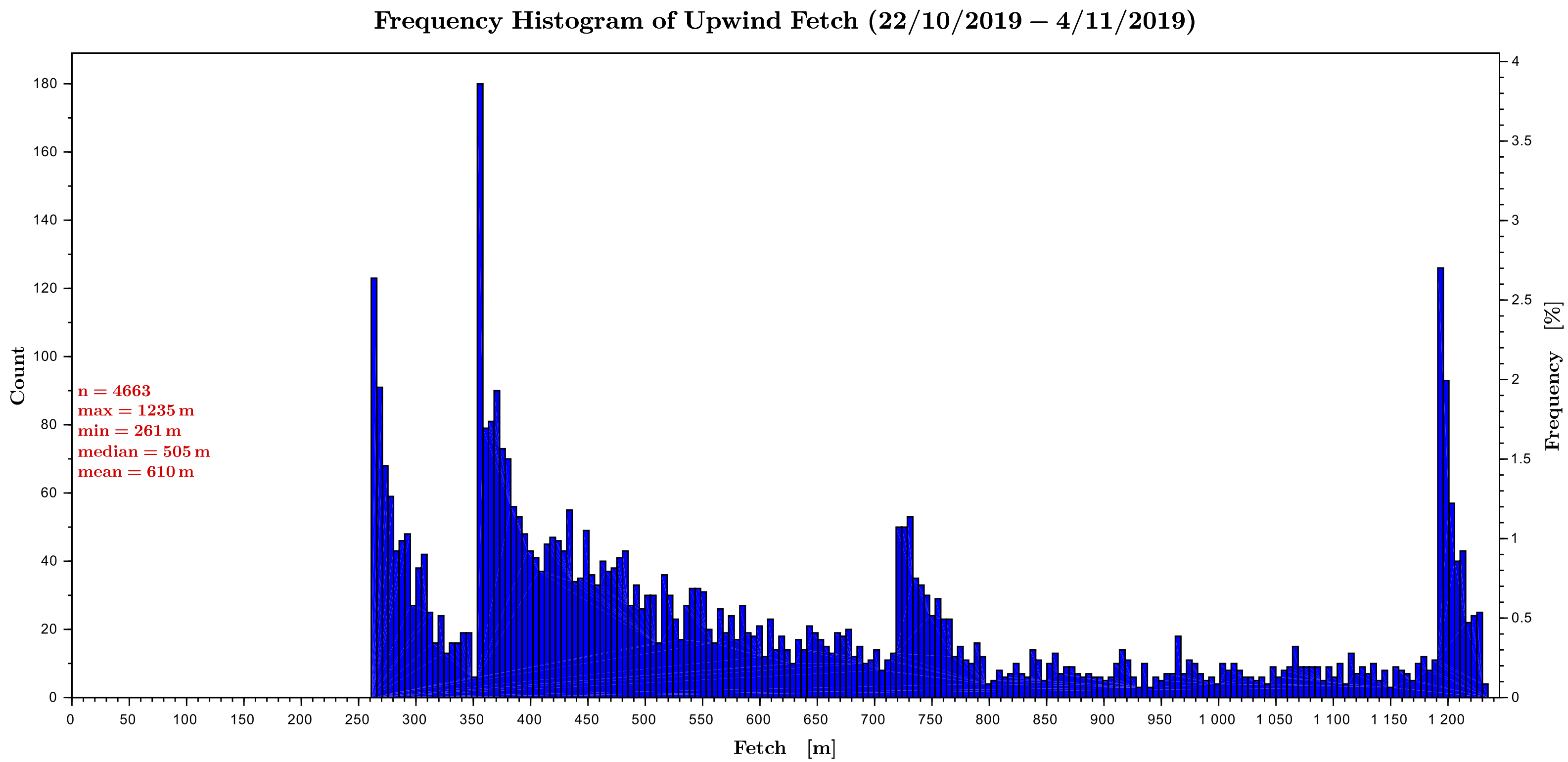

Figure P.6: DS2: distribution of fetch distances [m], where fetch was the upwind distance to the edge of the crop (see Appendix E, p. 359).

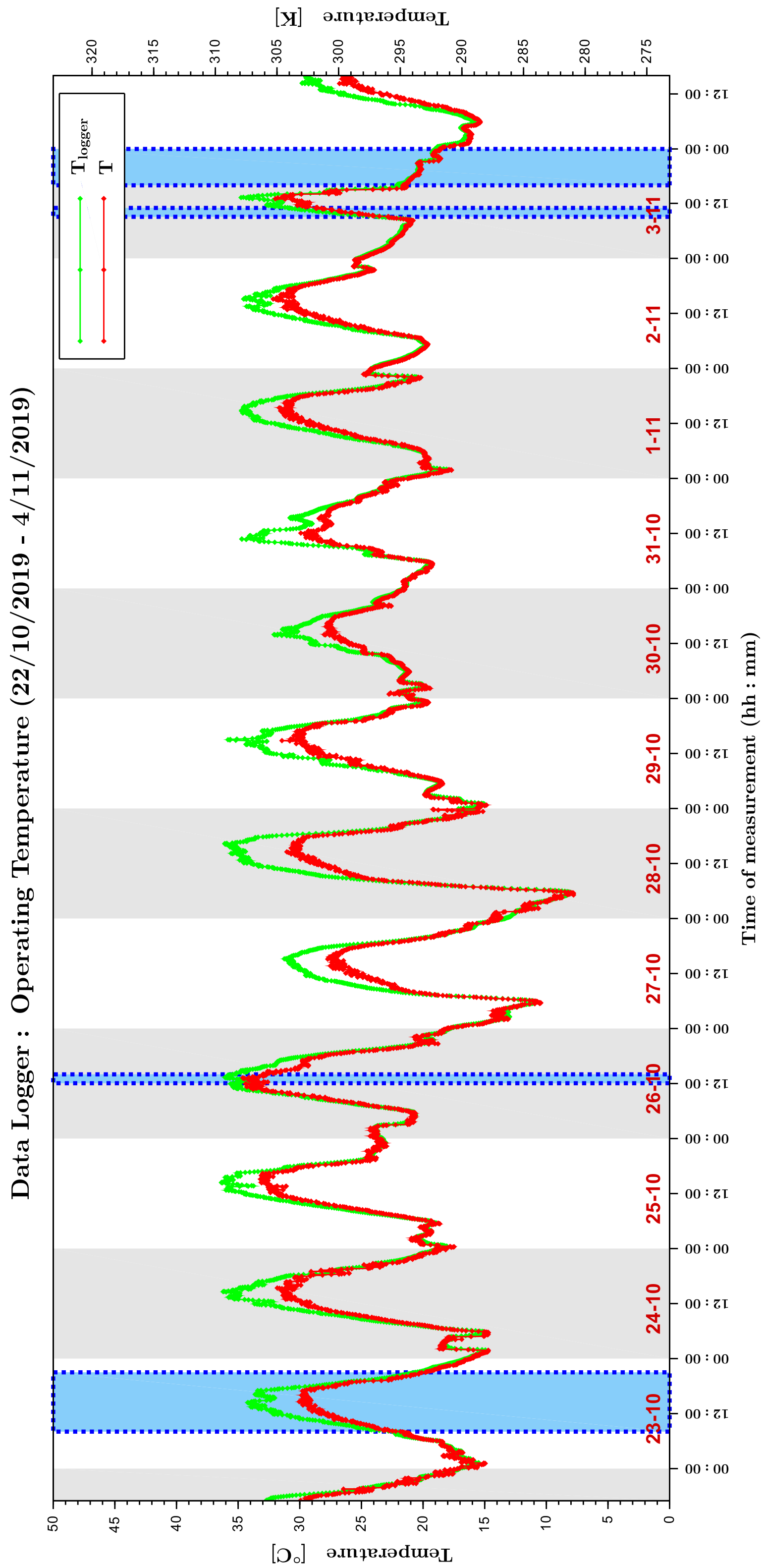

Figure P.7: DS2: temperature [°C] inside the logger's enclosure, measured every 60 s. The enclosure was actively vented to the surroundings by a fan. The shaded blue rectangles indicate when irrigation (23rd October) or rainfall occurred.

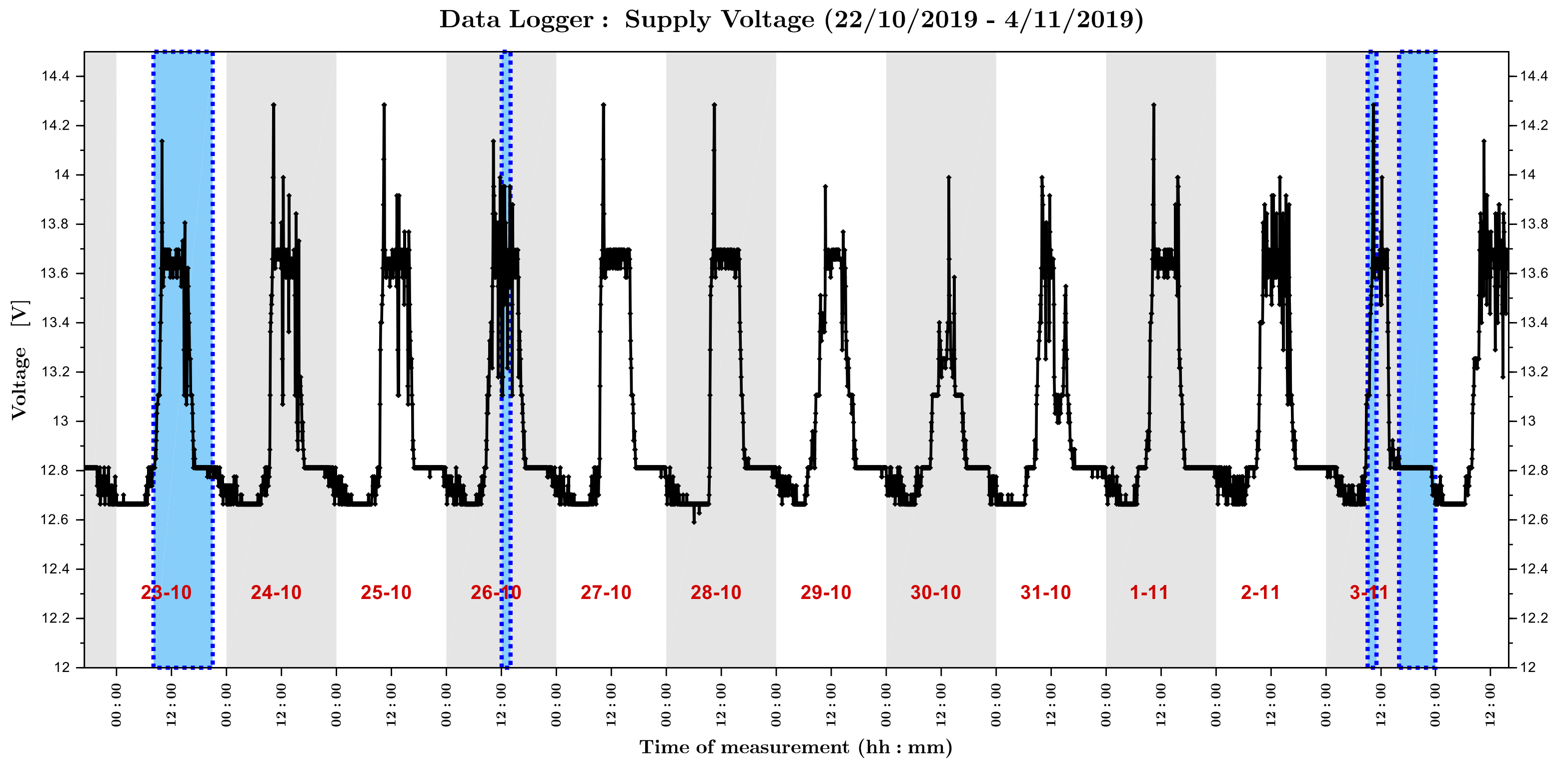

Figure P.8: DS2: logger's supply voltage [V] from a regulated 20 W solar panel and 12 V battery. The shaded blue rectangles indicate when irrigation (23$^{\text{rd}}$ October) or rainfall occurred.

This page intentionally left blank.

Appendix Q

ADDITIONAL WEATHER DATA FOR DS3

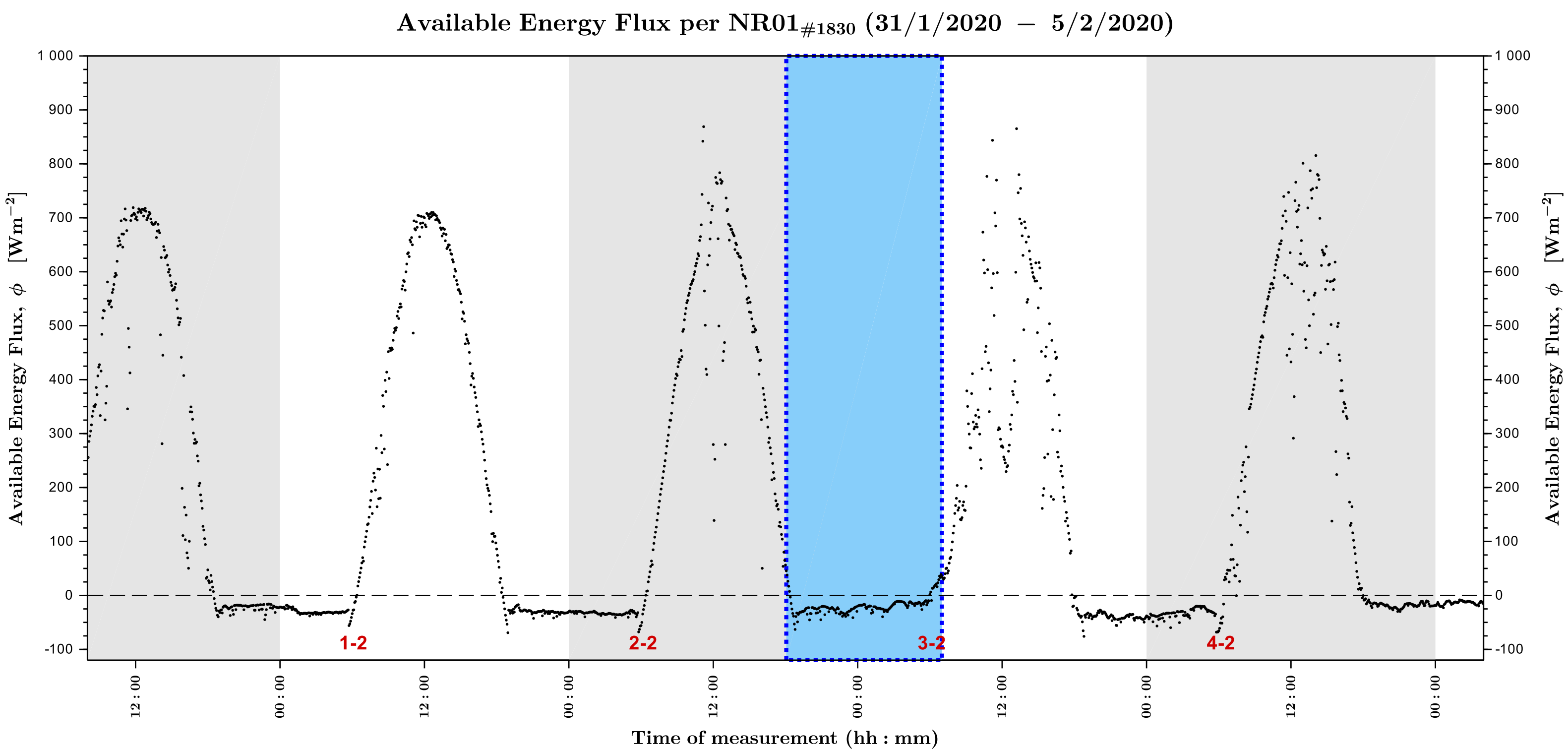

Figure Q.1: DS3: available energy flux, ϕ [Wm^{-2}]. The available energy flux was calculated by $\phi = R_N + G$ (where flux directions are as defined in § 0.3, p. xxxiii). The shaded blue rectangle indicates when the irrigation on the 2nd February occurred.

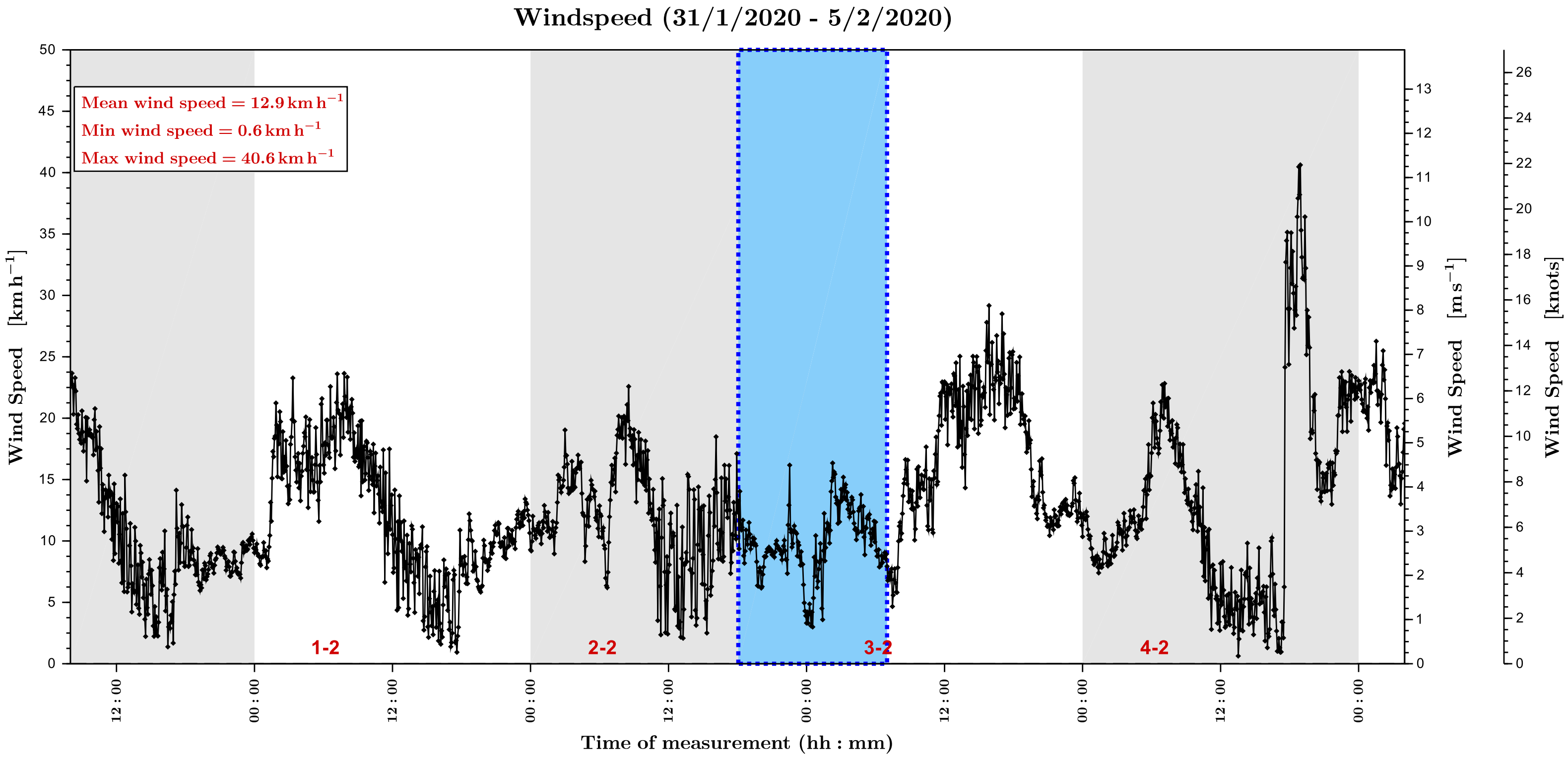

Figure Q.2: DS3: wind speed, W_{sp} [km h^{-1}], as measured by a 2-dimensional sonic anemometer in Field 16 at 5.5 m above the ground. The shaded blue rectangle indicates when the irrigation on the 2$^{\text{nd}}$ February occurred.

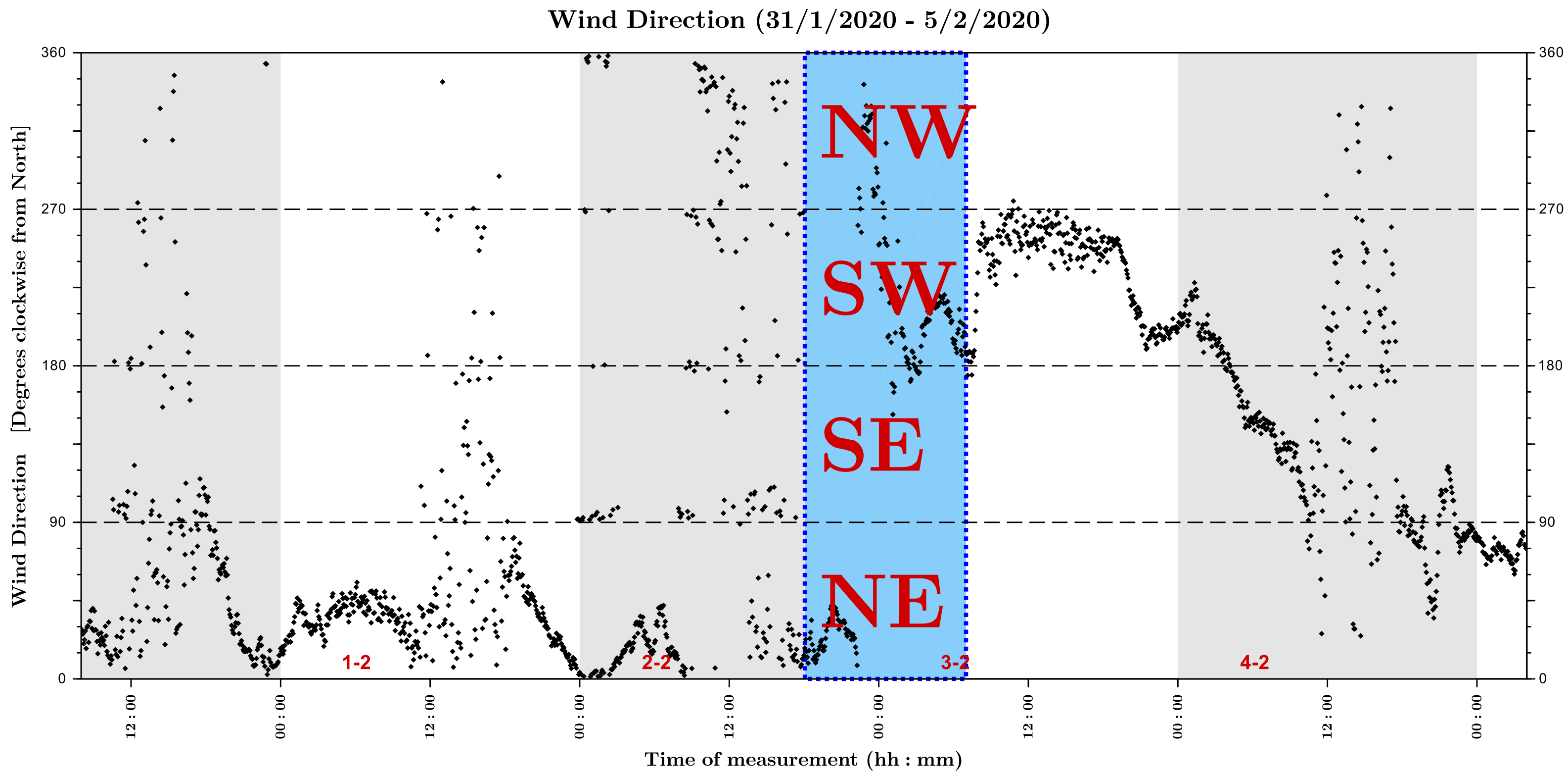

Figure Q.3: DS3: wind direction, W_{dir} [°] relative to grid North, as measured by a 2-dimensional sonic anemometer in Field 16 at 5.5 m above the ground. The shaded blue rectangle indicates when the irrigation on the 2nd February occurred.

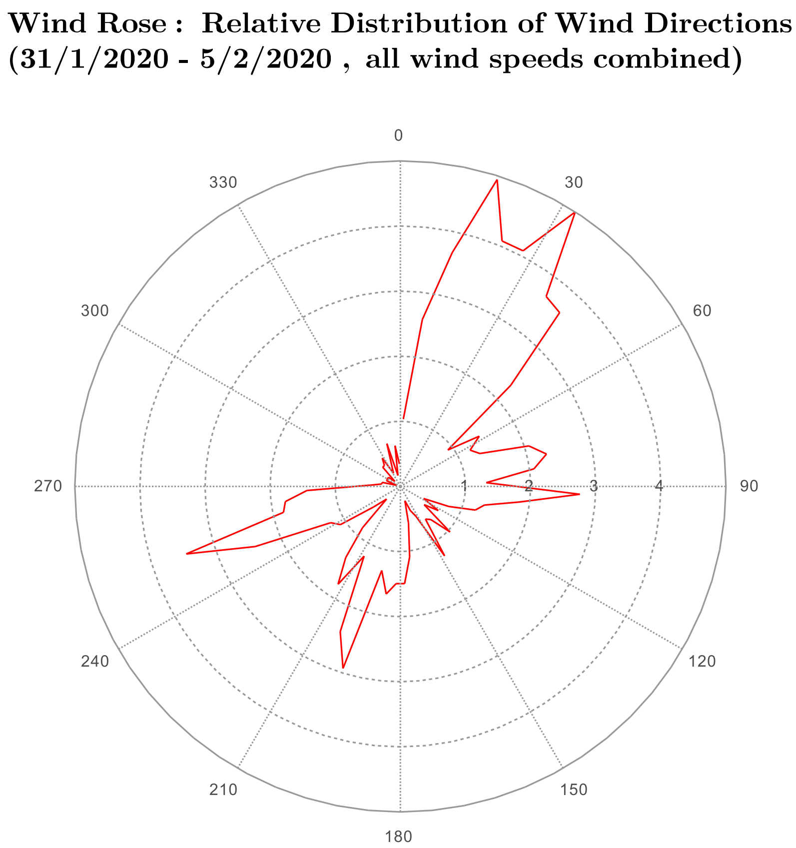

Figure Q.4: DS3: windrose showing the relative proportion of time with a given wind direction, as measured by a 2-dimensional sonic anemometer in Field 16 at 5.5 m above the ground.

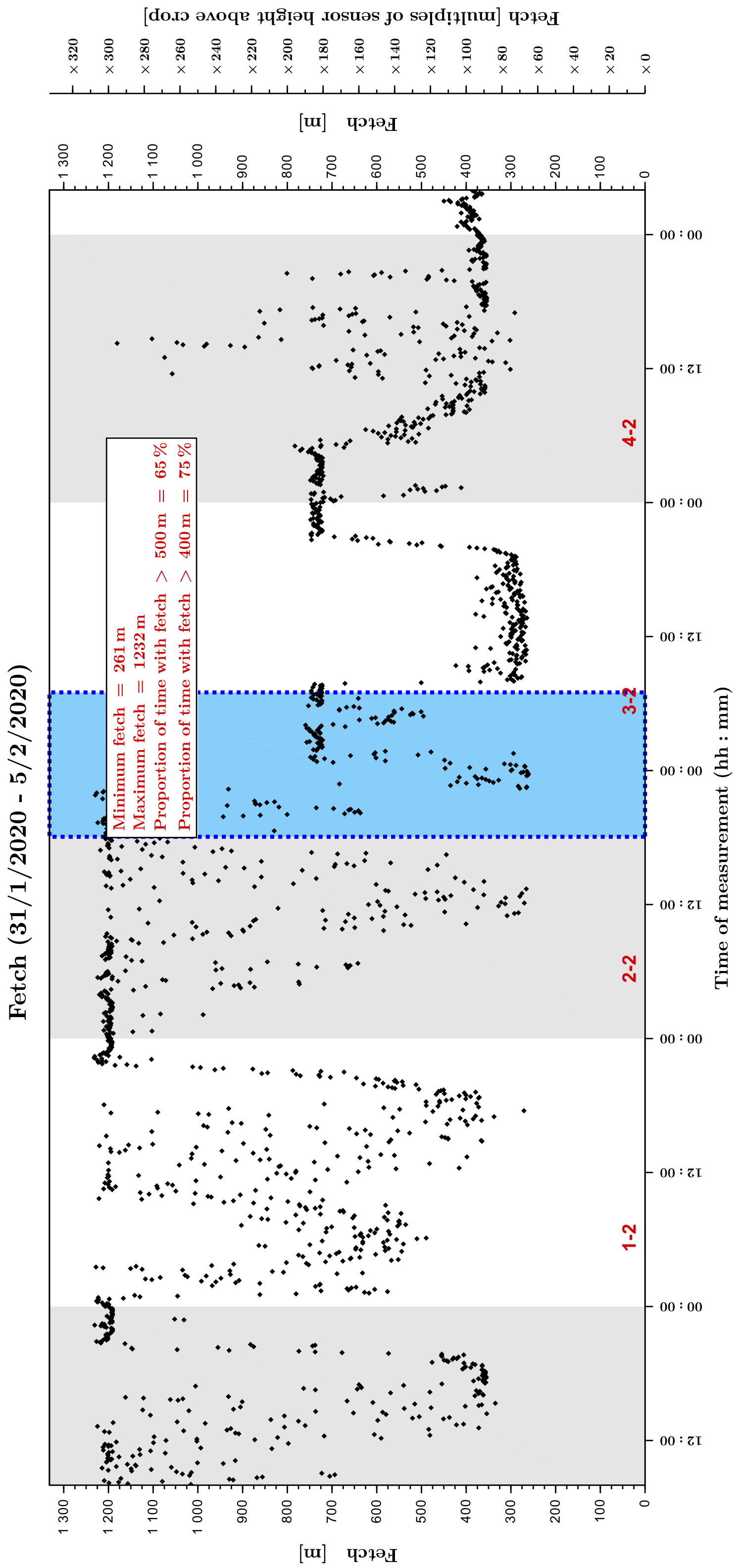

Figure Q.5: DS3: fetch, f [m], where fetch was the upwind distance to the edge of the crop (see Appendix E, p. 359). The shaded blue rectangle indicates when the irrigation on the 2nd February occurred.

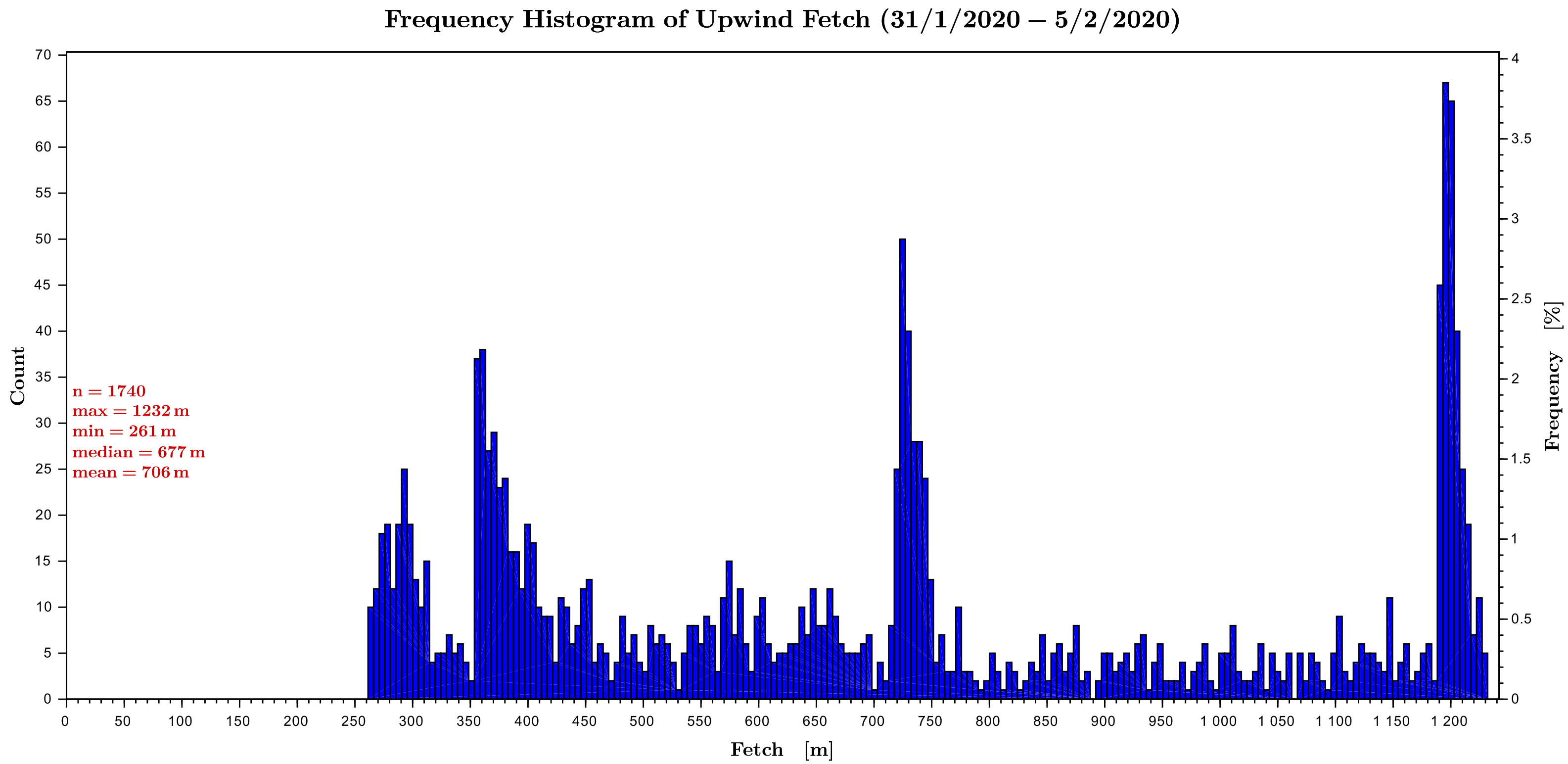

Figure Q.6: DS3: distribution of fetch distances [m], where fetch was the upwind distance to the edge of the crop (see Appendix E, p. 359).

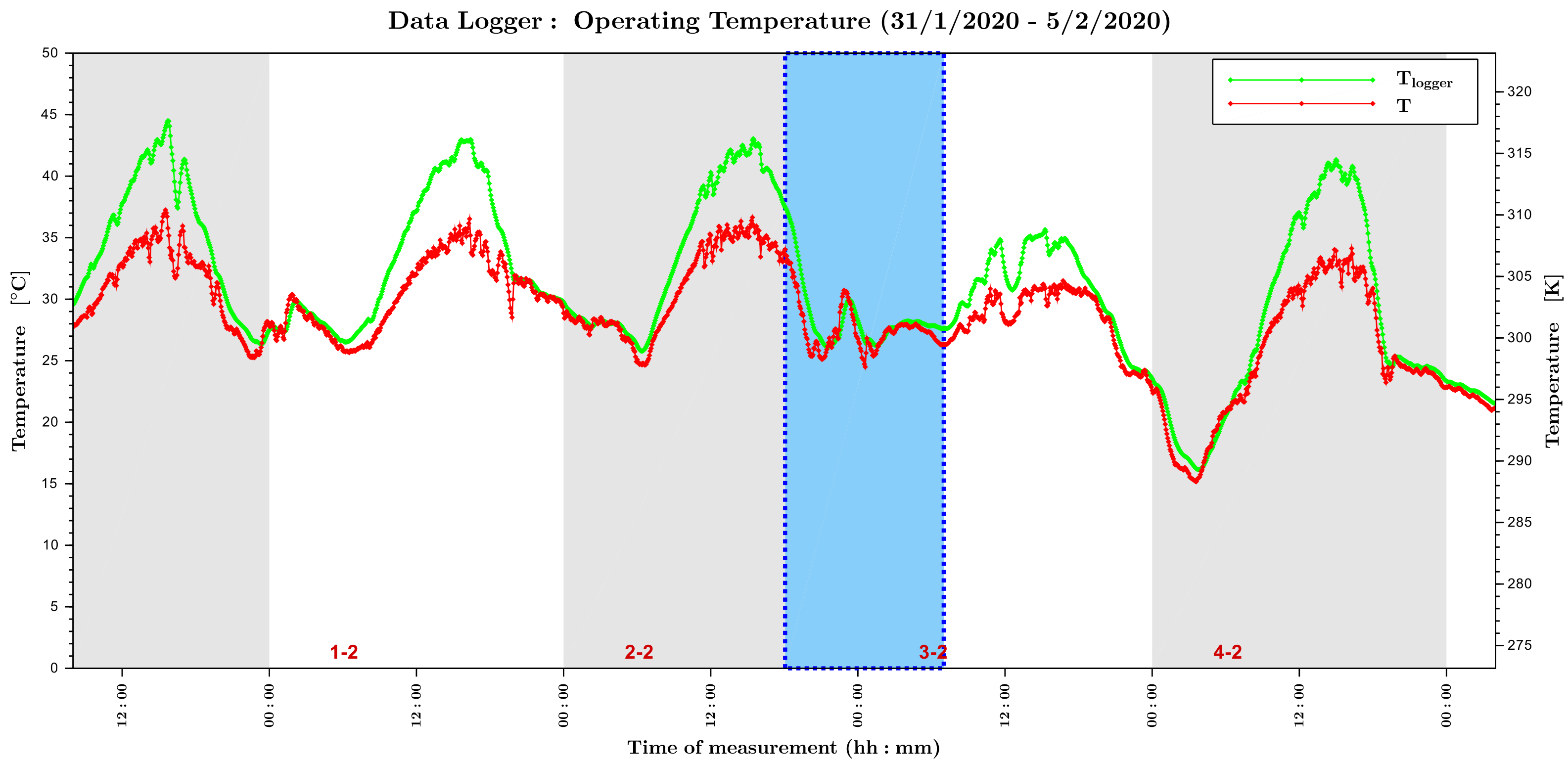

Figure Q.7: DS3: temperature [°C] inside the logger's enclosure, measured every 60 s. The enclosure was actively vented to the surroundings by a fan. The shaded blue rectangle indicates when the irrigation on the 2nd February occurred.

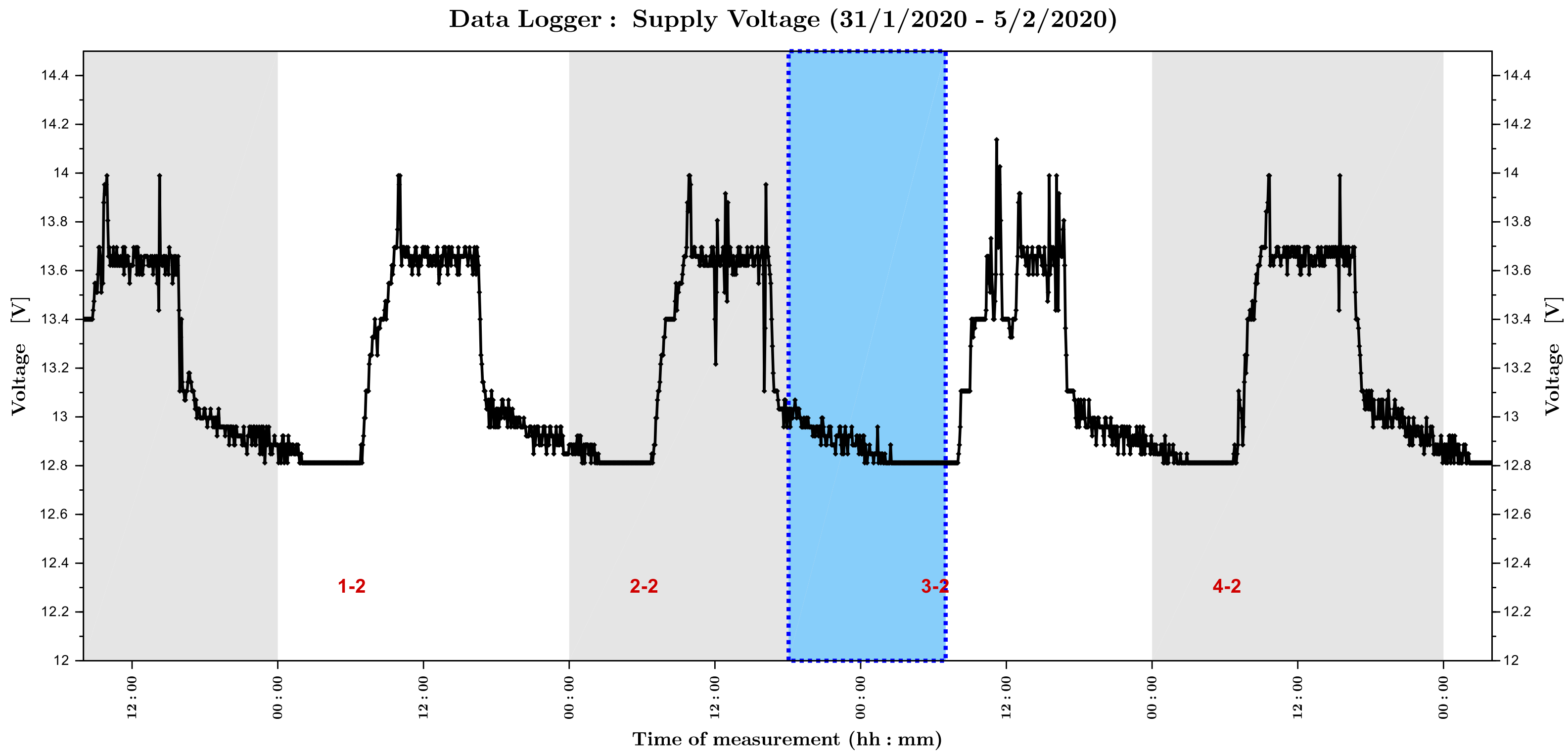

Figure Q.8: DS3: logger's supply voltage [V] from a regulated 20 W solar panel and 12 V battery. The shaded blue rectangle indicates when the irrigation on the 2nd February occurred.